U.PORTO

FEUP FACULDADE DE ENGENHARIA
UNIVERSIDADE DO PORTO

Master's Dissertation

Predicting the Failure of Structures with Second-Order Homogenisation and Nonlocal Damage Models

Guilherme Fonseca Gonçalves

Supervisor:
Dr. Igor André Rodrigues Lopes

Co-Supervisor:
Dr. Francisco Manuel Andrade Pires

Submitted in fulfillment of the requirements for
the degree of Master in Mechanical Engineering by
the Faculty of Engineering of the University of Porto

Porto, July 2024

CM2S

Computational Multi-Scale
Modeling of Solids and Structures

Aos meus avós, Manuel e Maria Delfina

Tomemos nas nossas mãos os destinos das nossas vidas.

Álvaro Cunhal

Predicting the Failure of Structures with Second-Order Homogenisation and Nonlocal Damage Models

Guilherme Fonseca Gonçalves

Abstract

The accurate prediction of structural failure under extreme loading scenarios is critical for industries such as aerospace and aeronautics. In this context, high-fidelity multi-scale approaches, allowing the prediction of macroscopic damage and fracture through the progressive failure of microstructural details, such as voids or cracks, face various numerical challenges. In this dissertation, strategies to tackle the issue of pathological mesh dependency at different spatial scales are assessed and compared. These mesh-regularisation approaches include nonlocal damage models and second-order computational homogenisation. In addition, a phase-field model towards the multi-scale modelling of fracture is implemented.

Integral type and gradient-enhanced nonlocal damage models are adopted for single-scale mesh regularisation. A staggered solution scheme is explored for the efficient and robust implementation of the gradient nonlocal model. A nonlocal model of integral type is implemented for both macro- and micro-scale problems, including coupled multi-scale setups. The predictions and performance of the two nonlocal approaches are assessed, establishing a detailed comparison rooted in their numerical aspects and formulations.

Multi-scale models based on first- and second-order computational homogenisation are used to model ductile failure, with RVEs containing voids and damage. The adoption of second-order approaches results in macro-regularisation, the extent of which is also related to micro-mesh dependency. The impact of the RVE length on these mesh-regularing effects is addressed, and the regularisation of the micro-problem is pursued with nonlocal damage of integral type. The simultaneous regularisation of the macroscopic and RVE balance problems results in a remarkable reduction of multi-scale pathological mesh dependency. Furthermore, an optimisation-based framework for relating single- and multi-scale macro-regularisation strategies is proposed. Second-order FE^2 predictions are used to calibrate the response of a macroscopic nonlocal model of integral type. A connection between the numerical regularisation parameters of both approaches is established, while also discussing the relevant limitations of this parallel.

Lastly, the staggered strategy for the solution of coupled problems is utilised to implement a phase-field fracture model, which is validated with reference results from the literature. Coupling scheme, mesh sensitivity and parametric analyses are carried out to assess the numerical and physical aspects of the phase-field approach. Thereafter, the model is employed to simulate the fracture of heterogeneous microstructures. Promising results are attained, with the prediction of transverse crack growth and coalescense for three different RVEs under tension. The potential of phase-field fracture models for the multi-scale modelling of structural failure is highlighted.

The various investigations conducted in this dissertation pave the road to the high-fidelity multi-scale modelling of damage and fracture for complex heterogeneous materials.

Keywords: Structural failure, Pathological mesh dependency, Gradient-enhanced and integral type nonlocal damage models, Multi-scale modelling, First- and second-order computational homogenisation, Phase-field fracture models, Finite element method, Finite strains, Heterogeneous materials

Previsão de Falhas Estruturais utilizando Homogenização de Segunda Ordem e Modelos de Dano Não-Local

Guilherme Fonseca Gonçalves

Resumo

A previsão precisa de falhas estruturais em cenários de carregamento extremos é fundamental para indústrias como a aeroespacial e a aeronáutica. Neste contexto, abordagens multi-escala de alta fidelidade, que permitem a previsão de dano e fratura macroscópicos através da falha progressiva de detalhes microestruturais, tais como vazios ou fissuras, enfrentam vários desafios numéricos. Nesta dissertação, são avaliadas e comparadas estratégias para resolver o problema da dependência patológica da malha a diferentes escalas espaciais. Estas abordagens de regularização incluem modelos de dano não-local e homogeneização computacional de segunda ordem. Além disso, é implementado um modelo de campo de fase no sentido da modelação multi-escala de fratura.

Modelos de dano não-local de tipo integral e gradiente são adotados para a regularização de problemas de escala única. Um esquema de solução escalonado é explorado para a implementação eficiente e robusta do modelo não-local gradiente. Um modelo não-local de tipo integral é implementado para problemas à macro- e micro-escalas, incluindo esquemas multi-escala acoplados. As previsões e o desempenho das duas abordagens não-locais são avaliados, estabelecendo-se uma comparação meticulosa com base nas suas formulações e aspetos numéricos.

Modelos multi-escala baseados em homogeneização computacional de primeira e segunda ordem são utilizados para modelar a falha de materiais dúcteis, com RVEs contendo vazios e dano. A adoção de abordagens de segunda ordem resulta na regularização da malha à macro-escala, cuja eficácia está também relacionada com a dependência da malha do RVE. O impacto do comprimento do RVE nestes efeitos de regularização da malha é abordado, e a regularização do problema da micro-escala é prosseguida com dano não local do tipo integral. A regularização simultânea dos problemas de equilíbrio macro- e microscópicos resulta numa redução notável da dependência patológica da malha às várias escalas. Além disso, é proposta uma abordagem baseada em otimização para relacionar estratégias de regularização da malha macro, em problemas a uma e a várias escalas. As previsões FE^2 de segunda ordem são utilizadas para calibrar a resposta de um modelo macroscópico não local de tipo integral. Estabelece-se uma ligação entre os parâmetros numéricos de regularização de ambas as estratégias, discutindo-se também as limitações relevantes deste paralelo.

Por último, o esquema de solução escalonado para problemas acoplados é utilizado para implementar um modelo de fratura de campo de fase, que é validado com resultados de referência da literatura. Estudos relativos ao esquema de acoplamento e à sensibilidade da malha e análises paramétricas são efetuados para avaliar os aspetos numéricos e físicos da abordagem de campo de fase. Em seguida, o modelo é utilizado para simular a fratura de microestruturas heterogéneas. São obtidos resultados promissores para três RVEs diferentes sob tensão, com a previsão do crescimento e coalescência de fendas transversais. O potencial dos modelos de fratura de campo de fases para a modelação multi-escala de falhas estruturais é realçado.

As várias investigações conduzidas nesta dissertação abrem caminho para a modelação multi-escala de alta fidelidade de dano e fratura em materiais heterogéneos complexos.

Palavras-chave: Falhas estruturais, Dependência patológica da malha, Modelos de dano não-local do tipo integral e gradiente, Modelação multi-escala, Homogeneização computacional de primeira e segunda ordem, Modelos de campo de fase para fratura, Método dos elementos finitos, Deformações finitas, Materiais heterogéneos

Agradecimentos

A realização deste trabalho e o percurso académico que lhe é subjacente não teriam sido possíveis sem o valioso contributo de terceiros, nas mais variadas frentes, aos quais não posso deixar de expressar formalmente a minha gratidão. Não sendo particularmente capaz na arte do agradecimento, espero que as linhas que se seguem façam justiça a todos esses contributos. Na falta de melhores palavras, aqui vai.

Adereço o meu primeiro agradecimento ao Dr. Igor Lopes, figura central do meu percurso na Faculdade de Engenharia. Tudo é simples, até o mais complexo e inesperado problema, quando se trabalha com alguém tão prestável e compreensivo, que alia a um elevado conhecimento técnico e científico uma humildade sem par. Não esquecerei todas as vezes em que, mesmo sem espaço no horário, encontrou tempo para apoiar o meu trabalho. Por isso, e por muito mais, obrigado. Deixo, também, um sentido agradecimento ao Dr. Francisco Pires, que teve um contributo chave no desenvolvimento deste trabalho, pela sua larga experiência, conhecimento, pragmatismo e honestidade. Aos meus dois orientadores, agradeço a oportunidade de trabalhar numa área que sempre me interessou, assim como todas as condições materiais e científicas que me proporcionaram na realização desta dissertação.

O grupo de trabalho em que me inseri inclui, também, alguns nomes que pretendo destacar pelo seu impacto concreto neste trabalho. Ao Eng. Rui Coelho, agradeço toda a ajuda que me ofereceu ao longo destes anos, ao atacar os mais variados problemas, desde questões estéticas às implementações no código acoplado. É, sem dúvida, outra pessoa marcante neste percurso. Ao meu colega de secretária, o Eng. António Carneiro, deixo uma palavra especial pela sua boa disposição e irrebatível disponibilidade. O seu contributo para a implementação de modelos de dano no código termo-mecânico foi imprescindível. Por último, um agradecimento ao Eng. José Luís Vila-Chã, pelo apoio à utilização e adaptação do GMMD. A todos os colegas do CM2S, um agradecimento sincero pela forma como me acolheram.

Além dos limites deste trabalho, todas as conversas, debates, trocas de ideias, experiências e surpresas deste percurso contribuiram para o meu crescimento e aprendizagem, na Faculdade de Engenharia e fora dela. Dito isto, deixo uma palavra especial a todos os colegas de curso e amigos que me acompanharam ao longo dos últimos cinco anos, com quem pude partilhar todos esses momentos. Daqui, destaco a minha companhia de todas as horas, a Kika, a quem agradeço a enorme e inabalável confiança que tem em mim. Não tendo tido um contributo científico para esta dissertação, deu-me a força necessária para encarar este desafio, como tantos outros, com um sorriso.

Agradeço, também, a todos os meus familiares, em especial à minha madrinha, Isabel, ao meu padrinho emprestado, Pedro, e aos meus irmãos, Tomás e Miguel. Finalmente, ao meu pai, Gil, e à minha mãe, Susana, agradeço, acima de tudo, os valores pessoais e humanos que me transmitiram, assim como todas as horas das suas vidas pessoais e profissionais que dedicaram à minha educação. A minha graduação como mestre em engenharia mecânica é o culminar de um caminho, já longo, de formação pessoal e científica, caminho este inseparável dos inúmeros privilégios que os meus pais, com muito amor, e muito suor, me proporcionaram ao longo da vida.

A todos e todas, por estes motivos, e por muitos outros, obrigado.

Guilherme Fonseca Gonçalves.

Contents

List of Figures xiii

List of Tables xxi

Chapter 1
Introduction 1
1.1 Context . . . 1
1.2 Motivation . . . 2
1.2.1 Nonlocal strategies for macro- and micro-regularisation . . . 2
1.2.2 Second-order homogenisation for macro-regularisation in FE^2 . . . 3
1.2.3 Phase-field models towards micro-scale fracture . . . 3
1.3 Contributions . . . 3
1.4 Dissertation outline . . . 5

Part I Theoretical Background 9

Chapter 2
Continuum Mechanics and the Finite Element Method 11
2.1 Preliminaries . . . 11
2.2 The continuum approximation . . . 11
2.3 Kinematics of deformation . . . 13
2.3.1 Deformation gradient . . . 14
2.3.2 Isochoric and volumetric deformations . . . 16
2.3.3 Polar decomposition of the deformation gradient . . . 17
2.3.4 Strain measures . . . 18
2.3.5 Spatial velocity gradient . . . 19
2.4 Forces and stress measures . . . 19
2.4.1 Cauchy stress tensor . . . 20
2.4.2 Deviatoric and hydrostatic stress components . . . 21
2.4.3 First Piola-Kirchhoff stress tensor . . . 21
2.4.4 Second Piola-Kirchhoff stress tensor . . . 22
2.4.5 Kirchhoff stress tensor . . . 22
2.5 Fundamental principles of thermodynamics . . . 22
2.5.1 Conservation of mass . . . 22
2.5.2 Momentum equilibrium . . . 22
2.5.3 First principle of thermodynamics . . . 23
2.5.4 Second principle of thermodynamics . . . 23
2.5.5 Clausius-Duhem inequality . . . 23
2.6 Constitutive theory . . . 24
2.6.1 Constitutive axioms . . . 24
2.6.2 Thermodynamics with internal variables . . . 25

2.6.3 The constitutive initial value problem . . . 26
2.7 Weak equilibrium formulation . . . 27
2.7.1 Spatial description . . . 27
2.7.2 Material description . . . 28
2.7.3 Quasi-static formulation . . . 28
2.8 Quasi-static initial boundary value problem . . . 28
2.9 Finite element method . . . 30
2.9.1 Approximate solution with the finite element method . . . 30
2.9.2 Time discretisation . . . 31
2.9.3 Spatial discretisation . . . 31
2.9.4 Newton-Raphson method . . . 36
2.10 Second-order continuum mechanics . . . 39
2.10.1 Second gradient of the displacement field . . . 39
2.10.2 Weak equilibrium equation . . . 39
2.10.3 Strong equilibrium . . . 40
2.10.4 Finite element solution for second-order problems . . . 40
2.10.5 Newton-Raphson method for problems including the second-gradient . . . 42

Chapter 3
Multi-Scale Models Based on Computational Homogenisation **43**
3.1 Introduction to multi-scale modelling . . . 43
3.2 Computational homogenisation . . . 45
3.2.1 Basic concept of computational homogenisation . . . 45
3.2.2 Representative volume element . . . 45
3.3 First-order computational homogenisation formulation . . . 47
3.3.1 Homogenised deformation gradient . . . 47
3.3.2 Multi-scale kinematics . . . 47
3.3.3 Micro-scale boundary conditions . . . 48
3.3.4 Hill-Mandel principle of macro-homogeneity . . . 51
3.3.5 Homogenised stress tensor . . . 53
3.4 Second-order computational homogenisation . . . 53
3.4.1 Introduction . . . 54
3.4.2 Kinematic homogenisation . . . 55
3.4.3 Multi-scale kinematics . . . 56
3.4.4 Micro-scale boundary conditions . . . 57
3.4.5 Higher-order stress tensor homogenisation . . . 58
3.5 Second-order homogensation formulation for porous RVEs . . . 58
3.5.1 RVE domain decomposition . . . 58
3.5.2 Kinematic homogenisation . . . 59
3.5.3 Multi-scale kinematics . . . 61
3.5.4 Micro-scale boundary conditions . . . 62
3.5.5 Higher-order stress homogenisation . . . 63
3.6 Numerical solution of large-strain multi-scale problems . . . 64

Chapter 4
Damage and Fracture Mechanics **67**
4.1 Introduction to fracture and continuum damage . . . 67
4.2 Nonlocal damage models of integral type . . . 68
4.2.1 Nonlocal theory of integral type . . . 69
4.2.2 Nonlocal averaging strategy . . . 70
4.3 Gradient-enhanced nonlocal damage . . . 72

4.3.1 Gradient-based nonlocal formulation . . . 73
4.3.2 Parallel with quasi-static heat diffusion . . . 74
4.4 Phase-field fracture . . . 75
4.4.1 General formulation for phase-field fracture . . . 76
4.4.2 Parallel with gradient nonlocal damage and quasi-static heat diffusion . . . 78

Part II Second-Order Homogenisation and Nonlocal Damage of Integral Type 81

Chapter 5
Implementing Nonlocal Damage of Integral Type 83
5.1 Introduction . . . 83
5.2 Constitutive model for nonlocal damage . . . 83
5.2.1 Constitutive model for finite strain elastoplasticity . . . 83
5.2.2 Isotropic explicit damage model . . . 85
5.2.3 Isotropic explicit nonlocal damage model of integral type . . . 85
5.3 Numerical Treatment . . . 85
5.3.1 Numerical integration procedure . . . 86
5.3.2 Nonlocal averaging procedure . . . 90
5.3.3 Linearisation of the local and nonlocal damage models . . . 91
5.4 Implementation . . . 96
5.4.1 Solution of a macro-scale problem with LINKS . . . 96
5.4.2 Existing code for micro-scale problems . . . 98
5.4.3 Implementation for macro-scale problems . . . 100
5.5 Numerical Examples . . . 102
5.5.1 Preliminary micro-scale tests . . . 103
5.5.2 Single-element tests . . . 105
5.5.3 Compact shear specimen . . . 108
5.5.4 Notched tensile specimen . . . 118
5.6 Discussion . . . 128

Chapter 6
Macro-Scale Regularisation with Second-Order Homogenisation 131
6.1 Introduction . . . 131
6.1.1 Ductile damage mechanisms . . . 131
6.1.2 Remarks on the computational homogenisation of softening media . . . 132
6.2 RVE generation and micro-scale analysis . . . 133
6.2.1 Generation of porous RVEs . . . 133
6.2.2 Preliminary micro-mechanical analysis . . . 135
6.3 Multi-scale simulations of a tensile specimen . . . 136
6.3.1 First-order multi-scale analysis . . . 137
6.3.2 Second-order multi-scale analysis . . . 141
6.3.3 Impact of the RVE length on the second-order multi-scale response . . . 144
6.4 Micro-scale mesh regularisation with integral nonlocal damage . . . 147
6.4.1 Implementation in LINKS^2 . . . 147
6.4.2 Preliminary micro-mechanical analysis . . . 149
6.5 Multi-scale analysis with nonlocal RVE damage . . . 153
6.5.1 First-order multi-scale analysis . . . 153
6.5.2 Second-order multi-scale analysis . . . 158
6.6 Discussion . . . 162

Chapter 7
Relating Nonlocal Damage of Integral Type and Second-Order Homogenisation **165**
7.1 On the comparison of macro-scale regularisation strategies . . . 165
7.2 Brief overview of the inverse identification problem . . . 168
7.2.1 The inverse problem . . . 168
7.3 Calibration of the local Engelen model . . . 170
7.3.1 Single-element calibration setup . . . 170
7.3.2 Direct calibration setup . . . 175
7.4 Calibrating the nonlocal radius . . . 178
7.5 Discussion . . . 182

Part III Gradient-Enhanced Nonlocal Damage and Phase-Field Fracture **185**

Chapter 8
Implementing Gradient-Enhanced Nonlocal Damage **187**
8.1 Introduction . . . 187
8.2 Finite element discretisation of the coupled problem . . . 187
8.2.1 Weak forms of momentum and damage balance . . . 187
8.2.2 Finite element discretisation . . . 188
8.3 Solution schemes for coupled multi-physics problems . . . 189
8.3.1 Staggered solution scheme . . . 190
8.4 Implementation . . . 192
8.4.1 Object-oriented programming . . . 192
8.4.2 Gradient-enhanced Engelen material model . . . 193
8.4.3 Damage averaging equation . . . 194
8.5 Numerical examples . . . 197
8.5.1 Single-element tests . . . 198
8.5.2 Plate with central hole . . . 200
8.5.3 Double-notched specimen . . . 207
8.6 Comparison with integral-type strategy . . . 211
8.6.1 Compact shear specimen . . . 211
8.6.2 Plate with central hole . . . 216
8.7 Discussion . . . 222

Chapter 9
Implementing Phase-Field Fracture Towards Multi-Scale Modelling of Damage **225**
9.1 Introduction . . . 225
9.2 Phase-field model for quasi-brittle hyperelastic materials . . . 225
9.2.1 Hyperelastic constitutive model . . . 226
9.2.2 Finite element discretisation of the phase-field equation . . . 226
9.3 Implementation . . . 227
9.3.1 Hyperelastic material model . . . 228
9.3.2 Phase-field equation . . . 228
9.4 Validation with pre-cracked plate benchmark . . . 231
9.5 Numerical examples . . . 234
9.5.1 Plate with central hole . . . 235
9.5.2 Composite RVE . . . 245
9.6 Discussion . . . 251

Chapter 10
Conclusions and Final Remarks **253**

10.1 Conclusions 253
10.1.1 Main contributions 254
10.1.2 Additional outcomes 255
10.2 Future challenges 256

Bibliography **259**

List of Figures

Chapter 1
Introduction **1**
1.1 LINKS logo. 4

Chapter 2
Continuum Mechanics and the Finite Element Method **11**
2.1 Schematic representation of the continuum approximation, adapted from Ferreira (2017). 12
2.2 Generic deformation of a body, taken from Coelho (2019). 13
2.3 Generic motion of a body, taken from de Souza Neto et al. (2008). 14
2.4 Deformation of two neighbouring material particles and its relation to the deformation gradient, taken from Coelho (2019). 15
2.5 Deformation of an infinitesimal volume element and its relation to the deformation gradient, taken from de Souza Neto et al. (2008). 15
2.6 Schematic representation of the isochoric and volumetric components of the deformation gradient, taken from Coelho (2019). 17
2.7 Schematic representation of the right and left polar decompositions of the deformation gradient, taken from Coelho (2019). 18
2.8 Representation of the Cauchy stress tensor, taken from de Souza Neto et al. (2008). . . 20
2.9 Cauchy stress components and principal stresses, taken from de Souza Neto et al. (2008). 20
2.10 Schematic representation of quasi-static initial boundary value problem, taken from Coelho (2019). 29
2.11 Schematic representation of the different steps for the application of the finite element method for the solution of the constitutive initial value problem, taken from Vieira (2018). 30
2.12 Representation of the spatial discretisation of a plane domain by a mesh of triangular finite elements and a schematic representation of the evolution of the shape functions associated with a generic finite element, (e), taken from Silva (2021). 33
2.13 Schematic representation of the mapping from the standard domain Γ onto Ω, by the transformation function, x, for a 4-noded biliniear quadratic element, taken from Coelho (2019). 36
2.14 Schematic representation of the Newton-Raphson iterative procedure and its quadratic rate of convergence, taken from Ferreira (2022). 37
2.15 Schematic representation of a second-order continuum body subjected to an arbitrary set of external forces, taken from Rodrigues Lopes and Andrade Pires (2021). . . 39
2.16 Schematic representation of an initially undeformed infinitesimal volume element (a), undergoing first- (b) and second-order (c) deformation modes. Taken from Silva (2021). 40
2.17 Schematic representation of the Q8F4L1 mixed finite element for second-order analysis, taken from Rodrigues Lopes (2019). 42

Chapter 3
Multi-Scale Models Based on Computational Homogenisation **43**
3.1 Schematic representation of the solution of a multi-scale problem with recourse to first-order computational homogenisation. Taken from Silva (2021). 45
3.2 Schematic representation of the RVE concept and the principle of separation of scales, adapted from Vieira (2018). 46
3.3 Schematic representation of the deformation of an RVE under with the Taylor boundary condition, taken from Silva (2021). 49
3.4 Schematic representation of the deformation of an RVE with the linear boundary condition, taken from Silva (2021). 50
3.5 Schematic representation of the deformation of an RVE with the periodic boundary condition, taken from Silva (2021). 51
3.6 Convergence of the homogenised properties with the increase of RVE size, for the different micro-scale boundary conditions. Taken from Rodrigues Lopes (2019). 52
3.7 Schematic representation of the solution of a multi-scale problem with recourse to second-order computational homogenisation. Taken from Silva (2021). 54
3.8 Schematic representation of the concept of generalised RVE size, which allows decoupling the RVE length and the number of microscopic features in the RVE model, taken from Rodrigues Lopes and Andrade Pires (2022b). 55
3.9 Schematic representation of the second-order homogenisation formulation for RVEs containing voids. Taken from dos Santos et al. (2023). 59
3.10 Schematic representation of the domain decomposition and boundaries of a generic porous RVE. Taken from dos Santos et al. (2023). 60
3.11 Schematic representation of a coupled multi-scale finite element analysis at large strains with path-dependent descriptions. Taken from Rodrigues Lopes (2019). 64
3.12 Schematic representation of numerical solution scheme for the micro-scale equilibrium problem with second-order homogenisation. Adapted from Rodrigues Lopes (2019). 65

Chapter 4
Damage and Fracture Mechanics **67**
4.1 Visual representation of the two nonlocal weighting functions presented in Equations (4.4) and (4.5). 70
4.2 Schematic representation of the two main strategies for nonlocal averaging, taken from Andrade et al. (2011). 71
4.3 Schematic representation of an arbitrary body with a discrete or a diffuse crack, adapted from Quintanas-Corominas et al. (2019). 76

Chapter 5
Implementing Nonlocal Damage of Integral Type **83**
5.1 Schematic representation of the general structure of the single-scale approach for the solution of macro-scale problems with LINKS, adapted from Ferreira (2017). 97
5.2 Representative volume element utilised in the micro-scale tests. 103
5.3 Distribution of nonlocal damage obtained with the new and legacy versions of LINKS, for each boundary condition. 104
5.4 Computational times recorded for the micro-scale example, with the three boundary conditions and each version of the nonlocal code. 105
5.5 Schematic representation of the boundary conditions applied to the single element under tension. 106

5.6 Effective Cauchy stress and damage evolutions found with the reduced integration single element, with the local and nonlocal damage models. . . . 106
5.7 Effective Cauchy stress and damage evolutions found with the complete integration single element, with the local damage model and the nonlocal damage model with two different values of the nonlocal radius. . . . 106
5.8 Evolution of the norm of the relative residual obtained with the Newton-Raphson method at different load increments, for the single-element setup and the local and nonlocal cases. . . . 107
5.9 Schematic representation of the boundary conditions applied to the compact shear specimen, based on the experimental test piece of Perdahcioglu et al. (2008). . . . 108
5.10 Finite element meshes used to discretize the shear specimen. . . . 108
5.11 Evolution of the horizontal reaction force for the local and nonlocal damage models, for both finite element meshes. . . . 109
5.12 Damage variable evolution for the local and nonlocal damage models, retrieved from a point in the deformation band for both finite element meshes. . . . 110
5.13 Local and nonlocal damage distributions at failure for the two finite element meshes. 111
5.14 Effective Cauchy stress distributions found with the local and nonlocal approaches. . 112
5.15 Evolution of the horizontal reaction force for nonlocal damage model, for both finite element meshes and several values of the nonlocal radius. . . . 113
5.16 Nonlocal damage evolution, retrieved from a point in the deformation band for both finite element meshes and several values of the nonlocal radius. . . . 114
5.17 Nonlocal damage distributions for the three additional values of the nonlocal radius. 114
5.18 Computational time associated with each simulation of the tensile specimen. . . . 115
5.19 Evolution of the norm of the relative residual throughout the Newton-Raphson procedure for the shear specimen simulations. . . . 116
5.20 Representation of the non-zero components of the global stiffness matrix for the shear specimen. . . . 117
5.21 Schematic representation of the boundary conditions applied to the tensile specimen. 118
5.22 Three finite element meshes used for the tensile specimen. . . . 119
5.23 Evolution of the vertical reaction force for the local and nonlocal damage models. . . 119
5.24 Damage variable evolution for the local and nonlocal models, retrieved at the tip of the notch. . . . 120
5.25 Damage distributions found for the local and nonlocal cases with the three finite element meshes. . . . 121
5.26 Evolution of the vertical reaction force for the local and nonlocal models, with a nonlocal radius of 0.1 mm. . . . 121
5.27 Damage distributions found for the nonlocal radius of 0.1 mm for the three finite element meshes. . . . 122
5.28 Evolution of the vertical reaction force for several values of the nonlocal radius. . . . 123
5.29 Damage distributions found for the medium mesh and several values of the nonlocal radius. . . . 123
5.30 Computational time associated with each simulation of the tensile specimen. . . . 124
5.31 Impact of adopting different solvers for the global system of equations on the computational times. . . . 124
5.32 Evolution of the vertical raction forces obtained with the bell-shaped weighting function and several values of the nonlocal radius. . . . 125
5.33 Damage distributions found with the bell-shaped weighting function, for the medium mesh and several values of the nonlocal radius. . . . 126
5.34 Damage distributions found with the two nonlocal averaging strategies and the two chosen nonlocal radii. . . . 127

Chapter 6
Macro-Scale Regularisation with Second-Order Homogenisation **131**
6.1 Void coalescense on metal sheets containing laser drilled holes, taken from Weck and Wilkinson (2008). . . . 132
6.2 Schematic representation of the macro- and micro-scale damage mechanisms influencing the failure of ductile materials, taken from Coelho (2019). . . . 133
6.3 Examples of the porous microstructures generated with GMMD. . . . 134
6.4 Finite element discretisation of the RVE employed in coupled analysis, with a single void with a 10% volume fracton. . . . 134
6.5 Stress-strain curves obtained for different values of the yield stress at failure, $\sigma_{y,2}$, with the medium RVE mesh. . . . 136
6.6 Damage contours found for a yield stress at failure of 300 MPa, for three equally spaced values of the load factor. . . . 136
6.7 Schematic representation of a quarter of the perturbed tensile specimen, inspired by the work of Kouznetsova (2002), and its three finite element discretisations. . . . 137
6.8 Reaction force curves obtained with first-order homogenisation for the tensile specimen, with the nine combinations of macro- and micro-scale meshes. . . . 138
6.9 Equivalent strain distributions at failure obtained with first-order homogenisation for the tensile specimen, with the nine combinations of macro- and micro-scale meshes. 139
6.10 Mirrored visualisation of two localisation patterns found with first-order homogenisation. . . . 140
6.11 Micro-mechanical responses attained with the coarse macro-scale mesh and the medium and fine RVEs. . . . 140
6.12 Reaction force curves obtained with second-order homogenisation for the tensile specimen, with the nine combinations of macro- and micro-scale meshes. . . . 142
6.13 Equivalent strain distributions at failure obtained with second-order homogenisation for the tensile specimen, with the nine combinations of macro- and micro-scale meshes. 143
6.14 Micro-scale mesh dependency found with second-order homogenisation. . . . 144
6.15 Impact of the RVE length on the mechanical response obtained with second-order homogenisation. . . . 145
6.16 Impact of the RVE length on the equivalent strain distributions obtained with second-order homogenisation for the tensile test piece. . . . 146
6.17 Comparing the impact of the RVE length on the mechanical response obtained with second-order homogenisation, for the three macro-scale meshes. . . . 147
6.18 Schematic representation of the master-slave scheme with dynamic scheduling, employed in the parallelisation of the coupled multi-scale problem. Taken from Rodrigues Lopes et al. (2018). . . . 149
6.19 Stress-strain curves obtained with different values of the nonlocal radius, for the coarse micro mesh. . . . 150
6.20 Stress-strain curves obtained with different values of the nonlocal radius, for the medium micro mesh. . . . 151
6.21 Stress-strain curves obtained with different values of the nonlocal radius, for the fine micro mesh. . . . 151
6.22 Effects of introducting nonlocal averaging in the stress-strain curves obtained for each micro-scale mesh. . . . 152
6.23 Effects of introducing nonlocal averaging in the resulting damage distributions at the micro-scale. . . . 152
6.24 Equivalent strain distributions at failure obtained with first-order homogenisation and nonlocal RVE damage, with the nine combinations of macro- and micro-scale meshes and a nonlocal radius of 0.2. . . . 155

6.25 Equivalent strain distributions at failure obtained with first-order homogenisation and nonlocal RVE damage, with the nine combinations of macro- and micro-scale meshes and a nonlocal radius of 0.1. . . . 156
6.26 Reaction force curves obtained with first-order homogenisation, for the three RVEs with the coarse macroscopic mesh, with local and nonlocal damage. . . . 157
6.27 Reaction force curves obtained with first-order homogenisation, for the three macroscopic meshes with the medium RVE, with local and nonlocal damage. . . . 157
6.28 Full regularisation of the multi-scale problem with the introduction of nonlocal damage at the micro-scale, with a nonlocal radius of 0.2 mm, using second-order homogenisation. . . . 159
6.29 Multi-scale mesh regularisation obtained with second-order homogenisation and nonlocal damage at the microscopic level. . . . 160
6.30 Full regularisation of the multi-scale problem with the introduction of nonlocal damage at the micro-scale, with a nonlocal radius of 0.1 mm, using second-order homogenisation. . . . 161
6.31 Full regularisation of the multi-scale problem with the introduction of nonlocal damage at the micro-scale using second-order homogenisation with an RVE length of 0.5 mm and a nonlocal radius of 0.05 mm. . . . 161

Chapter 7
Relating Nonlocal Damage of Integral Type and Second-Order Homogenisation **165**
7.1 Schematic representation of optimisation-based strategy employed in this chapter to relate the RVE length of second-order FE^2 and the nonlocal radius of an integral type single-scale damage model. . . . 167
7.2 Piglot logo (taken from www.github.com/CM2S/piglot). . . . 168
7.3 Schematic illustration of the inverse identification numerical procedure. . . . 169
7.4 Schematic representation of the calibration strategy employed in Section 7.3.1 to identify the parameters of the local Engelen model with first-order multi-scale simulations, based on the work of Fonseca Gonçalves (2022). . . . 171
7.5 Schematic of the loading cases applied to the single-element. . . . 171
7.6 Calibrated macroscopic single-element response using the tension loading case. . . . 173
7.7 Calibrated macroscopic single-element response using the shear loading case. . . . 173
7.8 Calibrated macroscopic single-element response adopting a multi-objective optimisation scheme, where both the tension and shear loading cases were included. . . . 174
7.9 Validation of the calibrated macroscopic Engelen models, using the single-element framework proposed by Fonseca Gonçalves (2022), against the first-order FE^2 response. 174
7.10 Calibrated macroscopic response of the tensile specimen, with the coarse macro-scale mesh. . . . 176
7.11 Calibrated macroscopic response of the tensile specimen, with the coarse macro-scale mesh. . . . 176
7.12 Calibrated macroscopic response of the tensile specimen, with the the second set of material properties, and the coarse macro-scale mesh. . . . 177
7.13 Calibrated macroscopic response of the tensile specimen, with the the second set of material properties, and the coarse macro-scale mesh. . . . 177
7.14 Reaction force curves obtained with the second-order FE^2 and the calibrated models, including the local model and the relations found between the nonlocal radius and the RVE length. . . . 180
7.15 Equivalent strain distributions obtained with both second-order FE^2 and the macroscopic calibrated nonlocal models. . . . 181

7.16 Numerical relation observed between the nonlocal radius and the RVE length, for the several calibration cases. . . . 182

Chapter 8
Implementing Gradient-Enhanced Nonlocal Damage **187**
8.1 Schematic representation of the staggered solution scheme adopted for the solution of the coupled system of equilibrium equations in this contribution. . . . 192
8.2 Schematic representation of the boundary conditions applied to the single element under tension. . . . 199
8.3 Effective Cauchy stress and damage evolutions found with the single-element setup, for the local and the gradient-enhanced nonlocal cases. . . . 199
8.4 Evolution of the norm of the relative residual obtained with the Newton-Raphson method at different load increments, for the single-element setup and the local and gradient nonlocal cases. . . . 200
8.5 Schematic representation of a quarter of a rectangular plate with a circular central hole, under a tensile load, and its finite element discretisation. . . . 201
8.6 Damage distributions found for the plate with a central hole, with local damage and the gradient-enhanced model, with two different values of the nonlocal length-scale parameter. . . . 202
8.7 Computational times recorded for the simulation of the plate with a central hole with two nonlocal lengths, three different implicit solvers and several numbers of coupling increments. . . . 203
8.8 Gradient-enhanced damage distributions found for the plate with a central hole, with two different numbers of coupling increments, n_c. . . . 204
8.9 Evolution of the norm of the relative residual obtained with the different implict solver, for different load increments, for the plate with central hole, with $l = 1$ mm. . . . 205
8.10 Evolution of the norm of the relative residual obtained with the different implict solver, for different load increments, for the plate with central hole, with $l = 5$ mm. . . . 206
8.11 Schematic representation of the double-notched specimen, taken from Andrade (2012) 207
8.12 Finite element meshes used to discretise the double-notched specimen. . . . 208
8.13 Reaction curves obtained with the gradient-enhanced and local models for the double-notched specimen, for the two finite element meshes and two values of the nonlocal length parameter. . . . 208
8.14 Damage distributions found for each mesh of the double-notched specimen, for the local and the two nonlocal cases. . . . 209
8.15 Nonlocal damage distributions found for each mesh of the double-notched specimen, for larger values of the nonlocal length parameter. . . . 210
8.16 Reaction curves obtained with the both nonlocal approaches and the local model for the compact shear specimen, for each finite element mesh. . . . 212
8.17 Nonlocal damage distributions found for each mesh of the compact shear specimen, for the two nonlocal models. . . . 213
8.18 Nonlocal damage distributions found for each mesh of the compact shear specimen, for the two nonlocal models and a nonlocal length of 10 mm. . . . 214
8.19 Computational times recorded for the nonlocal simulations of both meshes of the compact shear specimen. . . . 215
8.20 Reaction curves obtained with the both nonlocal approaches and the local model for the plate with a central hole, for several values of the nonlocal length parameter. . . . 217
8.21 Nonlocal damage distributions obtained with the two nonlocal strategies, for the plate with a central hole and $L = 0.5$ mm. . . . 218

8.22 Nonlocal damage distributions obtained with the two nonlocal strategies, for the plate with a central hole and several values of the nonlocal length parameter. 219
8.23 Strain and stress distributions obtained with the two nonlocal approaches for the plate with a central hole and a nonlocal length parameter of 1.0 mm. 220
8.24 Strain and stress distributions obtained with the two nonlocal approaches for the plate with a central hole and a nonlocal length parameter of 5.0 mm. 221
8.25 Computational times measured for all nonlocal simulations of the plate with a central hole. 221

Chapter 9
Implementing Phase-Field Fracture Towards Multi-Scale Modelling of Damage **225**
9.1 Schematic representation of the pre-cracked plate under tension, taken from Navidtehrani et al. (2021a). 231
9.2 Finite element meshes used to discretise the pre-cracked plate. 233
9.3 Reaction curve obtained for the pre-cracked plate benchmark, in comparison to the reference results (Navidtehrani et al., 2021a). 233
9.4 Phase-field variable distribution obtained for the pre-cracked benchmark, in comparison to the reference results (Navidtehrani et al., 2021a). 234
9.5 Results of the first simulation of the plate with a central hole with the phase-field model. 235
9.6 Reaction curves obtained with the two implicit solvers and different coupling increment ratios. 236
9.7 Reaction curves obtained for three values of the fracture toughness. 240
9.8 Phase-field variable distribution for the three values of the fracture toughness. 240
9.9 Reaction curves obtained for four values of the phase-field length-scale parameter. . . 241
9.10 Phase-field variable contours obtained for four values of the length-scale parameter. . 242
9.11 Finite element meshes utilised with the plate with central hole. 243
9.12 Reaction force curves obtained with the four different mesh sizes for the plate with central hole for different values of the phase-field length-scale parameter. 244
9.13 RVE 1: 10 fibres with 20% volume fraction, discretised in 3592 QUAD8 and TRI6 elements and 10987 nodes. 246
9.14 Phase-field variable contours obtained for RVE 1 and three different values of the length-scale parameter. 246
9.15 RVE 2: 39 fibres with 30% volume fraction, discretised in 3690 QUAD8 and TRI6 elements and 11297 nodes. 247
9.16 Phase-field variable contours obtained for RVE 2 and three different values of the fracture toughness. 248
9.17 RVE 3: 8 fibres with 15% volume fraction, discretised in 20800 F-bar QUAD4 elements and 21055 nodes. 249
9.18 Phase-field variable contours obtained for RVE 3, for three different values of the fracture toughness and three values of the phase-field length-scale. 250

List of Tables

Chapter 5
Implementing Nonlocal Damage of Integral Type **83**
5.1 Material properties adopted for the single-element tests. . . . 105
5.2 Material properties adopted for the notched tensile specimen. . . . 118
5.3 Computational times recorded for the Lagrangian and Eulerian nonlocal averaging strategies. . . . 126
5.4 Computational times recorded for the Lagrangian and Eulerian nonlocal averaging strategies, for a larger deformation of the tensile specimen. . . . 127

Chapter 6
Macro-Scale Regularisation with Second-Order Homogenisation **131**
6.1 Material properties of the porous RVEs. . . . 135
6.2 Computational times recorded for the micro-mechanical simulations of the Porous RVEs with different values of the nonlocal radius. . . . 151

Chapter 7
Relating Nonlocal Damage of Integral Type and Second-Order Homogenisation **165**
7.1 Numerical bounds and initial guess employed for each material parameter of the Engelen model. . . . 171
7.2 Second set of material properties of the porous RVEs. . . . 175
7.3 Recap of the calibrated macroscopic local damage models presented in Section 7.3.2. 178
7.4 Numerical bounds and initial guess employed for the calibration of the nonlocal radius. 178
7.5 Numerical relations found between the nonlocal radius and the RVE length, for each calibration case. . . . 179
7.6 Calibration loss values found for each case and RVE length. . . . 182

Chapter 8
Implementing Gradient-Enhanced Nonlocal Damage **187**
8.1 Material properties of the single finite element. . . . 198

Chapter 9
Implementing Phase-Field Fracture Towards Multi-Scale Modelling of Damage **225**
9.1 Material properties employed in the benchmarking example of the pre-cracked plate. 231
9.2 Material properties employed for the plate with central hole. . . . 235
9.3 Computational times recorded for the two implicit coupling solvers and the different time discretisation ratios. . . . 237
9.4 Coupling convergence rates obtained with Broyden's method and different coupling incrementation ratios. . . . 238

9.5 Coupling convergence rates obtained with the fixed-point method and different coupling incrementation ratios. 239
9.6 Elastic properties of RVE 1. 245
9.7 Critical displacements found for RVE 1 and each value of the length-scale parameter. 246
9.8 Critical displacements found for RVE 2 and each value of the fracture toughness. . . . 247
9.9 Elastic properties of RVE 3. 248
9.10 Critical displacements found for RVE 3 and each combination of fracture properties. . 249

CHAPTER 1

INTRODUCTION

1.1 Context

The accurate prediction of failure in structures and mechanical components is of great relevance to various industrial sectors, namely aerospace and aeronautics. High-fidelity multi-scale approaches for modelling structural performance under extreme loading scenarios and in the presence of material and geometrical nonlinearities have shown remarkable predictive capabilities. In this context, computational homogenisation, capturing complex path-dependent micro-phenomena, without assuming closed-form equations, has become one of the most popular scale-bridging strategies. Multi-scale models based on computational homogenisation, naturally accounting for the intricate behaviour of heterogeneous microstructures, allow predicting structural failure through the progressive degradation of microscopic material details, such as voids or cracks.

Nonetheless, the application of computational-homogenisation-based approaches to model multi-scale damage and structural failure faces several challenges. Some of them include the objectivity of scale transition in the presence of micro-scale softening, discussed by Gitman (2006), Gitman et al. (2007), and also possibly ill-posed initial boundary value problems at one or both spatial scales, due to the adoption of pointwise constitutive formulations. The former issue is not addressed in this dissertation. Instead, it focuses on the latter, which is known to lead to finite element solutions which are dependent on the underlying spatial discretisation. Several nonlocal strategies have been proposed in the literature to circumvent this issue, which is commonly known as *pathological mesh dependency*, and can regularise the balance problem at either or both scales. On the one hand, integral type models (Andrade et al., 2011, Pijaudier-Cabot and Bažant, 1987, Reis et al., 2018) introduce explicit nonlocal connections between neighbouring material points by conveniently modifying the constitutive relations. On the other hand, gradient-based nonlocal formulations (Engelen et al., 2003, Peerlings et al., 2001, 1996b) rely on adding an averaging equation to the global structural problem. Pivotal to both strategies is the introduction of a nonlocal intrinsic length-scale, which allows regularising mesh dependency up to moderate localisation.

Alternatively, multi-scale models based on second-order computational homogenisation naturally account for nonlocal and size effects, by employing a second-order continuum theory at the macro-level, also associated with the inclusion of a characteristic material length-scale. Therefore, the use of second-order multi-scale models leads to macro-regularisation, as first shown by Kouznetsova (2002). Moreover, the macroscopic characteristic length-scale arising from second-order computational homogenisation has been shown to be deeply related to the length of the underlying Representative Volume Element (RVE) (Kouznetsova et al., 2004b, Luscher, 2010, Ro-

drigues Lopes and Andrade Pires, 2021). However, the connection between the RVE length and macro-regularisation effects remains unexplored hitherito.

Furthermore, the application of phase-field approaches to model microscopic failure including fracture phenomena has gained traction in the research community (see for instance Bharali (2024), Bharali et al. (2021), Bijaya et al. (2023), Li and Xu (2022), Paggi et al. (2018)). Such formulations are based on treating cracks as diffuse entities, easing the handling of complex crack paths and topologies, characteristic of multiphasic microstructures, often containing competing damage mechanisms. These and other features, such as the regularisation of crack-tip singularities, make phase-field models particularly suitable for modelling the fracture of heterogeneous materials at lower spatial scales, and enable the modelling of strong localisation.

1.2 Motivation

The ultimate goal driving this dissertation is to assess and relate different strategies for the multi-scale modelling of structural failure. Particular attention is given to the problem of pathological mesh dependency at both micro- and macro-scales.

To this end, integral type and gradient-enhanced nonlocal strategies are pursued and compared, as competing solutions for single-scale mesh regularisation. In addition, a multi-scale model based on computational homogenisation is utilised to evaluate the mesh dependency of FE^2 predictions obtained with first- and second-order approaches. The impact of the RVE length on macro-regularisation effects is systematically analysed. The relationship between the characteristic lenght-scale parameters allowing macro-regularisation with nonlocal and second order multi-scale approaches is analysed. A phase-field model is also implemented and employed to analyse quasi-brittle fracture, with the goal of further improving the current formulation to enable the high-fidelity modelling of micro-scale damage and fracture.

1.2.1 Nonlocal strategies for macro- and micro-regularisation

In this dissertation, a pre-existing numerical implementation of a nonlocal model of integral type for micro-scale problems (see Reis et al. (2018)) was enhanced and extended for macroscopic cases. It was also compatibilised with a code structure for multi-scale finite element simulations based on first- and second-order homogenisation, to enable its employment for micro-regularisation in an FE^2 setup. The influence of its several features, particularly the nonlocal regularisation parameter, on the resulting mechanical response was analysed.

Additionally, a gradient-based nonlocal model is developed within a staggered solution scheme, to tackle the additional nonlocal averaging equation. In the literature, numerous authors have taken advantage of coupled solution schemes for multi-physcis problems, particularly thermomechanics and fluid-structure-interactions, increasingly available in commercial finite element software packages, to implement gradient-enhanced nonlocal formulations (Ostwald et al., 2019, Seupel et al., 2018). In this work, a recent implicit staggered strategy for the solution of thermomechanical macro-scale problems is exploited for the implementation of a gradient nonlocal model.

Although these two classes of nonlocal strategies stem from similar theoretical formulations, their numerical treatments are poles apart. Moreover, pratical comparisons between gradient and integral models are largely non-existent in the literature, notable exceptions being de Vaucorbeil et al. (2022), Nahrmann and Matzenmiller (2021), Peerlings et al. (1996a, 2001). With this in mind, the computational aspects, performance, and predictions of integral and gradient nonlocal approaches are systematically compared in this contribution.

1.2.2 Second-order homogenisation for macro-regularisation in FE^2

The macro-mesh dependency of FE^2 predictions is assessed with first- and second-order computational homogenisation. RVEs containing voids as damage precursors were adopted, with an isotropic explicit damage model coupled with a constitutive formulation for finite strain elasto-plasticity, to perform multi-scale simulations of ductile damage. The effect of the RVE length on the second-order multi-scale response is assessed, with emphasis on the mesh-regularising effects. The interdependence between micro- and macro-scale mesh dependency is also discussed, with the use of the nonlocal integral model to regularise the RVE balance problem.

To further study the macroscopic length-scale arising with the adoption of a second-order multi-scale approach, the macro-regularisation effects observed with second-order FE^2 are related to those resulting from the recently implemented nonlocal integral strategy within a single-scale approach. A connection is established between the nonlocal intrinsic parameter (single-scale) and the RVE length (multi-scale), and the limits of this parallel are extensively discussed.

1.2.3 Phase-field models towards micro-scale fracture

Considering the growing research interest in phase-field models for single- and multi-scale fracture, the development of such model was pursued. Conveniently, phase-field approaches share relevant computational similarities with gradient-enhanced nonlocal damage: both require the coupling of an additional Helmholtz equation with the underlying mechanical problem. Therefore, the same staggered solution scheme was employed to implement a phase-field model for brittle and quasi-brittle materials.

Although the developed phase-field model was limited to macro-scale analysis, some preliminary tests with microstructural models were performed, to showcase the potential of this approach in the context of high-fidelity multi-scale modelling of damage and fracture for complex heterogeneous materials.

1.3 Contributions

Attending to the context, motiavtion and main goals of this dissertation, discussed in the previous sections, its main scientific findings are highlighted in the following, as having advanced on the existing state-of-the-art:

1. *An assessment of macro-regularisation effects with second-order computational homogenisation:* the mesh dependency of FE^2 predictions obtained with multi-scale models based on first- and second-order homogenisation are extensively analysed. The relationship between mesh-dependent effects at the micro- and macro-scales is addressed, while also studying the impact of the RVE length, the numerical parameter for second-order macro-regularisation, on the resulting FE^2 response.

2. *Establishing a connection between single-scale nonlocal damage models and second-order multi-scale approaches:* an optimisation-based numerical procedure is employed to relate the numerical parameters for macro-regularisation with single-scale nonlocal models and multi-scale second-order approaches. The limits for establishing this parallel are discussed, as well as the ability of macroscopic nonlocal models to replicate the second-order FE^2 response.

3. *A numerical assessment of integral type and gradient-enhanced nonlocal models for ductile failure:* a systematic comparison between the two nonlocal approaches is performed, with particular emphasis on computational aspects. The structural responses predicted by both strategies for the same values of the nonlocal length parameter are analysed, including the global mechanical behaviour and also the resultiong damage, strain and stress distributions.

Given the scientific relevance of these studies, the preparation of journal articles presenting their methodology, analyses and conclusions is another outcome of this dissertation.

Moreover, throughout the development of this dissertation, several contributions have been made to the in-house implicit finite element code for multi-scale problems, LINKS (Large Strain Implicit Non-linear Analysis of Solids Linking Scales, see Figure 1.1). LINKS has been continuously developed by members of the CM2S (Computational Multi-scale Modelling of Solids and Structures) research group throughout the past decade, and allows the single- and multi-scale simulation of path-dependent heterogeneous materials at large strains. As aforementioned, it has been recently extended to address thermomechanical problems with a staggered solution scheme.To underscore the complex programming tasks involved in this work and its various parts, the main contributions to LINKS are listed in what follows:

1. **Single-scale nonlocal damage of integral type**: the pre-existing implementation of the integral type nonlocal model at the micro-scale was revisited and improved. Thereafter, this nonlocal model was extended for macro-scale analysis to allow comparing its macro-mesh regularisation effects to those observed for second-order FE^2. Several numerical procedures were programmed from scratch, while others were adopted from their micro-scale counterparts.

2. **Nonlocal damage of integral type for FE^2 problems**: furthermore, the improved version of the integral nonlocal model for micro-scale problems had to be compatibilised with the existing code structure for FE^2 simulations. This involved various modifications in the main routines for coupled simulations, and a review of parallel computing and the master-slave scheme employed by LINKS to solve multi-scale problems.

3. **Gradient-enhanced nonlocal damage at the macro-scale**: a gradient-enhanced nonlocal damage model was implemented in the recently developed thermomechanics branch of LINKS (Vila-Chã et al., 2023). This code structure allows tackling coupled multi-physics problems with both implicit and explicit staggered solution schemes. In addition, the entire code structure is built upon object-oriented programming principles. With this in mind, the material model and the solution of the nonlocal averaging equation were implemented in an object-oriented manner. It is also worth noting that this coupling scheme had not been used for problems other than thermomechanics before. This task not only allowed a systematic comparison between the two nonlocal models, but also paved the way for the implementation of the phase-field model.

4. **Phase-field models for macro-scale fracture**: lastly, the phase-field model for fracture was implemented in the thermomechanics branch, following the steps taken in the case of the gradient nonlocal model. An additional material model was programmed, and the previous code block for solving the nonlocal damage equation was modified to accomodate the solution of the phase-field balance problem. The implementated phase-field model was validated with benchmark results produced by Navidtehrani et al. (2021a).

Figure 1.1: LINKS logo.

1.4 Dissertation outline

The remainder of this dissertation is split into three separate parts, each one containing various chapters. At the end of the document, the main conclusions and final remarks are included, followed by the references. Hereinafter, a brief summary of each part and chapter is made.

Part I – Theoretical Background

The first part of the dissertation is devoted to the theoretical bases for the studies and numerical analyses presented in subsequent parts. Appropriate literature reviews are given in this part, regarding most of the building blocks of this work, including: first- and second-order continuum formulations, the finite element method, multi-scale models based on first- and second-order computational homogenisation, gradient-enhanced and integral type nonlocal damage models, and phase-field fracture.

– Chapter 2 – Continuum Mechanics and the Finite Element Method

This chapter addresses continuum mechanics, particularly its first- and second-order formulations, starting from the definition of the generic motion of an arbitrary deformable body to arrive at the strong and weak form statements of the governing equations. A brief summary of constitutive theory is also included. The spatial and time discretisation of the balance equations with the finite element method is described, with the adoption of the Newton-Raphson method for the solution of the nonlinear problem.

– Chapter 3 – Multi-Scale Models Based on Computational Homogenisation

The third chapter concerns multi-scale models based on computational homogenisation. The main concepts of computational homogenisation are addressed, while also comparing it to alternative scale-bridging frameworks. First- and second-order formulations are extensively discussed and derived. A particular second-order homogenisation strategy for porous RVEs is also presented. Lastly, some notions on the numerical solution of multi-scale (FE^2) balance problems are introduced.

– Chapter 4 – Damage and Fracture Mechanics

The final theoretical chapter adresses the main damage models considered in the context of this dissertation. A short summary of the distinctions between continuum damage and fracture mechanics is presented, before tackling the problem of pathological mesh dependency. Thereafter, the theoretical formulations of integral type and gradient-based nonlocal models are introduced. Finally, a generalised form of the phase-field approach to fracture is derived, after discussing its basic concepts.

Part II – Second-Order Homogenisation and Nonlocal Damage of Integral Type

The second part of this dissertation tackles the relationsthip between macro-scale mesh regularisation with two alernative strategies: a single-scale nonlocal model of integral type, and a multi-scale model based on second-order computational homogenisation. Throughout its three chapters, the limits of this parallel are discussed, emphasising the substantial foundational differences between the two macro-regularisation approaches. That said, this part ends with an assessment of their similarities with regard to macro-regularisation effects, by attempting to relate the value of the numerical parameters employed by each strategy for mesh regularisation: the nonlocal radius (single-scale) and the RVE length (multi-scale).

– Chapter 5 – Implementing Nonlocal Damage of Integral Type

This chapter presents the formulation and numerical treatment of the nonlocal model of integral type, while also describing its implementation in LINKS. The numerical integration algorithm is detailed and the linearisation of the nonlocal damage model is shown. Several examples demonstrate the consistency of the implementation and showcase the desired macro-mesh regularisation.

– Chapter 6 – Macro-Scale Regularisation with Second-Order Homogenisation

This chapter includes the systematic analysis of multi-scale modelling of softening and ductile damage, with the use of porous RVEs and first- and second-order homogenisation. The use of RVEs with voids as damage precursors is related to the microscopic mechanisms of ductile failure, and a few preliminary micro-mechanical studies are conducted with both local and nonlocal damage models. The FE^2 responses resulting from the adoption of first- and second-order homogenisation are compared, also for local and nonlocal damage at the RVE level. The impact of the RVE length on both the macro-regularisation effects and the overall mechanical response of materials is discussed.

– Chapter 7 – Relating Nonlocal Damage of Integral Type and Second-Order Homogenisation

The last chapter of Part II presents a novel optimisation-based approach to relate the macro-scale regularisation effects observed with nonlocal damage of integral type (Chapter 5) and the second-order multi-scale model (Chapter 6). A two-step methodology is employed to relate the two numerical regularisation parameters, the nonlocal radius and the RVE length, through an inverse identification scheme.

Part III – Gradient-Enhanced Nonlocal Damage and Phase-Field Fracture

The last part of this dissertation is comprised of two chapters, containing the implementation of the gradient-enhanced nonlocal damage model and the phase-field model for fracture. Taking advantage of the computational aspects shared between these two models, the staggered solution scheme for thermomechanical problems presented in Vila-Chã et al. (2023) was utilised.

– Chapter 8 – Implementing Gradient-Enhanced Nonlocal Damage

This chapter includes a comprehensive presentation on the numerical treatment of the gradient-enhanced nonlocal model, in the context of the adopted staggered scheme, starting from the finite element discretisation of the balance equations. The implementation of the material model and the damage averaing problem with an object-oriented approach is detailed. Thereafter, various numerical examples are shown to demonstrate the model's consistency and effectiveness. A preliminary assessment of particular aspects of the coupling scheme is also presented. Lastly, a practical comparison between integral and gradient nonlocal models is performed.

– Chapter 9 – Implementing Phase-Field Fracture Towards Multi-Scale Modelling of Damage

The nineth chapter presents the implementation of the phase-field model for fracture, including the finite element discretisation of the balance equations and their solution with the staggered solution scheme. A benchmark example from the literature is employed to validate the implementation, after which a few numerical studies are carried out. Finally, preliminary macro-scale simulations of composite RVEs are shown to demonstrate the potential of the phase-field approach in the context of multi-scale damage and fracture modelling.

Conclusions and Final Remarks

The main findings and accomplishments of this dissertation are summarised and reported in this concluding chapter, along with the planned future works.

Part I

Theoretical Background

CHAPTER 2

CONTINUUM MECHANICS AND THE FINITE ELEMENT METHOD

2.1 Preliminaries

This introductory chapter is dedicated to the fundamental principles governing the mechanical behaviour of continua under finite deformations, and also their numerical treatment. Sections 2.2 to 2.6 include a brief presentation of continuum mechanics and its main principles, starting with the continuum approximation and the kinematics of deformation, before assessing the typical force and stress measures, the equations of energy and momentum balance and the main concepts of constitutive theory. Thereafter, several sections are devoted to the presentation of the Finite Element Method (FEM) as the numerical tool for the solution of continuum mechanics problems. The main steps for the formulation of the discretised finite element equilibrium problem are assessed, starting from the establishment of the weak form balance statement in Section 2.7, in its different descriptions. Then, the quasi-static initial boundary value problem is presented in Section 2.8, after which the application of the finite element method and its fundamental concepts are discussed in Section 2.9. Finally, some relevant concepts on the mechanics of second-order continua are introduced in Section 2.10.

These sections follow the systematic approach taken by de Souza Neto et al. (2008). For further details on continuum mechanics and the finite element method, the interested reader can find extensive literature on these topics (see Bonet and Wood (1997), Holzapfel (2000), Oñate (2009), Tadmor et al. (2011), de Borst et al. (2012), Oñate (2013), Belytschko et al. (2014), Zienkiewicz et al. (2014) and Bonet et al. (2016)). Finally, higher-order theories, proposed in the pioneering contributions like the works of Cosserat and Cosserat (1909), Mindlin and Eshel (1968), Mindlin (1964), Toupin (1964), are extensively reviewed in Bertram (2017). The reader with particular interest in second-order continuum theories and their applications is referred to the works of Rodrigues Lopes (2019), Rodrigues Lopes and Andrade Pires (2021).

2.2 The continuum approximation

Throughout the past century, most of the progress in material modelling has been achieved by focusing on the physics of phenomenological descriptions at a particular length-scale. A key divide within phenomenological mechanical theories is the assumption of the *continuum approximation*.

On the one hand, discrete mechanical models treat matter as groups of individual particles or molecules, and are usually employed to treat the mechanics of low length- and time-scales. Since the 1990s, the computational modelling of material behaviour at such length-scales has intensified, with the growing popularity of advanced models like: *Density Functional Theory* (Becke, 1992, Geerlings et al., 2003, Grimme et al., 2011, Runge and Gross, 1984) for numerical predictions of atomic potentials, *Molecular Dynamics* (Ackbarow et al., 2007, Fermi et al., 1955, Stuart et al., 2000, Zhang et al., 2021) for the simulation of interactions at the atomic and molecular level, and *Coarse-grained Methods* (Groot and Warren, 1997, Rudd and Broughton, 1998) for the simulation of large molecular chains. In the context of mechanical engineering, some applications of these models have also been demonstrated, for instance, in the generation of statistically representative microstructural models (Li et al., 2018, Salnikov et al., 2015, Vila-Chã et al., 2021), the study of the fracture behaviour of cross-linked polymers (Meng et al., 2016, Vu-Bac et al., 2015), or the assessment of the structural response of nano-materials (Maekawa and Itoh, 1995, Wolf et al., 2005), including *Carbon Nanotubes* (Griebel and Hamaekers, 2004, Han and Elliott, 2007).

On the other hand, the continuum mechanics approach, based on the assumption of the continuum approximation, is an extremely powerful tool for the accurate description of the physical behaviour of matter at the macroscopic scale, without the need for detailed knowledge of its underlying micro- or nano-scopic structure (Bonet and Wood, 1997, de Souza Neto et al., 2008, Holzapfel, 2000). In essence, the continuum approximation postulates that a given body, $\mathscr{B}$, can be treated as a continuous distribution of material (see Figure 2.1), assuming that its dimensions are much larger than to interatomic or intermolecular distances[1]. Therefore, the complex structure of matter at lower length-scales is conceptually homogenised, and the continuum is treated as a group of material particles, $\boldsymbol{p}$. These material particles are defined as a cluster of molecules, and its physical behaviour is the consequence of the collective contribution of such molecules.

In the past decades, scientists and engineers have developed numerous high-fidelity continuum models, that allow describing the behaviour of several classes of materials for numerous operating conditions, and also for different length-scales. Throughout Chapters 3 and 4, some examples of the complex models that have been formulated within continuum mechanics and its assumptions are detailed.

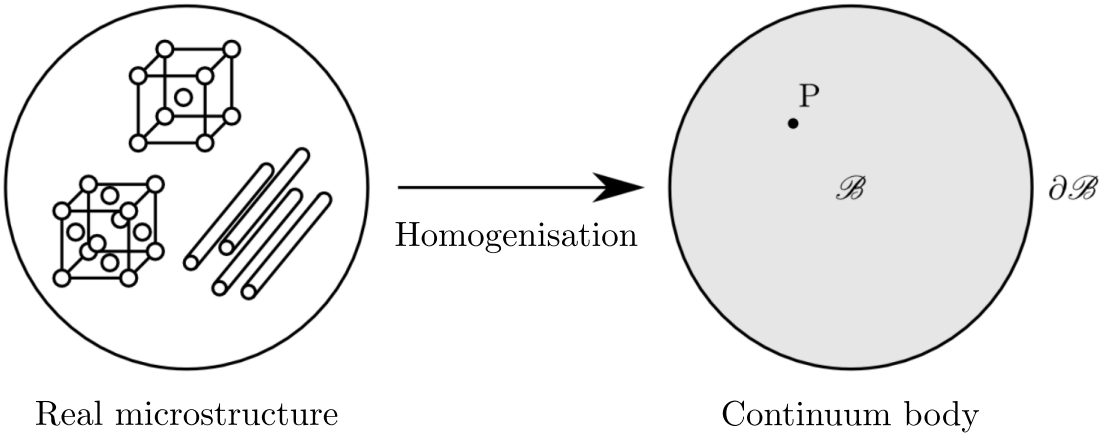

Figure 2.1: Schematic representation of the continuum approximation, adapted from Ferreira (2017).

[1]The continuum approximation can usually be assumed for lengths above 10 microns (10^{-5} m) (Matouš et al., 2017).

2.3 Kinematics of deformation

Let $\mathscr{B}$ be a body occupying an open region Ω of the three-dimensional Euclidian space $\mathscr{E}$, with a regular boundary $\partial\Omega$ in its *reference* configuration. Then, let $\boldsymbol{\varphi}$ be a one to one function that defines the *deformation* of the said body, $\mathscr{B}$, such that

$$\boldsymbol{\varphi} : \Omega \rightarrow \mathscr{E}. \tag{2.1}$$

This function, hence, defines the position of each material particle, $\boldsymbol{p}$, of $\mathscr{B}$ into the point

$$\boldsymbol{x} = \boldsymbol{\varphi}(\boldsymbol{p}), \tag{2.2}$$

where the said particle would be positioned in the *deformed* configuration of $\mathscr{B}$. Figure 2.2 depicts the generic deformation of a physical body. The region of $\mathscr{E}$ occupied by $\mathscr{B}$ will be denoted $\boldsymbol{\varphi}(\Omega)$. The displacement field, $\boldsymbol{u}$, will be a vector field defined by

$$\boldsymbol{u}(\boldsymbol{p}) = \boldsymbol{\varphi}(\boldsymbol{p}) - \boldsymbol{p}. \tag{2.3}$$

With that in mind, the position, $\boldsymbol{x}$, of a given material particle, $\boldsymbol{p}$, in the deformed configuration of

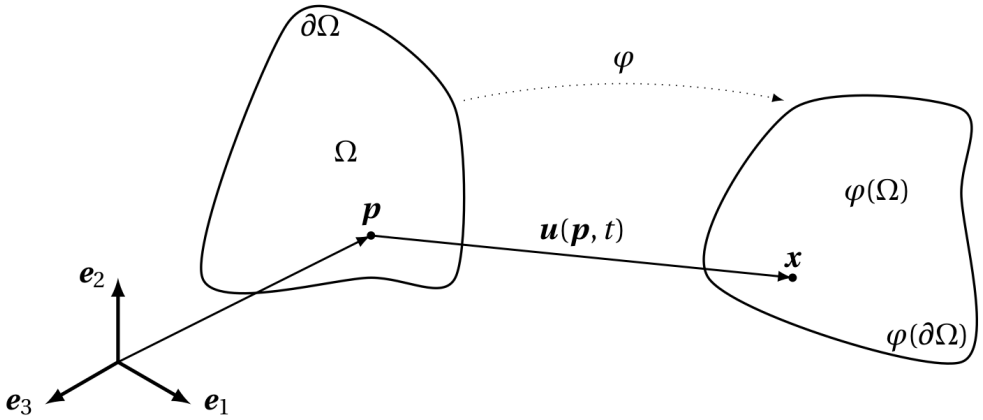

Figure 2.2: Generic deformation of a body, taken from Coelho (2019).

$\mathscr{B}$ can be recast as

$$\boldsymbol{x} = \boldsymbol{p} + \boldsymbol{u}(\boldsymbol{p}). \tag{2.4}$$

These notions can be used to describe the *motion* of a given body $\mathscr{B}$: its time-dependent deformation. The body's motion can be expressed as

$$\boldsymbol{\varphi} = \Omega \times \mathscr{B} \rightarrow \mathscr{E}, \tag{2.5}$$

where, for each instant, t, in a given interval of time, the map $\boldsymbol{\varphi}(\cdot, t)$ is a deformation of $\mathscr{B}$. During the motion $\boldsymbol{\varphi}$ of a material particle, $\boldsymbol{p}$, its position $\boldsymbol{x}$ at a given instant in time, t, is given by

$$\boldsymbol{x} = \boldsymbol{\varphi}(\boldsymbol{p}, t). \tag{2.6}$$

Furthermore, the region of $\mathscr{E}$ occupied by the body $\mathscr{B}$ at the instant t can be expressed as

$$\boldsymbol{\varphi}(\Omega, t), \tag{2.7}$$

while the displacement field of the motion can be written as

$$\boldsymbol{\varphi}(\boldsymbol{p}, t) = \boldsymbol{p} + \boldsymbol{u}(\boldsymbol{p}, t). \tag{2.8}$$

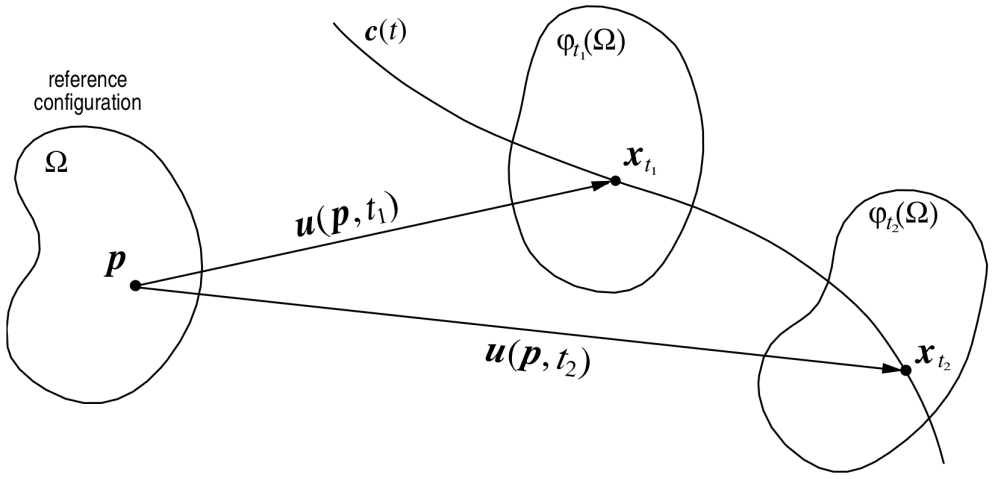

Figure 2.3: Generic motion of a body, taken from de Souza Neto et al. (2008).

The parametric curve, $\boldsymbol{c}(t)$, defined as:

$$\boldsymbol{c}(t) = \boldsymbol{\varphi}(\boldsymbol{p}, t), \tag{2.9}$$

describes the *trajectory* of a material particle, $\boldsymbol{p}$, during motion, as is depicted in Figure 2.3. For a given motion $\boldsymbol{\varphi}$, the *velocity* of a material particle, $\boldsymbol{p}$, is given by:

$$\dot{\boldsymbol{x}}(\boldsymbol{p}, t) = \frac{\partial \boldsymbol{\varphi}(\boldsymbol{p}, t)}{\partial t}. \tag{2.10}$$

Additionally, at each given time, t, the map $\boldsymbol{\varphi}(\cdot, t)$ is a one-to-one function, hence invertible. That being the case, the original material points can be expressed in terms of the position they occupy at a specific instant as

$$\boldsymbol{p} = \boldsymbol{\varphi}^{-1}(\boldsymbol{x}, t) = \boldsymbol{x} - \boldsymbol{u}(\boldsymbol{\varphi}^{-1}(\boldsymbol{x}, t), t). \tag{2.11}$$

The $\boldsymbol{\varphi}^{-1}$ map is called the reference map. Using this map, the velocity of a given material particle can be redefined as

$$\boldsymbol{v}(\boldsymbol{x}, t) = \dot{\boldsymbol{x}}(\boldsymbol{\varphi}^{-1}(\boldsymbol{x}, t), t). \tag{2.12}$$

This is the *spatial velocity* field, which yields the velocity of the material particle occupying x at time t. Even though both fields, $\boldsymbol{v}$ and $\dot{\boldsymbol{x}}$, represent the velocity of a material particle, they have different arguments. While $\dot{\boldsymbol{x}}$ has the material particle and time as arguments, $\boldsymbol{v}$ has spatial position and time. This motivates the following definitions: Let a general time-dependent (scalar, vectorial or tensorial) field α be defined over the body $\mathscr{B}$. If the domain of α is $\Omega \times \mathscr{B}$, i. e., if the value of α is expressed as a function of material particles and time, then α is said to be a *material field*. On the other hand, if its domain is $\boldsymbol{\varphi}_t(\Omega) \times \mathscr{B}$, then α is said to be a *spatial field*. Material and spatial fields also refer to different physical configurations. In a material description of a given field, the material body's motion is described with regards to its reference configuration. In a spatial description, however, the motion is described with the regards to fixed points in space, spatial positions, hence referring to a spatial configuration.

2.3.1 Deformation gradient

The *deformation gradient* of the motion $\boldsymbol{\varphi}$ is the second-order tensor $\boldsymbol{F}$ defined by

$$\boldsymbol{F}(\boldsymbol{p}, t) = \nabla_{\boldsymbol{p}}(\boldsymbol{\varphi}(\boldsymbol{p}, t)) = \frac{\partial \boldsymbol{x}_t}{\partial \boldsymbol{p}}, \tag{2.13}$$

where $\nabla_{\boldsymbol{p}}(\cdot)$ is the material divergence operator. This tensor can also be written as

$$\boldsymbol{F} = \boldsymbol{I} + \nabla_{\boldsymbol{p}} \boldsymbol{u}. \tag{2.14}$$

Figure 2.4 depicts the relative positions of two neighbouring particles before and after deformation. Their initial positions are $\boldsymbol{p}$ and $\boldsymbol{p}+\mathrm{d}\boldsymbol{p}$, in a generic continuum body $\mathscr{B}$. After motion, the positions of these two particles are $\boldsymbol{x}$ and $\boldsymbol{x}+\mathrm{d}\boldsymbol{x}$. That being the case, the cartesian components of $\boldsymbol{F}$ can be deduced as

$$F_{ij} = \frac{\partial x_i}{\partial p_j} = \delta_{ij} + \frac{\partial u_i}{\partial p_j}. \tag{2.15}$$

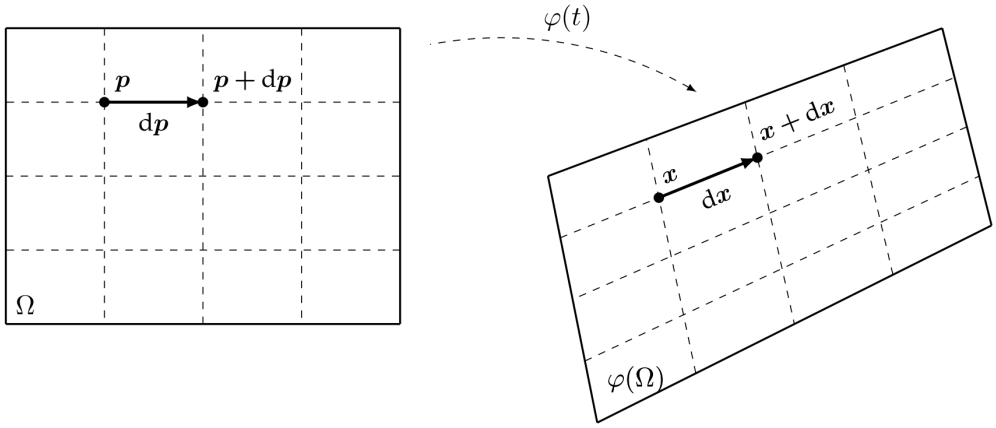

Figure 2.4: Deformation of two neighbouring material particles and its relation to the deformation gradient, taken from Coelho (2019).

Figure 2.5 illustrates the deformation of an infinitesimal volume element, within the larger deformation of the body $\mathscr{B}$. The infinitesimal volume, $\mathrm{d}v_0$, is defined by the infinitesimal vectors $\mathrm{d}\boldsymbol{a}$, $\mathrm{d}\boldsymbol{b}$ and $\mathrm{d}\boldsymbol{c}$, associated with a material particle $\boldsymbol{p}$ in the reference configuration.

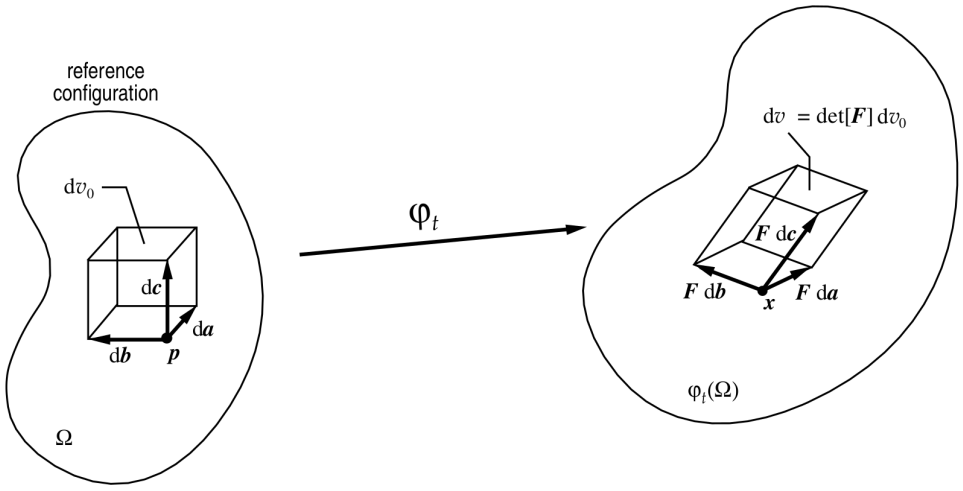

Figure 2.5: Deformation of an infinitesimal volume element and its relation to the deformation gradient, taken from de Souza Neto et al. (2008).

In the reference configuration, the infinitesimal volume element can be defined through the triple product

$$\mathrm{d}v_0 = (\mathrm{d}\boldsymbol{a} \times \mathrm{d}\boldsymbol{b}) \cdot \mathrm{d}\boldsymbol{c}. \tag{2.16}$$

In the deformed configuration, $\boldsymbol{\varphi}_t$ maps the infinitesimal vectors into $\boldsymbol{F}\mathrm{d}\boldsymbol{a}$, $\boldsymbol{F}\mathrm{d}\boldsymbol{b}$ and $\boldsymbol{F}\mathrm{d}\boldsymbol{c}$. Consequently, infinitesimal volume element in the deformed configuration can be expressed as

$$\mathrm{d}v = (\boldsymbol{F}\mathrm{d}\boldsymbol{a} \times \boldsymbol{F}\mathrm{d}\boldsymbol{b}) \cdot \boldsymbol{F}\mathrm{d}\boldsymbol{c}. \tag{2.17}$$

With this in mind, it follows that

$$J \equiv \det\boldsymbol{F} = \frac{\mathrm{d}v_0}{\mathrm{d}v}. \tag{2.18}$$

i.e. the determinant of the deformation gradient represents, locally, the ratio of volume change. Consequently, if the determinant of the deformation gradient, denoted as $\det\boldsymbol{F}$ or J, were to be null, the infinitesimal volume would collapse into a material particle. Such a scenario is deemed physically unacceptable, as the deformation map must maintain a one-to-one correspondence, preventing the body from self-intersecting. Therefore, in any deformed configuration of a body, J must satisfy

$$J > 0. \tag{2.19}$$

2.3.2 Isochoric and volumetric deformations

Any deformation can be locally decomposed into a purely *isochoric*, $\boldsymbol{F}_{\mathrm{iso}}$, i.e. volume-preserving, deformation and a purely *volumetric*, $\boldsymbol{F}_{\mathrm{vol}}$, deformation, as is illustrated in Figure 2.6. Therefore, the deformation gradient can also be decomposed as

$$\boldsymbol{F} = \boldsymbol{F}_{\mathrm{iso}}\boldsymbol{F}_{\mathrm{vol}} = \boldsymbol{F}_{\mathrm{vol}}\boldsymbol{F}_{\mathrm{iso}}. \tag{2.20}$$

These two types of deformation can be defined as follows:

1. In an *Isochoric Deformation*, as was previously stated, the volume of the deformed body remains constant, i.e. only shape distortion is present. In a deformation of this sort, $J = 1$.

2. A *Volumetric Deformation* consists of uniform contraction/expansion - only volume change is present. That being the case, the deformation gradient of any volumetric deformation is a spherical tensor

$$\boldsymbol{F}_{\mathrm{vol}} = \alpha\boldsymbol{I}, \tag{2.21}$$

where α is the corresponding contraction/expansion ratio.

With this decomposition in mind, the local rate of volume change, expressed in Equation (2.18), can be recast as

$$J = \det(\boldsymbol{F}_{\mathrm{vol}}) = \det(\alpha\boldsymbol{I}) = \alpha^3, \tag{2.22}$$

since the isochoric component of the deformation gradient has no contribution to volume changes. From this relation, one can derive the following expression for the volumetric component:

$$\boldsymbol{F}_{\mathrm{vol}} = (J)^{1/3}\boldsymbol{F}. \tag{2.23}$$

Finally, with Equation (2.20) in mind, the isochoric component can be rewritten as

$$\boldsymbol{F}_{\mathrm{iso}} = (J)^{-1/3}\boldsymbol{F}. \tag{2.24}$$

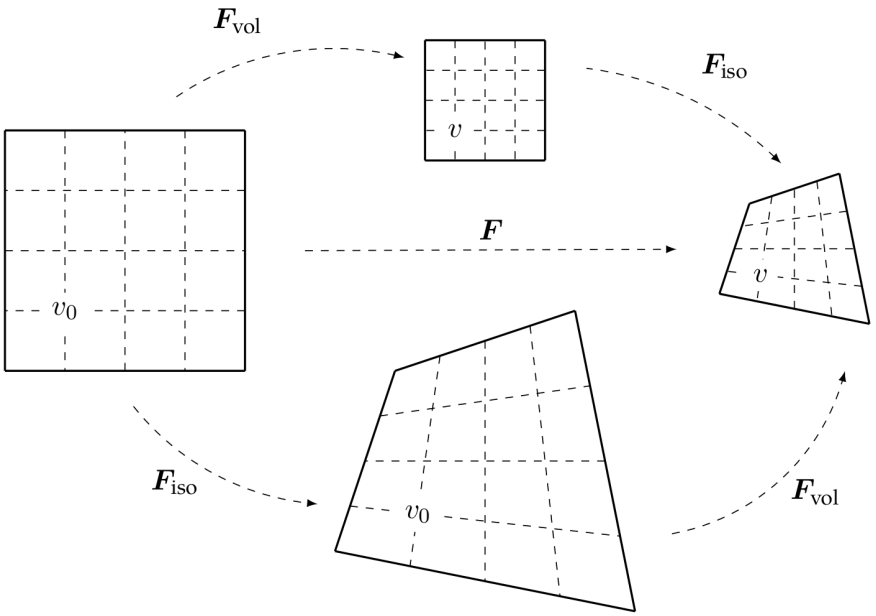

Figure 2.6: Schematic representation of the isochoric and volumetric components of the deformation gradient, taken from Coelho (2019).

2.3.3 Polar decomposition of the deformation gradient

The deformation gradient might also be deconstructed into *pure stretch* and *pure rotation* components. In other words, the deformation gradient can be divided into *deformed* and *undeformed* components. The *polar decomposition theorem* states that

$$\boldsymbol{F} = \boldsymbol{R}\boldsymbol{U} = \boldsymbol{V}\boldsymbol{R}, \tag{2.25}$$

where $\boldsymbol{R}$ is the proper orthogonal tensor, denoting local rotation, and $\boldsymbol{U}$ and $\boldsymbol{V}$ are symmetric positive definite tensors, the right and left stretch tensors, respectively. Analogously, these tensors are associated with the right and left decompositions of the deformation gradient. Additionally, the stretch tensors are related by the rotation as follows:

$$\boldsymbol{V} = \boldsymbol{R}\boldsymbol{U}\boldsymbol{R}^T. \tag{2.26}$$

Furthermore, these stretch tensors can also be expressed as

$$\boldsymbol{U} = \sqrt{\boldsymbol{C}}, \quad \boldsymbol{V} = \sqrt{\boldsymbol{B}}, \tag{2.27}$$

where $\boldsymbol{C}$ and $\boldsymbol{B}$ are the right and left *Cauchy-Green strain tensors*. These and other strain measures are introduced in the Section 2.3.4. Figure 2.7 depicts the right and left polar decompositions of the deformation gradient.

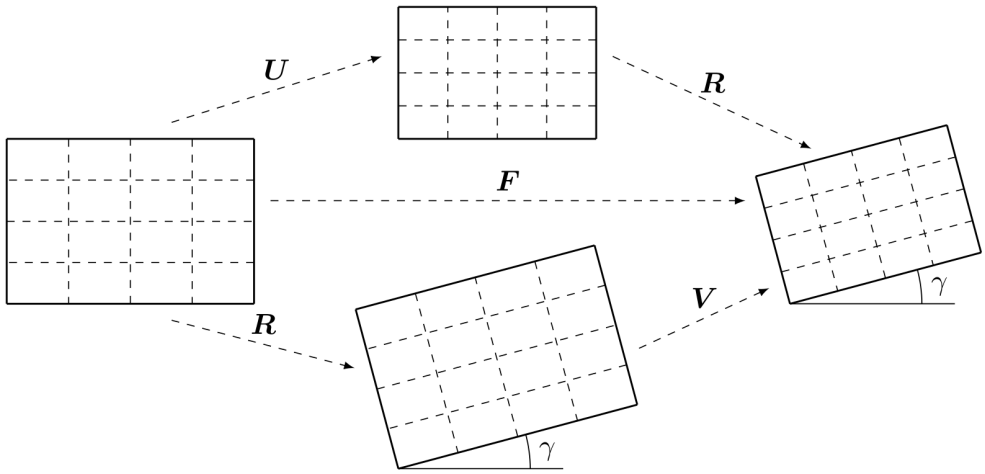

Figure 2.7: Schematic representation of the right and left polar decompositions of the deformation gradient, taken from Coelho (2019).

2.3.4 Strain measures

In this subsection, the main strain measures utilised in the context of continuum mechanics are assessed. Firstly, the right and left Cauchy-Green strain tensors, previously mentioned when discussing the polar decomposition of the deformation gradient, are defined as

$$\begin{aligned} \boldsymbol{C} &= \boldsymbol{U}^2 = \boldsymbol{F}^T\boldsymbol{F}, \\ \boldsymbol{B} &= \boldsymbol{V}^2 = \boldsymbol{F}\boldsymbol{F}^T. \end{aligned} \tag{2.28}$$

The *Green-Lagrange* strain tensor, in turn, is given by

$$\begin{aligned} \boldsymbol{E}^{(2)} &= \frac{1}{2}(\boldsymbol{C}-\boldsymbol{I}) \\ &= \frac{1}{2}[\nabla_p\boldsymbol{u} + (\nabla_p\boldsymbol{u})^T + (\nabla_p\boldsymbol{u})^T\nabla_p\boldsymbol{u}]. \end{aligned} \tag{2.29}$$

If $\boldsymbol{E}^{(2)} = 0$, no deformation occurs, as $\boldsymbol{C} = \boldsymbol{U} = \boldsymbol{I}$, translating into a deformation gradient that is an orthogonal tensor and, hence, rigid body motion. The Green-Lagrange strain tensor, however, is a particular member of the *Lagrangian strain tensor* family, defined by

$$\boldsymbol{E}^{(m)} = \begin{cases} \frac{1}{m}(\boldsymbol{U}^m - \boldsymbol{I}) & m \neq 0 \\ \ln\|\boldsymbol{U}\| & m = 0 \end{cases} \tag{2.30}$$

It is also possible to define the *Eulerian strain tensors*. Based on the *left* stretch tensor, Eulerian strain tensors are defined by

$$\boldsymbol{\varepsilon}^{(m)} = \begin{cases} \frac{1}{m}(\boldsymbol{V}^m - \boldsymbol{I}) & m \neq 0 \\ \ln\|\boldsymbol{V}\| & m = 0. \end{cases} \tag{2.31}$$

These two strain tensor families are related by

$$\boldsymbol{\varepsilon}^{(m)} = \boldsymbol{R}\boldsymbol{E}^{(m)}\boldsymbol{R}^T. \tag{2.32}$$

The Cauchy-Green strain tensors can also be written in terms of the displacement gradient, as

$$\begin{aligned} \boldsymbol{C} &= \boldsymbol{I} + \nabla_p\boldsymbol{u} + (\nabla_p\boldsymbol{u})^T + (\nabla_p\boldsymbol{u})^T\nabla_p\boldsymbol{u}, \\ \boldsymbol{B} &= \boldsymbol{I} + \nabla_p\boldsymbol{u} + (\nabla_p\boldsymbol{u})^T + (\nabla_p\boldsymbol{u})\nabla_p\boldsymbol{u}^T. \end{aligned} \tag{2.33}$$

In many engineering problems, the displacement gradient is assumed to be small enough that the second-order terms of Equation (2.33) may be neglected. In this case, *infinitesimal* or *small deformation theory* is assumed. In such cases, one may write

$$\boldsymbol{C} \approx \boldsymbol{B} \approx \boldsymbol{I} + \nabla_p \boldsymbol{u} + (\nabla_p \boldsymbol{u})^T. \tag{2.34}$$

From this equation, it can be easily shown that, for small strains,

$$\boldsymbol{\varepsilon}^{(m)} \approx \boldsymbol{E}^{(m)} \approx \boldsymbol{\varepsilon}. \tag{2.35}$$

2.3.5 Spatial velocity gradient

The spatial velocity $\boldsymbol{v}$ was defined in Equation (2.12), where its dependence on the current position $\boldsymbol{x}$ is noticeable. To conclude this overview on the kinematics of continua, the spatial velocity gradient, $\boldsymbol{L}$, is briefly assessed. This gradient results from deriving $\boldsymbol{v}$ with respect to the spatial position $\boldsymbol{x}$, which yields

$$\boldsymbol{L} = \nabla_{\boldsymbol{x}}(\boldsymbol{v}) \tag{2.36}$$

Using the chain rule, one can writte

$$\boldsymbol{L} = \frac{\partial}{\partial t}\left(\frac{\partial \varphi}{\partial \boldsymbol{p}}\right)\frac{\partial \boldsymbol{p}}{\partial \boldsymbol{x}} = \dot{\boldsymbol{F}}\boldsymbol{F}^{-1}. \tag{2.37}$$

The velocity gradient is normally separated into its symmetric and skew components. The symmetric part is denoted by $\boldsymbol{D}$ and is often called *stretch rate tensor* or *rate of deformation tensor*; conversely, the skew tensor (hereafter represented by $\boldsymbol{W}$) is referred to as the spin tensor. These tensors are expressed as

$$\begin{aligned} \boldsymbol{D} &= \mathrm{sym}(\boldsymbol{L}) = \frac{1}{2}\left(\boldsymbol{L} + \boldsymbol{L}^T\right), \\ \boldsymbol{W} &= \mathrm{skew}(\boldsymbol{L}) = \frac{1}{2}\left(\boldsymbol{L} - \boldsymbol{L}^T\right). \end{aligned} \tag{2.38}$$

2.4 Forces and stress measures

Thus far, no references have been made to *forces* and how they are transferred within continuous media. Three distinct classes can be defined for the forces acting on a body, depending on their nature:

1. *Boundary Forces*: These forces are applied on the surface or boundary of the body by exterior agents. They can result from the contact with other bodies or fluids, for instance. These forces have units of force per unit area.

2. *Body Forces*: These forces are exerted in the interior of the body. Classical examples of boundary forces are gravitational and magnetic forces. The units of Body Forces are force per unit mass or force per unit volume.

3. *Interior Forces*: These are the internal interactions between adjacent parts of a body, which are transmitted across the surface that separates them. They are of central importance in regards to structural and mechanical problems and their units are force per unit area.

Therefore, boundary forces and interior forces are essentially of the same nature, and are often collectively referred to as *surface forces*. The concept of *stress* arises from the need to describe surface forces mathematically.

2.4.1 Cauchy stress tensor

Consider a point $\boldsymbol{x}$ on a surface with a normal unit vector $\boldsymbol{n}$. The traction force $\boldsymbol{t}$ is given by

$$\boldsymbol{t}(\boldsymbol{x},\boldsymbol{n},t) = \boldsymbol{\sigma}(\boldsymbol{x},t)\cdot\boldsymbol{n}, \tag{2.39}$$

where the second order tensor $\boldsymbol{\sigma}(\boldsymbol{x},t)$ is the Cauchy stress tensor. Equation (2.39) is schematically illustrated in Figure 2.8.

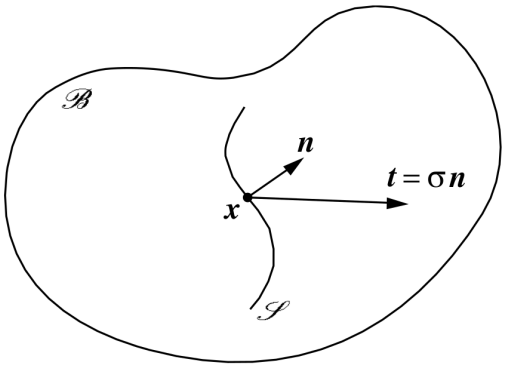

Figure 2.8: Representation of the Cauchy stress tensor, taken from de Souza Neto et al. (2008).

This tensor is often called the real stress tensor, as it is defined in the deformed configuration of the solid and it is also a *symmetric* tensor,

$$\boldsymbol{\sigma} = \boldsymbol{\sigma}^T. \tag{2.40}$$

Furthermore, the Cauchy stress tensor can be written in terms of an orthonormal basis $\{e_1,e_2,e_3\}$:

$$\boldsymbol{\sigma} = \sigma_{ij}\, e_i \otimes e_j \tag{2.41}$$

and its components can be expressed as

$$\sigma_{ij} = (\boldsymbol{\sigma} e_i)\cdot e_j, \tag{2.42}$$

where the vector $\boldsymbol{\sigma} e_i$ is the force per unit area exerted across a surface whose unit vector is e_i. This component of the Cauchy stress tensor, σ_{ij}, is the magnitude of the projection of $\boldsymbol{\sigma} e_i$ in the direction of e_j. In an arbitray infinitesimal cube, as represented in Figure 2.9, the stress components σ_{11}, σ_{22} and σ_{33} represent the tractions normal to its faces. On the other hand, the components σ_{12}, σ_{13}, σ_{21}, σ_{23}, σ_{31} and σ_{32} are the shear tractions acting parallel to the faces.

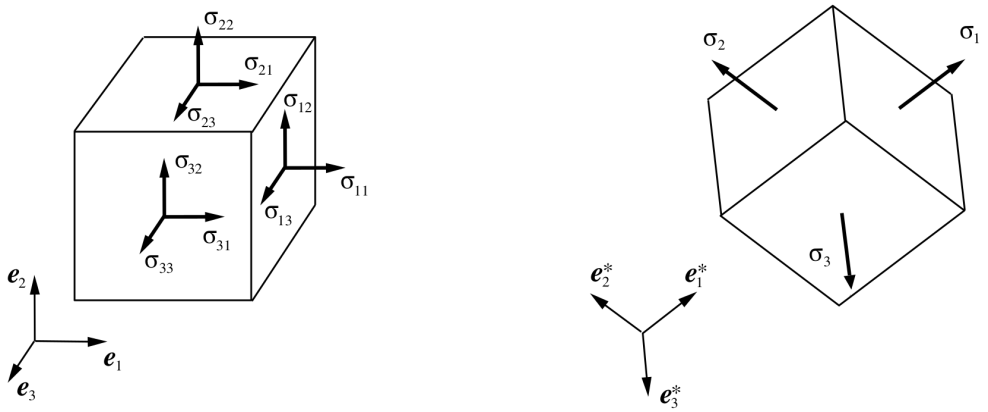

Figure 2.9: Cauchy stress components and principal stresses, taken from de Souza Neto et al. (2008).

Due to the symmetry of the Cauchy stress tensor, there exists an orthonormal basis $\{e_1^*, e_2^*, e_3^*\}$, for which all the shear components of the tensor vanish. The normal components, σ_i^*, are the eigenvalues of $\boldsymbol{\sigma}$ and are called the *Principal Cauchy stresses*. The directions defined by the basis $\{e_1^*, e_2^*, e_3^*\}$ are named the *principal stress directions*, and are also depicted in Figure 2.9.

2.4.2 Deviatoric and hydrostatic stress components

It is often convenient, particularly for the purpose of constitutive modelling, to split the stress tensor $\boldsymbol{\sigma}$ into the sum of a *spherical* and *traceless* component

$$\boldsymbol{\sigma} = \boldsymbol{s} + p\boldsymbol{I}, \tag{2.43}$$

where the invariant

$$p \equiv \frac{1}{3} I_1(\boldsymbol{\sigma}) = \frac{1}{3} \mathrm{tr}\boldsymbol{\sigma} \tag{2.44}$$

is the *hydrostatic pressure*, also referred to as *hydrostatic stress* or *mean stress*, and

$$\boldsymbol{s} \equiv \boldsymbol{\sigma} - p\boldsymbol{I} = \mathbf{I}_d : \boldsymbol{\sigma}, \tag{2.45}$$

where $\mathbf{I}_d$ is a fourth-order traceless tensor, named the *deviatoric stress* or *stress deviator*. The tensor

$$p\boldsymbol{I} = \frac{1}{3}(\boldsymbol{I} \otimes \boldsymbol{I}) : \boldsymbol{\sigma} \tag{2.46}$$

is called the *spherical stress tensor*. Similarly to the isochoric/volumetric decomposition of a deformation phenomena, the hydrostatic component of the stress tensor is associated with the uniform traction/compression of a solid, whereas the deviatoric component of the stress tensor is associated to its distortion.

2.4.3 First Piola-Kirchhoff stress tensor

The first Piola-Kirchhoff stress tensor is an alternative representation of the stress state. In the definition of the Cauchy stress tensor, the traction vector, $\boldsymbol{t}$, that measures the force exerted across a material surface per unit *deformed* area, was defined. Its counterpart $\boldsymbol{t}_0$, which measures, the force that acts across any surface per unit *reference* area, at the point of interest, is crucial for the formulation of the First Piola-Kirchhoff stress tensor. These traction vectors are related by

$$\boldsymbol{t}_0 = \frac{\mathrm{d}a}{\mathrm{d}a_0} \boldsymbol{t}, \tag{2.47}$$

where $\mathrm{d}a$ and $\mathrm{d}a_0$ are the infinitesimal area elements normal to unit vectors $\boldsymbol{n}$ and $\boldsymbol{n}_0$. These vectors are established in the deformed and reference configuration, respectively, i.e. $\mathrm{d}a_0$ is the material counterpart of $\mathrm{d}a$. Using Equation (2.39), the previous equation may be recast as

$$\boldsymbol{t}_0 = \frac{\mathrm{d}a}{\mathrm{d}a_0} \boldsymbol{\sigma}\boldsymbol{n}, \tag{2.48}$$

which yields

$$\boldsymbol{t}_0 = J\boldsymbol{\sigma}\boldsymbol{F}^T\boldsymbol{n}_0. \tag{2.49}$$

As a result, the first Piola-Kirchhoff is defined by

$$\boldsymbol{P} = J\boldsymbol{\sigma}\boldsymbol{F}^T, \tag{2.50}$$

In essence, what separates the First Piola-Kirchhoff stress tensor from the Cauchy stress tensor is the fact that, while the former is not entirely a material entity, as a tensor, it has one index attatched to the deformed configuration and another attatched to the reference configuration. This is the reason for this tensor to be generally unsymmetric. Adding to this, like the deformation gradient, $\boldsymbol{F}$, the first Piola-Kirchhoff stress tensor is a two-point tensor, which relates the current force to the original undeformed area.

2.4.4 Second Piola-Kirchhoff stress tensor

The Second Piola-Kirchhoff stress tensor can be defined as

$$\boldsymbol{S} = J\boldsymbol{F}^{-1}\boldsymbol{\sigma}\boldsymbol{F}^{-\top}. \tag{2.51}$$

It is worth noting that similarly to the Cauchy stress tensor, the second Piola-Kirchhoff stress tensor is also symmetric.

2.4.5 Kirchhoff stress tensor

Lastly, the Kirchhoff stress tensor, $\boldsymbol{\tau}$, is defined by

$$\boldsymbol{\tau} = J\boldsymbol{\sigma}. \tag{2.52}$$

Note that the Kirchhoff stress tensor is also symmetric, and its components are frequently obtained using Cauchy principal stresses.

2.5 Fundamental principles of thermodynamics

The strain and stress measures presented in previous sections, on their own, are not enough to construct a model that correctly describes the behaviour of a continuum body. To construct such model, its foundations, the universal laws that must be abided by, are needed. The fundamental laws that govern the behaviour of every continuum body are presented in this section.

2.5.1 Conservation of mass

The principle of mass conservation states that

$$\dot{\rho} + \rho \mathrm{div}_x(\dot{\boldsymbol{u}}) = 0, \tag{2.53}$$

where ρ denotes the mass per unit volume in the deformed configuration, $\dot{\rho}$ is its derivative with respect to time and $\mathrm{div}_x(\cdot)$ is the spatial divergence operator.

2.5.2 Momentum equilibrium

Considering the deformed configuration, the conservation of linear momentum can be expressed by

$$\begin{cases} \mathrm{div}_x\boldsymbol{\sigma} + \boldsymbol{b} = \rho\ddot{\boldsymbol{u}}, & \text{in } \boldsymbol{\varphi}(\Omega) \\ \boldsymbol{t} = \boldsymbol{\sigma}\boldsymbol{n}, & \text{in } \boldsymbol{\varphi}(\partial\Omega) \end{cases}, \tag{2.54}$$

where $\boldsymbol{b}$ is the body force per unit volume and n is the outward normal to the boundary in the deformed configuration. These equations described what is often referred to as the *strong* or *local* form of the equilibrium and establish a relation between the forces, stresses and displacements of the continuum. The first equation of Eq. (2.54) is also known as Cauchy's equation of motion. The strong form can also be expressed using a material description, such that

$$\begin{cases} \mathrm{div}_p\boldsymbol{P} + \boldsymbol{b}_0 = \rho_0\ddot{\boldsymbol{u}}, & \text{in } \Omega \\ \boldsymbol{t}_0 = \boldsymbol{P}\boldsymbol{n}_0, & \text{in } \partial\Omega \end{cases} \tag{2.55}$$

where $\boldsymbol{b}_0$ is the body force per unit reference volume, ρ_0 is the mass per unit of reference volume and $\boldsymbol{n}_0$ is the outward normal to the boundary in the reference configuration. These quantities can be related to their spatial counterparts through

$$\begin{aligned} \boldsymbol{b}_0 &= J\boldsymbol{b}, \\ \rho_0 &= J\rho. \end{aligned} \tag{2.56}$$

2.5.3 First principle of thermodynamics

The first principle of thermodynamics postulates the *conservation of energy*. Before introducing this principle mathematically, it is convenient to establish the following double contraction

$$\boldsymbol{\sigma} : \boldsymbol{D}, \tag{2.57}$$

which represents the stress power per unit volume in the deformed configuration of a body, where $\boldsymbol{D}$ is the *stretch rate tensor*. The first principle of thermodynamics is mathematically expressed, in the current configuration, as

$$\rho \dot{e} = \boldsymbol{\sigma} : \boldsymbol{D} + \rho r - \mathrm{div}_x \boldsymbol{q}. \tag{2.58}$$

where $\dot{e}$ is the first derivative of the specific internal energy with respect to time, r is the density of heat production and $\boldsymbol{q}$ is the heat flux. In words, the rate of internal energy per unit deformed volume must be equal to the sum of stress power and heat production per unit deformed volume minus the spatial divergence of the heat flux.

2.5.4 Second principle of thermodynamics

The second principle of thermodynamics postulates the *irreversibility of entropy production*. It can be expressed mathematically, in the current configuration, by the expression

$$\rho \dot{s} + \mathrm{div}_x \left[\frac{\boldsymbol{q}}{\theta} \right] - \frac{\rho r}{\theta} \geq 0. \tag{2.59}$$

where $\dot{s}$ is the first derivative of the specific entropy with respect to time and θ is the temperature.

2.5.5 Clausius-Duhem inequality

The combination of the first and second principles of thermodynamics results in the following inequality

$$\rho \dot{s} + \mathrm{div}_x \left[\frac{\boldsymbol{q}}{\theta} \right] - \frac{1}{\theta} (\rho \dot{e} - \boldsymbol{\sigma} : \boldsymbol{D} + \mathrm{div}_x \boldsymbol{q}) \geq 0. \tag{2.60}$$

The introduction of the *specific free energy*, ψ, also known as the *Helmholtz free energy per unit mass*, defined by

$$\psi = e - \theta s, \tag{2.61}$$

along with the identity

$$\rho \dot{s} + \mathrm{div}_x \left[\frac{\boldsymbol{q}}{\theta} \right] = \frac{1}{\theta} \mathrm{div}_x \boldsymbol{q} - \frac{1}{\theta^2} \boldsymbol{q} \cdot \nabla_x \theta, \tag{2.62}$$

into the above fundamental inequality, results in the *Clausius-Duhem Inequality*

$$\boldsymbol{\sigma} : \boldsymbol{D} - \rho \left(\dot{\psi} + s \dot{\theta} \right) - \frac{1}{\theta} \boldsymbol{q} \cdot \boldsymbol{g} \geq 0, \tag{2.63}$$

where the spatial temperature gradient, $\boldsymbol{g}$, is defined as

$$\boldsymbol{g} = \nabla_x \theta. \tag{2.64}$$

The left-hand side of Equation (2.63) represents the dissipation per unit deformed volume. Making use of Equation (2.56), this inequality can be written in terms of the dissipation per unit reference volume as

$$\boldsymbol{\tau} : \boldsymbol{D} - \rho_0 \left(\dot{\psi} + s \dot{\theta} \right) - \frac{J}{\theta} \boldsymbol{q} \cdot \boldsymbol{g} \geq 0. \tag{2.65}$$

2.6 Constitutive theory

The conservation principles stated in Section 2.5 are valid for any continuum body, irrespective of its material. To define the physical behaviour of different materials, *constitutive models* must be introduced. In this section, the concepts that define the constitutive approach adopted in this work are briefly introduced.

2.6.1 Constitutive axioms

In this section, the fundamental principles that must be respected by any constitutive model are assessed. Firstly, the difference between a thermokinetic process and a calorodynamic process of $\mathscr{B}$ must be assessed. According to Truesdell (1984), the former is a pair of functions of fields

$$\boldsymbol{\varphi}(\boldsymbol{p},t) \text{ and } \theta(\boldsymbol{p},t), \tag{2.66}$$

while the latter is a set of functions

$$\boldsymbol{\sigma}(\boldsymbol{p},t), e(\boldsymbol{p},t), s(\boldsymbol{p},t), r(\boldsymbol{p},t), \boldsymbol{b}(\boldsymbol{p},t) \text{ and } \boldsymbol{q}(\boldsymbol{p},t), \tag{2.67}$$

whose fields satisfy momentum balance, as well as both principles of Thermodynamics. Having established the difference btween a thermokinetic and a calordynamic process, the constitutive axioms of thermodynamic determinism, material objectivity and material symmetry may now be presented.

Thermodynamic determinism

In thermodynamics, materials are generally represented by constitutive relations, which must hold the principle of thermodynamically compatible determinism (Truesdell, 1984). Specifically, this axiom postulates the following:

Axiom 1 *For a point $\boldsymbol{p}$ in a given body $\mathscr{B}$ at time t, the history of the thermokinetic process to which it has been subject up to and including the time t determines a calorodynamic process for $\mathscr{B}$ at $\boldsymbol{p}$.*

It is worth noting that, for simple materials, the calorodynamic process of a point $\boldsymbol{p}$ is only function of the history of the thermokinetic process at the same point, that is, of the local history of the thermokinetic process (de Souza Neto et al., 2008). Therefore, there must exist a set of constitutive functionals $\mathfrak{F}$, $\mathfrak{B}$, $\mathfrak{H}$ and $\mathfrak{J}$ of the histories of $\boldsymbol{F}$, θ and $\boldsymbol{g}$ in a point $\boldsymbol{p}$, such that

$$\begin{aligned}
\boldsymbol{\sigma}(\boldsymbol{p},t) &= \mathfrak{F}\left(\boldsymbol{F}^t(\boldsymbol{p}),\theta^t(\boldsymbol{p}),\boldsymbol{g}^t(\boldsymbol{p})\right),\\
\psi(\boldsymbol{p},t) &= \mathfrak{B}\left(\boldsymbol{F}^t(\boldsymbol{p}),\theta^t(\boldsymbol{p}),\boldsymbol{g}^t(\boldsymbol{p})\right),\\
s(\boldsymbol{p},t) &= \mathfrak{H}\left(\boldsymbol{F}^t(\boldsymbol{p}),\theta^t(\boldsymbol{p}),\boldsymbol{g}^t(\boldsymbol{p})\right),\\
\boldsymbol{q}(\boldsymbol{p},t) &= \mathfrak{J}\left(\boldsymbol{F}^t(\boldsymbol{p}),\theta^t(\boldsymbol{p}),\boldsymbol{g}^t(\boldsymbol{p})\right),
\end{aligned} \tag{2.68}$$

where $(\cdot)^t$ denotes the history of $(\cdot)^t$ up to the time instant t. Finally, the Clausius-Duhem inequality (Section 2.5.5) must be verified for every thermokinetic process of $\mathscr{B}$.

Material objectivity

The axiom of material objectivity or frame invariance essentially states that *the material response is independent of the observer.* The motion $\boldsymbol{\varphi}^*$ is related to the motion $\boldsymbol{\varphi}$ by a change in the observer if it can be expressed as

$$\boldsymbol{\varphi}^*(\boldsymbol{p},t) = \boldsymbol{y}(t) + \boldsymbol{Q}(t)\left[\boldsymbol{\varphi}(\boldsymbol{p},t) - \boldsymbol{x}_0\right] \tag{2.69}$$

where $\boldsymbol{y}(t)$ is a translation and $\boldsymbol{Q}(t)$ is a rotation around a given point $\boldsymbol{x}_0$. Furthermore, the deformation gradient as viewed by the second observer can be written as

$$\boldsymbol{F}^* = \boldsymbol{Q}\boldsymbol{F} \tag{2.70}$$

Accordingly, the other fields transform as follows

$$\begin{aligned} \boldsymbol{\sigma} \rightarrow \boldsymbol{\sigma}^* &= \boldsymbol{Q}\boldsymbol{\sigma}\boldsymbol{Q}^\top, \\ \boldsymbol{q} \rightarrow \boldsymbol{q}^* &= \boldsymbol{Q}\boldsymbol{q}, \\ \boldsymbol{g} \rightarrow \boldsymbol{g}^* &= \boldsymbol{Q}\boldsymbol{g}, \end{aligned} \tag{2.71}$$

while scalar fields remain constant after transformation. Therefore, for any transformation similar to Equation (2.69), the material objectivity principle requires the constitutive relations to verify

$$\begin{aligned} \boldsymbol{\sigma}^*(\boldsymbol{p},t) &= \mathfrak{F}\left(\boldsymbol{F}^{t*}(\boldsymbol{p}),\theta^t(\boldsymbol{p}),\boldsymbol{g}^{t*}(\boldsymbol{p})\right), \\ \psi(\boldsymbol{p},t) &= \mathfrak{B}\left(\boldsymbol{F}^{t*}(\boldsymbol{p}),\theta^t(\boldsymbol{p}),\boldsymbol{g}^{t*}(\boldsymbol{p})\right), \\ s(\boldsymbol{p},t) &= \mathfrak{H}\left(\boldsymbol{F}^{t*}(\boldsymbol{p}),\theta^t(\boldsymbol{p}),\boldsymbol{g}^{t*}(\boldsymbol{p})\right), \\ \boldsymbol{q}^*(\boldsymbol{p},t) &= \mathfrak{J}\left(\boldsymbol{F}^{t*}(\boldsymbol{p}),\theta^t(\boldsymbol{p}),\boldsymbol{g}^{t*}(\boldsymbol{p})\right). \end{aligned} \tag{2.72}$$

Material symmetry

The symmetry group $\mathscr{S}$ of a solid material is the set of rotations $\boldsymbol{Q}$ that does not change the response functionals of the constitutive model, i.e

$$\begin{aligned} \mathfrak{F}\left(\boldsymbol{F}^t,\theta^t,\boldsymbol{g}^t\right) &= \mathfrak{F}\left([\boldsymbol{F}\boldsymbol{Q}]^t,\theta^t,\boldsymbol{g}^t\right) \\ \mathfrak{B}\left(\boldsymbol{F}^t,\theta^t,\boldsymbol{g}^t\right) &= \mathfrak{B}\left([\boldsymbol{F}\boldsymbol{Q}]^t,\theta^t,\boldsymbol{g}^t\right) \\ \mathfrak{H}\left(\boldsymbol{F}^t,\theta^t,\boldsymbol{g}^t\right) &= \mathfrak{H}\left([\boldsymbol{F}\boldsymbol{Q}]^t,\theta^t,\boldsymbol{g}^t\right) \\ \mathfrak{J}\left(\boldsymbol{F}^t,\theta^t,\boldsymbol{g}^t\right) &= \mathfrak{J}\left([\boldsymbol{F}\boldsymbol{Q}]^t,\theta^t,\boldsymbol{g}^t\right) \end{aligned} \tag{2.73}$$

The symmetry group $\mathscr{S}$ is a set of rotations (such that $Q \in \mathscr{S}$), so it is also a subset of the proper orthogonal group[2], $\mathscr{O}^+$. The principle of material symmetry imposes the symmetries of the constitutive model to be consistent with the symmetries of the material. An isotropic solid has its symmetry group coincident with the proper orthogonal group.

2.6.2 Thermodynamics with internal variables

The approach described in Section 2.6.1 for the establishment of the constitutive equations is too general and difficult to use in practice. Thermodynamics with internal variables is often employed to simplify this process. In essence, its underlying hypothesis states that *given a point $\boldsymbol{p}$, a finite set of state variables will completely define the thermodynamic state (defined by $\boldsymbol{\sigma}$, ψ, s and $\boldsymbol{q}$) of a thermodynamic process.* Additionally, the thermodynamic state is only a function of the instantaneous value of the state variables, not of their history.

In solid mechanics problems, one can assume that the thermodynamic state of a point can be expressed in terms of a set of state variables,

$$\{\boldsymbol{F},\theta,\boldsymbol{g},\boldsymbol{\alpha}\}, \tag{2.74}$$

where $\boldsymbol{F}$, θ and $\boldsymbol{g}$ are the instantaneous values of the deformation gradient, the temperature and the spatial temperature gradient, whereas

$$\boldsymbol{\alpha} = \{\alpha_k\} \tag{2.75}$$

[2] $\mathscr{O}^+$ is the set of all proper orthogonal rotations. A proper orthogonal rotation tensor must verify $\det\boldsymbol{Q} = 1$. For further details see section 2.2.6 of de Souza Neto et al. (2008).

is the vector of internal state variables, which are associated with internal dissipative mechanisms (de Souza Neto et al., 2008).

Furthermore, the free-energy function can now be expressed in terms of the aforementioned state variables. However, in order to satisfy the second law of thermodynamics, it must not be a function of $\boldsymbol{g}$ (Coleman and Gurtin, 1967). That being the case, the free-energy function can be written as

$$\psi = \psi(\boldsymbol{F}, \theta, \boldsymbol{\alpha}). \tag{2.76}$$

Its temporal derivative now becomes

$$\dot{\psi} = \frac{\partial \psi}{\partial \boldsymbol{F}} : \dot{\boldsymbol{F}} + \frac{\partial \psi}{\partial \theta}\dot{\theta} + \sum_{k=1}^{n} \frac{\partial \psi}{\partial \alpha_k}\dot{\alpha}_k, \tag{2.77}$$

where n is the number of variables in the set defined in Equation (2.75). Additionally, expressing the stress power as

$$\boldsymbol{\sigma} : \boldsymbol{D} = \boldsymbol{\sigma}\boldsymbol{F}^{-\top} : \dot{\boldsymbol{F}} \tag{2.78}$$

the Clausius-Duhem inequality reduces to

$$\left(\boldsymbol{\sigma}\boldsymbol{F}^{-\top} - \rho\frac{\partial \psi}{\partial \boldsymbol{F}}\right) : \dot{\boldsymbol{F}} - \rho\left(s + \frac{\partial \psi}{\partial \theta}\right)\dot{\theta} - \rho\sum_{k=1}^{n}\left(\frac{\partial \psi}{\partial \alpha_k}\dot{\alpha}_k\right) - \frac{1}{\theta}\boldsymbol{q}\cdot\boldsymbol{g} \geq 0. \tag{2.79}$$

Similarly, in the reference configuration one has

$$\left(\boldsymbol{P} - \rho_0\frac{\partial \psi}{\partial \boldsymbol{F}}\right) : \dot{\boldsymbol{F}} - \rho_0\left(s + \frac{\partial \psi}{\partial \theta}\right)\dot{\theta} - \rho_0\sum_{k=1}^{n}\left(\frac{\partial \psi}{\partial \alpha_k}\dot{\alpha}_k\right) - \frac{J}{\theta}\boldsymbol{q}\cdot\boldsymbol{g} \geq 0 \tag{2.80}$$

The axiom of thermodynamic determinism imposes that Equation (2.80) holds for any thermokinetic process, i.e. any pair of functions $\{\dot{\boldsymbol{F}}(t), \dot{\theta}(t)\}$. This implies that

$$\begin{aligned} \boldsymbol{P} &= \rho_0\frac{\partial \psi}{\partial \boldsymbol{F}}, \\ s &= -\frac{\partial \psi}{\partial \theta}. \end{aligned} \tag{2.81}$$

The first equation of Equation (2.81) can also be written in terms of the Cauchy and Kirchhoff stress tensors, such that

$$\begin{aligned} \boldsymbol{\sigma} &= \frac{1}{J}\rho_0\frac{\partial \psi}{\partial \boldsymbol{F}}\boldsymbol{F}^{-\top}, \\ \boldsymbol{\tau} &= \rho_0\frac{\partial \psi}{\partial \boldsymbol{F}}\boldsymbol{F}^{-\top}. \end{aligned} \tag{2.82}$$

2.6.3 The constitutive initial value problem

Within the scope of this work, thermal effects were neglected. That being the case it becomes convenient to summarise the general internal variable-based constitutive equations in the *purely mechanical case*. By removing the thermally related terms of the above theory, the following set of mechanical constitutive equations is attained:

$$\begin{cases} \psi = \psi(\boldsymbol{F}, \boldsymbol{\alpha}), \\ \boldsymbol{P} = \rho_0\frac{\partial \psi}{\partial \boldsymbol{F}}, \\ \dot{\boldsymbol{\alpha}} = f(\boldsymbol{F}, \boldsymbol{\alpha}). \end{cases} \tag{2.83}$$

Having establish these equations, the basic constitutive problem is defined as follows: *'Given the history of the deformation gradient (and the history of temperature and temperature gradient, if thermal effects are considered), find the free-energy and stress according to the constitutive law conceptually expressed by Equation* (2.68)*'*. If the internal variable approach is adopted in the formulation of the constitutive equations, the generic constitutive problem reduces to the fundamental *mechanical constitutive initial value problem* (de Souza Neto et al., 2008), which can be written in the spatial description:

Problem 2.1 *Given the initial values of the internal variables,* $\boldsymbol{\alpha}(t_0)$*, and the history of the deformation gradient*

$$\boldsymbol{F}(t), \quad t \in [t_0, t_f], \tag{2.84}$$

find the functions for $\boldsymbol{\sigma}(t)$ *and* $\boldsymbol{\alpha}(t)$*, for the Cauchy stress tensor and the set of internal variables, such that the constitutive equations*

$$\begin{aligned} \boldsymbol{\sigma} &= \rho \frac{\partial \psi}{\partial \boldsymbol{F}} \boldsymbol{F}^T, \\ \psi &= \psi(\boldsymbol{F}, \boldsymbol{\alpha}), \\ \dot{\boldsymbol{\alpha}} &= f(\boldsymbol{F}, \boldsymbol{\alpha}), \end{aligned} \tag{2.85}$$

are satisfied for every $t \in [t_0, t_f]$.

In the material description:

Problem 2.2 *Given the initial values of the internal variables* $\boldsymbol{\alpha}(t_0)$ *and the history of the deformation gradient,*

$$\boldsymbol{F}(t), \quad t \in [t_0, t_f], \tag{2.86}$$

find the functions $\boldsymbol{P}(t)$ *and* $\boldsymbol{\alpha}(t)$*, for the first Piola-Kirchhoff stress tensor and the set of internal variables, such that the constitutive equations*

$$\begin{aligned} \boldsymbol{P} &= \rho_0 \left. \frac{\partial \psi}{\partial \boldsymbol{F}} \right|_t, \\ \psi &= \psi(\boldsymbol{F}, \boldsymbol{\alpha}), \\ \dot{\boldsymbol{\alpha}} &= f(\boldsymbol{F}, \boldsymbol{\alpha}), \end{aligned} \tag{2.87}$$

are satisfied for every $t \in [t_0, t_f]$.

2.7 Weak equilibrium formulation

The strong form of the momentum balance has been stated in Section 2.5.2 (see Equation (2.54) and Equation (2.55)). In this section, the momentum balance is stated in its corresponding *weak*, *global* or *integral* form. In practical terms, as a general solution to the differential problem is often difficult to obtain, the weak or global form of the equilibrium equations is used to obtain a solution with less restrictions in terms of continuity and differentiability.

2.7.1 Spatial description

The spatial version of the equilibrium equation can be written, in the weak form, according to an Eulerian description

$$\int_{\boldsymbol{\varphi}(\Omega)} [\boldsymbol{\sigma} : \nabla_x(\boldsymbol{\eta}) - (\boldsymbol{b} - \rho \ddot{\boldsymbol{u}}) \cdot \boldsymbol{\eta}] \, \mathrm{d}v = \int_{\boldsymbol{\varphi}(\partial\Omega)} \boldsymbol{t} \cdot \boldsymbol{\eta} \, \mathrm{d}a = 0, \ \ \forall \boldsymbol{\eta} \in \mathcal{V}, \tag{2.88}$$

where $\boldsymbol{\eta}$ is the virtual displacement vector and $\mathcal{V}$ is the set of admissible virtual displacements.

2.7.2 Material description

The weak form of momentum equilibrium can also be written using a material description. With Equation (2.50) in mind, and according to identity

$$\nabla_x \boldsymbol{a} = \nabla_p \boldsymbol{a} \boldsymbol{F}^{-1}, \tag{2.89}$$

for any valid vector field $\boldsymbol{a}$, it is possible to relate the spatial and material gradient of a field. Finally, considering

$$\int_{\boldsymbol{\varphi}(\Omega)} \boldsymbol{a}(x)\,\mathrm{d}v = \int_{\Omega} J(\boldsymbol{p})\boldsymbol{a}(\boldsymbol{\varphi}(\boldsymbol{p}))\,\mathrm{d}v, \tag{2.90}$$

valid for any scalar field a, the weak form in a material description is given by

$$\int_{\Omega} [\boldsymbol{P} : \nabla_p(\boldsymbol{\eta}) - (\boldsymbol{b}_0 - \rho_0 \ddot{\boldsymbol{u}}) \cdot \boldsymbol{\eta}]\,\mathrm{d}v - \int_{\partial\Omega} \boldsymbol{t}_0 \cdot \boldsymbol{\eta}\,\mathrm{d}a = 0, \ \ \forall \boldsymbol{\eta} \in \mathcal{V}. \tag{2.91}$$

2.7.3 Quasi-static formulation

Bearing in mind that dynamical effects are not considered in the present work, the weak form statements can be reduced to their quasi-static form. In such case, under a spatial description, the weak form can be recast as

$$\int_{\boldsymbol{\varphi}(\Omega)} \left[\boldsymbol{\sigma} : \nabla_{\boldsymbol{x}}(\boldsymbol{\eta}) - \boldsymbol{b} \cdot \boldsymbol{\eta}\right] \mathrm{d}v - \int_{\boldsymbol{\varphi}(\partial\Omega)} \boldsymbol{t} \cdot \boldsymbol{\eta}\,\mathrm{d}a = 0, \quad \forall \boldsymbol{\eta} \in \mathcal{V}. \tag{2.92}$$

Lastly, the material weak form becomes

$$\int_{\Omega} \left[\boldsymbol{P} : \nabla_{\boldsymbol{p}}(\eta) - \boldsymbol{b}_0 \cdot \boldsymbol{\eta}\right] \mathrm{d}v - \int_{\partial\Omega} \boldsymbol{t}_0 \cdot \boldsymbol{\eta}\,\mathrm{d}a = 0, \quad \forall \boldsymbol{\eta} \in \mathcal{V}. \tag{2.93}$$

2.8 Quasi-static initial boundary value problem

Following the establishment of the constitutive initial value problem (Section 2.6.3) and the quasi-static version of the weak form statement (Section 2.7.3), the quasi-static initial boundary value problem can also be established.

Recall the body $\mathscr{B}$, from Section 2.3. Consider that the history of prescribed body forces

$$\boldsymbol{b}(\boldsymbol{x}, t), \quad t \in \left[t_0, t_f\right], \tag{2.94}$$

is known. Additionally, consider that the following boundary conditions are imposed on the body:

1. **Natural boundary condition**: history of the prescribed surface traction $\boldsymbol{t}(\boldsymbol{x}, t)$ over the boundary $\partial\Omega_t$ of $\mathscr{B}$ in its reference configuration.

2. **Essential boundary condition**: prescribed boundary displacement field $\bar{\boldsymbol{u}}$ over the boundary $\partial\Omega_u$ of $\mathscr{B}$ in its reference configuration. The boundary displacements become

$$\bar{\boldsymbol{\varphi}}(\boldsymbol{p}, t) = \boldsymbol{p} + \bar{\boldsymbol{u}}(\boldsymbol{p}, t), \quad t \in \left[t_0, t_f\right], \boldsymbol{p} \in \partial\Omega_u \tag{2.95}$$

   For the sake of simplicity, it is assumed that $\partial\Omega_u \cap \partial\Omega_t = \emptyset$. The set of displacements that satisfies the essential boundary condition allows us to define the set of *kinematically admissible displacements* of $\mathscr{B}$, given by

$$\mathscr{K} = \left\{\boldsymbol{u} : \Omega \times \mathscr{R} \to \mathscr{U} \mid \boldsymbol{u}(\boldsymbol{p}, t) = \overline{\boldsymbol{u}}(\boldsymbol{p}, t), t \in \left[t_0, t_f\right], \boldsymbol{p} \in \partial\Omega_u\right\}. \tag{2.96}$$

Furthermore, assume that the body is constituted of a generic material, for which the internal variable set, $\boldsymbol{\alpha}$, is known at the initial time instant t_0, such that

$$\boldsymbol{\alpha}(\boldsymbol{p}, t_0) = \boldsymbol{\alpha}_0(\boldsymbol{p}). \tag{2.97}$$

The fundamental *quasi-static initial boundary value problem* can now be posed in its spatial version (de Souza Neto et al., 2008):

Problem 2.3 *Find a kinematically admissible displacement function, $\boldsymbol{u} \in \mathscr{X}$, such that, for all $t \in [t_0, t_f]$, the following equation is satisfied*

$$\int_{\varphi(\Omega,t)} \left[\boldsymbol{\sigma}(t) : \nabla_{\boldsymbol{x}} \boldsymbol{\eta} - \boldsymbol{b}(t) \cdot \boldsymbol{\eta}\right] \mathrm{d}v - \int_{\varphi(\partial\Omega_t,t)} \boldsymbol{t}(t) \cdot \boldsymbol{\eta} \mathrm{d}a = 0, \quad \forall \boldsymbol{\eta} \in \mathscr{V}_t \tag{2.98}$$

The space of virtual displacements at time t is defined by

$$\mathscr{V}_t = \left\{\boldsymbol{\eta} : \varphi(\Omega, t) \to \mathscr{U} \mid \boldsymbol{\eta} = \boldsymbol{0} \text{ on } \varphi(\partial\Omega_u, t)\right\} \tag{2.99}$$

and, at each point of $\mathscr{B}$, the Cauchy stress is given by

$$\boldsymbol{\sigma}(t) = \frac{1}{J(t)} \boldsymbol{P}(t) \boldsymbol{F}(t)^T \tag{2.100}$$

where $\boldsymbol{P}(t)$ is the solution of constitutive initial value problem (Problem 2.2) with prescribed deformation gradient

$$\boldsymbol{F}(t) = \nabla_p \boldsymbol{\varphi}(\boldsymbol{p}, t) = \boldsymbol{I} + \nabla_p \boldsymbol{u}(\boldsymbol{p}, t). \tag{2.101}$$

The quasi-static initial boundary value problem is illustrated in Figure 2.10, and can also be written in its material version:

Problem 2.4 *Find a kinematically admissible displacement function, $\boldsymbol{u} \in \mathscr{X}$, such that, for all $t \in [t_0, t_f]$,*

$$\int_{\Omega} \left[\boldsymbol{P}(t) : \nabla_p \boldsymbol{\eta} - \boldsymbol{b}_0(t) \cdot \boldsymbol{\eta}\right] \mathrm{d}v - \int_{\partial\Omega_t} \boldsymbol{t}_0(t) \cdot \boldsymbol{\eta} \mathrm{d}a = 0, \quad \forall \boldsymbol{\eta} \in \mathscr{V} \tag{2.102}$$

where

$$\mathscr{V} = \left\{\boldsymbol{\eta} : \Omega \to \mathscr{U} \mid \boldsymbol{\eta} = \boldsymbol{0} \text{ on } \partial\Omega_u\right\} \tag{2.103}$$

and the Piola-Kirchhoff stress, $\boldsymbol{P}(t)$, is the solution of the initial value problem (Problem 2.2) with prescribed deformation gradient (Equation (2.101)).

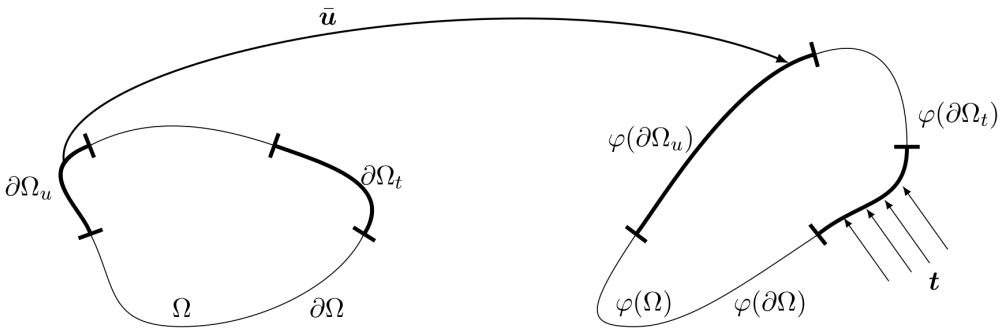

Figure 2.10: Schematic representation of quasi-static initial boundary value problem, taken from Coelho (2019).

2.9 Finite element method

Having established the incremental weak form of the quasi-static mechanical constitutive initial boundary value problem, an approximated solution can now be obtained with the *finite element method*, presented in what follows.

2.9.1 Approximate solution with the finite element method

Analytical solutions of the quasi-static initial boundary value problem, presented in Section 2.8, are almost impossible to obtain whenever complex geometries or nonlinear phenomena are considered. This calls for the use of numerical strategies for the solution of the system of partial differential equations, of which the finite element method is likely one of the most popular. That being said, the application of the finite element method to solve the quasi-static initial boundary value problem is discussed in this section. The temporal and spatial discretisation of the governing equations are assessed in Section 2.9.2 and Section 2.9.3, respectively. Finally, the Newton-Raphson method is introduced in Section 2.9.4 as the main algorithm for the solution of nonlinear equations. Figure 2.11 illustrates the main steps for the application of the finite element method to solve the mechanical constitutive initial value problem presented in Section 2.6.3.

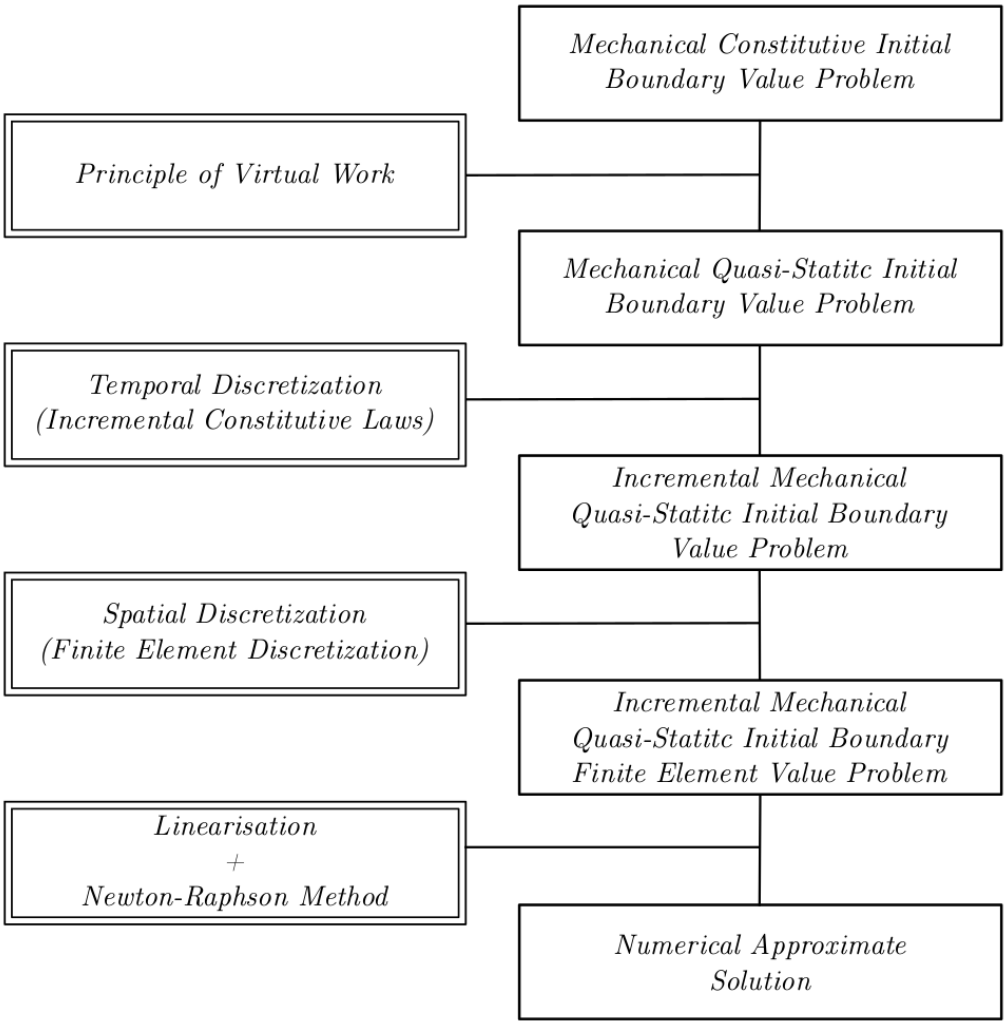

Figure 2.11: Schematic representation of the different steps for the application of the finite element method for the solution of the constitutive initial value problem, taken from Vieira (2018).

2.9.2 Time discretisation

When attempting to solve path-dependent problems, like the mechanical testing of elastoplastic or elasto-viscoplastic materials, path-dependent formulations of the FEM are necessary for the accurate depiction of the time evolution and history-dependent behaviour of the material. In such problems, an *incremental strategy*, resorting to a *time* (or *pseudo-time*) *discretisation* is adopted in order to transform the constitutive equations into *n time-discrete* increments of the given time domain, $[t_0, t_f]$. With this in mind, an *incremental constitutive function*, $\hat{\boldsymbol{\sigma}}$ and $\hat{\boldsymbol{P}}$, for the Cauchy and First Piola-Kirchhoff stress tensors, may be defined as

$$\boldsymbol{\sigma}_{n+1} = \hat{\boldsymbol{\sigma}}(\boldsymbol{F}_{n+1}, \boldsymbol{\alpha}_n), \tag{2.104}$$

and

$$\boldsymbol{P}_{n+1} = \hat{\boldsymbol{P}}(\boldsymbol{F}_{n+1}, \boldsymbol{\alpha}_n), \tag{2.105}$$

where $\boldsymbol{\alpha}_n$ is a set of internal variables at time t_n, $\boldsymbol{F}_{n+1}$ is the deformation gradient at time t_{n+1} and $\boldsymbol{\sigma}_{n+1}$ and $\boldsymbol{P}_{n+1}$ are expected to converge to the exact solution as the time increments are reduced. The evolution of the internal variables is also discretised in n time increments:

$$\boldsymbol{\alpha}_{n+1} = \hat{\boldsymbol{P}}(\boldsymbol{F}_{n+1}, \boldsymbol{\alpha}_n). \tag{2.106}$$

Applying this incremental strategy ensures that the constitutive equations are path-independent within each increment, but retain their path-dependence throughout the whole time domain.

At this point, the *incremental quasi-static mechanical constitutive initial boundary value problem* can written in its spatial description as follows

Problem 2.5 *Given the set of internal variables $\boldsymbol{\alpha}_n$ at t_n, the prescribed body and traction force fields $\boldsymbol{b}_{n+1}$ and $\boldsymbol{t}_{n+1}$ at t_{n+1}, and the prescribed deformationg gradient $\boldsymbol{F}_{n+1}$ at t_{n+1}, find the kinematically admissible displacement field $\boldsymbol{u}_{n+1} \in \mathscr{K}_{n+1}$ such that the body $\mathscr{B}$ is in equilibrium as stated by the Virtual Work Principle*

$$\int_{\Omega_{n+1}} \left[\hat{\boldsymbol{\sigma}}(\boldsymbol{F}_{n+1}, \boldsymbol{\alpha}_n) : \nabla\boldsymbol{\eta} - \boldsymbol{b}_{n+1} \cdot \boldsymbol{\eta}\right] \mathrm{d}v - \int_{\partial\Omega_{n+1}} \boldsymbol{t}_{n+1} \cdot \boldsymbol{\eta} \mathrm{d}a = 0, \quad \forall \boldsymbol{\eta} \in \mathscr{V}, \tag{2.107}$$

where the space of kinematically admissible displacement fields $\mathscr{K}_{n+1}$ is defined by

$$\mathscr{K}_{n+1} = \left\{\boldsymbol{u} : \Omega \times \mathscr{R} \to \mathscr{U} \mid \boldsymbol{u}_{n+1}(\boldsymbol{X}) = \boldsymbol{u}_{presc,n+1}(\boldsymbol{X}), \quad \boldsymbol{X} \in \partial\Omega_{motion,0}\right\}. \tag{2.108}$$

and also in its material description:

Problem 2.6 *Given the set of internal variables $\boldsymbol{\alpha}_n$ at t_n, the prescribed body and traction forces fields $\boldsymbol{b}_{0,n+1}$ and $\boldsymbol{t}_{0,n+1}$ at t_{n+1}, and the prescribed deformationg gradient $\boldsymbol{F}_{n+1}$ at t_{n+1}, find the kinematically admissible displacement field $\boldsymbol{u}_{n+1} \in \mathscr{K}_{n+1}$ such that the body $\mathscr{B}$ is in equilibrium as stated by the Virtual Work Principle*

$$\int_{\Omega_0} \left[\hat{\boldsymbol{P}}(\boldsymbol{F}_{n+1}, \boldsymbol{\alpha}_n) : \nabla_0\boldsymbol{\eta} - \boldsymbol{b}_{0,n+1} \cdot \boldsymbol{\eta}\right] \mathrm{d}v - \int_{\partial\Omega_0} \boldsymbol{t}_{0,n+1} \cdot \boldsymbol{\eta} \mathrm{d}a = 0, \quad \forall \boldsymbol{\eta} \in \mathscr{V}, \tag{2.109}$$

where the space of kinematically admissible displacement fields $\mathscr{K}_{n+1}$ is defined by

$$\mathscr{K}_{n+1} = \left\{\boldsymbol{u} : \Omega \times \mathscr{R} \to \mathscr{U} \mid \boldsymbol{u}_{n+1}(\boldsymbol{X}) = \boldsymbol{u}_{presc,n+1}(\boldsymbol{X}), \quad \boldsymbol{X} \in \partial\Omega_{motion,0}\right\}. \tag{2.110}$$

2.9.3 Spatial discretisation

The *spatial discretisation*, commonly known as the *finite element discretisation*, is the main ingredient of the FEM. In essence, it comprises the division of the domain Ω of a given body $\mathscr{B}$ into a finite

number of non-overlapping subdomains, known as *finite elements*. Each finite element, e, occupies a region of the domain, Ω^e, such that

$$\Omega \approx {}^h\Omega = \bigcup_{e=1}^{n_{\text{elem}}} \Omega^e, \tag{2.111}$$

where ${}^h\Omega$ is the region occupied by the sum of all the n_{elem} elements, i.e. the discretised continuum domain Ω.

Interpolation of fields

Each generic finite element e is defined by its set of n_{nodes} nodes and $N_i^e(x)$ *shape functions* or *interpolation functions*, associated with a certain i node of the element. Even thought these shape functions are defined by elements geometry, they must always satisfy the Kroenecker delta property, i.e.

$$N_i^e(x^j) = \delta_{ij} = \begin{cases} 1, & \text{if } j = i, \\ 0, & \text{if } j \neq i \end{cases} \tag{2.112}$$

which states that each shape function must have unit value in its respective node i, and null value in all other nodes of the element. Moreover, the shape functions of a generic element e may be arranged in the form of an *interpolation matrix*, $\mathbf{N}^e$, given by

$$\mathbf{N}^e(\boldsymbol{x}) = \begin{bmatrix} \text{diag}[N_1^e(\boldsymbol{x})] & \text{diag}[N_2^e(\boldsymbol{x})] & \cdots & \text{diag}[N_n^e(\boldsymbol{x})] \end{bmatrix}, \tag{2.113}$$

where each diagonal matrix is a square $(n_{\text{dof}} \times n_{\text{dof}})$ matrix

$$\text{diag}\left[N_i^e(\boldsymbol{x})\right] = \begin{bmatrix} N_i^e(\boldsymbol{x}) & 0 & \cdots & 0 \\ 0 & N_i^e(\boldsymbol{x}) & \cdots & 0 \\ \vdots & \vdots & \ddots & \vdots \\ 0 & 0 & \cdots & N_i^e(\boldsymbol{x}) \end{bmatrix}_{n_{\text{dof}} \times n_{\text{dof}}}. \tag{2.114}$$

A *global interpolation matrix*, $\mathbf{N}^g$ can also be defined as

$$\mathbf{N}^g(\boldsymbol{x}) = \begin{bmatrix} \text{diag}[N_1^g(\boldsymbol{x})] & \text{diag}[N_2^g(\boldsymbol{x})] & \cdots & \text{diag}[N_n^g(\boldsymbol{x})] \end{bmatrix}, \tag{2.115}$$

written in terms of the n_{poin} nodes within the finite element mesh. The diagonal matrix $\text{diag}[N_i^g(\boldsymbol{x})]$ is defined identically to its element counterpart,

$$\text{diag}\left[N_i^g(\boldsymbol{x})\right] = \begin{bmatrix} N_i^g(\boldsymbol{x}) & 0 & \cdots & 0 \\ 0 & N_i^g(\boldsymbol{x}) & \cdots & 0 \\ \vdots & \vdots & \ddots & \vdots \\ 0 & 0 & \cdots & N_i^g(\boldsymbol{x}) \end{bmatrix}_{n_{\text{dof}} \times n_{\text{dof}}}. \tag{2.116}$$

Note that $n_{poin} < n_{elem} \times n_{nodes}$, as adjacent elements will share nodes. Figure 2.12 depicts the discretisation of a plane domain in triangular finite elements.

The approximation of the displacement field $\boldsymbol{u}(\boldsymbol{x})$ also plays a key role in the finite element method formulation. The discretised version of the displacement field, ${}^h\boldsymbol{u}(\boldsymbol{x})$, is given by the interpolation of nodal displacement values, such that

$$\boldsymbol{u}(\boldsymbol{x}) \approx {}^h\boldsymbol{u}(\boldsymbol{x}) = \mathbf{N}^g(\boldsymbol{x})\mathbf{u}, \;\; \forall {}^h\boldsymbol{u} \in {}^h\mathcal{K}, \tag{2.117}$$

where $\mathbf{u}$ is the global vector of nodal displacements, given by

$$\mathbf{u} = \left\{ u_1^1, \ldots, u_1^{n_{\text{dof}}}, \ldots, u_j^i, \ldots, u_{n_{\text{points}}}^1, \ldots, u_{n_{\text{points}}}^{n_{\text{dof}}} \right\}^T, \tag{2.118}$$

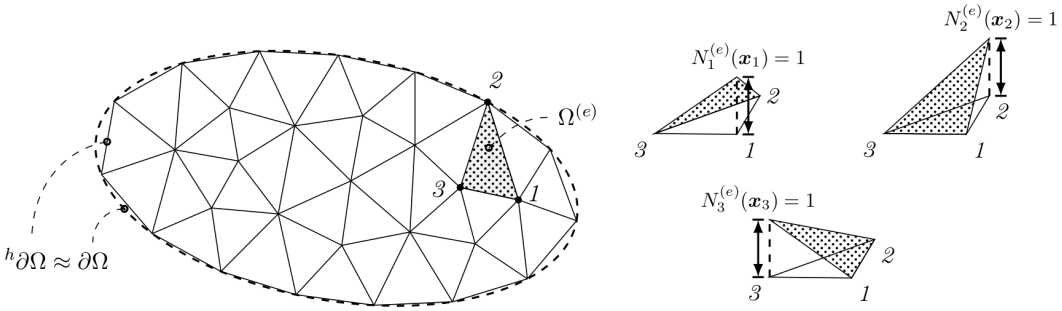

Figure 2.12: Representation of the spatial discretisation of a plane domain by a mesh of triangular finite elements and a schematic representation of the evolution of the shape functions associated with a generic finite element, (e), taken from Silva (2021).

where u_j^i is the i-th component of the nodal displacement of the global nodel j. Kinematic constraints must be followed by the components of $\mathbf{u}$ on $\partial\Omega_u$. As a result of the spatial discretisation, a set $^h\mathcal{K}$ can also be defined as

$$^h\mathcal{K} = \left\{ {}^h\boldsymbol{u}\boldsymbol{x} = \sum_{j=1}^{n_{\text{points}}} \boldsymbol{u}_j N_j^g \boldsymbol{x} \quad \| \quad \boldsymbol{u}_j = \hat{\boldsymbol{u}}(x_j) \quad \text{if} \quad x_j \in \partial\Omega \right\}, \tag{2.119}$$

where u_j and $\hat{u}(x_j)$ are the displacement vector and the prescribed displacement at node j. The virtual displacements over the domain can also be defined as

$$\boldsymbol{\eta}\boldsymbol{x} \approx {}^h\boldsymbol{\eta}\boldsymbol{x} = \boldsymbol{N}^g \boldsymbol{x}\boldsymbol{\eta}, \quad \forall\, {}^h\boldsymbol{\eta} \in {}^h\mathcal{V}, \tag{2.120}$$

with its corresponding set of admissible displacements, $^h\mathcal{V}$, defined as

$$^h\mathcal{V} = \left\{ {}^h\boldsymbol{\eta}\boldsymbol{x} = \sum_{j=1}^{n_{\text{points}}} \boldsymbol{\eta}_j N_j^g \boldsymbol{x} \quad \| \quad \boldsymbol{\eta}_j = 0 \quad \text{if} \quad x_j \in \partial\Omega \right\}. \tag{2.121}$$

Discretisation of the equilibrium equations

At this point it is convenient to introduce the *global discrete symmetric gradient operator*, denoted $\boldsymbol{B}^g$, as well as the *global discrete spatial gradient operator*, which is, in turn, denoted by $\boldsymbol{G}^g$. Both of these matrices are essential to the establishment of the incremental version of the equilibrium equations. In two-dimensional problems, such as plane strain problems, as the ones discussed in the present work, these matrices are given by

$$\mathbf{B}^g = \left[\begin{array}{cc|cc|c|cc} \frac{\partial N_1^g}{\partial x} & 0 & \frac{\partial N_2^g}{\partial x} & 0 & \cdots & \frac{\partial N_{n_{\text{points}}}^g}{\partial x} & 0 \\ 0 & \frac{\partial N_1^g}{\partial y} & 0 & \frac{\partial N_2^g}{\partial y} & \cdots & 0 & \frac{\partial N_{n_{\text{points}}}^g}{\partial y} \\ \frac{\partial N_1^g}{\partial y} & \frac{\partial N_1^g}{\partial x} & \frac{\partial N_2^g}{\partial y} & \frac{\partial N_2^g}{\partial x} & \cdots & \frac{\partial N_{n_{\text{points}}}^g}{\partial y} & \frac{\partial N_{n_{\text{points}}}^g}{\partial x} \end{array}\right], \tag{2.122}$$

$$\mathbf{G}^g = \left[\begin{array}{cc|cc|c|cc} \frac{\partial N_1^g}{\partial x} & 0 & \frac{\partial N_2^g}{\partial x} & 0 & \cdots & \frac{\partial N_{n_{\text{points}}}^g}{\partial x} & 0 \\ 0 & \frac{\partial N_1^g}{\partial x} & 0 & \frac{\partial N_2^g}{\partial x} & \cdots & 0 & \frac{\partial N_{n_{\text{points}}}^g}{\partial x} \\ \frac{\partial N_1^g}{\partial y} & 0 & \frac{\partial N_2^g}{\partial y} & 0 & \cdots & \frac{\partial N_{n_{\text{points}}}^g}{\partial y} & 0 \\ 0 & \frac{\partial N_1^g}{\partial y} & 0 & \frac{\partial N_2^g}{\partial y} & \cdots & 0 & \frac{\partial N_{n_{\text{points}}}^g}{\partial y} \end{array}\right]. \tag{2.123}$$

Analogously, the element counterparts of these discrete operators can be written as

$$\mathbf{B}^e = \left[\begin{array}{cc|cc|c|cc} \frac{\partial N_1^e}{\partial x} & 0 & \frac{\partial N_2^e}{\partial x} & 0 & \cdots & \frac{\partial N_{n_{\text{points}}}^e}{\partial x} & 0 \\ 0 & \frac{\partial N_1^e}{\partial y} & 0 & \frac{\partial N_2^e}{\partial y} & \cdots & 0 & \frac{\partial N_{n_{\text{points}}}^g}{\partial y} \\ \frac{\partial N_1^e}{\partial y} & \frac{\partial N_1^e}{\partial x} & \frac{\partial N_2^e}{\partial y} & \frac{\partial N_2^e}{\partial x} & \cdots & \frac{\partial N_{n_{\text{points}}}^e}{\partial y} & \frac{\partial N_{n_{\text{points}}}^e}{\partial x} \end{array}\right], \tag{2.124}$$

$$\mathbf{G}^e = \left[\begin{array}{cc|cc|c|cc} \frac{\partial N_1^e}{\partial x} & 0 & \frac{\partial N_2^e}{\partial x} & 0 & \cdots & \frac{\partial N_{n_{\text{points}}}^e}{\partial x} & 0 \\ 0 & \frac{\partial N_1^e}{\partial x} & 0 & \frac{\partial N_2^e}{\partial x} & \cdots & 0 & \frac{\partial N_{n_{\text{points}}}^e}{\partial x} \\ \frac{\partial N_1^e}{\partial y} & 0 & \frac{\partial N_2^e}{\partial y} & 0 & \cdots & \frac{\partial N_{n_{\text{points}}}^e}{\partial y} & 0 \\ 0 & \frac{\partial N_1^e}{\partial y} & 0 & \frac{\partial N_2^e}{\partial y} & \cdots & 0 & \frac{\partial N_{n_{\text{points}}}^e}{\partial y} \end{array}\right]. \tag{2.125}$$

Having defined these operators, it is now possible to derive the *spatial incremental discretised quasi-static mechanical initial boundary value problem* or, put simply, the spatial version of the *finite element equilibrium equations*:

Problem 2.7 *Given the set of internal variables $\boldsymbol{\alpha}_n$ at t_n, the prescribed body and traction forces fields $\mathbf{b}_{n+1}$ and $\mathbf{t}_{n+1}$ at t_{n+1}, and the prescribed deformation gradient $\boldsymbol{F}_{n+1}$ at t_{n+1}, find the kinematically admissible nodal displacement field $\mathbf{u}_{n+1} \in {}^h\mathscr{K}_{n+1}$ such that the body $\mathscr{B}$ is in equilibrium:*

$$\mathbf{r}(\mathbf{u}_{n+1}) = \mathbf{f}^{\text{int}}(\mathbf{u}_{n+1}) - \mathbf{f}^{\text{ext}}_{n+1} = \mathbf{0}, \tag{2.126}$$

where $\mathbf{f}^{\text{int}}$ and $\mathbf{f}^{\text{ext}}_{n+1}$ are the global vectors of internal and external forces defined as

$$\begin{aligned} \mathbf{f}^{\text{int}} &= \int_{\boldsymbol{\varphi}_{n+1}({}^h\Omega)} (\mathbf{B}^g)^T \hat{\boldsymbol{\sigma}}(\boldsymbol{F}(\mathbf{u}_{n+1}), \boldsymbol{\alpha}_n) \mathrm{d}v, \\ \mathbf{f}^{\text{ext}}_{n+1} &= \int_{\boldsymbol{\varphi}_{n+1}({}^h\Omega)} (\mathbf{N}^g)^T \mathbf{b}_{n+1} \mathrm{d}v, + \int_{\boldsymbol{\varphi}_{n+1}(\partial^h\Omega_{\text{traction}})} (\mathbf{N}^g)^T \mathbf{t}_{n+1} \mathrm{d}a. \end{aligned} \tag{2.127}$$

In a similar fashion, the discretised balance equations can be recast under the material description:

Problem 2.8 *Given the set of internal variables $\boldsymbol{\alpha}_n$ at t_n, the prescribed body and traction forces fields $\mathbf{b}_{0,n+1}$ and $\mathbf{t}_{0,n+1}$ at t_{n+1}, and the prescribed deformation gradient $\boldsymbol{F}_{n+1}$ at t_{n+1}, find the kinematically admissible nodal displacement field $\mathbf{u}_{n+1} \in {}^h\mathscr{K}_{n+1}$ such that the body $\mathscr{B}$ is in equilibrium:*

$$\mathbf{r}(\mathbf{u}_{n+1}) = \mathbf{f}^{\text{int}}(\mathbf{u}_{n+1}) - \mathbf{f}^{\text{ext}}_{n+1} = \mathbf{0}, \tag{2.128}$$

where $\mathbf{f}^{\text{int}}$ and $\mathbf{f}^{\text{ext}}_{n+1}$ are the global vectors of internal and external forces defined as

$$\begin{aligned} \mathbf{f}^{\text{int}} &= \int_{{}^h\Omega} (\mathbf{G}^g)^T \hat{\mathbf{P}}(\boldsymbol{F}(\mathbf{u}_{n+1}), \boldsymbol{\alpha}_n) \mathrm{d}v, \\ \mathbf{f}^{\text{ext}}_{n+1} &= \int_{{}^h\Omega} (\mathbf{N}^g)^T \mathbf{b}_{0,n+1} \mathrm{d}v, + \int_{\partial^h\Omega_{\text{traction}}} (\mathbf{N}^g)^T \mathbf{t}_{0,n+1} \mathrm{d}a. \end{aligned} \tag{2.129}$$

Since the domain is spatially discretised, in order to obtain the global nodal force vectors, the elementary nodal forces must be assembled. This operation is usually performed with the finite element assembly operator, A:

$$\mathbf{f}^{\text{int}} = \mathop{\mathsf{A}}_{e=1}^{n_{\text{elem}}} (\mathbf{f}^{\text{int}})^e, \tag{2.130}$$

$$\mathbf{f}^{\text{ext}}_{n+1} = \mathop{\mathsf{A}}_{e=1}^{n_{\text{elem}}} (\mathbf{f}^{\text{ext}}_{n+1})^e. \tag{2.131}$$

Essentially, the global force associated to a given global node is calculated by the sum of the contributions of all the elements which share that given global node. In turn, computing the element counterparts of the internal ($(\mathbf{f}^{\text{int}})^e$) and external ($(\mathbf{f}^{\text{ext}}_{n+1})^e$) force vectors becomes mandatory. This is done according to the following equations:

$$\begin{aligned}(\mathbf{f}^{\text{int}})^e &= \int_{\boldsymbol{\varphi}_{n+1}({}^h\Omega^e)} (\mathbf{B}^e)^T \hat{\boldsymbol{\sigma}}(\boldsymbol{F}(\mathbf{u}_{n+1}), \boldsymbol{\alpha}_n) \mathrm{d}v, \\ (\mathbf{f}^{\text{ext}}_{n+1})^e &= \int_{\boldsymbol{\varphi}_{n+1}({}^h\Omega^e)} (\mathbf{N}^e)^T \mathbf{b}_{n+1} \mathrm{d}v, + \int_{\boldsymbol{\varphi}_{n+1}(\partial^h\Omega^e_{\text{traction}})} (\mathbf{N}^e)^T \mathbf{t}_{n+1} \mathrm{d}a.\end{aligned} \tag{2.132}$$

Finally, in the material description, these vectors can be written as

$$\begin{aligned}(\mathbf{f}^{\text{int}})^e &= \int_{h^e_{\Omega^e}} (\mathbf{G}^e)^T \hat{\mathbf{P}}(\boldsymbol{F}(\mathbf{u}_{n+1}), \boldsymbol{\alpha}_n) \, \mathrm{d}v, \\ (\mathbf{f}^{\text{ext}}_{n+1})^e &= \int_{{}^h\Omega^e} (\mathbf{N}^e)^T \mathbf{b}_{0,n+1} \, \mathrm{d}v + \int_{\partial^h\Omega^e_{\text{traction}}} (\mathbf{N}^e)^T \mathbf{t}_{0,n+1} \, \mathrm{d}a.\end{aligned} \tag{2.133}$$

Numerical integration

The weak formulation established the equilibrium equations in their integral form. This is particularly useful because it allows for the solution of these equations through numerical integration. Generally, these integrals are solved through a quadrature rule known as the *Gaussian quadrature rule*. In general terms, a Gaussian quadrature approximates an integral of a function f over a domain Γ by the evaluation of the function on n_{gauss} points, such that

$$\int_\Gamma f(\boldsymbol{\xi}) \mathrm{d}\boldsymbol{\xi} \approx \sum_{i=1}^{n_{\text{gaus}}} w_i f\left(\boldsymbol{\xi}_i\right) \tag{2.134}$$

where $\boldsymbol{\xi}_i \left(i = 1, \ldots, n_{\text{gaus}}\right)$ are the coordinates of the Gauss points and $w_i \left(i = 1, \ldots, n_{\text{gaus}}\right)$ are the corresponding weights.

Furthermore, the Gaussian quadrature rule guarantees an exact solution to a defined integral if its integration interval is $[-1; +1]$ and if enough integration points are utilised. With that in mind, the computation of integrals, such as the ones expressed in Equation (2.130) and Equation (2.131), in the natural domain of each element is common practice. That being the case, the integration of a function g over a domain Ω, with the function $\boldsymbol{x} : \Gamma \rightarrow \Omega$ mapping the standard domain Γ onto Ω (see Figure 2.13), can be written in terms of a transformation of variables by

$$\int_\Omega g(\boldsymbol{x}) \mathrm{d}\boldsymbol{x} = \int_\Gamma g(\boldsymbol{x}(\boldsymbol{\xi})) \, j(\boldsymbol{\xi}) \mathrm{d}\boldsymbol{\xi} \approx \sum_{i=1}^{n_{\text{gaus}}} w_i g\left(\boldsymbol{x}\left(\boldsymbol{\xi}_i\right)\right) j\left(\boldsymbol{\xi}_i\right), \tag{2.135}$$

where

$$j(\boldsymbol{\xi}) = \det\left[\frac{\partial \boldsymbol{x}}{\partial \boldsymbol{\xi}}\right] \tag{2.136}$$

is the determinant of the transformation jacobian. It is also worth noting that the integration can be performed not only over a domain Ω but also on the boundary $\partial\Omega$. The use of numerical integration techniques is at the heart of the finite element method as a numerical tool and its ability to solve complex partial differential problems.

Incremental loading scheme

The use of a time discretisation scheme (Section 2.9.2), which results in the use of incremental constitutive functions, warrants the use an incremental loading scheme. In this work, only proportional loading is employed, meaning that equal portions of the body forces and surface tractions are applied at each time increment t.

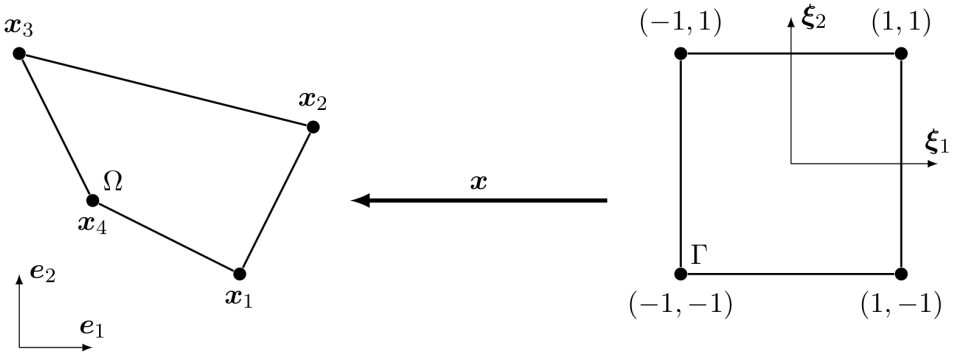

Figure 2.13: Schematic representation of the mapping from the standard domain Γ onto Ω, by the transformation function, x, for a 4-noded biliniear quadratic element, taken from Coelho (2019).

Throughout this work, the term *Load Factor* is mentioned several times, particularly in graphical representations. The load factor is the incremental measure of the finite element procedure, generally going from 0 to 1 as the load increments go from 0 to N, where N is the total number of increments of the adopted time discretisation scheme.

2.9.4 Newton-Raphson method

The finite element equilibrium equations are often nonlinear, either due to material, geometrical, frictional or other factors. In fact, many of the physical problems discussed in this text are concerned to the finite element simulation of solids undergoing finite strains, with nonlinear material models. That said, a robust numerical method must be employed to obtain a valid solution. The Newton-Raphson method is of particular interest, given its quadratic rate of convergence, and suitability for robust nonlinear incremental finite element schemes.

The key feature of the Newton-Raphson method is the linearisation of the nonlinear discretised incremental equilibrium equation, linearised on the current iterative value. Each iteration solves this linearised equation and essentially obtains an estimate of the solution, which is, then, used as the linearisation point for the next iteration. The procedure is repeated until the error of the solution is below a given tolerance. Figure 2.14 depicts this iterative process and its quadratic rate of convergence.

Recall Equation (2.126) and assume that the k-th iteration of the Newton-Raphson method is being solved. The global displacement vector at the previous iteration $\boldsymbol{u}_{n+1}^{(k-1)}$ is known. Upon linearisation, the function becomes

$$\begin{aligned}\mathbf{r}\left(\mathbf{u}_{n+1}^{(k)}\right) &\approx \mathbf{r}\left(\mathbf{u}_{n+1}^{(k-1)}\right) + \left.\frac{\partial \mathbf{r}}{\partial \mathbf{u}_{n+1}}\right|_{\mathbf{u}_{n+1}^{(k-1)}} \left(\mathbf{u}_{n+1}^{(k)} - \mathbf{u}_{n+1}^{(k-1)}\right) \\ &= \mathbf{r}^{(k-1)} + \mathbf{K}_T\left(\mathbf{u}_{n+1}^{(k)} - \mathbf{u}_{n+1}^{(k-1)}\right) \\ &= \mathbf{r}^{(k-1)} + \mathbf{K}_T \delta\mathbf{u}^{(k)}\end{aligned} \tag{2.137}$$

where $\mathbf{K}_T$ is the *global tangent stiffness matrix*. Using the linearised version of the function, the value of $\mathbf{u}_{n+1}^{(k)}$ is obtained from the solution of the system of equations

$$\mathbf{K}_T \delta\mathbf{u}^{(k)} = -\mathbf{r}^{(k-1)} \tag{2.138}$$

by

$$\mathbf{u}_{n+1}^{(k)} = \mathbf{u}_{n+1}^{(k-1)} + \delta\mathbf{u}^{(k)} \tag{2.139}$$

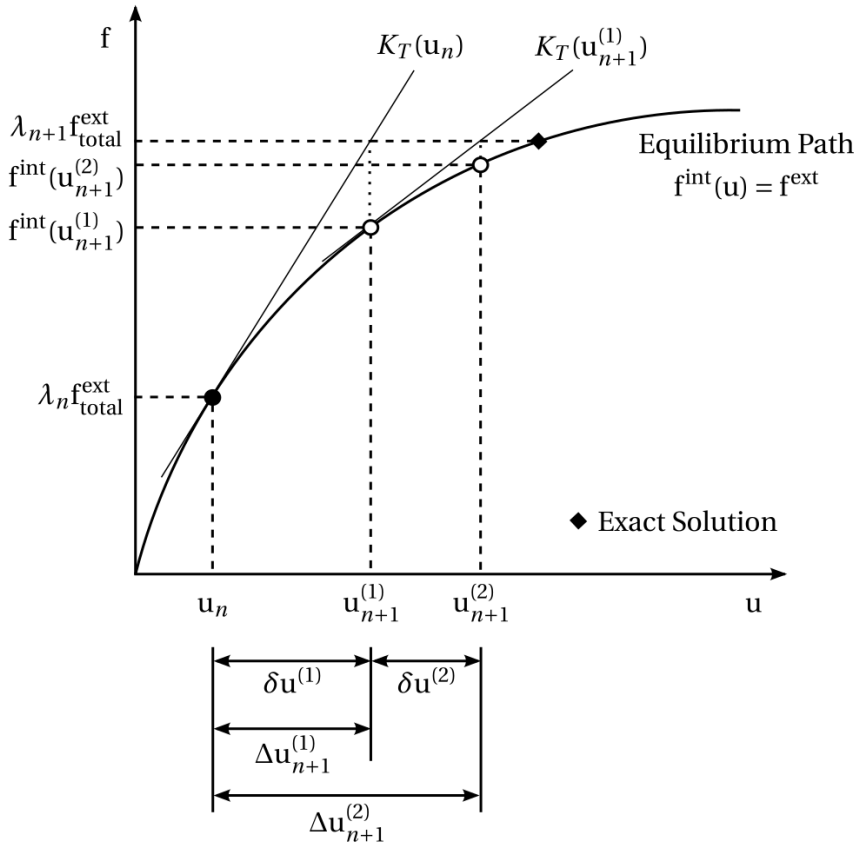

Figure 2.14: Schematic representation of the Newton-Raphson iterative procedure and its quadratic rate of convergence, taken from Ferreira (2022).

This iterative process is repeated until a certain convergence tolerance is satisfied at an iteration m, that is, until

$$\frac{|\mathbf{r}^{(m)}|}{|\mathbf{f}^{\mathrm{ext}}_{n+1}|} \leq \epsilon_{\mathrm{tol}} \tag{2.140}$$

is verified, where ϵ_{tol} is the predefined convergence tolerance. The converged value $\mathbf{u}^{(m)}_{n+1}$ then becomes the displacement vector after the increment $n+1$, that is

$$\mathbf{u}_{n+1} = \mathbf{u}^{(m)}_{n+1}. \tag{2.141}$$

The global tangent stiffness matrix is given by the assembly of all element tangent stiffness matrices, that is,

$$\mathbf{K}_T = \bigwedge_{e=1}^{n_{\mathrm{elem}}} \mathbf{K}^e_T. \tag{2.142}$$

Up to this point, no reference was made whether the terms in the Newton-Raphson method are evaluated in a spatial or material version. In a spatial version, the element tangent stiffness matrix of the element e given by

$$\mathbf{K}^e_T = \int_{\boldsymbol{\varphi}_{n+1}({}^c\Omega^c)} \mathbf{G}^\top \mathbf{a} \mathbf{G} \mathrm{d}v. \tag{2.143}$$

The fourth order tensor $\mathbf{a}$ is known as the consistent spatial tangent modulus, and is given by

$$\mathrm{a}_{ijkl} = \frac{1}{J}\frac{\partial \tau_{ij}}{\partial F_{km}} F_{lm} - \sigma_{il}\delta_{jk}, \tag{2.144}$$

where δ_{jk} is the Kroenecker delta. Alternatively, in a material version, the element tangent stiffness matrix of the element e becomes

$$\mathbf{K}_T^e = \int_{h_{\Omega^e}} \mathbf{G}^{\mathrm{T}} \mathbf{A} \mathbf{G} \mathrm{d}v. \tag{2.145}$$

Similarly, the fourth order tensor $\mathbf{A}$ is known as the consistent material tangent modulus, defined by

$$\mathrm{A}_{ijkl} = \frac{\partial P_{ij}}{\partial F_{kl}}. \tag{2.146}$$

The material and spatial elasticity tensors are related by

$$\mathrm{a}_{ijkl} = \frac{1}{J} \mathrm{A}_{imkn} F_{jm} F_{ln}. \tag{2.147}$$

Box 2.1 summarises the main steps for the solution of a given load increment of the nonlinear equations with the Newton-Raphson method.

Box 2.1 Newton-Raphson solution technique for a given increment of the nonlinear finite element equilibrium equations.

1. Initialize iterative counter, $k := 1$;
2. Set initial guess for displacements, $\mathbf{u}_{n+1}^{(0)} = \mathbf{u}_n$;
3. Compute initial residual force vector:

$$\mathbf{r}\left(\mathbf{u}_{n+1}^{(0)}\right) = \mathbf{f}^{\mathrm{int}}\left(\mathbf{u}_n\right) - \lambda_{n+1} \mathbf{f}_{\mathrm{total}}^{\mathrm{ext}}; \tag{2.148}$$

4. Compute consistent spatial tangent modulus:

$$\mathrm{a}_{ijkl} = \frac{1}{J} \mathrm{A}_{imkn} F_{jm} F_{ln} = \frac{1}{J} \frac{\partial P_{im}}{\partial F_{kn}} F_{jm} F_{ln}; \tag{2.149}$$

5. Compute and assemble elemental tangent stiffness matrices:

$$\mathbf{K}_T^e = \sum_{i=1}^{n_{\mathrm{gauss}}} w_i \mathbf{G}_i^T \mathbf{a}_i \mathbf{G}_i j_i, \quad \mathbf{K}_T = \bigwedge_{e=1}^{n_{\mathrm{elem}}} \mathbf{K}_T^e; \tag{2.150}$$

6. Increment iteration counter, $k := k + 1$;
7. Solve the equilibrium system of equations:

$$\delta \mathbf{u} = -\mathbf{K}_T^{-1}\left(\mathbf{u}_n^{(k-1)}\right) \mathbf{r}\left(\mathbf{u}_n^{(k-1)}\right); \tag{2.151}$$

8. Update displacements:

$$\mathbf{u}_{n+1}^{(k)} = \mathbf{u}_{n+1}^{(k-1)} + \delta \mathbf{u}; \tag{2.152}$$

9. Update deformation gradient:

$$\boldsymbol{F}_{n+1} = \left[\boldsymbol{I} - \nabla_{\boldsymbol{x}} \boldsymbol{u}_{n+1}^{(k)}\right]^{-1}. \tag{2.153}$$

2.10 Second-order continuum mechanics

In the context of this dissertation, a second-order continuum formulation is of the utmost importance for the multi-scale modelling of strain localisation effects. With this in mind, this section is dedicated to a brief presentation of a formulation for second-order continua at large strains.

2.10.1 Second gradient of the displacement field

Consider a second-order continuum body occupying the domain Ω in the reference configuration, which is subjected to external body forces $\boldsymbol{b}_0$, external boundary tractions $\boldsymbol{t}_0$ and double tractions $\boldsymbol{r}_0$ on part of its boundary $\partial\Omega^N$, and line forces $\boldsymbol{s}_0$ on Γ^N, as illustrated in Figure 2.15. In addition to the deformation gradient $\boldsymbol{F}$, the material constitutive behaviour of this body is also driven by the second gradient of the displacement field $\mathbf{G}$:

$$\mathbf{G} = \nabla_{\boldsymbol{p}} \boldsymbol{F} = \nabla_{\boldsymbol{p}} \left(\nabla_{\boldsymbol{p}} \boldsymbol{u} \right) \Rightarrow \mathrm{G}_{ijk} = \frac{\partial u_i}{\partial p_j \partial p_k}, \tag{2.154}$$

which can be seen as the gradient of the deformation gradient and is a symmetric fourth-order tensor.

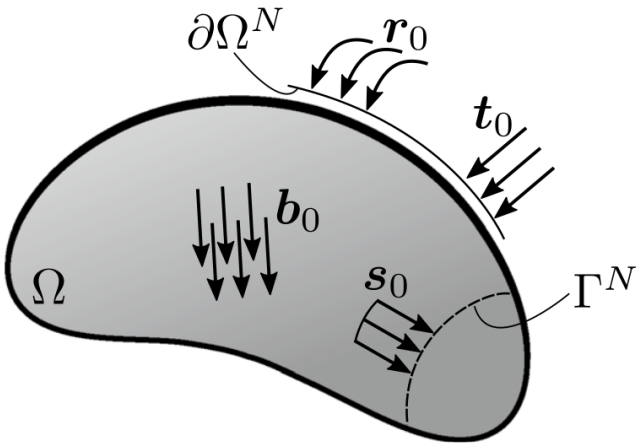

Figure 2.15: Schematic representation of a second-order continuum body subjected to an arbitrary set of external forces, taken from Rodrigues Lopes and Andrade Pires (2021).

In this case, the conjugate of the second-gradient of displacements, $\mathbf{G}$, is the higher-order stress, denoted by $\mathbf{Q}$. Polizzotto (2016) proposed a physical interpretation for these quantities, arguing that when the second-gradient is considered in the deformation kinematics of a continuum body, its infinitesimal volume elements, associated with particular points of the domain, undergo second-order deformation modes (illustrated in Figure 2.16), which must be accounted for in the strain energy density function.

2.10.2 Weak equilibrium equation

Rodrigues Lopes (2019) employ a variational approach to derive the weak equilibrium equation for second-order continua, based on the work of Kouznetsova (2002). This is done by resorting to the *Principle Virtual Work*, which states that the internal virtual work, accounting for the contribution of the higher-order stress and the second gradient, must equal the variation of the external work. In the context of second-gradient continua, the contribution of the double tractions $\boldsymbol{r}_0$, which are

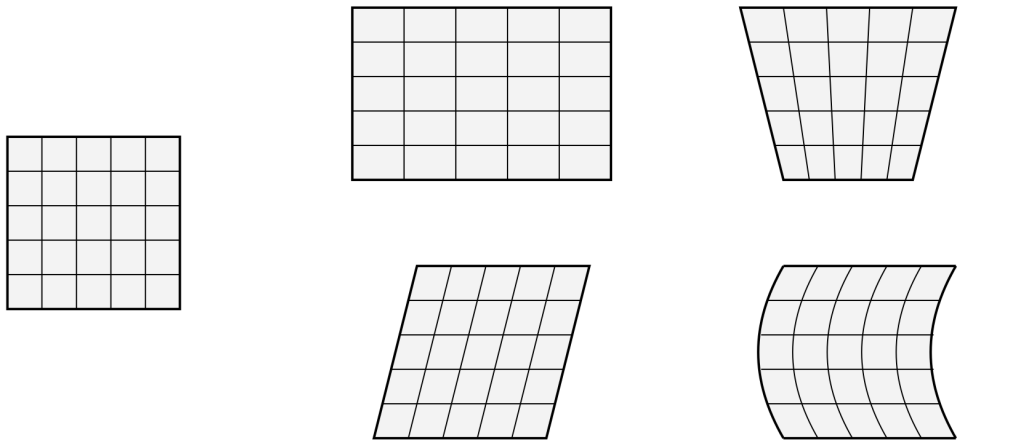

(a) Undeformed (b) 1^{st}-order modes (c) 2^{nd}-order modes

Figure 2.16: Schematic representation of an initially undeformed infinitesimal volume element (a), undergoing first- (b) and second-order (c) deformation modes. Taken from Silva (2021).

dual to the normal displacements gradient $D_0\delta\boldsymbol{u} = \nabla_{\boldsymbol{p}}\delta\boldsymbol{u}\cdot\boldsymbol{N}$, is also included. Therefore the weak equilibrium equation, in the material description, reads:

$$\int_\Omega (\boldsymbol{P}:\delta\boldsymbol{F} + \mathbf{Q}\vdots\delta\mathbf{G})dV = \int_\Omega \boldsymbol{b}_0\cdot\delta\boldsymbol{u}dV + \int_{\partial\Omega^N}\boldsymbol{t}_0\cdot\delta\boldsymbol{u}dA + \int_{\partial\Omega^N}\boldsymbol{r}_0\cdot D_0\delta\boldsymbol{u}dA + \int_{\Gamma^N}\boldsymbol{s}_0\cdot\delta\boldsymbol{u}dA, \quad (2.155)$$

where $\boldsymbol{r}_0$ are the external double tractions on the boundary and s_0 represents the external line forces.

2.10.3 Strong equilibrium

The strong form of the equilibrium can be attained through some algebraic manipulations of the weak form statement, detailed in Section 2.10.2. For the sake of brevity, such manipulations are not included in this section and the interested reader is referred to the work of Rodrigues Lopes (2019). The strong form of the equilibrium equations for second-gradient continua is expressed by the following set of equations:

$$\begin{array}{rcll} \boldsymbol{b}_0 &=& \mathrm{div}(\mathrm{div}\,\mathbf{Q}) - \mathrm{div}\,\boldsymbol{P}, & \text{in } \Omega \\ \boldsymbol{t}_0 &=& \boldsymbol{P}\cdot\boldsymbol{N} - \mathrm{div}\,\mathbf{Q}\cdot\boldsymbol{N} + \mathrm{div}^t\boldsymbol{N}(\mathbf{Q}\cdot\boldsymbol{N})\cdot\boldsymbol{N} - \mathrm{div}^t(\mathbf{Q}\cdot\boldsymbol{N}), & \text{on } \partial\Omega \\ \boldsymbol{r}_0 &=& (\mathbf{Q}\cdot\boldsymbol{N})\cdot\boldsymbol{N}, & \text{on } \partial\Omega \\ \boldsymbol{s}_0 &=& \|(\mathbf{Q}\cdot\boldsymbol{N})\cdot\boldsymbol{m}\|, & \text{on } \Gamma \end{array} \quad (2.156)$$

where div^t denotes the tangential divergence operator and m is the unit vector tangent to the surface $\partial\Omega$ and normal to the line Γ^{n_0}.

2.10.4 Finite element solution for second-order problems

When utilising numerical techniques, like the finite element method, to discretise and solve the weak equilibrium equation for first-order continuum formulations, only C^0 continuity of the displacement field must be ensured, which is the most common for conventional element types. In the case of second-gradient formulations, C^1 continuity must also be guaranteed, either with sofisticated adaptions of C^0, or with pure C^1 elements. This has motivated the community to explore several strategies for the formulation of C^1 continuous elements, including the contributions of

Petera and Pittman (1994), where the shape functions are not explicitly defined, penalty-based approaches (Papanicolopulos et al., 2009, Zervos, 2008), staggered schemes (Bagni and Askes, 2015), discontinuous-Galerkin method (Nguyen and Noels, 2014) and mixed approaches based on Lagrange multipliers (Kouznetsova et al., 2001, Luscher, 2010, Matsushima et al., 2002, Phunpeng and Baiz, 2015), which have shown remarkable success in the context second-order homogenisation.

In this dissertation, a mixed formulation, detailed in Rodrigues Lopes and Andrade Pires (2021), was employed to guarantee C^1 continuity with C^0 elements. Mixed finite elements are defined by introducing an additional independent variable consisting of the relaxed deformation gradient field, denoted by $\hat{\boldsymbol{F}}$, in addition to the displacement field, $\boldsymbol{u}$. Furthermore, the compatibility between $\hat{\boldsymbol{F}}$ and the actual deformation gradient, computed from the displacement field (see Equation (2.14)), is weakly enforced with Lagrange multipliers, λ. The weak equilibrium statement must, then, be modified to ensure compatibility. Neglecting external line forces, $\boldsymbol{s}_0$, Equation (2.155) can be recast as

$$\int_\Omega \left(\boldsymbol{P} : \delta \boldsymbol{F} + \mathbf{Q} \vdots \nabla^s_{\boldsymbol{p}} \delta \hat{\boldsymbol{F}} - \delta \left[\lambda : \left(\boldsymbol{F} - \hat{\boldsymbol{F}} \right) \right] \right) dV = \int_\Omega \boldsymbol{b}_0 \cdot \delta \boldsymbol{u} dV + \int_{\partial\Omega^N} \boldsymbol{t}_0 \cdot \delta \boldsymbol{u} dA + \int_{\partial\Omega} \boldsymbol{R}_0 : \hat{\boldsymbol{F}} dA, \quad (2.157)$$

where $\nabla^s_{\boldsymbol{p}}$ denotes the symmetric material gradient operator, and

$$\boldsymbol{R}_0 = \boldsymbol{r}_0 \otimes \boldsymbol{N}. \quad (2.158)$$

Additionally, the second-gradient of displacements can be obtained as follows:

$$\mathbf{G} = \nabla^s_{\boldsymbol{p}} \delta \hat{\boldsymbol{F}} \Rightarrow \mathrm{G}_{ijk} = \frac{1}{2} \left(\frac{\partial \hat{F}_{ij}}{\partial p_k} + \frac{\partial \hat{F}_{ik}}{\partial p_j} \right). \quad (2.159)$$

Finally, the enforcement of compatibility on the external boundaries arises naturally if the domain is properly discretised (Kouznetsova, 2002).

Spatial discretisation

Mixed finite elements are characterised by an independent interpolation of the displacement field $\boldsymbol{u}$, the relaxed deformation gradient field $\hat{\boldsymbol{F}}$ and the Lagrange multipliers field λ, which is defined through:

$$\boldsymbol{u} = \sum_{k=1}^{n_{nu}} H^u_k u_k = \mathbf{H}^u \mathbf{u}, \quad (2.160)$$

$$\hat{\boldsymbol{F}} = \sum_{k=1}^{n_{nF}} H^F_k \hat{F}_k = \mathbf{H}^F \hat{\boldsymbol{F}}, \quad (2.161)$$

$$\boldsymbol{\lambda} = \sum_{k=1}^{n_\lambda} H^\lambda_k \lambda_k = \mathbf{H}^\lambda \lambda, \quad (2.162)$$

where $\mathbf{H}^u$ denotes the shape function matrix for both the displacements and coordinates interpolation, $\mathbf{H}^F$ is the matrix with interpolation functions for the deformation gradient and $\mathbf{H}^\lambda$ for the Lagrange multipliers.

Since all problems discussed in this work are limited to a 2D analysis, only the bi-dimensional Q8F4L1 mixed element, proposed by Matsushima et al. (2002), was utilised, since it showcases a decent balance between computational cost and accuracy (Kouznetsova, 2002, Rodrigues Lopes, 2019). This quadrilateral element, illustrated in Figure 2.17, employs 8 nodes for displacements and geometry interpolation, with quadratic shape functions, 4 nodes and bi-linear shape functions for the interpolation of the deformation gradient, and a single node for the Lagrange multiplier field, which is constant in the element domain. This results in a total of 36 degrees of freedom and a 2×2 Gauss integration scheme suffices for this element type.

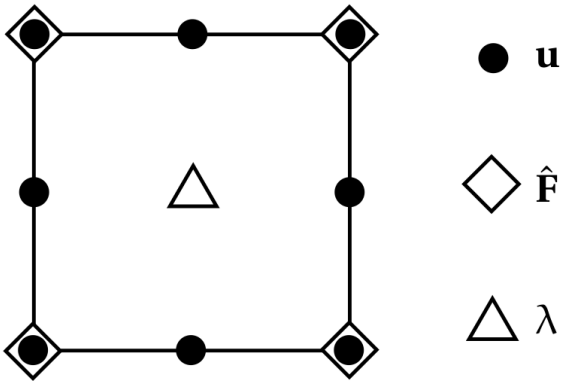

Figure 2.17: Schematic representation of the Q8F4L1 mixed finite element for second-order analysis, taken from Rodrigues Lopes (2019).

Discretising the modified weak form statement for second-order continua, expressed in Equation (2.157), the finite element equilibrium equations are obtained:

$$\mathbf{r} = \left\{ \begin{array}{c} \mathbf{r}^u \\ \mathbf{r}^F \\ \mathbf{r}^\lambda \end{array} \right\} = \left\{ \begin{array}{c} \int_{\Omega^d} (\mathbf{G}^u)^T \mathbf{P} \mathrm{d}V - \int_{\Omega^d} (\mathbf{G}^u)^T \mathbf{H}^\lambda \mathrm{d}V\lambda - \int_{\Omega^d} (\mathbf{N}^u)^T \mathbf{b}_0 \, \mathrm{d}V - \int_{\partial\Omega^d} (\mathbf{N}^u)^T \mathbf{t}_0 \, \mathrm{d}A \\ \int_{\Omega^d} \left(\mathbf{G}^F\right)^T \mathbf{Q} \mathrm{d}V + \int_{\Omega^d} \left(\mathbf{H}^F\right)^T \mathbf{H}^\lambda \mathrm{d}V\lambda - \int_{\partial\Omega^d} \left(\mathbf{H}^F\right)^T \mathbf{R}_0 \, \mathrm{d}A \\ \int_{\Omega^d} \left(\mathbf{H}^\lambda\right)^T \mathbf{H}^F \, \mathrm{d}V\hat{\mathbf{F}} - \int_{\Omega^d} \left(\mathbf{H}^\lambda\right)^T \mathbf{G}^u \, \mathrm{d}V\mathbf{x} \end{array} \right\} = \mathbf{0}, \tag{2.163}$$

where $\mathbf{G}^u$ is the displacement discrete gradient operator, defined in Equation (2.123), and $\mathbf{G}^F$ is the analogous operator for the deformation gradient.

2.10.5 Newton-Raphson method for problems including the second-gradient

In Section 2.10.4, it was shown that the discretisation and solution of a second-order continua equilibrium problem with the finite element method warrants the introduction of some additional independent variables. With this in mind, the Newton-Raphson method must be modified to solve the nonlinear finite element equilibrium equation (Equation (2.163)). In this case, the residual vector must be linearised with respect to the additional variables, as demonstrated in what follows:

$$\Delta\mathbf{r} = \frac{\partial \mathbf{r}}{\partial \mathbf{u}} \Delta\mathbf{u} + \frac{\partial \mathbf{r}}{\partial \hat{\boldsymbol{F}}} \Delta\hat{\boldsymbol{F}} + \frac{\partial \mathbf{r}}{\partial \lambda} \Delta\lambda, \tag{2.164}$$

where the partial derivatives are computed for each residual sub-vector, $\mathbf{r}^u$, $\mathbf{r}^F$ and $\mathbf{r}^\lambda$ to attain the cofficient sub-matrices that compose the linear system of equations:

$$\left[\begin{array}{ccc} \mathbf{k}^{uu} & \mathbf{k}^{uF} & \mathbf{k}^{u\lambda} \\ \mathbf{k}^{Fu} & \mathbf{k}^{FF} & \mathbf{k}^{F\lambda} \\ \mathbf{k}^{\lambda u} & \mathbf{k}^{\lambda F} & \mathbf{k}^{\lambda\lambda} \end{array} \right]^{(k)} \left\{ \begin{array}{c} \Delta\mathbf{u} \\ \Delta\hat{\mathbf{F}} \\ \Delta\lambda \end{array} \right\}^{(k+1)} = -\left\{ \begin{array}{c} \mathbf{r}^u \\ \mathbf{r}^F \\ \mathbf{r}^\lambda \end{array} \right\}^{(k)}, \tag{2.165}$$

with the unknown variables being updated through

$$\left\{ \begin{array}{c} \mathbf{u} \\ \hat{\mathbf{F}} \\ \lambda \end{array} \right\}^{(k+1)} = \left\{ \begin{array}{c} \mathbf{u} \\ \hat{\mathbf{F}} \\ \lambda \end{array} \right\}^{(k)} + \left\{ \begin{array}{c} \Delta\mathbf{u} \\ \Delta\hat{\mathbf{F}} \\ \Delta\lambda \end{array} \right\}^{(k+1)}. \tag{2.166}$$

For the sake of brevity, the expressions for each sub-matrix of Equation (2.165) were not presented, but the interested reader is referred to the work of Rodrigues Lopes and Andrade Pires (2021).

CHAPTER 3

MULTI-SCALE MODELS BASED ON COMPUTATIONAL HOMOGENISATION

3.1 Introduction to multi-scale modelling

The emergence of the advanced materials with optimised properties and features in recent years is inseparable from the study of material behaviour at varios length-scales. Materials with optimised properties often possess highly nonlinear heterogeneous multiphasic microstructures, where underlying mechanisms and phenomena play critical roles (Ferreira, 2022). As a result, an accurate description of their behaviour poses issues to traditional continuum models. On the one hand, macroscopic phenomenological models require large sets of material parameters to be calibrated for a given set of conditions through time-consuming and expensive experiments. On the other hand, performing direct numerical simulations, by taking into account all the heterogeneities from the lower scales, leads to problems with unfeasible dimension for realistic engineering applications.

Multi-scale modelling methodologies, particularly the ones based on homogenisation procedures, have gained traction the past two decades, since they allow the treatment of macroscopic materials and solids as hierarchical objects, whose observable behaviour is deeply linked to underlying mechanisms and features embedded at their microstructure. Such multi-scale modelling approaches allow predicting the macro-scale response of solids by resolving their topological, physical and statistical details at lower length- and time-scales. This is done by employing *scale-bridging* strategies, which define and quantify the relation between material behaviour at different modelling levels. According to Matouš et al. (2017), scale-bridging strategies can be classified as follows:

1. *Concurrent methods*, in essence, address multiple time- and length-scales in a single domain, simultaneously, often with different methodologies. These approaches generally include adaptive schemes in order to select the regions of interest in the macroscopic domain, to alleviate computational demand. If such adaptive schemes are not adopted, concurrent strategies coincide with the *Direct Numerical Simulation* (DNS) of the multi-scale problem, including all of its microscopic details. In practice, DNS approaches are mostly used to validate the numerical results of more intricate predictive strategies. A few examples of works on concurrent multi-scale methods include Fish (2006), Temizer and Wriggers (2011), Zhang et al. (2012).

2. In *Hierarchical methods*, the scales are linked hierarchically, i.e. different scales are resolved in the same part of a domain. The link between both scales is typically made via *homogenisation*

theorems. Such theorems include *computational homogenisation*, the main scale-bridging strategy employed in this work, in which two or more length-scales are coupled for the solution of mechanical problems. However, other theorems, such as analytical or numerical homogenisation procedures, have also been utilised in the literature, and do not necessarily imply a direct coupling between scales. For instance, numerical homogenisation includes parameter identification procedures, in which the microscopic behaviour of materials is used to calibrate their constitutive parameters at the macro-scale (see Fonseca Gonçalves (2022)). Data-driven and machine-learning-based approaches can also be employed to accelerate coupled multi-scale simulations, by replacing the micro-scale continuum model with a *surrogate*, that mirrors the response of the former at a lower computational cost. Adaptative Clustering-based Reduced Order Models (ACROMs, see Ferreira et al. (2022a) for further details) and Physically Recurrent Neural Networks (PRNNs, see Maia et al. (2023)) are two prime examples of this.

3. Finally, *Hybrid methods* are a mix of strategies that reveal features of the two aforementioned classes. Some examples of hybrid methods are: multi-grid methods (Miehe and Bayreuther, 2007), quasi-continuum methods (Tadmor et al., 1996), wavelet-based methods, generalized finite element method (Plews and Duarte, 2015).

In the literature, the modelling of several classes of materials has been enhanced with the introduction of multi-scale strategies. This is the case for the mechanical behaviour of composite materials (Elmasry et al., 2023, Kanouté et al., 2009, Orifici et al., 2008, Soutis and Beaumont, 2005), including degradative environmental effects (Ferreira Rocha et al., 2024). It is also the case for metals, where multi-scale models have been developed to predict the response of dual-phase steels which undergo mechanically-induced martensitic transformation (Cardoso Coelho et al., 2023, de Carvalho et al., 2022, Rodrigues Lopes et al., 2023, Vieira de Carvalho et al., 2022). Lastly, these advanced modelling strategies have also allowed interesting investigations into the behaviour of metamaterials (dos Santos et al., 2024, Jamshidian et al., 2020, Kochmann et al., 2019, Lu and Tong, 2023).

The use of multi-scale modelling methodologies allows not only describing the behaviour of existing materials with enhanced accuracy, but also developing novel material solutions for specific applications. In the so-called Age of New Materials, developments in engineering and materials science have allowed researchers to tailor the microscopic arrangement of materials and structures to achieve the desired macroscopic properties or design considerations. In this context, Horstemeyer (Horstemeyer, 2012, 2018) proposed the Integrated Computational Materials Engineering (ICME) paradigm, to accelerate the development of new materials by fostering collaborative research efforts. The ICME paradigm aims to integrate design, manufacturing and materials science by forging process-structure-property-performance relationships and combining it with multi-scale process-structure and structure-property modeling over different length scales.

The following sections present the multi-scale model employed in this dissertation. Section 3.2 introduces the fundamental concepts of computational homogenisation, including the Representative Volume Element (RVE). Thereafter, Section 3.3 and Section 3.4 present the formulations for multi-scale models based on first- and second-order homogenisation, respectively. Section 3.5 presents the adaptations required for the second-order formulation to model RVEs containing voids. Finally, Section 3.6 discusses the solution of large-strain multi-scale problems.

The variational theory introduced by de Souza Neto and co-workers is the basis for the multi-scale models presented in this chapter (Blanco et al., 2016b, de Souza Neto et al., 2015, de Souza Neto and Feijóo, 2010). Regarding second-order homogenisation, the works of Blanco et al. (2016a), Rodrigues Lopes (2019), Rodrigues Lopes and Andrade Pires (2021), Rodrigues Lopes and Andrade Pires (2022b), Rodrigues Lopes et al. (2023) provide additional mathematical and numerical details.

3.2 Computational homogenisation

The multi-scale models employed in the context of this dissertation are based on computational homogenisation for scale-bridging. In this section, a brief introduction to this topic is presented, starting with its basic concept in Section 3.2.1, before discussing the importance of the Representative Volume Element in Section 3.2.2.

3.2.1 Basic concept of computational homogenisation

Multi-scale models based on computational homogenisation were first developed during the 1990s and 2000s (Feyel and Chaboche, 2000, Ghosh et al., 1995, Guedes and Kikuchi, 1990, Kouznetsova et al., 2001, Smit et al., 1998). These models rely on averaging techniques to derive the macroscopic constitutive response from a Representative Volume Element (RVE), which accounts for material details and properties at lower length-scales. These length-scales are bridged by the convenient homogenisation of relevant fields, resulting in a set of microscopic constraints. In essence, the macro-scale problem is solved with a standard finite element solution scheme, with the nuance that the solution of the mechanical constitutive initial boundary value problem at each macro-scale integration point is replaced by the solution of the microscopic equilibrium problem, with the prescription of the macroscopic deformation gradient. After the RVE balance problem is solved, the relevant fields, e.g. the First Piola-Kirchhoff stress tensor and the consistent tangent modulus, are homogenised and up-scaled. This solution technique is depicted in Figure 3.1.

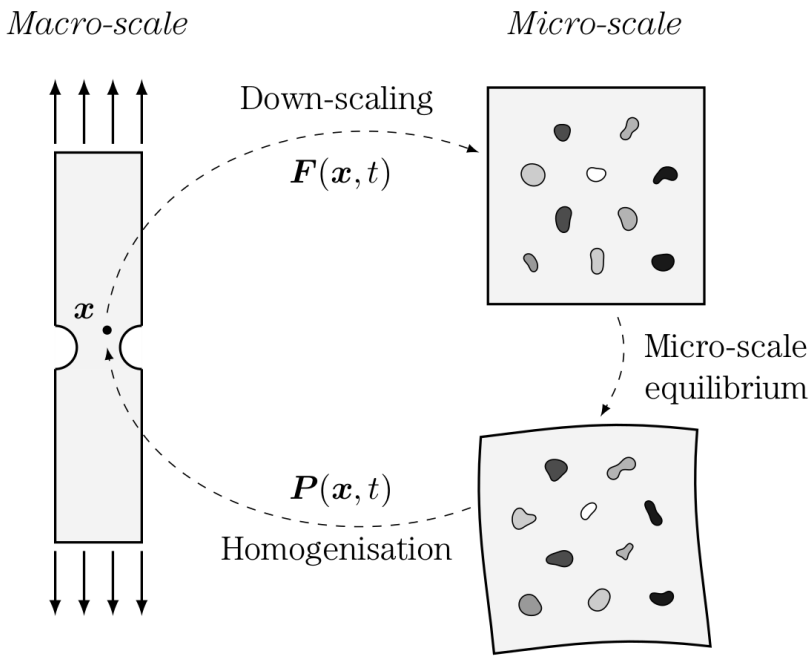

Figure 3.1: Schematic representation of the solution of a multi-scale problem with recourse to first-order computational homogenisation. Taken from Silva (2021).

3.2.2 Representative volume element

Multi-scale models based on computational homogenisation rely on the continuous exchange of information between two or more length-scales. In this framework, the RVE is a means from which the micro-scale is represented and homogenised. In other words, the RVE is used to capture the microstructural features of a given material, so that their influence on the macroscopic behaviour of solids and structures can be considered. The concept of a representative volume element was

firstly introduced by Hill (1965). The RVE can be interpreted as the smallest volume of material where the assumption of material continuity is still valid (de Souza Neto et al., 2008). According to Hill, the RVE is a sample of material with a structure that is typical, on average, of the entire material, and has enough microscopic defects to make the mechanical properties independent of boundary values. Gitman et al. (2007) produced a comprehensive discussion on the RVE concept, its existence and numerical and experimental attempts at RVE size determination. An important conclusion from their investigation is that, in the context of computational homogenisation, an RVE only exists for statistically homogeneous materials and material responses, since the scale-bridging strategy is reliant on this premise.

Generally speaking, the RVE should be large enough to accurately capture the microstructure of the material, while also being significantly smaller than the macro-scale domain, to comply with the *principle of separation of scales*. In essence, the RVE size, l_{RVE}, must relate to the size of microstructural features, l, and to the dimension of the macroscopic structure, L, as follows:

$$l << l_{\text{RVE}} << L. \tag{3.1}$$

Figure 3.2 depicts a representative volume element and its relation to a particular point in the macroscopic structure, while also highlighting the characteristic dimensions that compose the principle of separation of scales.

The aforementioned microstructural features, depending on the material, may include grain boundaries, cracks, voids, inclusions or other deffects. Since porous RVEs are utilised in this work (see Chapter 6), it is convenient to decompose the undeformed domain of a generic RVE, Ω_μ, into two distinct regions:

$$\Omega_\mu = \Omega_\mu^s \bigcup \Omega_\mu^v, \tag{3.2}$$

where Ω_μ^s and Ω_μ^v denote the volume of the RVE occupied by the solid and void regions. Here, the subscript $(\cdot)_\mu$ is used to identify a micro-scale quantity. Following this notation, together with the one from Chapter 2, the boundary of the RVE is $\partial\Omega_\mu$.

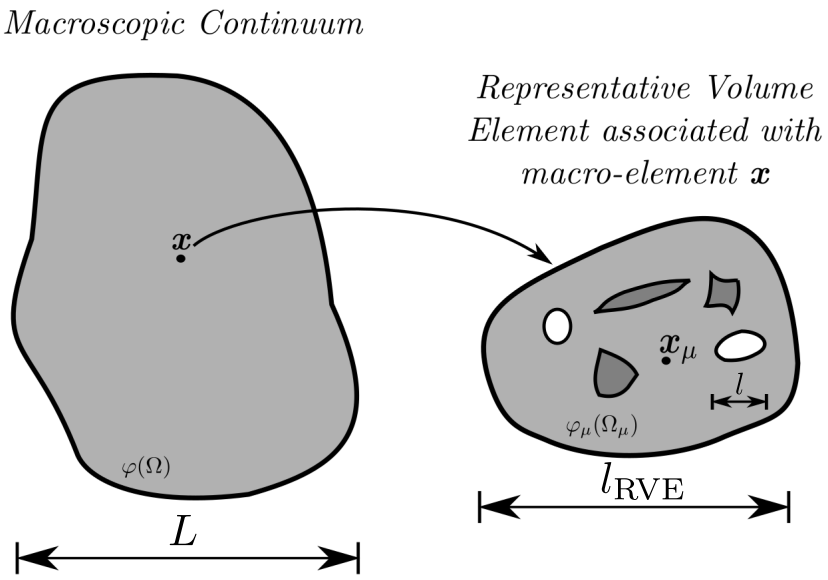

Figure 3.2: Schematic representation of the RVE concept and the principle of separation of scales, adapted from Vieira (2018).

3.3 First-order computational homogenisation formulation

In this section, the solution of the multi-scale problem based on first-order computational homogenisation is addressed. The present formulation is based on the *Method of Multi-scale Virtual Power* (Blanco et al., 2016b), which ensures variational consistency across length-scales. Section 3.3.1 presents the homogenisation of the macroscopic deformation gradient, Section 3.3.2 discusses multi-scale kinematics, and Section 3.3.4 touches on the Hill-Mandel principle of macro-homogeneity. Thereafter, Section 3.3.3 presents the various boundary conditions that can be applied to the microscopic domain. Lastly, Section 3.3.5 assesses the homogenisation of the micro-scale First Piola-Kirchhoff stress tensor.

3.3.1 Homogenised deformation gradient

Homogenisation is the averaging technique which allows the transition of quantities from one length scale to the other. Through homogenisation, the macro-scale properties at a given point $\boldsymbol{x}$ are a volume average of such properties down at the microscopic level. For example, given a certain field $\boldsymbol{A}(\boldsymbol{x}, t)$ over a certain continuum body at the macro-scale, its value can be obtained from the equivalent field at the micro-scale, $\boldsymbol{A}_\mu(\boldsymbol{x}_\mu, t)$ by

$$\boldsymbol{A}(\boldsymbol{x}, t) = \frac{1}{v_{0,\mu}} \int_{\Omega_\mu} \boldsymbol{A}_\mu(\boldsymbol{x}_\mu, t)\, \mathrm{d}v, \tag{3.3}$$

where $\boldsymbol{x}_\mu$ is a point at the microscopic domain and $v_{0,\mu}$ is the volume of the RVE in its reference configuration. This way, homogenisation allows for the definition of macroscopic properties as volume averages of their counterparts at the micro-scale.

The Homogenised Deformation Gradient, $\boldsymbol{F}$, for instance, at a given material point $\boldsymbol{p}$ of the continuum body relates to its micro-scale counterpart by

$$\boldsymbol{F}(\boldsymbol{p}, t) = \frac{1}{v_{0,\mu}} \int_{\Omega_\mu} \boldsymbol{F}_\mu(\boldsymbol{p}_\mu, t)\, \mathrm{d}v, \tag{3.4}$$

where $\boldsymbol{p}_\mu$ is a generic infinitesimal material point of the RVE domain. Recalling equation 2.14, the deformation gradient can be rewritten as

$$\boldsymbol{F}(\boldsymbol{p}, t) = \boldsymbol{I} + \frac{1}{v_{0,\mu}} \int_{\Omega_\mu} \nabla_{\boldsymbol{p}} [\boldsymbol{u}_\mu(\boldsymbol{p}_\mu, t)]\, \mathrm{d}v. \tag{3.5}$$

Through the application of Gauss's theorem, the integration over the domain Ω_μ can be recast as an integration over the boundary $\partial\Omega_\mu$, such that

$$\boldsymbol{F}(\boldsymbol{p}, t) = \boldsymbol{I} + \frac{1}{v_{0,\mu}} \int_{\partial\Omega_\mu} \boldsymbol{u}_\mu(\boldsymbol{p}_\mu, t) \otimes \boldsymbol{n}_{0,\mu}(\boldsymbol{p}_\mu)\, \mathrm{d}v, \tag{3.6}$$

where $\boldsymbol{n}_{0,\mu}$ is the unit vector normal to the external boundary of the RVE in its reference configuration. This last expression allows for the expression of the macro-scale deformation gradient as a function of the micro-scale displacement field $\boldsymbol{u}_\mu$ over the boundary of the RVE.

3.3.2 Multi-scale kinematics

The prescription of a macroscopic deformation gradient places a constraint on the set of admissible displacement fields over the RVE's boundary. That being the case, the condition for *kinematic admissibility* can be expressed as

$$\boldsymbol{u}_\mu \in \mathcal{K}_\mu^*, \tag{3.7}$$

where $\mathcal{K}_\mu^*$ denotes the minimally constrained set of *kinematically admissible microscopic displacements*, given by

$$\mathcal{K}_\mu^* \equiv \left\{ \boldsymbol{u}_\mu, \text{sufficiently regular} \middle| \int_{\partial\Omega_\mu} \boldsymbol{u}_\mu(\boldsymbol{p}_\mu, t) \otimes \boldsymbol{n}_{0,\mu}(\boldsymbol{p}_\mu)\, \mathrm{d}a = v_{0,\mu}[\boldsymbol{F}(\boldsymbol{x}, t) - \boldsymbol{I}] \right\}. \tag{3.8}$$

The microscopic displacement field, $\boldsymbol{u}_\mu$, may be split into its linear component, which is directly linked to the macroscopic deformation gradient, and the *displacement fluctuation*, $\tilde{\boldsymbol{u}}_\mu$, as follows:

$$\boldsymbol{u}_\mu(\boldsymbol{p}_\mu, t) = [\boldsymbol{F}(\boldsymbol{x}, t) - \boldsymbol{I}] \cdot \boldsymbol{p}_\mu + \tilde{\boldsymbol{u}}_\mu(\boldsymbol{p}_\mu, t). \tag{3.9}$$

In this context, since the linear displacement is a known quantity, the microscopic displacement fluctuation, $\tilde{\boldsymbol{u}}_\mu$, is the unknown variable of the RVE equilibrium problem. Furthermore, the microscopic deformation gradient can be expressed as a sum of the macroscopic deformation gradient, which translates into an homogeneous deformation of the RVE, and a second term, expressed as a function of the displacement fluctuation field, such that

$$\boldsymbol{F}_\mu(\boldsymbol{x}, t) = \boldsymbol{F}(\boldsymbol{x}, t) + \nabla_{\boldsymbol{p}}[\tilde{\boldsymbol{u}}_\mu(\boldsymbol{p}_\mu, t)]. \tag{3.10}$$

Introducing Equation (3.4) into the decomposition above,

$$\boldsymbol{F}(\boldsymbol{x}, t) = \boldsymbol{F}(\boldsymbol{x}, t) + \frac{1}{v_{0,\mu}} \int_{\Omega_\mu} \nabla_{\boldsymbol{p}}[\tilde{\boldsymbol{u}}_\mu(\boldsymbol{x}_\mu, t)]\, \mathrm{d}v. \tag{3.11}$$

From the last equation, it can be concluded that

$$\int_{\Omega_\mu} \nabla_{\boldsymbol{p}}[\tilde{\boldsymbol{u}}_\mu(\boldsymbol{x}_\mu, t)]\, \mathrm{d}v = \boldsymbol{0}, \tag{3.12}$$

defining the *minimal kinematically admissible constraint*. Additionally, this equation can be rewritten, using the Gauss Theorem, as

$$\int_{\partial\Omega_\mu} \tilde{\boldsymbol{u}}_\mu(\boldsymbol{x}_\mu, t) \otimes \boldsymbol{n}_{0,\mu}(\boldsymbol{p}_\mu)\, \mathrm{d}a = \boldsymbol{0}. \tag{3.13}$$

Consequently, the *minimally constrained space of displacement fluctuations* is defined by:

$$\mathcal{K}_\mu^* \equiv \left\{ \tilde{\boldsymbol{u}}_\mu, \text{sufficiently regular} \middle| \int_{\partial\Omega_\mu} \tilde{\boldsymbol{u}}_\mu(\boldsymbol{x}_\mu, t) \otimes \boldsymbol{n}_{0,\mu}(\boldsymbol{p}_\mu)\, \mathrm{d}a = \boldsymbol{0} \right\}. \tag{3.14}$$

Additional constraints may be placed upon the RVE. Therefore, the *actual set of kinematically admissible fluctuation fields*, $\tilde{\mathcal{K}}_\mu$, may be defined, such that,

$$\tilde{\boldsymbol{u}}_\mu \in \tilde{\mathcal{K}}_\mu \subset \tilde{\mathcal{K}}_\mu^*. \tag{3.15}$$

3.3.3 Micro-scale boundary conditions

In this subsection, a set of micro-scale boundary condition models are introduced. In essence, they define the level of kinematic constraint imposed on the RVE, by restricting the initial set of possible displacement fluctuations, $\tilde{\mathcal{K}}_\mu^*$, into $\tilde{\mathcal{K}}_\mu$. The level of constraint is dependent on the chosen model. In the context of the present dissertation, the following micro-scale boundary condition are of interest:

1. *Taylor Boundary Condition*
2. *Linear Boundary Condition*

3. *Periodic Boundary Condition*

4. *Uniform Traction Boundary Condition*

The microscopic boundary conditions are listed in order of decreasing kinematic constraint, meaning that the Taylor Condition is the one associated with the greatest kinematic constraint of the RVE. That being the case, it can be written that

$$^{Tay}\tilde{\mathcal{K}}_\mu \subset^{Lin} \tilde{\mathcal{K}}_\mu \subset^{Per} \tilde{\mathcal{K}}_\mu \subset^{Uni} \tilde{\mathcal{K}}_\mu \equiv \tilde{\mathcal{K}}^*_\mu, \tag{3.16}$$

where the Uniform Traction Boundary Condition is equivalent to the minimum kinematic constraint imposed upon the RVE.

Taylor boundary condition

The Taylor Boundary Condition is the simplest and most restrictive of all the models under consideration. It states that the displacement fluctuation is null over the entirety of the RVE,

$$\tilde{\boldsymbol{u}}_\mu(\boldsymbol{p}_\mu, t) = \boldsymbol{0}, \forall \boldsymbol{p}_\mu \in \Omega_\mu, \tag{3.17}$$

for every microscopic point $\boldsymbol{p}_\mu$ contained within the RVE.

Figure 3.3 represents a possible deformation of an arbitrary RVE, with respect to the Taylor Boundary Condition. The deformation is, naturally, homogeneous.

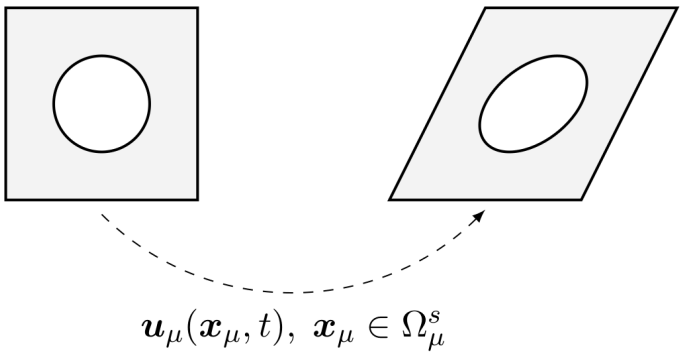

Figure 3.3: Schematic representation of the deformation of an RVE under with the Taylor boundary condition, taken from Silva (2021).

For the Taylor Boundary Condition, the set of kinematically admissible displacement fluctuations is given by:

$$^{Tay}\mathcal{K}^*_\mu \equiv \left\{ \tilde{\boldsymbol{u}}_\mu, \text{sufficiently regular} \middle| \tilde{\boldsymbol{u}}_\mu(\boldsymbol{p}_\mu, t) = \boldsymbol{0}, \forall \boldsymbol{p}_\mu \in \Omega_\mu \right\}. \tag{3.18}$$

Linear boundary condition

The Linear Boundary Condition is less kinematically restrictive than the Taylor Condition, as it enforces null displacement fluctuations on the boundary of the RVE,

$$\tilde{\boldsymbol{u}}_\mu(\boldsymbol{p}_\mu, t) = \boldsymbol{0}, \forall \boldsymbol{p}_\mu \in \partial\Omega_\mu. \tag{3.19}$$

Figure 3.4 represents a possible deformation of an arbitrary RVE, with respect to the Linear Boundary Condition. As can be seen, the deformation of the RVE's boundary is uniform, while the deformation of the rest of the RVE can fluctuate.

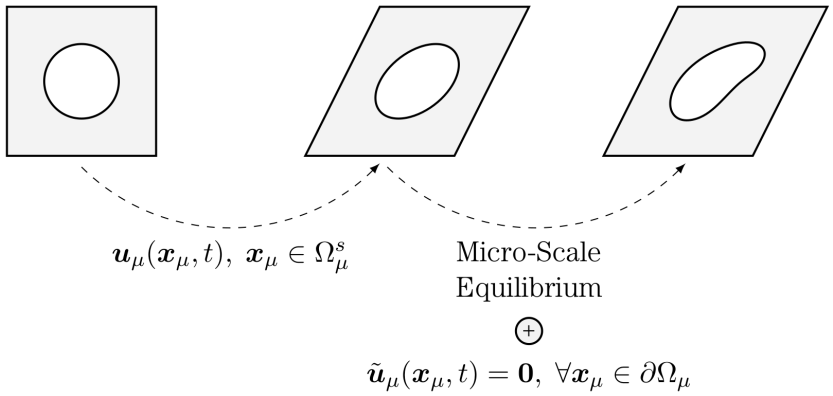

Figure 3.4: Schematic representation of the deformation of an RVE with the linear boundary condition, taken from Silva (2021).

For the Linear Boundary Condition, the set of kinematically admissible displacement fluctuations is given by:

$$^{Lin}\mathcal{K}^*_\mu \equiv \left\{ \tilde{\boldsymbol{u}}_\mu, \text{sufficiently regular} \middle| \, \tilde{\boldsymbol{u}}_\mu(\boldsymbol{p}_\mu, t) = \mathbf{0}, \forall \boldsymbol{p}_\mu \in \partial\Omega_\mu \right\}. \tag{3.20}$$

Periodic boundary condition

The Periodic Boundary Condition is of common use in the micro-mechanical simulation of materials with periodic microstructures. In these cases, these materials' microstructure may be portrayed as a periodic pattern of RVE's. As the periodicity must remain true in the deformed configurations of the RVE, the resulting displacements in opposite sides of the boundary must be compatible. For this purpose, the boundary of the RVE is divided into a given number of pairs, n_{pairs}, as follows

$$\partial\Omega_\mu = \bigcup_{i=1}^{n_{pairs}} \partial\Omega_{\mu,i}, \tag{3.21}$$

where the subscript i identifies each pair. To guarantee the compaitbility of each pair, it must be composed of a positive and a negative part, $\partial\Omega^+_{\mu,i}$ and $\partial\Omega^-_{\mu,i}$, respectively, such that,

$$\partial\Omega_{\mu,i} = \partial\Omega^+_{\mu,i} \bigcup \partial\Omega^-_{\mu,i}. \tag{3.22}$$

Figure 3.5 represents a possible deformation of an arbitrary RVE, with respect to the Periodic Boundary Condition. As can be seen, the boundary of the RVE is subdivided in different parts with compatible displacements, to guarantee microscopic equilibrium.

For each microscopic point, $\boldsymbol{p}^+_\mu$ cointained in a given part of the RVE's boundary, $\partial\Omega^+_{\mu,i}$, there must exist a corresponding point ,$\boldsymbol{p}^-_\mu \in \partial\Omega^-_{\mu,i}$, such that

$$\boldsymbol{n}^+_{0,\mu,i} = -\boldsymbol{n}^-_{0,\mu,i}, \tag{3.23}$$

where $\boldsymbol{n}^+_{0,\mu,i}$ and $\boldsymbol{n}^-_{0,\mu,i}$ are the unit vectors normal to the boundary of the RVE, in points $\boldsymbol{p}^+_\mu$ and $\boldsymbol{p}^-_\mu$, respectively. Furthermore, the displacement fluctuations on opposite sides of the boundary cannot be prescribed independently, therefore, the periodic boundary condition can be established as

$$\tilde{\boldsymbol{u}}_\mu(\boldsymbol{p}^+_\mu, t) = \tilde{\boldsymbol{u}}_\mu(\boldsymbol{p}^-_\mu, t). \tag{3.24}$$

The resulting space of kinematically admissible displacement fluctuations is given by

$$\begin{aligned} ^{Per}\mathcal{K}^*_\mu \equiv \Big\{ \tilde{\boldsymbol{u}}_\mu, \text{sufficiently regular} | \tilde{\boldsymbol{u}}_\mu(\boldsymbol{p}^+_\mu, t) = \tilde{\boldsymbol{u}}_\mu(\boldsymbol{p}^-_\mu, t), \\ \forall \partial\Omega_{\mu,i} \wedge \forall \boldsymbol{p}^+_\mu, \boldsymbol{p}^-_\mu \in \partial\Omega_{\mu,i} \Big\}. \end{aligned} \tag{3.25}$$

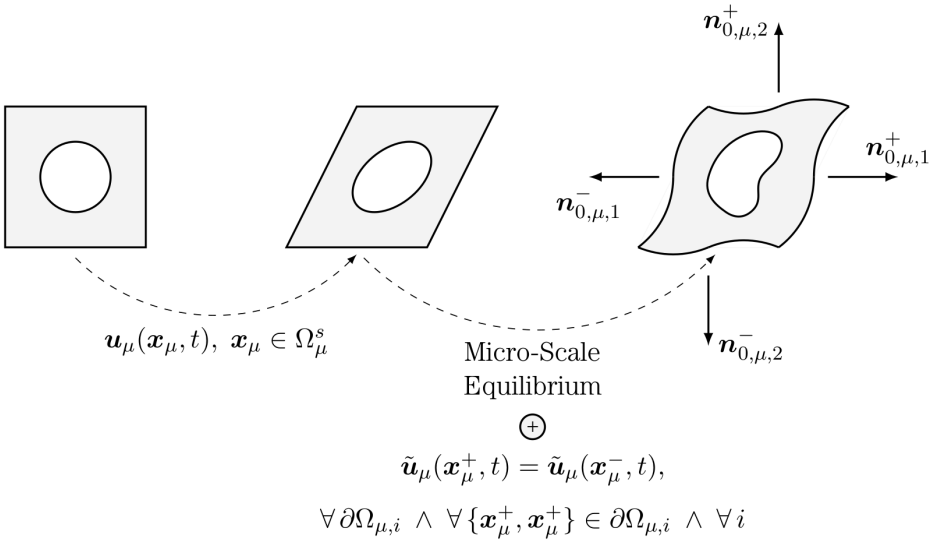

Figure 3.5: Schematic representation of the deformation of an RVE with the periodic boundary condition, taken from Silva (2021).

Uniform traction boundary condition

The Uniform Traction boundary condition is established by the condition of least constraint of the microscopic equilibrium problem, resulting in a space that is equivalent to the minimally constrained space of displacement fluctuations. Therefore, for this boundary condition, the space of kinematically admissible displacement fluctuations can be written as

$$^{Uni}\mathcal{K}^*_\mu \equiv \left\{ \tilde{\boldsymbol{u}}_\mu, \text{sufficiently regular} \middle| \int_{\partial\Omega_\mu} \tilde{\boldsymbol{u}}_\mu(x_\mu, t) \otimes \boldsymbol{n}_{0,\mu}(\boldsymbol{p}_\mu)\, \mathrm{d}a = \boldsymbol{0} \right\} \tag{3.26}$$

The size of the RVE has an impact on the average properties obtained through homogenisation, as smaller RVEs will have average properties that are more susceptible to their specific microscopic features. That being the case, there exists a minimum size of the RVE that allows for its average properties to actually represent the macroscopic response. A notable aspect of the periodic boundary condition is that is results in a faster convergence of the homogenised properties, with an increasing RVE size, thus reducing the necessary computational effort. This is depicted in Figure 3.6.

3.3.4 Hill-Mandel principle of macro-homogeneity

Up until now, the link between scales has been set solely by the homogenisation of micro-scale properties. The *Hill-Mandel Principle of Macro-Homogeneity* completes this link by establishing energetic compatibility between scales. The principle states that the stress power at the macro-scale must be equal to the volume average of the microscopic stress power over the RVE, such that,

$$\boldsymbol{P}(x,t) : \dot{\boldsymbol{F}}(x,t) = \frac{1}{v_{0,\mu}} \int_{\Omega_\mu} \boldsymbol{P}_\mu(\boldsymbol{p}_\mu, t) : \dot{\boldsymbol{F}}_\mu(\boldsymbol{p}_\mu, t) \mathrm{d}v, \tag{3.27}$$

where $\dot{\boldsymbol{F}}$ is the macroscopic deformation gradient rate, or virtual macroscopic deformation gradient, and $\dot{\boldsymbol{F}}_\mu$ is its microscopic counterpart. Moreover, $\boldsymbol{P}$ and $\boldsymbol{P}_\mu$ are the macro and micro-scale First Piola-Kirchhoff stress tensors, respectively. Recalling Equation (3.10), the time derivative microscopic deformation gradient analogously relates to its macroscopic equivalent by:

$$\dot{\boldsymbol{F}}_\mu(\boldsymbol{x}, t) = \dot{\boldsymbol{F}}(\boldsymbol{x}, t) + \nabla_{\boldsymbol{p}} \left[\dot{\boldsymbol{u}}_\mu \left(\boldsymbol{p}_\mu, t \right) \right]. \tag{3.28}$$

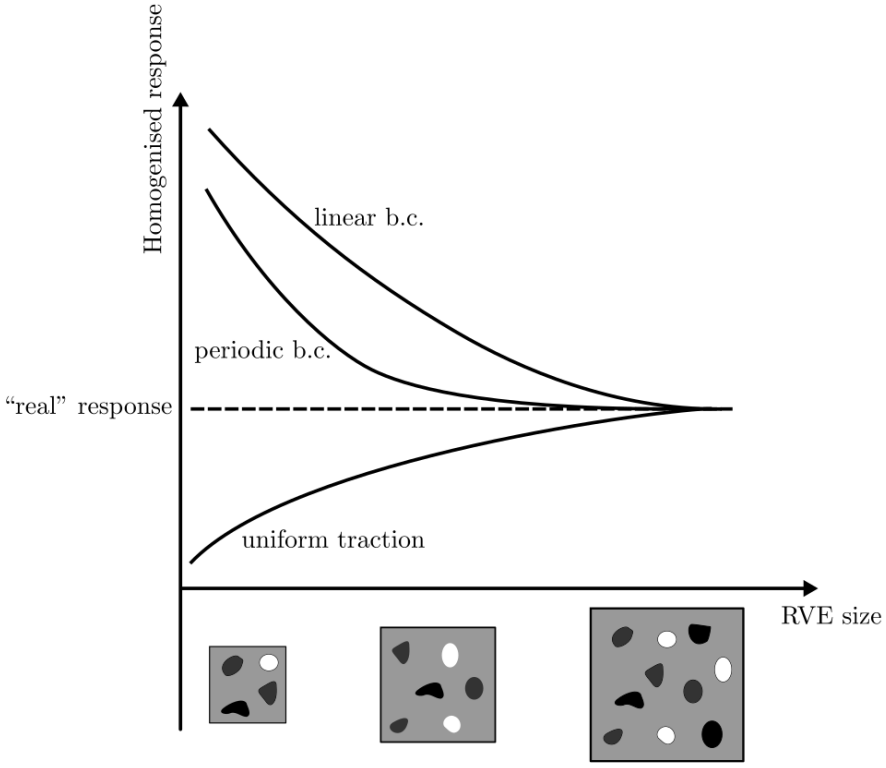

Figure 3.6: Convergence of the homogenised properties with the increase of RVE size, for the different micro-scale boundary conditions. Taken from Rodrigues Lopes (2019).

Combining the previous two expressions, it follows that

$$\boldsymbol{P}(\boldsymbol{x},t):\dot{\boldsymbol{F}}(\boldsymbol{x},t)=\boldsymbol{P}(\boldsymbol{x},t):\dot{\boldsymbol{F}}(\boldsymbol{x},t)+\frac{1}{v_{0,\mu}}\int_{\Omega_\mu}\boldsymbol{P}_\mu\left(\boldsymbol{p}_\mu,t\right):\nabla_{\boldsymbol{p}}\left[\dot{\boldsymbol{u}}_\mu\left(\boldsymbol{p}_\mu,t\right)\right]\mathrm{d}v, \tag{3.29}$$

and, as a result:

$$\int_{\Omega_\mu}\boldsymbol{P}_\mu\left(\boldsymbol{p}_\mu,t\right):\nabla_{\boldsymbol{p}}\left[\dot{\tilde{\boldsymbol{u}}}_\mu\left(\boldsymbol{p}_\mu,t\right)\right]\mathrm{d}v=0,\forall\dot{\tilde{\boldsymbol{u}}}_\mu\in\mathscr{V}_\mu, \tag{3.30}$$

where $\mathscr{V}_\mu$ stands for the space of virtual kinematically admissible displacements of the RVE, which coincides with actual space of kinematically admissible fluctuations, i.e., $\mathscr{V}_\mu\equiv\tilde{\mathscr{K}}_\mu$. Through integration by parts of the left-hand side of Equation (3.30) and considering the absence of body forces on the voids present in the RVE, i.e.,

$$\boldsymbol{b}_{0,\mu}\left(\boldsymbol{p}_\mu,t\right)=0,\forall\boldsymbol{p}_\mu\in\Omega_\mu^v, \tag{3.31}$$

it follows from the strong form of equilibrium at the micro-scale:

$$\begin{aligned}\int_{\Omega_\mu}\boldsymbol{P}_\mu\left(\boldsymbol{p}_\mu,t\right):\nabla_{\boldsymbol{p}}\left[\dot{\tilde{\boldsymbol{u}}}_\mu\left(\boldsymbol{p}_\mu,t\right)\right]\mathrm{d}v=&\int_{\partial\Omega_\mu}\boldsymbol{t}_{0,\mu}\left(\boldsymbol{p}_\mu,t\right)\cdot\dot{\tilde{\boldsymbol{u}}}_\mu\mathrm{d}a\\&+\int_{\Omega_\mu^s}\boldsymbol{b}_{0,\mu}\left(\boldsymbol{p}_\mu,t\right)\cdot\dot{\tilde{\boldsymbol{u}}}_\mu\mathrm{d}v\end{aligned} \tag{3.32}$$

Considering Equation (3.30) and that both terms on the right-hand side of the expression above are independent of each other, the Hill-Mandel principle is verified if and only if

$$\begin{aligned} \int_{\partial\Omega_\mu} \boldsymbol{t}_{0,\mu}\left(\boldsymbol{p}_\mu, t\right)\cdot\dot{\tilde{\boldsymbol{u}}}_\mu \mathrm{d}a = 0, \forall\,\dot{\tilde{\boldsymbol{u}}}_\mu \in \mathscr{V}_\mu, \text{ and} \\ \int_{\Omega^s_\mu} \boldsymbol{b}_{0,\mu}\left(\boldsymbol{p}_\mu, t\right)\cdot\dot{\tilde{\boldsymbol{u}}}_\mu \mathrm{d}v = 0, \forall\,\dot{\tilde{\boldsymbol{u}}}_\mu \in \mathscr{V}_\mu. \end{aligned} \tag{3.33}$$

Through Equation (3.33), resulting from the Hill-Mandel principle, one may then interpret the body and surface forces, $\boldsymbol{b}_{0,\mu}$ and $\boldsymbol{t}_{0,\mu}$, respectively, as reactions of the kinematical constraints enforced on the RVE.

3.3.5 Homogenised stress tensor

Throughout the course of this section, the homogenisation principle has been presented, and the deformation gradient has been homogenised. The First Piola-Kirchhoff stress tensor can also be homogenised, such that

$$\boldsymbol{P}(\boldsymbol{p}, t) = \frac{1}{v_{0,\mu}}\int_{\Omega_\mu} \boldsymbol{P}_\mu(\boldsymbol{x}_\mu, t)\,\mathrm{d}v. \tag{3.34}$$

This expression can be rewritten as

$$\boldsymbol{P}(\boldsymbol{p}, t) = \frac{1}{v_{0,\mu}}\int_{\Omega_\mu} \boldsymbol{P}_\mu(\boldsymbol{x}_\mu, t)(\nabla_p \boldsymbol{p}_\mu)^T\,\mathrm{d}v, \tag{3.35}$$

which, integrating by parts and taking the microscopic equilibrium into account, leads to

$$\boldsymbol{P}(\boldsymbol{p}, t) = \frac{1}{v_{0,\mu}}\left[\int_{\partial\Omega_\mu} \boldsymbol{t}_\mu(\boldsymbol{x}_\mu, t)\otimes\boldsymbol{p}_\mu\,\mathrm{d}a - \int_{\Omega_\mu} \boldsymbol{b}_\mu(\boldsymbol{x}_\mu, t)\otimes\boldsymbol{p}_\mu\,\mathrm{d}v\right]. \tag{3.36}$$

Expression (3.36) allows for the calculation of the macroscopic First Piola-Kirchhoff stress tensor from the volume and surface reactive forces on the RVE.

Even though the homogenisation procedure is done using the First Piola-Kirchhoff stress tensor, the Cauchy stress tensor is also often needed. The Cauchy stress tensor can be expressed in terms of the homogenised First Piola-Kirchhoff stress tensor and the homogenised deformation gradient, as follows:

$$\boldsymbol{\sigma} = \frac{1}{\det\boldsymbol{F}}\boldsymbol{P}\boldsymbol{F}^T. \tag{3.37}$$

3.4 Second-order computational homogenisation

In the context of this dissertation, a multi-scale model based on second-order computational homogenisation was employed, in addition to the standard first-order homogenisation approach. This model adopts a second-order continuum formulation at the macro-scale, and a first-order formulation at the RVE level, with the adoption of second-order homogenisation to transition the higher-order gradient and stresses from one scale to the other.

With this in mind, the present section delves into multi-scale models based on second-order computational homogenisation. Section 3.4.1 introduces its distinctive elements relative to the first-order approach, before describing the mathematical formulation of multi-scale models based on second-order homogenisation in subsequent sections. Sections 3.4.2 and 3.4.3 address kinematic homogenisation of a second-order continuum and multi-scale kinematics framework employed in this context, respectively. Section 3.4.4 presents a set of micro-scale boundary conditions for multi-scale models based on second-order homogenisation. Finally, Section 3.4.5 outlines the homogenisation of higher-order stresses from a first-order continuum formulation at the RVE level. Although the principle of multi-scale virtual power for second-order homogenisation and the corresponding micro-scale equilibrium problem are not included in this section, the interested reader is referred to Rodrigues Lopes and Andrade Pires (2022b).

3.4.1 Introduction

Second-order computational homogenisation was first introduced by Kouznetsova (Kouznetsova et al., 2004a, Kouznetsova, 2002), and further employed and developed by several other authors (Blanco et al., 2016a, Lesičar, 2015, Lesičar et al., 2016, Luscher, 2010, Rodrigues Lopes, 2019, Rodrigues Lopes and Andrade Pires, 2022a, Rodrigues Lopes et al., 2023). In essence, multi-scale models based on second-order computational homogenisation are simply an extension of the ones based upon the first-order scheme, and the overall idea is relatively similar, with the only major difference resting on the kinematical information passed from the macro-scale to the microscopic equilibrium problem, and vice-versa. However, this yields significant differences in the predictions of the two formulations, with second-order homogenisation reliably describing the multi-scale behaviour of solids under second-order deformation modes (recall Figure 2.16), and also accounting for the presence of size effects. Figure 3.7 illustrates the solution of a multi-scale equilibrium problem with the second-order scheme, in which the macroscopic solid is modelled with a second-gradient continuum formulation, while the RVE domain is treated as a first-order continuum. In this case, the second-order gradient must also be homogenised and down-scaled, while the resulting higher-order stresses must be computed using the microscopic First Piola-Kirchhoff tensor and homogenised. A second-order constitutive law is obtained through this homogenisation procedure, even though the micro-scale domain is modelled as a first-order continuum.

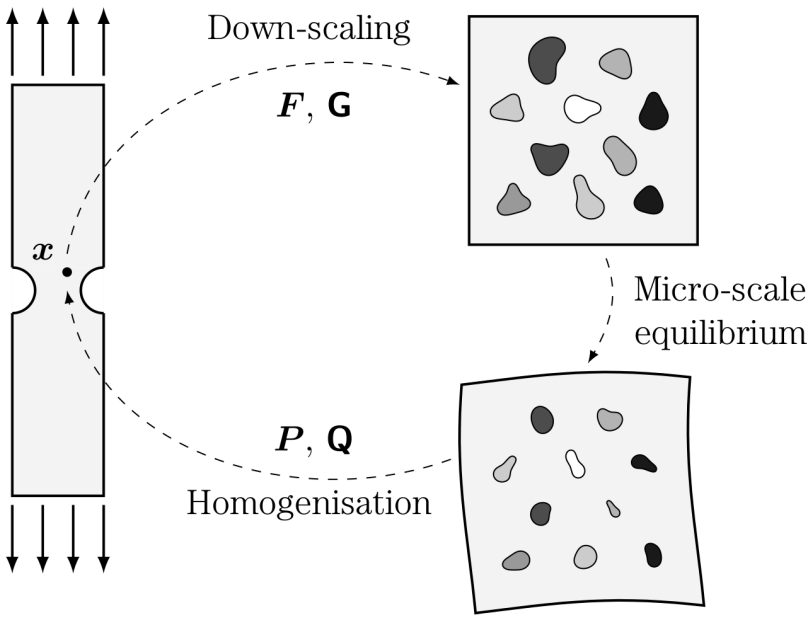

Figure 3.7: Schematic representation of the solution of a multi-scale problem with recourse to second-order computational homogenisation. Taken from Silva (2021).

The inclusion of the second gradient of displacements in the kinematical description of the macroscopic continuum domain implies the introduction of a characteristic length at this scale. In the context of second-order homogenisation, this macroscopic characteristic length is linked to the value of the RVE length. Hence, the multi-scale predictions of second-order models are numerically dependent on the value of the RVE length, whereas, with first-order homogenisation, the RVE length does not play any role. Additionally, the scale separation principle, which postulates that the RVE size must be much smaller than the macroscopic structural length (recall Section 3.2.1), is relaxed under the adoption of the second-order framework, since a linear variation of the macro-deformation is assumed within the RVE. For this reason, second-order homogenisation is also particularly suitable for the analysis of very small structures Rodrigues Lopes (2019).

Fully second-order multi-scale models have also been formulated in the literature (see Rodrigues Lopes and Andrade Pires (2022) for instance), but are not addressed here.

At this point, the distinction between the RVE length and the RVE size, discussed by Rodrigues Lopes and co-workers (Rodrigues Lopes and Andrade Pires, 2022b, Rodrigues Lopes et al., 2023), should be addressed. The RVE size is related to the amount of microscopic features included in an RVE model, i.e. the number of grains in a polycrystalline microstructure or the number of fibres or inclusions in a reinforced polymeric RVE. This quantity is linked to the representativeness of the RVE model, associated to the convergence of its homogenised properties with the increase in the number of microscopic features (recall Figure 3.6). The interested reader is referred to the work of Marques da Silva et al. (2023), in which a detailed analysis on the influence of the number of grains on the representativeness of polycrystalline RVEs is presented. Rodrigues Lopes and Andrade Pires (2022b) introduced the concept of the *generalised RVE size*, s_{RVE}, which is a measure of the number of micro-constituents included in the RVE model. The generalised RVE size is, thus, conceptually independent of the RVE length l_{RVE}, as illustrated in Figure 3.8, and controls the representativeness of the homogenised response. Conversely, the RVE length, despite not playing any role in first-order homogenisation approaches, is relevant in the context of second-order multi-scale models, since it is linked with the nonlocality of the macroscopic response. That said, the RVE length can be viewed as a numerical parameter, which should be calibrated to obtain a suitable macro-scale response, which is independent of the generalised RVE size.

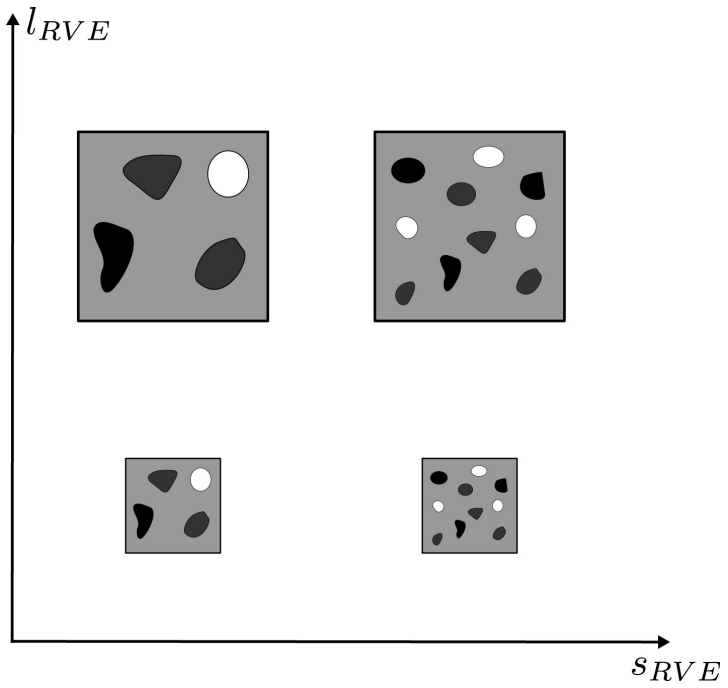

Figure 3.8: Schematic representation of the concept of generalised RVE size, which allows decoupling the RVE length and the number of microscopic features in the RVE model, taken from Rodrigues Lopes and Andrade Pires (2022b).

3.4.2 Kinematic homogenisation

For second-order multi-scale models, the homogenisation of the macroscopic deformation gradient, $\boldsymbol{F}$, follows the same procedure as for first-order homogenisation (recall Equation (3.3)). Moreover, the second gradient of displacements must also be homogenised, which is not as straightforward since the RVE domain is modelled as a first-order continuum. That being the case, Ro-

drigues Lopes (2019) suggests the following homogenisation procedure:

$$\mathbf{G} = \frac{1}{v_{0,\mu}} \int_{\Omega_\mu} \nabla_{\boldsymbol{p}} \left[\boldsymbol{u}_\mu \left(\boldsymbol{p}_\mu \right) \right] \otimes \boldsymbol{p}_\mu \cdot \boldsymbol{J}^{-1} \, \mathrm{d}v \tag{3.38}$$

where $\boldsymbol{J}$ is the second-order moment of volume tensor:

$$\boldsymbol{J} = \frac{1}{v_{0,\mu}} \int_{\Omega_\mu} \boldsymbol{p}_\mu \otimes \boldsymbol{p}_\mu \mathrm{d}v. \tag{3.39}$$

3.4.3 Multi-scale kinematics

Taking into account the macroscopic second-order deformation gradient, the microscopic displacement field can now be decomposed into three components: the linear displacement and the displacement fluctuation parts, already present in the first-order homogenisation formulation, but also a quadratic displacement. That said, the decomposition of the microscopic displacement field, $\boldsymbol{u}_\mu$, in multi-scale models based on second-order homogenisation, reads:

$$\boldsymbol{u}_\mu \left(\boldsymbol{p}_\mu \right) = \boldsymbol{u}_M + (\boldsymbol{F} - \boldsymbol{I}) \cdot \boldsymbol{p}_\mu + \frac{1}{2} \mathbf{G} : \left(\boldsymbol{p}_\mu \otimes \boldsymbol{p}_\mu - \boldsymbol{J} \right) + \tilde{\boldsymbol{u}}_\mu \left(\boldsymbol{p}_\mu \right), \forall \boldsymbol{p}_\mu \in \Omega_\mu. \tag{3.40}$$

where $\boldsymbol{u}_M$ is the macroscopic displacement field. While the term $(-1/2\mathbf{G} : \boldsymbol{J})$ might be required for an accurate characterisation of the external power per volume unit, it may also induce a rigid body movement in the RVE (Blanco et al., 2016a). Since inertia and external body forces are not considered in this dissertation, this term can be neglected, recasting the expression of the microscopic displacement field as:

$$\boldsymbol{u}_\mu \left(\boldsymbol{p}_\mu \right) = \boldsymbol{u}_M + (\boldsymbol{F} - \boldsymbol{I}) \cdot \boldsymbol{p}_\mu + \frac{1}{2} \mathbf{G} : \left(\boldsymbol{p}_\mu \otimes \boldsymbol{p}_\mu \right) + \tilde{\boldsymbol{u}}_\mu \left(\boldsymbol{p}_\mu \right), \forall \boldsymbol{p}_\mu \in \Omega_\mu. \tag{3.41}$$

With this in mind, the microscopic deformation gradient, $\boldsymbol{F}_\mu$ can be written as

$$\boldsymbol{F}_\mu \left(\boldsymbol{p}_\mu \right) = \nabla_{\boldsymbol{p}} \left[\boldsymbol{u}_\mu \left(\boldsymbol{p}_\mu \right) \right] + \boldsymbol{I} = \boldsymbol{F} + \boldsymbol{G} \cdot \boldsymbol{p}_\mu + \nabla_{\boldsymbol{p}} \tilde{\boldsymbol{u}}_\mu \left(\boldsymbol{p}_\mu \right), \forall \boldsymbol{p}_\mu \in \Omega_\mu. \tag{3.42}$$

Furthermore, without loss of generality, the origin of the micro-coordinate system is conveniently located at the RVE's centroid, such that

$$\int_{\Omega_\mu} \boldsymbol{p}_\mu \mathrm{d}v = \mathbf{0}. \tag{3.43}$$

Introducing the definition of the microscopic displacement gradient (Equation (3.42)) into the expression for the homogenised deformation gradient (Equation (3.4)), and taking the assumption that the centroid of the RVE is located at the origin of the microscopic coordinate system into account (Equation (3.43)), one may write:

$$\boldsymbol{F} = \boldsymbol{F} + \frac{1}{v_{0,\mu}} \left[\mathbf{G} \cdot \int_{\Omega_\mu^\Omega} \boldsymbol{p}_\mu \mathrm{d}v + \int_{\Omega_\mu} \nabla_{\boldsymbol{p}} \left[\tilde{\boldsymbol{u}}_\mu \left(\boldsymbol{p}_\mu \right) \right] \right] \Leftrightarrow \int_{\Omega_\mu} \nabla_{\boldsymbol{p}} \tilde{\boldsymbol{u}}_\mu = \mathbf{0}, \tag{3.44}$$

which can also be expressed as the following boundary condition:

$$\int_{\Omega_\mu} \nabla_{\boldsymbol{p}} \left[\tilde{\boldsymbol{u}}_\mu \left(\boldsymbol{p}_\mu \right) \right] = \int_{\partial\Omega_\mu} \tilde{\boldsymbol{u}}_\mu \otimes \boldsymbol{n}_{0,\mu} \left(\boldsymbol{p}_\mu \right) \mathrm{d}a = \mathbf{0}, \tag{3.45}$$

and is identical to the uniform traction boundary condition (or minimal kinematically admissible constraint), leading to the minimally constrained space of displacement fluctuations, defined for the first-order homogenisation scheme in Equation (3.14).

Analogously, introducing Equation (3.42) into Equation (3.38), while also considering the definitions of Equations (3.40) and (3.43) yields the following volumetric constraint:

$$\int_{\Omega_\mu} \nabla_{\boldsymbol{p}} \left[\tilde{\boldsymbol{u}}_\mu \left(\boldsymbol{p}_\mu \right) \right] \otimes \boldsymbol{p}_\mu \cdot \boldsymbol{J}^{-1} \, \mathrm{d}v = \boldsymbol{0}. \tag{3.46}$$

Developing the above expression through integration by parts, it may split into volumetric and boundary integral terms:

$$\int_{\partial\Omega_\mu} \left[\tilde{\boldsymbol{u}}_\mu \left(\boldsymbol{p}_\mu \right) \otimes \boldsymbol{n}_{0,\mu} \left(\boldsymbol{p}_\mu \right) \otimes \boldsymbol{p}_\mu \right] \cdot \boldsymbol{J}^{-1} \, \mathrm{d}a - \int_{\Omega_\mu} \tilde{\boldsymbol{u}} \left(\boldsymbol{p}_\mu \right) \mathrm{d}v \otimes \boldsymbol{J}^{-1} = \boldsymbol{0}. \tag{3.47}$$

For second-order computational homogenisation, the minimal constraints that define the kinematically admissible space are given by Equations (3.45) and (3.47). That being said, the minimally constrained space of displacement fluctuations (previously expressed in Equation (3.15) for the first-order homogenisation formulation) is now defined as:

$$\begin{aligned} \tilde{\mathscr{K}}_\mu^* \equiv \Bigg\{ \tilde{\boldsymbol{u}}_\mu, \text{ sufficiently regular } \mid \int_{\partial\Omega_\mu} \tilde{\boldsymbol{u}}_\mu \left(\boldsymbol{p}_\mu \right) \otimes \boldsymbol{n}_{0,\mu} \left(\boldsymbol{p}_\mu \right) \mathrm{d}a = \boldsymbol{0} \quad \wedge \\ \int_{\partial\Omega_\mu} \left[\tilde{\boldsymbol{u}}_\mu \left(\boldsymbol{p}_\mu \right) \otimes \boldsymbol{n}_{0,\mu} \left(\boldsymbol{p}_\mu \right) \otimes \boldsymbol{p}_\mu \right] \cdot \boldsymbol{J}^{-1} \, \mathrm{d}a - \int_{\Omega_\mu} \tilde{\boldsymbol{u}} \left(\boldsymbol{p}_\mu \right) \mathrm{d}v \otimes \boldsymbol{J}^{-1} = \boldsymbol{0} \Bigg\}. \end{aligned} \tag{3.48}$$

3.4.4 Micro-scale boundary conditions

In the context of second-order homogenisation, only two boundary conditions were considered, other than the minimal constraint condition (Equation (3.48)): the Periodic and the Direct boundary conditions. In the following, their corresponding spaces of kinematically admissible displacement fluctuations are presented.

Periodic boundary condition

Relative to the periodic boundary condition presented in the context of first-order homogenisation (see Section 3.3.3), additional considerations must be admitted here, so that the kinematic admissibility is still guaranteed within the second-order homogenisation scheme. The periodic boundary condition is defined by:

$$\tilde{\boldsymbol{u}} \left(\boldsymbol{p}_\mu^+ \right) = \tilde{\boldsymbol{u}} \left(\boldsymbol{p}_\mu^- \right), \forall \boldsymbol{p}_\mu^+ \in \partial\Omega_\mu^+, \forall \boldsymbol{p}_\mu^- \in \partial\Omega_\mu^-, \tag{3.49}$$

and

$$\boldsymbol{n}_{0,\mu} \left(\boldsymbol{p}_\mu^+ \right) = -\boldsymbol{n}_{0,\mu} \left(\boldsymbol{p}_\mu^- \right), \forall \boldsymbol{p}_\mu^+ \in \partial\Omega_\mu^+, \forall \boldsymbol{p}_\mu^- \in \partial\Omega_\mu^-. \tag{3.50}$$

From these equations, the minimal kinematical admissibility criterion stated in Equation (3.45) is automatically satisfied. To also satisfy the minimal constraint (Equation (3.47)), it becomes convenient to prescribe each of its terms independently, i.e.:

$$\int_{\partial\Omega_\mu} \left[\tilde{\boldsymbol{u}}_\mu \left(\boldsymbol{p}_\mu \right) \otimes \boldsymbol{n}_{0,\mu} \left(\boldsymbol{p}_\mu \right) \otimes \boldsymbol{p}_\mu \right] \mathrm{d}a = \boldsymbol{0}, \tag{3.51}$$

$$\int_{\Omega_\mu} \tilde{\boldsymbol{u}} \left(\boldsymbol{p}_\mu \right) \mathrm{d}v = \boldsymbol{0}. \tag{3.52}$$

Considering solely RVEs with rectangular shapes, defined by a constant normal vector on each surface, Equation (3.51) can be developed and adequately recast as

$$\int_{\partial\Omega_\mu^{+_s}} \tilde{\boldsymbol{u}} \left(\boldsymbol{p}_\mu \right) \mathrm{d}a = \boldsymbol{0}, \quad \text{for each positive surface } s. \tag{3.53}$$

Therefore, within the second-order homogenisation framework, the actual space of kinematically admissible displacement fluctuations for the periodic boundary condition is given by:

$$
\begin{aligned}
{}^{\text{Per}}\tilde{\mathscr{K}}_\mu \equiv \Big\{ \tilde{\boldsymbol{u}}_\mu, \text{sufficiently regular} \mid \tilde{\boldsymbol{u}}_\mu\left(\boldsymbol{p}_\mu^+\right) = \tilde{\boldsymbol{u}}_\mu\left(\boldsymbol{p}_\mu^-\right), \int_{\Omega_\mu} \tilde{\boldsymbol{u}}\left(\boldsymbol{p}_\mu\right) \mathrm{d}v = \boldsymbol{0}, \\
\int_{\partial\Omega_\mu^{+,s}} \tilde{\boldsymbol{u}}\left(\boldsymbol{p}_\mu\right) \mathrm{d}a = \boldsymbol{0}, \quad \text{for each positive surface } s. \Big\}.
\end{aligned}
\tag{3.54}
$$

Direct boundary condition

For the sake of completeness, it is worth addressing the direct boundary condition, which is the second-order equivalent to the linear condition, previously presented in the context of first-order homogenisation (see Section 3.3.3). This condition is simply defined by:

$$
\tilde{\boldsymbol{u}}\left(\boldsymbol{p}_\mu\right) = \boldsymbol{0}, \forall \boldsymbol{p}_\mu \in \partial\Omega_\mu, \tag{3.55}
$$

and immediately verifies both constraints Equations (3.45) and (3.51). That being the case, only the volumetric constraint (Equation (3.52)) needs to be imposed in order to satisfy all minimal constraints. The resulting set of kinematically admissible displacement fluctuations reads:

$$
{}^{\text{Dir}}\tilde{\mathscr{K}}_\mu \equiv \left\{ \tilde{\boldsymbol{u}}_\mu, \text{ sufficiently regular } \mid \tilde{\boldsymbol{u}}\left(\boldsymbol{p}_\mu\right) = \boldsymbol{0}, \forall \boldsymbol{p}_\mu \in \partial\Omega_\mu, \int_{\Omega_\mu} \tilde{\boldsymbol{u}}\left(\boldsymbol{p}_\mu\right) \mathrm{d}v = \boldsymbol{0} \right\}. \tag{3.56}
$$

3.4.5 Higher-order stress tensor homogenisation

Finally, the homogenised higher-order stress tensor $\mathbf{Q}$ is given by:

$$
\mathbf{Q} = \frac{1}{v_{0,\mu}} \int_{\Omega_\mu} \left(\boldsymbol{P}_\mu \otimes \boldsymbol{p}_\mu\right)^S \mathrm{d}v, \tag{3.57}
$$

whereas the homogenised First Piola-Kirchhoff stress tensor is still computed as the volume average of its counterpart microscopic stress field Equation (3.36).

3.5 Second-order homogensation formulation for porous RVEs

Several authors have extended standard first-order homogenisation formulations to RVEs containing voids (Blanco et al., 2023, Feijóo et al., 2023, Rocha et al., 2018). In the case of second-order homogenisation, the volumetric constraint in Equation (3.48) cannot be imposed in the entire domain, but solely in the RVE solid part, if the voids are not discretised with finite elements. In this dissertation, the formulation described in dos Santos et al. (2023), dos Santos et al. (2024) was adopted to address this issue. Figure 3.9 depicts the solution strategy of second-order homogenisation-based models for RVEs containing voids.

3.5.1 RVE domain decomposition

Figure 3.10 depicts the structure of an arbitrary porous RVE. Recalling Equation (3.2), the domain of a porous RVE, Ω_μ can be decomposed into its continuum portion, Ω_μ^s, and the region occupied by voids, Ω_μ^v. with Ω_μ^v composed of:

$$
\Omega_\mu^v = \sum_{k=1}^{n_{v,i}} \Omega_\mu^{v,i_k} + \sum_{j=1}^{n_{v,b}} \Omega_\mu^{v,b_j}, \tag{3.58}
$$

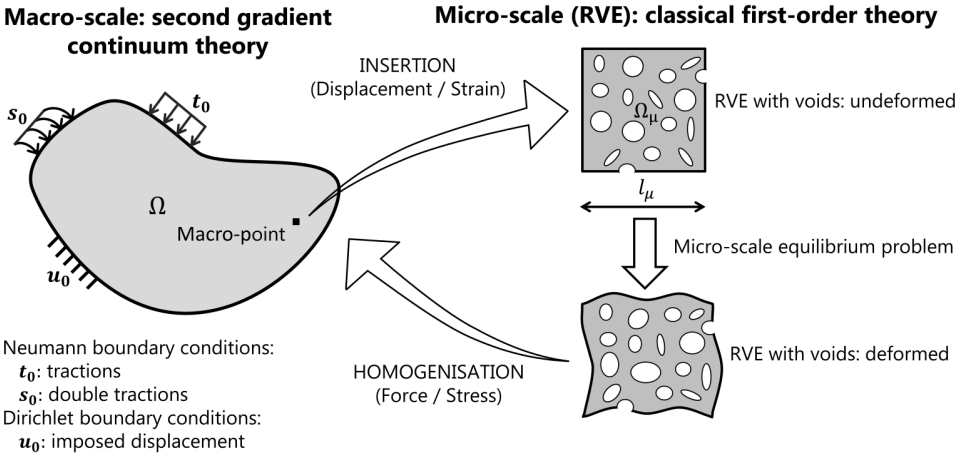

Figure 3.9: Schematic representation of the second-order homogenisation formulation for RVEs containing voids. Taken from dos Santos et al. (2023).

where Ω_μ^{v,i_k} defines the domain of the internal void k, Ω_μ^{v,b_j} denotes the domain of the boundary void j, $n_{v,i}$ represents the number of internal voids, and $n_{v,b}$ is the number of boundary voids.

In regards to the domain boundaries, $\partial\Omega_\mu^{s,b}$ indicates the outer boundary of the RVE solid component, and is given by

$$\partial\Omega_\mu^{s,b} = \sum_{m=1}^{n_{s,b}} \partial\Omega_\mu^{s,b_m}, \tag{3.59}$$

where $\partial\Omega_\mu^{s,b_m}$ defines the solid outer boundary m, and $n_{s,b}$ is the number of solid outer boundaries. Moreover, the internal boundary of the voids $\partial\Omega_\mu^{s,v}$ can be defined as

$$\partial\Omega_\mu^{s,v} = \sum_{k=1}^{n_{s,v}} \partial\Omega_\mu^{s,v_k} \tag{3.60}$$

where $\partial\Omega_\mu^{s,v_k}$ defines the void internal boundary k, and $n_{s,v}$ is the number of voids with internal boundaries. Furthermore, the outer boundary of the void regions $\partial\Omega_\mu^{v,b}$, represented in Figure 3.10 with dashed lines, can be expressed as

$$\partial\Omega_\mu^{v,b} = \sum_{j=1}^{n_{v,b}} \partial\Omega_\mu^{v,b_j}, \tag{3.61}$$

where $\partial\Omega_\mu^{v,b_j}$ defines the void outer boundary j, and $n_{v,b}$ is the number of voids with outer boundaries. In this context, the RVE outer boundary $\partial\Omega_\mu$ is composed of:

$$\partial\Omega_\mu = \partial\Omega_\mu^{s,b} \bigcup \partial\Omega_\mu^{v,b}, \tag{3.62}$$

and the boundary for the RVE solid portion $\partial\Omega_\mu^s$ is given by:

$$\partial\Omega_\mu^s = \partial\Omega_\mu^{s,b} \bigcup \partial\Omega_\mu^{s,v}. \tag{3.63}$$

3.5.2 Kinematic homogenisation

In the presence of voids, the averaging of macro-scale kinematical quantities must be appropriately adapted. The homogenisation related to the macro-scale displacement field for porous RVEs is given by

$$\boldsymbol{u}_M = \frac{1}{v_{0,\mu}^s} \int_{\Omega_\mu^s} \boldsymbol{u}_\mu \mathrm{d}v. \tag{3.64}$$

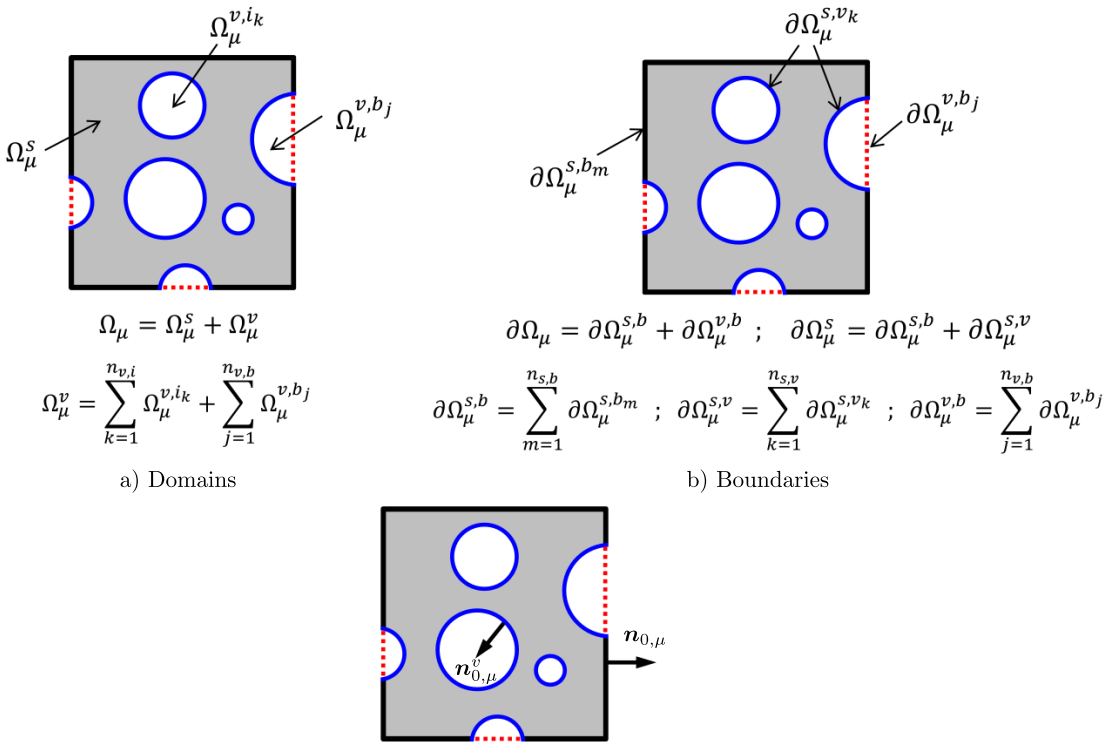

Figure 3.10: Schematic representation of the domain decomposition and boundaries of a generic porous RVE. Taken from dos Santos et al. (2023).

In the case of the macroscopic first-order deformation gradient, Equation (3.3) is rewritten to perform the averaging procedure solely on the solid domain of the RVE:

$$\boldsymbol{F} = \frac{1}{v_{0,\mu}^s}\left[\int_{\Omega_\mu^s} \boldsymbol{F}_\mu \mathrm{d}v - \int_{\partial\Omega_\mu^{s,v}} \tilde{\boldsymbol{u}} \otimes \boldsymbol{n}_{0,\mu}^v \mathrm{d}a - \int_{\partial\Omega_\mu^{s,b}} \tilde{\boldsymbol{u}} \otimes \bar{\boldsymbol{n}}_{0,\mu} \mathrm{d}a\right], \tag{3.65}$$

with $\boldsymbol{n}_{0,\mu}^v$ denoting the normal unit vector at the void inner boundary Figure 3.10 c), and $\bar{\boldsymbol{n}}_{0,\mu}$ denoting a constant mean normal in the solid part of the RVE boundary, $\partial\Omega_\mu^{s,b}$. In dos Santos et al. (2023), it is shown that the constant mean normal can be written as

$$\bar{\boldsymbol{n}}_{0,\mu} = \frac{1}{a_\mu^{s,b}} \int_{\partial\Omega_\mu^{s,b}} \boldsymbol{n}_{0,\mu} \mathrm{d}a, \tag{3.66}$$

where $\boldsymbol{n}_{0,\mu}$ is the normal unit vector at the RVE outer solid boundary and

$$a_\mu^{s,b} = \left|\partial\Omega_\mu^{s,b}\right| = \int_{\partial\Omega_\mu^{s,b}} \mathrm{d}a \tag{3.67}$$

denotes the surface area of the outer solid part. This demonstrates that $\bar{\boldsymbol{n}}_{0,\mu}$ is the mean normal, meaning that its associated boundary integral maintains kinematical consistency in the homogenisation related to the first-order macro-scale deformation gradient (Feijóo et al., 2023). It should also be remarked that the mean normal term vanishes for a periodic microstructure.

Furthermore, for the second-gradient of displacements, Equation (3.38) must be recast as fol-

lows to account for the presence of voids in the RVE:

$$\mathbf{G} = \frac{1}{v^s_{0,\mu}}\left[\int_{\Omega^s_\mu} \nabla_p \boldsymbol{u}_\mu \otimes \boldsymbol{p}_\mu \cdot \boldsymbol{J}^{-1} \mathrm{d}v - \int_{\partial\Omega^{s,v}_\mu} \tilde{\boldsymbol{u}} \otimes \boldsymbol{n}^v_{0,\mu} \otimes \boldsymbol{p}_\mu \cdot \boldsymbol{J}^{-1} \mathrm{d}a \right. \\ \left. - \int_{\partial\Omega^s_\mu,b} \tilde{\boldsymbol{u}} \otimes \bar{\bar{\boldsymbol{X}}} \cdot \boldsymbol{J}^{-1} \mathrm{d}a\right], \tag{3.68}$$

where $\bar{\bar{\boldsymbol{X}}}$ is a constant second-order tensor. Equation (3.68) has two noteworthy features. Firstly, the boundary void-solid integral (i.e., associated with $\partial\Omega^{s,v}_\mu$) arises to account for the effect of fluctuations on the void boundaries due to the fact that the kinematics is defined only over the solid component of the RVE. Secondly, the homogenisation formula for $\mathbf{G}$ must also avoid spurious macro-scale second gradient when considering a uniform displacement fluctuation field. In this context, the integral on the RVE outer solid boundary ($\partial\Omega^{s,b}_\mu$) related to $\bar{\bar{\boldsymbol{X}}}$ aims to remove spurious macro-scale second gradients for porous RVEs. That said, in order to prevent such spurious macro-gradients, dos Santos et al. (2023) derive the following expression for $\bar{\bar{\boldsymbol{X}}}$:

$$\bar{\bar{\boldsymbol{X}}} = \frac{1}{a^{s,b}_\mu}\int_{\partial\Omega^{s,b}_\mu} \boldsymbol{n}_{0,\mu} \otimes \boldsymbol{p}_\mu \mathrm{d}a - \frac{1}{a^{s,b}_\mu} v^s \boldsymbol{I}. \tag{3.69}$$

3.5.3 Multi-scale kinematics

Combining Equations (3.40) and (3.64) results in the conservation of the macro-scale displacement field for porous RVEs:

$$\boldsymbol{u}_M = \boldsymbol{u}_M + (\boldsymbol{F}-\boldsymbol{I})\cdot\frac{1}{v^s_\mu}\int_{\Omega^s_\mu}\boldsymbol{p}_\mu \mathrm{d}v + \frac{1}{2}\mathbf{G} : \left[\frac{1}{v^s_{0,\mu}}\int_{\Omega^s_\mu}(\boldsymbol{p}_\mu\otimes\boldsymbol{p}_\mu)\mathrm{d}v - \boldsymbol{J}\right] + \frac{1}{v^s_{0,\mu}}\int_{\Omega^s_\mu}\tilde{\boldsymbol{u}}\mathrm{d}v \Leftrightarrow \\ (\boldsymbol{F}-\boldsymbol{I})\cdot\frac{1}{v^s_{0,\mu}}\int_{\Omega^s_\mu}\boldsymbol{p}_\mu \mathrm{d}v + \frac{1}{2}\mathbf{G} : \left[\frac{1}{v^s_{0,\mu}}\int_{\Omega^s_\mu}(\boldsymbol{p}_\mu\otimes\boldsymbol{p}_\mu)\mathrm{d}v - \boldsymbol{J}\right] + \frac{1}{v^s_{0,\mu}}\int_{\Omega^s_\mu}\tilde{\boldsymbol{u}}\mathrm{d}v = \boldsymbol{0}. \tag{3.70}$$

By introducing Equations (3.65) and (3.68) into the above expression, dos Santos et al. (2023) arrive at the set of micro-scale constraints, which include a volumetric one:

$$\int_{\partial\Omega^{s,b}_\mu}\tilde{\boldsymbol{u}}\mathrm{d}v = \boldsymbol{0}; \tag{3.71}$$

and two independent boundary constraints:

$$\int_{\partial\Omega^{s,b}_\mu}\tilde{\boldsymbol{u}}\otimes(\boldsymbol{n}_{0,\mu}-\bar{\boldsymbol{n}}_{0,\mu})\mathrm{d}a = \boldsymbol{0}, \tag{3.72}$$

$$\int_{\partial\Omega^{s,b}_\mu}\tilde{\boldsymbol{u}}\otimes(\boldsymbol{n}_{0,\mu}\otimes\boldsymbol{p}_\mu-\bar{\bar{\boldsymbol{X}}})\mathrm{d}a = \boldsymbol{0}. \tag{3.73}$$

Therefore, the set of admissible fluctuation displacements that satisfies these constraints may be defined by $\mathscr{K}^*_\mu$, such that $\tilde{\boldsymbol{u}} \in \mathscr{K}^*_\mu$ and $\delta\tilde{\boldsymbol{u}} \in \mathscr{K}^*_\mu$:

$$\mathscr{K}^*_\mu = \left\{\tilde{\boldsymbol{u}} \text{ sufficiently regular in } \Omega^s_\mu, \int_{\partial\Omega^{s,b}_\mu}\tilde{\boldsymbol{u}}\otimes(\boldsymbol{n}_{0,\mu}-\bar{\boldsymbol{n}}_{0,\mu})\mathrm{d}a = \boldsymbol{0}, \right. \\ \left. \int_{\partial\Omega^{s,b}_\mu}\tilde{\boldsymbol{u}}\otimes(\boldsymbol{n}_{0,\mu}\otimes\boldsymbol{p}_\mu-\bar{\bar{\boldsymbol{X}}})\mathrm{d}a = \boldsymbol{0}, \int_{\Omega^s_\mu}\tilde{\boldsymbol{u}}\mathrm{d}v = \boldsymbol{0}\right\}. \tag{3.74}$$

Although this represents the set of minimally constrained displacement fluctuation fields, more restrictive subsets may be conveniently defined. Following the constraints usually employed in first-order homogenisation models, null or periodic fluctuations on the RVE boundary may be defined as subsets of solutions that still satisfy the kinematic admissibility.

3.5.4 Micro-scale boundary conditions

The description of the two micro-scale boundary conditions, other than the minimal constraints, must also be revised for porous RVEs.

Periodic boundary condition

With regard to the periodic boundary conditions, to account for the boundaries of the solid component of the RVE, it is redefined as follows

$$\tilde{\boldsymbol{u}}^{+} = \tilde{\boldsymbol{u}}^{-} \Leftrightarrow \tilde{\boldsymbol{u}}\left(\boldsymbol{p}_{\mu}^{+}\right) = \tilde{\boldsymbol{u}}\left(\boldsymbol{p}_{\mu}^{-}\right), \quad \forall \boldsymbol{p}_{\mu}^{+} \in \partial\Omega_{\mu}^{s,b+}, \quad \forall \boldsymbol{p}_{\mu}^{-} \in \partial\Omega_{\mu}^{s,b-} \tag{3.75}$$

with superscripts $(\cdot)^{+}$ and $(\cdot)^{-}$ denoting opposite RVE boundaries, i.e., $\partial\Omega_{\mu}^{s,b+} = \partial\Omega_{\mu}^{s,b} \bigcap \partial\Omega_{\mu}^{+}$ and $\partial\Omega_{\mu}^{s,b-} = \partial\Omega_{\mu}^{s,b} \bigcap \partial\Omega_{\mu}^{-}$, such that

$$\boldsymbol{n}_{0,\mu}\left(\boldsymbol{p}_{\mu}^{+}\right) = -\boldsymbol{n}_{0,\mu}\left(\boldsymbol{p}_{\mu}^{-}\right), \quad \forall \boldsymbol{p}_{\mu}^{+} \in \partial\Omega_{\mu}^{s,b+}, \forall \boldsymbol{p}_{\mu}^{-} \in \partial\Omega_{\mu}^{s,b-}. \tag{3.76}$$

Therefore, in order for Equation (3.76) to be verified, if an RVE has voids intersecting its boundary, there must be a corresponding void intersection on the opposite side of the microstructure, i.e. the RVE must be periodic. Otherwise, this formulation of the periodic boundary condition cannot be applied.

Assuming RVEs with rectangular shapes, characterised by a constant normal vector on each surface, the introduction of the periodic condition in Equation (3.73) yields:

$$\int_{\partial\Omega_{\mu}^{s,b}} \tilde{u}_i \left(n_{0,\mu,j}\, p_k - \bar{\bar{X}}_{jk}\right) \mathrm{d}a = \int_{\partial\Omega_{\mu}^{s,b+,j}} \tilde{u}_i \left[\left(p_k^{+} - p_k^{-}\right) - 2\bar{\bar{X}}_{jk}\right] \mathrm{d}a = 0, \quad \text{for each positive surface } j, \tag{3.77}$$

where index notation is conveniently applied to represent the expression. Moreover, the coordinates of a pair of points $p_k^{+}$and p_k^{-} on a face with normal N_j are equal, as long as $j \neq k$, or

$$\left(p_k^{+} - p_k^{-}\right)_j = l_{0,k}\delta_{jk}, \tag{3.78}$$

where $l_{0,k}$ is the undeformed RVE length in the direction k, and δ_{jk} is the Kroenecker delta (see Equation (2.112)). Thus, since $\bar{\bar{X}}_{jk}$ is also a constant value, Equation (3.77) can be reduced to

$$\int_{\partial\Omega_{\mu}^{s,b+(j)}} \tilde{u}_i \mathrm{d}a = \mathbf{0}. \tag{3.79}$$

After these considerations, the set of micro-scale solutions for the periodic boundary condition is defined by

$$\begin{aligned} {}^{\mathrm{Per}}\tilde{\mathscr{K}}_{\mu} = \Bigg\{ & \tilde{\boldsymbol{u}} \text{ sufficiently regular in } \Omega_{\mu}^{s}, \tilde{\boldsymbol{u}}\left(\boldsymbol{p}_{\mu}^{+}\right) = \tilde{\boldsymbol{u}}\left(\boldsymbol{p}_{\mu}^{-}\right), \int_{\Omega_{\mu}^{s}} \tilde{\boldsymbol{u}} \mathrm{d}v = \mathbf{0}, \\ & \int_{\partial\Omega_{\mu}^{s,b+(i)}} \tilde{\boldsymbol{u}} \mathrm{d}a = \mathbf{0}, \text{ for each positive surface } i \Bigg\}. \end{aligned} \tag{3.80}$$

In the case of RVEs without voids in its domain, this constraint is similar to the periodic constraint presented in Section 3.4.4.

Direct boundary condition

The direct boundary condition, in turn, is defined by

$$\tilde{\boldsymbol{u}}(\boldsymbol{p}_\mu) = \boldsymbol{0}, \quad \forall \boldsymbol{p}_\mu \in \partial\Omega_\mu^{s,b}. \tag{3.81}$$

Consequently, the resulting set of admissible solutions is given by

$$^{\text{Dir}}\tilde{\mathscr{K}}_\mu = \left\{ \tilde{\boldsymbol{u}} \text{ sufficiently regular in } \Omega_\mu^s, \tilde{\boldsymbol{u}}(\boldsymbol{p}_\mu) = \boldsymbol{0}, \forall \boldsymbol{p}_\mu \in \partial\Omega_\mu^{s,b}, \int_{\Omega_\mu^s} \tilde{\boldsymbol{u}} \mathrm{d}v = \boldsymbol{0} \right\}. \tag{3.82}$$

Finally, note that $^{\text{Dir}}\tilde{\mathscr{K}}_\mu \subset {}^{\text{Per}}\tilde{\mathscr{K}}_\mu \subset \tilde{\mathscr{K}}_\mu^*$, thus the solutions obtained with direct and periodic boundary conditions respect the minimal kinematic admissible constraint.

3.5.5 Higher-order stress homogenisation

In the formulation presented in dos Santos et al. (2023), the first- and higher-order stress measures are homogenised through the computation of boundary integrals, for numerical reasons.

For porous RVEs, one can recast Equation (3.36) for the homogenisation of the First Piola-Kirchhoff stress tensor as

$$\boldsymbol{P} = \frac{1}{v_{0,\mu}} \int_{\partial\Omega_\mu^s} \boldsymbol{P}_\mu \mathrm{d}v. \tag{3.83}$$

Through the application of the Divergence theorem, the above equation may be rewritten as

$$\boldsymbol{P} = \frac{1}{v_{0,\mu}} \left[\int_{\partial\Omega_\mu^s} \boldsymbol{P}_\mu \cdot \boldsymbol{n}_{0,\mu} \otimes \boldsymbol{p}_\mu \mathrm{d}a - \int_{\Omega_\mu^s} \mathrm{div}_{\boldsymbol{p}} \left(\boldsymbol{P}_\mu\right) \otimes \boldsymbol{p}_\mu \mathrm{d}v \right]. \tag{3.84}$$

where $\mathrm{div}_{\boldsymbol{p}}(\cdot)$ is the microscopic material divergence operator. Considering $\partial\Omega_\mu^s = \partial\Omega_\mu^{s,b} \bigcup \partial\Omega_\mu^{s,v}$:

$$\boldsymbol{P} = \frac{1}{v_{0,\mu}} \left[\int_{\partial\Omega_\mu^{s,b}} \boldsymbol{P}_\mu \cdot \boldsymbol{n}_{0,\mu} \otimes \boldsymbol{p}_\mu \mathrm{d}a + \int_{\partial\Omega_\mu^{s,v}} \boldsymbol{P}_\mu \cdot \boldsymbol{n}_{0,\mu}^v \otimes \boldsymbol{p}_\mu \mathrm{d}a - \int_{\Omega_\mu^s} \mathrm{div}_{\boldsymbol{p}} \left(\boldsymbol{P}_\mu\right) \otimes \boldsymbol{p}_\mu \mathrm{d}v \right]. \tag{3.85}$$

Conversely, the homogenisation of the higher-order stress tensor (Equation (3.57)) reads

$$\mathbf{Q} = \frac{1}{v_{0,\mu}} \int_{\partial\Omega_\mu^s} (\boldsymbol{P}_\mu \otimes \boldsymbol{p}_\mu)^S \mathrm{d}v. \tag{3.86}$$

As demonstrated by Blanco et al. (2016b), the above expression may be recast as

$$\mathbf{Q} = \frac{1}{2v_{0,\mu}} \left[\int_{\partial\Omega_\mu^s} \boldsymbol{P}_\mu \cdot \boldsymbol{n}_{0,\mu} \otimes \boldsymbol{p}_\mu \otimes \boldsymbol{p}_\mu \mathrm{d}a - \int_{\Omega_\mu^s} \mathrm{div}_{\boldsymbol{p}} \left(\boldsymbol{P}_\mu\right) \otimes \boldsymbol{p}_\mu \otimes \boldsymbol{p}_\mu \mathrm{d}v \right], \tag{3.87}$$

and with $\partial\Omega_\mu^s = \partial\Omega_\mu^{s,b} \bigcup \partial\Omega_\mu^{s,v}$:

$$\begin{aligned} \mathbf{Q} = \frac{1}{2v_{0,\mu}} \Bigg[& \int_{\partial\Omega_\mu^{s,b}} \boldsymbol{P}_\mu \cdot \boldsymbol{n}_{0,\mu} \otimes \boldsymbol{p}_\mu \otimes \boldsymbol{p}_\mu \mathrm{d}a + \int_{\partial\Omega_\mu^{s,v}} \boldsymbol{P}_\mu \cdot \boldsymbol{n}_{0,\mu}^v \otimes \boldsymbol{p}_\mu \otimes \boldsymbol{p}_\mu \mathrm{d}a \\ & - \int_{\Omega_\mu^s} \mathrm{div}_{\boldsymbol{p}} \left(\boldsymbol{P}_\mu\right) \otimes \boldsymbol{p}_\mu \otimes \boldsymbol{p}_\mu \mathrm{d}v \Bigg]. \end{aligned} \tag{3.88}$$

3.6 Numerical solution of large-strain multi-scale problems

In this dissertation, the finite element method was employed to solve the multi-scale equilibrium problem. While the macro-scale problem is addressed with the standard finite element solution technique (recall Section 2.9), addditional numerical treatment is required at the micro-scale, due to the nature of micro-constraints. In the following, the solution technique for multi-scale solid mechanics problems at large strains, with computational homogenisation is succinctly presented. The numerical strategies for the enforcement of micro-scale boundary conditions are not addressed here, and the interested reader is referred to the works of Javili et al. (2017), Kaczmarczyk et al. (2008), Nguyen et al. (2017), Reis and Andrade Pires (2014), Rodrigues Lopes et al. (2021).

Since a large-strain formulation is assumed at both scales, and path-dependent constitutive models are adopted at the RVE level, the macroscopic response is also path-dependent. In this scenario, the constitutive functional in Equation (2.104) represents the micro-scale problem and stress homogenisation procedure, where the macro-internal variables, $\boldsymbol{\theta}$, can be interpreted as the underlying RVE state. This micro-state is characterised by a set of microscopic internal variables, $\boldsymbol{\beta}$, the microscopic geometry defined by the update RVE coordinates and the micro-stress field. The RVE state must be preserved during the iterative solution of the macroscopic problem to ensure state updates can be executed within each incremental step, considering the load history. Additionally, the incrementation at both scales must be consistent. Sub-incrementation strategies have been proposed to enhance the robustness of the RVE iterative solution and reduce computational time for multi-scale analysis while maintaining consistency between incremental schemes at both scales (Reis and Andrade Pires, 2013, Somer et al., 2009). Figure 3.11 provides a schematic representation of the multi-scale analysis involving large strains at both scales, highlighting the incremental consistency between scales and the importance of the RVE state.

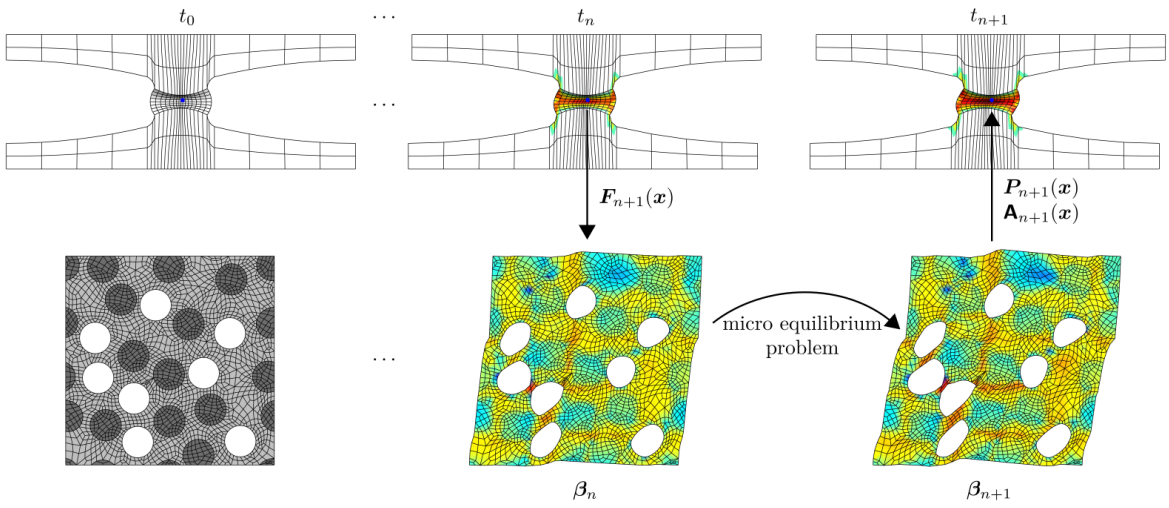

Figure 3.11: Schematic representation of a coupled multi-scale finite element analysis at large strains with path-dependent descriptions. Taken from Rodrigues Lopes (2019).

Lastly, Figure 3.12 illustrates the numerical procedure for the solution of the micro-scale equilibrium problem. After the macro-scale deformation gradients are inserted into the RVE, an iterative loop over is perfomed with the Newton-Raphson method until an acceptable solution is found. In this formulation, since no external forces are considered, the residual vector coincides with the internal forces, which must be null. After the micro-scale Newton-Rapshon scheme finds convergence, the stresses are homogenised and up-scaled.

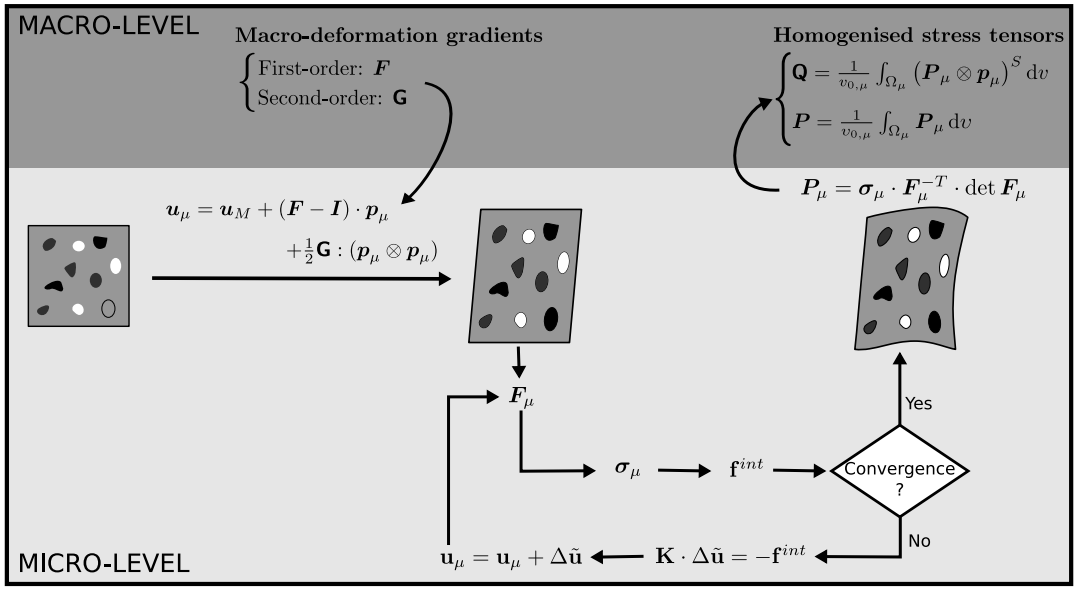

Figure 3.12: Schematic representation of numerical solution scheme for the micro-scale equilibrium problem with second-order homogenisation. In the case of first-order homogenisation, the higher-order gradients and stresses vanish. Adapted from Rodrigues Lopes (2019).

CHAPTER 4

DAMAGE AND FRACTURE MECHANICS

4.1 Introduction to fracture and continuum damage

Two major branches of failure theories can be employed in the context of structural integrity: *continuum damage mechanics* (CDM) and *fracture mechanics*. The former introduces the concept of continuum damage, which is associated with material softening and eventual failure without imposing any discontinuities in the displacement field. In this setting, cracks are implicitely considered through the damage variable, which progressively reduces the material load bearing capacity, but are not directly modelled. Conversely, fracture-based approaches presuppose the explicit modelling of crack interfaces, leading to discontinuities in the resulting displacement field and substantial increases in geometrical complexity. Although combined methods, which couple continuum damage with discontinuous approaches to fracture, have also emerged (Hambli, 2001, Simone et al., 2003), they are not addressed in this contribution. In what follows, these two approaches, their issues and modelling capabilities, are discussed.

A quantitative notion of *damage* was first introduced by Kachanov (1958) to predict the brittle creep failure of metals. A few years later, Rabotnov (1963) formulated the basis for CDM theories, which have been extensively utilised to predict the failure of several classes of materials since then. In the past decades, CDM, which originally started as a phenomenological theory of damage and fracture, has been strenghtened with robust theoretical frameworks of material science, nonlinear continuum mechanics, irreversible thermodynamics, micromechanics, computational mechanics, etc., and now has been established as a precise and systematic discipline for damage and fracture analysis (Murakami, 2012). Pivotal contributions to the development of CDM-based models for material degradation include Bažant et al. (1984), Gurson (1977), Lemaitre (1985a,b), Tvergaard and Needleman (1984), which were accompanied by the formulation of efficient numerical algorithms for the computational modelling of softening media (see for instance de Souza Neto et al. (1994), de Souza Neto (2002)).

However, a significant issue affecting most continuum models for failure is the emergence of *pathological mesh dependency* due to the assumption of pointwise constitutive formulation. This yields local degradation effects which are insensitive to the behaviour of surrounding material points. In essence, first-order continuum theories rely on the assumption that the lower-scale physical phenomena that drive the material response at the macroscopic level occur at a spatial scale much smaller than that of the structure (Section 2.2) inherently neglecting size effects (Andrade et al., 2011). When such assumption is violated, i.e. when the deformation field wavelength approaches the material characteristic length, first-order continuum formulations are no longer appropriate.

Consequently, structural problems involving localisation and softening become inobjective if modelled with a standard local approach to CDM, since the partial differential equilibrium equations lose ellipticity, or hyperbolicity, in the case of dynamical problems. This leads to ill-posed initial boundary value problems (recall Section 2.8), which no longer have a unique solution, as it is dependent upon spatial discretization (Bažant and Pijaudier-Cabot, 1988). In practice, this inhibits the convergence of finite element predictions with mesh refiniment, as the aforementioned mesh dependency results in spurious damage and strain concentration in specific elements of the domain. In this context, several *nonlocal* CDM strategies have been proposed to circumvent this numerical issue, stemming from the works of Bažant et al. (1984), Pijaudier-Cabot and Bažant (1987) and a few others. In addition, Bažant (1991, 1994), among others, enirched the description of material degradation with nonlocal theories with arguments rooted in micro-mechanics and materials science.

The simpler approaches to fracture mechanics are based on *linear elastic fracture mechanics* (LEFM), which is, in turn, formulated upon Griffith's theroy of brittle fracture (Griffith, 1921). In essence, this theory postulates that a crack will propagate in a material when the reduction in potential energy due to crack growth is greater than or equal to the increase in surface energy due to the creation of new free surfaces. Further developments by Irwin (1957), allowing the theoretical prediction of stresses near the crack front, have enabled the modelling of brittle failure. Nonetheless, for problems in which the fracture process zone is large in relation to the dimensions of the geometry, e.g. ductile fracture in metals or delamination in composites, LEFM can no longer provide valid predictions. For such problems, several computational strategies to model fracture have been proposed in the past decades, including: continuous and adaptive remeshing (Mediavilla Varas, 2005), the virtual crack closure technique (Krueger, 2004, Rybicki and Kanninen, 1977), the extended finite element method (Moës et al., 1999) and crack tip elements (Bouhala et al., 2013, Fu et al., 2020, Song and Wolf, 1997), and cohesive zone models (Mi et al., 1998, Schellekens and de Borst, 1993, Turon et al., 2007). Despite their computational efficiency, most discrete fracture models require the explicit tracking of evolving fracture surfaces, which can often prove to be a cumbersome task. In practice, the theory of fracture mechanics is intrinsically not self-contained, in spite of its versatility and popularity in both academic and engineering communities. Extrinsic (sometimes *ad hoc*) criteria have to be introduced to determine when and where a crack nucleates, how much it propagates and in which orientation (Mandal et al., 2019). With this in mind, *smeared crack* methods, which treat cracks as diffusive entities and not geometrical discontinuities, have been adopted to bypass many of the concerns posed by discrete computational approaches. More recently, *phase-field* fracture models have gained considerable popularity. These models were initially formulated by Francfort and co-workers (Bourdin et al., 2000, 2008, Francfort and Marigo, 1998), who proposed a phase-field approximation of the variational formulation for Griffith's theory of brittle fracture.

In this chapter, the theoretical framework of the three damage models implemented and utilised in the context of this dissertation are layed out. Section 4.2 introduces nonlocal theory of integral type, emphasising a few notable elements of nonlocal averaging strategies. Section 4.3 presents an alternative implicit gradient-based nonlocal model, formulated through a Taylor expansion of the integral nonlocal weighting function. Finally, Section 4.4 addresses phase-field models for fracture, describing the general formulation adopted in this contribution. The implementation of the three models is detailed in Chapters 5, 8 and 9, respectively.

4.2 Nonlocal damage models of integral type

During the 1960s and 1970s, nonlocal continuum formulations were developed by several authors (see for instance Edelen et al. (1971), Edelen and Laws (1971), Kröner (1967)). In the 1980s, nonlocal theory of integral type was applied to damage mechanics by contributions such as Bažant et al.

(1984), Belytschko et al. (1986), Pijaudier-Cabot and Bažant (1987) and others, who explored the possibility of eliminating mesh dependency with the introduction of nonlocal interactions based on appropriately selected weighting functions. This nonlolcal strategy saw significant application and development in the context of quasi-brittle material failure (Benvenuti et al., 2002, Comi, 2001, de Vree et al., 1995, Jirásek, 1998). However, it has since also been extended to treat ductile damage (Andrade et al., 2009, 2011, 2014b).

In essence, integral nonlocal damage theory relies on the homogenisation of a given damage-related local quantity using adequate weighting functions, and within a nonlocal domain determined by the *nonlocal intrinsic length-scale parameter*. This nonlocal averaging procedure is presented in Section 4.2.1, in relation to a local damage variable, where an integral operator is employed to establish nonlocal interactions between different points in the domain to ensure mesh regularisation. In this scenario, since the material behaviour at a given point is dependent on these nonlocal interactions, the numerical treatment of the mechanical balance problem must also be nonlocal. This motivated extensive research on consistent tangent operators for integral nonlocal models in the past decades, with some notable contributions by Andrade et al. (2014a), Belnoue et al. (2009), Jirásek and Patzak (2002), Pijaudier-Cabot and Huerta (1991). The adequate formulation of these tangent operators has been shown to be essential for the stability of nonlocal models of integral type, particularly in the case of highly nonlinear deformation paths, commonly found in the modelling of ductile damage.

Some modern advancements on integral type nonlocal formulations include the adoption of an evolving intrinsic parameter (Jirásek and Desmorat, 2019, Pijaudier-Cabot et al., 2004, Rastiello et al., 2018, Shutov and Klyuchantsev, 2023), and the study of particular scenarios of nonlocal interaction, such as the relationship between two points in opposite sides of a crack (Rastiello et al., 2018). Reis et al. (2018) utilised integral nonlocal damage to model the progressive failure of heterogeneous micro-structures, while also discussing the interactions between two nonlocal materials and the symmetry of the nonlocal operator in the case a periodic boundary condition is employed. Lenz and Mahnken (2023) also explored the use of integral nonlocal models to study the effect of residual strains on the response of composites via mean-field homogenisation. The authors utilised a novel numerical scheme to tackle the computational cost of the nonlocal assembly and averaging procedures with parallelisation. Romano et al. (2017) adopted an integral nonlocal model to address the failure of elastic nano-beams.

In the following, additional details regarding the formulation of nonlocal models of integral type are presented. After describing the basic concepts of nonlocal theory in Section 4.2.1, the nonlocal averaging procedure and some of its relevant aspects are discussed in Section 4.2.2. In Chapter 5, the finite element implementation of a nonlocal model of integral type is detailed.

4.2.1 Nonlocal theory of integral type

The fundamental concept underlying any nonlocal approach in physics and mathematics is the replacement of a locally calculated variable with a nonlocal counterpart. In the case of nonlocal theory of integral type, the nonlocal variable is computed through an averaging procedure in the neighbourhood of the point of interest. For instance, the local field, $A\{\boldsymbol{y}\}$, is replaced with its nonlocal counterpart, $\bar{A}\{\boldsymbol{y}\}$, defined as

$$\bar{A}\{\boldsymbol{y}\} = \int_{\Omega^{\mathrm{nl}}} \beta\{\boldsymbol{y},\boldsymbol{\xi}\} A\{\boldsymbol{\xi}\} \mathrm{d}V\{\boldsymbol{\xi}\}, \tag{4.1}$$

where $\beta\{\cdot,\cdot\}$ is the nonlocal averaging operator, often referred to as a *kernel* function (Fish et al., 2012), Ω^{nl} denotes the nonlocal integration domain and $\boldsymbol{y}$ and $\boldsymbol{\xi}$ are the global coordinates of two neighbouring points. To guarantee a uniform evolution of $\beta\{\cdot,\cdot\}$, it must comply with a normalising condition, such that

$$\int_{\Omega^{\mathrm{nl}}} \beta\{\boldsymbol{y},\boldsymbol{\xi}\} \mathrm{d}V\{\boldsymbol{\xi}\} = 1. \tag{4.2}$$

With the goal of meeting this condition, a regularisation procedure is often carried out, using the following expression

$$\beta\{\boldsymbol{y},\boldsymbol{\xi}\} = \frac{\alpha\{\boldsymbol{y},\boldsymbol{\xi}\}}{\int_{\Omega^{\mathrm{nl}}} \alpha\{\boldsymbol{y},\boldsymbol{\xi}\}\mathrm{d}V\{\boldsymbol{\xi}\}}, \tag{4.3}$$

where $\alpha\{\cdot,\cdot\}$ is a weighting function, defined as

$$\alpha\{\boldsymbol{y},\boldsymbol{\xi}\} = \exp\left[\frac{-\|\boldsymbol{y}-\boldsymbol{\xi}\|^2}{2R^2}\right], \tag{4.4}$$

where R is the *nonlocal intrinsic length*, also referred to as the nonlocal radius. Alternatively, the bell-shaped function proposed in Andrade et al. (2011) can also be used:

$$\alpha\{\boldsymbol{y},\boldsymbol{\xi}\} = \left\langle 1 - \frac{\|\boldsymbol{y}-\boldsymbol{\xi}\|^2}{R^2} \right\rangle^2, \tag{4.5}$$

where $\langle\cdot\rangle$ are the *Macauley* brackets. Nevertheless, Equation (4.4) was adopted in most of the examples presented in this work. These two functions are plotted in Figure 4.1. Contrarily to the exponential weighting function in Equation (4.4), the bell-shaped function (Equation (4.5)) achieves $\alpha\{\boldsymbol{y},\boldsymbol{\xi}\} = 0$, if point ξ is at distance equal to R from point $\boldsymbol{y}$.

With this in mind, nonlocal theory of integral type replaces the local damage variable, D, with its nonlocal counterpart, $\bar{D}$, computed as

$$\bar{D}\{\boldsymbol{y}\} = \int_{\Omega^{\mathrm{nl}}} \beta\{\boldsymbol{y},\boldsymbol{\xi}\}D\{\boldsymbol{\xi}\}\mathrm{d}V, \tag{4.6}$$

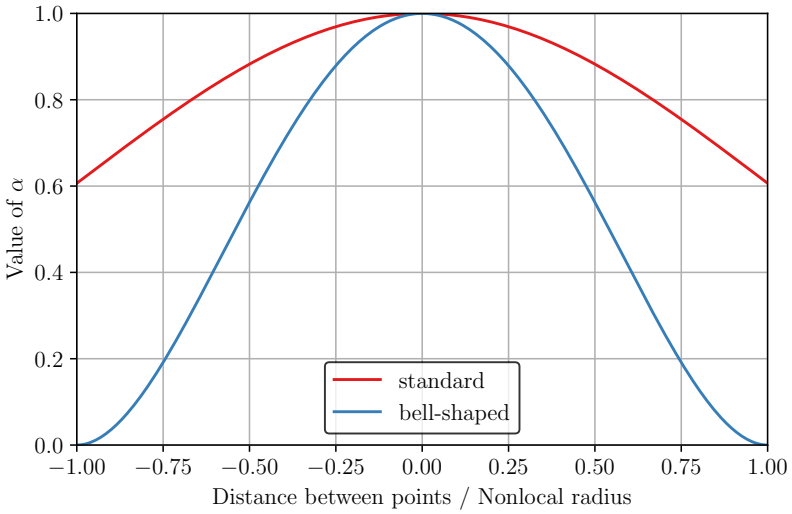

Figure 4.1: Visual representation of the two nonlocal weighting functions presented in Equations (4.4) and (4.5).

4.2.2 Nonlocal averaging strategy

Some additional numerical aspects regarding the implementation of this nonlocal approach should be assessed. The nonlocal domain of each point, $\boldsymbol{y}$, is defined with a circumference with a radius of R. This circumference contains the $\boldsymbol{\xi}$ points that contribute to the nonlocal averaging of $D\{\boldsymbol{y}\}$, and delimits the nonlocal domain, Ω^{nl}. This domain can be evaluated at different configurations of the body, as shown in Figure 4.2, leading to different constitutive models. The three main strategies for the evaluation of the nonlocal domains are the following:

1. With the *Eulerian* approach, the nonlocal domain and the nonlocal integral are both computed in the deformed configuration, meaning that updated Gauss point coordinates are used to determine the integration domain and the values of the weighting function (see Equation (4.4)).
2. Within a *Lagrangian* approach, the nonlocal domain and the nonlocal integral are determined in the reference configuration, i.e. their values remain constant during the deformation of the body.
3. With the *updated-Lagragian* approach, the nonlocal domain is updated in the beginning of each load increment, but remains unaltered during its iterative cycle.

Andrade et al. (2011) observed that no significant differences arise with the use of these three strategies. That being the case, the Lagrangian-type strategy was employed in most of the examples presented in this dissertation, meaning that the value of the nonlocal operator $\beta\{\cdot,\cdot\}$ is only computed in the first pseudo-time increment of each simulation, after which the same integration points 'j' are considered to be in the nonlocal circumference of Gauss point 'i' irregardless of their deformation path, as is depicted in Figure 4.2b.

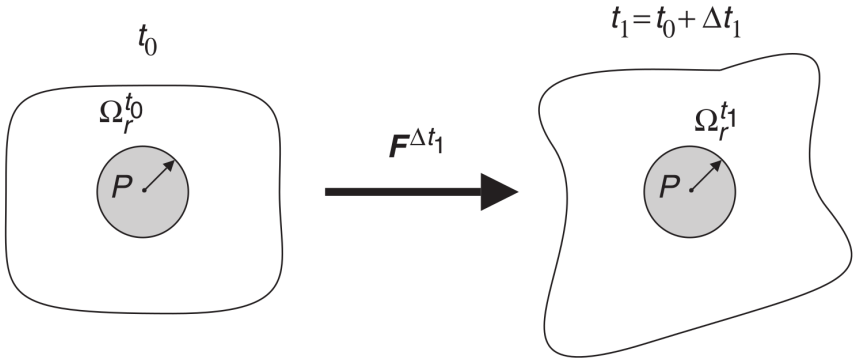

(a) Eulerian-type averaging.

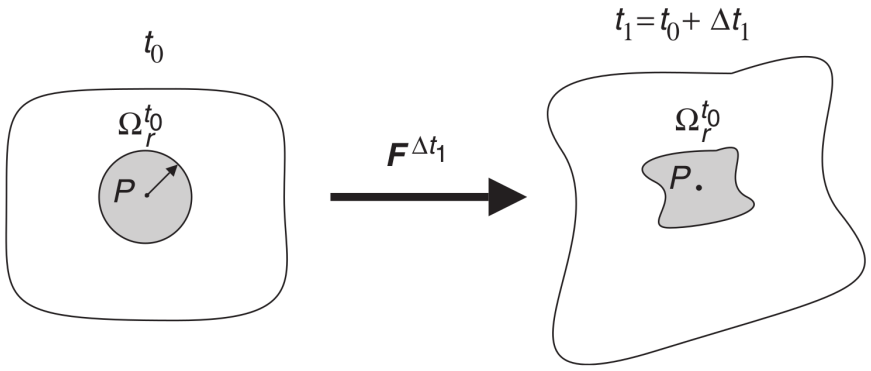

(b) Lagragian-type averaging.

Figure 4.2: Schematic representation of the two main strategies for nonlocal averaging, taken from Andrade et al. (2011).

Regarding the nonlocal operator, from the observation of Equation (4.3), one can infer that the nonlocal operator might not be symmetric for every combination of $\boldsymbol{y}$ and $\boldsymbol{\xi}$, i.e. there can exist pairs of points with which it is found that

$$\beta\{\boldsymbol{y},\boldsymbol{\xi}\} \neq \beta\{\boldsymbol{\xi},\boldsymbol{y}\}. \tag{4.7}$$

This occurs whenever the nonlocal circumference of a given point intersects the boundary of the physical domain, for instance. In such cases, the resulting tangent stiffness operator for the Newton-Raphson method can be unsymmetric, which hinders computational performance.

Lastly, the invariability of kernels was assumed, as is common in nonlocal approaches of integral type. Mathematically speaking, this translates into

$$\dot{\beta}\{\boldsymbol{y},\boldsymbol{\xi}\} = 0, \tag{4.8}$$

which, in essence, means that the kernel is independent of the history of the problem. That being the case, in computational terms, the kernel remains unaltered when the body undergoes deformation, it is simply evaluated at different configurations. This hypothesis and its advantages from a numerical perspective are discussed by Andrade et al. (2011).

4.3 Gradient-enhanced nonlocal damage

Gradient-enhanced continuum formulations arised in the 1980s with pioneering contributions such as the works of Aifantis and co-workers (Aifantis, 1984, Triantafyllidis and Aifantis, 1986) who introduced the concept of gradient plasticity. Since then, *strain gradient plasticity* formulations have been the focus of extensive research, both from a numerical (De Borst and Muehlhaus, 1992, Engelen et al., 2003, Mühlhaus and Alfantis, 1991, Polizzotto, 2009) and an empirical (Fleck et al., 1994) standpoint. The gradient-enhancement of continuum can also be applied in the context of damage mechanics (Comi, 1999, César de Sá et al., 2006, de Borst et al., 1998, de Borst, R. et al., 1996, Lacy et al., 1999, Mühlhaus et al., 1994, Peerlings et al., 1996b), where a nonlocal formulation is achieved through the introduction of an intrinsic length-scale linked with the gradient diffusion of damage, effectively circumventing pathological mesh sensitivity. In contrast with the integral nonlocal strategy, addressed in Section 4.2, gradient-based models rely on the coupling of an additional equation with the standard finite element equilibrium problem, to ensure nonlocality. This results in treating the mechanical problem and the nonlocal interactions in a separate fashion, allowing the pointwise formulation of the material model and conveniently maintaining the local-like format of the mechanical equilibrium equations (Andrade et al., 2011). A relevant consequence is preventing the emergence of numerous additional non-zero stiffness coefficients associated with the integral approach, thus preserving the sparsity of the mechanical stiffness matrix. However, it also requires an adequate solution scheme to guarantee the stability and convergence of the coupled problem. This issue is discussed in Section 8.3.

In this dissertation, an implicit gradient-enhanced nonlocal model was employed. Its formulation is addressed in Section 4.3.1, where its explicit couterpart is also mentioned. Nonlocal models incorporating variable intrinsic length-scale parameters have also gained traction within gradient-based approaches (Geers et al., 1998, Mandal et al., 2019, Poh and Sun, 2017, Rajput et al., 2023, s. Saroukhani et al., 2013, Sarkar et al., 2019). These models have not been included in the present contribution.

More recently, several implementation strategies for gradient-enhanced damage models have been proposed to take advantage of the growing capabilites of commercial and research finite element codes. The solution strategies embedded in many finite element programs for the treatment of multi-physics problems, particularly thermomechanical ones, has opened opportunities for simple and unified implementations of gradient nonlocal models (Azinpour et al., 2018, Junker et al., 2022, Ostwald et al., 2019, Seupel et al., 2018). In fact, the implementation strategy followed in the context of this dissertation adopts a pre-existing solution method for thermomechanical problems, as detailed in Chapter 8. The parallel between the gradient-enhancement of damage and the thermal heat diffusion problem is of particular interest due to the similarity of the governing equation that must be coupled with the standard mechanical problem. This parallel is discussed in Section 4.3.2.

4.3.1 Gradient-based nonlocal formulation

In their seminal work, Bažant et al. (1984) postulated that the nonlocal theory of integral type, presented in Section 4.2.1 can be utilised to derive a gradient-based nonlocal formulation. To this end, the local variable of interest, in this case, the local damage variable, must be expanded into a Taylor series:

$$D(\boldsymbol{x}+\boldsymbol{\xi}) = D(\boldsymbol{x}) + \nabla_{\boldsymbol{x}} D(\boldsymbol{x}) \cdot \boldsymbol{\xi} + \frac{1}{2!}\nabla^2_{\boldsymbol{x}} D(\boldsymbol{x}) \cdot^2 \boldsymbol{\xi}^2 + \frac{1}{3!}\nabla^3_{\boldsymbol{x}} D(\boldsymbol{x}) \cdot^3 \boldsymbol{\xi}^3 + \frac{1}{4!}\nabla^4_{\boldsymbol{x}} D(\boldsymbol{x}) \cdot^4 \boldsymbol{\xi}^4 + \dots, \tag{4.9}$$

where $(\cdot)^n$ is the n-th order inner product operator and $\boldsymbol{\xi}^n$ denotes the n-th factor of the dyadic product of $\boldsymbol{\xi}$ with itself. Assuming isotropy and substituting Equation (4.9) into Equation (4.6) leads to

$$\bar{D} = D + c\nabla^2_{\boldsymbol{x}} D + d\nabla^4_{\boldsymbol{x}} D + \dots, \tag{4.10}$$

where the coefficients c, d, ... , are determined with the kernel function (Equation (4.3)) and the averaging volume. Neglecting higher-order terms, the nonlocal damage variable can be rewritten as

$$\bar{D} = D + c\nabla^2_{\boldsymbol{x}} D, \tag{4.11}$$

in which c is equivalent to the square of the intrinsic length-scale parameter, inherent to the gradient-based nonlocal formulation, i.e. $c = l^2$.

Equation (4.11) is the additional damage-related equation associated with *explicit* gradient-enhanced nonlocal approaches (Peerlings et al., 2001). Nonetheless, as remarked by Peerlings et al. (1996b), Equation (4.11) is not suitable for standard numerical analysis, due to the explicit dependence of the nonlocal variable on the local damage gradient. This would warrant the adoption of C^1 continuity of the displacement field (Lasry and Belytschko, 1988) and, thus, the adoption of C^1 continuous finite elements (recall Section 2.10.4). To avoid this, most numerical strategies for explicit gradient damage employ mixed formulations relying on a three-field problem, in which a consistency condition is included (de Borst et al., 1998, Engelen et al., 2003). Moreover, it has been shown that explicit gradient models are only *weakly nonlocal*, i.e. spatial interactions are confined to an infinitesimal neighbourhood, while implicit gradient and integral models are *strongly nonlocal* (Engelen et al., 2003, Peerlings et al., 2001).

To bypass these issues, the gradient of the local damage variable may be *implicitely* redefined by differentiating Equation (4.10):

$$\nabla^2_{\boldsymbol{x}} \bar{D} = \nabla^2_{\boldsymbol{x}} D + c\nabla^4_{\boldsymbol{x}} D + d\nabla^6_{\boldsymbol{x}} D + \dots, \tag{4.12}$$

which yields

$$\nabla^2_{\boldsymbol{x}} D = \nabla^2_{\boldsymbol{x}} \bar{D} - c\nabla^4_{\boldsymbol{x}} D - d\nabla^6_{\boldsymbol{x}} D - \dots. \tag{4.13}$$

Substituting the above expression into Equation (4.10):

$$\bar{D} - \nabla^2_{\boldsymbol{x}} \bar{D} = D + (d-c)\nabla^4_{\boldsymbol{x}} D + \dots. \tag{4.14}$$

Neglecting higher-order terms, the final equation for implicit gradient-enhanced nonlocal damage is achieved:

$$\bar{D} - l^2\nabla^2_{\boldsymbol{x}} \bar{D} = D, \tag{4.15}$$

where l is the aforementioned length-scale parameter of the nonlocal gradient enhancement. The following natural boundary condition must also be considered:

$$\nabla_{\boldsymbol{x}} \bar{D} \cdot \boldsymbol{N} = 0, \tag{4.16}$$

where $\boldsymbol{N}$ is the unit vector normal to the boundary of the domain. With this approach, the gradient nonlocal damage, $\bar{D}$ is treated as an independent variable, which must comply with the partial

differential equation in Equation (4.15), and allows utilising standard C^0 continuous finite element interpolation, contrarily to explicit gradient-enhanced nonlocal formulations. That said, higher-order implicit gradient formulations have also been derived (de Borst and Verhoosel, 2016), considering the fourth or fourth and sixth order terms in Equation (4.12). Such formulations require C^1 and C^2 continuity of the finite element interpolation, but have not been included in this dissertation.

Despite the significant differences in the numerical treatment of implicit gradient and integral type nonlocal models, the gradient formulation can be considered an approximation of the original integral nonlocal model (Peerlings et al., 2001), resulting from the Taylor expansion of the nonlocal kernel (Equation (4.3)).

4.3.2 Parallel with quasi-static heat diffusion

Equation (4.15) is an Helmholtz equation, similarly to the general form of quasi-static thermal balance. As aforementioned, this parallel between heat diffusion and the damage averaging equation has been particularly relevant due to the widespread adoption of solution schemes for thermomechanical problems in the context of gradient formulations, particularly in commercial finite element codes. Since the implementation of a gradient nonlocal model was based on existing code for thermomechanical problems, this comparison is expanded in this section. Ostwald et al. (2019) provides a comprehensive discussion on the parallel between quasi-static heat diffusion and gradient-enhanced damage averaging, which guided the following review.

The general form of the heat equation, for homogeneous and isotropic materials, and assuming a temperature-independent heat capacity, c_p, reads

$$\rho c_p \dot{\theta} - k_t \nabla^2_{\boldsymbol{x}} \theta = r_\theta(\theta, \boldsymbol{F}, \boldsymbol{\alpha}, t, \boldsymbol{x}), \tag{4.17}$$

where θ and $\dot{\theta}$ denote the temperature and its first time-derivative, k_t is the thermal condutivity, and r_θ is a spatial heat source, depending on the temperature itself, the deformation gradient, a given set of internal variables, $\boldsymbol{\alpha}$, the time instant, t, and the spatial point, x. Assuming quasi-static heat diffusion, the first derivative term vanishes, i.e.

$$- k_t \nabla^2_{\boldsymbol{x}} \theta = r_\theta(\theta, \boldsymbol{F}, \boldsymbol{\alpha}, \boldsymbol{x}). \tag{4.18}$$

The above expression, containing a gradient and a heat source term, may be utilised as the basis for the numerical implementation of Equation (4.15), where nonlocal damage, $\bar{D}$, is the independent variable, for a properly analogous thermal problem. The definition of the analogous heat diffusion problem relies on establishing a particular heat source, such as:

$$- k_t \nabla^2_{\boldsymbol{x}} \theta = q + r_{\text{mec}}. \tag{4.19}$$

where r_{mec} denotes the mechanically dissipated heat, which, within a coupled solution scheme, can be utilised to transfer the local damage variable, D, from the mechanical problem into the averaging equation. Furthermore, the thermal condutivity, k_t, in the damage equation, is analogous to the nonlocal length-scale parameter, while the remaining term in the right-hand side of Equation (4.19), q, can be viewed as a temperature-dependent linear heat source defined by

$$q = -\theta. \tag{4.20}$$

In addition to this, the natural boundary condition of the damage averaging problem (Equation (4.15)) is equivalent to the assumption of a continuum body with adiabatic boundaries, i.e. no heat flux can be transferred to the external environment. Another relevant boundary condition for most problems involving the nonlocal model is the prescription of an initial null damage in the entire domain, analogous to the prescription of an initial null global temperature.

Section 8.4.3 details the numerical implementation of the damage averaging equation in the thermomechanical branch of LINKS, following the parallel presented in this section.

4.4 Phase-field fracture

Despite being rooted in fracture mechanics, both historically and conceptually, phase-field models are smeared crack continuous approaches for the prediction of crack propagation and structural failure under severe localisation. Such formulations offer various advantages in relation to alternative smeared and discrete fracture models. On the one hand, by modelling cracks as diffuse entities, the need for crack tracking is eliminated, and complex crack topologies in two and three dimensions can be handled with relative ease. Notable examples of the application of phase-field models for predicting complex crack paths are presented by Borden et al. (2016), Kristensen et al. (2020), Msekh et al. (2015), Paggi and Reinoso (2017), Quintanas-Corominas et al. (2019), Wu et al. (2021), Zhou et al. (2018). On the other hand, its thermodynamical consistency, versatility and ease of implementation distance phase-field approaches from most other continuous fracture models. Its energy-based formulation provides a suitable a suitable platform for the simple yet rigorous fracture thermodynamics principles (Navidtehrani et al., 2021b).

Having been the focus of extensive research in the past decade, phase-field approaches have been employed in numerous fracture problems, including: elastoplasticity coupeld with fracture (Fang et al., 2019, Miehe et al., 2016), shape memory alloys (Simoes and Martínez-Pañeda, 2021). functionally-graded materials (Hirshikesh et al., 2019, Kumar et al., 2021), fatigue (Schreiber et al., 2021), dynamic fracture (Borden et al., 2012, McAuliffe and Waisman, 2016), delamination in composite materials (Quintanas-Corominas et al., 2020), metamaterials (Abali et al., 2021), and hydrogen-embrittled structures (Kristensen et al., 2020). This broad scope of application underscores the versatility and compelling numerical aspects of phase-field models.

More recently, the integration of phase-field strategies within multi-scale modelling frameworks has been pursued by various authors, although developments are still limited. Paggi et al. (2018) presented a mixed approach, combining cohesive elements with phase-field, to predict the fracture of solar-grade polycrystalline silicon with competing failure modes. Khadyko et al. (2024) coupled phase-field fracture with crystal plasticity, while Li and Xu (2022) utilised it to predict fracture in heterogeneous concrete composite microstructures. Tan and Martínez-Pañeda (2021) proposed a concurrent multi-scale approach to model the fracture of composite materials, coupling the phase-field approach with CZM and R-curve behaviour, i.e. evolving fracture toughness. Patil and co-workers (Patil et al., 2018a, 2019, 2018b) also employed concurrent approaches to model the brittle and quasi-brittle failure of composites, with high degrees of heterogeneity. He et al. (2020) made use of a numerical homogenisation procedure and a phase-field model to predict the failure of elastic heterogeneous porous media. Bijaya et al. (2023) studied the fracture of architected materials with a DNS approach and phase-field. Noentheless, efforts to incorporate microstructures undergoing severe localisation, modelled with a phase-field approach, into multi-scale models based on computational homogenisation are still limited hitherito. Noteworthy exceptions include the contributions of Bharali and co-workers (Bharali, 2024, Bharali et al., 2021), who proposed a variationally consistent computational-homogenisation-based multi-scale framework for the phase-field fracture of heterogeneous materials.

Finally, it should be remarked that various authors have drawn comparisons between phase-field fracture models and gradient-enhanced nonlocal damage (see for instance Azinpour et al. (2018), de Borst and Verhoosel (2016)). This comparison was not considered in the context of this dissertation, since the gradient (Chapter 8) and phase-field (Chapter 9) models were implemented for two different constitutive models and material classes.

With this in mind, Section 4.4.1 elaborates on the basic concepts of the phase-field fracture approach and derives a general formulation of the phase-field balance equation. Lastly, Section 4.4.2 presents the parallel between gradient-enhanced, phase-field, and quasi-static heat diffusion equations, which is the basis for the implementation of a phase-field model in the thermomechanics branch of LINKS, detailed in Section 9.3.

4.4.1 General formulation for phase-field fracture

Consider an physical body occupying an arbitrary region, Ω, in the three-dimensional Euclidean space, with external boundary $\partial\Omega$ and outwards unit normal vector $\boldsymbol{N}$, as illustrated in Figure 4.3.

With a phase-field fracture model, the nucleation and growth of cracks are described by a smeared continuous scalar *phase-field*: $\phi \in [0;1]$. Said phase-field functions as a continuum damage variable, being null when the material point is perfectly undamaged and unitary at failure. The smearing of cracks is controlled by a phase-field length-scale parameter l. The aim of this diffuse representation is to introduce, over a given discontinuous surface, Γ, the following approximation of the fracture energy (Bourdin et al., 2000):

$$\Phi = \int_{\boldsymbol{\varphi}(\Gamma)} G_c \, \mathrm{d}a \approx \int_{\boldsymbol{\varphi}(\Omega)} G_c \gamma(\phi, \nabla_{\boldsymbol{x}}(\phi)) \mathrm{d}v, \quad \text{for } l \to 0, \tag{4.21}$$

where γ is the so-called crack surface density functional and G_c is the material's fracture toughness (Griffith, 1921). Equation (4.21) is the so-called Γ-convergence concept, which states that the phase-field approach recovers the sharp crack representation, as the length-scale parameter, l, approaches zero. In practice, infinitesimal phase-field length-scales yield infinite crack nucleation stresses, inducing non-physical behaviour Borden et al. (2012). For this reason, researchers have proposed empirical formulas for estimating a physical value for this parameter (see for instance Quintanas-Corominas et al. (2019)). Notwithstanding, the phase-field approximation of discontinuous fracture phenomena is essentially based on considering diffuse cracks, surrounded by sharp phase-field gradients, ultimately controlled by the length-scale parameter.

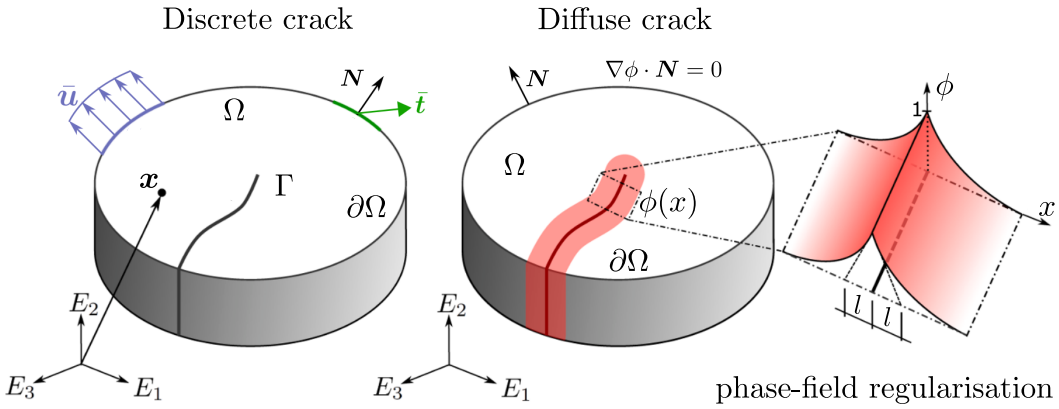

Figure 4.3: Schematic representation of an arbitrary body with a discrete or a diffuse crack, adapted from Quintanas-Corominas et al. (2019).

The weak form of momentum balance must be recast to account for new terms involving the fracture process. To this end, a scalar stress-like quantity, ω, which is work conjugate to the phase-field, ϕ, is introduced, as well as a phase-field microstress vector, denoted by $\boldsymbol{\xi}$, that is work conjugate to the gradient of the phase-field, $\nabla_{\boldsymbol{x}}\phi$. In the following, the phase-field is assumed to be driven solely by the solution to the displacement problem, thus, no external traction is associated with ϕ. In the absence of body forces, the weak momentum balance statement is derived in the spatial description through the application of the principle of virtual work:

$$\int_{\boldsymbol{\varphi}(\Omega)} \{\boldsymbol{\sigma}^* : \nabla_{\boldsymbol{x}}(\boldsymbol{\eta}) + \omega\kappa + \boldsymbol{\xi} \cdot \nabla_{\boldsymbol{x}}(\kappa)\} \mathrm{d}v = \int_{\boldsymbol{\varphi}(\partial\Omega)} (\boldsymbol{t} \cdot \boldsymbol{\eta}) \mathrm{d}a, \quad \forall \boldsymbol{\eta} \in \mathcal{V}, \quad \forall \kappa \in \mathscr{F}, \tag{4.22}$$

where $\boldsymbol{\eta}$ is the virtual displacement vector and $\mathcal{V}$ is the set of admissible virtual displacements, whereas κ is the virtual phase-field and $\mathscr{F}$ is its corresponding admissible set. Equation (4.22) must

hold for an arbitrary deformed configuration of Ω, and for any kinematically admissible variations of the virtual quantities. Thus, by application of the Gauss divergence theorem, the strong form of spatial force balances are given by:

$$\begin{aligned} &\nabla_{\boldsymbol{x}} \cdot \boldsymbol{\sigma} = 0 \\ &\nabla_{\boldsymbol{x}} \cdot \boldsymbol{\xi} - \omega = 0 \end{aligned} \qquad \text{in } \boldsymbol{\varphi}(\Omega), \tag{4.23}$$

subject to the following natural boundary conditions:

$$\begin{aligned} &\boldsymbol{\sigma} \cdot \boldsymbol{N} = \boldsymbol{t} \\ &\boldsymbol{\xi} \cdot \boldsymbol{N} = 0 \end{aligned} \qquad \text{on } \boldsymbol{\varphi}(\partial\Omega). \tag{4.24}$$

Moreover, since the phase-field formalism relies on energetic considerations, one must define the total potential energy of the body:

$$W(\boldsymbol{\varepsilon}(\mathbf{u}), \phi, \nabla_{\boldsymbol{x}}\phi) = \psi(\boldsymbol{\varepsilon}(\mathbf{u}), g(\phi)) + \varphi(\phi, \nabla_{\boldsymbol{x}}\phi) \tag{4.25}$$

where ψ is the elastic strain energy density, φ is the fracture energy density. It should remarked that, since the derivation presented here is for a generic material model, at either infinitesimal or finite strains, the elastic potential energy has been assumed to depend on a generic kinematical quantity, $\boldsymbol{\varepsilon}$. In practice the strain energy potential may assume numerous forms dependending on the material model at hand, and several strain measures may be used to define it. It is also noteworthy that the fracture energy diminishes with the increase in the phase-field variable, through the *degradation function*, $g(\phi)$, which, as the name implies, controls the continuum degradation of the material. In general terms, it must fulfill the following conditions:

$$g(0) = 1, \quad g(1) = 0, \quad g'(\phi) \leq 0 \text{ for } 0 \leq \phi \leq 1. \tag{4.26}$$

At this point, one may write the fracture energy density as

$$\varphi(\phi, \nabla_{\boldsymbol{x}}\phi) = G_c \gamma(\phi, \nabla_{\boldsymbol{x}}\phi) = G_c \frac{1}{4c_w l} \left(w(\phi) + l^2 |\nabla_{\boldsymbol{x}}\phi|^2 \right). \tag{4.27}$$

where $w(\phi)$ is the geometric crack function, which must comply with the following conditions:

$$w(0) = 0, \quad w(1) = 1, \quad w'(\phi) \geq 0 \text{ for } 0 \leq \phi \leq 1. \tag{4.28}$$

In addition, c_w is a scaling constant, related to the geometric crack function:

$$c_w = \int_0^1 \sqrt{w(\zeta)} \mathrm{d}\zeta. \tag{4.29}$$

Phase-field crack or damage growth is driven by the strain energy stored in the solid, as characterized by the undamaged elastic strain energy density ψ_0. Moreover, to prevent crack propagation under compressive strain states, the driving force for fracture can be decomposed into active ψ_0^+ and inactive ψ_0^- parts (Miehe et al., 2010):

$$\psi(\varepsilon(\mathbf{u}), g(\phi)) = \psi^+(\varepsilon(\mathbf{u}), \phi) + \psi_0^-(\varepsilon(\mathbf{u})) = g(\phi)\psi_0^+(\varepsilon(\mathbf{u})) + \psi_0^-(\varepsilon(\mathbf{u})) \tag{4.30}$$

However, this energetic split was not pursued in the context of this dissertation, and is suggested as a future development. That said, fracture by the total undamaged elastic strain energy ψ_0, irregardless of the deformation path.

Also, since damage is an irreversible process the following must hold for the any deformation path and material model:

$$\dot{\phi} \geq 0. \tag{4.31}$$

To enforce irreversibility, a history field variable, coined *history-dependent maximum strain energy*, $\mathscr{H}$ may be introduced. This history-dependent variable which must satisfy the Karush-Kuhn-Tucker conditions (Navidtehrani et al., 2021b):

$$\psi_0 - \mathscr{H} \leq 0, \quad \dot{\mathscr{H}} \geq 0, \quad \dot{\mathscr{H}}\left(\psi_0 - \mathscr{H}\right) = 0. \tag{4.32}$$

Accordingly, for a given time instant, t, over a total time t_f, the history-dependent maximum strain energy may be defines as

$$\mathscr{H} = \max_{t\in[0,t_f]} \psi_0(t) \tag{4.33}$$

Consequently, the total potential energy of the solid, expressed in Equation (4.25) can be recast as:

$$W = g(\phi)\mathscr{H} + \frac{G_c}{4c_w}\left(\frac{1}{l}w(\phi) + l|\nabla\phi|^2\right) \tag{4.34}$$

Finally, to arrive at the generalised form of the phase-field equation, the fracture micro-stress variables ω and $\boldsymbol{\xi}$ must be addressed. The scalar micro-stress ω is defined as:

$$\omega = \frac{\partial W}{\partial \phi} = g'(\phi)\mathscr{H} + \frac{G_c}{4c_w l}w'(\phi), \tag{4.35}$$

while the phase-field micro-stress vector, $\boldsymbol{\xi}$ reads,

$$\boldsymbol{\xi} = \frac{\partial W}{\partial \nabla_{\boldsymbol{x}}\phi} = \frac{l}{2c_w}G_c\nabla_{\boldsymbol{x}}\phi. \tag{4.36}$$

Inserting Equations (4.35) and (4.36) into the phase-field balance equation (Equation (4.23)):

$$\frac{G_c}{2c_w}\left(\frac{w'(\phi)}{2l} - l\nabla^2\phi\right) + g'(\phi)\mathscr{H} = 0. \tag{4.37}$$

4.4.2 Parallel with gradient nonlocal damage and quasi-static heat diffusion

Although the Equation (4.42) is more intricate than the gradient damage averaging problem in Equation (4.15), the most popular degradation and geometric crack functions yield a reasonably simpler expression for the phase-field balance. In the present dissertation, the following degradation function was assumed:

$$g(\phi) = (1-\phi)^2 + \chi, \tag{4.38}$$

where χ is a small, positive-valued constant that is introduced to prevent ill-conditioning when $\phi = 1$. A value of $\chi = 1\times10^{-7}$ was adopted as suggested by Navidtehrani et al. (2021a). Moreover, the geometric crack function was defined as

$$w(\phi) = \phi^2, \tag{4.39}$$

for simplicity. This, in turn, yields

$$c_w = \int_0^1 \sqrt{\phi^2}\,\mathrm{d}\phi = \frac{1}{2}. \tag{4.40}$$

Considering the functions expressed in Equations (4.38) and (4.39) and their respective derivatives, Equation (4.37) may be recast as follows

$$G_c\left(\frac{\phi}{l} - l\nabla^2_{\boldsymbol{x}}(\phi)\right) + 2(1-\phi)\mathscr{H} = 0, \tag{4.41}$$

rearranging the above equation, one reaches the format a common format of phase-field balance, which was used for the implementation tasks reported in Chapter 9:

$$-G_c l\nabla^2_{\boldsymbol{x}}(\phi) = -2(1-\phi)\mathscr{H} - \frac{G_c}{l}\phi. \tag{4.42}$$

Similarly to Equation (4.15), Equation (4.42) is a Helmholtz equation, which can be related to quasi-static heat diffusion for numerical purposes. In this case, the analogous thermal problem is relatively more complex, since the history-dependent energetic variable, $\mathscr{H}$, is entangled with the phase-field, ϕ. With this in mind, the thermal balance problem analogous to Equation (4.42) may be defined as

$$-k_t \nabla_{\boldsymbol{x}}^2 \theta = q(\theta, r_{\text{mec}}) + r_{\text{mec}}, \tag{4.43}$$

where q is a linear heat source which depends not only on the temperature but also on the mechanically dissipated heat, given by

$$q(\theta, r_{\text{mec}}) = -\theta\, r_{\text{mec}} - m\theta, \tag{4.44}$$

where m is a coefficient of the heat source, in this case:

$$m = \frac{G_c}{l}, \tag{4.45}$$

whereas the mechanically dissipated heat is conveniently defined as

$$r_{\text{mec}} = -2\mathscr{H}. \tag{4.46}$$

Finally, in the phase-field analogy, the thermal condutivity is the product of the fracture toughness and material length-scale (see Equations (4.42) and (4.43)). The computational implementation of the phase-field balance equation, making use of the thermal analogy, is reported in Section 9.3.2.

Part II

Second-Order Homogenisation and Nonlocal Damage of Integral Type

CHAPTER 5

IMPLEMENTING NONLOCAL DAMAGE OF INTEGRAL TYPE

5.1 Introduction

In this chapter, the implementation of a nonlocal damage model of integral type is detailed. This nonlocal model was already available in LINKS (recall Section 1.3) for micro-scale analysis, and the main ingredients for its formulation are presented in Reis et al. (2018), which was the main guiding reference for its extension to macroscopic problems. In this dissertation, the nonlocal model was extended for macro-scale problems, such that it could be related to second-order computational homogenisation, as discussed in Chapter 1.

Having addressed nonlocal theory of integral type in Section 4.2, Section 5.2 presents the constitutive framework of the Engelen damage model, employed in this chapter. Section 5.3 describes the numerical treatment of the nonlocal Engelen model, while Section 5.4 discusses its implementation in the macro-scale code of LINKS, mentioning the existing routines for micro-scale problems and their usability in this new context. Section 5.5 reports four numerical examples of the newly implemented nonlocal model, before summarising the main conclusions from this chapter in Section 5.6

5.2 Constitutive model for nonlocal damage

In this section, the constitutive framework employed to formulate the nonlocal damage model at the macro-scale is outlined. Firstly, in Section 5.2.1, the model for elastoplasticity at finite strains is described. Thereafter, the isotropic explicit local damage model is presented in Section 5.2.2, before detailing the equivalent nonlocal damage model of integral-type for ductile materials at finite strains in Section 5.2.3. The constitutive methodology used in this section was based on the work of Reis et al. (2018), since it describes the implementation of the same model at the micro-scale.

5.2.1 Constitutive model for finite strain elastoplasticity

The von Mises constitutive model for finite strain elastoplasticity was employed as the basis for the introduction of nonlocal damage. A multiplicative hyperelasto-plastic framework (de Souza Neto et al., 2008, Simo and Hughes, 1998) was adopted. Therefore, the deformation gradient is decomposed as

$$\boldsymbol{F} = \boldsymbol{F}^e \boldsymbol{F}^p, \tag{5.1}$$

where $\boldsymbol{F}^e$ and $\boldsymbol{F}^p$ are the elastic and plastic components of the deformation gradient, respectively. The polar decomposition (see Section 2.3.3) can be used with the same multiplicative strategy, resulting in the following relations

$$\boldsymbol{F}^e = \boldsymbol{R}^e \boldsymbol{U}^e = \boldsymbol{V}^e \boldsymbol{R}^e, \tag{5.2}$$

where $\boldsymbol{R}^e$, $\boldsymbol{U}^e$ and $\boldsymbol{V}^e$ are the elastic rotation and right and left stretch tensors. Similar expressions could also be established for their plastic counterparts:

$$\boldsymbol{F}^p = \boldsymbol{R}^p \boldsymbol{U}^p = \boldsymbol{V}^p \boldsymbol{R}^p. \tag{5.3}$$

Furthermore, the logarithmic elastic strain tensor can be written as

$$\boldsymbol{\varepsilon}^e = \ln \boldsymbol{V}^e. \tag{5.4}$$

This strain tensor can also be decomposed in two parts:

$$\boldsymbol{\varepsilon} = \boldsymbol{\varepsilon}^e + \boldsymbol{\varepsilon}^p. \tag{5.5}$$

The use of this spatial strain measure to describe elastic deformation at finite strains is particularly convenient, as it leads to substantial simplifications in the stress integration algorithm allowing a natural extension of the elastic predictor/plastic corrector to the finite strain range (de Souza Neto et al., 2008). Moreover, the Kirchhoff stress tensor, $\boldsymbol{\tau}$, which is the conjugate stress measure to the logarithmic elastic strain tensor, can be defined as

$$\boldsymbol{\tau} = \mathbf{D}^{\mathrm{e}} : \boldsymbol{\varepsilon}^e = \mathbf{D}^{\mathrm{e}} : (\boldsymbol{\varepsilon} - \boldsymbol{\varepsilon}^p), \tag{5.6}$$

where $\mathbf{D}^{\mathrm{e}}$ is the isotropic fourth-order elasticity tensor. Another relevant building block of the constitutive model is the adoption of a hyperelastic law based on a free-energy potential that assumes the general form

$$\psi(\boldsymbol{\varepsilon}^e, \boldsymbol{\alpha}). \tag{5.7}$$

Similarly to what was seen in Section 2.6.2, through the dissipation inequality, it can be shown (de Souza Neto et al., 2008) that the above potential yields the following constitutive relation for the Kirchhoff stress tensor:

$$\boldsymbol{\tau} = \rho_0 \frac{\partial \psi}{\partial \boldsymbol{\varepsilon}^e}. \tag{5.8}$$

Furthermore, with the adoption of the von Mises criterion, the yield function is given by

$$\Phi(\boldsymbol{\tau}, \bar{\varepsilon}^p) = \tau_{\mathrm{eq}}(\boldsymbol{\tau}) - \tau_y(\bar{\varepsilon}^p) \leq 0, \tag{5.9}$$

where τ_{eq} is the von Mises equivalent stress and τ_y denotes the current yield stress, which, under the assumption of linear hardening, is defined as

$$\tau_y(\bar{\varepsilon}^p) = \tau_{y,0} + H\bar{\varepsilon}^p, \tag{5.10}$$

where $\tau_{y,0}$ is the initial yield stress, H is the hardening modulus and $\bar{\varepsilon}^p$ is the accumulated plastic strain. Moreover, the Prandtl Reuss plasticity law is used to predict the evolution of the plastic strain tensor:

$$\dot{\boldsymbol{\varepsilon}}^p = \dot{\gamma} \boldsymbol{N}, \tag{5.11}$$

$$\boldsymbol{N} = \sqrt{\frac{3}{2}} \frac{\boldsymbol{\tau}^d}{\|\boldsymbol{\tau}^d\|}, \tag{5.12}$$

where $\boldsymbol{\tau}^d$ is the deviatoric component of the stress tensor, $\boldsymbol{N}$ is the plastic flow vector and the plastic multiplier rate, $\dot{\gamma}$, is driven by the loading/unloading and consistency conditions:

$$\phi \leq 0, \;\; \dot{\gamma} \geq 0, \;\; \dot{\phi}\dot{\gamma} = 0. \tag{5.13}$$

5.2.2 Isotropic explicit damage model

The fundamental concept behind continuum damage models is the introduction of one of more *damage variables* - internal state variables whose value affects the physical properties of the material. In this work, an isotropic explicit damage model, based on the von Mises constitutive model for finite strain plasticity, was employed. This model is hereupon referred to as the Engelen damage model. In this case, it is assumed that every stress component is affected equally by the presence of damage, which is modelled using a single damage variable, D, such that

$$\boldsymbol{\tau}^* = (1-D)\boldsymbol{\tau}, \tag{5.14}$$

where $\boldsymbol{\tau}^*$ is the *damaged* Kirchhoff stress tensor. If the material is undamaged, D is equal to 0, whereas if the material is completely damaged and unable to support any load, D is equal to 1. With this in mind, it can be said that the damaged stress tensor reflects the internal degradation of the material (Lemaitre, 1985b).

Furthermore, constitutive functionals for the evolution of the stress tensor, $\boldsymbol{\tau}$, and the damage variable, D, can now be defined:

$$\begin{aligned} \boldsymbol{\tau} &= \widehat{\boldsymbol{\tau}}\{\boldsymbol{\varepsilon}, \boldsymbol{\alpha}\}, \\ D &= \widehat{D}\{\boldsymbol{\varepsilon}, \boldsymbol{\alpha}, \boldsymbol{\tau}\}, \end{aligned} \tag{5.15}$$

where $\widehat{\boldsymbol{\tau}}$ and $\widehat{D}$ are the stress and damage functionals, respectively, $\boldsymbol{\varepsilon}$ is a given kinematic quantity and $\boldsymbol{\alpha}$ is the set of internal variables. The stress functional, crucially, is independent of the damage variable, making this an *explicit* damage model. In implicit damage models, the stress functional, $\widehat{\boldsymbol{\tau}}$, is also dependent on D, which makes its implementation more complex.

In this case, a simple explicit damage law, governed by the evolution of the rate of accumulated plastic strain, $\dot{\bar{\varepsilon}}^p$ was assumed. That being said, the damage law is defined by

$$\dot{D} = \frac{\dot{\bar{\varepsilon}}^p}{\varepsilon_f}, \tag{5.16}$$

where ε_f is a scalar quantity comprising the critical value of the accumulated plastic strain.

5.2.3 Isotropic explicit nonlocal damage model of integral type

Recalling Equation (4.6),in nonlocal theory of integral type, the original damage variable is replaced by its nonlocal counterpart, which is computed through nonlocal averaging (see Equation (4.1)):

$$\bar{D}\{\boldsymbol{y}\} = \int_{\Omega^{\mathrm{nl}}} \beta\{\boldsymbol{y}, \boldsymbol{\xi}\} D\{\boldsymbol{\xi}\} \mathrm{d}V, \tag{5.17}$$

where $\beta\{\cdot,\cdot\}$ is the kernel operator presented in Section 4.2.1 and defined in Equation (4.3). Therefore, Equation (5.14) can be recast as

$$\boldsymbol{\tau}^* = (1-\bar{D})\boldsymbol{\tau}. \tag{5.18}$$

Having established these equations, the nonlocal damage model of integral type is fully defined as an extension of the von Mises constitutive model coupled with an isotropic explicit local damage model.

5.3 Numerical Treatment

In Chapter 2, fundamental concepts of continuum mechanics problems and their solution with the finite element method were addressed. Morever, Section 5.2 presented the constitutive model for the finite strain elastoplasticity coupled with nonlocal damage, set to be employed in the present

chapter. In this section, the computational treatment of the material model, in its local and nonlocal versions, is described. The work of de Souza Neto et al. (2008) was used as the main guiding reference regarding the numerical treatment of an elastoplastic constitutive model at large strains. Additionally, the work of Reis et al. (2018) provided a valuable insights regarding the implementation of the nonlocal damage model.

With this in mind, Section 5.3.1 presents the numerical integration of the elastoplastic constitutive equations. Thereafter, the nonlocal averaging procedure is discussed in Section 5.3.2 and the linearisation of the local and nonlocal models is detailed in Section 5.3.3.

5.3.1 Numerical integration procedure

Within the framework of computational elastoplasticity, it becomes necessary to adopt a numerical algorithm for the integration of the rate constitutive equations. In these cases, the overall finite element solution scheme is highly dependent on the accuracy of the particular numerical algorithm adopted (de Souza Neto et al., 2008). In this work, the elastic predictor/plastic corrector algorithm was adopted, in conjunction with an exponential backward Euler time discretisation for the integration of the elastoplastic constitutive equations. Furthermore, for the solution of the return-mapping equations, the Newton-Raphson method (Section 2.9.4) was employed. In this section the numerical strategy employed for the integration of the rate constitutive equations, which is often referred to as the *state update procedure*, is presented in detail.

Time discretisation

The first step towards the implementation of the state update procedure is the adoption of a time discretisation scheme. In this work, an *exponential* backward Euler (fully implicit) scheme was adopted. The choice of an algorithm based on an exponential map integrator is common in the context of finite strain plasticity, as it results in a volume-preserving update formula for the plastic component of the deformation gradient. Therefore, the elastoplastic constitutive problem at finite strains can be posed, as stated in de Souza Neto et al. (2008):

Problem 5.1 *Given $\boldsymbol{F}^e_n$ and $\boldsymbol{\alpha}_n$ at the beginning of the interval $[t_n, t_{n+1}]$ and given the prescribed incremental deformation gradient, $\boldsymbol{F}_\Delta$, for this interval, solve the following system of algebraic equations*

$$\begin{aligned} \boldsymbol{F}^e_{n+1} &= \boldsymbol{F}_\Delta \boldsymbol{F}^e_n \boldsymbol{R}^{eT}_{n+1} \exp\left[-\Delta\gamma \left.\frac{\partial \psi}{\partial \boldsymbol{\tau}}\right|_{n+1} \right] \boldsymbol{R}^e_{n+1} \\ \boldsymbol{\alpha}_{n+1} &= \boldsymbol{\alpha}_n + \Delta\gamma \boldsymbol{H}_{n+1} \end{aligned} \tag{5.19}$$

for the unknowns $\boldsymbol{F}^e_{n+1}, \boldsymbol{\alpha}_{n+1}$ and $\Delta\gamma$, subjected to the constraints

$$\Delta\gamma \geq 0, \quad \Phi(\boldsymbol{\tau}_{n+1}, \boldsymbol{A}_{n+1}) \leq 0, \quad \Delta\gamma\Phi(\boldsymbol{\tau}_{n+1}, \boldsymbol{A}_{n+1}) = 0, \tag{5.20}$$

with

$$\boldsymbol{\tau}_{n+1} = \rho_0 \left.\frac{\partial \psi}{\partial \boldsymbol{\varepsilon}^e}\right|_{n+1}, \quad \boldsymbol{A}_{n+1} = \rho_0 \left.\frac{\partial \psi}{\partial \boldsymbol{\alpha}}\right|_{n+1}, \tag{5.21}$$

and the kinematic relations

$$\begin{aligned} \boldsymbol{\varepsilon}^e_{n+1} &= \ln \boldsymbol{V}^e_{n+1}, \\ \boldsymbol{V}^e_{n+1} &= \left[\boldsymbol{F}^e_{n+1} \left(\boldsymbol{F}^e_{n+1}\right)^T \right]^{\frac{1}{2}}, \\ \boldsymbol{R}^e_{n+1} &= \left[\boldsymbol{V}^e_{n+1}\right]^{-1} \boldsymbol{F}^e_{n+1}, \end{aligned} \tag{5.22}$$

where Ψ is the plastic flow potential of the material, H is the material's hardening modulus and $\boldsymbol{A}$ are the thermodynamical forces associated to the dissipative phenomena at play.

Elastic predictor/return-mapping algorithm

Having established the time discretisation of the elastoplastic constitutive equations, it becomes convenient to outline the two-step state update algorithm, which is used to compute the stresses, strains and state variables at time t_{n+1} at a given Gauss point i. That being said, the mathematical operations presented in this section are related to quantities which are evaluated at the integration points of the finite element mesh, as the subscripts $(\cdot)_i$ indicate. In practice, a loop over the integration points of the structure is done to perform the numerical integration procedure.

Elastic trial state

In the first step, the displacement increment, $\Delta\boldsymbol{u}$ is assumed to result in purely elastic deformation. That being said, the deformation gradient increment must be determined, according to a discretized version of Equation (2.14):

$$\boldsymbol{F}_{\Delta,i} = \boldsymbol{I} + \nabla_n[\Delta\boldsymbol{u}], \tag{5.23}$$

with which the deformation gradient at time t_{n+1} and Gauss point i can be written as

$$\boldsymbol{F}_{n+1,i} = \boldsymbol{F}_{\Delta,i}\boldsymbol{F}_{n,i}. \tag{5.24}$$

Thereafter, the left Cauchy-Green strain tensor is determined as

$$\begin{aligned} \boldsymbol{B}^e_{n,i} &= \exp\left[2\boldsymbol{\varepsilon}^e_{n,i}\right], \\ \boldsymbol{B}^e_{n+1,i} &= \boldsymbol{F}_{\Delta,i}\boldsymbol{B}^e_{n,i}\left(\boldsymbol{F}_{\Delta,i}\right)^T. \end{aligned} \tag{5.25}$$

At this point, the elastic trial state can be computed as follows:

$$\begin{aligned} &\boldsymbol{\varepsilon}^{e,\text{trial}}_{n+1,i} = \ln\left[\boldsymbol{V}^{e,\text{trial}}_{n+1,i}\right] = \frac{1}{2}\ln\left[\boldsymbol{B}^{e,\text{trial}}_{n+1,i}\right], \\ &\bar{\varepsilon}^{\text{p,trial}}_{n+1.i} = \bar{\varepsilon}^{\text{p}}_{n.i}, \\ &D^{\text{trial}}_{n+1,i} = D_{n,i}, \\ &\boldsymbol{\tau}^{d,\text{trial}}_{n+1,i} = 2G\mathbf{I}_d : \boldsymbol{\varepsilon}^{e,\text{trial}}_{n+1,i}. \end{aligned} \tag{5.26}$$

The last line of Equation (5.26) is particularly relevant as it concerns the determination of the deviatoric trial stress tensor, $\boldsymbol{\tau}^{d,\text{trial}}_{n+1}$, using the material's shear modulus, G and the fourth-order deviatoric identity tensor, $\mathbf{I}_d$. Having obtained the elastic trial state, the final step of the elastic predictor stage is the evaluation of the von Mises yield function,

$$\Phi(\boldsymbol{\tau}^{d,\text{trial}}_{n+1,i}, \bar{\varepsilon}^{\text{p,trial}}_{n+1.i}) = \tau_{eq}(\boldsymbol{\tau}^{d,\text{trial}}_{n+1,i}) - \tau_y(\bar{\varepsilon}^{\text{p,trial}}_{n+1.i}) \leq 0. \tag{5.27}$$

In this work, a linear piecewise interpolation strategy was employed to obtain the numerical hardening curve and, hence, the numerical hardening modulus, from a set of sampling points. Finally, if Equation (5.27) is satisfied, the elastic trial state is deemed valid, and the state variables are updated according to

$$(\cdot)_{n+1} = (\cdot)^{trial}_{n+1}. \tag{5.28}$$

In such cases, the return-mapping algorithm is not used. Otherwise, the elastic trial state is invalid, as the displacement increment did not result in purely elastic deformation. That being the case, the return-mapping algorithm is used to update the state variables. A brief overview of the state update procedure for multiplicative finite strain elastoplasticity is presented in Box 5.1.

Box 5.1 State update procedure for multiplicative finite strain elastoplasticity coupled with isotropic explicit damage.

1. For each i Gauss point, given incremental displacement $\Delta\boldsymbol{u}$, update the deformation gradient:

$$\boldsymbol{F}_{\Delta,i} := \boldsymbol{I} + \nabla_n[\Delta\boldsymbol{u}], \quad \boldsymbol{F}_{n+1,i} := \boldsymbol{F}_{\Delta,i}\boldsymbol{F}_{n,i}; \tag{5.29}$$

2. Compute elastic trial state:

$$\begin{aligned}
&\boldsymbol{B}^e_{n,i} := \exp\left[2\boldsymbol{\varepsilon}^e_{n,i}\right],\\
&\boldsymbol{B}^e_{n+1,i} := \boldsymbol{F}_{\Delta,i}\boldsymbol{B}^e_{n,i}\left(\boldsymbol{F}_{\Delta,i}\right)^T,\\
&\boldsymbol{\varepsilon}^{e,\text{trial}}_{n+1,i} := \ln\left[\boldsymbol{V}^{e,\text{trial}}_{n+1,i}\right] = \frac{1}{2}\ln\left[\boldsymbol{B}^{e,\text{trial}}_{n+1,i}\right],\\
&\boldsymbol{\tau}^{d,\text{trial}}_{n+1,i} = 2G\mathbf{I}_d : \boldsymbol{\varepsilon}^{e,\text{trial}}_{n+1,i},\\
&\bar{\varepsilon}^{\text{p,trial}}_{n+1.i} := \bar{\varepsilon}^{\text{p}}_{n,i},\\
&D^{\text{trial}}_{n+1,i} := D_{n,i};
\end{aligned} \tag{5.30}$$

3. Check plastic admissibility:

$$\text{IF}\,\Phi(\boldsymbol{\tau}^{d,\text{trial}}_{n+1,i}, \bar{\varepsilon}^{\text{p,trial}}_{n+1.i}) \leq 0; \tag{5.31}$$

THEN set $(\cdot)_{n+1} := (\cdot)^{\text{trial}}_{n+1}$ and EXIT
ELSE GOTO Algorithm 2 (update $\boldsymbol{\tau}, \boldsymbol{\varepsilon}^{\text{e}}, \bar{\varepsilon}^{\text{p}}$ and D).

Return-mapping algorithm

Whenever the displacement increment, $\Delta\boldsymbol{u}$, results in some plastic deformation, Equation (5.27) is not satisfied and the elastic trial step is not valid. In such cases, a return-mapping algorithm must be employed to recover an admissible material state. This is done by enforcing the return to the yield surface, by finding an incremental plastic multiplier, $\Delta\gamma$, that satisfies the system of return-mapping equations. After simplification, this system can be reduced to the single-equation return-mapping:

$$\Phi(\boldsymbol{\tau}^d_{n+1,i}, (\bar{\varepsilon}^p_{n,i} + \Delta\gamma_i)) = \tau_{eq}(\boldsymbol{\tau}^d_{n+1,i}) - \tau_y(\bar{\varepsilon}^p_{n,i} + \Delta\gamma_i) = 0. \tag{5.32}$$

For the sake of convenience, the trial stresses are often utilised in this procedure, resulting in

$$\tau_{eq}\left(\boldsymbol{\tau}^{d,\text{trial}}_{n+1,i}\right) - 3G\Delta\gamma_i - \tau_y\left(\bar{\varepsilon}^p_{n,i} + \Delta\gamma_i\right) = 0. \tag{5.33}$$

This is a nonlinear equation on $\Delta\gamma_i$, which is solved with the Newton-Raphson method (Section 2.9.4). Having found a new admissible state, the logarithmic elastic strain must be updated as

$$\boldsymbol{\varepsilon}^e_{n+1,i} = \boldsymbol{\varepsilon}^{e,\text{trial}}_{n+1,i} - \Delta\gamma_i \boldsymbol{N}^{\text{trial}}_{n+1,i}, \tag{5.34}$$

where

$$\boldsymbol{N}^{\text{trial}}_{n+1,i} = \sqrt{\frac{3}{2}}\frac{\boldsymbol{\tau}^{d,\text{trial}}_{n+1,i}}{\|\boldsymbol{\tau}^{d,\text{trial}}_{n+1,i}\|}. \tag{5.35}$$

The stress tensor and the state variables must also be updated according to:

$$\boldsymbol{\tau}_{n+1,i} = \mathbf{D}^{\mathrm{e}} : \boldsymbol{\varepsilon}^{e}_{n+1,i}, \tag{5.36}$$

$$\bar{\varepsilon}^{p}_{n+1,i} = \bar{\varepsilon}^{p}_{n,i} + \Delta\gamma_i, \tag{5.37}$$

$$D_{n+1,i} = \frac{\bar{\varepsilon}^{p}_{n+1,i}}{\varepsilon_f}. \tag{5.38}$$

Furthermore, the damaged stress tensor must also be computed for the local damage model:

$$\boldsymbol{\tau}^{*}_{n+1,i} = \left(1 - D_{n+1,i}\right)\boldsymbol{\tau}_{n+1,i}. \tag{5.39}$$

Finally, in order to compute the vector of internal forces (see Equation (2.132)), the damaged Kirchhoff stress tensor must be converted into the damaged Cauchy stress tensor, according to:

$$\boldsymbol{\sigma}^{*}_{n+1,i} := \frac{1}{\det \boldsymbol{F}_{n+1,i}}\boldsymbol{\tau}^{*}_{n+1,i} \tag{5.40}$$

The return-mapping procedure adopted in this work is summarised in Box 5.2.

Remark 1 *To maintain consistency with the notation used for the elastic trial step, the equations concerning the return-mapping algorithm retain the notation associated with the particular Gauss point, i, at which the state update procedure is taking place.*

Box 5.2 Return mapping algorithm for multiplicative finite strain elastoplasticity coupled with isotropic explicit damage.

---

1. Using the Newton-Raphson method, find the incremental plastic multiplier $\Delta\gamma_i$ that satisfies:

$$\tau_{eq}\left(\boldsymbol{\tau}^{d,\mathrm{trial}}_{n+1,i}\right) - 3G\Delta\gamma_i - \tau_y\left(\bar{\varepsilon}^{p}_{n,i} + \Delta\gamma_i\right) = 0. \tag{5.41}$$

2. Update the logarithmic elastic strain tensor and the Kirchhoff stress tensor:

$$\boldsymbol{\varepsilon}^{e}_{n+1,i} := \boldsymbol{\varepsilon}^{e,\mathrm{trial}}_{n+1,i} - \Delta\gamma_i \boldsymbol{N}^{\mathrm{trial}}_{n+1,i}, \tag{5.42}$$

$$\boldsymbol{\tau}_{n+1,i} := \mathbf{D}^{\mathrm{e}} : \boldsymbol{\varepsilon}^{e}_{n+1,i}. \tag{5.43}$$

3. Update the effective plastic strain and the local damage variable:

$$\bar{\varepsilon}^{p}_{n+1,i} := \bar{\varepsilon}^{p}_{n,i} + \Delta\gamma_i, \tag{5.44}$$

$$D_{n+1,i} := \frac{\bar{\varepsilon}^{p}_{n+1,i}}{\varepsilon_f}. \tag{5.45}$$

4. Update the local damaged stress tensor:

$$\boldsymbol{\tau}^{*}_{n+1,i} := \left(1 - D_{n+1,i}\right)\boldsymbol{\tau}_{n+1,i}. \tag{5.46}$$

5. Update the damaged Cauchy stress tensor in order to compute the vector of internal forces:

$$\boldsymbol{\sigma}^{*}_{n+1,i} := \frac{1}{\det \boldsymbol{F}_{n+1,i}}\boldsymbol{\tau}^{*}_{n+1,i} \tag{5.47}$$

5.3.2 Nonlocal averaging procedure

In the case of the nonlocal damage model, for each pseudo-time increment, after the local state update procedure has been performed, the nonlocal integral must be computed, in order to obtain the nonlocal damage variable. This integral is computed numerically, using the Gaussian quadrature rule (see Section 2.9.3). That being said, the discretized version of Equation (5.17) can be written as

$$\bar{D}_{n+1,i} = \sum_{j=1}^{N_{\text{Gauss}}^{nl}} w_j J_j \beta_{ij} D_{n+1,j}, \tag{5.48}$$

where $\bar{D}_{n+1,i}$ is the nonlocal damage at Gauss point 'i' and time increment t_{n+1}, w_j, J_j, $D_{n+1,j}$ are the weight, jacobian and local damage variable for Gauss point 'j' and β_{ij} is the nonlocal operator evaluated at the two integration points. As was mentioned in Section 4.2.2, a Lagrangian-type strategy was employed in this work, hence the value of β is only computed in the first pseudo-time increment of each simulation.

Furthermore, having computed the nonlocal integral, the state update procedure described in Section 5.3.1 must be performed to obtain the local damage variable and the stress and strain state at time increment t_{n+1}. The final step in the nonlocal averaging procedure is the homogenisation of the stress tensor with the nonlocal damage variable at each integration point, i.e.

$$\boldsymbol{\tau}^*_{n+1,i} = (1 - \bar{D}_{n+1,i})\boldsymbol{\tau}_{n+1,i}. \tag{5.49}$$

Similarly to the local case, the damaged Cauchy stress tensor must be obtained (Equation (5.40)) in order to compute the vector of internal focers. The general state update and nonlocal averaging algorithm for an isotropic explicit nonlocal damage model is presented in Box 5.3.

Box 5.3 State update procedure and nonlocal averaging algorithm for an isotropic explicit damage model based on the von Mises constitutive model at finite strains.

1. For each i Gauss point, determine the weight of the non-local integral related to j Gauss point, β_{ij}. Given the adoption of the Lagrangian averaging approach, this is only carried out once at the problem initialisation stage;

2. State-update over all integration Gauss points, i, (local approach to update the stress tensor and the damage variable) - GOTO Algorithm 1;

3. Determine the non-local damage variable for all Gauss points i, $\bar{D}_{n+1,i}$:

$$\bar{D}_{n+1,i} := \sum_{j=1}^{N_{\text{Gauss}}^{nl}} w_j J_j \beta_{ij} D_{n+1,j}, \tag{5.50}$$

4. Compute the damaged stress tensor for all Gauss points, i:

$$\boldsymbol{\tau}^*_{n+1,i} := \left(1 - \bar{D}_{n+1,i}\right)\boldsymbol{\tau}_{n+1,i}. \tag{5.51}$$

5. Obtain the damaged Cauchy stress tensor for the calculation of the internal forces:

$$\boldsymbol{\sigma}^*_{n+1,i} = \frac{1}{\det \boldsymbol{F}_{n+1,i}} \boldsymbol{\tau}^*_{n+1,i}. \tag{5.52}$$

Remark 2 *It should be remarked that, because a local state update strategy is employed before the nonlocal averaging procedure, the computation of the damaged stress tensor should be performed*

carefully. As shown in Section 5.3.1, the local damaged stress tensor is computed after a valid stress state is found with the return-mapping algorithm. That being the case, to obtain the nonlocal damaged stress tensor, the undamaged stress tensor must be used in the right-hand side of Equation (5.49). In computational terms, this means that the local update of the damaged stress tensor must either be reverted before computing the nonlocal damaged stress tensor or avoided in the case a nonlocal model is assumed.

5.3.3 Linearisation of the local and nonlocal damage models

The final step of the numerical implementation of the model is the derivation of the consistent tangent stiffness matrix for both the local and nonlocal damage models. In this section, the consistent linearisation of the local and nonlocal damage models is presented, while the derivation of the elastoplastic consistent tangent modulus for the von Mises constitutive model is also detailed.

As discussed in Section 2.9.4, the global tangent stiffness is obtained through the assembly of the contribution of each element of the domain. The expression for the element tangent stiffness matrix was also shown in Equation (2.143), in its spatial format, and in Equation (2.145), in its material version. Nevertheless, the spatial description was used to obtain the consistent tangent stiffness, which, in its discrete version, is given by

$$\mathbf{K}_T^e = \sum_{i=1}^{N_{\text{Gauss}}^e} w_i J_i \boldsymbol{G}_i^\top \mathbf{a}_i \boldsymbol{G}_i \mathrm{d}v. \tag{5.53}$$

Furthermore, the general expression for the spatial tangent modulus, $\mathbf{a}$, was also shown in Equation (2.144). That being said, it becomes convenient to establish the expression of this fourth-order tensor for the von Mises constitutive model. Through the application of the chain rule, the expression for the components of the spatial tangent modulus can be recast as

$$\mathrm{a}_{ijkl} = \frac{1}{\det \boldsymbol{F}} \left[\frac{\partial \boldsymbol{\tau}}{\boldsymbol{\varepsilon}^{e,\text{trial}}} : \frac{\boldsymbol{\varepsilon}^{e,\text{trial}}}{\partial \boldsymbol{B}^{e,\text{trial}}} : \frac{\partial \boldsymbol{B}^{e,\text{trial}}}{\partial \boldsymbol{F}} \right]_{ijkl} - \sigma_{il}\delta_{jk}, \tag{5.54}$$

for a given integration point and at a pseudo-time increment, t_{n+1}. These three derivatives are usually presented in their tensor format, i.e.

$$\mathrm{a}_{ijkl} = \frac{1}{\det \boldsymbol{F}} [\mathbf{D} : \mathbf{L} : \mathbf{B}]_{ijkl} - \sigma_{il}\delta_{jk}, \tag{5.55}$$

where $\mathbf{D}$ is the *consistent tangent modulus*, given by

$$\mathbf{D} = \frac{\partial \boldsymbol{\tau}}{\partial \boldsymbol{\varepsilon}^{e,\text{trial}}}. \tag{5.56}$$

Additionally, the fourth-order tensor, $\mathbf{L}$, is defined as

$$\mathbf{L} = \frac{\partial \ln \left[\boldsymbol{B}^{e,\text{trial}} \right]}{\partial \boldsymbol{B}^{e,\text{trial}}}, \tag{5.57}$$

wheareas the cartesian components of the fourth-order tensor, $\mathbf{B}$, are expressed as

$$\mathrm{B}_{ijkl} = \delta_{ik} \left(\boldsymbol{B}^{e,\text{trial}} \right)_{jl} + \delta_{jk} \left(\boldsymbol{B}^{e,\text{trial}} \right)_{il}. \tag{5.58}$$

That being said, the following subsections are dedicated to the derivation of the consistent tangent modulus, $\mathbf{D}$, for the various relevant cases.

Remark 3 *For the sake of simplicity, the notation related to the integration point at which a given quantity is evaluated, $(\cdot)_i$, was dropped in the derivation of the elastoplastic consistent tangent and the consistent tangent modulus for the local damage model.*

Elastoplastic consistent tangent modulus

By definition, the elastoplastic consistent tangent modulus is given by

$$\mathbf{D}^{\text{ep}}_{n+1} = \frac{\partial \boldsymbol{\tau}_{n+1}}{\partial \boldsymbol{\varepsilon}^{e,\text{trial}}_{n+1}}. \tag{5.59}$$

In order to derive the mathematical expression of the elastoplastic consistent tangent modulus for the von Mises constitutive model and the numerical integration algorithm presented in Section 5.3.1, the complete formula for the updated Kirchhoff stress tensor is derived first. For a given Gauss point, i, and load increment, t_{n+1}, the updated stress tensor can be decomposed in its volumetric and deviatoric parts

$$\boldsymbol{\tau}_{n+1} = \boldsymbol{\tau}^{p}_{n+1} + \boldsymbol{\tau}^{d}_{n+1}, \tag{5.60}$$

which are updated as follows:

$$\boldsymbol{\tau}^{p}_{n+1} = \boldsymbol{\tau}^{p,trial}_{n+1}, \tag{5.61}$$

$$\boldsymbol{\tau}^{d}_{n+1} = 2G\left(1 - \frac{\Delta\gamma 3G}{q^{\text{trial}}_{n+1}}\right)\boldsymbol{\tau}^{d,trial}_{n+1}, \tag{5.62}$$

where

$$q^{\text{trial}}_{n+1} = \sqrt{\frac{3}{2}\boldsymbol{\tau}^{d}_{n+1} : \boldsymbol{\tau}^{d}_{n+1}}. \tag{5.63}$$

Furthermore, considering the procedure for the computation of the elastic trial state presented in Section 5.3.1, the updated stress components can be recast as

$$\boldsymbol{\tau}^{p}_{n+1} = K\,\boldsymbol{I}\otimes\boldsymbol{I} : \boldsymbol{\varepsilon}^{e,\text{trial}}_{n+1}, \tag{5.64}$$

$$\boldsymbol{\tau}^{d}_{n+1} = \left(1 - \frac{\Delta\gamma 3G}{q^{\text{trial}}_{n+1}}\right)2G\,\mathbf{I}_d : \boldsymbol{\varepsilon}^{e,\text{trial}}_{n+1}, \tag{5.65}$$

where K is the material's bulk modulus. Moreover, given the volumetric/deviatoric decomposition of the fourt-order elasticity tensor:

$$\mathbf{D}^{\text{e}} = K\,\boldsymbol{I}\otimes\boldsymbol{I} + 2G\,\mathbf{I}_d, \tag{5.66}$$

the final expression for the updated Kirchhoff stress tensor is obtained:

$$\boldsymbol{\tau}_{n+1} = K\,\boldsymbol{I}\otimes\boldsymbol{I} : \boldsymbol{\varepsilon}^{e,\text{trial}}_{n+1} + \left(1 - \frac{\Delta\gamma 3G}{q^{\text{trial}}_{n+1}}\right)2G\,\mathbf{I}_d : \boldsymbol{\varepsilon}^{e,\text{trial}}_{n+1} \tag{5.67}$$

$$= \left(\mathbf{D}^{\text{e}} - \frac{\Delta\gamma 6G^2}{q^{\text{trial}}_{n+1}}\mathbf{I}_{\text{d}}\right) : \boldsymbol{\varepsilon}^{e,\text{trial}}_{n+1}. \tag{5.68}$$

That being the case, Equation (5.59) can be rewritten as

$$\mathbf{D}^{\text{ep}}_{n+1} = \frac{\partial}{\partial \boldsymbol{\varepsilon}^{e,\text{trial}}_{n+1}}\left[\left(\mathbf{D}^{\text{e}} - \frac{\Delta\gamma 6G^2}{q^{\text{trial}}_{n+1}}\mathbf{I}_{\text{d}}\right) : \boldsymbol{\varepsilon}^{e,\text{trial}}_{n+1}\right]. \tag{5.69}$$

Through the application of tensor differentiation rules to the above expression:

$$\begin{aligned}
\mathbf{D}^{\text{ep}}_{n+1} &= \frac{\partial}{\partial \boldsymbol{\varepsilon}^{e,\text{trial}}_{n+1}}\left(\mathbf{D}^{\text{e}} : \boldsymbol{\varepsilon}^{e,\text{trial}}_{n+1}\right) - \frac{\partial}{\partial \boldsymbol{\varepsilon}^{e,\text{trial}}_{n+1}}\left(\frac{\Delta\gamma 6G^2}{q^{\text{trial}}_{n+1}}\mathbf{I}_{\text{d}} : \boldsymbol{\varepsilon}^{e,\text{trial}}_{n+1}\right), \\
&= \mathbf{D}^{\text{e}} - 6G^2\left(\frac{1}{q^{\text{trial}}_{n+1}}\mathbf{I}_{\text{d}} : \boldsymbol{\varepsilon}^{e,\text{trial}}_{n+1} \otimes \frac{\partial\Delta\gamma}{\partial \boldsymbol{\varepsilon}^{e,\text{trial}}_{n+1}} - \frac{\Delta\gamma}{(q^{\text{trial}}_{n+1})^2}\mathbf{I}_{\text{d}} : \boldsymbol{\varepsilon}^{e,\text{trial}}_{n+1} \otimes \frac{\partial q^{\text{trial}}_{n+1}}{\partial \boldsymbol{\varepsilon}^{e,\text{trial}}_{n+1}} + \frac{\Delta\gamma}{q^{\text{trial}}_{n+1}}\mathbf{I}_{\text{d}}\right), \\
&= \mathbf{D}^{\text{e}} - 6G^2\left(\frac{1}{q^{\text{trial}}_{n+1}}\boldsymbol{\varepsilon}^{e,\text{trial}}_{d,n+1} \otimes \frac{\partial\Delta\gamma}{\partial \boldsymbol{\varepsilon}^{e,\text{trial}}_{n+1}} - \frac{\Delta\gamma}{(q^{\text{trial}}_{n+1})^2}\boldsymbol{\varepsilon}^{e,\text{trial}}_{d,n+1} \otimes \frac{\partial q^{\text{trial}}_{n+1}}{\partial \boldsymbol{\varepsilon}^{e,\text{trial}}_{n+1}} + \frac{\Delta\gamma}{q^{\text{trial}}_{n+1}}\mathbf{I}_{\text{d}}\right).
\end{aligned} \tag{5.70}$$

At this point, the partial derivatives included in the expression above should also be derived. Regarding the partial derivative of q_{n+1}^{trial} with respect to $\boldsymbol{\varepsilon}_{n+1}^{e,\text{trial}}$, one can start with the application of the chain rule, to arrive at

$$\frac{\partial q_{n+1}^{\text{trial}}}{\partial \boldsymbol{\varepsilon}_{n+1}^{e,\text{trial}}} = \frac{\partial q_{n+1}^{\text{trial}}}{\partial \boldsymbol{\tau}_{n+1}^{d,\text{trial}}} : \frac{\partial \boldsymbol{\tau}_{n+1}^{d,\text{trial}}}{\partial \boldsymbol{\varepsilon}_{n+1}^{e,\text{trial}}}. \tag{5.71}$$

The first term can be simplified by resorting to the definition of the derivative of the norm of a tensor with respect to the tensor itself:

$$\frac{\partial q_{n+1}^{\text{trial}}}{\partial \boldsymbol{\tau}_{n+1}^{d,\text{trial}}} = \sqrt{\frac{3}{2}} \frac{\boldsymbol{\tau}_{n+1}^{d,\text{trial}}}{\|\boldsymbol{\tau}_{n+1}^{d,\text{trial}}\|}. \tag{5.72}$$

Conversely, the derivation of the second term reads

$$\frac{\partial \boldsymbol{\tau}_{n+1}^{d,\text{trial}}}{\partial \boldsymbol{\varepsilon}_{n+1}^{e,\text{trial}}} = \frac{\partial \left(2G\mathbf{I}_d : \boldsymbol{\varepsilon}_{n+1}^{e,\text{trial}}\right)}{\partial \boldsymbol{\varepsilon}_{n+1}^{e,\text{trial}}} = 2G \frac{\partial \left(\mathbf{I}_d : \boldsymbol{\varepsilon}_{n+1}^{e,\text{trial}}\right)}{\partial \boldsymbol{\varepsilon}_{n+1}^{e,\text{trial}}} = 2G\mathbf{I}_d. \tag{5.73}$$

Combining Equations (5.72) and (5.73) yields

$$\frac{\partial q_{n+1}^{\text{trial}}}{\partial \boldsymbol{\varepsilon}_{n+1}^{e,\text{trial}}} = \frac{\boldsymbol{\tau}_{n+1}^{d,\text{trial}}}{\|\boldsymbol{\tau}_{n+1}^{d,\text{trial}}\|} : \frac{\partial \boldsymbol{\tau}_{n+1}^{d,\text{trial}}}{\partial \boldsymbol{\varepsilon}_{n+1}^{e,\text{trial}}} = 2G\sqrt{\frac{3}{2}} \frac{\boldsymbol{\tau}_{n+1}^{d,\text{trial}}}{\|\boldsymbol{\tau}_{n+1}^{d,\text{trial}}\|}. \tag{5.74}$$

For the sake of convenience, one may define the *unit flow vector*:

$$\bar{\boldsymbol{N}}_{n+1} \equiv \sqrt{\frac{2}{3}} \boldsymbol{N}_{n+1} = \frac{\boldsymbol{\tau}_{n+1}^{d,\text{trial}}}{\|\boldsymbol{\tau}_{n+1}^{d,\text{trial}}\|}, \tag{5.75}$$

such that the previous derivative can be recast as

$$\frac{\partial q_{n+1}^{\text{trial}}}{\partial \boldsymbol{\varepsilon}_{n+1}^{e,\text{trial}}} = 2G\sqrt{\frac{3}{2}} \bar{\boldsymbol{N}}_{n+1}. \tag{5.76}$$

To compute the derivative of the incremental plastic multiplier with respect to the elastic trial strain tensor, Equation (5.33) is recalled. Considering the adoption of linear hardening, the aforementioned equation can be rewritten as follows

$$q_{n+1}^{\text{trial}} - 3G\Delta\gamma - \left(\tau_0 + H(\bar{\varepsilon}^p + \Delta\gamma)\right) = 0, \tag{5.77}$$

where H is the *hardening modulus* of the material, which represents the slope of the hardening curve. In the case of linear hardening, this quantity is a constant. Therefore, after some manipulation, one can arrive at

$$\Delta\gamma = \frac{1}{3G + H}\left(q_{n+1}^{\text{trial}} - \tau_0 - H\bar{\varepsilon}^p\right). \tag{5.78}$$

Finally, the derivative of the plastic multiplier is given by

$$\begin{aligned} \frac{\partial \Delta\gamma}{\partial \boldsymbol{\varepsilon}_{n+1}^{e,\text{trial}}} &= \frac{1}{3G + H} \frac{\partial q_{n+1}^{\text{trial}}}{\partial \boldsymbol{\varepsilon}_{n+1}^{e,\text{trial}}} \\ &= \frac{2G}{3G + H}\sqrt{\frac{3}{2}} \bar{\boldsymbol{N}}_{n+1}. \end{aligned} \tag{5.79}$$

Having arrived at the expressions for the two derivatives, the elastoplastic consistent tangent modulus consistent with the constitutive and numerical strategy adopted in this work is given by

$$\begin{aligned}\mathbf{D}^{\mathrm{ep}} =& \mathbf{D}^{\mathrm{e}} - \frac{\Delta\gamma 6G^2}{q^{\mathrm{trial}}_{n+1}}\mathbf{I}_{\mathrm{d}} + 6G^2\left(\frac{\Delta\gamma}{q^{\mathrm{trial}}_{n+1}} - \frac{1}{3G+H}\right)\bar{\boldsymbol{N}}_{n+1}\otimes\bar{\boldsymbol{N}}_{n+1} \\ =& 2G\left(1 - \frac{\Delta\gamma 3G}{q^{\mathrm{trial}}_{n+1}}\right)\mathbf{I}_{\mathrm{d}} \\ &+ 6G^2\left(\frac{\Delta\gamma}{q^{\mathrm{trial}}_{n+1}} - \frac{1}{3G+H}\right)\bar{\boldsymbol{N}}_{n+1}\otimes\bar{\boldsymbol{N}}_{n+1} + K\boldsymbol{I}\otimes\boldsymbol{I}.\end{aligned} \tag{5.80}$$

Consistent tangent modulus for the local damage model

After arriving at the consistent tangent modulus for the von Mises model, it is also paramount to derive the consistent tangent modulus for the local damage model. Starting from the application of the same definition of Equation (5.59) to the damaged stress tensor, one may write

$$\mathbf{D}^{*}_{n+1} = \frac{\partial\boldsymbol{\tau}^{*}_{n+1}}{\partial\boldsymbol{\varepsilon}^{e,\mathrm{trial}}_{n+1}}, \tag{5.81}$$

which, recalling the definition of the local damaged stress tensor, can be recast as

$$\begin{aligned}\mathbf{D}^{*}_{n+1} &= \frac{\partial}{\partial\boldsymbol{\varepsilon}^{e,\mathrm{trial}}_{n+1}}\left[(1-D_{n+1})\,\boldsymbol{\tau}_{n+1}\right] \\ &= \frac{\partial\boldsymbol{\tau}_{n+1}}{\partial\boldsymbol{\varepsilon}^{e,\mathrm{trial}}_{n+1}} - D_{n+1}\frac{\partial\boldsymbol{\tau}_{n+1}}{\partial\boldsymbol{\varepsilon}^{e,\mathrm{trial}}_{n+1}} - \boldsymbol{\tau}_{n+1}\otimes\frac{\partial D_{n+1}}{\partial\boldsymbol{\varepsilon}^{e,\mathrm{trial}}_{n+1}}.\end{aligned} \tag{5.82}$$

The above expression can also be simplified with the introduction of the elastoplastic consistent tangent modulus:

$$\mathbf{D}^{*}_{n+1} = (1-D_{n+1})\,\mathbf{D}^{\mathrm{ep}}_{n+1} - \boldsymbol{\tau}_{n+1}\otimes\frac{\partial D_{n+1}}{\partial\boldsymbol{\varepsilon}^{e,\mathrm{trial}}_{n+1}} \tag{5.83}$$

Furthermore, the derivative of the damage variable, D_{n+1}, in relation to the logarithmic elastic trial deformation tensor can be obtained through the application of the chain rule:

$$\frac{\partial D_{n+1}}{\partial\boldsymbol{\varepsilon}^{e,\mathrm{trial}}_{n+1}} = \frac{\partial D_{n+1}}{\partial\Delta\gamma}\frac{\partial\Delta\gamma}{\partial\boldsymbol{\varepsilon}^{e,\mathrm{trial}}_{n+1}}, \tag{5.84}$$

which, recalling the definition of the damage law and the previously obtained derivative of the plastic multiplier, yields

$$\frac{\partial D_{n+1}}{\partial\boldsymbol{\varepsilon}^{e,\mathrm{trial}}_{n+1}} = \frac{1}{\varepsilon_f}\frac{2G}{3G+H}\sqrt{\frac{3}{2}}\bar{\boldsymbol{N}}_{n+1}. \tag{5.85}$$

That being the case, the final expression for the consistent tangent modulus of the local damage model is as follows:

$$\mathbf{D}^{*}_{n+1} = (1-D_{n+1})\,\mathbf{D}^{\mathrm{ep}}_{n+1} - \frac{2G}{\varepsilon_f\,(3G+H)}\sqrt{\frac{3}{2}}\boldsymbol{\tau}_{n+1}\otimes\bar{\boldsymbol{N}}_{n+1} \tag{5.86}$$

Consistent tangent modulus for the nonlocal damage model

The final derivation presented in this section is that of the consistent tangent modulus for the nonlocal damage model. In this section, the nomenclature related to the integration points was recovered. The starting point for the derivation of the consistent tangent modulus for the nonlocal

model is the substitution of the local damage variable in Equation (5.83) with its nonlocal counterpart, such that

$$\mathbf{D}^{*}_{n+1,ij} = \left(1-\bar{D}_{n+1,i}\right)\mathbf{D}^{\text{ep}}_{n+1,ij} - \boldsymbol{\tau}_{n+1,i} \otimes \frac{\partial \bar{D}_{n+1,i}}{\partial \boldsymbol{\varepsilon}^{e,\text{trial}}_{n+1,j}}. \tag{5.87}$$

Recalling the definition of the discrete nonlocal damage variable, introduced in Equation (5.48), the derivative of the nonlocal damage variable can be written as

$$\begin{aligned}\frac{\partial \bar{D}_{n+1,i}}{\partial \boldsymbol{\varepsilon}^{e,\text{trial}}_{n+1,j}} &= \frac{\partial}{\partial \boldsymbol{\varepsilon}^{e,\text{trial}}_{n+1,j}} \sum_{k=1}^{N^{\text{nl}}_{\text{Gauss}}} w_k J_k \beta_{ik} D_k \\ &= w_j J_j \beta_{ij} \frac{\partial D_j}{\partial \boldsymbol{\varepsilon}_j},\end{aligned} \tag{5.88}$$

where the derivative of the local damage variable at Gauss point j is computed according to Equation (5.85), such that the following expression is obtained for the consistent tangent modulus of the nonlocal damage model:

$$\mathbf{D}^{*}_{n+1,ij} = \left(1-\bar{D}_{n+1,i}\right)\mathbf{D}^{\text{ep}}_{n+1,ij} - \frac{w_j J_j \beta_{ij} 2G}{\varepsilon_f (3G+H)} \sqrt{\frac{3}{2}}\, \boldsymbol{\tau}_{n+1,i} \otimes \bar{\boldsymbol{N}}_{n+1,j}. \tag{5.89}$$

Global tangent stiffness for the nonlocal damage model

To conclude the numerical treatment of the nonlocal damage model, the general algorithm for the assembly of the global tangent stiffness is presented. In this case, the discrete expression for the element tangent stiffness is

$$\mathbf{K}^{nl}_{T} = \sum_{i=1}^{N^{e}_{\text{Gauss}}} w_i J_i \mathbf{G}^{T}_{i} \sum_{j=1}^{N^{nl}_{\text{Gauss}}} \mathbf{a}_{ij} \mathbf{G}_j, \tag{5.90}$$

where the nonlocal spatial tangent modulus, for Gauss points i and j, is given by

$$\mathbf{a}_{ij} = \frac{1}{2 \det \boldsymbol{F}_i} \left[\mathbf{D}^{*}_{ij} : \mathbf{L}_j : \mathbf{B}_j\right] - \Sigma_i \delta_{ij}, \tag{5.91}$$

where the components of the fourth-order tensor Σ are defined as

$$\Sigma_{ijkl} = \sigma^{*}_{il} \delta_{jk}. \tag{5.92}$$

Furthermore, as the expressions for the remaining fourth-order tensors have been established (see Equation (5.89), Equation (5.57) and Equation (5.58)), the algorithm for the assembly of the global tangent stiffness is presented in Box 5.4.

Box 5.4 Algorithm for the assembly of the global tangent stiffness matrix for an isotropic explicit nonlocal damage model based on the von Mises constitutive model at finite strains (adapted from Reis et al. (2018)).

1. Loop over all Gauss points i:
   i. Determine the discrete gradient operator $\mathbf{G}_i$, w_i, J_i and $\det \boldsymbol{F}_i$;
   ii. Loop over Gauss points j, in the influence area of i, with $D_j > 0$:
      a. Determine $\mathbf{G}_j$ and elastic trial for left Cauchy-Green $\boldsymbol{B}^e_j$;
      b. Compute the non-local consistent tangent $\mathbf{D}_{ij}$;
      c. Obtain the tensor derivative $\mathbf{L}_j$ and the tensor $\mathbf{B}_j$;
      d. Build array with the spatial tangent modulus $\mathbf{a}_{ij}$;
      e. Assemble this contribution to the global stiffness matrix:

$$\mathbf{K}_T^{nl} = \mathbf{K}_T^{nl} + w_j J_i \mathbf{G}_i^T \mathbf{a}_{ij} \mathbf{G}_j. \tag{5.93}$$

5.4 Implementation

In this section, the implementation of the nonlocal damage model for 2D plane strain macro-scale problems is detailed. The overall structure of LINKS is briefly presented in Section 5.4.1. In Section 5.4.2, the existing code for nonlocal models at the micro-scale is discussed, assessing the routines and code blocks that could also be utilised for macroscopic problems. The optimisation of the legacy version is also presented, particularly regarding the state update routines for nonlocal models. In Section 5.4.3 the remaining aspects of the implementation for macroscopic analysis are described.

5.4.1 Solution of a macro-scale problem with LINKS

The structure of LINKS for the solution of macro-scale problems, depicted in Figure 5.1, is perfectly standard when it comes to the application of the finite element method to solve both small and large strain problems (Ferreira, 2017). In this section, the various routines that make up this code structure are briefly introduced, in order to contextualise the necessary changes for the implementation of the nonlocal damage model.

The logical steps shown in Figure 5.1 take place within the LINKS main routine for the solution of single-scale macroscopic problems, and can be systematised as follows:

1. The first step is to read the input data, allocate and initialise the necessary variables. At this stage, the global connectivities and the vector of external forces and prescribed displacements are also built, and the load incrementation is setup.

2. Thereafter, a loop over the load/displacement increments is performed, according to the user-prescribed incremental proportional load factor.

   (a) To solve the equilibrium problem for each load increment, an iterative scheme is employed with the Newton-Raphson method (see Section 2.9.4).

      i. In the beginning of each equilibrium iteration, global tangent stiffness matrix is assembled and the system of equilibrium equations is solved.

      ii. Thereafter, the state update procedure takes place, culminating in the update of the vector of internal forces, before a new equilibrium iteration begins.

(b) The iterative cycle for each load increment is only terminated when a predefined convergence tolerance is surpassed. Alternatively, the cycle can be interrupted if the iterations are diverging or if a negative jacobian is found for any element in the state update procedure. In such instances, the load increment is reduced and a new cycle of equilibrium iterations starts.

3. After a converged solution is found for each increment, the results are written in predefined output files.

The simulation of the macro-scale problem is concluded when converged equilibrium solutions are found for all load/displacement increments.

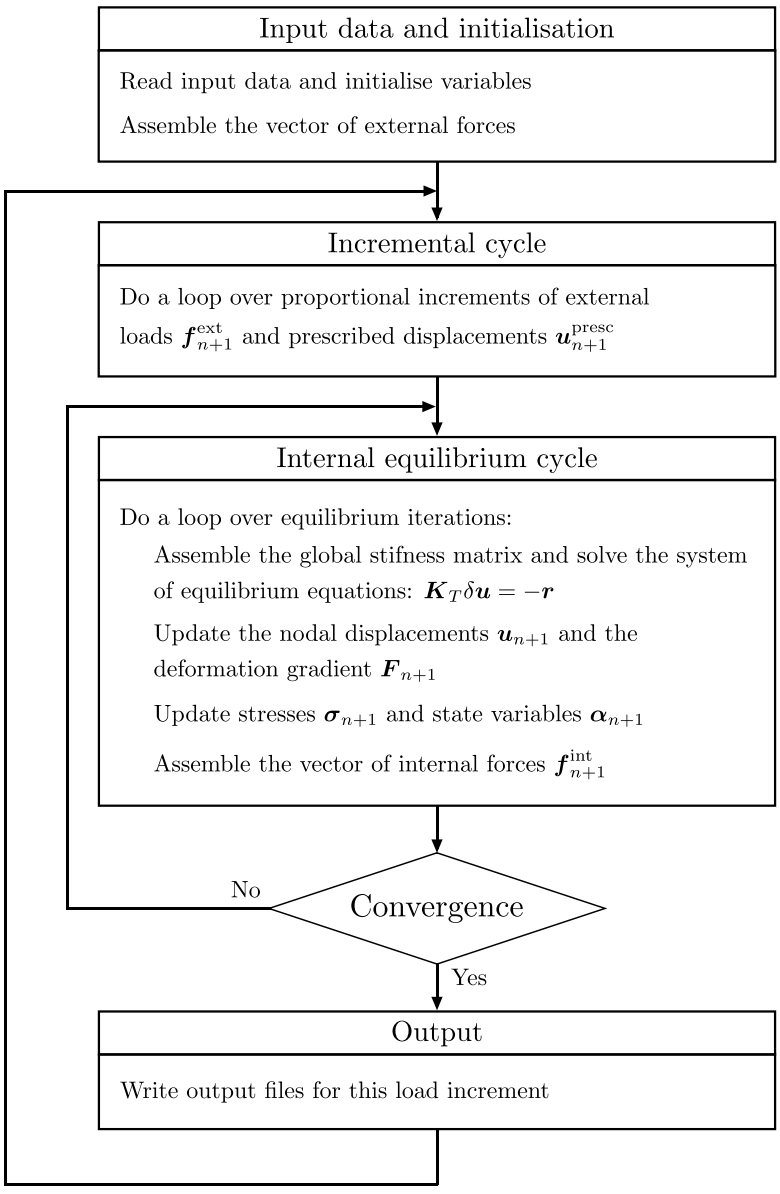

Figure 5.1: Schematic representation of the general structure of the single-scale approach for the solution of macro-scale problems with LINKS, adapted from Ferreira (2017).

5.4.2 Existing code for micro-scale problems

As has been mentioned, the nonlocal damage model of integral type was already available in LINKS, at the micro-scale. That being the case, the existing code related to nonlocal models is briefly described in this section, identifying routines that could also be employed at the macro-scale, and discussing opportunities for improvement.

The routines related to the nonlocal averaging operator and the code block for reading the input data related to the nonlocal model were re-utilised. These include the initialisation and update of the kernels and Gauss point coordinates, depending on the averaging strategy, but also the existing code block to read the input for nonlocal models for micro-problems.

Adding to this, the consistent tangent and state update routines were also already available. In regards to the consistent tangent code, the assembly operations for micro-scale cases are dependent on the boundary condition in use. Therefore, only the routine for the computation of the nonlocal consistent tangent modulus could be used (see further details in Section 5.4.3). In the case of the state update procedure for the nonlocal Engelen model, most of the code could be directly applied for macro-scale problems. Nevertheless, these state update routines were revisited and subjected to a few notable changes, in an attempt to improve their efficiency and overall organisation. The hierarchical code structure involved in the numerical state update procedure is described in what follows:

1. The state update routines available in LINKS are integrated in *interfaces for the computation of element internal forces*, in which a loop over all elements in the domain is performed. These interfaces are contained in the main single-scale codes, and call the *routines for the computation of the internal force vector*, according to the element class. For instance, F-Bar elements (see Neto et al. (2005)) and mixed elements for second-order formulations (recall Section 2.10.4) can be used, other than standard displacement-based finite elements.

2. Thereafter, within the element internal force routines, the *state update procedure* for the material model in use is called, before assembling the element contribution to the force vector.

3. The actual state update routine contains the algorithmic steps and operations described in Section 5.3.1, in the case of the Engelen model.

In the micro-scale code, there existed a specific element interface for computing the internal force vectors for nonlocal models. Since the existing nonlocal model can deal with heterogeneous RVEs, this interface then conveniently calls either the standard or the nonlocal element internal force routine. In this section, the existing version of the nonlocal routine for the computation of element internal force vectors is presented and discussed, before outlining the new structure of this numerical procedure. The existing version of the code is hereupon referred to as the *legacy* version.

Legacy version

In the legacy version, the structure of the nonlocal element internal force routine was the following:

1. A loop over all nonlocal elements and Gauss points is performed, where the incremental deformation gradient is determined and applied, to extract the logarithmic strains. The four components of the logarithmic strain tensor are then stored as the first index of a third-order tensor, where the second and third indices are the Gauss point and element identifications, respectively.

2. If an Eulerian averaging strategy is adopted, a new loop over all nonlocal elements is performed, where the coordinates of all Gauss points are re-computed, before updating the value of the nonlocal kernels for each pair of interacting points.

3. Thereafter, the third-order tensor is introduced into the legacy state update procedure for the nonlocal Engelen model, to compute the elastic trial state. This routine includes the following logical steps:

   (a) A loop over all nonlocal integration points is performed to carry out the local state update procedure (which includes the aforementioned trial state, as described in Section 5.3.1). An incremental local damage variable is computed:

   $$\Delta D_i := \frac{\Delta \gamma_i}{\varepsilon_f}, \tag{5.94}$$

   and stored in a second-order tensor, whose indices are the Gauss point and element identifications.

   (b) After performing the local state update, the averaging procedure described in Section 5.3.2 takes place, making use of the second-order tensor to homogenise the incremental local damage:

   $$\Delta \bar{D}_i := \sum_{j=1}^{N_{\text{Gauss}}^{nl}} w_j J_j \beta_{ij} \Delta D_j. \tag{5.95}$$

   Finally, the nonlocal damage variable is computed as

   $$\bar{D}_{n+1,i} := \bar{D}_{n,i} + \Delta \bar{D}_i, \tag{5.96}$$

   and the damaged Kirchhoff stress tensor is obtained.

4. Finally, the element vector of internal forces is updated.

The possibility of adopting an Eulerian averaging strategy imposes some restrictions on the structure of this numerical procedure. On the one hand, it must be preceeded by the determination of the incremental deformation gradient, to allow the update of the Gauss point coordinates. On the other hand, the actual nonlocal averaging operation must take place after the Eulerian update of the nonlocal domain of each point. An additional code block must also be included for the update of the element internal force vectors.

In spite of this, a few suboptimal programming choices were identified in the legacy version of this routine. Firstly, the employment of two global tensors, could pose memory issues for problems with refined meshes. Secondly, it was found that an alternative algorithmic strategy could be employed, to reduce the number of separate code blocks and element loops that made up the legacy procedure.

New version

In the following, a new version of the nonlocal routine for computing the element internal force vectors is proposed:

1. The same loop is performed within the Gauss points of the structure, in order to compute the incremental deformation gradient. Crucially, the final step of this loop, in the new version, is the local state update procedure, which is carried out by resorting to the standard state update routine for the Engelen model, which was already implemented in LINKS.

   (a) However, the structure of the local Engelen state update routine was modified to facilitate its use in the nonlocal case. In essence, logical conditions were introduced to accomodate the use of both local and nonlocal models.

   (b) The same incremental strategy was adopted for the update of the damage variable since it was observed that this benefited the convergence rate.

(c) To facilitate the manipulation of the various damage variables at play, the array of state variables was modified for the Engelen model[1]. In the legacy version, this array was made up of six variables in 2D cases: four logarithmic strains, the accumulated plastic strain and the damage variable. The array of state variables was modified such that, in the new version, it included the four logarithmic strain components, the accumulated plastic strain, and the local and nonlocal damage variables. If the local model is adopted, the seventh component of this array is always null. In the nonlocal case, the sixth component of the array is used to store the increment of local damage, whereas the nonlocal damage variable is stored in the seventh component. This change in the array of state variables required the adjustment of all legacy nonlocal routines.

2. After the first loop, the Eulerian nonlocal update can be performed.

3. Since the local state update was already carried out, the following step is the nonlocal averaging procedure, which makes use of the incremental local damage stored in the array of state variables. This array is a global variable, included in the material module in LINKS, and eliminates the need for the second-order tensor of the legacy code. Moreover, the existing implementation of the nonlocal averaging procedure suffered only minor changes to comply with the new variable structure.

4. Finally, the same legacy code block is used to compute the updated vector of internal forces.

The new version of this numerical procedure offers a few advantages in terms of efficiency and memory requirements. By adopting the array of state variables and making use of an existing state update routine for the local Engelen model, two loops were merged, and the necessity for the legacy global tensors vanished.

5.4.3 Implementation for macro-scale problems

Having discussed the existing code for the nonlocal model of integral type, this section presents the additional changes required for is employment in macro-scale problems.

The code block that reads the input data related to the nonlocal damage model, which was previously limited to micro-scale analyses, was extended for macro-scale cases. This set of input data includes the number of materials modelled with the nonlocal approach, the nonlocal radius, the weighting function and the nonlocal averaging type. Additionally, the initialisation of the nonlocal operator must also be performed before entering the incremental loop. That being said, the code block for the initialisation of the nonlocal operator and other variables related to the nonlocal averaging procedure was introduced in the beginning of the main routine for macro-scale anlaysis.

Furthermore, as mentioned in Section 5.4.2, LINKS contains interface routines, which call adequate functions for computing both the element consistent tangent and element vector of internal forces. Regarding the state update, the existing interface was compatibilised with macro-scale analysis and employes the improved version of the legacy code. However, to include the nonlocal model in the macro-scale code, an interface routine for computing the element stiffness matrix was created, given the relevant differences between the macro- and micro-scale procedures in this regard. Notwithstanding, the strategy employed at the micro-scale to compute the element stiffness matrices and assemble the global stiffness matrix with the nonlocal damage model guided the implementation of the analogous procedures at the macro-scale. That said, in what follows, the implementation tasks related to the assmbly of the global tangent stiffness and also to the computation of the element stiffness matrices are detailed.

[1]The array of state variables is specific to each material model, and is a *global* numerical entity. The legacy version of the nonlocal code was exclusively implemented with the Engelen model, meaning that only the Engelen state variable array was modified. However, in case additional models are compatibilised with the nonlocal model of integral type, their array of state variables should also be adapted.

Element stiffness computation for the nonlocal case

A new routine for the computation of the element stiffness matrices in nonlocal cases was implemented for macro-scale analysis. Recalling Box 5.4, the adoption of a nonlocal damage model leads to element stiffness matrices that include contributions from neighbouring integration points inside the nonlocal domain. With this in mind, the new routine for computing the nonlocal element stiffness contributions yields a third-order tensor, containing the stiffness of element i contributed by each neighbouring element j, which is the third index of the aforementioned tensor. Furthermore, the routine also produces a vector of nonlocal connectivities for element i, which is necessary for the correct assembly of the element contributions into the global tangent stiffness.

That said, the structure of the new routine is the following:

1. After the initialisation and allocation of local variables, the incremental deformation gradient is computed, as well as its determinant and the product between the weight and determinant of the Jacobian matrix, for all integration points of the structure. To store the incremental deformation gradient, a fourth-order tensor is allocated, which essentially maps the 3×3 second-order tensor for each integration point of each element of the structure. To store the other two quantities, which are scalars, second-order tensors are allocated.

2. A loop over the Gauss points of the structure is performed to initialise relevant variables for each Gauss point, i, such as the Kirchhoff stress tensor and the number of integration points, j, inside the nonlocal domain of Gauss point i.

   (a) Thereafter, a new loop over the integration points, j related to Gauss point i is carried out. In this loop, the existing function for computing the nonlocal consistent tangent modulus is called for each pair of Gauss points, i and j.

      i. The tangent modulus is computed according to Equation (5.89), starting with the estimation of the elastoplastic tangent modulus, for the pair of integration points. To this end, it should be mentioned that some relevant variables, such as the undamaged Kirchhoff stress tensor, must be recovered for both Gauss points.

      ii. Thereafter, the tangent component associated with the nonlocal damage model, $\bar{\mathbf{D}}^{*}_{n+1,ij}$, is computed, i.e.

$$\bar{\mathbf{D}}^{*}_{n+1,ij} = \frac{w_j J_j \beta_{ij} 2G}{\varepsilon_f (3G+H)} \sqrt{\frac{3}{2}} \boldsymbol{\tau}_{n+1,i} \otimes \bar{\boldsymbol{N}}_{n+1,j}. \tag{5.97}$$

      iii. The final constitent tangent is obtained by subtracting the nonlocal component:

$$\mathbf{D}^{*}_{n+1,ij} = \left(1 - \bar{D}_{n+1,i}\right) \mathbf{D}^{\mathrm{ep}}_{n+1,ij} - \bar{\mathbf{D}}^{*}_{n+1,ij}. \tag{5.98}$$

3. After the consistent tangent modulus is obtained, the following code block concerns the computation of the spatial tangent modulus for each pair of Gauss points. In this case, a logical condition is in place to distinguish cases in which the i and j integration points are the same - the stiffness contribution of the Gauss point itself.

4. Finally, having computed the spatial tangent modulus, the tangent stiffness matrix is computed and stored in the first two indices of the aforementioned third-order tensor, while the third index stores the identification number of integration point j, while also saving the respective nonlocal connectivities.

Global tangent stiffness subroutines

Within the larger solution scheme for macro-scale problems, presented in Section 5.4.1, the computation of each elementary stiffness matrix and its assembly in the global stifness matrix are done in

a single loop over the elements of the structure. After the conclusion of this loop, the global system of equilibrium equations is solved.

That being said, in the beginning of the aforementioned element loop for the computation of the stiffness matrix, a logical condition was introduced to differentiate this procedure for nonlocal problems. That being the case, the loop over the elements, in the nonlocal case, is structured as follows:

1. At the beginning of the nonlocal element loop, another logical condition to separates the procedures for elements with local and nonlocal models. For elements with local models, the standard LINKS procedure for macro-scale problems is employed.

2. For elements with nonlocal models, since the element stiffness matrix includes the contributions from the elements inside the nonlocal circumference, a third-order tensor is allocated to store the stiffness contributions from each of these neighbouring elements. The first and second dimensions of this tensor are the number of elementary degrees of freedom, while the third dimension is the number of elements contained in the nonlocal circumference of the element in question. Finally, a vector, whose size is the number of elements contained in the nonlocal domain, must also be allocated, to store the nonlocal connectivities.

3. The computation of this third-order tensor is done as previously described, in the new routine for estimating the nonlocal element stifness.

4. Having computed this tensor, the final step in the element loop is to assemble each contribution in the global stiffness matrix. To do this, a loop over the elements contained in the vector of nonlocal connectivities is carried out, to assemble the contribution associated to each of these elements, using the standard LINKS routine for macro-scale global stiffness assembly, which suffered minor changes to comply with the nonlocal case.

5. After the loop over the neighbouring elements is concluded, third-order tensor and the connectivities vector are deallocated.

Finally, it should be remarked that LINKS uses a Coordinate List (COO) format to store the non-zero components of the global stiffness matrix, given the fact that it is generally sparse. That being the case, a scalar parameter, M, is used to define the maximum number of non-zero elements of the stiffness matrix. Given that nonlocal interactions result in increased contributions stiffness contributions from neighbouring elements, this scalar parameter has to be adapted for nonlocal problems, using a logical condition. That said, for macro-scale problems including nonlocal material models, the following formula was employed:

$$M = N_{\text{elem}} \times N_{\text{dof}} \times N_{\text{dof}} \times N_{\text{max}}^{nl} + N_{\text{sym}}, \tag{5.99}$$

where N_{elem} is the number of elements, N_{dof} is the number of element degrees of fredoom, N_{max}^{nl} is the maximum number of integration points contained in a single nonlocal domain, and N_{sym} is the number of equations in the global system, added here in the case symmetrisation is enabled.

5.5 Numerical Examples

In this section, some numerical examples are presented, to validate the implementation of the nonlocal damage model. Firstly, given that the model was already implemented at the micro-scale, some preliminary tests were performed with benchmark micro-mechanical examples to ensure that the new strategy for the state update and nonlocal averaging procedures, presented in Section 5.4.2, is valid. The results obtained for these micro-mechanical cases are presented in Section 5.5.1. Thereafter, single-element tests were performed at the macro-scale. Since the new ver-

sion of the state update procedure had already been assessed, the focus of these tests was to evaluate the rate of convergence of the Newton-Raphson method. This was done to evaluate the validity of the global tangent stiffness computation routines, and the results are discussed in Section 5.5.2.

Thereafter, two realistic setups were introduced to assess the elimination of pathological mesh dependency with nonlocal damage model of integral type. The first one is the simulation of a compact shear specimen is discussed in Section 5.5.3. The final example is the simulation of a notched specimen under a tensile load and is presented in Section 5.5.4.

5.5.1 Preliminary micro-scale tests

Micro-scale benchmark examples were used for the validation of the new state update procedure, given that this allowed a direct comparison with the legacy version of the code. These examples involved the simulation of a heterogeneous RVE, using different micro-mechanical boundary conditions (recall Section 3.3.3), under the following prescribed global deformation gradient:

$$\boldsymbol{F} = \begin{bmatrix} 1.000 & 0.002 \\ 0.002 & 1.000 \end{bmatrix}. \tag{5.100}$$

Figure 5.2 depicts the structure of the square RVE, of 40×40 mm, which is composed of a matrix, fibres and voids. The volume fraction of inclusions is 40%, with 8 circular voids and 15 circular fibres, both with a diameter of 6 mm. The fibres were modelled as isotropic elastic materials, with a Young's modulus of 74 GPa and a Poisson's ratio of 0.2. Moreover, the Engelen model was used with the nonlocal approach to define the material behaviour of the matrix, with a Young's modulus of 30 GPa, a Poisson's ratio of 0.3. A linear hardening curve was defined by with points of accumulated plastic strain and the von mises equivalent stress:

$$\bar{\varepsilon}^p = 0 \quad \text{when} \quad \sigma^{\text{eq}} = 93\,\text{MPa}, \tag{5.101}$$

$$\bar{\varepsilon}^p = 1 \quad \text{when} \quad \sigma^{\text{eq}} = 193\,\text{MPa}. \tag{5.102}$$

A critical accumulated plastic strain of 0.8 was adopted. A nonlocal radius of 1/40th of the RVE length was selected. Finally, the RVE was discretized in 2377 8-noded quadrilateral elements with reduced integration and 7498 nodes.

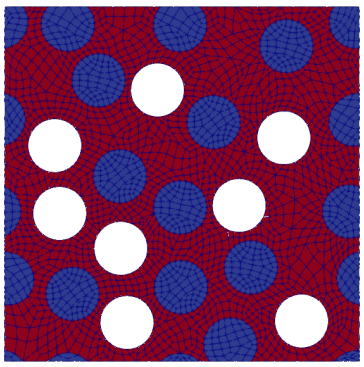

Figure 5.2: Representative volume element utilised in the micro-scale tests. The matrix is rendered in red, while the fibres are rendered in blue.

The RVE was simulated with the new and the legacy version of the code, for the following micro-mechanical boundary conditions: the linear boundary condition, the periodic boundary condition and the uniform traction boundary condition. Figure 5.3 depicts the nonlocal damage distributions obtained for these cases, for each version of the code. From the observation of these results,

it can be inferred that the new implementation yielded valid results. Additionally, identical rates of convergence for the Newton-Raphson method were found. Furthermore, Figure 5.4 depicts the computational times recorded for each boundary condition and the two versions of the code. The changes in the numerical state update procedures resulted in a slight reduction of the overall computational cost of the nonlocal model. However, considering that a relatively low nonlocal radius was adopted, this improvement is likely associated with significant time savings for larger values of this parameter.

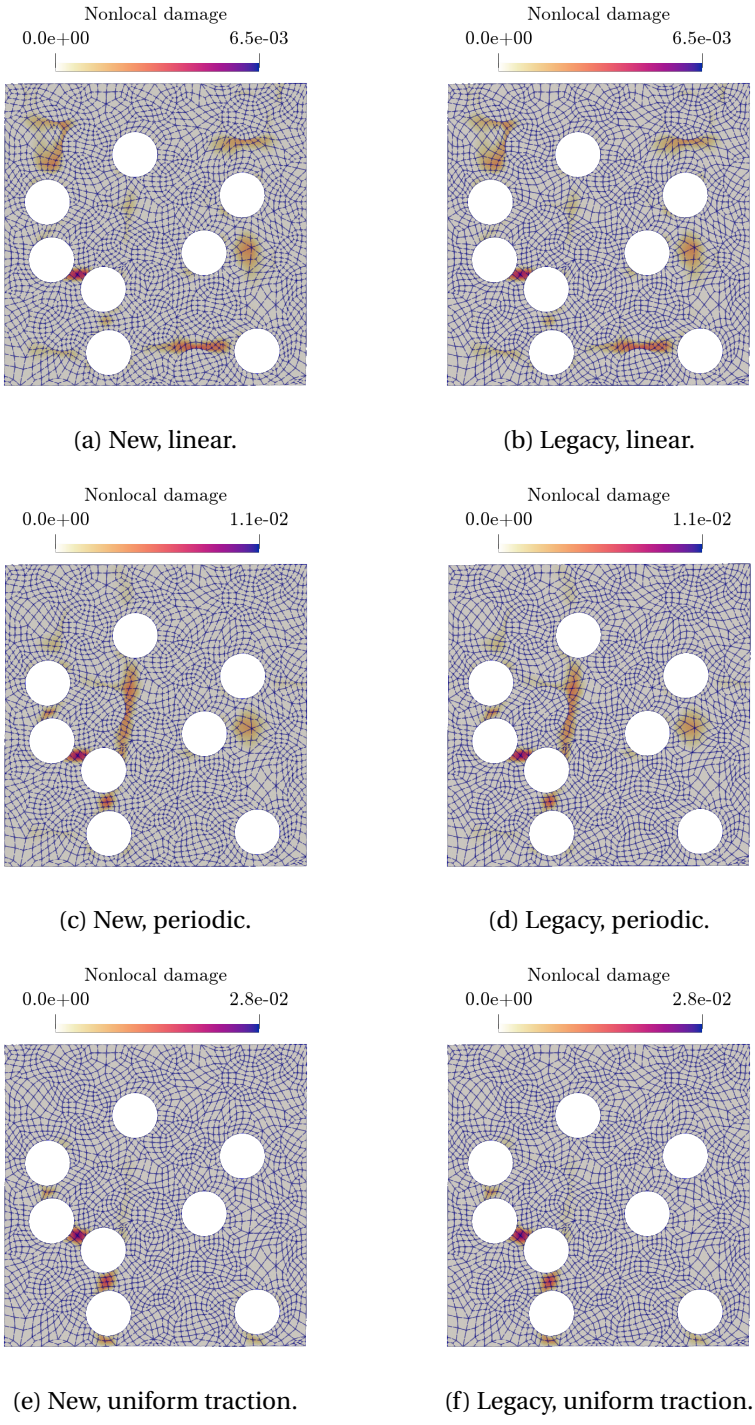

(a) New, linear.

(b) Legacy, linear.

(c) New, periodic.

(d) Legacy, periodic.

(e) New, uniform traction.

(f) Legacy, uniform traction.

Figure 5.3: Distribution of nonlocal damage (plotted in the deformed configurations) obtained with the new and legacy versions of LINKS, for each boundary condition.

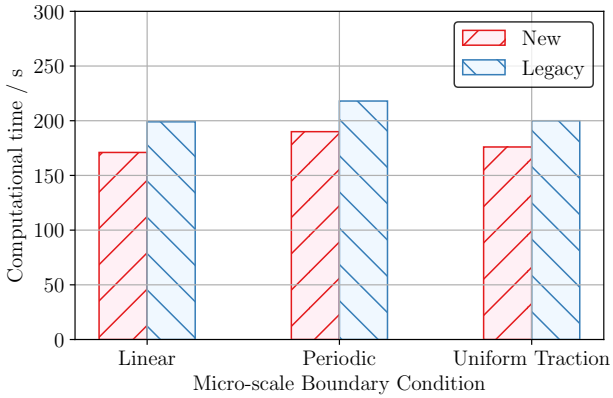

Figure 5.4: Computational times recorded for the micro-scale example, with the three boundary conditions and each version of the nonlocal code.

5.5.2 Single-element tests

Having observed that the new state update procedure yields valid results for the micro-scale examples, the first set of macro-scale tests concerned the simulation of a 1×1 mm^2 square, modelled with a single finite element, under tension. The boundary conditions applied to the single element are illustrated in Figure 5.5. Furthermore, two element types were used in this section: a 4-noded quadrilateral element with reduced integration (1 Gauss point) and a 4-noded quadrilateral element with complete integration (4 Gauss points). In the first case, nonlocal averaging does not take place, due to the presence of a single integration point. That being said, these tests were performed with both the local and nonlocal damage models for the sake of comparison. Finally, the material properties used for the matrix in Section 5.5.1 were assigned to the single element and are recapped in Table 5.1.

Figure 5.6 presents the effective Cauchy stress and damage evolutions obtained for the reduced integration single element, with the local and nonlocal approaches. As can be seen, the results obtained for these two cases overlap, as was expected, given the absence of nonlocal averaging. Figure 5.7 illustrates the evolution of the same quantitites, for the single element with complete integration. In this case, the presence of nonlocal averaging meant that the local and nonlocal responses no longer overlap. With the local model, a greater value of damage was found, thereby resulting in a greater degree of softening, in comparison to the nonlocal cases.

Additionally, it was seen that different values of the nonlocal radius led to different results. This is due to the fact that, in this case, adopting a nonlocal radius of 0.7 mm results in the inclusion of only three integration points in each nonlocal circumference. On the contrary, a nonlocal radius of 1.0 mm results in four nonlocal circumferences which include the four Gauss points. Through the observation of Figure 5.7, it can be inferred that an increase in the number of Gauss points included in the nonlocal domain yields a stiffer material response. That being the case, a greater degree of softening was observed for the lower value of the nonlocal radius. In spite of this, in terms of softening and damage, the local case clearly stands out from its nonlocal counterparts.

Table 5.1: Material properties adopted for the single-element tests. Legend: E denotes the Young's modulus; ν denotes the Poisson coefficient; ε_f denotes the critical accumulated plastic strain; $\sigma_{y,0}$ denotes the initial yield stress; $\sigma_{y,1}$ denotes the yield stress at $\bar{\varepsilon}^p = 1$.

E / GPa	ν / -	ε_f / -	$\sigma_{y,0}$ / MPa	$\sigma_{y,1}$ / MPa
30	0.30	0.80	93	193

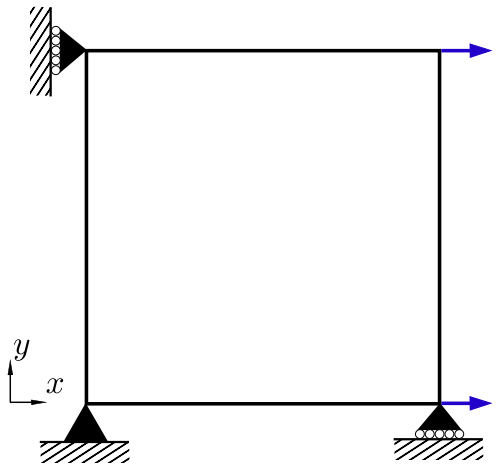

Figure 5.5: Schematic representation of the boundary conditions applied to the single element under tension. Horizontal displacements of 20% of the element's length were prescribed.

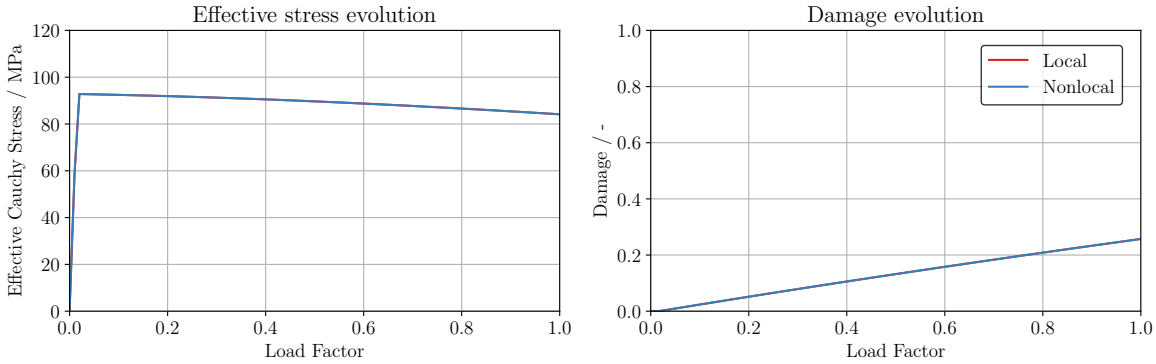

Figure 5.6: Effective Cauchy stress (left) and damage (right) evolutions found with the reduced integration single element, with the local and nonlocal damage models.

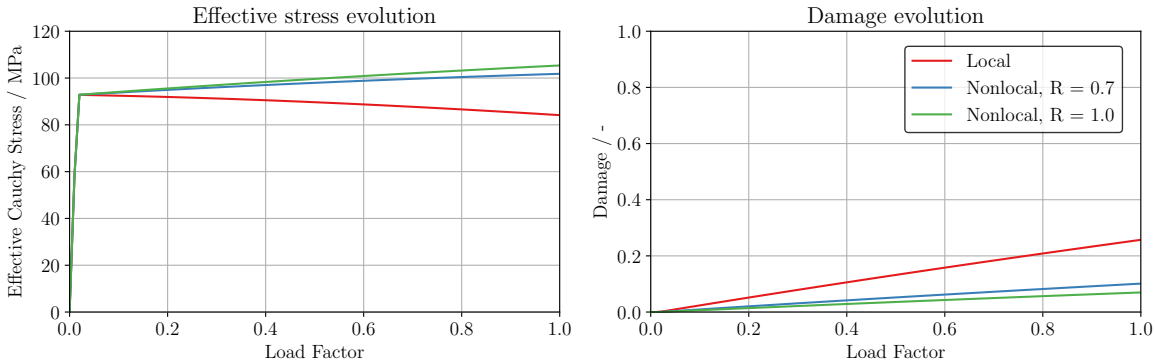

Figure 5.7: Effective Cauchy stress (left) and damage (right) evolutions found with the complete integration single element, with the local damage model and the nonlocal damage model with two different values of the nonlocal radius.

Adding to this, the convergence behaviour of the Newton-Raphson method, observed for the complete integration cases, is depicted in Figure 5.8, for different load increments. The results observed for the nonlocal cases, generally matching the rates of convergence of their local counterpart, indicate that the implementation of the nonlocal model of integral type is coherent. As can be seen, a quadratic rate of convergence of the Newton-Raphson method was obtained.

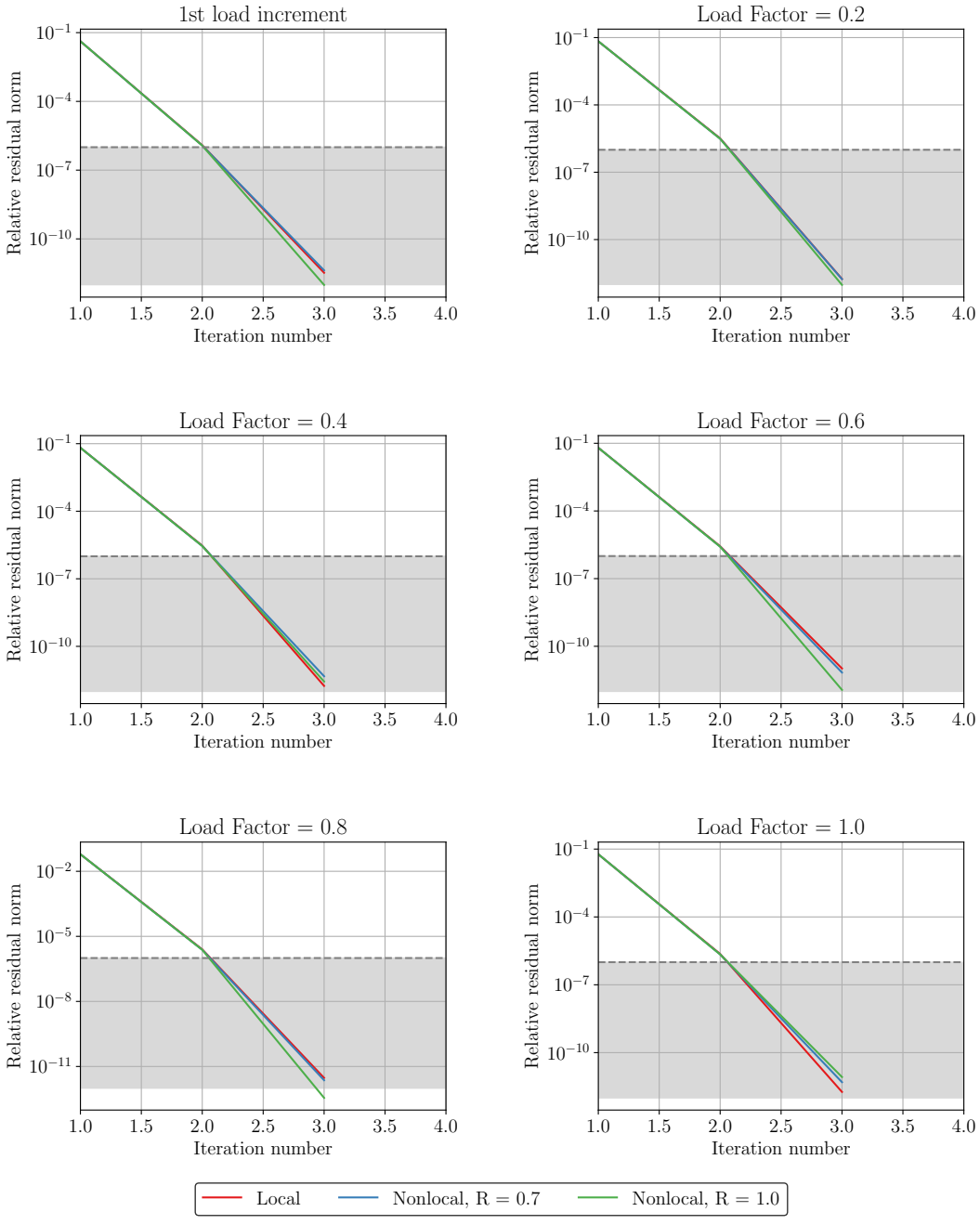

Figure 5.8: Evolution of the norm of the relative residual obtained with the Newton-Raphson method at different load increments, for the single-element setup and the local and nonlocal cases. Relative norms shown in %.

5.5.3 Compact shear specimen

In this section, the simulation of a compact shear specimen, with local and nonlocal damage models, is analysed. The boundary conditions applied to the specimen are depicted in Figure 5.9, where a 1 mm horizontal displacement was prescribed on its upper half.

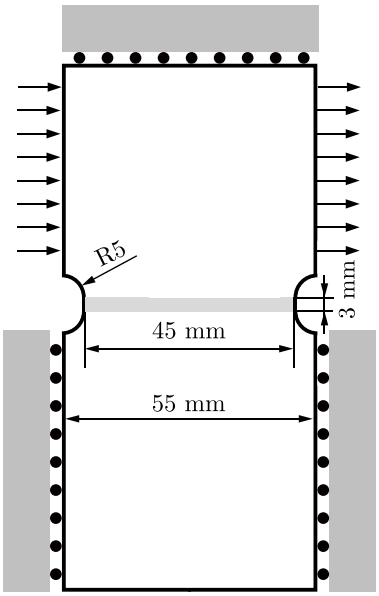

Figure 5.9: Schematic representation of the boundary conditions applied to the compact shear specimen, based on the experimental test piece of Perdahcioglu et al. (2008).

The same material properties from Table 5.1 were adopted. The finite element meshes employed in this case are shown in Figure 5.10. The output from a specific integration point was requested to evaluate the evolution of the damage variable locally. In this case, one of the elements on the deformation band of the specimen was selected (see Figure 5.10).

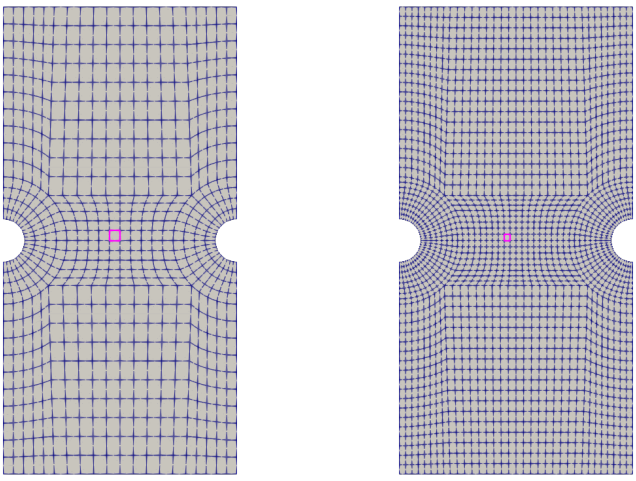

(a) Coarse mesh. (b) Fine mesh.

Figure 5.10: Finite element meshes used to discretize the shear specimen. The elements for which the Gauss point output was requested are highlighted. Coarse mesh: 660 QUAD8 elements, 2117 nodes. Fine mesh: 2024 QUAD8 elements, 6309 nodes.

Figure 5.11 depicts the reaction forces obtained with the local and nonlocal approaches for this example and both meshes. Given the dimensions of the test piece, the value of the nonlocal radius was 10 mm. The use of different finite element meshes resulted in considerably different mechanical responses in the local case, whose response, showcasing a considerable degree of softening, was seen to be mesh-dependent. For the nonlocal model, the reaction force curves obtained for each mesh overlap, and no significant softening is observed, meaning that the mesh dependence pathology has been overcome by the implementation presented in this work.

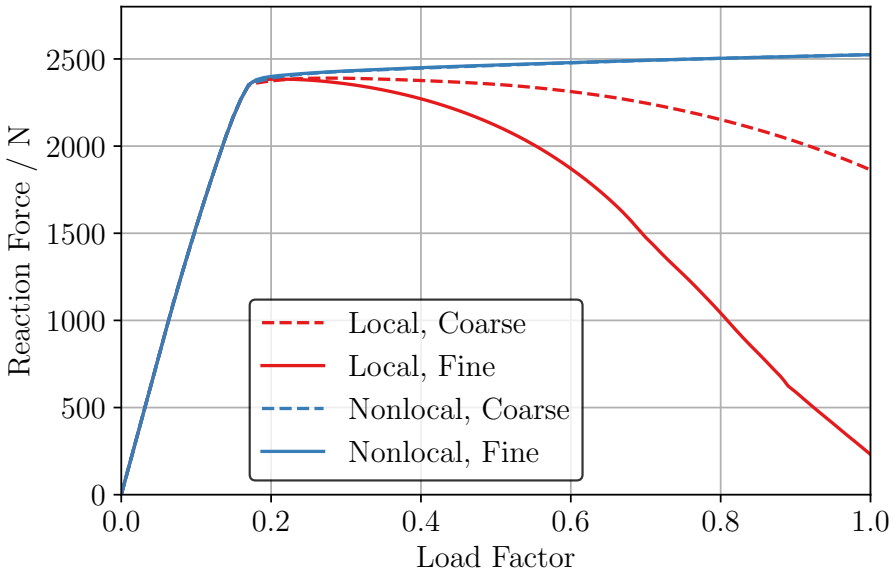

Figure 5.11: Evolution of the horizontal reaction force for the local and nonlocal damage models, for both finite element meshes. Results for a nonlocal radius of 10 mm.

The damage at the requested Gauss point is illustrated in Figure 5.12, and was relatively low for both local and nonlocal approaches. In the case of the nonlocal approach, the damage grew steadily in a quasi-linear manner after initiation occurred. In the local case, however, the value of the local damage variable stabilised at a certain value of displacement, which differed for the two meshes. To better visualise the onset and propagation of damage, the distributions found with the local and nonlocal cases are shown in Figure 5.13. In the local case, the onset of damage was highly localised along the middle axis of the deformation band. This, in turn, led to a noticeable degree of element distortion, which, after a given load increment, became so significant that the lower half of the specimen could not offer much resistance to the displacement of its upper counterpart, whose motion was almost rigid. Nevertheless, the onset of damage and element distortion was highly localised in the element layer below the middle axis. That being the case, since the output was requested from an element above the axis, the appearance of the plateau seen in Figure 5.12 represents the initiation of the rigid displacement of the upper half of the specimen. Furthermore, the occurrence of damage localisation is even more present in the case of the finer mesh, further highlighting the mesh dependency of the local damage model. In the nonlocal case, these phenomena were not observed, as the entire deformation band became damaged in an almost homogeneous fashion, avoiding spurious damage localisation. Moreover, the nonlocal damage distributions found for both meshes were identical. Finally, Figure 5.14 depicts the effective stress distributions obtained with the local and nonlocal models, for a Load Factor of 0.8. For this load increment, the fine mesh specimen, in the local case, is practically unloaded, showcasing the effect of the different degrees of damage localisation on the mechanical response of the material.

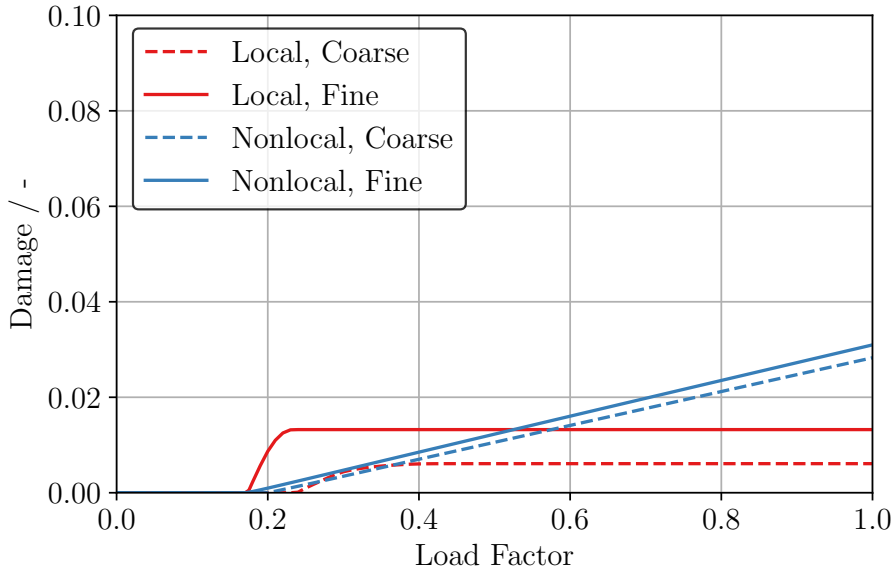

Figure 5.12: Damage variable evolution for the local and nonlocal damage models, retrieved from a point in the deformation band for both finite element meshes. Results for a nonlocal radius of 10 mm.

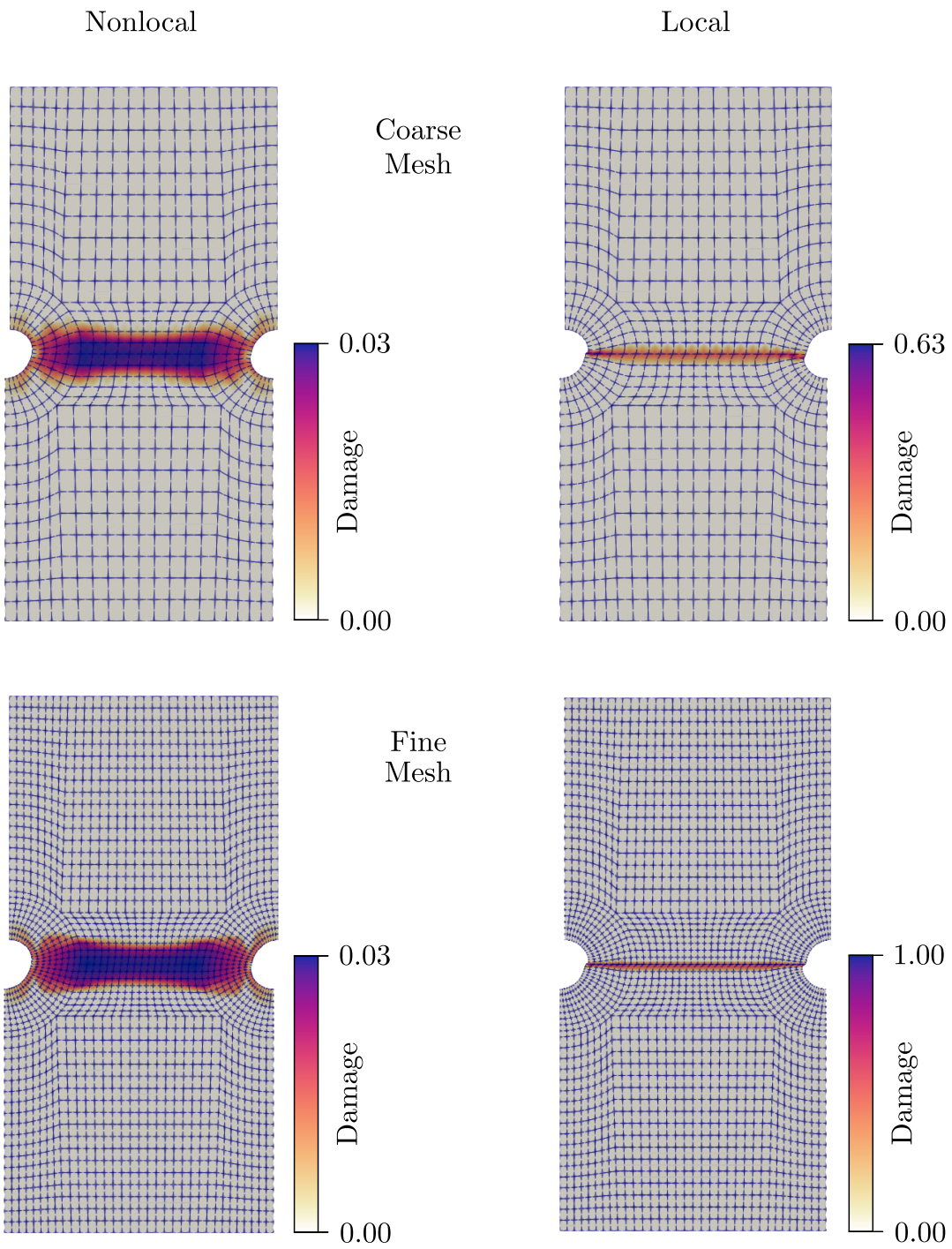

Figure 5.13: Local and nonlocal damage distributions at failure (plotted in the deformed configurations) for the two finite element meshes. Nonlocal results obtained with a radius of 10 mm. Colour indicates the damage model, linestyle indicates the mesh.

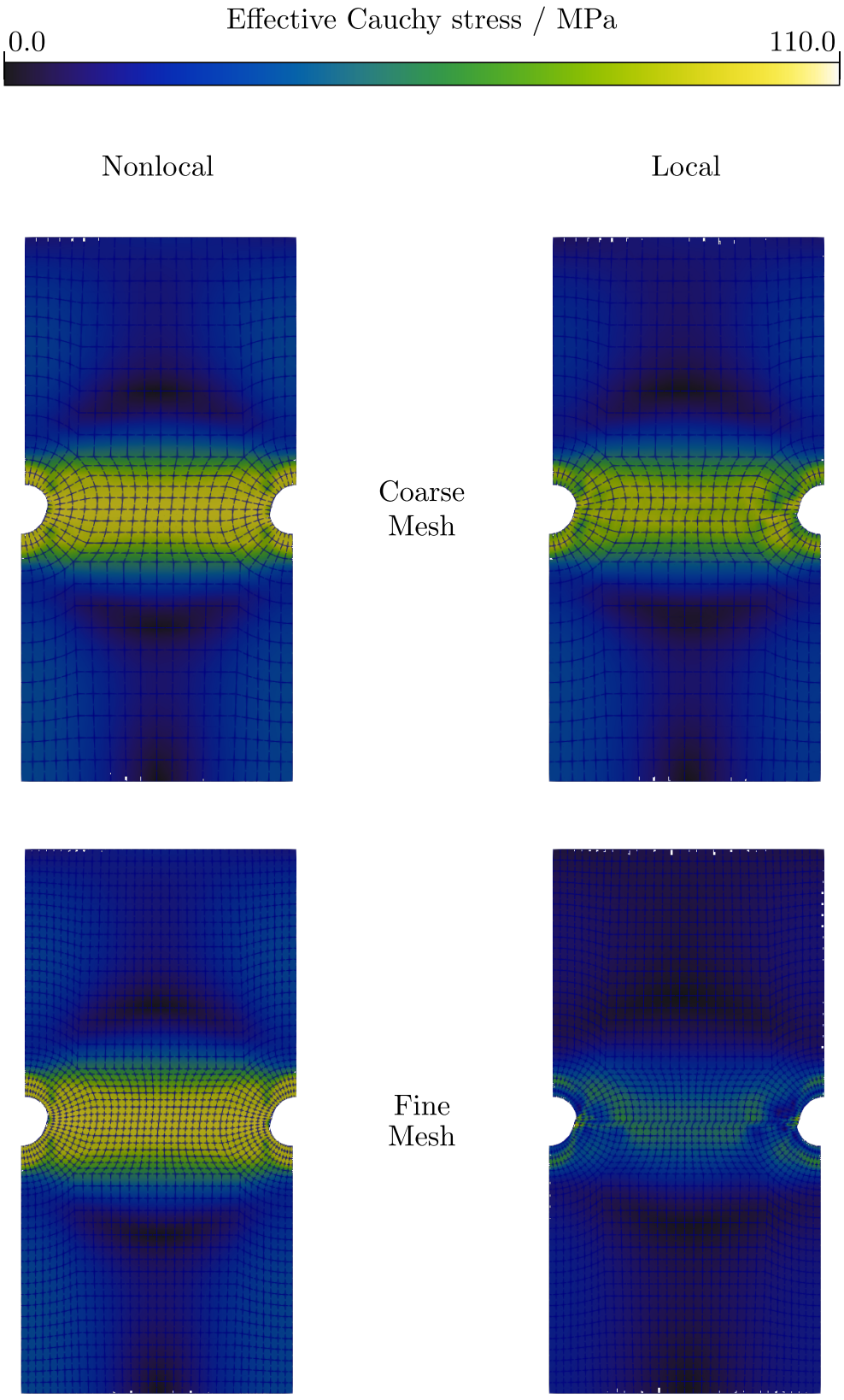

Figure 5.14: Effective Cauchy stress distributions (plotted in the deformed configurations) found with the local and nonlocal approaches, for Load Factor = 0.8. Nonlocal results obtained with a radius of 10 mm. Colour indicates the damage model, linestyle indicates the mesh.

To assess the impact of the nonlocal radius on the mechanical response of the specimen, the simulations of the two meshes were repeated for a nonlocal radius of 2.5, 5 and 7.5 mm. The reaction force curves found with the different nonlocal radii are shown in Figure 5.15. Increasing the value of the nonlocal radius is seen to lead to a convergence of the reactions, while also slightly reducing the presence of softening. Adding to this, Figure 5.16 illustrates the evolution of nonlocal damage observed in each case. For greater values of the nonlocal radius, the damage at the integration point in question decreases, since a greater degree of nonlocal averaging is present. The deviation between the damage values found for each mesh is also reduced by adopting larger values of the nonlocal regularisation parameter. Figure 5.17 depicts the global nonlocal damage distributions found for these additional values of the nonlocal radius, demonstrating the redistribution of damage over a larger region of the specimen for greater values of this parameter.

Another relevant aspect of adopting a nonlocal damage model of integral type, with different values of the nonlocal length parameter, is its impact on the computational cost of simulations. The computational times measured for the different simulations of the compact shear specimen are shown in Figure 5.18. Two distinct factors were associated to relevant increases in the computational time: the selection of the fine shear specimen mesh, and the adoption of a nonlocal damage model. This second factor, for all values of the nonlocal radius, and for the fine mesh in particular, is associated to a computational cost increase of two orders of magnitude. The introduction of the nonlocal averaging loops in the algorithmic solution procedure can, thus, be associated to a significant increase in the computational cost. In addition, the loss of stiffness matrix sparsity due to the presence of nonlocal interactions is also a relevant numerical aspect affecting the computing time. Moreover, in this case, the value of the nonlocal radius did not lead to significant distinctions in the computational cost. This is likely due to the limited range of values in consideration, relative to the dimensions of the specimen. The higher computing time, for both meshes, was found for the lower value of the nonlocal radius, 2.5 mm, albeit the differences were not significant. This observation was relatively unexpected, given that increase the nonlocal radius should lead to greater nonlocal loops for all integration points of the specimen, and larger numbers of non-zero elements of the stiffness matrix. This was seen to be related to the convergence behaviour of the Newton-Raphson method, which was different for different values of the nonlocal radius.

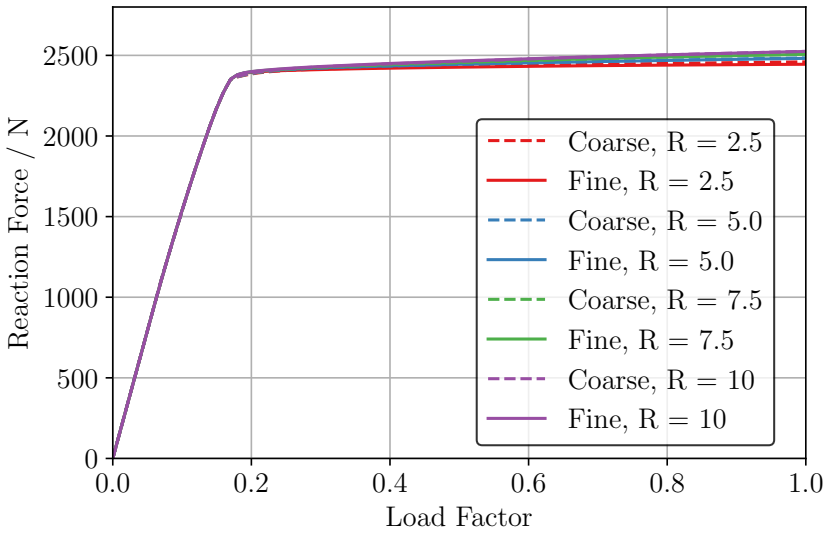

Figure 5.15: Evolution of the horizontal reaction force for nonlocal damage model, for both finite element meshes and several values of the nonlocal radius. Colour indicates the nonlocal radius, linestyle indicates the mesh.

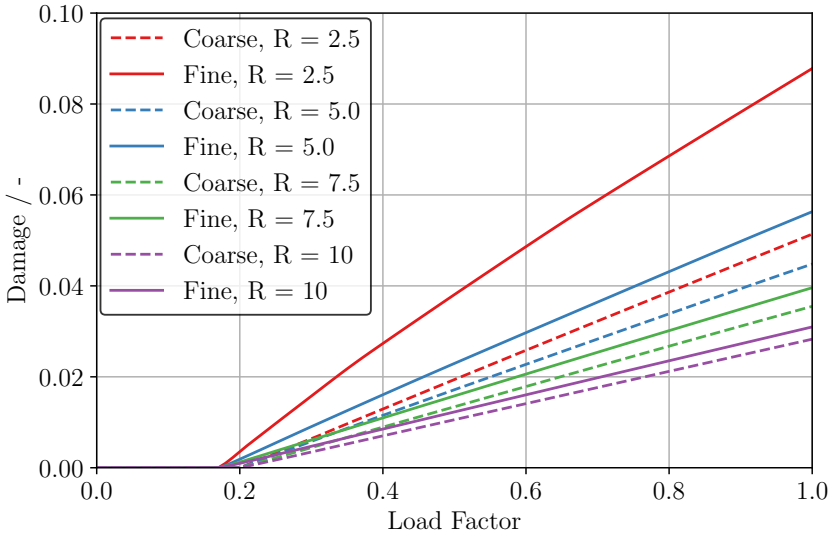

Figure 5.16: Nonlocal damage evolution, retrieved from a point in the deformation band for both finite element meshes and several values of the nonlocal radius. Colour indicates the nonlocal radius, linestyle indicates the mesh.

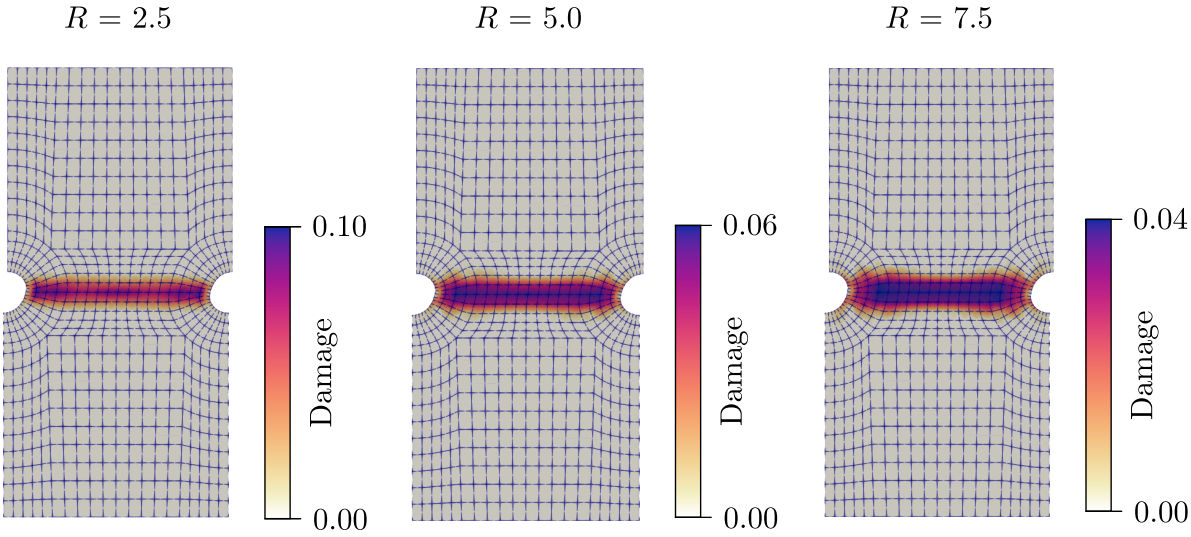

Figure 5.17: Nonlocal damage distributions (plotted in the deformed configuration) for the three additional values of the nonlocal radius. Results obtained with the coarse mesh, values of the nonlocal radius shown in mm.

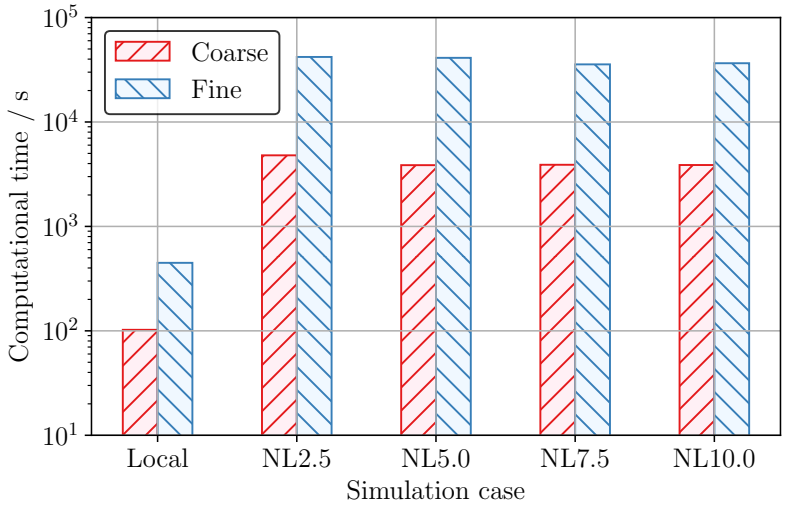

Figure 5.18: Computational time associated with each simulation of the tensile specimen, for both meshes. Legend: NL - Nonlocal; 2.5, 5.0, 7.5 and 10.0 - nonlocal radius / mm.

The convergence of the Newton-Raphson method for the coarse mesh cases is depicted in Figure 5.19, through the evolution of the norms of the relative residuals, at different load increments. Quadratic rates of convergence were observed for both local and nonlocal models, at every load increment. Nevertheless, a few observations can be drawn from the convergence analysis. Firstly, with the exclusion of the first and last load increments included in Figure 5.19, the local model required more equilibrium iterations to find an admissible solution to the numerical problem. This may be related to the ill-posedness of the initial boundary value problem, which leads to excessive localisation and, in this case, element distortion.

Furthermore, for the nonlocal model, the convergence of the Newton-Raphson method presents slight variations according to the value of the nonlocal radius. In the case of the coarse mesh, shown in Figure 5.18, the computational cost of the simulations was similar for all nonlocal radius values, although larger nonlocal domains were expected to yield computing time increases. In Figure 5.19, the lower values of the nonlocal radius, particularly 2.5 mm, are associated with slightly lower convergence rates.

That being said, for this particular problem, there seem to be two opposing factors, which greatly influence the cost of the nonlocal simulations: the size of the averaging domain and the convergence of the nonlinear algorithm. Both of these factors are linked to the value of the nonlocal intrinsic length. On the one hand, it is clear that a greater value of the nonlocal radius increases the computational cost of each equilibrium iteration. On the other hand, the use of lower values of the nonlocal radius yielded a slight reduction in the convergence rate of the Newton-Raphson method. This can imply that, for such values of the nonlocal radius, this geometry, finite element meshes, and material properties, pathological mesh dependency has not been effectively eliminated. It could also be linked with the occurrence of element distortion or other instability problems, which can lead to lower convergence rates. However, several factors could be related to this observation, and it is not clear wether this can be generalised for other geometries and loading scenarios.

As the final ingredient for the discussion of these results, the structure of the global stiffness matrices obtained for the local and nonlocal cases tested with the coarse mesh are depicted in Figure 5.20. It can be seen that greater values of the nonlocal radius lead to a significant increase in the number of non-zero elements of the global stiffness matrix, whose sparsity is reduced. This effect is one of the main drawbacks of nonlocal models of integral type, since most finite element programs are designed around the manipulation of sparse matrices, for efficiency, which is no longer the case

here. Furthermore, it can be seen that the global stiffness matrix obtained for a nonlocal radius of 2.5 mm is relatively similar to that of the local approach, which couled be another indication that, for the coarse mesh of the specimen, this value of the nonlocal intrinsic length is insufficient.

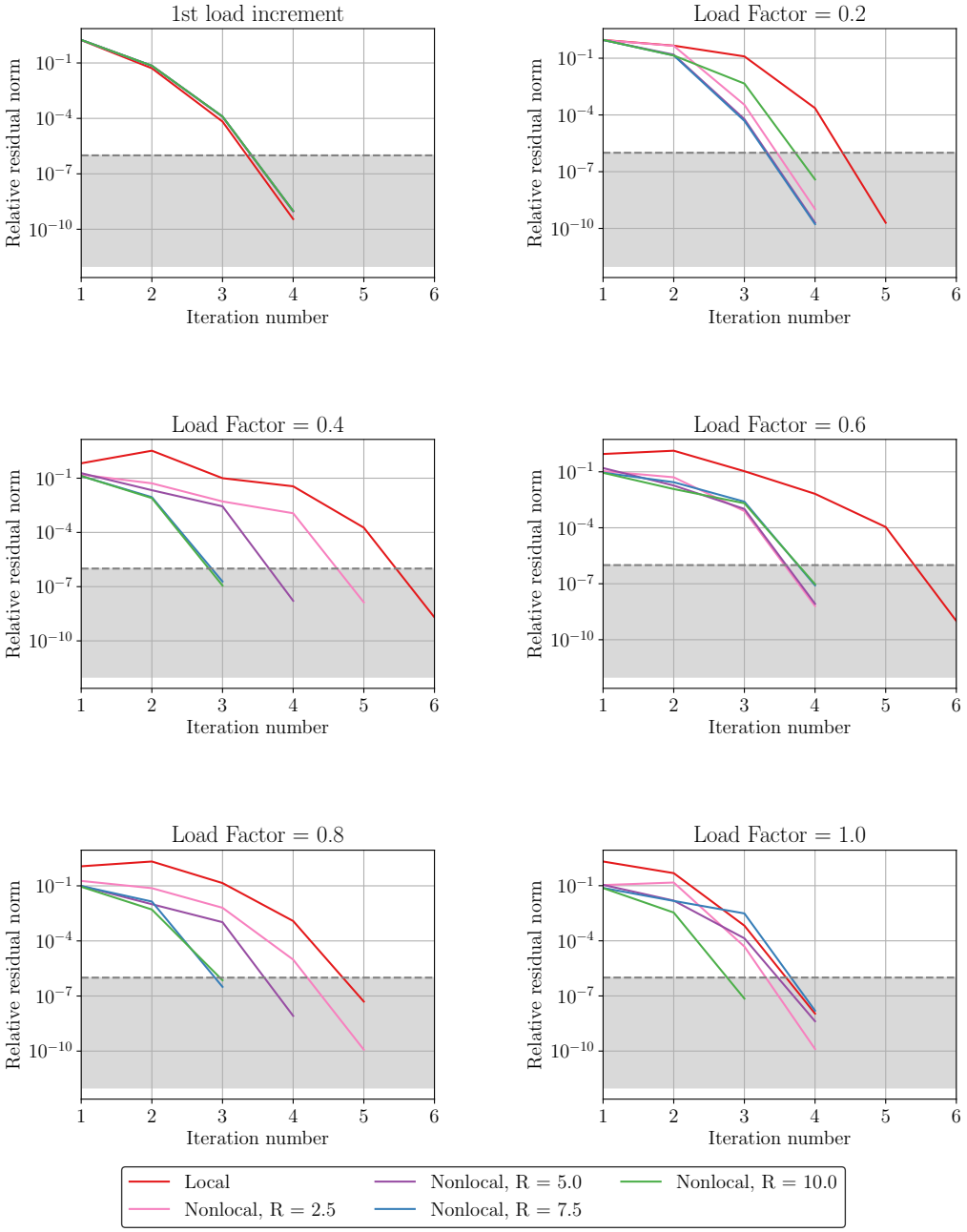

Figure 5.19: Evolution of the norm of the relative residual throughout the Newton-Raphson procedure for the shear specimen simulations with the coarse mesh, at different load increments. In this case, the prescribed displacement was divided in 100 proportional increments.

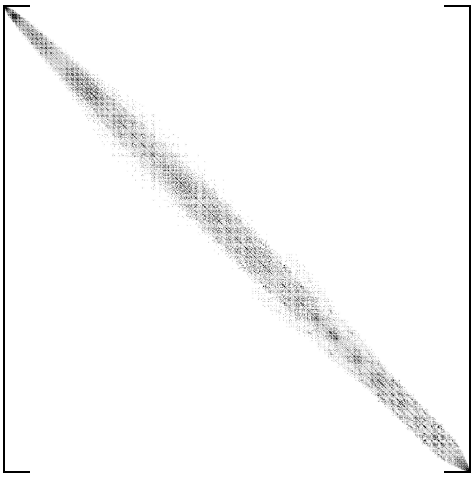

(a) Local.

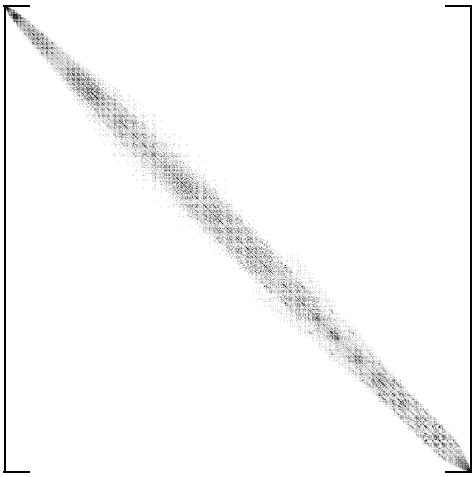

(b) Nonlocal, R = 2.5.

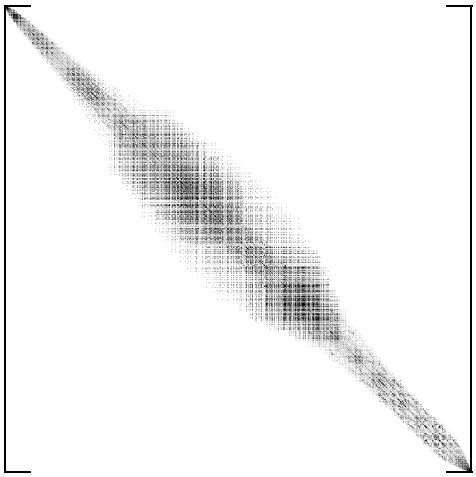

(c) Nonlocal, R = 5.0.

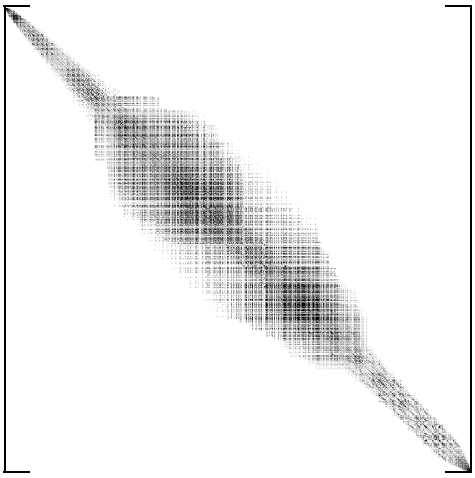

(d) Nonlocal, R = 7.5

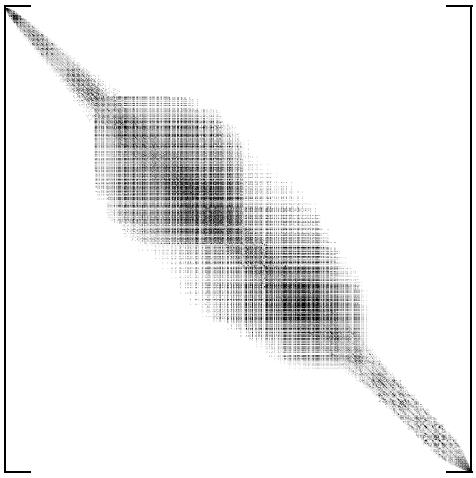

(e) Nonlocal, R = 10.0

Figure 5.20: Representation of the non-zero components of the global stiffness matrix, for the shear specimen and the coarse mesh. Values of the nonlocal radius presented in mm

5.5.4 Notched tensile specimen

Having discussed the simulation of the compact shear specimen with local and nonlocal damage models in Section 5.5.3, a new realistic macro-scale specimen is introduced in the present section. In this case, a notched tensile test piece was employed, to complement the analysis of the shear specimen. The test piece geometry and the corresponding boundary conditions are depicted in Figure 5.21, where a vertical displacement of 0.5 mm was applied. To study the impact of the spatial discretisation on the mechanical responses obtained with the local and nonlocal approaches, three finite element meshes, which are shown in Figure 5.22, were devised. Furthermore, to perform a local comparison of the damage obtained in the notch of the specimen, the output of stresses, strains and state variables was also requested at one of the integration points of the element on the lower tip of the notch, for all meshes (see Figure 5.22). Finally, Table 5.2 presents a new set of material properties adopted for this specimen.

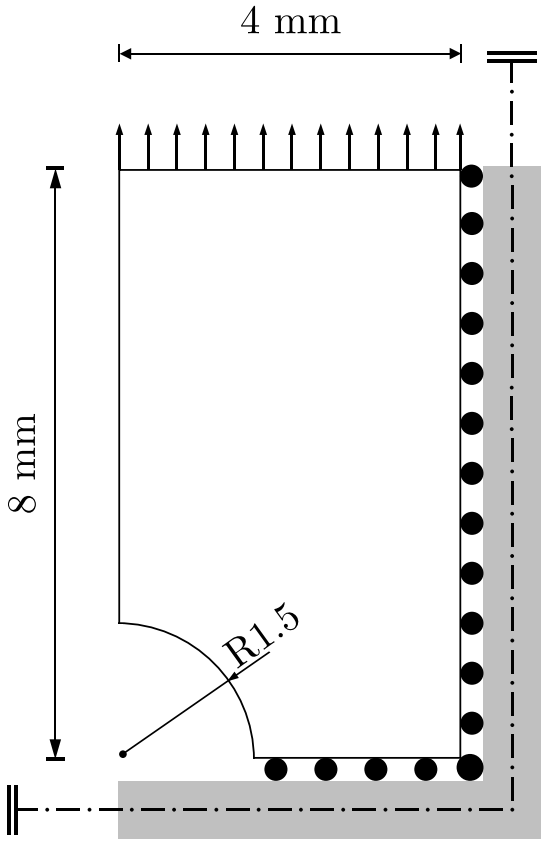

Figure 5.21: Schematic representation of the boundary conditions applied to the tensile specimen.

Table 5.2: Material properties adopted for the notched tensile specimen. Legend: E denotes the Young's modulus; ν denotes the Poisson coefficient; ε_f denotes the critical accumulated plastic strain; $\sigma_{y,0}$ denotes the initial yield stress; $\sigma_{y,1}$ denotes the yield stress at $\bar{\varepsilon}^p = 1$.

E / GPa	ν / -	ε_f / -	$\sigma_{y,0}$ / MPa	$\sigma_{y,1}$ / MPa
210	0.30	2.00	243	250

Figure 5.23 depicts the evolution of the vertical reaction force obtained for the local and nonlocal models and the three meshes. Given the general dimensions of the notched specimen, an initial nonlocal radius of 0.4 mm was assigned. The introduction of nonlocal averaging was seen to re-

duce the observed level of mesh dependency, even though three very distinct spatial discretisations of the specimen were considered. Figure 5.24 shows the damage variable evolution found for the same cases, where the impact of adopting a nonlocal model in the elimination of spurious damage localisation is clearly apparent. This is further illustrated in Figure 5.25, where similar damage distributions were found for the three meshes by adopting a nonolocal model. In contrast, the damage localisation bands obtained with the local model are visibly dependent on the mesh size.

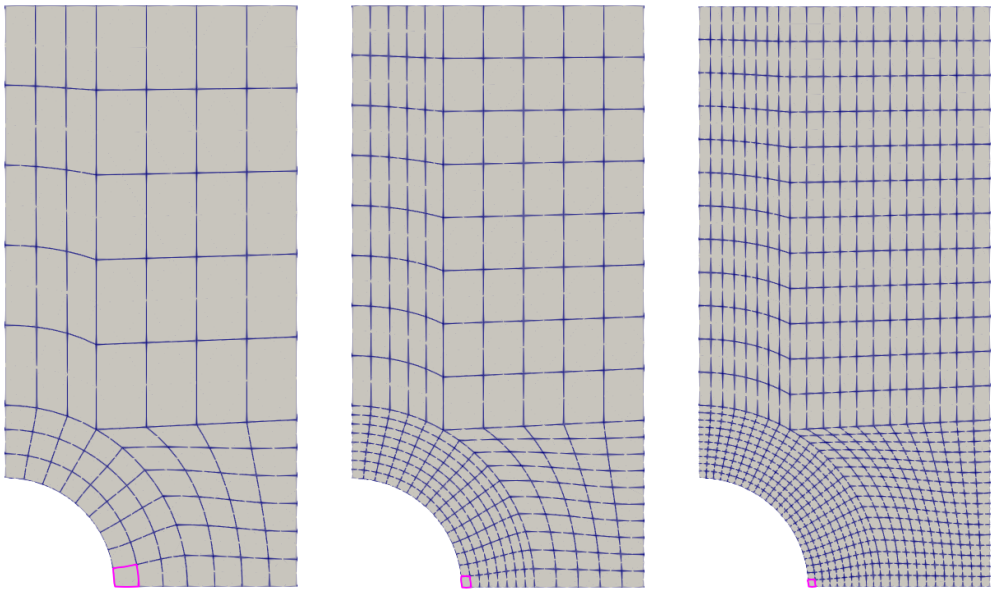

(a) Coarse mesh. (b) Medium mesh. (c) Fine mesh.

Figure 5.22: Three finite element meshes used for the tensile specimen specimen. The elements at which the Gauss point output was requested at the end of each load increment are highlighted. Coarse mesh: 86 QUAD8 elements, 301 nodes. Medium mesh: 250 QUAD8 elements, 823 nodes. Fine mesh: 672 QUAD8 elements, 2133 nodes.

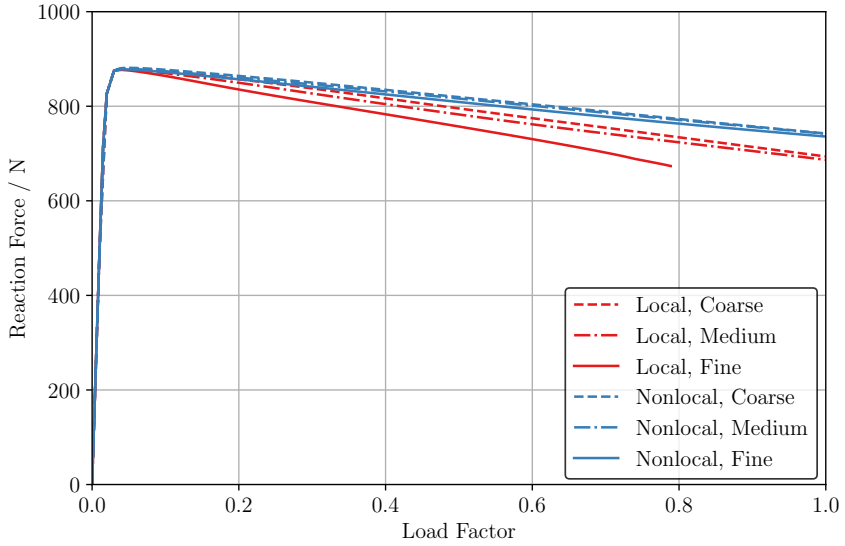

Figure 5.23: Evolution of the vertical reaction force for the local and nonlocal damage models, for both meshes. Results for a nonlocal radius of 0.4 mm. Colour indicates the damage model, linestyle indicates the finite element mesh.

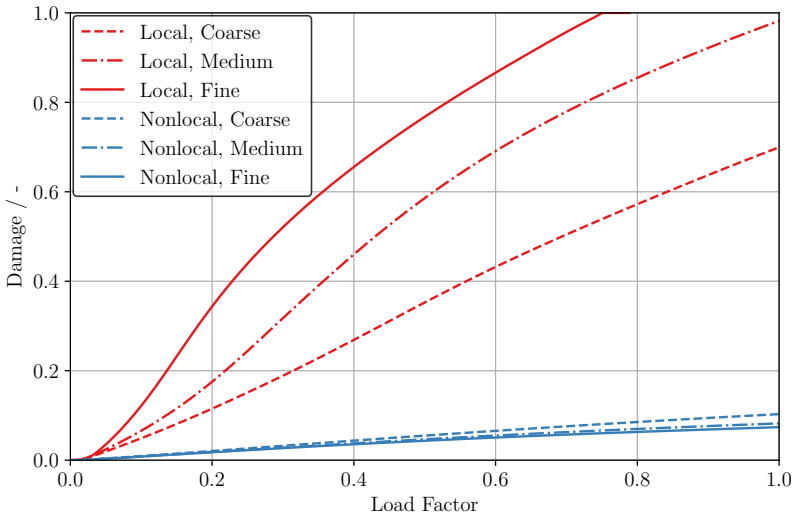

Figure 5.24: Damage variable evolution for the local and nonlocal models, retrieved at the tip of the notch, for both meshes. Results for a nonlocal radius of 0.4 mm. Colour indicates the damage model, linestyle indicates the finite element mesh..

Adopting a nonlocal model resulted in significantly lower values of the damage variable at the notch tip (Figure 5.24). However, this reduction is intrinsically linked with the presence of nonlocal averaging, which redistributes damage within a greater region of the specimen (Figure 5.25). This, in turn, explains why the discrepancy between the damage evolution at the notch tip is much greater than the difference between the reaction forces obtained for the local and nonlocal cases (Figure 5.23). Even though the damage variable is generally much lower in the nonlocal case, the damaged area is significantly greater, which yields a similar global response of the specimen, where the main distinction is the elimination of softening-induced mesh dependence in the nonlocal case.

Having performed this first regularisation study for the notched tensile specimen, the remainder of this section is split into several segments, in which specific features of the nonlocal model are assessed in isolation. These features include: the lower and upper bounds of the nonlocal length-scale parameter, the impact of adopting different numerical techniques to solve the global system of equations on the computational cost, and also aspects of the nonlocal averaging procedure.

Lower limit of the nonlocal radius

In Section 5.5.3, it was seen that, for sufficiently low values of the nonlocal radius, the rates of convergence of the Newton-Raphson method would slightly decrease. However, in this section, the analysis on the lower limit of the value of this parameter is pushed further, by repeating the simulation of the notched tensile specimen with a nonlocal radius of 0.1 mm. The resulting reaction force curves are plotted in Figure 5.26, where the local responses are also shown. In comparison to the reactions plotted in Figure 5.23, a greater level of mesh dependency was found for the nonlocal cases. Moreover, the adoption of this value of the nonlocal radius resulted in coincident local and nonlocal responses for the coarse mesh, since this characteristic length-scale is insufficient for the regularisation of this specific mesh.

These observations are further illustrated in Figure 5.27, where the nonlocal damage distributions found for these cases are shown. The damage contour for the coarse mesh is identical to the one found with a local model (see Figure 5.25a). Adding to this, although the introduction of the nonlocal regularisation parameter is noticeable in the damage distributions for the medium and fine meshes, some differences can also be observed, underscoring the fact that this value of the nonlocal radius is not sufficient to achieve the regularisation with these specific macro-meshes.

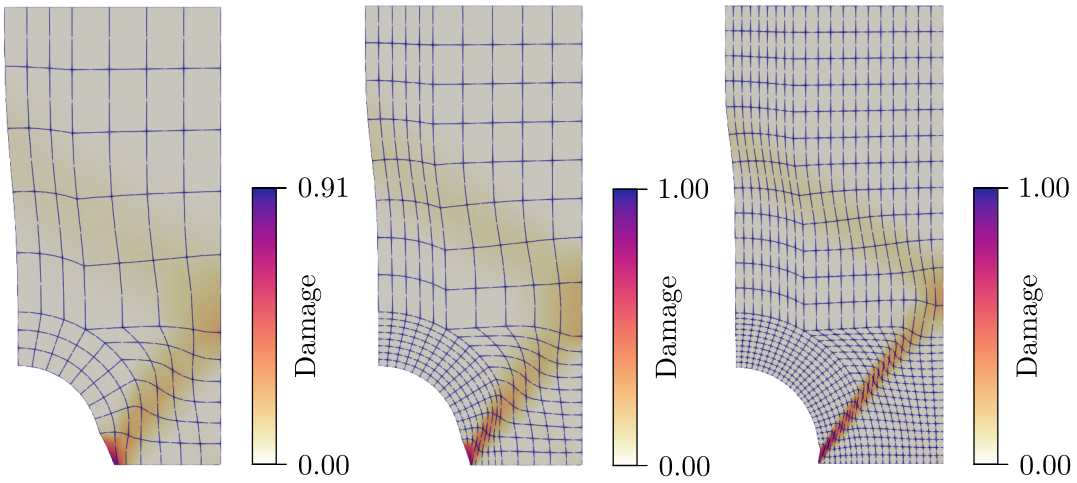

(a) Local case.

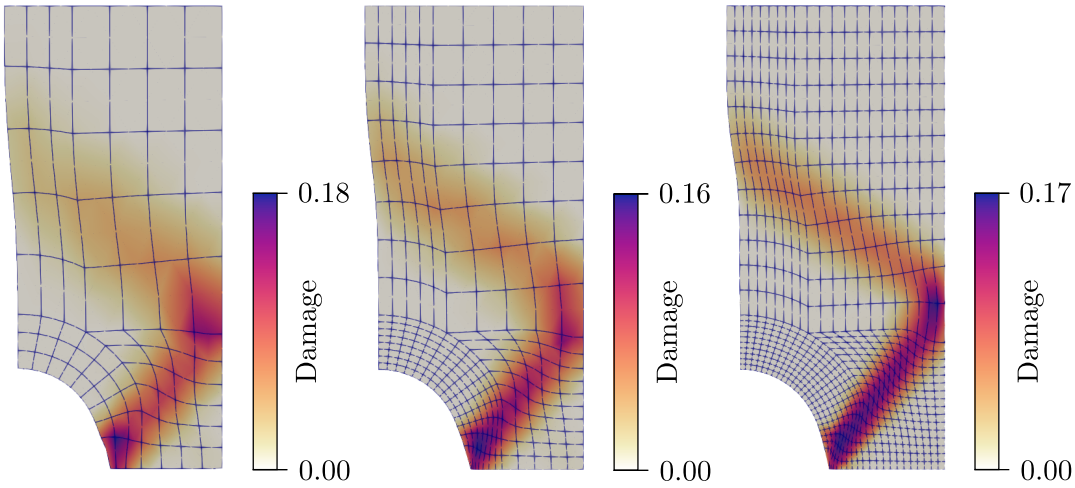

(b) Nonlocal case.

Figure 5.25: Damage distributions (plotted in the deformed configurations) found for the local and nonlocal cases with the three finite element meshes. Results for a nonlocal radius of 0.4 mm.

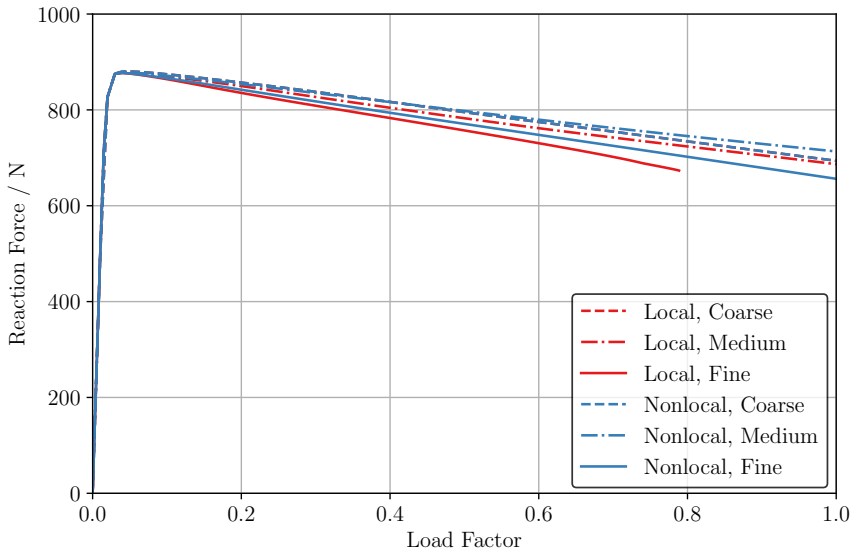

Figure 5.26: Evolution of the vertical reaction force for the local and nonlocal models, with a nonlocal radius of 0.1 mm. Results shown for the three meshes. Colour indicates the damage model, linestyle indicates the finite element mesh.

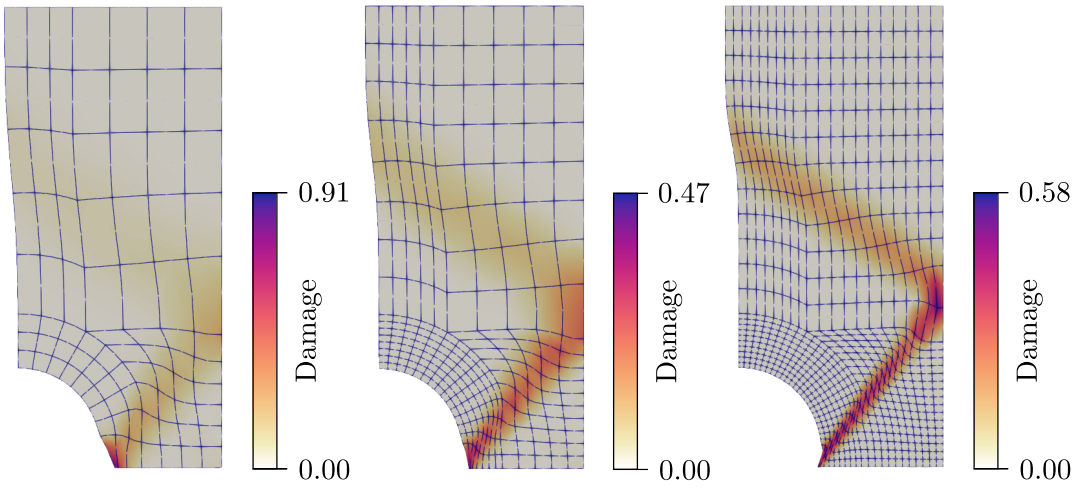

Figure 5.27: Damage distributions (plotted in the deformed configurations) found for the nonlocal radius of 0.1 mm for the three finite element meshes.

Upper limit of the nonlocal radius

The simulation of the tensile specimen was repeated with several other values of the nonlocal radius, to assess the existence of an upper bound for this parameter. To this end, the following additional values were considered: 0.8, 1.2, 1.6 and 2.0 mm; where the last value is large enough that a point in the centre of the specimen interacts with all points in the same horizontal line. The resulting reaction force curves are shown in Figure 5.28, where the nonlocal response is, once again, seen to converge for larger values of the nonlocal radius, with decreasing softening.

Additionally, Figure 5.29 depicts the damage contours obtained for the local case and five different values of the nonlocal radius, with the medium spatial discretisation of the specimen. Greater values of the nonlocal radius yield the redistribution of damage over a larger area of the specimen, also resulting in overall lower values of damage. Damage is also seen to concentrate in particular areas of the finite element mesh, which vary with the adopted nonlocal radius. However, the fact that the integral type averaging procedure is based on the interactions between Gauss points seems to result in the concentration of damage in more densely populated ares of the mesh. This effect is the most observable for the larger values of the nonlocal radius. Lastly, it should be noted that the damage distribution obtained for a nonlocal radius of 2.0 mm was not included, because it was identical to the one obtained with 1.6 mm.

Another relevant factor in this analysis is the impact of the nonlocal radius on the computational cost of these simulations. Such an analysis was already reported in Section 5.5.3, but with a smaller sample size. That said, Figure 5.30 shows the computational times recorded for the simulation of the tensile specimen with local and nonlocal models, with the various values of the nonlocal radius, the three meshes. Once again, exponential increases in the computational cost are associated to both the introduction of nonlocal averaging and the employment of finer meshes. Moreover, a clear increase was also observed for larger values of the nonlocal radius, for all meshes. This observation could not be made in Section 5.5.3, since the range of nonlocal radius values in consideration was not as wide. Regarding the lower values of this parameter, only for the fine mesh was a slight increase in the computational cost recorded for $R = 0.1$ mm. This effect, once again, is related to the rates of convergence of the Newton-Raphson method, although it was not observed for the remaining cases. Another relevant note is the fact that, for the coarse mesh and a nonlocal radius of 0.1 mm, even though no damage averaging took place, a computational cost increase was recorded. This is due to the fact that, even though the nonlocal circumferences of all Gauss points in the specimen did not include any additional point, the code still went over all the loops and logical steps described in Sections 5.3 and 5.4.

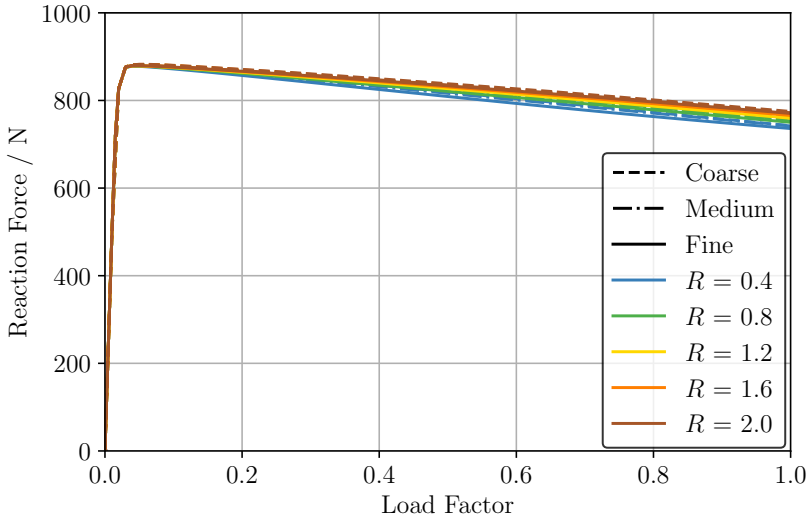

Figure 5.28: Evolution of the vertical reaction force for several values of the nonlocal radius. Results shown for the three meshes. Colour indicates the value of the nonlocal radius, linestyle indicates the finite element mesh.

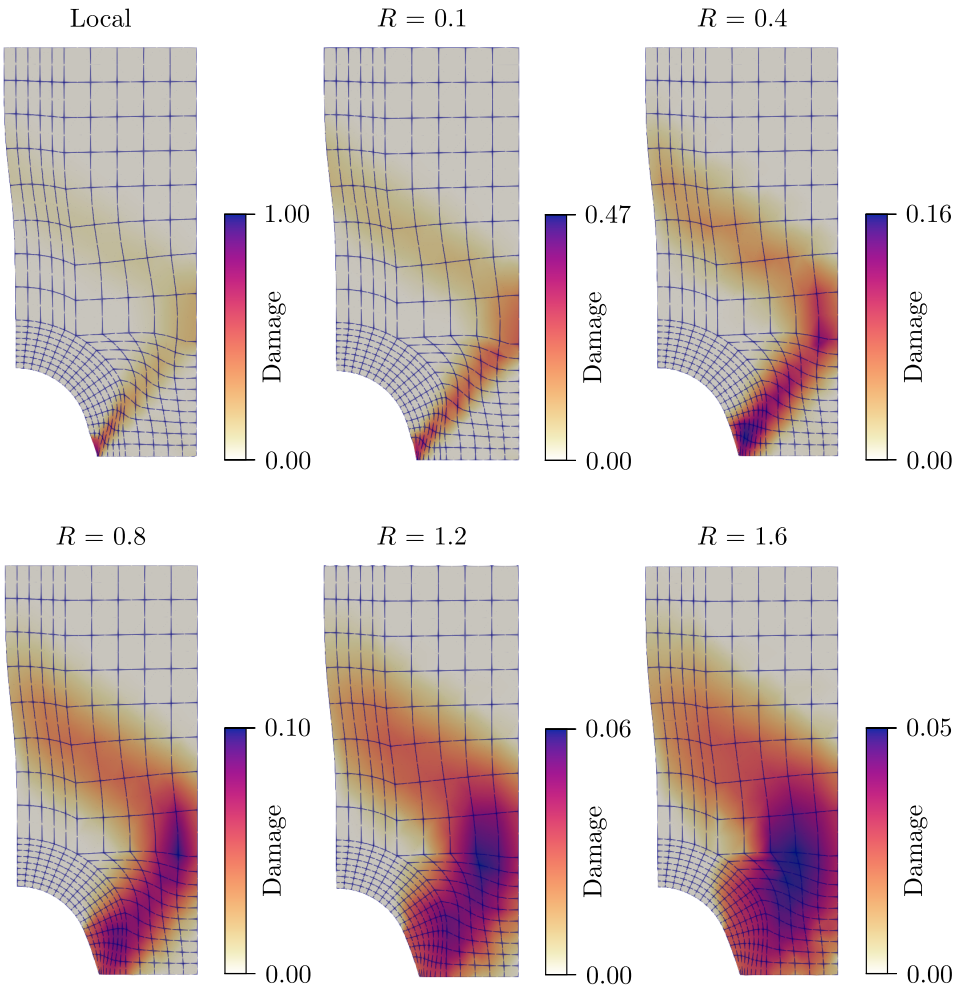

Figure 5.29: Damage distributions (plotted in the deformed configurations) found for the medium mesh and several values of the nonlocal radius.

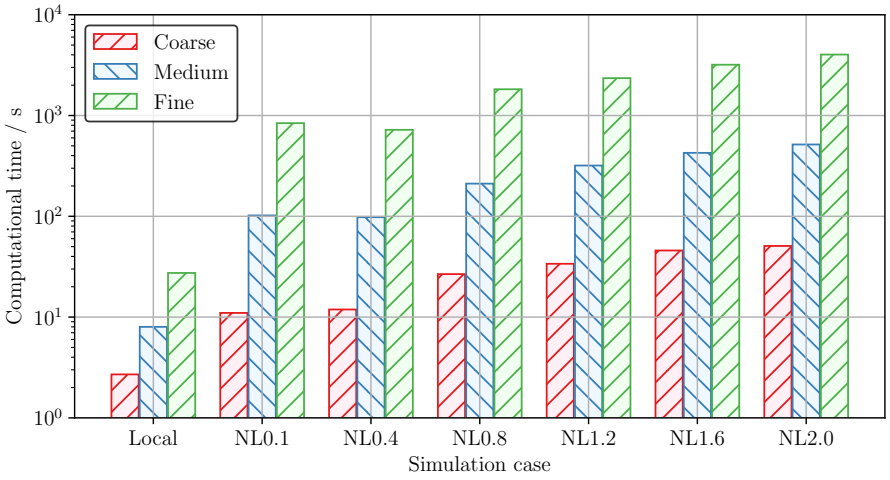

Figure 5.30: Computational time associated with each simulation of the tensile specimen, for both meshes. Legend: NL - Nonlocal; 0.1, 0.4, 0.8, 1.0, 1.2, 1.6, and 2.0 - respective nonlocal radius.

Impact of the solver on the computational cost

In Section 5.5.3 the adoption of larger values of the nonlocal radius increased the number of non-zero elements of the global stiffness matrix, yielding a reduction in the overall matrix sparsity. However, most numerical techniques employed to solve the global system of finite element equilibrium equations were designed to solve sparse systems. This is the case for the solver commonly employed by LINKS, Intel's PARDISO (Schenk and Gärtner, 2011). With this in mind, the simulations of the medium mesh were repeated for all values of the nonlocal radius, using an alternative solver, MA41, which, despite also being designed for sparse systems, can deal with the lack of symmetry introduced by nonlocal averaging (recall Section 4.2.1). Figure 5.31 shows the computational times recorded for the aforementioned simulations, with the two solvers. Adopting the MA41 solver did not modify the overall results, and yielded slight time savings, in comparison to PARDISO. However, this was found for almost all cases, including the local one. In addition, the computing time increased for larger values of the nonlocal radius for the MA41 solver, indicating that it is also not the most adequate alternative in this setting.

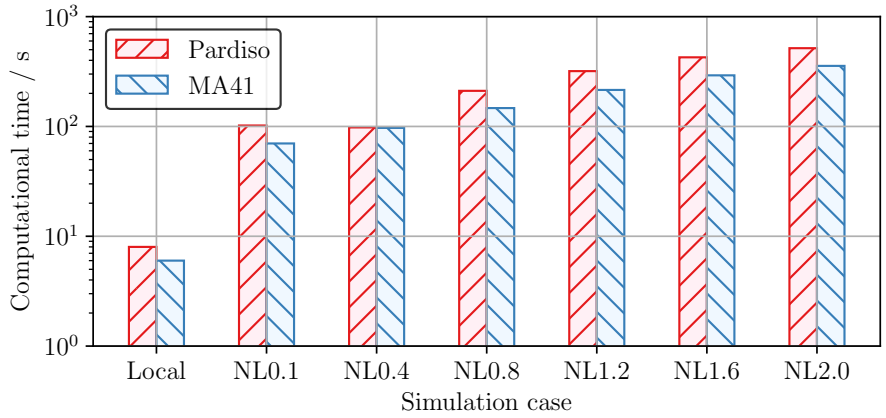

Figure 5.31: Impact of adopting different solvers for the global system of equations on the computational times. Computational times recorded for the medium mesh cases. Legend: NL - Nonlocal; 0.1, 0.4, 0.8, 1.2, 1.6, and 2.0 - nonlocal radius / mm.

As a final note, it should be remarked that the other elements of the finite element program, other than the solver, are designed to deal with sparse matrices. An example of this is the use of a COO format to store the stiffness coefficients, mentioned in Section 5.4. With this in mind, even if an adequate solver was selected in these cases, the non-sparsity of the stiffness matrix would probably still lead to increased computing times.

Bell-shaped function for nonlocal averaging

Up until this point, the standard weighting function (see Equation (4.4)) has been utilised in all nonlocal examples. To assess the impact of selecting different weighting functions on nonlocal predictions, the simulations with the medium mesh of the tensile specimen were repeated with the bell-shaped function (see Equation (4.5)). Figure 5.32 depicts the reaction force curves obtained with the bell-shaped functions and the nonlocal radii of 0.4, 0.8, 1.2, 1.6 and 2.0 mm. In comparison to the analogous cases with the standard function, depicted in Figure 5.28, the global mechanical response of the nonlocal cases is seen to converge faster with the value of this parameter. To further visualise the effects of adopting the bell-shaped function, Figure 5.33 illustrates the damage distributions obtained for the nonlocal radii of 0.8, 1.2, and 1.6 mm. On the one hand, lower damage values were generally found with the alternative weighting function, for the three values of the nonlocal radius. On the other hand, lower areas of damage redistribution were also found with this function, in comparison to the standard one. Recalling Figure 4.1, the differences in the two weighting functions justify the stiffer response observed in this case. Since a sharper averaging gradient is adopted, the same local damage is homogenised within a smaller area and resulting in overall lower damage values. This, in turn, also explains the faster convergence of the nonlocal responses with the bell-shaped function.

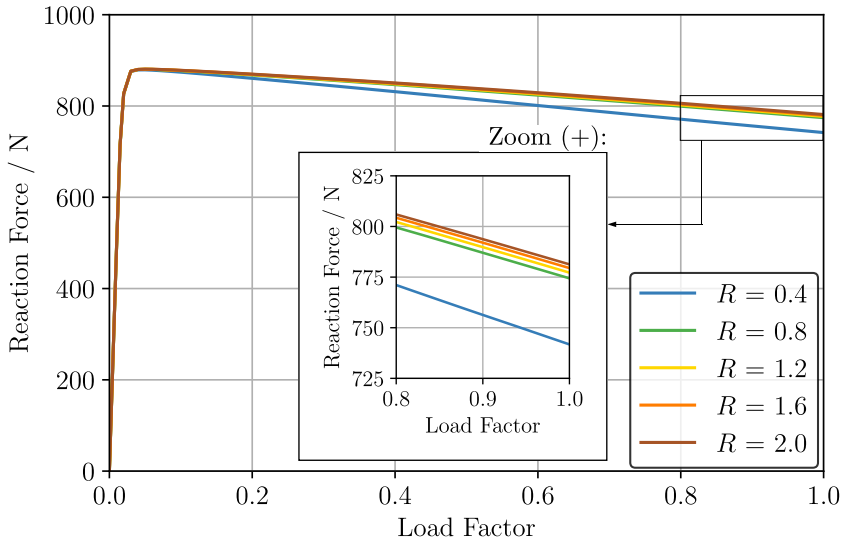

Figure 5.32: Evolution of the vertical raction forces obtained with the bell-shaped weighting function and several values of the nonlocal radius, for the medium mesh. Values of the nonlocal radius presented in mm.

Lagrangian and Eulerian nonlocal averaging

As the final analysis of the implemented nonlocal model of integral type for macro-scale problem, this segment aims to explore the impact of the nonlocal averaging strategy (recall Figure 4.2b) on the

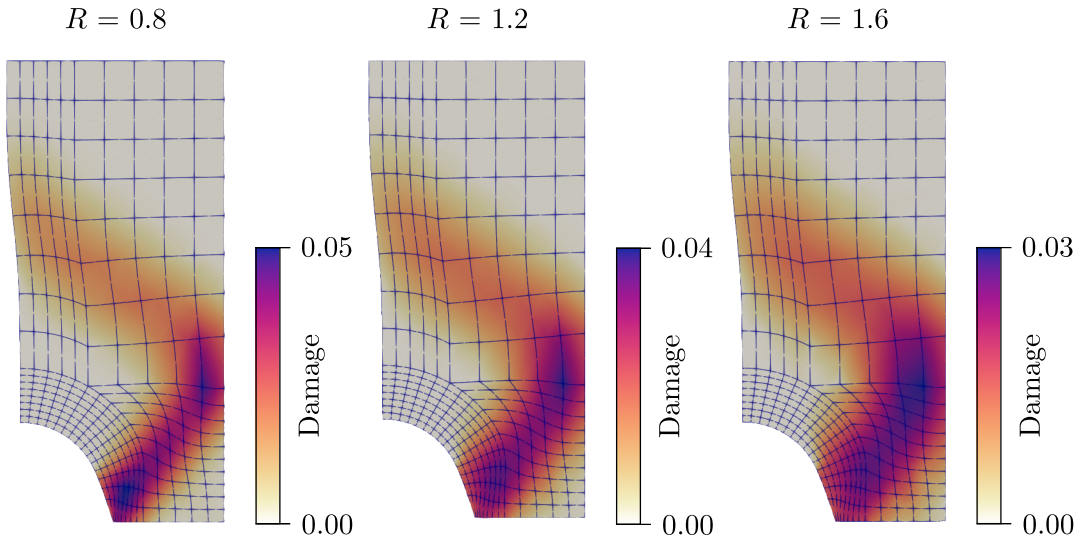

Figure 5.33: Damage distributions (plotted in the deformed configurations) found with the bell-shaped weighting function, for the medium mesh and several values of the nonlocal radius.

resulting mechanical response and also the computational cost. To this end, the simulation of the tensile specimen was repeated, with the medium mesh, the standard weighting function and two values of the nonlocal radius: 0.4 and 2.0 mm. The mechanical responses found for both nonlocal averaging strategies were identical, but some differences were found in terms of the computational cost. Table 5.3 reports the computational times measured for each nonlocal averaging type and nonlocal radius. As expected, adopting an Eulerian averaging type, which requires the update of the nonlocal domain of each integration point at the beginning of each equilibrium iteration, led to a computational cost increase.

Table 5.3: Computational times recorded for the Lagrangian and Eulerian nonlocal averaging strategies. Results obtained with the medium mesh. Time measures shown in seconds.

Averaging strategy	$R = 0.4$	$R = 2.0$
Lagrangian	98	516
Eulerian	149	553

To push this analysis further, the four simulations were repeated with a three times larger prescribed displacement, while also adopting a new critical plastic strain, ε_f, of 6 (also three times greater). The resulting damage distributions for the four cases are shown in Figure 5.34, while the recorded computational times are shown in Table 5.4. For a nonlocal radius of 2.0 mm, the Eulerian strategy overperformed, taking less computational resources to solve the problem for a three times larger displacement, while also recording a lower computational time than the Lagrangian strategy. This is linked to the fact that, for a tensile loading scenario, the extension of the material results in a progressive reduction of the number of points contained in each nonlocal domain, with the Eulerian strategy. Furthermore, for a nonlocal radius of 2.0 mm, almost all points in the notched section of the specimen are already nonlocally linked in the undeformed configuration, hence, its transverse compression throughout the simulation does not add many integration points to the original nonlocal domains in this region. Conversely, for a nonlocal radius of 0.4 mm, this is not true, justifying the similar computational costs observed for the two strategies. On the one hand, the extension of the upper part of the specimen results in a reduction of the nonlocal interactions. On the other hand, for the lower nonlocal radius, the transverse compression of the notched section leads to an

increase of the nonlocal interactions with the Eulerian strategy.

Finally, in spite of the differences observed in terms of computational cost, the mechanical responses attained with the two strategies remained very similar even with the increased deformation of the notched tensile specimen.

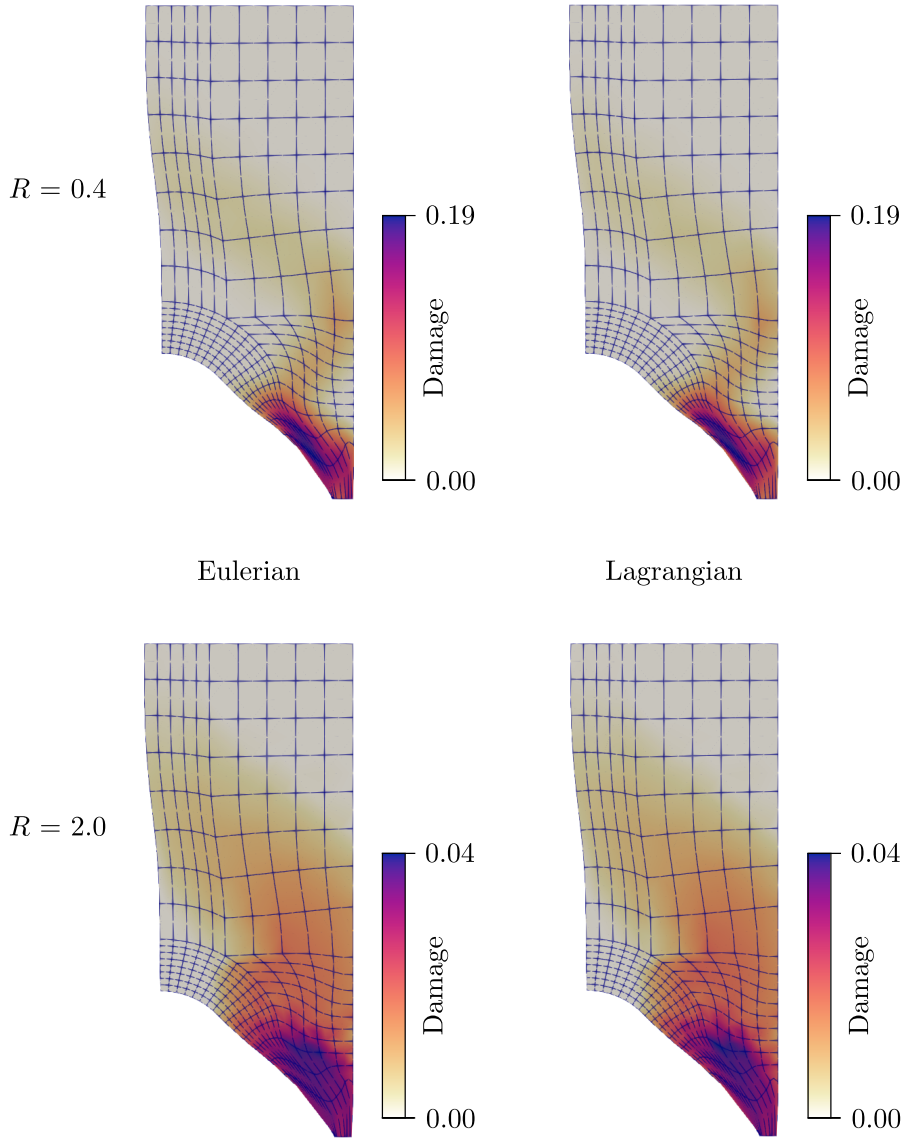

Figure 5.34: Damage distributions (plotted in the deformed configurations) found with the two nonlocal averaging strategies and the two chosen nonlocal radii. Results obtained for the medium mesh.

Table 5.4: Computational times recorded for the Lagrangian and Eulerian nonlocal averaging strategies, for a larger deformation of the tensile specimen. Results obtained with the medium mesh. Time measures shown in seconds.

Averaging strategy	$R = 0.4$	$R = 2.0$
Lagrangian	179	563
Eulerian	185	521

5.6 Discussion

In this chapter, the implementation of a nonlocal damage model of integral type for macro-scale problems has been extensively discussed. Section 5.5 presented various numerical analyses of the nonlocal model and its several features. The preliminary micro-scale examples shown in Section 5.5.1 demonstrated that the improved version of the state update procedure yielded relative time savings for all microscopic boundary conitions in consideration. Thereafter, quadratic rates of convergence were obtained with the Newton-Raphson method in the single-element tests reported in Section 5.5.2, showcasing the consistency of the implementation. In Sections 5.5.3 and 5.5.4, the employment of the integral nonlocal approach allowed the regularisation of localisation problems.

Moreover, particular emphasis was placed on the influence of the nonlocal length-scale parameter and the limits for its value. Adopting large values of the nonlocal radius led to non-sparse global stiffness matrices, as a result of the interactions between a greater number of points in the structure. Moreover, it was also observed that the value of the nonlocal radius has to be selected in accordance with the finite element mesh at hand, since it must be large enough that neighbouring integration points can interact. That being the case, it could be said that the optimal value of the nonlocal radius, for each geometry, boundary conditions and finite element mesh is that which, simultaneously:

1. Accurately captures the behaviour of the material under damage and moderate localisation;

2. Is large enough that it can effectively regularise the localisation problem, for the selected finite element discretisations of the geometry.

If possible, the nonlocal radius should also not be large enough that it leads to a significant increase in the computational cost of each equilibrium iteration, by largely increasing the number of non-zero elements of the global stiffness matrix. This increase is problematic, since many of the numerical procedures employed in the finite element problems are tailored for sparse systems of equations. In addition, for the compact shear specimen (Section 5.5.3), a lower value of the nonlocal radius led to slighly lower convergence rates of the Newton-Raphson method. However, this effect was not further investigated and remains unanswered, since several factors could be behind this observation.

The main focus of this chapter was to study the implementation and the numerical aspects of the nonlocal model of integral type. This meant that selecting representative values of the nonlocal radius was not a priority. Notwithstanding, in practical terms, since the nonlocal intrinsic length is a *material parameter*, its value should be calibrated empirically for the material of interest, to ensure physically meaningful results. Thereafter, the setup of the numerical problem, including the spatial discretisation, should be devised such that the numerical efficiency and stability of the finite element solution is also guaranteed.

In Section 5.5.4, other aspects of the nonlocal model were also analysed. Regarding the nonlocal averaging procedure, the selection of the weighting function was seen to have a relevant impact on the resulting mechanical response. For the two alternatives considered in this work, the bell-shaped function led to lower values of damage, distributed within lower areas of the domain. Furthermore, in spite of having a notable effect on the computational cost of simulations, adopting distinct nonlocal averaging strategies did not produce significant differences in the mechanical response of the notched specimen. It was also concluded that, when large nonlocal radius values are adopted, yielding a non-sparse stiffness matrix, the numerical techniques employed to solve the global system of equations should be revisited.

Concerning the present implementation of the nonlocal model, a few future optimisation tasks have been identified. Firstly, as discussed in Section 5.4, the array of state variables was modified for the Engelen material model, to allow manipulating two different damage variables: the actual nonlocal damage variable, and the local damage increment. This solution proved to be effective in

this scenario, where a single material model has been employed with nonlocal damage of integral type. However, as had been remarked, this means that, upon adopting nonlocal averaging with a different material model, its array of state variables also has to be modified. To avoid having to alter the array of state variables for several material models, the local damage increment could be stored as a global variable in an alternative fashion, for instance, by resorting to the *nonlocal module*, which already includes quantities like the nonlocal radius. Additionally, the code could also be enhanced to avoid unnecessary resource expenditures, in cases in which nonlocal averaging does not take place, for instance, as was seen in Section 5.5.4 for the coarse mesh and a nonlocal radius of 0.1 mm. The macro-scale nonlocal code should also be extended for 2D plane stress and 3D problems. Lastly, an integral model with an evolving nonlocal radius could be considered as a future enhancement of the present implementation.

CHAPTER 6

MACRO-SCALE REGULARISATION WITH SECOND-ORDER HOMOGENISATION

6.1 Introduction

Chapter 5 was dedicated to the formulation and study of a nonlocal damage model of integral type as a strategy for the attenuation of pathological mesh dependency for single-scale problems. In the present chapter, the regularisation of multi-scale softening problems is discussed, with the employment of first- and second-order computational homogenisation. Porous RVEs were utilised in multi-scale simulations, since the existence of voids within the RVE is a source of geometrical nonlinearity, which, in turn, promotes softening behaviour (see Figure 5.11 of Kouznetsova (2002)). Porous RVEs are also often employed to model the microstructure of ductile materials, since their failure is intrinsically linked to void growth. That said, Section 6.1.1 presents a brief review on ductile failure and its underlying damage mechanisms. Additionally, Section 6.1.2 discusses the application of computational-homogenisation-based multi-scale approaches for the prediction of softening and ductile failure, with particular emphasis on the adoption of second-order multi-scale models.

Thereafter, the generation and analysis of porous RVEs is detailed in Section 6.2. Multi-scale simulations of softening with first- and second-order computational homogenisation are presented in Section 6.3. The regularisation of the micro-scale problem is discussed in Section 6.4, starting with a few notes on the implementation of nonlocal damage for coupled problems, before repeating the micro-scale analyses. Multi-scale simulations performed with nonlocal damage at the RVE level and first- and second-order homogenisation are presented in Section 6.5. Finally, Section 6.6 discusses the main conclusions that can be drawn from the contents of the present chapter. As a final note, it should be mentioned that the analyses presented in this chapter were greatly inspired by the seminal work of Kouznetsova (2002).

6.1.1 Ductile damage mechanisms

The onset and propagation of structural defects are inseparable from the nucleation and growth of damage mechanisms at the microscopic level. The progressive failure of ductile materials, particularly metals, is the result of the nucleation, growth and coalescense of internal voids, as first observed by Tipper (1949). Since then, this phenomena has been extensively studied, with the development of numerous phenomenological models, such as the pioneering work of Gurson (1977).

Figure 6.1 illustrates the different stages of the progressive failure of ductile materials.

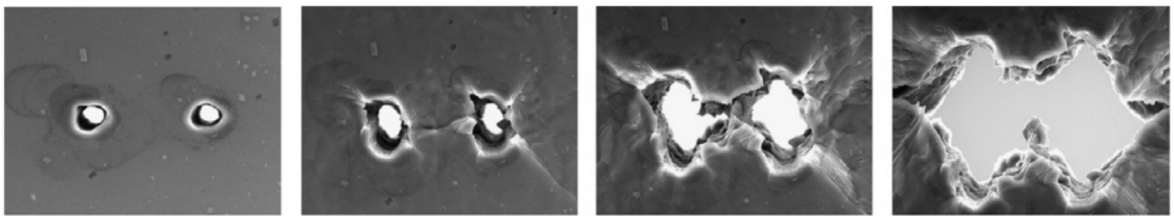

Figure 6.1: Void coalescense on metal sheets containing laser drilled holes, taken from Weck and Wilkinson (2008).

The failure of ductile materials is an intrinsically multi-scale phenomenon, as is illustrated in Figure 6.2. In the past decades, several numerical studies have been conducted on the nonlinear behaviour of ductile materials and its relation to the underlying microscopic damage mechanisms. The micro-scale analysis of the yield response of metals, for instance, has been addressed by several authors (dos Santos et al., 2022, 2023, Pinto Carvalho et al., 2018). In these studies, the presence of voids in the RVE is associated with damage, since their increase in size is related to a reduction of the microstructure's load bearing capacity. The impact of the void volume fraction, morphology and distribution on the mechanical behaviour of various materials has also been documented (De Cola et al., 2016, Tang et al., 2022, Xie et al., 2022).

Most contributions cited in this section employ porous RVEs to assess the yield response of ductile materials and its connection with microstructural features. In this chapter, porous RVEs have been adopted to promote macro-scale softening in a multi-scale scheme, which, in the absence of a regularisation strategy, is associated with macro-mesh dependency.

6.1.2 Remarks on the computational homogenisation of softening media

As aforementioned, the main focus of this chapter is the regularisation of multi-scale softening problems. In this context, Kouznetsova (2002) demonstrated that the adoption of second-order homogenisation allows for this regularising effect at the macro-scale. This is due to the introduction of an intrinsic macroscopic length-scale, implicit to the use of second-gradient continuum theory. Within a coupled scheme based on computational homogenisation, this length-scale parameter is linked with the length of the RVE. Kouznetsova et al. (2004b) performed several numerical analyses to study the influence of the RVE length on the macroscopic response of complex geometries. The authors were able to demonstrate that, the RVE length is deeply related to the length-scale of the macroscopic second-order continuum. They have also shown that, while the RVE length and the macroscopic length-scale can be explicitly related in the case of linear elasticity, the presence of material and geometrical nonlinearities affects this relationship. It is also stated that the value of this macro-scale characteristic length evolves throughout the loading path, as nonlinear effects also vary. Furthermore, Luscher (2010) concluded that, in second-order multi-scale models, the resulting macroscopic characteristic length is not an inherent property of the RVE model, its size and features, but rather an intricate combination and interaction of macro-scale geometry and forces with microscopic heterogeneity and response. This is also analysed in Rodrigues Lopes and Andrade Pires (2021), where the author states that the choice of an appropriate RVE for second-order homogenisation schemes is hampered by the need to select a representative model with the length that properly defines the macroscopic nonlocal behaviour. In the limit, it may happen that the RVE with an appropriate length does not contain a representative number of constituents and the RVE length needed to provide a representative response overestimates the physical material characteristic length, leading to results that do not describe the real behaviour.

Another relevant aspect of the computational homogenisation of softening media is the exis-

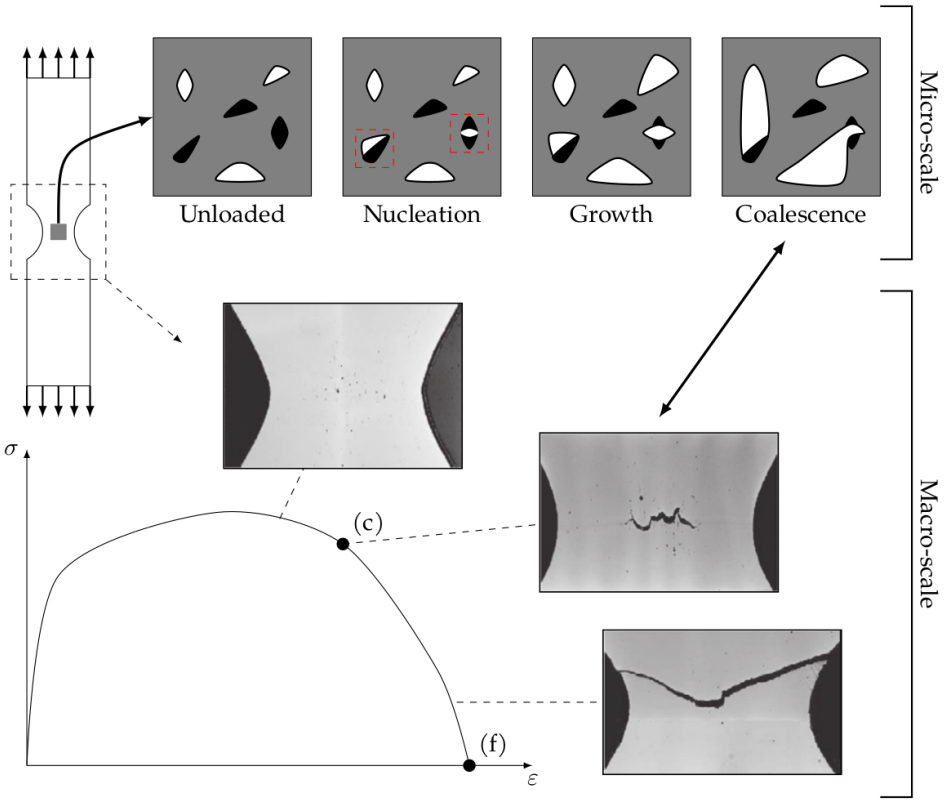

Figure 6.2: Schematic representation of the macro- and micro-scale damage mechanisms influencing the failure of ductile materials, taken from Coelho (2019).

tence of the RVE. Gitman et al. (2007) demonstrates that, contrarily to what is observed for linear elasticity or the hardening regime, the mechanical response of quasi-brittle RVEs experiencing softening does not converge as their size increases, with first-order homogenisation. From this observation, the authors concluded that, for this particular case, the RVE does not exist, since the micro-scale model is no longer statistically homogeneous due to the presence of localisation and its consequences on the initial boundary value problem. This results in losing the objectivity of the separation of scales. In spite of this, the representativeness of the porous RVEs employed in this chapter is outside the scope of this dissertation. These micro-models were adopted to promote macroscopic softening within a multi-scale simulation setup, and assess the mesh-dependent effects observed with first- and second-order homogenisation schemes. That being the case, the representativeness of the homogenised micro-scale response, in relation to the actual material behaviour is not addressed.

6.2 RVE generation and micro-scale analysis

Having presented the microscopic damage mechanisms governing ductile failure, and also given some insights into its computational multi-scale modelling, the generation of porous RVEs is reported in Section 6.2.1, along with the details on the microscopic model, before a preliminary micro-mechanical analysis is shown in Section 6.2.2.

6.2.1 Generation of porous RVEs

To simulate ductile failure within a coupled multi-scale finite element framework, the presence of voids was considered at the micro-scale, as mentioned in Section 6.1.1. To generate RVEs with

the desired microstructural descriptors, GMMD, an in-house tool for computational RVE generation, was employed. In the context of this dissertation, GMMD had to be slightly adapted to allow the inclusion of voids in the resulting microstructural models. GMMD, utilises an adaptive multi-temperature isokinetic time-driven molecular dynamics scheme to produce high-fidelity RVEs (see Ferreira et al. (2022b), Vila-Chã et al. (2021) for further details). In this case, a single material phase was assumed, and the relevant microstructural descriptors are as follows: i) the number of voids, ii) the void volume fraction and iii) the void distribution. For the sake of simplicity, only circular voids were considered in the present 2D analysis, although GMMD supports several other shapes. In addition, a minimum distance between voids was established, to avoid meshing issues. Figure 6.3 shows some of the RVEs generated in this context.

With the goal of studying the regularisation of a multi-scale softening problem in mind, the RVE depicted in Figure 6.4, with 10% void volume fraction, was ultimately selected for its simplicity, a key factor in guaranteeing the stability of the multi-scale simulations. Furthermore, since RVE morphology studies are outside the scope of this dissertation, considering other options, with several voids and different configurations, did not offer many advantages. Adding to this, the Periodic Boundary Condition (recall Section 3.3.3) was employed with the first-order homogenisation, since it produces the intermediate response, among the available sets of micro-constraints (see Figure 3.6). That said, the chosen RVE was discretised in 8-noded quadratic quadrilateral elements, QUAD8, with reduced intergation, for three different characteristic mesh sizes (as shown in Figure 6.4).

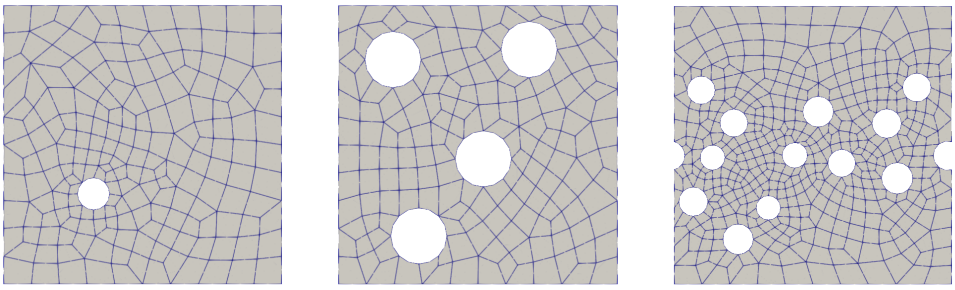

(a) RVE with 1 void with a 1% vol. fraction.

(b) RVE with 4 voids with a 10% vol. fraction.

(c) RVE with 13 voids with a 10% vol. fraction.

Figure 6.3: Examples of the porous microstructures generated with GMMD.

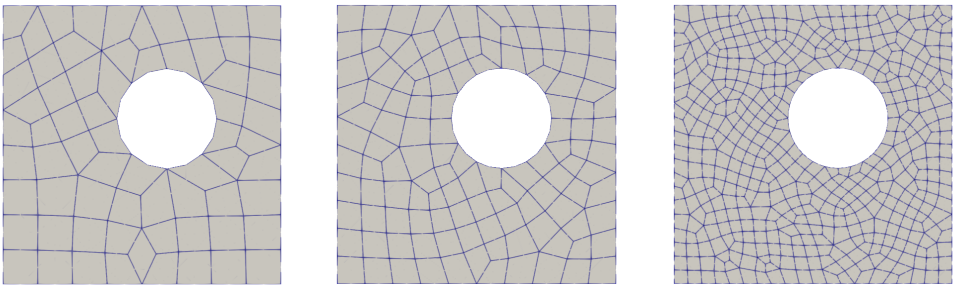

(a) Coarse mesh, 68 elements and 244 nodes.

(b) Medium mesh, 125 elements and 427 nodes.

(c) Fine mesh, 487 elements and 1565 nodes.

Figure 6.4: Finite element discretisation of the RVE employed in coupled analysis, with a single void with a 10% volume fracton.

6.2.2 Preliminary micro-mechanical analysis

The von Mises constitutive model for finite strain elastoplasticity, coupled with isotropic local explicit damage, i.e. the local Engelen model (described in Section 5.2), was adopted at the micro-scale. Considering the nonlinear effects associated with the presence of voids in the micro-model, the micro-scale equilibrium problem is *mesh-dependent*, regardless of the adoption of continuum damage at the RVE level. However, the inclusion of damage amplifies the tendency for softening, by introducing a material source of nonlinearity. This reduces the micro-scale deformation levels required to achieve the desired macro-scale strain localisation in the context of the multi-scale regularisation studies presented in subsequent sections. Moreover, the introduction of damage at the micro-scale allows modelling void coalescense, even for an RVE containing a single void, if damage propagates from the void to one of the boundaries. This is possible due to the adoption of the periodic boundary condition.

Table 6.1 summarises the main mechanical properties of the porous RVEs employed in the present chapter, generally corresponding to the properties of a steel alloy. Furthermore, a linear hardening law was assumed, with an initial yield stress of 243 MPa. To select a value of the hardening slope which would allow a reasonable amount of softening, a preliminary micro-mechanical study was conducted. The medium mesh RVE was simulated with the following prescribed deformation gradient:

$$\boldsymbol{F} = \begin{bmatrix} 0.800 & 0.000 \\ 0.000 & 1.200 \end{bmatrix}; \tag{6.1}$$

with five values of the yield stress at failure, i.e. the yield stress at $\bar{\varepsilon}^p = \varepsilon_f = 1$: 250 MPa, 300 MPa, 350 MPa, 400 MPa and 450 MPa. The results are depicted in Figure 6.5, in which some degree of softening can be observed for every value of the yield stress at failure. Nonetheless, the value of 300 MPa was chosen to ensure the occurrence of softening for a wider range of loading scenarios. Figure 6.6 depicts the evolution of the damage distribution for the chosen value of the hardening slope, where the combined effects of void presence and material softening can be observed. The resulting damage band, by propagating from the void to the RVE boundaries, approximates the occurrence of void coalescense.

Table 6.1: Material properties of the porous RVEs. Legend: E denotes the Young's modulus; ν denotes the Poisson coefficient; ε_f denotes the critical accumulated plastic strain; $\sigma_{y,0}$ denotes the initial yield stress. The yield stress at failure was fixed at 300 MPa after the preliminary analysis depicted in Figure 6.5.

E / GPa	ν / -	ε_f / -	$\sigma_{y,0}$ / MPa
210	0.30	1.00	243

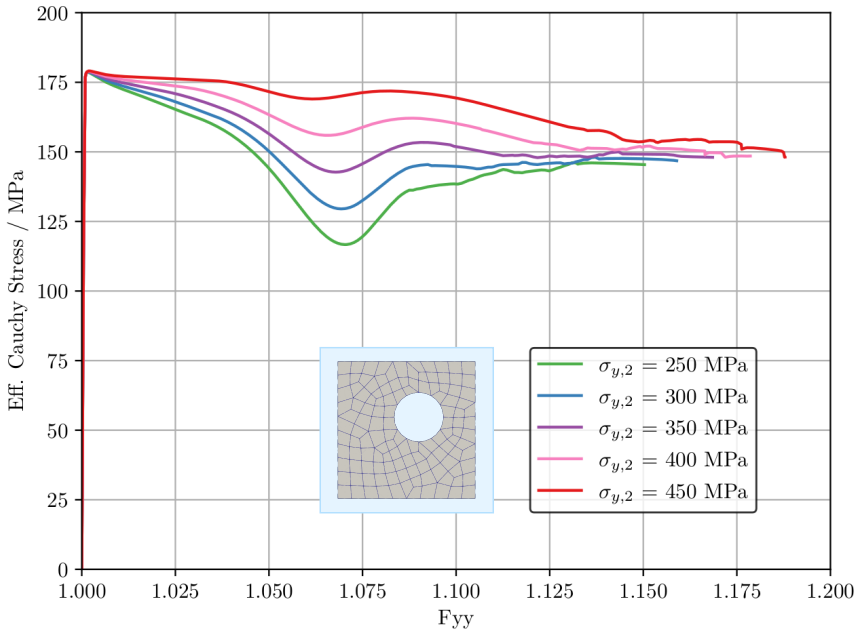

Figure 6.5: Stress-strain curves obtained for different values of the yield stress at failure, $\sigma_{y,2}$, with the medium RVE mesh.

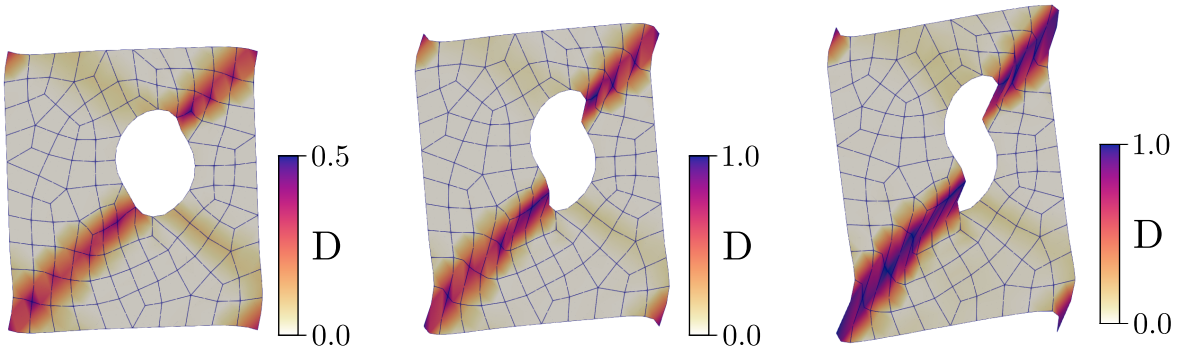

(a) $\Delta = 0.27$. (b) $\Delta = 0.54$. (c) $\Delta = 0.81$.

Figure 6.6: Damage contours found for a yield stress at failure of 300 MPa, for three equally spaced values of the load factor.

6.3 Multi-scale simulations of a tensile specimen

Having defined the micro-mechanical model to be used in this coupled analysis, a tensile specimen inspired by the analysis of chapter 6.2 of Kouznetsova (2002) was devised. In the finite element setup, only a quarter of the actual tensile specimen is actually simulated, taking advantage of two symmetry conditions. Furthermore, the test piece contains a geometrical perturbation, a 1% width reduction, to promote localisation at the macro-scale (see illustration in Figure 6.7a). A vertical displacement of 0.5 mm was applied at the upper boundary of the specimen, as shown in Figure 6.7a. Three different finite element discretisations of the specimen were generated, as shown in Figure 6.7, using 8-noded quadratic quadrilateral elements, QUAD8, with reduced intergation.

In Section 6.3.1, this multi-scale problem is tackled with first-order computational homogenisation. The results and the limitations of the first-order coupled approach in this context are commented, with the discussion of Section 6.1.2 in mind. Thereafter, the multi-scale analysis is repeated

using second-order homogenisation in Section 6.3.2. The impact of the RVE length on the numerical solution is addressed in Section 6.3.3, with some remarks on its mesh regularising effect.

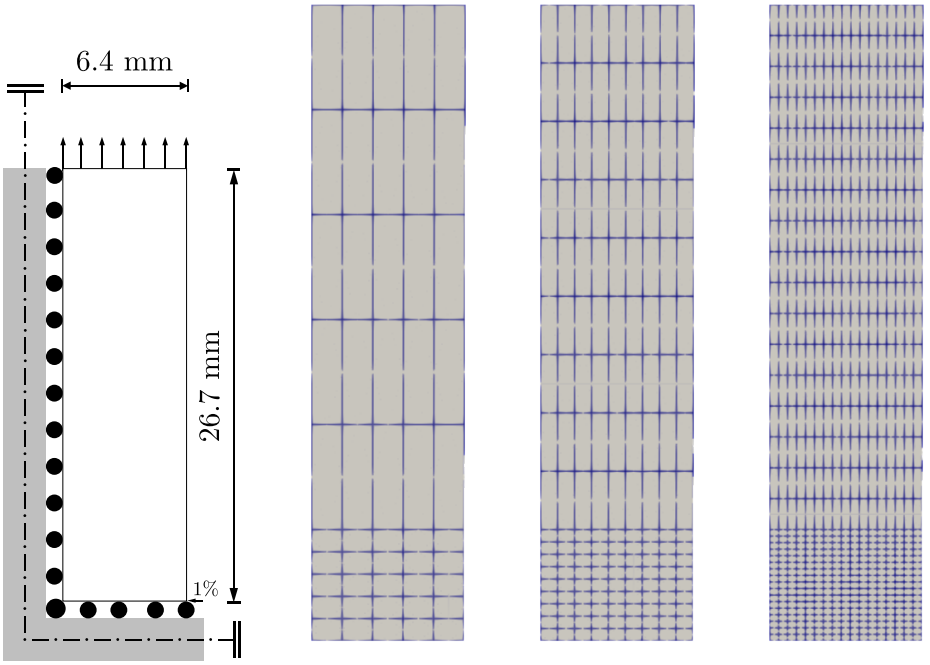

(a) Schematic.

(b) Coarse, 50 elements and 181 nodes.

(c) Medium, 162 elements and 541 nodes.

(d) Fine, 578 elements and 1837 nodes.

Figure 6.7: Schematic representation of a quarter of the perturbed tensile specimen, inspired by the work of Kouznetsova (2002), and its three finite element discretisations.

6.3.1 First-order multi-scale analysis

Figure 6.8 shows the reaction curves obtained by simulating the tensile specimen, with the nine combinations of macro- and micro-scale meshes, employing first-order homogenisation. The mechanical response of the specimen was seen to vary both in terms of macro- and micro-scale spatial discretisation. On one end of the spectrum, the simulation of the coarse-meshed tensile specimen, coupled with the coarse RVE mesh, only aborted near the actual prescribed displacement, due to the lack of convergence in the Newton-Raphson scheme (see Remark 4). On the other end, the combination of the fine macro- and micro-scale meshes resulted in the premature collapse of the simulation before it reached 15% of the prescribed displacement. That being the case, with first-order homogenisation, the global response of the specimen was shown to be dependent on the finite element discretisations of the problem at both scales. This was expected, since a first-order continuum approach at the macro-scale is not adequate for modelling a localisation problem, without the addition of an intrinsic length-scale parameter. Furthermore, as had been discussed in Section 6.2.2, the inclusion of material and geometrical softening in the RVE model leads to mesh dependency at the micro-scale. In these cases, and RVE length of 1 mm was adopted, although this parameter is known to have no influence on first-order multi-scale predictions.

Adding to that, Figure 6.9 illustrates the strain distributions at failure found for each case. As can be observed, several localisation patters were found for this set of simulations. Considering the symmetry conditions imposed on the specimen, an "X-type" shear strain band (Tang et al., 2018) was expected (see the works of Labergere et al. (2014), Li et al. (2016), Mir et al. (2018) for further evidence). Only two simulations showcased this localisation pattern: the coarse-macro, medium-micro and the coarse-macro, fine-micro cases. Figure 6.10a depicts the X-type localisa-

tion band obtained with the coarse-macro, fine-micro case, by mirroring the strain distribution obtained for the quarter of the test piece. The remaining localisation patterns, within the symmetry conditions assumed in this setup, do not seem to bear physical meaning. Figure 6.10b shows the full mirrored version of another strain band, found for several cases with combinations of the finer meshes, which was associated to a stiff macro-scale response and the premature abortion of the simulations. This demonstrates that, since the macro-scale mesh is not regularised with first-order homogenisation, the presence of spurious deformation modes is not circumvented.

Finally, it should also be observed that, the two cases that captured the expected localisation band shared the same macro-scale mesh. However, since they were associated to different RVE meshes, their reaction curves differed substantially (see Figure 6.8). Figure 6.11 depicts the influence of softening at the microscopic level on the resulting macro-scale response. For the fine RVE, since the micro-mechanical equilibrium problem is mesh-dependent, localisation occurs within a thinner band, causing the specimen to fail earlier in comparison with the medium-micro case.

In essence, employing a multi-scale model based on first-order homogenisation has led to macro-mesh dependency, which has been observed in the resulting reaction curves but also in the strain localisation patterns found for each case.

Remark 4 *Premature termination was found for many of the multi-scale simulations presented in this chapter. At this point, it is relevant to note that, in all cases, this is linked to excessive localisation at the micro-scale level, yielding considerable levels of element distortion, which, in turn, result in micro-scale negative jacobians, inhibiting the convergence of the multi-scale Newton-Raphson scheme.*

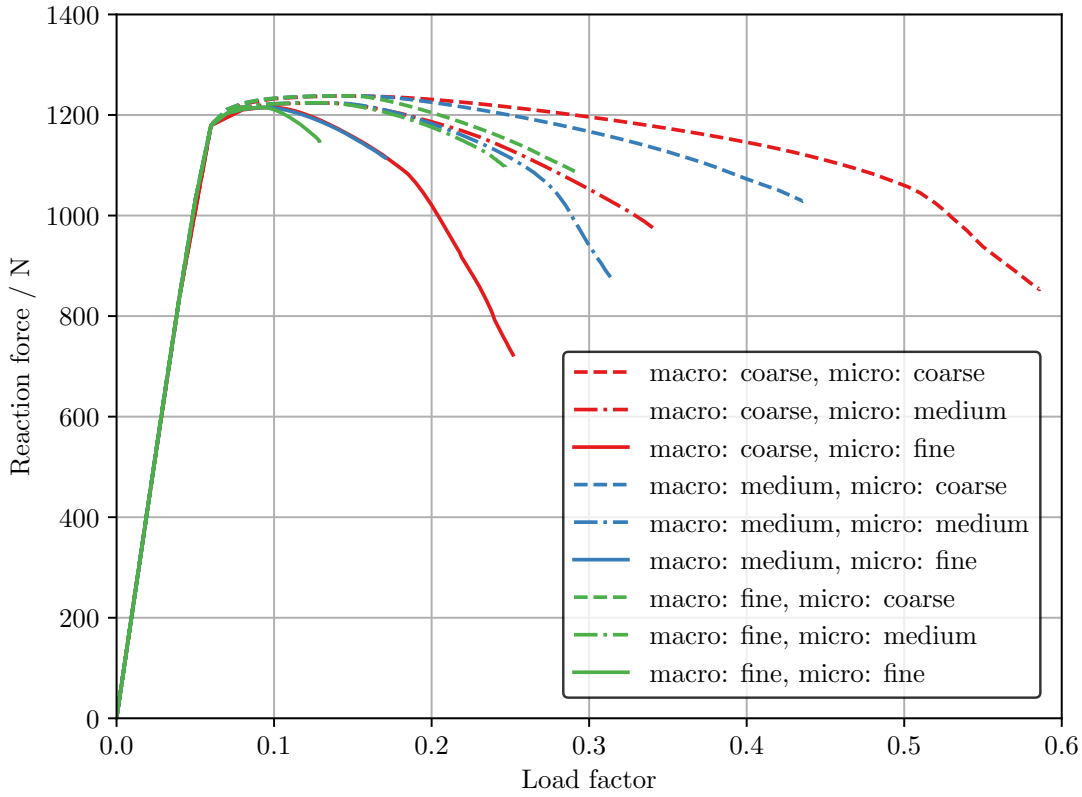

Figure 6.8: Reaction force curves obtained with first-order homogenisation for the tensile specimen, with the nine combinations of macro- and micro-scale meshes. Linestyle indicates the micro-scale mesh, while colour indicates the macro-scale mesh.

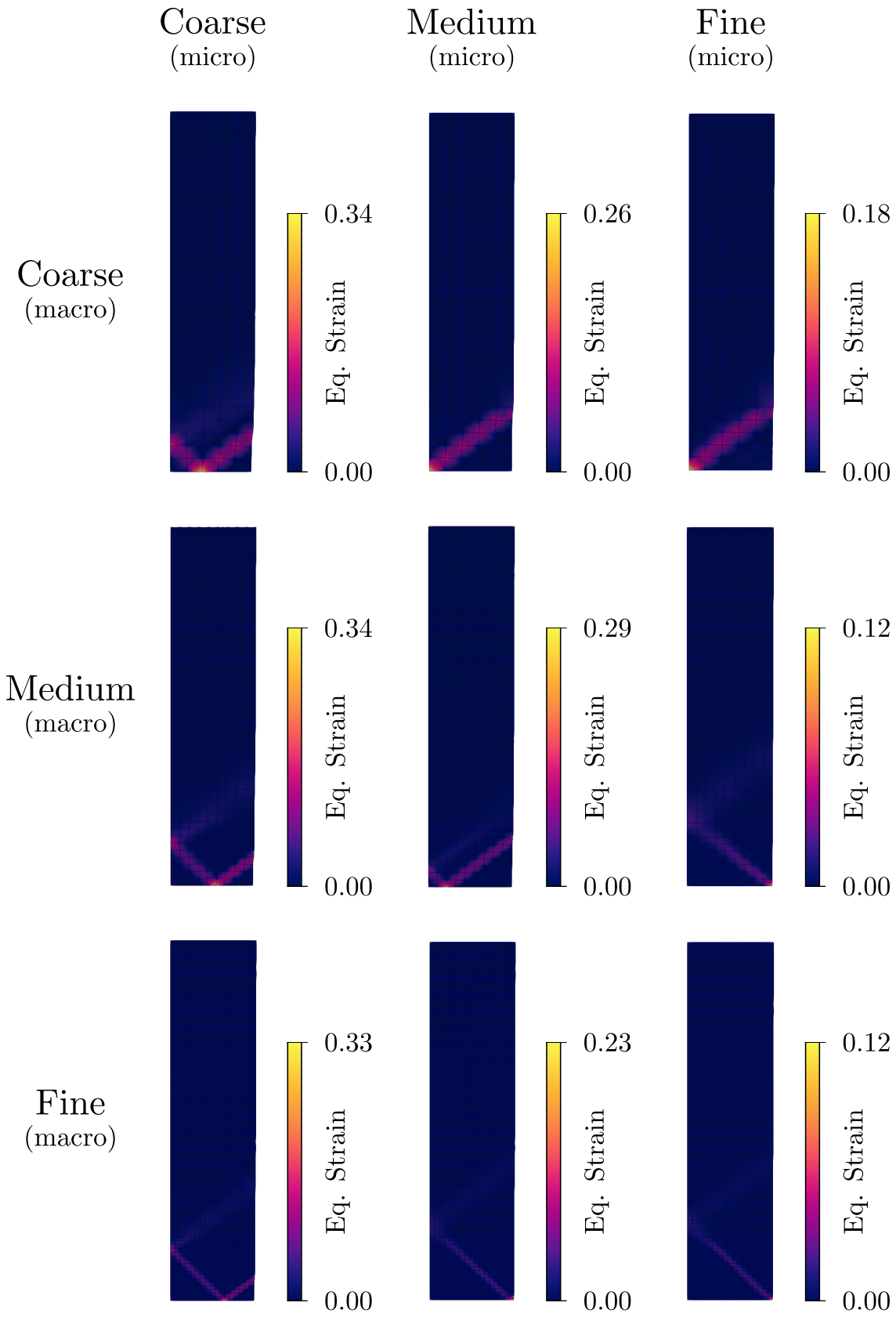

Figure 6.9: Equivalent strain distributions at failure obtained with first-order homogenisation for the tensile specimen, with the nine combinations of macro- and micro-scale meshes.

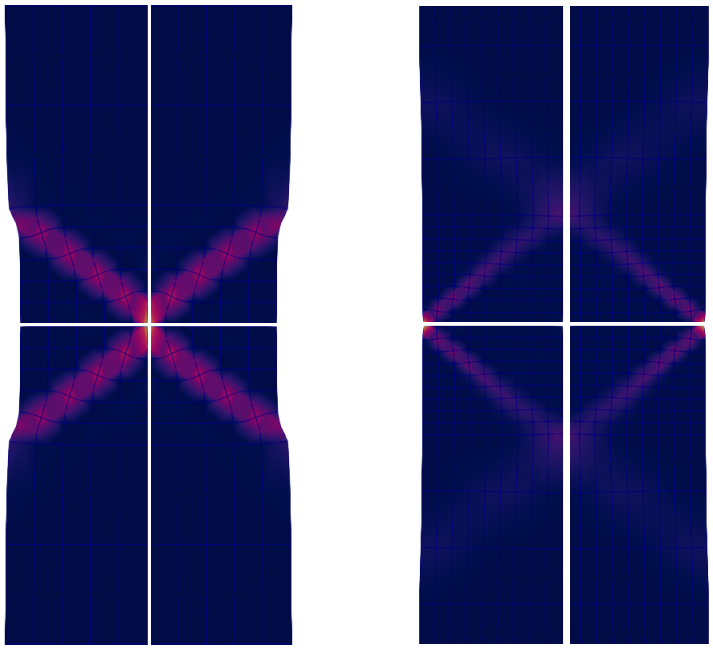

(a) Coarse-macro, fine-micro case.

(b) Medium-macro, fine-micro case.

Figure 6.10: Mirrored visualisation of two localisation patterns found with first-order homogenisation. The deformed configurations were multiplied by a scale factor of 5 for visualisation purposes.

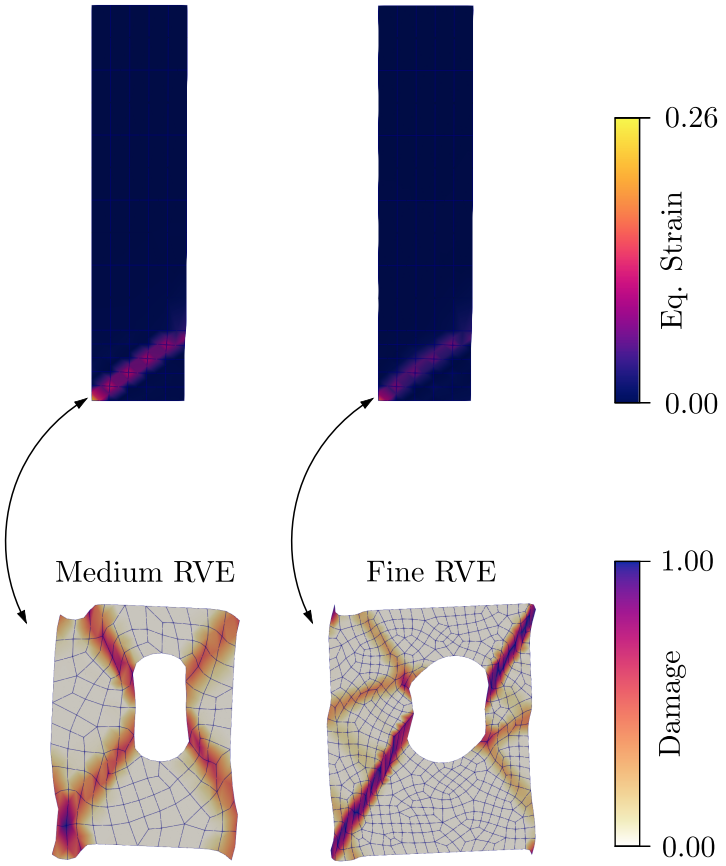

Figure 6.11: Micro-mechanical responses attained with the coarse macro-scale mesh and the medium and fine RVEs.

6.3.2 Second-order multi-scale analysis

To repeat the simulations reported in Section 6.3.1 with second-order computational homogenisation, three adjustments were necessary. Firstly, at the macro-scale, since a second-gradient continua is assumed, a Q8F4L1 mixed element (see Section 2.10.4) was employed for the spatial discretisation of the specimen. Since this mixed element has the same number of nodes as the QUAD8 element, utilised in the first-order cases, the finite element meshes used in the present section are identical to the ones depicted in Figure 6.7. Secondly, regarding the micro-scale model, an alternative RVE boundary condition was adopted, in order to deal with the second-order gradients coming from the macro-scale correctly. In this dissertation, the periodic condition (see Section 3.4.4), adapted for porous RVEs as described in Section 3.5.4, was employed. In dos Santos et al. (2023), this set of micro-constraints was shown to performed particularly well against Direct Numerical Simulations. Thirdly, an additional boundary condition, associated to the deformation gradient, is demanded by the description of the macroscopic domain as a second-order continuum. In this case, to adequately impose the symmetry conditions on the specimen, the following components of the deformation gradient were prescribed in the nodes belonging to the axes of symmetry (Kouznetsova, 2002):

$$F_{12} = F_{21} = 0. \tag{6.2}$$

The nine simulations documented in Section 6.3.1 were repeated with second-order homogenisation, assuming an initial RVE length of 1 mm (the impact of this parameter is further investigated in Section 6.3.3). Figure 6.12 shows the resulting reaction force curves, where a significant reduction of the macro-scale mesh dependency is observed. This is related to the introduction of an intrinsic macro length-scale parameter, which regularises the softening problem at the specimen level. Employing second-order homogenisation also impacts the resulting strain distributions. As shown in Figure 6.13, the inclusion of the second-gradient of displacements prevents the occurrence of spurious deformation patterns, contrarily to what was observed with first-order homogenisation.

However, for the fine-macro, coarse-micro case, localisation was observed at the top of the specimen. This strain distribution is not representative of the response of ductile materials under uniaxial tension, and its occurrence is likely related to the adoption of a second-order continuum formulation at the macro-scale. As was mentioned in Section 6.1.2, the length of the RVE, in a multi-scale scheme based on second-order computational homogenisation, is linked with the macro-scale characteristic length-scale parameter. Nevertheless, the relation between these two quantities is influenced by the presence of nonlinearities. With this in mind, for this particular combination of macro- and micro-scale meshes, this RVE length probably yielded an excessive macroscopic characteristic length, which ceases to function just as a regularisation parameter, exerting a significant influence in the mechanical response of the specimen. This, in turn, leads to the localisation of strain at the top of the tensile test piece, where the displacement is applied, in spite of the geometrical perturbation and the symmetry conditions. The analysis presented in Section 6.3.3 discusses the occurrence of localisation at the top of the specimen in greater detail.

Furthermore, Figures 6.12 and 6.13 indicate that the micro-scale problem is still not regularised. This micro-scale mesh dependency is further illustrated in Figure 6.14, where the macro- and micro-scale response of the coarse-meshed tensile specimen are shown for the three RVE meshes. In this setup, there is a clearly observable dependency of the microscopic localisation band on the spatial discretisation of the RVE. Additionally, even for the same RVE mesh, the greater the degree of softening at the microscopic level, the less effective is the macro-scale regularisation with second-order homogenisation. This is observable in Figure 6.12, since the variability between reaction curves of the same macro-scale mesh increases with the refinemenet of the RVE discretisation. This seems to indicate that, in a coupled multi-scale simulation of softening, the mesh regularisation at the macro-scale cannot be entirely separated from the regularisation of the microscopic equilibrium problem.

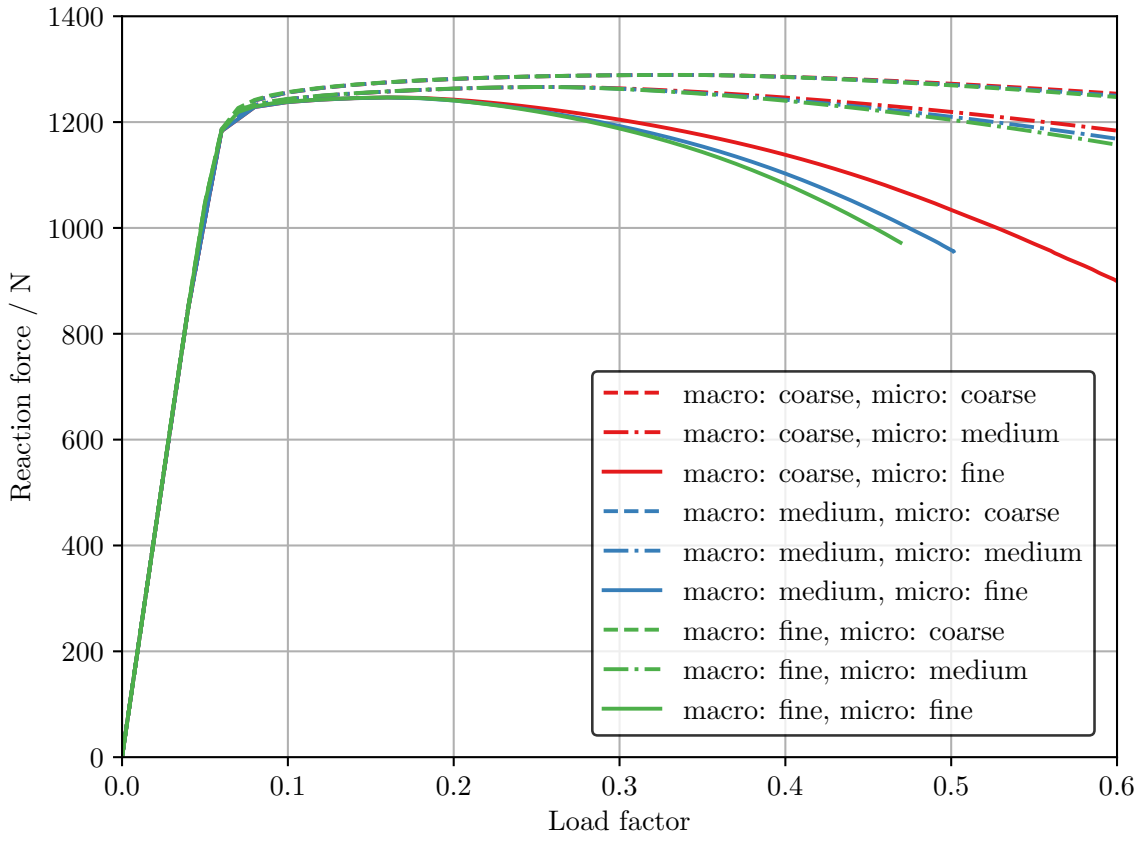

Figure 6.12: Reaction force curves obtained with second-order homogenisation for the tensile specimen, with the nine combinations of macro- and micro-scale meshes. Linestyle indicates the micro-scale mesh, while colour indicates the macro-scale mesh.

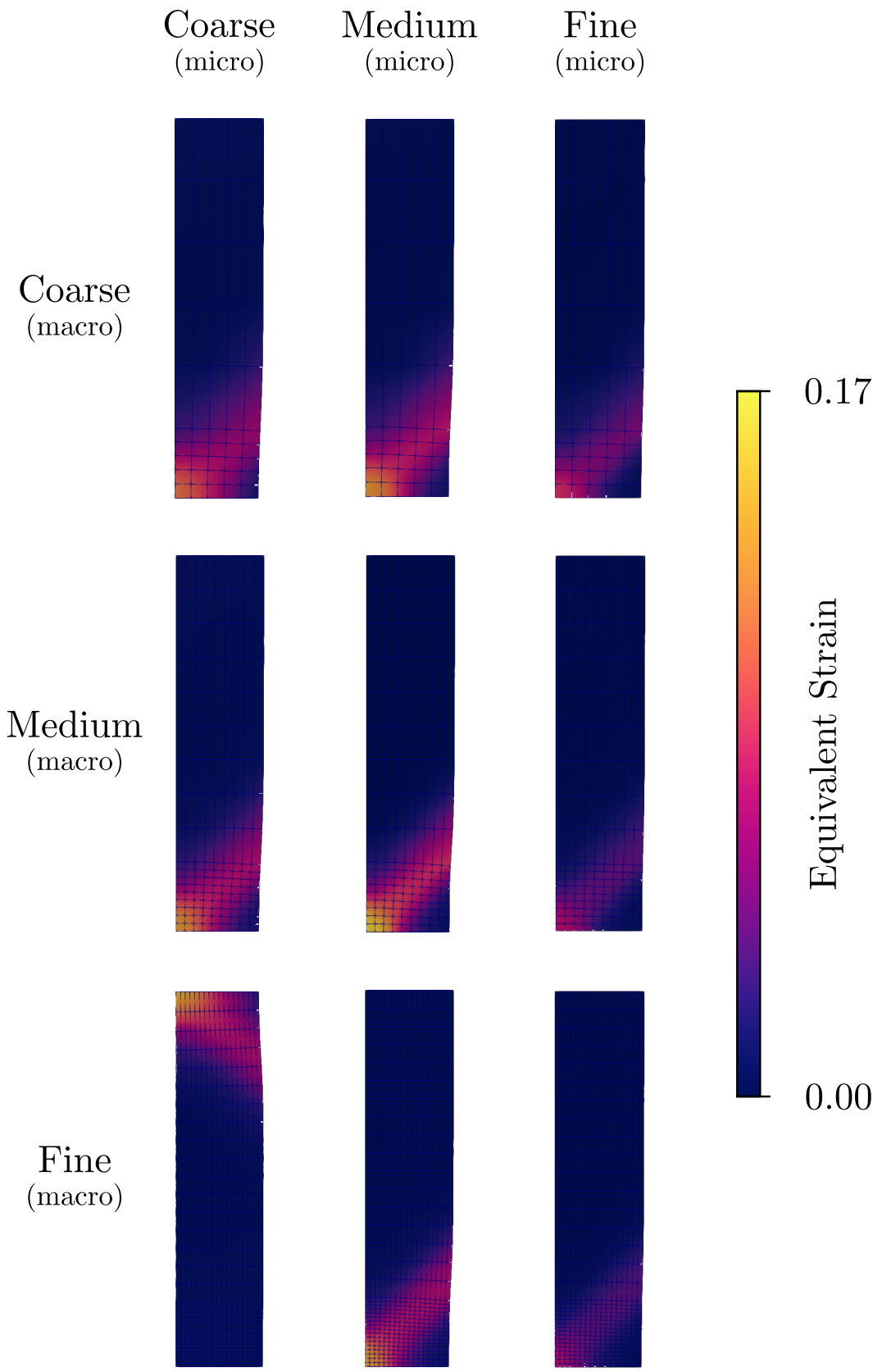

Figure 6.13: Equivalent strain distributions at failure obtained with second-order homogenisation for the tensile specimen, with the nine combinations of macro- and micro-scale meshes.

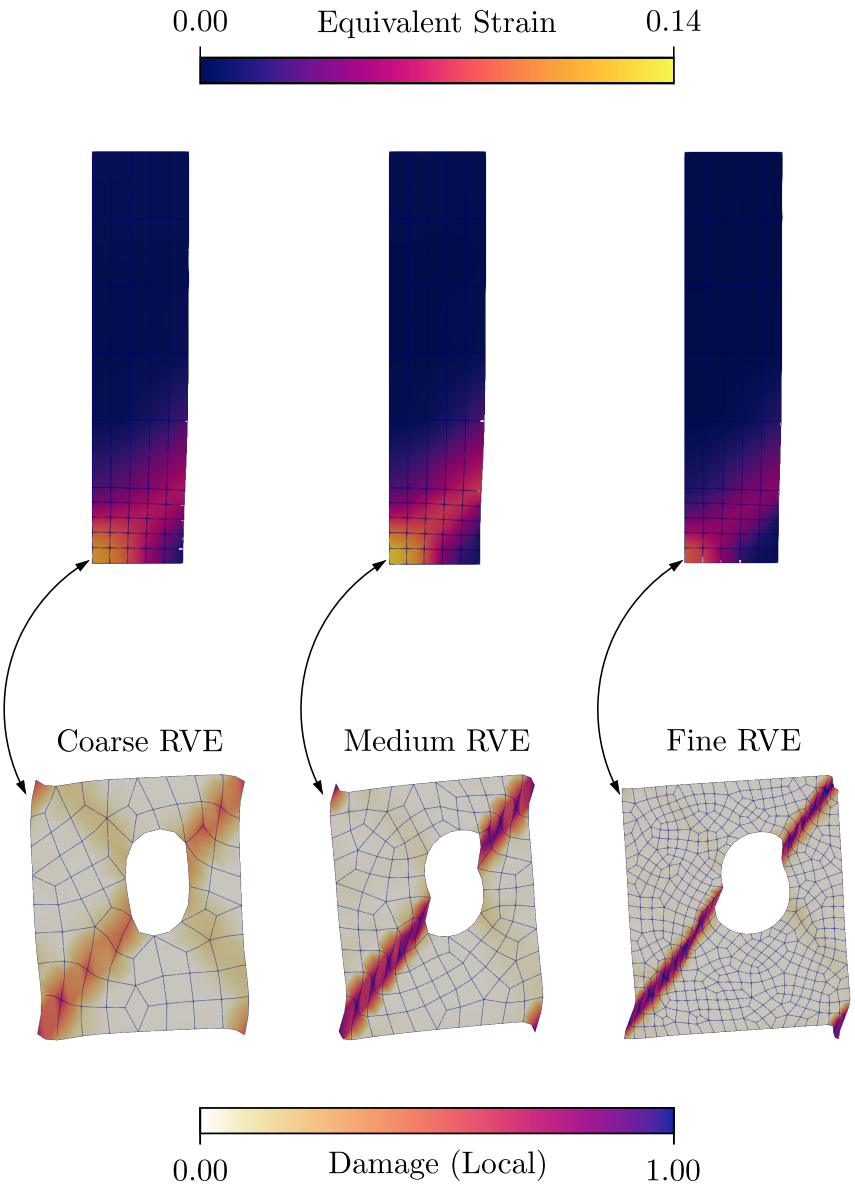

Figure 6.14: Micro-scale mesh dependency found with second-order homogenisation, shown through the damage distributions at failure, obtained with the coarse macro-scale mesh of the tensile specimen.

6.3.3 Impact of the RVE length on the second-order multi-scale response

As was discussed in Section 6.1.2, the length of the RVE in second-order homogenisation is deeply linked to the intrinsic length-scale introduced at the macroscopic level. Since this material parameter is key to the mesh regularising effect observed with second-order homogenisation, its impact on the mechanical response of the tensile test piece is assessed here. In this section, the second-order multi-scale simulations of the tensile test piece were repeated considering different values of the RVE length, but keeping the generalised RVE size constant, meaning that the same RVE from Figure 6.4 was employed.

Figure 6.15 depicts the reaction curves obtained for a range of RVE length values, for the medium meshes at the macro- and micro-scales. The increase in the RVE length is clearly linked to a de-

crease in the degree of softening observed in the global mechanical response of the specimen. In fact, for an RVE length of 10 mm, almost no softening is observed. To further illustrate the influence of the RVE length on the macroscopic characteristic length, Figure 6.16 shows the equivalent strain distributions found for some of the l_{RVE} values. For this combination of macro- and micro-scale meshes, RVE lengths below 1 mm are shown to lead to the expected localisation pattern. However, for values greater than 1 mm, localisation occurred at the upper region of the specimen, similarly to what had been reported in Section 6.3.2. Once again, the observation of these strain distributions is coincident with excessive values of the RVE length, which seems to corroborate the hypothesis suggested in Section 6.3.2. In the extreme case of an RVE length of 10 mm, the strain distribution is almost uniform, justifying the lack of significant softening seen in Figure 6.16. Furthermore, considering the dimensions of the specimen, shown back in Figure 6.7a, it becomes apparent that some of these values of RVE length are disproportionate. Regarding the use of second-order homogenisation for the regularisation of macro-scale problems, there is an upper bound for the RVE length, above which it ceases to serve this purpose. The definition of this upper bound, according to the previously discussed relation between the RVE length and macroscopic characteristic length, should vary according to the physical problem and its sources of nonlinearity. Nonetheless, regardless of its value, the upper bound may be defined as the maximum RVE length which results in physically admissible responses. Above this value, the adoption of a second-gradient continuum formulation fundamentally alters the mechanical behaviour of the material, instead of eliminating (or reducing) the dependency on the spatial discretisation of the macroscopic domain, leading to non-physical mechanical behaviour.

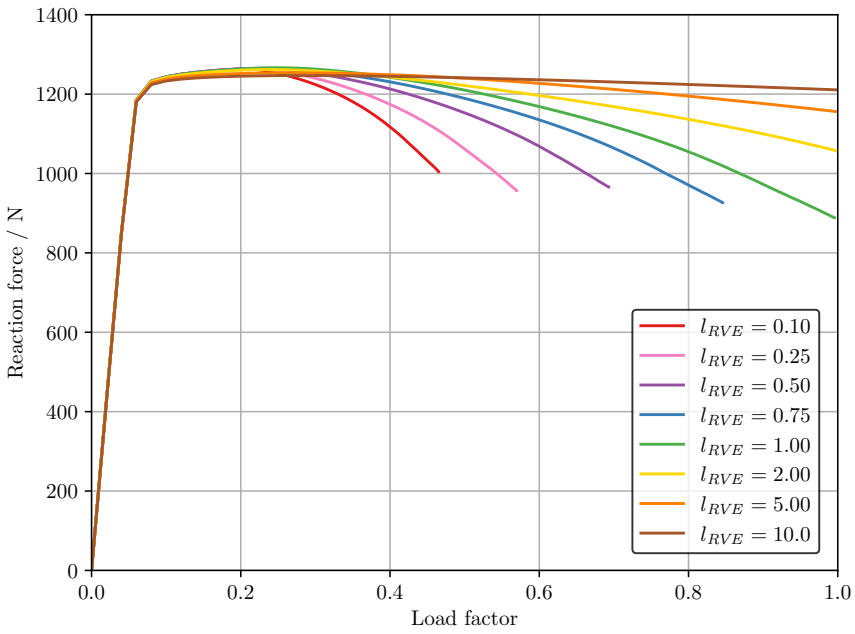

Figure 6.15: Impact of the RVE length on the mechanical response obtained with second-order homogenisation. Results obtained with the medium macro- and micro-scale meshes. RVE length expressed in mm.

Finally, to assess the lower bound of the RVE length for the regularisation effect of second-order homogenisation, Figure 6.17 compares the reaction curves obtained for various RVE lengths, and for the three discretisations of the tensile specimen. The response of the three meshes converged with the increase in the RVE length, highlighting the mesh-regularising effect of second-order homogenisation. Nevertheless, the rate of this convergence is also dependent on the characteristic size of each mesh. That said, from a theoretical standpoint, should the RVE length be low enough,

the second- and first-order homogenisation responses would coincide. The lower bound for this parameter to act as a macro-scale regularisation parameter is, thus, the minimum length for which macro-mesh dependency is eliminated or attenuated, to an acceptable degree.

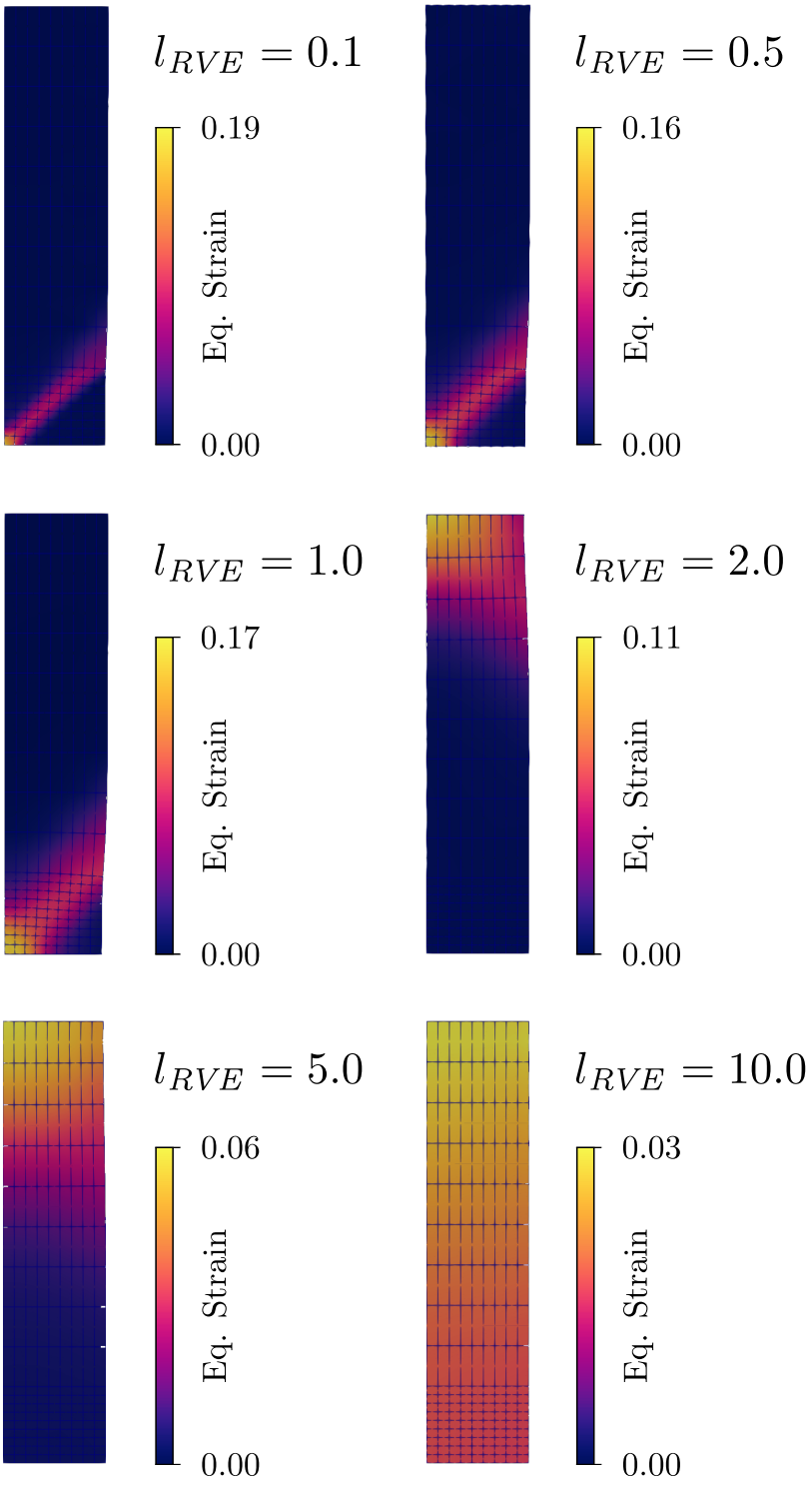

Figure 6.16: Impact of the RVE length on the equivalent strain distributions obtained with second-order homogenisation for the tensile test piece. Results for the medium macro- and micro-scale meshes. RVE length expressed in mm.

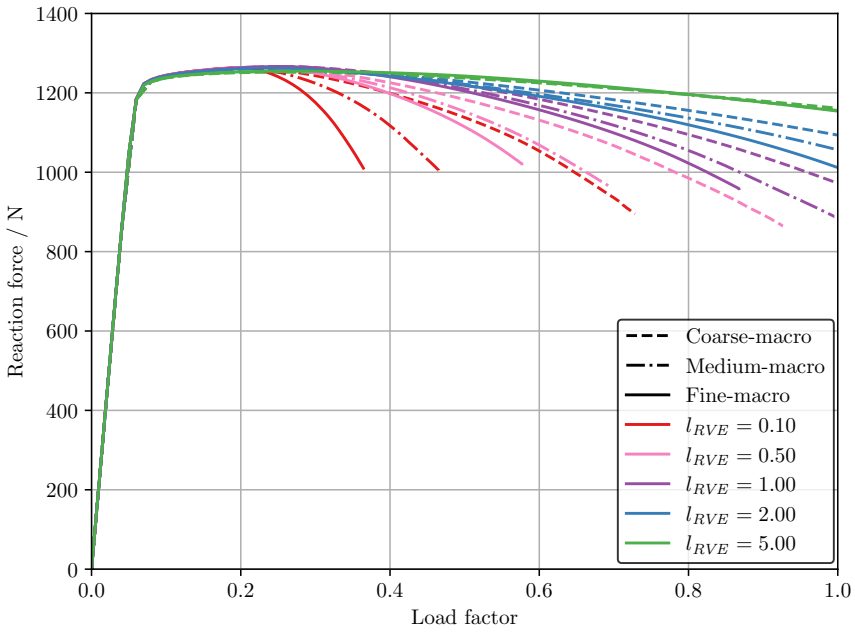

Figure 6.17: Comparing the impact of the RVE length on the mechanical response obtained with second-order homogenisation, for the three macro-scale meshes. Results obtained with medium RVE mesh. Linestyle indicates the macro-scale mesh, colour indicates the RVE length, expressed in mm.

6.4 Micro-scale mesh regularisation with integral nonlocal damage

The use of local damage and the presence of voids at the RVE level introduce material and geometrical nonlinearities in the micro-mechanical problem, respectively. It has been shown that, with this approach at the micro-scale, and using first-order homogenisation, there is mesh dependency at both scales. Furthermore, with the introduction of second-order homogenisation, the macro-scale is regularised, but mesh depdency remains at the RVE level. With this in mind, the introduction of nonlocal damage of integral type at the micro-scale is studied as a possible solution to this problem, bearing in mind that this can only directly reduce the mesh dependency caused by material softening.

To perform these studies, nonlocal damage of integral type at the micro-scale had to be correctly implemented within the the coupled code of the in-house finite element code, LINKS. An old version of the code for micro-scale nonlocal damage was already in place in the coupled structure of LINKS. However, in the context of this dissertation, it suffered major changes to accomodate the present features of the nonlocal damage model of integral type, mainly the possibility of adopting several nonlocal materials. The overall solution method of multi-scale problems with LINKS is presented in Section 6.4.1, along with the main steps for the compatibilisation of the nonlocal model implemented in Chapter 5 with the coupled code. Thereafter, a preliminary micro-scale regularisation study is reported in Section 6.4.2.

6.4.1 Implementation in LINKS^2

Section 5.4 presented a brief description of the implementation of a nonlocal damage model for macro-scale analysis. As was mentioned, this model was already available for micro-scale problems, but some additional changes were introduced to optimise the overall code structure. In order to employ these models at the RVE level in FE^2 analysis, it was necessary to introduce these routines

in the coupled code structure, hereupon referred to as LINKS^2. This did not require any additional theoretical or conceptual work (like the one presented in Section 5.3), but warranted the full compatibilisation of these routines with the coupled code structure, including the variable management strategy. That said, in what follows, the LINKS^2 strategy for the solution of large-strain multi-scale problems is briefly discussed, before outlining the necessary steps for the introduction of nonlocal damage for coupled analysis.

The works of Reis and Andrade Pires (2013), Rodrigues Lopes et al. (2018), Rodrigues Lopes et al. (2021) provide a detailed overview of the numerical scheme employed by LINKS^2 to find the solution for large-strain multi-scale problems based on computational homogenisation. In essence, the code makes use of an adaptive sub-incremental strategy at the RVE level to ensure the robustness and efficiency of the Newton-Raphson method in the multilevel finite element (ML-FEM) framework, in the presence of several sources of non-linearity. This strategy enlarges the convergence bowl of the Newton-Raphson procedure at the micro-scale, and allows larger macroscopic deformation gradients. It also significantly reduces the overall computational cost of ML-FEM analyses, while maintaining the quadratic rates of asymptotic convergence of the Newton-Raphson method at the macro-scale. Furthermore, LINKS^2 employs a master-slave scheme with dynamic scheduling to solve different parts of the multi-scale problem in separate central processing units (CPUs).

This master-slave algorithm naturally suits the nested structure of coupled multi-scale problems, and allows the parallelisation of FE^2 simulations. The master CPU deals with the global problem and distributes sub-problems among several slave processors, that work in parallel. In the context of coupled multi-scale simulations, the master is responsible for the solution of the macro-equilibrium problem and distributes the macro-Gauss points among the slaves, that solve RVE equilibrium problems and perform homogenisation in parallel. This procedure is illustrated in Figure 6.18.

With this in mind, the implementation of micro-scale nonlocal damage within the coupled code involved the following steps:

1. *Input data reading, allocations and initialisations*: the code blocks for reading the nonlocal input data, such as the value of the nonlocal radius, the nonlocal weighting function in use, and others, had to be included in the routine with which the master CPU reads such data in LINKS^2. Thereafter, the necessary memory was allocated for the storage of the input data, which also had to be introduced in the main routines for the solution of the micro-scale equilibrium problem.

2. *Master-slave variable broadcast*: since the solution of the microscopic problem is solved in a parallel fashion, some variables need to be broadcast from the master CPU, which loops over all RVEs to read their properties. In this context, the nonlocal input data has to be broadcasted from the master CPU to the slaves, before allocating the necessary arrays for the solution of the micro-problem with each slave.

3. *Micro-scale local-global interface routines*: for the solution of the microscopic equilibrium problem, LINKS^2 includes two interface routines, responsible for setting local micro-scale variables from global counterparts, and vice-versa. That being the case, in these routines, the global arrays of the nonlocal radius or the nonlocal material flags are converted into the local values of these variables, and vice-versa.

4. *Maximum number of non-zero elements of the stiffness matrix*: a formula similar to the one presented in Section 5.4, for the calculation of this variable, was introduced at the micro-scale for single-scale and coupled analysis, to avoid excessive memory usage.

Additionally, to simulate RVEs with nonlocal damage within a second-order multi-scale scheme, the routines for the assembly of micro-scale stiffness matrices for second-order boundary condition

types had to be compatibilised with the interface routines for computing the micro-scale stiffness in nonlocal cases.

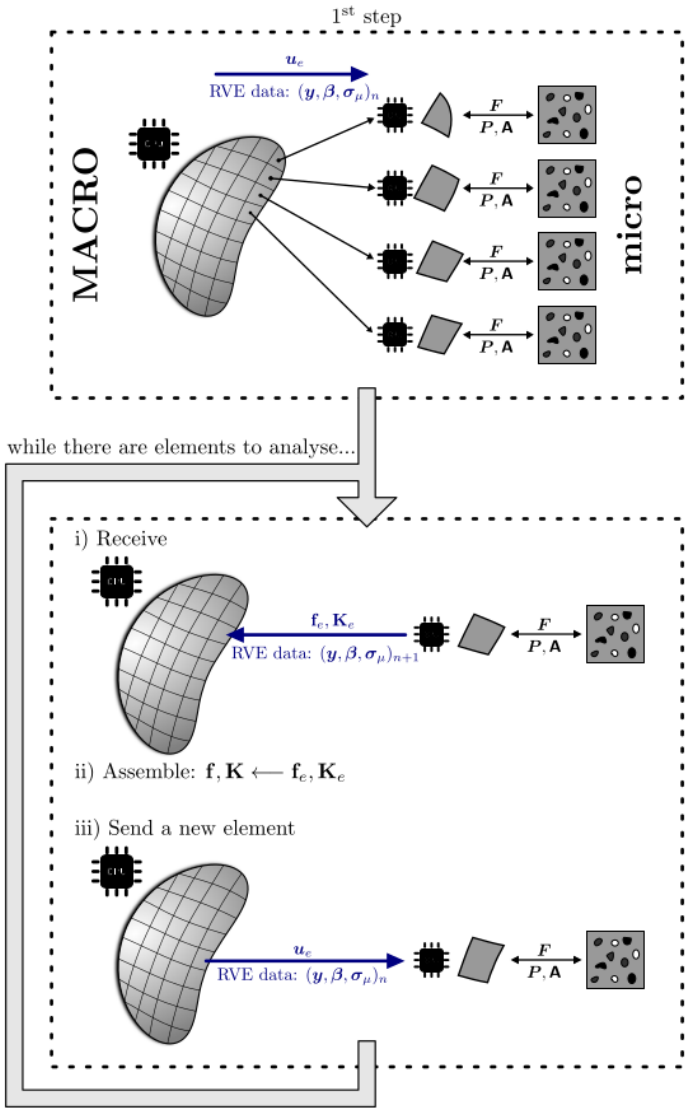

Figure 6.18: Schematic representation of the master-slave scheme with dynamic scheduling, employed in the parallelisation of the coupled multi-scale problem. Taken from Rodrigues Lopes et al. (2018).

6.4.2 Preliminary micro-mechanical analysis

Before assessing the regularisation of the micro-scale problem, different values of the nonlocal radius were tested for each mesh (same RVE meshes shown in Figure 6.4). The macroscopic deformation gradient history at a Gauss point near the bottom-left tip of the tensile specimen was retrieved from the first-order coupled simulation of the coarse-medium case, to provide a realistic deformation path for the single-scale simulations of the RVEs. In these cases, the value of the nonlocal radius is expressed as a fraction of the RVE length.

The results for the coarse, medium and fine microscopic meshes are shown in Figure 6.19, Figure 6.20 and Figure 6.21, respectively, and highlight the impact of the nonlocal radius on the mechanical response of the porous microstructures. In general, as the value of the nonlocal radius increased, its effect on the micro-mechanical response of the RVE decreased. This is due to the fact

that, after a certain point, the RVEs no longer experienced significant softening, thus the effect of further increasing the nonlocal radius was reduced.

Adding to this, the computational times recorded for the aforementioned simulations are reported in Table 6.2. Greater values of the nonlocal radius bring about an exponential increase in the computational cost of simulations, for all three meshes. However, the mesh refinement is also a relevant factor. For the coarse RVE, the computational time increases around 18 and 4.5 times, from the local case and a nonlocal radius of 0.1 to a radius of 0.3, respectively. For the fine RVE, these increases are of 111 and 6.5 times, highlighting the significant effect of combining a finer mesh with a larger nonlocal radius. Similar effects had already been observed in Chapter 5, and are due to the inclusion of more integration points in the nonlocal averaging domain. Nonetheless, this has particular importance in this context, since these RVEs are set to be employed in coupled multi-scale analyses, where computationally demanding micro-mechanical models lead to cumbersome simulation times, since they take part in the solution of the constitutive behaviour of every Gauss point of the macroscopic domain.

Considering the fact that, for each of the three meshes, increasing the nonlocal radius above 0.2 yielded little effects in the global RVE response, and the computational burden of increasing the value of this parameter, the regularisation of the micro-scale problem was studied for the following values: 0.1 and 0.2. The results are depicted in Figures 6.22 and 6.23, where stress-strain curves and the damage distributions found for the three meshes are shown, for the local and nonlocal approaches. Figure 6.22 shows that increasing the value of the nonlocal radius reduces the degree of softening and mesh dependency. Considering that geometrical nonlinearities, inherent to porous RVEs, have not been addressed by the introduction of damage averaging, the stress strain curves obtained with the nonlocal model show a reasonable degree of regularisation, particularly for a nonlocal radius of 0.2. Additionally, Figure 6.23 also highlights the significant differences observed with local and nonlocal approaches. With the former, strain and damage localisation is completely mesh-dependent, and unitary damage was reached with all three meshes, for damage localisation bands with distinct thicknesses. With the latter, the maximum damage is greatly reduced, due to the presence of nonlocal averaging, and, for a nonlocal radius of 0.2, the damage distributions of the three RVEs are essentially identical. Building on these conclusions, and also bearing computational cost in mind, 0.2 was adopted as the preferred value of the nonlocal radius for the coupled analyses presented in Section 6.5.

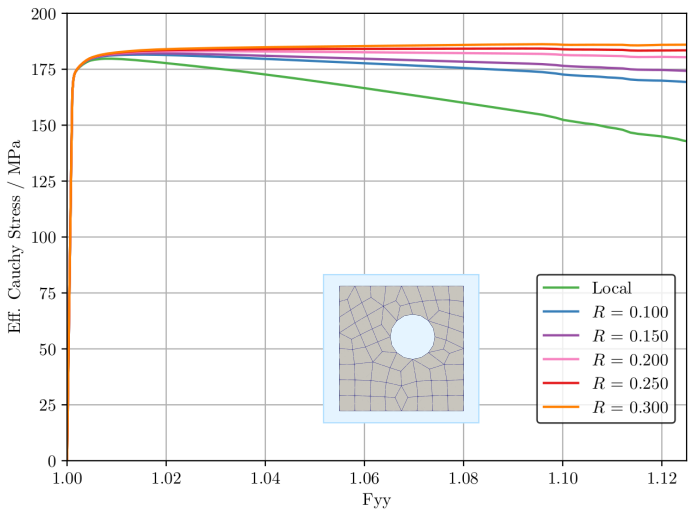

Figure 6.19: Stress-strain curves obtained with different values of the nonlocal radius, for the coarse micro mesh.

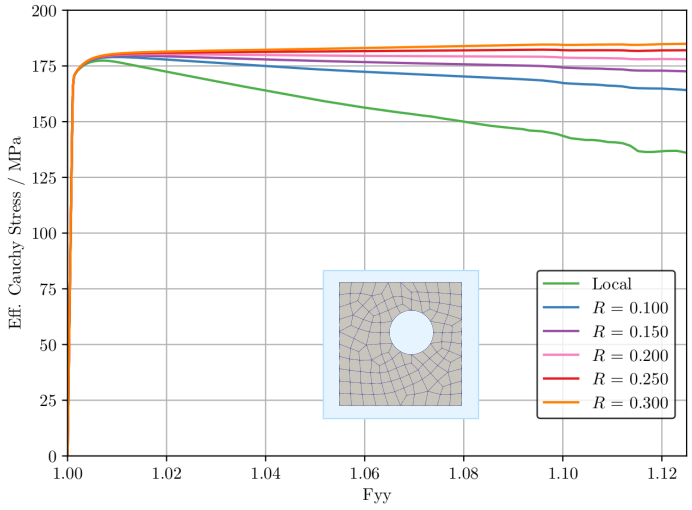

Figure 6.20: Stress-strain curves obtained with different values of the nonlocal radius, for the medium micro mesh.

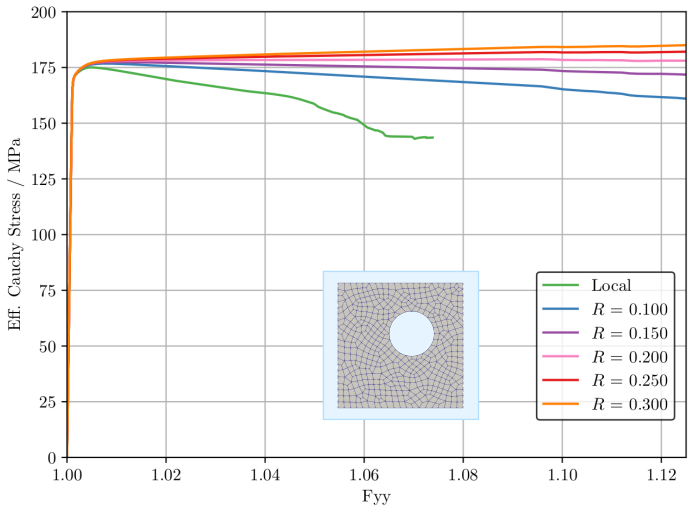

Figure 6.21: Stress-strain curves obtained with different values of the nonlocal radius, for the fine micro mesh.

Table 6.2: Computational times recorded for the micro-mechanical simulations of the Porous RVEs with different values of the nonlocal radius. Time measures expressed in seconds.

		Nonlocal radius		
RVE mesh	Local	0.1	0.2	0.3
Coarse	5	20	55	89
Medium	10	61	145	287
Fine	40	682	2631	4442

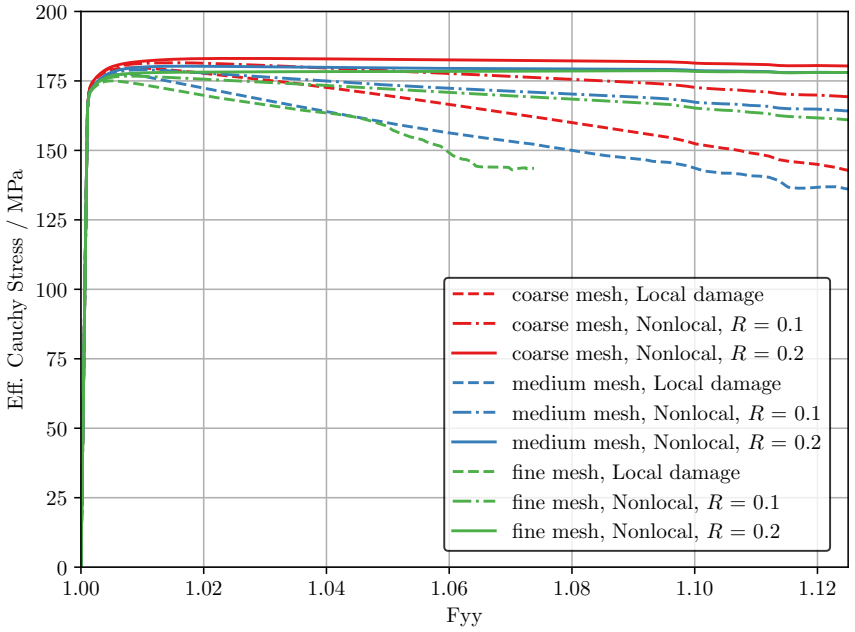

Figure 6.22: Effects of introducting nonlocal averaging in the stress-strain curves obtained for each micro-scale mesh. Colour indicates the micro-scale mesh and linestyle indicates the nonlocal radius value.

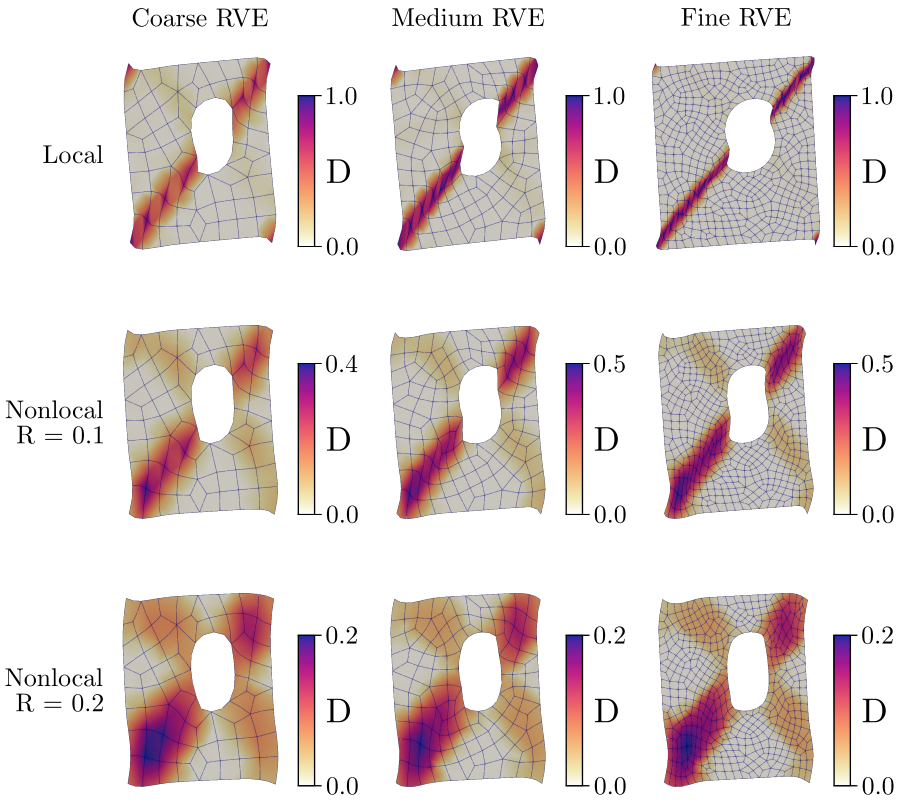

Figure 6.23: Effects of introducing nonlocal averaging in the resulting damage distributions at the micro-scale.

6.5 Multi-scale analysis with nonlocal RVE damage

Having studied the mesh regularisation of the micro-scale problem in a single-scale approach, the effects of introducing nonlocal damage of integral type at the RVE level within a coupled multi-scale scheme are presented here. In Section 6.5.1, this is done with first-order computational homogenisation, and the possibility of regularising the softening problem at one scale without addressing the other is discussed. Finally, microscopic nonlocal damage is introduced with second-order homogenisation, and the results are reported in Section 6.5.2.

6.5.1 First-order multi-scale analysis

The analysis presented in Section 6.3.1, demonstrated that utilising first-order computational homogenisation schemes to model multi-scale localisation problems does not guarantee obtaining the correct deformation pattern (see illustration in Figure 6.10). Out of the nine cases depicted in Figure 6.9, only two captured the expected X-type strain band. Therefore, it was demonstrated that macro-scale mesh dependency not only influenced the global mechanical response of the specimen and the width of the deformation band, but also the resulting localisation pattern.

The nine simulations were repeated for a nonlocal radius of 0.2 mm. Figure 6.24 depicts the localisation bands observed for the various combination of meshes. The introduction of nonlocal damage, led to different strain distributions, none of which resembles the X-type band. These results raise questions on the possibility of regularising the RVE mesh if the macro-scale problem is still mesh-dependent, which implies that attaining the physical strain band for ductile failure is not guaranteed. In this particular case, obtaining these deformation patterns could be due to the fact that the micro-mechanical response does not undergo sufficient softening, as a result of an excessive value of the nonlocal radius. With this in mind, the simulations were repeated with a nonlocal radius of 0.1, which had also been tested in Section 6.4.2. The resulting localisation patterns for the nine cases are shown in Figure 6.25. With a reduced nonlocal radius, several X-type strain bands were observed. This could indicate that, with first-order homogenisation, a nonlocal radius of 0.2 produced excessively stiff RVEs, which, in turn, led to the localisation bands shown in Figure 6.24.

With a radius of 0.1, employing the coarse mesh at the macro-scale yielded three apparently physical strain distributions. Figure 6.26 showcases the reaction force curves attained for the coarse macro-scale mesh, with the three RVE meshes, using local and nonlocal damage. The introduction of nonlocal averaging at the micro-scale resulted in a reduction of the observed RVE mesh dependency, while also leading to a decrease in macroscopic softening. While the micro-scale problem does not seem to be fully regularised, the presence of unadressed geometrical nonlinearities, the adoption of a lower value of the nonlocal radius, and the mesh dependency still present at the macro-scale, could all contribute to this. Adding to this, the use of the medium RVE with the medium and fine meshes at the macro-scale also resulted in the X-type band, which had not been found with local damage (see Figure 6.9). Figure 6.27 depicts the reaction force curves for the three macroscopic meshes, using the medium RVE and both local and nonlocal damage. In this case, the employment of a nonlocal damage model at the micro-scale, by reducing the degree of microscopic softening, avoided spurious strain modes. Nevertheless, the global response of the tensile specimen was still largely dependent on its discretisation.

In Section 6.3.2, it had been observed that effectively regularising the macro-scale cannot be separated from mesh-dependent effects at the RVE level. However, introducing the second-gradient of macroscopic displacements largely prevented the occurrence of spurious deformation modes. In this case, although introducing nonlocal damage at the micro-scale undoubtedly reduces the likelihood of mesh-dependent localisation, several factors come into play and, in some cases, its effects on the macro-scale response were unexpected. Since the use of first-order homogenisation does not guarantee that the desirable localisation pattern is attained, a varied set of strain distributions was reported in this section. On the one hand, this is another demonstration that mesh regular-

isation or dependency at both length-scales cannot be entirely separated. However, regularising the micro-scale mesh while the macroscopic problem is still prone to spurious localisation is particularly troublesome, as shown here. On the other hand, the localisation patterns found with a nonlocal radius of 0.1 show that the degree of RVE softening also influences the arisal of spurious strain modes. With local damage, since the RVEs were more prone to localisation, the tensile specimen was also more likely to experience such strain modes, instead of the X-type shear band.

These results further emphasise the deep connection between the various mesh-dependent effects present at each length-scale. Introducting a micro-mesh regularisation strategy does not guarantee attaing physically meaningful localisation bands, since the macro-scale boundary value problem is still ill-posed.

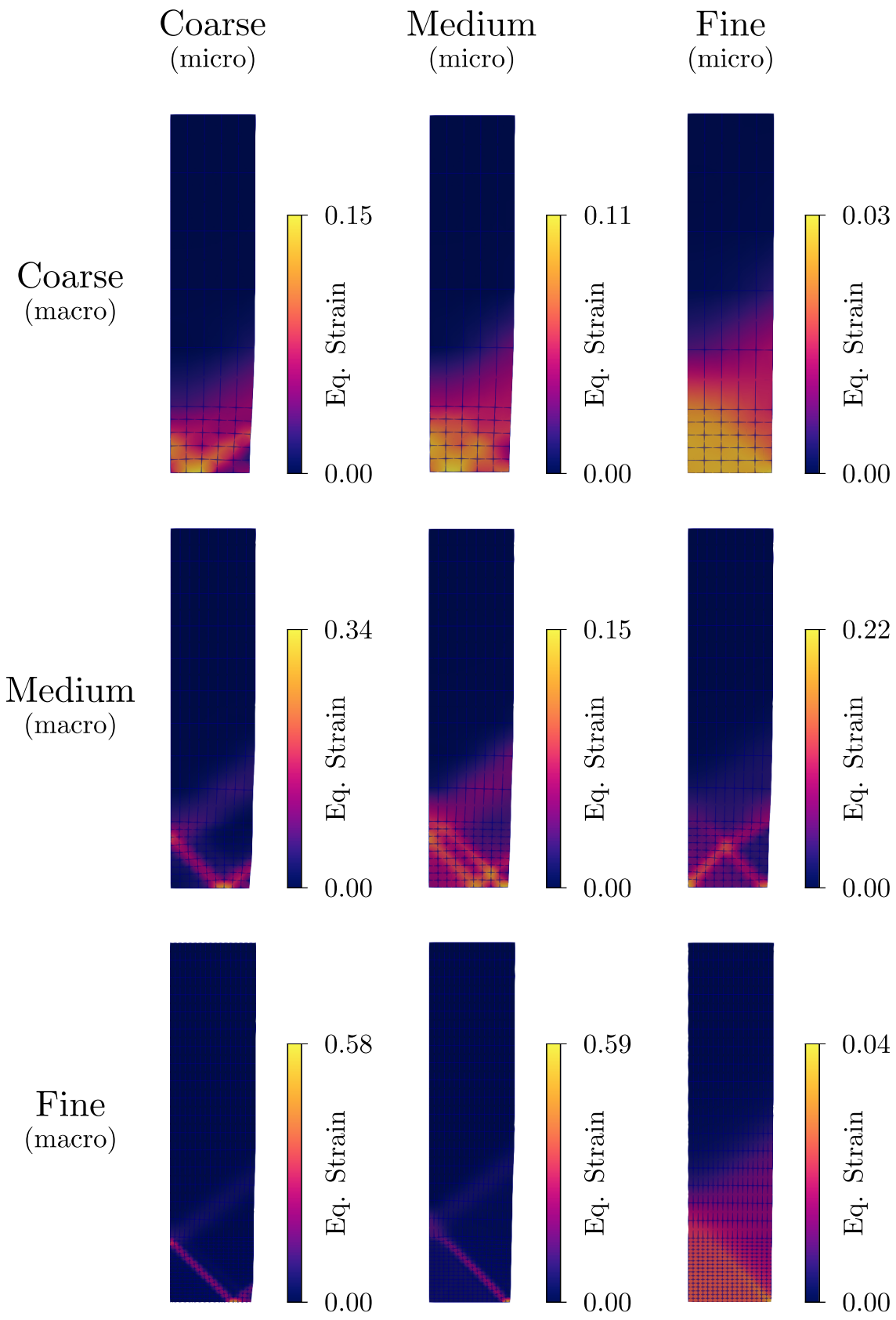

Figure 6.24: Equivalent strain distributions at failure obtained with first-order homogenisation and nonlocal RVE damage, with the nine combinations of macro- and micro-scale meshes and a nonlocal radius of 0.2.

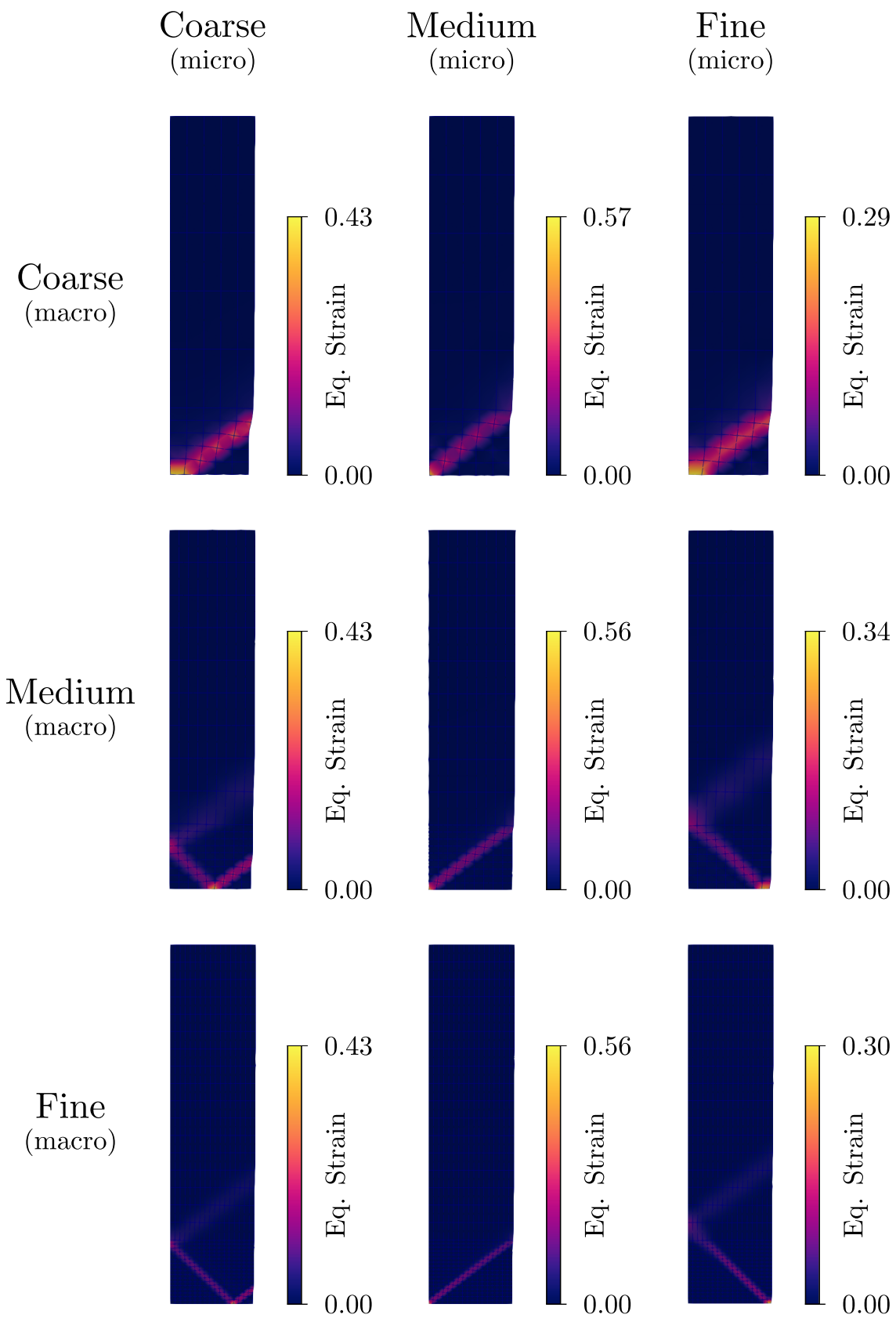

Figure 6.25: Equivalent strain distributions at failure obtained with first-order homogenisation and nonlocal RVE damage, with the nine combinations of macro- and micro-scale meshes and a nonlocal radius of 0.1.

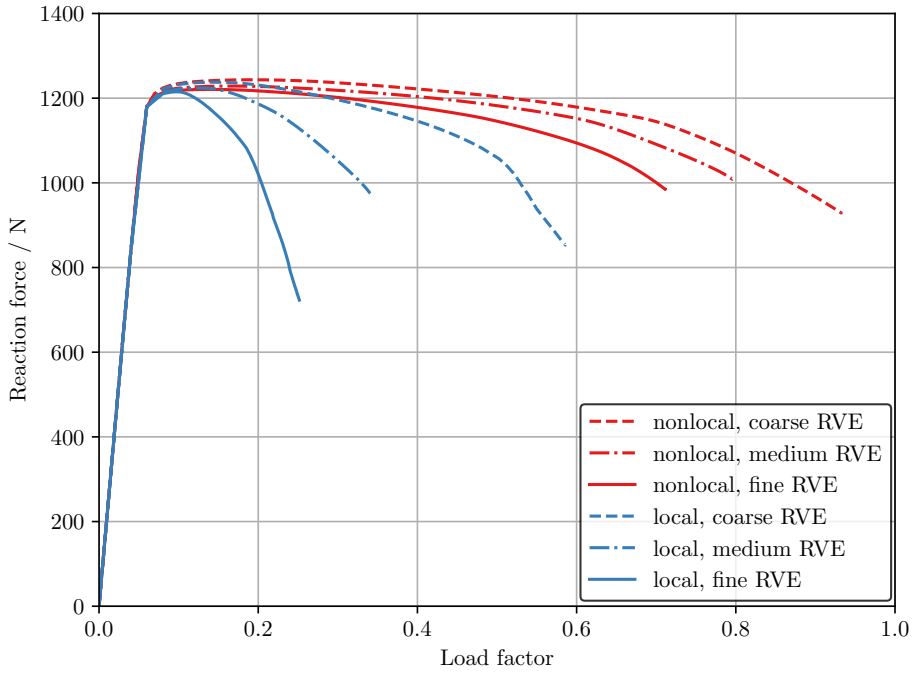

Figure 6.26: Reaction force curves obtained with first-order homogenisation, for the three RVEs with the coarse macroscopic mesh, with local and nonlocal damage. Results obtained for a nonlocal radius of 0.1.

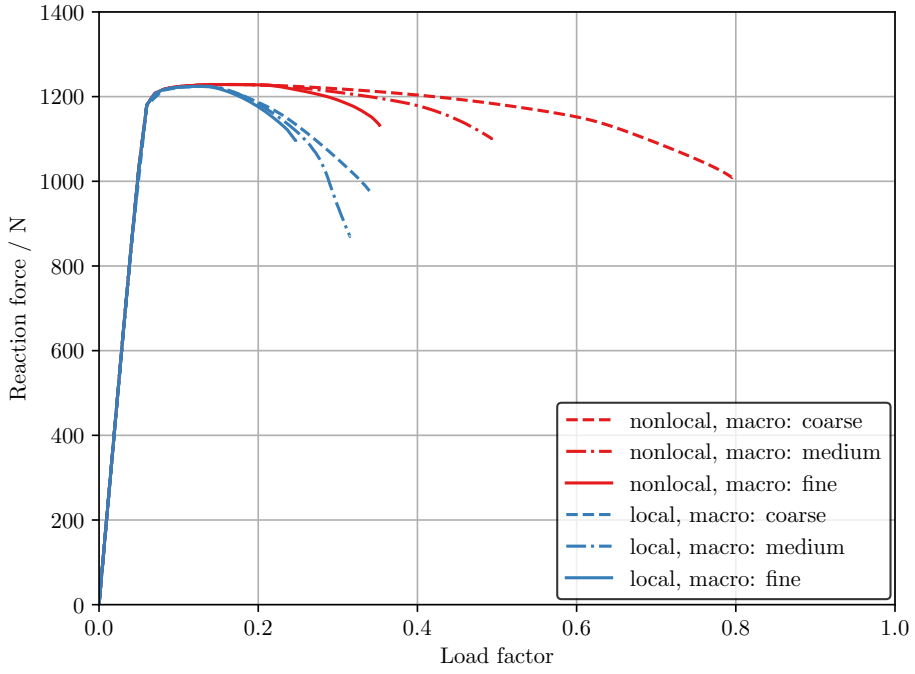

Figure 6.27: Reaction force curves obtained with first-order homogenisation, for the three macroscopic meshes with the medium RVE, with local and nonlocal damage. Results obtained for a nonlocal radius of 0.1.

6.5.2 Second-order multi-scale analysis

In this section, the nine combinations of macro- and micro-scale meshes were simulated with second-order computational homogenisation and nonlocal damage. The first set of numerical parameters was comprised of an RVE length of 1 mm and a nonlocal radius of 0.2 mm, at the RVE level. Figure 6.28 depicts the resulting reaction force curves, with a remarkable agreement between the nine cases. In comparison with the results of Section 6.3.2, where local RVE damage was assumed, the degree of micro-scale mesh dependency was greatly reduced. This is further illustrated in Figure 6.29, where the macroscopic strain distributions for the coarse macro-scale mesh are shown, along with the resulting damage contour, for the three RVE meshes, at the tip of the specimen. In this case, there is a greater degree of strain distribution, which could imply that the adoption of a nonlocal damage model at the micro-scale, for the same RVE length, yielded a larger macroscopic characteristic length, due to the reduced level of softening. Considering the damage distributions shown in Figure 6.29, the significant reduction in macro- and micro-mesh depdency could also be linked to a reasonable decrease in the observed macro-scale softening. That being the case, and recalling the fact that this nonlocal radius value was seen to lead to spurious strain modes in Section 6.5.1, the simulation of the tensile specimen was repeated, for the nine mesh combinations and the following two sets of numerical parameters: a 1 mm RVE length and a 0.1 mm RVE nonlocal radius, which was seen to produce significantly different macro-responses in Section 6.5.1, in comparison to a radius of 0.2 mm; and a 0.5 mm RVE length, with a 0.05 mm nonlocal radius, i.e. still 10% of the RVE length. The resulting reaction forces are plotted in Figures 6.30 and 6.31, for the RVE lengths of 1 and 0.5 mm, respectively. The adoption of the two alternative numerical parameter sets yielded reaction curves essentially identical to the ones obtained for the original RVE length and nonlocal radius.

On the one hand, these results showcase the importance of addressing mesh dependency at both scales, since the simultaneous regularisation of both scales led to practically coincident responses for the nine different setups strengthens the argument that the mesh-dependent and regularising effects at each length-scale are not entirely separable. Furthermore, the fact that modifying the value of the RVE length led resulted in negligible changes in the reactions could indicate that, for a mesh-regularised RVE model, the second-order macro-response converges faster with the RVE length (recall discussion in Section 6.3.3). On the other hand, this reduction in the micro- and macro-mesh dependency is likely inseparable from the reduced degree of softening observed here. With this in mind, these conclusions should be put to the test for a more adequate loading scenario, since, in the absence of spurious localisation, either at the micro- or macro-scale, or at both, the displacement applied to the tensile specimen did not result in significant softening. However, such analysis could not be carried out in time due to computational time concerns.

Finally, from the observation of Figures 6.28 and 6.29, the few deviations that still exist between the nine responses are linked to micro-scale considerations. This could be due to the previously mentioned geometrical nonlinearities, inherent to the microstructure of porous RVEs, which are not addressed by the regularisation strategy adopted at this length-scale, since nonlocal averaging only explicitly controls the distribution of damage. Secondly, the value of the micro-scale nonlocal radius could still be increased to reduce these deviations. Nonetheless, the combination of these and other factors resulted in very minor differences between the nine responses, and the employment of a mesh regularisation strategy at each scale has proven successful, within the previously discussed caveats.

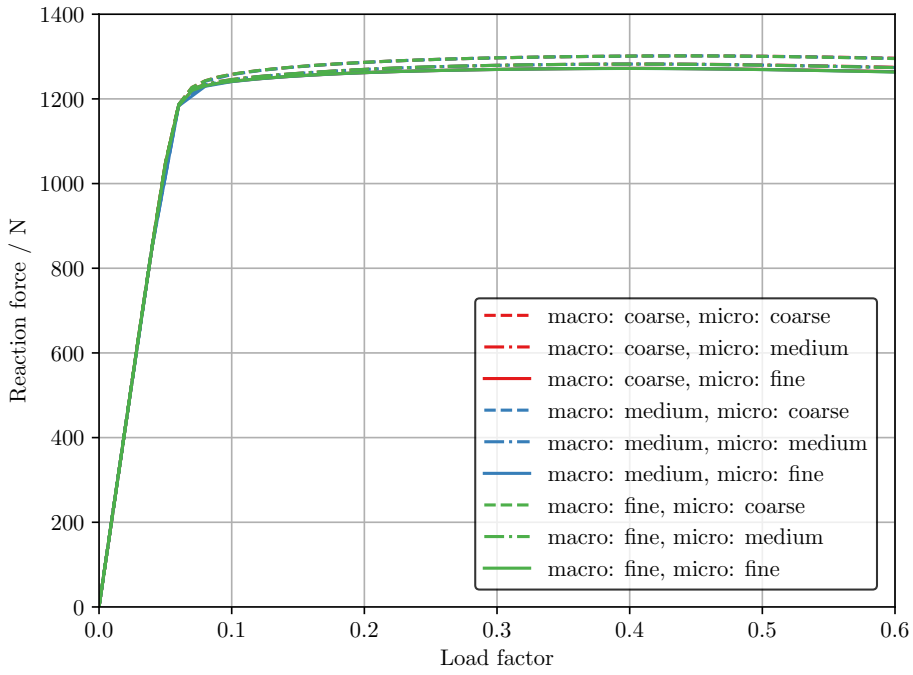

Figure 6.28: Full regularisation of the multi-scale problem with the introduction of nonlocal damage at the micro-scale, with a nonlocal radius of 0.2 mm, using second-order homogenisation. An RVE length of 1 mm was adopted.

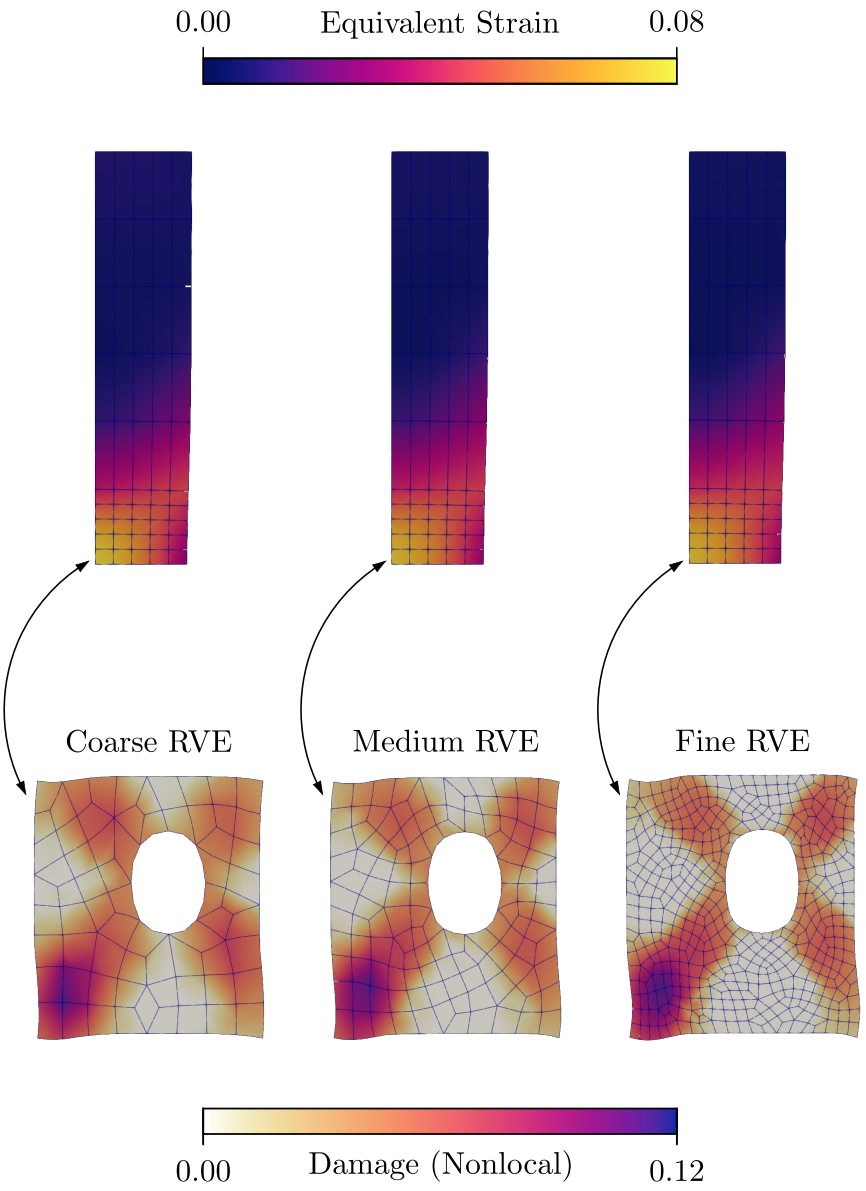

Figure 6.29: Multi-scale mesh regularisation obtained with second-order homogenisation and nonlocal damage at the microscopic level, shown through the damage distributions at failure, found with the coarse macro-scale mesh of the tensile specimen.

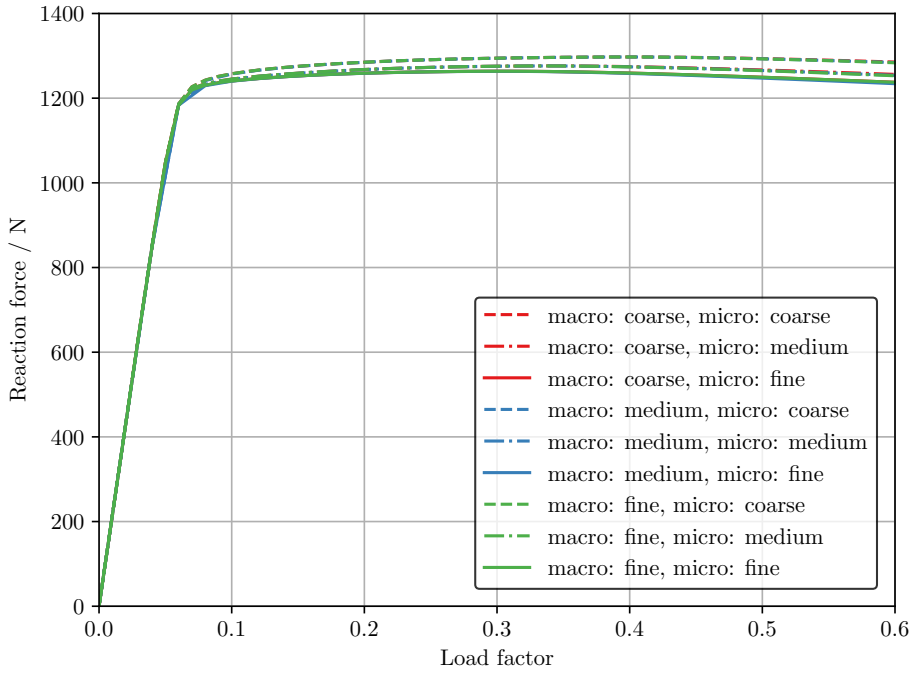

Figure 6.30: Full regularisation of the multi-scale problem with the introduction of nonlocal damage at the micro-scale, with a nonlocal radius of 0.1 mm, using second-order homogenisation. An RVE length of 1 mm was adopted.

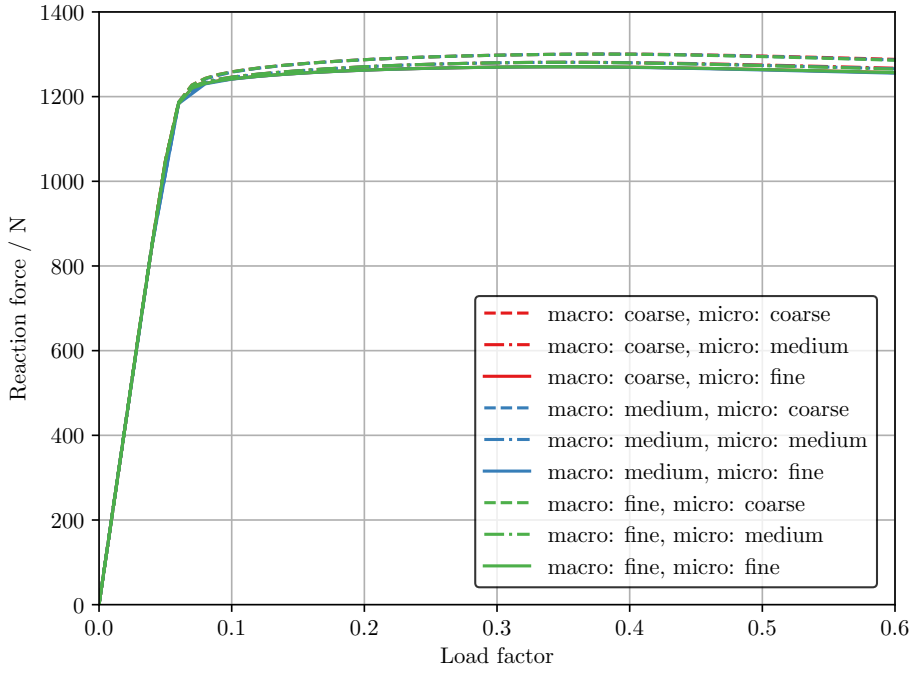

Figure 6.31: Full regularisation of the multi-scale problem with the introduction of nonlocal damage at the micro-scale using second-order homogenisation with an RVE length of 0.5 mm and a nonlocal radius of 0.05 (0.1 × 0.5) mm.

6.6 Discussion

This chapter presented numerous multi-scale simulations of softening and ductile damage, adopting first- and second-order computational homogenisation. The first-order FE^2 predictions obtained with RVE local damage, reported in Section 6.3.1, showcased several issues, including spurious mesh-dependent localisation, but also the arisal of non-physical localisation bands. In addition, the observed mesh dependency was not limited to the macro-scale, with the multi-scale reaction curves and strain contours depending on the spatial discretisation of the RVE. Conversely, with the adoption of second-order computational homogenisation in Section 6.3.2, a significant reduction in the macro-mesh dependency was observed. As discussed in Kouznetsova (2002), the characteristic macro length-scale parameter, associated to the second-order continuum formulation, regularises the softening problem at the specimen level. The appearance of non-physical strain bands was also circumvented with the adoption of the second-order multi-scale model. However, the micro-scale problem was still not regularised, and the macro-mesh dependency of the second-order FE^2 predictions (Figure 6.12) was seen to slightly increase for the finer RVE meshes, associated with a higher degree of softening. This underscores the interdependence of mesh-dependent and mesh-regularising effects at both length-scales.

A more detailed study on the impact of the RVE length on the second-order multi-scale response of the tensile specimen was reported in Section 6.3.3. Greater values of this numerical parameter were seen to substantially reduce the observed level of softening, while, for some extreme cases, localisation did not occur and softening was eliminated altogether. These values of the RVE length were seen to result in non-physical responses of the tensile specimen, and were deemed excessive. Additionally, the second-order FE^2 predictions of the three macro-meshes were seen to converge with the increase in the RVE length. In light of these facts, the following bounds for treating the RVE length as a numerical macro-regularisation parameter were defined:

1. Upper bound: the maximum RVE length which results in physically admissible responses;

2. Lower bound: minimum RVE length that attenuates macro-mesh dependency to a minimum acceptable degree.

Furthermore, to tackle the micro-mesh dependency of the FE^2 responses, nonlocal damage was introduced at the RVE level in Section 6.5, after some preliminary micro-mechanical studies in Section 6.4.2. With first-order homogenisation, this was seen to produce unexpected outcomes, with additional spurious strain modes appearing at the macro-scale for a nonlocal raidus of 0.2 mm, as shown in Section 6.5.1. For a nonlocal radius of 0.1 mm, X-type strain bands were recovered for some combinations of meshes, indicating that the previous nonlocal radius likely yielded an excessively stiff micro-response, for this particular multi-scale setup. Notwithstanding, these results highlighted, once more, the dependence of multi-scale mesh-dependent effects. In said setting, since the macro-scale problem was ill-posed, although mesh dependency was largely limited at the micro-scale, there was no guarantee of obtaining the physical localisation band and, thus, regularising the multi-scale response with respect to the micro-mesh.

With nonlocal damage at the RVE level and second-order homogenisation linking the scales, macro- and micro-mesh dependency were both greatly reduced (Section 6.5.2). That said, this was accompanied by a significant decrease in macro-softening, which is the primary factor driving mesh-dependent effects at this length-scale. With this in mind, the simulations were repeated for i) a lower value of the nonlocal radius, and ii) for both lower values of the RVE length and nonlocal radius. Practically identical FE^2 responses were found for the alternative values of the regularisation parameters, implying that the value of the prescribed displacement, which remained unchanged throughout the whole chapter, could be insufficient to promote reasonable macro-softening in the absence of spurious localisation at both scales. Nonetheless, the extent of multi-scale regularision observed in this case, where dependency was tackled at the two scales simultaneously, contrasting

with the remaining examples, seems to strengthen the argument that the presence and elimination of these effects at both scales are interdependent. Finally, the fact that the second-order responses obtained for the two RVE length values were identical, with the presence of nonlocal damage at the micro-scale, demonstrates that the convergence of the second-order FE^2 predictions with the value of the RVE length is dependent on the micro-response. Indeed, the convergence of second-order multi-scale predictions is related to the value of the characteristic length-scale parameter, whose relation with the RVE length is affected by several factors, including the macro-scale loading scenario, but also the micro-constitutive response. Hence, for a micro-scale model less prone to localisation and softening, the FE^2 predictions of different macro-meshes should converge for lower values of the RVE length, in comparison to a mesh-dependent micro-response.

CHAPTER 7

RELATING NONLOCAL DAMAGE OF INTEGRAL TYPE AND SECOND-ORDER HOMOGENISATION

7.1 On the comparison of macro-scale regularisation strategies

In single-scale mechanical problems where strain localisation occurs, nonlocal averaging strategies can prevent pathological mesh dependency, as shown in Chapter 5. This kind of strategy cannot be employed in more complex multi-scale simulation schemes to regularise macro-scale mesh dependency. Alternatively, regularisation can be achieved by employing second-order homogenisation, as demonstrated in Chapter 6. Both strategies, despite their significant differences, share a common trait: the introduction of an intrinsic material length parameter. On the one hand, in nonlocal damage models of integral type, this parameter is the nonlocal radius, that explicitly defines a nonlocal domain for each Gauss point the structure, within which damage averaging occurs. In the context of this dissertation, since nonlocal models with evolving nonlocal parameters were not considered, this macroscopic length-scale remains constant throughout the entire deformation path. On the other hand, second-order homogenisation implicitly introduces a macro-characteristic length, through the adoption of a second-gradient continuum formulation. This macroscopic length-scale, in turn, is known to be deeply related to the RVE length (as extensively discussed in Chapter 6). The introduction of these macroscopic length-scales plays a crucial role in the elimination of mesh dependency and determine the extent to which regularisation and strain redistribution occurs. In the present chapter, these two macro-scale regularisation strategies are compared, to the extent that such comparison is possible, considering the significant differences between single-scale nonlocal damage and a multi-scale model based on second-order homogenisation.

In Chapter 6, the limits of utilising the RVE length as a numerical parameter for macro-mesh regularisation were discussed. It was concluded that there exists an upper bound, above which the value of the RVE length becomes excessive, resulting in a macroscopic characteristic length which ceases to act as a regularisation parameter and fundamentally alters the mechanical response of the material. However, since the relation between the RVE length and this macro-regularisation parameter is dependent on several macro- and micro-scale factors, defining a numerical value for this upper bound is not trivial. In regards to its lower bound, it was demonstrated that for excessively low values of the RVE length, mesh-dependent localisation is not attenuated to an acceptable degree, even though, once again, it was not possible to define this lower bound numerically.

In the case of nonlocal damage of integral type, implemented and analysed for macroscopic problems in Chapter 5, there is a clear lower bound for regularisation, which is dependent on the characteristic size of the finite element discretisation. If the value of the nonlocal radius is lower than all distances between integration points, all nonlocal circumferences in the domain would only include the respective points, recovering the local damage case. For excessively large values of the nonlocal radius, the regularisation effect is not lost, contrarily to what is found with second-order homogenisation. However, several issues arise, particularly regarding the loss of sparsity of the stiffnes matrix and the resulting increase in computational cost, as well as the resulting damage distributions, which do not seem to bear much physical resemblance. That said, although there is no upper bound for the macro-regularisation parameter, after a certain value of the averaging radius, the physical meaning of the predictions obtained with nonlocal damage of integral type is questionable.

Taking these aspects into account, this chapter presents an optimisation-based strategy to relate the regularisation of macroscopic localisation problems with second-order homogenisation and nonlocal damage. The relationship between the nonlocal radius in integral approaches and the RVE length in 2nd order homogenisation is analysed. In essence, the FE^2 predictions documented in Chapter 6 were employed as the reference for the calibration of the macroscopic nonlocal damage model of integral type. This way, by calibrating the nonlocal model using the multi-scale responses for RVE lengths, the values of the regularisation parameters introduced by the two macro-scale regularisation strategies could be related. That said, the proposed calibration setup, illustrated in Figure 7.1, is comprised of two main steps:

1. Firstly, the parameters of the local Engelen model (recall its full description back in Section 5.2.2) are calibrated using the multi-scale responses obtained with first-order homogenisation. Since these two approaches are associated with mesh-dependent localisation, the calibration setup equates them, such that the multi-scale constitutive response, based on the material properties and features of the RVE model, can be up-scaled and adequately captured by a macroscopic Engelen model.

2. Secondly, the macroscopic nonlocal radius is calibrated for the tensile specimen using the second-order multi-scale responses attained with several RVE lengths. In this context, having calibrated the remaining parameters of the nonlocal Engelen model in the first step of the calibration scheme is essential for ensuring that an isolated relation between the values of the nonlocal radius and the RVE length is obtained. This way, the introduction of nonlocal damage averaging in the single-scale setup is assumed to be equivalent to the inclusion of the second-gradient of displacements in the multi-scale scheme.

Lastly, it should be remarked that, despite relating the RVE length and the nonlocal radius, this approach does not directly relate the two macroscopic length-scale parameters that characterise the two regularisation strategies. This is the case because the intrinsic length-scale emerging in second-order multi-scale models is only implicitly defined through the RVE length. As discussed in Chapter 6, the relation between the RVE length and the actual macro-regularisation parameter is dependent on several aspects of the multi-scale setup.

Bearing this in mind, the structure of this chapter is the following. In Section 7.2, a brief theoretical overview of the inverse identification problem is presented, introducing the numerical tool employed for this purpose and the corresponding optimisation algorithm and strategy. In Section 7.3, the identification of the local Engelen parameters is discussed, with the comparison of two distinct calibration setups. Section 7.4 reports the calibration of the macroscopic nonlocal radius with second-order multi-scale responses of the tensile specimen. Finally, Section 7.5 presents a discussion of the overall calibration strategy and the relationship observed between the values of the two regularisation parameters, while also summarising the main takeaways from this chapter.

Step 1: Equate local (mesh-dependent) models.

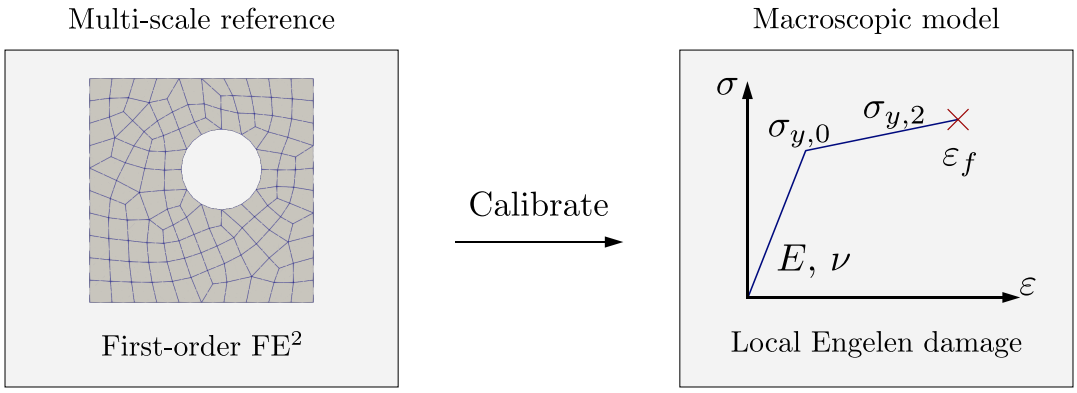

Goal 1: calibrate the 5 local material parameters.

Step 2: Equate the two regularisation strategies.

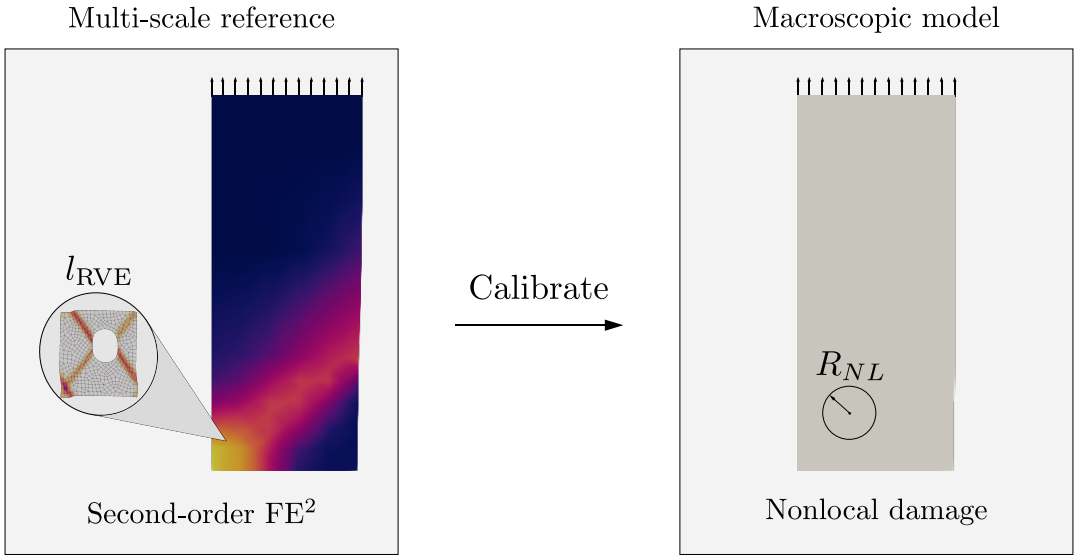

Goal 2: relate the RVE length and the nonlocal radius.

Figure 7.1: Schematic representation of optimisation-based strategy employed in this chapter to relate the RVE length of second-order FE^2 and the nonlocal radius of an integral type single-scale damage model.

7.2 Brief overview of the inverse identification problem

Effecient procedures for the inverse identification of material parameters have been pursued by several authors (Andrade-Campos et al., 2007, Cardoso Coelho et al., 2024, Carvalho Alves et al., 2023, Ferreira et al., 2023, Kuhn et al., 2022, Martins et al., 2018). These strategies have been particularly useful in the case of complex path-dependent constitutive models, where finding adequate sets of parameters for different materials can pose serious challenges in terms of engineering practice. Determining an extensive number of material parameters often requires non-standard or multiple experiments, resulting in a large dimensionality of the optimisation space (Cardoso Coelho et al., 2024). Additionally, although some parameters can be directly related to physically measurable quantities, others must be identified through trial-and-error processes, often involving the visual assessment of experimental data, which is an extremely time-consuming task (Mirkhalaf et al., 2017). Among others, optimisation-based approaches for the inverse identification of constitutive parameters, integrating finite element simulations in the numerical procedure, offer an efficient solution to these issues.

In this chapter, an optimisation-based framework for inverse identification, employing finite element analysis within an iterative scheme, is employed. This identification strategy is schematically illustrated in Figure 7.3. To this end, piglot (Parameter Identification via Global Optimisation, see Figure 7.2), a numerical toolbox taylored for the automated optimisation of constitutive responses from numerical solvers, is adopted. Moreover, the Bayesian optimiser is used with a recently proposed composite optimisation approach available in piglot. Nonetheless, its formulation and numerical aspects are not addressed here. The interested reader is referred to Brochu et al. (2010), Frazier (2018), Mockus (1994) for further details on Bayesian optimisation, and to Cardoso Coelho et al. (2024) for the presentation of the composite strategy. That said, Section 7.2.1 presents a brief summary of the inverse identification problem.

Figure 7.2: Piglot logo (taken from www.github.com/CM2S/piglot).

7.2.1 The inverse problem

Consider an arbitrary set of constitutive parameters, $\boldsymbol{\theta}$, that should be identified. It is assumed that the incremental finite element procedure defines a function, f^i, for a given quantity of interest, i, of the type

$$\hat{y}^i(t) = f^i(t, \boldsymbol{\theta}), \tag{7.1}$$

where $\hat{y}^l$ may designate any output field from the numerical solution. It should be remarked that the function is not only dependent on the material parameters and time, but these dependencies are relaxed for notational convenience. As a reference for this field, consider the response $y^i(t)$. In the end, the optimal values, $\boldsymbol{\theta}^*$, that better fit the incremental response in comparison with the reference should be identified. This procedure may be formulated as an optimisation problem such that

$$\boldsymbol{\theta}^* = \underset{\boldsymbol{\theta} \in \mathscr{A}}{\arg\min}\, J(\boldsymbol{\theta}), \tag{7.2}$$

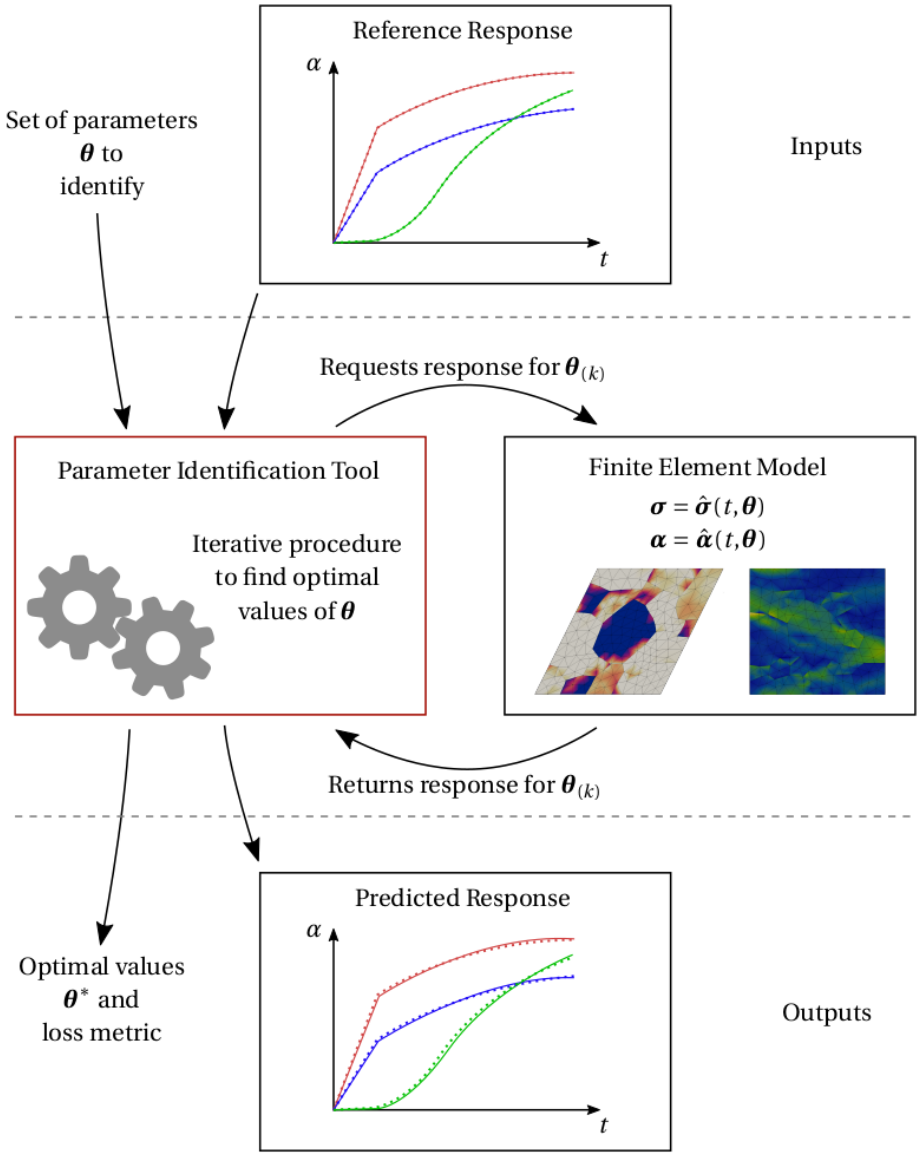

Figure 7.3: Schematic illustration of the inverse identification numerical procedure.

where $J(\boldsymbol{\theta})$ denotes a cost function, uniquely dependent on the constitutive parameters, and $\mathscr{B}$ is the domain of the parameters. Without loss of generality, in multi-objective optimisation, one may desire to use several fields and/or loading conditions, leading to the following expression

$$J(\boldsymbol{\theta}) = \sum_{i=1}^{N_L} \mathscr{L}^i \left(y^i, f^i \right), \tag{7.3}$$

where $\mathscr{L}^i$ is the loss function on the reference and predicted functionals, for the i-th field and N_L is the number of fields to consider. Generally speaking, this loss function should account for the distance between both responses, and therefore, should be minimal when these are equal. The parameter identification problem is, thus, to find the optimal values, $\boldsymbol{\theta}^*$, that minimise $J(\boldsymbol{\theta})$.

In this work, the *Normalised Mean Squared Error* (NMSE) loss function was utilised. This function is expressed as

$$\mathscr{L}^i_{NMSE}(\theta) = \frac{1}{N^i} \frac{\sum_{n=1}^{N^i} (y^i_n - \hat{y}^i_n)^2}{\sum_{n=1}^{N^i} (y^i_n)^2}. \tag{7.4}$$

7.3 Calibration of the local Engelen model

In this section, the response of a macroscopic local Engelen model is calibrated with the first-order FE^2 response of the porous microstructures presented in Chapter 6. The goal of this task is to replicate the first-order response with an equivalent macroscopic model such that, thereafter, the adoption of second-order homogenisation and the introduction of nonlocal averaging, in the multi-scale and single-scale setups, respectively, can be equated, and the macroscopic characteristic length parameters observed for each case can be related in an isolated fashion.

With this in mind, two strategies were tested with respect to the calibration of the macroscopic local Engelen model. The first one, presented in Section 7.3.1, was based on the work by Fonseca Gonçalves (2022), where the multi-scale responses of macroscopic single-elements to small displacements were used to calibrate constitutive models for large strain elastoplasticity. Conversely, the second approach calibrates the response of the tensile test piece directly, as is detailed in Section 7.3.2.

7.3.1 Single-element calibration setup

Fonseca Gonçalves (2022) proposed a framework for the calibration of macroscopic constitutive models using multi-scale simulations of single finite elements coupled with complex microstructural models of polycrystalline materials. It was observed that employing multi-objective calibration schemes, in which the response of the coupled single-elements to various loading scenarios were included in the optimisation problem, yielded more robust macroscopic models. Moreover, it was noted that, even though the reference single-element responses were attained for relatively low deformations, the resulting calibrated models could replicate the actual FE^2 response and experimental results for large displacements.

With this in mind, the same calibration framework, depicted in Figure 7.4, was utilised to identify the values of the five material parameters of the Engelen model. The medium mesh RVE (recall Figure 6.4) was utilised as the reference microstructural model in this section. Furthermore, two loading scenarios were devised for the coupled single-element setup: a tension case and a simple shear case (see illustrations in Figure 7.5). Table 7.1 reports the numerical bounds and initial guesses employed for the identification of the five material parameters. Furthermore, the Bayesian optimiser was used, with the composite setting, and a limit of 75 iterations. Three separate calibrated models were attained, using the following setups:

1. *Tension*: the first calibrated model was obtained by including solely the reaction force curve of the single-element tension case in the optimisation problem. The reference and the calibrated reaction force evolutions are depicted in Figure 7.6, along with the resulting material parameters;

2. *Shear*: the second setup is similar to the first one, but employing the reaction force curve resulting from the shear loading case. The calibrated response and the respective macroscopic constitutive parameters are shown in Figure 7.7;

3. *Multi-objective*: the final setup includes the reaction forces extracted from the two FE^2 loading scenarios in the optimisation problem[1], yielding the calibrated reactions and parameters reported in Figure 7.8.

[1] For optimisation purposes, the two reaction curves had the same weight in the multi-objective function.

Table 7.1: Numerical bounds and initial guess employed for each material parameter of the Engelen model.

	E / GPa	ν / -	ε_f / -	$\sigma_{y,0}$ / MPa	$\sigma_{y,2}$ / MPa
Lower bound	100	0.10	0.01	100	150
Initial guess	150	0.30	0.30	200	300
Upper bound	200	0.50	1.00	350	5000

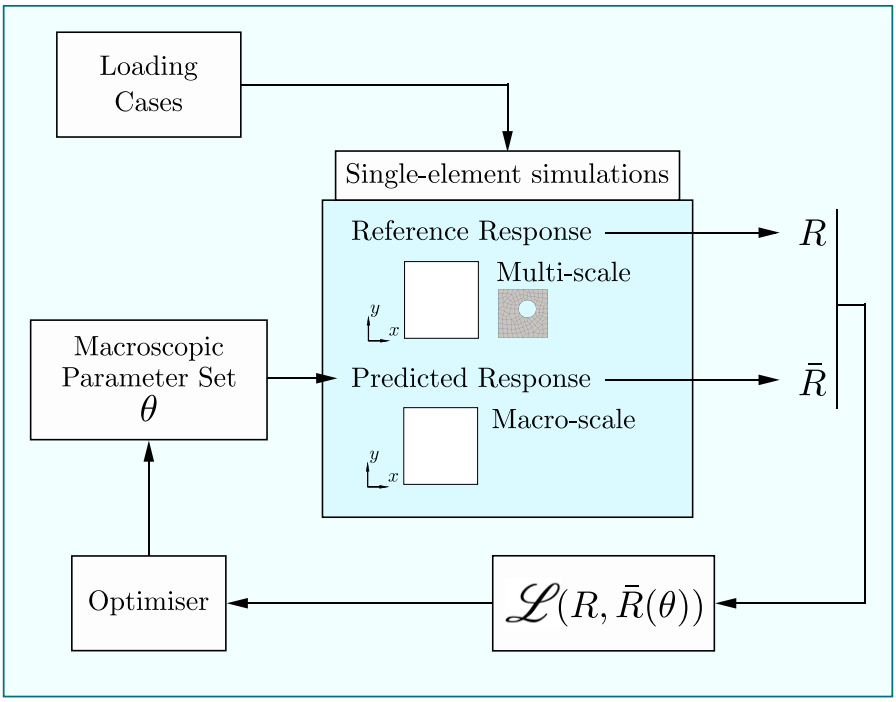

Figure 7.4: Schematic representation of the calibration strategy employed in Section 7.3.1 to identify the parameters of the local Engelen model with first-order multi-scale simulations, based on the work of Fonseca Gonçalves (2022).

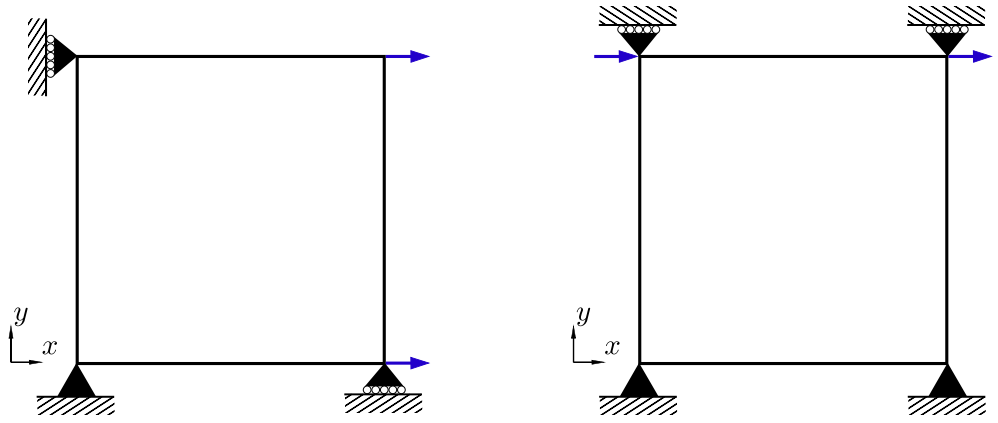

(a) Tension, displacements of 8% length.

(b) Shear, displacements of 2% length.

Figure 7.5: Schematic of the loading cases applied to the single-element.

Reasonably low calibration loss values were obtained for all three setups. The multi-objective case yielded the greatest value of the calibration loss, as reported in Fonseca Gonçalves (2022). This is explained by the fact that, in this calibration scheme, the optimiser must find a set of material parameters that fit reasonably well with both FE^2 responses. That said, since the macroscopic constitutive model cannot fully capture the complex constitutive behaviour of its multi-scale counterpart, no set of parameters fits both reference reaction curves with the same accuracy which was found for the single-objective cases.

Regarding the values of the calibrated parameters, there seems to exist some degree of interdependence between the value of the second yield stress, $\sigma_{y,2}$, and the critical equivalent plastic strain, ε_f. This observation is related to the influence of these parameters on the onset of softening observed in the simulations. Decreasing the values of either of these two parameters amplifies the degree of softening, hence, the optimiser likely balanced their ideal values in a relative fashion. This is showcased by the fact that, for the three models, the greater the value of the calibrated second yield stress, the lower the value of the calibrated critical strain, and vice-versa.

Moreover, the combination of elastic parameters attained in the shear case differs significantly from the ones reported for the other two models. Since, for a single loading direction, there are several combinations of the elastic parameters that yield the same response, this could lead to minor or no deviations in the actual calibrated elastic responses. That being the case, only the value of the initial yield stress, $\sigma_{y,0}$, can be effectively compared. The tension case recorded the greatest value for this parameter, while the same calibrated initial yield stress was found for the multi-objective and shear models.

Having analysed the calibrated response and parameters, the validation of these models was performed, with recourse to the tensile specimen. To compare the calibrated response with the first-order multi-scale reference, the coarse macro-scale mesh (recall Figure 6.7) of the test piece was simulated using the three sets of macroscopic parameters. The results, depicted in Figure 7.9, show that only the tension model could replicate the reference response with reasonable agreement.

These deviations could have several explanations, most of which are linked to the validity, or lack thereof, of the framework proposed in Fonseca Gonçalves (2022) for this particular application. Recalling the discussion of Section 6.1.2, the presence of significant softening at the micro-scale raises questions regarding the objectivity of the principle of scale separation, one of the fundamental assumptions in Fonseca Gonçalves (2022). While the RVEs adopted in this dissertation are associated with micro-softening and localisation, the analyses presented by Fonseca Gonçalves (2022) were performed with polycrystalline microstructures in the hardening regime. Furthermore, it seems that the macroscopic constitutive model, with which the RVE response is being captured, could lack the ability to evaluate the microstructure's *tendency for softening*. Since the Engelen model only contains parameters related to a certain degree of softening (the hardening slope and the critical strain), it may be unable to account for the material and geometrical nonlinearities of the RVE model, which comprise its tendency for softening, whose presence in the mechanical response of the multi-scale model is dependent on the loading conditions. This could explain the fact that the tension model better approximated the FE^2 reference in the validation task, since, in the multi-scale scheme of Chapter 6, the tensile test piece subjects the RVEs to essentially tensile deformation gradients. Therefore, since the degree of softening found in the tension single-element case is closer to the one found with the tensile specimen, in comparison to the other two loading scenarios, it performed better in the validation procedure.

Adding to this, the calibrated elastic parameters for the shear case actually resulted in a distinct linear-elastic response and a lower stiffness of the tensile specimen. This fact is likely related to the presence of the void, which particularly affects the RVE's stiffness under shear loads. This further highlights the inability of the adopted macroscopic constitutive model to fully capture the nonlinear features and load-dependent behaviour of the adopted micro-mechanical model.

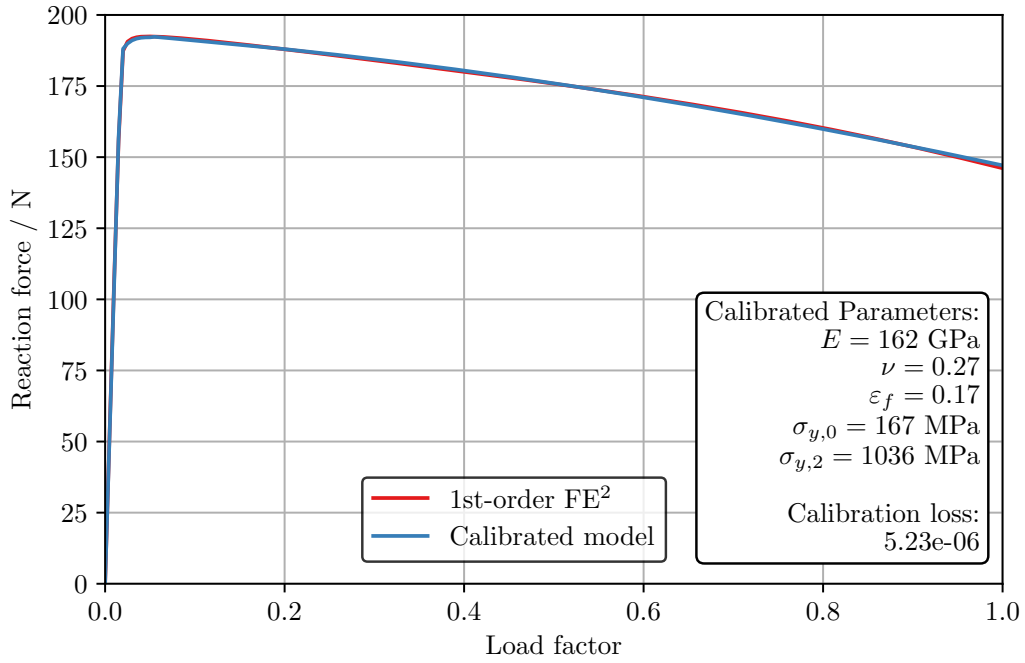

Figure 7.6: Calibrated macroscopic single-element response using the tension loading case. First-order coupled response obtained with the medium-mesh RVE.

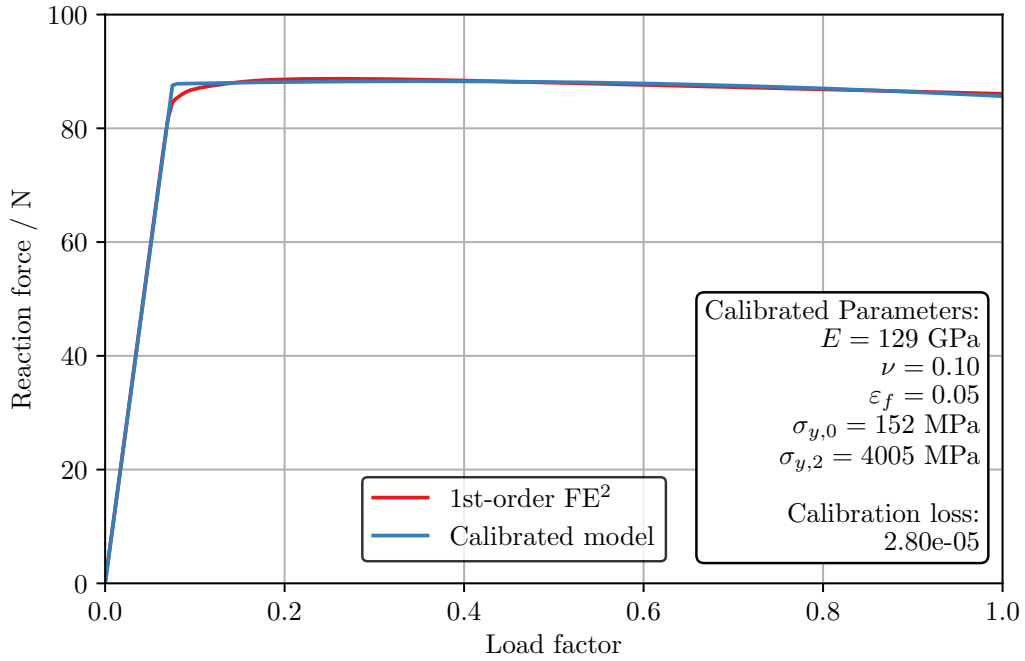

Figure 7.7: Calibrated macroscopic single-element response using the shear loading case. First-order coupled response obtained with the medium-mesh RVE.

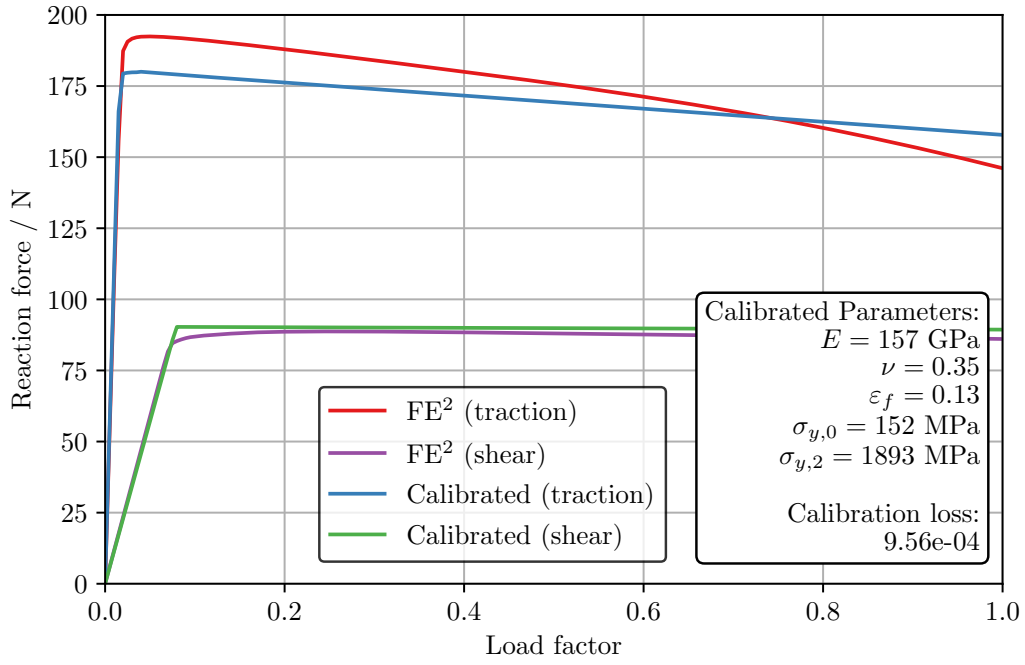

Figure 7.8: Calibrated macroscopic single-element response adopting a multi-objective optimisation scheme, where both the tension and shear loading cases were included. First-order coupled response obtained with the medium-mesh RVE.

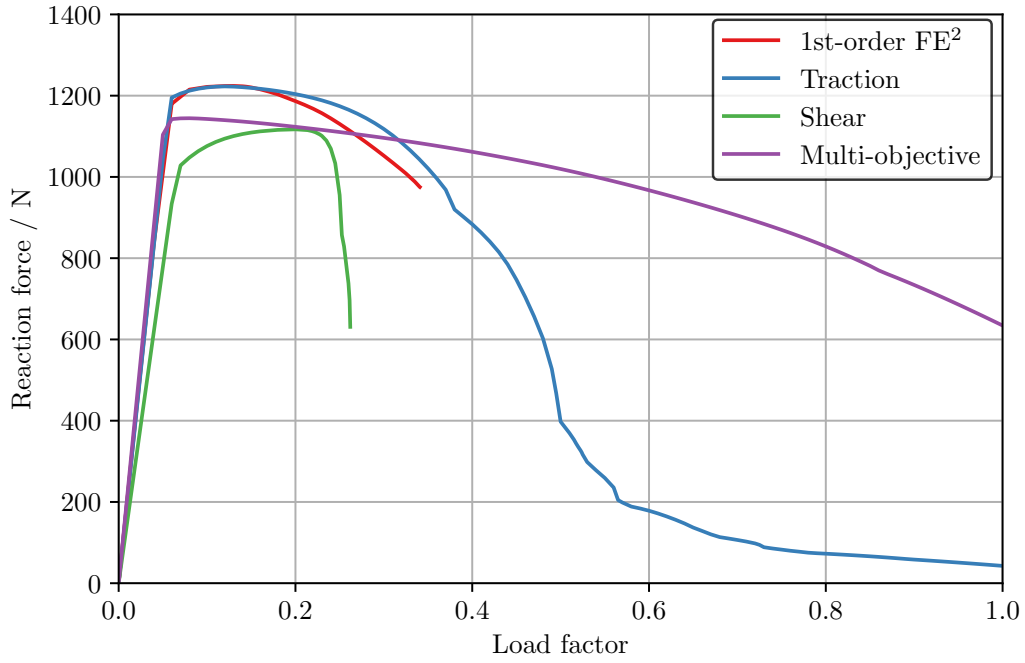

Figure 7.9: Validation of the calibrated macroscopic Engelen models, using the single-element framework proposed by Fonseca Gonçalves (2022), against the first-order FE^2 response. First-order coupled response obtained with the medium-mesh RVE used as reference.

7.3.2 Direct calibration setup

Bearing the results of Section 7.3.1 in mind, an alternative setup for the calibration of the local Engelen model is proposed here. In essence, drawing from the fact that the macroscopic model can only capture the multi-scale response for a particular set of loading conditions and, thus, for a specific degree of softening, it was concluded that such models should be calibrated using the actual first-order FE^2 responses obtained with the tensile test piece. With this strategy, a macroscopic model should be *directly* calibrated, using the respective macro-scale mesh, for each first-order multi-scale response, i.e. for each degree of softening.

One issue posed by the adoption of this direct calibration setup is the fact that, since the optimisation tool is performing numerical simulations with a mesh-dependent model, there is no guarantee that the X-type strain band arises for the optimal set of parameters, if the optimisation problem only includes the reactions, as was done in Section 7.3.1. That said, in this case, the equivalent strain extracted from the Gauss point at the tip of the tensile specimen was introduced in the optimisation scheme, making it multi-objective[2], with a global and a local reference. In Section 6.3.1 it was observed that only two combinations of macro- and micro-scale meshes yielded the desired localisation pattern. Hence, only those two multi-scale responses are considered as adequate references for calibration with the direct strategy.

The same bounds, initial guesses and iterations of the Bayesian optimiser were used. The results obtained with this setup are shown in Figures 7.10 and 7.11 for the coarse-macro, medium-micro and coarse-macro, fine-micro FE^2 cases, respectively. With this strategy, the macroscopic models replicate the FE^2 response for the tensile specimen with remarkable accuracy.

Regarding the calibrated parameters, relatively low values of the critical strain, ε_f were found, once again, as well as the interdependence with the hardening slope. Adding to the parameter dependence, these low values of the critical strain could be linked to the fact that a coupled multi-scale scheme, for the same material parameters, is much more prone to localisation, due to the RVE's inherent material and geometrical features. This could also explain the relatively lower calibration loss found for the coarse-macro, medium-micro case Figure 7.10, for which a lower degree of softening is observed, in comparison to its coarse-macro, fine-micro counterpart (Figure 7.11). Moreover, the variability of the elastic parameters seems to confirm their interdependence, aforementioned in Section 7.3.1. In theses cases, however, the values of the calibrated initial yield stresses are almost coincident.

Given the limited number of cases from Section 6.3.1 that could be used as calibration references, the tensile specimen was simulated with a different set of material properties at the micro-scale, for the same two combinations of meshes. The alternative material properties employed at the RVE level are reported in Table 7.2, maintain the same hardening slope and correspond to the typical properties of an aluminum alloy. The resulting calibrated responses and parameters are shown in Figures 7.12 and 7.13. A similar level of accuracy was found for the alternative set of RVE properties.

Table 7.2: Second set of material properties of the porous RVEs. Legend: E denotes the Young's modulus; ν denotes the Poisson coefficient; ε_f denotes the critical accumulated plastic strain; $\sigma_{y,0}$ denotes the initial yield stress; $\sigma_{y,2}$ denotes the second yield stress, at $\bar{\varepsilon}^p = \varepsilon_f$.

E / GPa	ν / -	ε_f / -	$\sigma_{y,0}$ / MPa	$\sigma_{y,2}$ / MPa
70	0.33	1.00	100	123

[2]Once again, the same weight was adopted for each of the fields in the optimisation procedure.

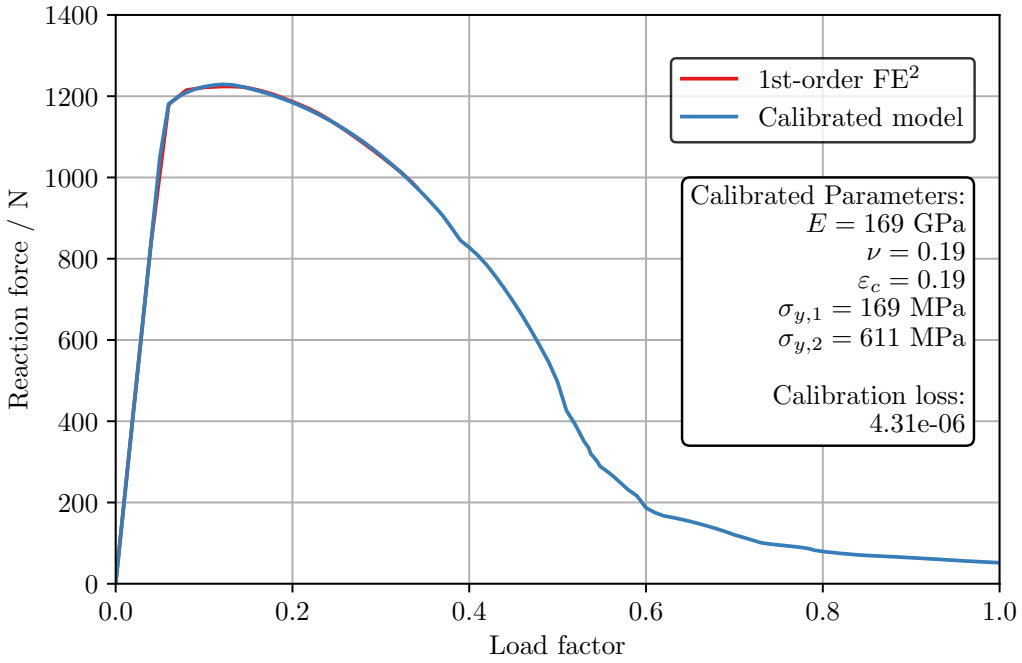

Figure 7.10: Calibrated macroscopic response of the tensile specimen, with the coarse macro-scale mesh. First-order coupled response obtained with the medium-mesh RVE used as reference.

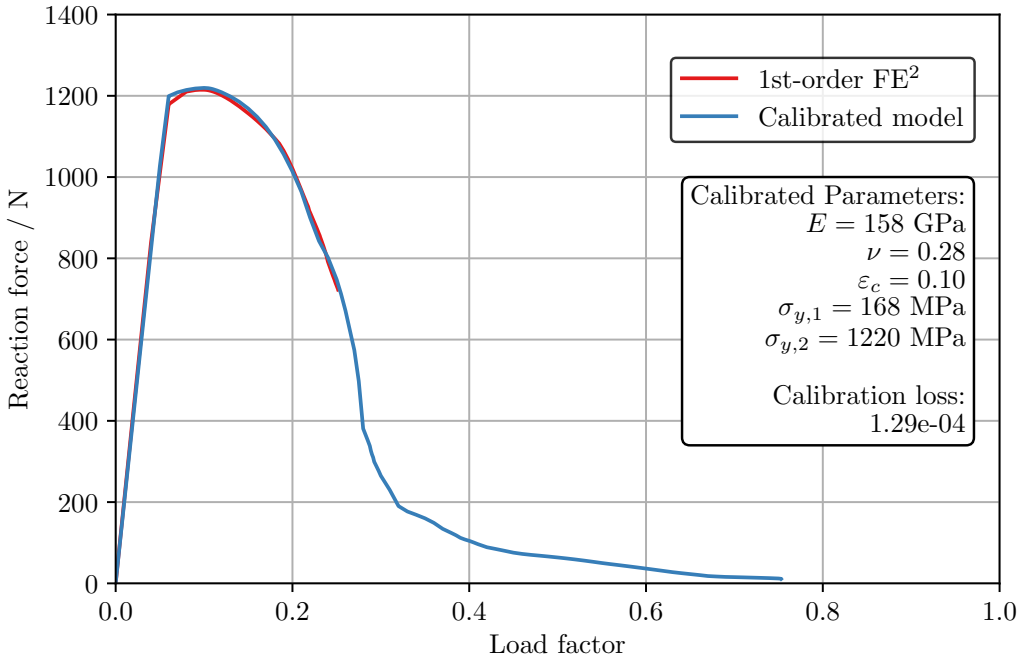

Figure 7.11: Calibrated macroscopic response of the tensile specimen, with the coarse macro-scale mesh. First-order coupled response obtained with the fine-mesh RVE used as reference.

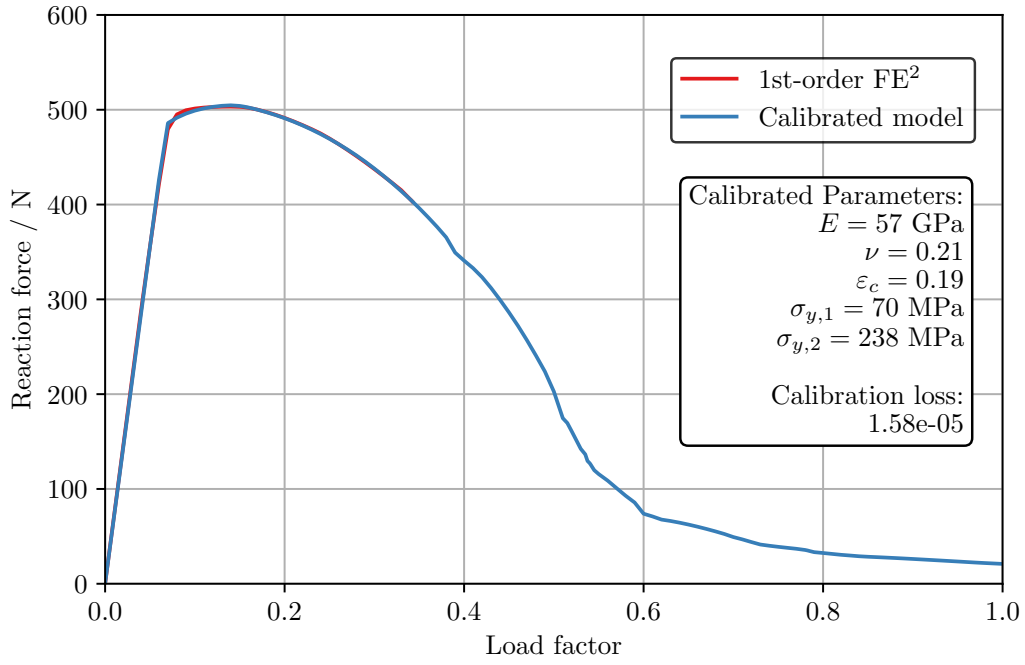

Figure 7.12: Calibrated macroscopic response of the tensile specimen, with the the second set of material properties, and the coarse macro-scale mesh. First-order coupled response obtained with the medium-mesh RVE used as reference.

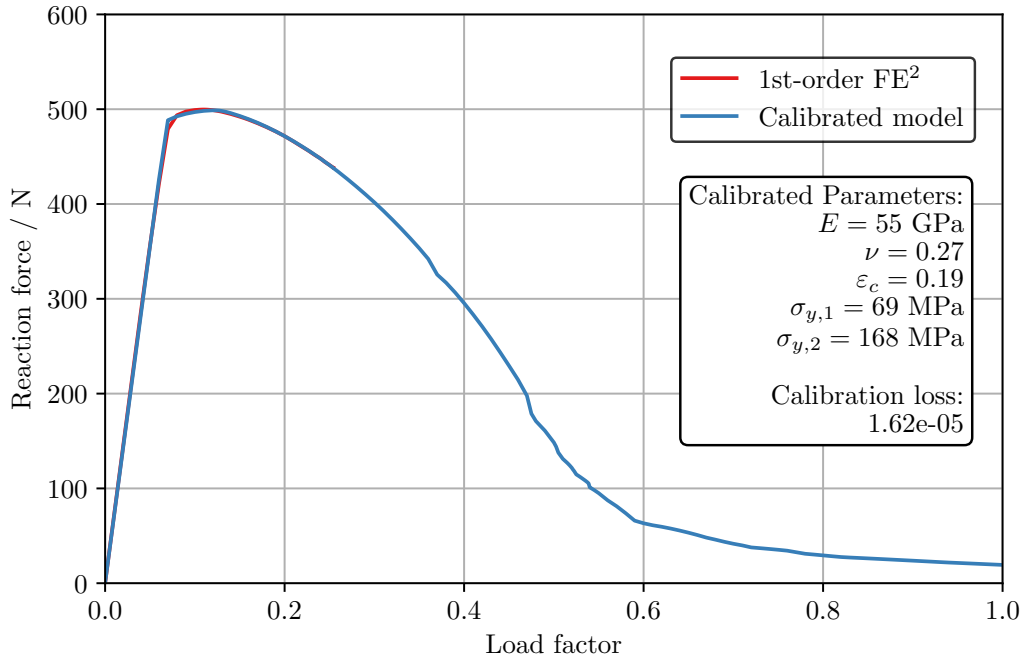

Figure 7.13: Calibrated macroscopic response of the tensile specimen, with the the second set of material properties, and the coarse macro-scale mesh. First-order coupled response obtained with the fine-mesh RVE used as reference.

7.4 Calibrating the nonlocal radius

In Section 7.3, calibrated macroscopic responses were obtained for four first-order multi-scale simulations of the tensile specimen. Table 7.3 presents a recap of the constitutive parameters calibrated for each case, where Steel and Aluminum refer to the two sets of RVE material properties (see Tables 6.1 and 7.2, respectively), and CM and CF refer to the two combinations of meshes: coarse-macro, medium-micro and coarse-macro, fine-micro, respectively.

In this section, the second step of the calibration procedure presented in Section 7.1 and Figure 7.1 is assessed. In what follows, nonlocal damage is introduced in these macroscopic models, and the value of the nonlocal radius is calibrated with the second-order FE^2 responses obtained for the respective combination of meshes and RVE properties. The remaining macro-scale parameters are the ones obtained through calibration, reported in Table 7.3. To assess the relation between the two macro-regularisation material parameters, these calibration procedures were performed for several values of the RVE length.

Table 7.3: Recap of the calibrated macroscopic local damage models presented in Section 7.3.2. Legend: E denotes the Young's modulus; ν denotes the Poisson coefficient; ε_f denotes the critical accumulated plastic strain; $\sigma_{y,0}$ denotes the initial yield stress; $\sigma_{y,2}$ denotes the second yield stress, at $\bar{\varepsilon}^p = \varepsilon_f$.

Model	Calibration loss	E / GPa	ν / -	ε_f / -	$\sigma_{y,0}$ / MPa	$\sigma_{y,2}$ / MPa
Steel CM	4.31×10^{-6}	169	0.19	0.19	169	611
Steel CF	1.29×10^{-4}	158	0.28	0.10	168	1220
Aluminum CM	1.58×10^{-5}	57	0.21	0.19	70	238
Aluminum CF	1.62×10^{-5}	55	0.27	0.19	69	168

Considering the observations of Section 6.3.3, the following RVE lengths were utilised: 0.10, 0.25, 0.50, 0.75 and 1.00 mm. Above these values, the RVE length significantly alters the mechanical behaviour of the specimen, ceasing to act solely as a mesh regularisation parameter. Table 7.4 reports the numerical bounds and initial guess employed in this section. The iterations of the Bayesian optimiser, with the composite setting, were reduced to 50, since this identification problem is limited to a single material parameter.

Table 7.4: Numerical bounds and initial guess employed for the calibration of the nonlocal radius. Values presented in mm.

Lower bound	Initial guess	Upper bound
0.5	2	5

Figures 7.14 and 7.15 present the reference and calibrated reaction forces and strain distributions, respectively, for the Steel CM case. The nonlocal radius obtained for each RVE length is also reported in these figures. The calibrated value of the nonlocal radius increases for greater RVE lengths. This tendency was expected, since greater values of these two parameters are both associated with a greater redistribution of strains, within the previously discussed bounds.

Additionally, two contrary observations must be made, regarding the accuracy of the calibrated nonlocal models. On the one hand, a notable difference was found in regards to the reaction force curves (shown in Figure 7.14). While the calibrated macroscopic models exhibit a quasi-linear decay of the reactions from the yielding point onwards, the second-order multi-scale responses show a reasonable degree of nonlinearity, with more hardening after yielding and a more pronounced

softening. This is likely due to the two distinct continuum formulations adopted at the macro-scale. The employment of a second-order formulation in the FE^2 cases not only serves to eliminate pathological mesh dependency, but also allows attaing more complex mechanical responses, particularly in problems including relevant size effects. On the other hand, the strain distributions found for the two strategies are identical (shown in Figure 7.15). For equivalent macroscopic length-scale parameters, the introduction of these two regularisation strategies yielded comparable results, in terms of strain redistribution. This observation highlights the practical similarities of adopting a nonlocal damage model, in a single-scale case, or second-order homogenisation, in a multi-scale setting, to eliminate macroscopic mesh dependency. This also demonstrates the importance of including a local measure of strain in the calibration scheme, especially since the macroscopic continuum formulations are no longer equivalent, and the first-order continuum model could not be adequately calibrated through the reactions.

For the three remaining cases, identical patterns were found, regarding the calibrated reactions and equivalent strain contours. For brevity, such results are not presented. That said, Table 7.5 reports the calibrated values of the nonlocal radius, for each setup and RVE length, and Table 7.6 shows the respective calibration losses. As observed for the Steel CM case, greater values of the RVE length resulted in greater calibrated nonlocal radii. Furthermore, the obtained nonlocal radius values were all larger than their respective RVE length. As aforementioned, the RVE length is not the actual macroscopic characteristic length parameter in multi-scale schemes based on second-order homogenisation, instead being connected to its value. With this in mind, and also considering the identical strain contours obtained with the two strategies, one can infer that the values of this second-order macroscopic length-scale should be closer to the calibrated nonlocal radii. Regarding the attained calibration losses, very similar values were observed for all four cases and RVE lengths, without any discernible pattern. The values shown in Table 7.6 are considerably larger than the losses reported in Section 7.3, which is justified by the issues found in the calibration of the second-order FE^2 reactions.

Finally, Figure 7.16 depicts the evolution of the calibrated nonlocal radius as a function of the RVE length, for the four cases. A notable tendency for the increase of the nonlocal radius with the increase of the RVE length was found, even though some degree of variability is also observed in the numerical relation between these parameters. As discussed in Section 6.1.2, the connection between the RVE length and the macroscopic characteristic parameter in second-order multi-scale schemes is not straightfoward, depending on several factors. That said, a clear and simple relation between the two numerical parameters for macro-regularisation - the RVE length and the nonlocal radius - should not be expected. Nevertheless, the main distinctions and similarities between the two strategies for macro-scale mesh regularisation have been analysed, and a clear tendency has been identified in regards to the relation established by their corresponding length-scale parameters.

Table 7.5: Numerical relations found between the nonlocal radius and the RVE length, for each calibration case. Values of both parameters are presented in mm.

	RVE length				
Case	0.10	0.25	0.50	0.75	1.00
Steel CM	1.47	1.80	2.21	2.61	2.70
Steel CF	1.19	1.19	1.66	1.89	2.03
Aluminum CM	1.35	1.95	2.29	2.33	2.97
Aluminum CF	1.19	1.95	2.55	3.13	3.32

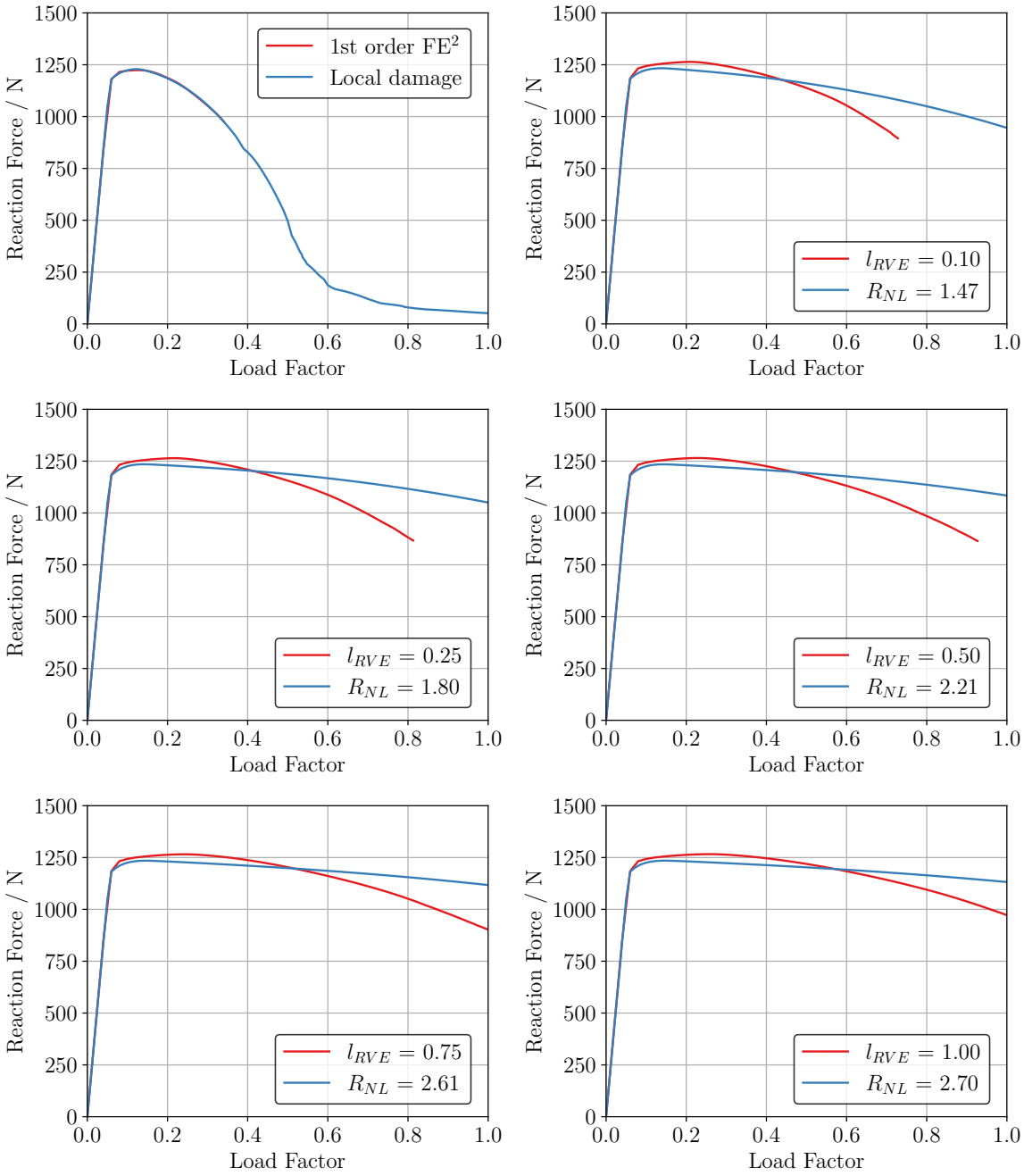

Figure 7.14: Reaction force curves obtained with the second-order FE^2 and the calibrated models, including the local model and the relations found between the nonlocal radius and the RVE length. Results obtained for the Steel CM case. RVE length and nonlocal radius values presented in mm.

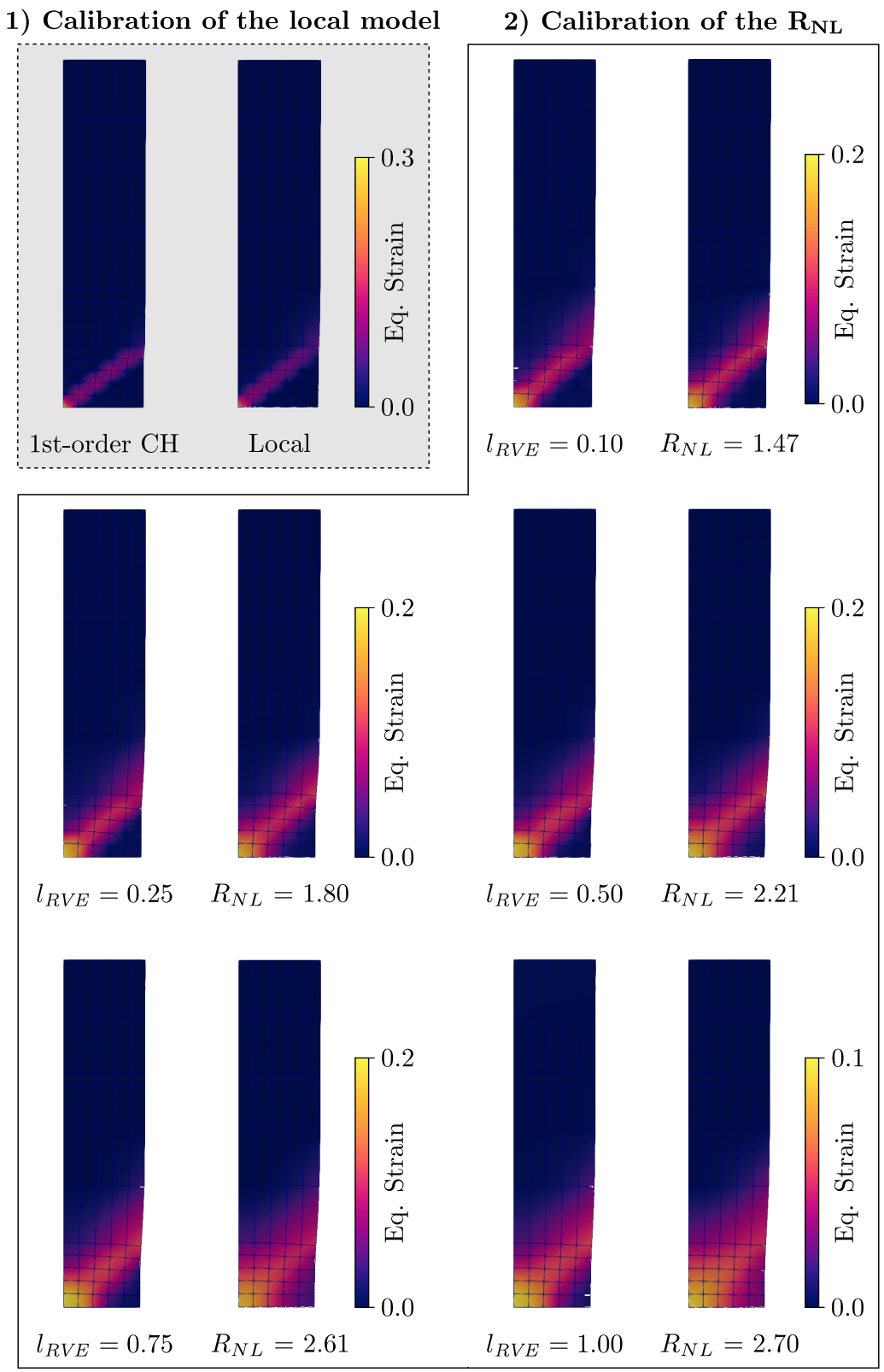

Figure 7.15: Equivalent strain distributions obtained with both second-order FE^2 and the macroscopic calibrated nonlocal models. Results obtained for the Steel CM case. RVE length and nonlocal radius values presented in mm.

Table 7.6: Calibration loss values found for each case and RVE length, expressed in mm.

	RVE length				
Case	0.10	0.25	0.50	0.75	1.00
Steel CM	9.0×10^{-3}	9.1×10^{-3}	8.5×10^{-3}	8.6×10^{-3}	8.5×10^{-3}
Steel CF	6.5×10^{-2}	9.0×10^{-3}	7.3×10^{-3}	8.8×10^{-3}	9.9×10^{-3}
Aluminum CM	7.6×10^{-3}	8.8×10^{-3}	7.9×10^{-3}	5.0×10^{-2}	8.7×10^{-3}
Aluminum CF	4.9×10^{-3}	7.4×10^{-3}	7.4×10^{-3}	1.5×10^{-2}	1.7×10^{-2}

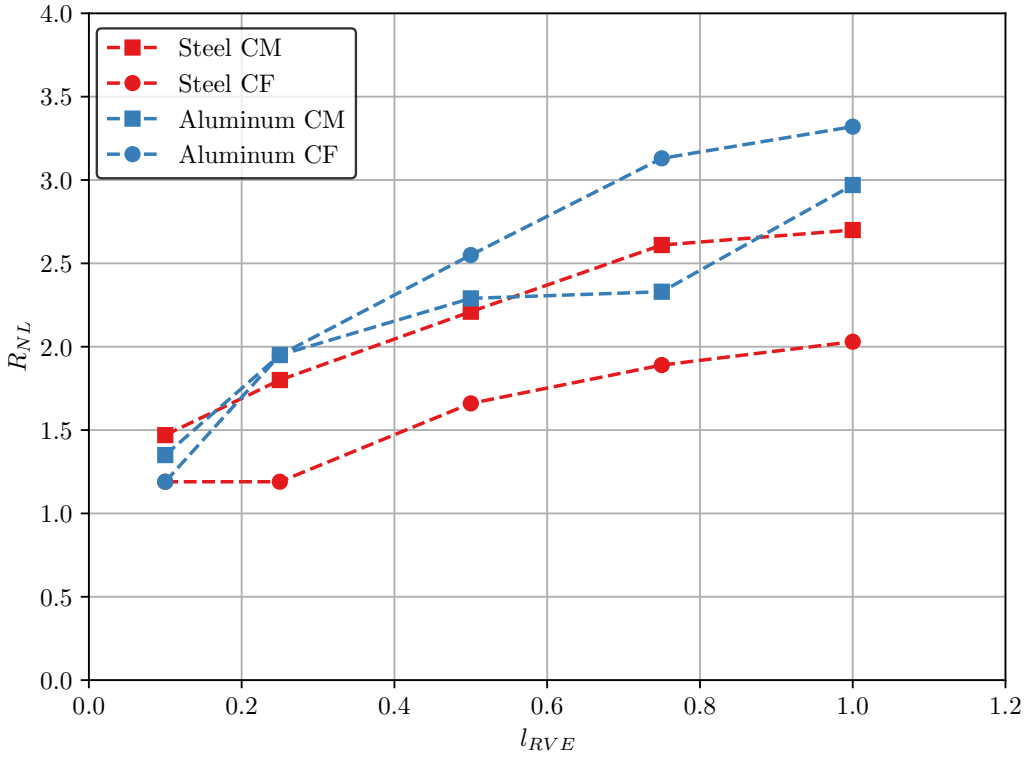

Figure 7.16: Numerical relation observed between the nonlocal radius and the RVE length, for the several calibration cases.

7.5 Discussion

In this chapter, the macro-regularisation effects obtained with a nonlocal damage model and second-order FE^2 are related. In spite of the significant distinctions between single-scale nonlocal damage and second-order multi-scale models, a numerical relation between the nonlocal radius and the RVE length has been established through the two-step optimisation-based approach, which aimed at equating the macro-mesh regularisation effects introduced by each strategy. This relation is illustrated in Figure 7.16, where greater values of the RVE length are seen to lead to larger calibrated nonlocal radii, for the four cases presented in Section 7.4. This tendency was accompanied by some degree of variability, which could be due to various sources of uncertainty, particularly the calibration procedure and its associated error. The relation between the RVE length and the resulting macroscopic characteristic length-scale in second-order FE^2, which is dependent on numerous numerical aspects, could also be behind some of these variations. Notwithstanding, the calibrated

nonlocal strain distributions, depicted in Figure 7.15, showcased remarkable agreement with the FE^2 references for all values of the RVE length.

Furthermore, it is worth noting that this numerical relation should also be dependent on particular features of the adopted nonlocal model. For instance, the use of the alternative bell-shaped nonlocal weigthing function (Equation (4.5)) would likely have yielded different calibrated nonlocal radii. In addition, the employment of an evolving nonlocal radius could be an interesting future prospect, since the value of the second-order macroscopic length-scale changes throughout the deformation path. This has been shown by Kouznetsova et al. (2004b), Rodrigues Lopes and Andrade Pires (2021), and is related to the nonlinearity of the reactions observed in the FE^2 cases in Figure 7.14, in contrast with the single-scale responses.

Finally, in Section 7.3.1, it was seen that the upscaling framework proposed by Fonseca Gonçalves (2022) was not valid for this particular identification problem, due to several relevant distinctions between the two calibration setups. The two most relevant aspect are the loss of objectivity of scale separation brought about by micro-softening and the inability of the macroscopic Engelen model to capture the nonlinear load-dependent response of porous RVEs. In fact, it was seen that the macroscopic model could only capture a certain degree of softening, and not the actual tendency for softening and localisation of the RVE. This motivated the adoption of a direct calibration scheme in Section 7.3.2, which yielded much better results.

Part III

Gradient-Enhanced Nonlocal Damage and Phase-Field Fracture

CHAPTER 8

IMPLEMENTING GRADIENT-ENHANCED NONLOCAL DAMAGE

8.1 Introduction

This chapter describes the computational implementation of a gradient-enhanced nonlocal damage model, making use of the staggered solution scheme available in LINKS for thermodynamical problems. The formulation of gradient nonlocal approaches was presented in Section 4.3, as a Taylor expansion of the integral nonlocal kernel. Instead of explicitly relating neighbouring material points, gradient approaches rely on an addition of a damage averaging equation, which is coupled to the mechanical problem to achieve nonlocality. That said, despite being a formal approximation of the integral model, these two nonlocal strategies are completely different in terms of numerical treatment. With this in mind, the implementation of the gradient-enhanced model also allows the comparison of the two single-scale nonlocal approaches, which is underexplored hitherito.

In this context, Section 8.2 presents the finite element discretisation of the gradient damage averaging equation (Equation (4.15)). Thereafter, Section 8.3 discusses solution schemes for coupled problems, with particular emphasis on strongly coupled staggered approaches. Section 8.4 details the main steps for the implementation of the gradient model in LINKS. Section 8.5 includes three numerical examples to assess the robustness of the implementation, before performing a systematic comparison between the gradient and integral (Chapter 5) nonlocal strategies in Section 8.6. Lastly, Section 8.7 summarises the main outcomes of this chapter.

8.2 Finite element discretisation of the coupled problem

In this section the finite element discretisation of the gradient damage averaging equation is derived, based on similar expositions by de Borst and Verhoosel (2016), Peerlings et al. (1996b). Section 8.2.1 presents the weak form statement of the damage equation, before assessing the finite element interpolation of fields and the discretisation of said equation in Section 8.2.2.

8.2.1 Weak forms of momentum and damage balance

In the absence of body forces, the quasi-static version of the weak form statement reads

$$\int_{\boldsymbol{\varphi}(\Omega)} \left[\boldsymbol{\sigma} : \nabla_{\boldsymbol{x}}(\boldsymbol{\eta})\right] \mathrm{d}v - \int_{\boldsymbol{\varphi}(\partial\Omega)} \boldsymbol{t} \cdot \boldsymbol{\eta} \mathrm{d}a = 0, \quad \forall \boldsymbol{\eta} \in \mathcal{V}, \tag{8.1}$$

under a spatial description. Considering the presence of damage in the material, the above expression must be recast accounting for the effective stresses

$$\int_{\boldsymbol{\varphi}(\Omega)} \left[\boldsymbol{\sigma}^* : \nabla_{\boldsymbol{x}}(\boldsymbol{\eta})\right] \mathrm{d}v - \int_{\boldsymbol{\varphi}(\partial\Omega)} \boldsymbol{t}\cdot\boldsymbol{\eta}\mathrm{d}a = 0, \quad \forall \boldsymbol{\eta} \in \mathcal{V}. \tag{8.2}$$

Conversely, through the principle of virtual work, the weak form of the gradient-enhanced damage averaging equation (Equation (4.15)) may be written as

$$\int_{\boldsymbol{\varphi}(\Omega)} \zeta \left[\bar{D} - l^2\nabla^2_{\boldsymbol{x}}(\bar{D}) - D\right] \mathrm{d}v = 0, \quad \forall \zeta \in \mathscr{M}, \tag{8.3}$$

where l is the nonlocal length-scale parameter, ζ is the virtual nonlocal damage and $\mathscr{M}$ is the set of admissible virtual nonlocal damage values. Resorting to the natural boundary condition in Equation (4.16) and the divergence theorem, Equation (8.3) can be rewritten as follows

$$\int_{\boldsymbol{\varphi}(\Omega)} \nabla_{\boldsymbol{x}}(\zeta)\cdot l^2\nabla_{\boldsymbol{x}}(\bar{D})\mathrm{d}v = \int_{\boldsymbol{\varphi}(\Omega)} \zeta\left(D-\bar{D}\right)\mathrm{d}v, \quad \forall \zeta \in \mathscr{M}. \tag{8.4}$$

8.2.2 Finite element discretisation

Having established the weak form statements of momentum and damage balance, in the following, the finite element discretisation of the coupled problem is detailed.

Interpolation of fields

Recalling Section 2.9.3 and eq. (2.117), the displacement field is interpolated as follows. The discretised version of the displacement field, ${}^h\boldsymbol{u}(\boldsymbol{x})$, is given by the interpolation of nodal displacement values, such that

$$\boldsymbol{u}(\boldsymbol{x}) \approx {}^h\boldsymbol{u}(\boldsymbol{x}) = \mathbf{N}^g(\boldsymbol{x})\mathbf{u}, \tag{8.5}$$

where $\mathbf{N}^g$ is the global displacement interpolation function and $\mathbf{u}$ is the global vector of nodal displacements, given by

$$\mathbf{u} = \left\{u_1^1, \ldots, u_1^{n_{\text{dof}}}, \ldots, u_j^i, \ldots, u_{n_{\text{points}}}^1, \ldots, u_{n_{\text{points}}}^{n_{\text{dof}}}\right\}^T, \tag{8.6}$$

where u_j^i is the i-th component of the nodal displacement of the global nodel j. The virtual displacement, $\boldsymbol{\eta}$ are discretised in a similar fashion, as mentioned din Section 2.9.3. Conversely, the nonlocal damage may also be discretised:

$$\bar{D}(\boldsymbol{x}) \approx {}^h\bar{D}(\boldsymbol{x}) = \bar{\mathbf{N}}^g(\boldsymbol{x})\bar{\mathbf{D}}, \tag{8.7}$$

where $\bar{\mathbf{N}}^g$ is the global damage interpolation function and $\bar{\mathbf{D}}$ is the global nonlocal damage vector , given by

$$\bar{\mathbf{D}} = \left\{\bar{D}_1, \bar{D}_2, \ldots, \bar{D}_j, \ldots, \bar{D}_{n_{\text{points}}}\right\}^T, \tag{8.8}$$

where $\bar{D}_j$ is the nonlocal damage at global node j. Finally, the virtual nonlocal damage field is also discretised with recourse to $\bar{\mathbf{N}}^g$.

Discretised equilibrium equations

The weak equilibrium equations in Equations (8.2) and (8.4) may be recast in discretised formats. Similarly to what was described in Section 2.9.3, the discretised mechanical equilibrium equation reads

$$\int_{\boldsymbol{\varphi}({}^h\Omega)} (\mathbf{B}^g)^T\boldsymbol{\sigma}^*\mathrm{d}v = \int_{\boldsymbol{\varphi}(\partial^h\Omega)} (\mathbf{N}^g)^T\mathbf{t}\mathrm{d}a, \tag{8.9}$$

where $(\mathbf{B}^g)$ is the global discrete symmetric gradient operator (Equation (2.122)). Moreover, the discretised damage averaging equation may be written as follows

$$\int_{\boldsymbol{\varphi}(^h\Omega)} l^2 (\nabla_{\boldsymbol{x}} (\bar{\mathbf{N}}^g))^T \nabla_{\boldsymbol{x}} (\bar{D}) \mathrm{d}v = \int_{\boldsymbol{\varphi}(^h\Omega)} (\bar{\mathbf{N}}^g)^T \left(D - \bar{D}\right) \mathrm{d}v. \tag{8.10}$$

It should be noted that the right-hand side of the above equation regards the evaluation of the local-nonlocal damage differential at each integration point of the structure. That said, while D is Gauss point quantity in the mechanical problem, the value of $\bar{D}$ at each point must be obtained through the interpolation of the nodal nonlocal damage values. Equations (8.9) and (8.10) yield the following space-discrete time-continuous mechanical and damage residuals, which must be solved at every time instant, t

$$\mathbf{r}_u = \mathbf{f}_u^{\text{int}} - \mathbf{f}_u^{\text{ext}} = \mathbf{0}, \tag{8.11}$$

$$\mathbf{r}_D = \mathbf{f}_D^{\text{int}} - \mathbf{f}_D^{\text{ext}} = \mathbf{0}, \tag{8.12}$$

where

$$\begin{aligned}
\mathbf{f}_u^{\text{int}} &= \int_{\boldsymbol{\varphi}(^h\Omega)} (\mathbf{B}^g)^T \boldsymbol{\sigma}^* \mathrm{d}v, \\
\mathbf{f}_u^{\text{ext}} &= \int_{\boldsymbol{\varphi}(\partial^h\Omega)} (\mathbf{N}^g)^T \mathbf{t} \mathrm{d}a, \\
\mathbf{f}_D^{\text{int}} &= \int_{\boldsymbol{\varphi}(^h\Omega)} l^2 (\nabla_{\boldsymbol{x}} (\bar{\mathbf{N}}^g))^T \nabla_{\boldsymbol{x}} (\bar{D}) \mathrm{d}v, \\
\mathbf{f}_D^{\text{ext}} &= \int_{\boldsymbol{\varphi}(^h\Omega)} (\bar{\mathbf{N}}^g)^T \left(D - \bar{D}\right) \mathrm{d}v.
\end{aligned} \tag{8.13}$$

The time discretisation of Equations (8.11) and (8.12) leads to the fully discrete coupled problem, summarised here as

$$\mathbf{r}_u^{n+1} \left(\mathbf{u}_{n+1}, \bar{\mathbf{D}}_{n+1}\right) = \mathbf{0}, \tag{8.14}$$

$$\mathbf{r}_D^{n+1} \left(\mathbf{u}_{n+1}, \bar{\mathbf{D}}_{n+1}\right) = \mathbf{0}, \tag{8.15}$$

for each pseudo-time increment, $t_{n+1} \in [t_0, t_f]$. Once these residuals are available, the iterative Newton-Rapshon method can be employed to solve the system of equations for the displacement, $\Delta\mathbf{u}_{n+1}$, and nonlocal damage, $\Delta\bar{\mathbf{D}}_{n+1}$, increments at time step t_{n+1}:

$$\begin{bmatrix} \mathbf{K}_{uu} & \mathbf{K}_{uD} \\ \mathbf{K}_{Du} & \mathbf{K}_{DD} \end{bmatrix}_{n+1}^{i} \begin{bmatrix} \delta\mathbf{u} \\ \delta\bar{\mathbf{D}} \end{bmatrix}_{n+1}^{i+1} = - \begin{bmatrix} \mathbf{r}_u \\ \mathbf{r}_D \end{bmatrix}_{n+1}^{i}. \tag{8.16}$$

with i and $i+1$ denoting the iterations of the solution scheme. The emergence of coupling terms in the global stiffness matrix, $\mathbf{K}_{uD}$ and $\mathbf{K}_{Du}$, is noteworthy, particularly since $\mathbf{K}_{uD} \neq \mathbf{K}_{Du}^T$ (see for intance de Borst and Verhoosel (2016)). This results in non-symmetric global stiffness matrices for the coupled problem, which can bring about numerical issues, if not appropriately addressed. Furthermore, as mentioned in Section 8.1, several numerical techniques have been proposed in the literature for the efficient and consistent solution of the nonlinear coupled system of equations in Equation (8.16). These numerical strategies are reviewed in Section 8.3, including the general description of the staggered approach adopted in this contribution.

8.3 Solution schemes for coupled multi-physics problems

This section presents a general overview of the different solution techniques for coupled multi-physics problems. Several approaches have been proposed in recent decades, including field elimination, operator splitting, fractional-step methods, staggered or partitioned solution schemes and monolithic solution methods. Nonetheless, while field elimination techniques are limited to linear problems, operator splitting, fractional-step, and staggered solution methods have been shown

to be essentially synonymous for most multi-physics scenarios (Danowski, 2014). That said, two main strategies for the solution of coupled problems are discussed herein: staggered and monolithic schemes.

Monolithic methods essentially consist in the simultaneous solution of the coupled system of equations (in this case Equation (8.16)), fulfilling coupling conditions exactly (Vila-Chã et al., 2023). These methods have been extensively utilised for several multi-physics problems, including fluid-structure interactions (Barker and Cai, 2010, Walhorn et al., 2005), thermomechanics (Danowski, 2014, Romero, 2010), electro-mechanics (Rochus et al., 2006), and also gradient-enhanced and phase-field models (Bharali et al., 2022, Gerasimov and De Lorenzis, 2016, Seupel et al., 2018, Wick, 2017, Wu et al., 2020). Furthermore, some contributions have proposed three-field formulations including both thermal effects and gradient-enhanced nonlocal damage, with the adoption of monolithic solvers (Felder et al., 2022, Sarkar et al., 2020). In general, together with implicit time integration techniques, monolithic schemes can provide unconditional stability and are typically robust. However, the stability and robustness of monolithic schemes rely on the adoption of adequate preconditioning strategies, and require extensive development and maintenance cost, while also lacking flexibility (Vila-Chã et al., 2023). Bearing this in mind, the solution scheme implemented in LINKS by Vila-Chã et al. (2023) is a staggered one.

Staggered solution methods emerged in the 1970s and have been comprehensively discussed in the contributions of Felippa and co-workers Felippa and Park (1980), Felippa et al. (2001). These strategies rely on partitioning the coupled multi-physics problem into smaller blocks, which are addressed separately, easing complexity and memory requirements. This separation results in an elimination of the coupling terms of the coupled stifness matrix (recall Equation (8.16)), which is conveniently compensated by adopting the residual to include the coupling contributions to a specific field. Staggered strategies have also been applied in several multi-physics contexts, particularly for gradient-enhanced damage (Azinpour et al., 2018, Nahrmann and Matzenmiller, 2021, Rajput et al., 2023, Tran et al., 2023) and phase-field fracture models (Azinpour et al., 2021, Hofacker and Miehe, 2012, Lu et al., 2020, Luo, 2023, Quintanas-Corominas et al., 2019, Seleš et al., 2019, Storvik et al., 2021).

Staggered solution methods can be categorised into: one-way loosely coupled, two-way loosely coupled and two-way strongly-coupled schemes. In a one-way coupling scheme, there is a primary coupling field, from which information is passed into the second physical field, but not vice-versa. With this approach, the primary field is completely decoupled from the other. Regarding two-way coupling methods, commonly referred to as *fully coupled* schemes, the main difference resides in the exchange of variables between the two separate problems. In the loosely coupled or explicit case, the primary coupling field is computed, at a given pseudo-time step, t_n, and passed to the second problem, where the second coupling variable is estimated at t_n. The value of this second coupling variable at t_n is then utilised to compute the first coupling field at t_{n+1}, i.e. a time offset of the coupling effect arises and equilibrium is not achieved at the end of each pseudo-time step (Danowski, 2014). Conversely, the strongly coupled or implicit case, the coupling variables are exchanged and updated in both problems several times within a designated iterative cycle for the same coupling increment, until the convergence criterion is met. Another relevant distinction between the two-way coupling methods is their stability. While the strongly coupled is *unconditionally stable*, having the same temporal stability properties of the monolithic scheme (Vila-Chã et al., 2023), the loosely coupled strategy is *conditionally stable*. With this discussion in mind, the coupling method employed in this dissertation was a two-way strongly coupled one and is detailed in Section 8.3.1, although other variants of the staggered scheme are also available in LINKS.

8.3.1 Staggered solution scheme

By tackling the two coupled problems in a separate fashion, the adoption of a staggered solution scheme allows de-coupling the global system of equations, previously expressed in Equation (8.16),

such that:

$$\begin{bmatrix} \mathbf{K}_{uu} & \mathbf{0} \\ \mathbf{0} & \mathbf{K}_{DD} \end{bmatrix}_{n+1}^{i} \begin{bmatrix} \delta\mathbf{u} \\ \delta\bar{\mathbf{D}} \end{bmatrix}_{n+1}^{i+1} = - \begin{bmatrix} \mathbf{r}_u \\ \mathbf{r}_D \end{bmatrix}_{n+1}^{i}, \tag{8.17}$$

where the displacement and damage residuals must include the coupling information in the form of external loads, instead of considering these effects in the stiffness matrix. This is only possible since the mechanical problem is solved at a constant temperature value and damage averaging is carried out at a fixed configuration.

The two-way strongly coupled staggered strategy adopted in this work is illustrated in Figure 8.1. The displacement field is the primary coupling variable and the mechanical problem is solved first for fixed nonlocal damage values, followed by the solution of the damage averaging problem at a fixed configuration. Furthermore, the last converged nonlocal damage, $\bar{\mathbf{D}}_n$, is employed as the initial guess for the first iteration of each coupling increment, to compute $\mathbf{u}_{n+1}^{1}$. However, (Vila-Chã et al., 2023) suggest the adoption of polynomial extrapolation to produce the initial guess, $\bar{\mathbf{D}}_{n+1}^{*}$. For second-order polynomial extrapolation, for instance, one would have:

$$\bar{\mathbf{D}}_{n+1}^{*} = 3\bar{\mathbf{D}}_n - 3\bar{\mathbf{D}}_{n-1} + \bar{\mathbf{D}}_{n-2}. \tag{8.18}$$

Nevertheless, polynomial extrapolation was not pursued in the context of this contribution and remains as an future enhancement of this solution scheme. In addition, the coupling convergence criterion adopted here is based on the relative norm of the nodal nonlocal damage vector, i.e. convergence is found when

$$\frac{||\bar{\mathbf{D}}_{n+1}^{k} - \bar{\mathbf{D}}_{n+1}^{k-1}||}{||\bar{\mathbf{D}}_n||} = \frac{||\Delta\bar{\mathbf{D}}_{n+1}^{k-1}||}{||\bar{\mathbf{D}}_n||} < \epsilon_{\text{tol}}, \tag{8.19}$$

where ϵ_{tol} is the coupling tolerance and k denotes the k-th iteration of the implicit coupling cycle.

A relevant aspect of strongly coupled staggered schemes is the fact that, in spite of their unconditional stability, the convergence of the implicit inter-field loop, depicted in the grey box of Figure 8.1, is not guaranteed and cane take an excessive number of iterations. Consequently, several methods for the solution of the inter-field coupling loop have been proposed in the literature. The following presents a brief overview of the implicit solvers considered in the context of this dissertation, which were already available in LINKS:

1. *Fixed-point method:* the fixed-point algorithm is the simplest solver available, and only necessitates one residual evaluation per nonlinear iteration.

2. *Aitken relaxation:* the Aitken relaxation method, requiring one residual evaluation and also the previous iteration, was introduced by Irons and Tuck (1969). It has been extensively utilised in staggered solution schemes (for instance by Danowski (2014)).

3. *Broyden's method:* Broyden's method is a quasi-Newton nonlinear algorithm, with increased memory requirements and numerical complexity. Vila-Chã et al. (2023) performed a numerical assessment of these implicit solvers and concluded that Broyden's method was generally the best-performing algorithm.

The reader is referred to Vila-Chã et al. (2023) for additional details on these implicit algorithms.

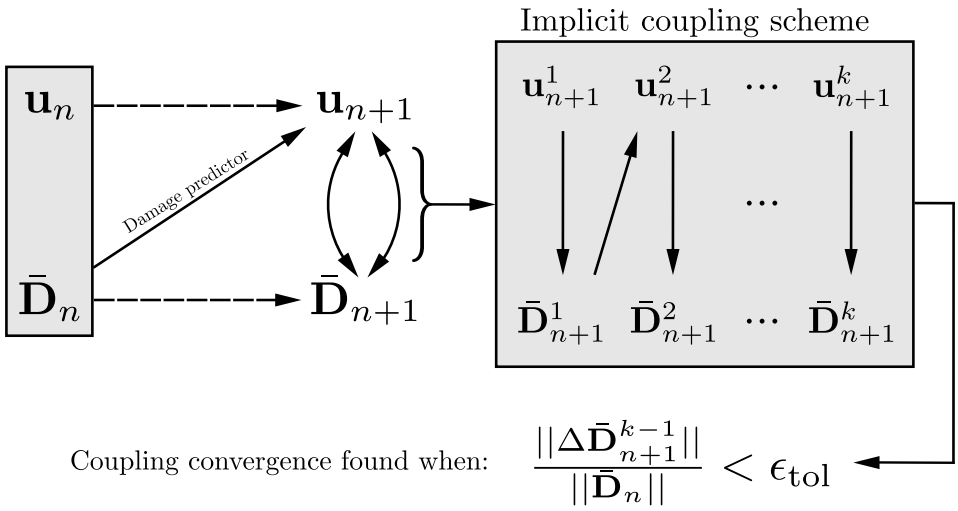

Figure 8.1: Schematic representation of the staggered solution scheme adopted for the solution of the coupled system of equilibrium equations in this contribution.

8.4 Implementation

The implementation of the gradient-enhanced nonlocal model in LINKS is detailed in this section. Since a staggered scheme was used to solve the coupled problem, the mechanical and damage routines are separate, interacting through their respective residuals (Equation (8.17)). The solution scheme also presupposes the use of two parallel CPUs, one for each problem. Furthermore, the LINKS code branch for the solution of thermomechanical problems, in which the staggered coupling scheme is available, is programmed using *object-oriented* code design. That said, some basic concepts of object-oriented programming are given in Section 8.4.1.

Furthermore, the implicit gradient-enhancement was implemented for the Engelen damage model, described in Section 5.2.2. However, the Engelen material model had to be implemented in the thermomechanical branch of LINKS, using object-oriented programming, to comply with the remaining structure of the code. The new implementation of the Engelen model is presented in Section 8.4.2, pointing out the main nuances of this version, in comparison to the standard local Engelen routines. Finally, Section 8.4.3 addresses the use of the thermal code in LINKS to implement and solve the damage averaging equation.

8.4.1 Object-oriented programming

Object-oriented (OO) software design rose to proeminence in the 1980s (Bobrow and Stefik, 1982, Moon, 1986) and is based on the concept of *objects*, which are reusable components containing both data and procedures in the form of *attributes* and *methods*, respectively. This contrasts with standard procedural programming, in which data and functionality are treated separately. OO language constructs are provided by Fortran 2003 and subsequent standard levels (Metcalf et al., 2011), and inherently promote code modularity and data-hiding—both critical concepts for flexible software design (Pinto Carvalho, 2021). In what follows, some of the key points of OO programming are discussed.

A significant advantage of OO programming is its focus on code reuse, primarily through *inheritance*. Inheritance allows objects to inherit properties and methods from other objects, establishing an "is a" relationship. For example, a 'Car' object can inherit from a more general 'Vehicle' object, adopting its attributes and methods while adding specific features unique to cars. This hierarchical structure promotes reuse and reduces redundancy, enabling developers to build on existing code. Polymorphism is another fundamental concept in OO programming, allowing objects to be treated

as instances of their parent class rather than their specific class. This means different objects can be accessed through the same interface, even if their implementations differ. For instance, both 'Car' and 'Airplane' classes might implement a 'fuelControl' method. Through polymorphism, a program can call 'fuelControl' on a list of vehicles without knowing their specific object, enhancing versatility and maintainability. Encapsulation, another key OO software design principle, conceals an object's internal state and requires all interactions to occur through its methods. This data hiding ensures objects can be used and modified without unintended interference from other parts of the program, guaranteeing modularity.

Finally, design patterns offer standardised solutions to common design problems in OO programming. Popularised by the work of Gamma et al. (1995), these patterns are categorised into creational, structural, and behavioral patterns. They provide best practices refined through experience, offering a shared vocabulary for developers and improving the overall design and architecture of software systems. Using design patterns enhances the robustness and flexibility of OO programs, making it a powerful paradigm for complex software development.

8.4.2 Gradient-enhanced Engelen material model

Many aspects of the numerical strategy presented in Section 5.3, for the treatment of the local Engelen damage model remain valid for the mechanical code of its gradient-enhancement. That said, in this section, the new material model implemented in the thermomechanics branch of LINKS and its key features are outlined, while the few required adaptations of the local damage model are also mentioned.

Within an OO approach, distinct material models are introduced as objects, which contain both state variables and properties as attributes and procedures, such as the state update and the computation of the consistent tangent, as methods. The implemented OO Engelen material model contains the following methods:

1. An initialisation or *constructor* procedure which, as the name implies, constructs the relevant instances of the material class, such as its ID within the LINKS material database;
2. A procedure for reading the material properties, in this case, the elastic parameters, the critical equivalent plastic strain and the hardening curve points;
3. The state update procedure;
4. The consistent tangent determination procedure;
5. A procedure of thermomechanical material models, allowing the computation of mechanically dissipated heat, to be transfered to the thermal problem.
6. Procedures for building the relevant Gauss point outputs of the specific material type.

The state update and consistent tangent code blocks are discussed in what follows. The importance of computing, storing and relaying the equivalent to the mechanically dissipated heat, i.e. the local damage, is also emphasised. The remaining methods were not addressed since their structure is essentially standardised within LINKS.

State update procedure

The numerical integration strategy for the local Engelen model, presented in Section 5.3.1 remains largely consistent for the gradient-enhanced setup, with particular differences regarding the state update procedure and the management of damage variables. For the sake of brevity, only said differences were addressed.

The integral type model presented in Chapter 5 relied on the nonlocal averaging of an incremental local damage varaible to improve stability and convergence. Conversely, the gradient averaging of damage is achieved by relating the local damage variable to its nonlocal counterpart and its gradients (recall Equation (4.15)). With this in mind, the total local damage variable is required in the gradient case, hence, it must be conveniently stored and sent to the damage averaging problem as an analogous quantity to the mechanically dissipated heat (recall the discussion in Section 4.3.2), since it is the only variable in the gradient-enhanced equation that comes explicitly from the mechanical problem.

Furthermore, since a staggered approach was adopted in this dissertation, the damaged stress tensor is computed at the end of each solution of the mechanical problem with the nonlocal damage variable obtained in the previous solution of the damage problem. Consequently, the nonlocal damage variable is imported in the beginning of the mechanical state update procedure, which is almost entirely bypassed if damage is equal to one, since completely damaged elements no longer contribute to the internal forces. In this setting, if a loosely coupled scheme is employed, a pseudo-time offset emerges between the mechanical and damage problems. However, since the strongly coupled approach was employed, and considering that the convergence of the nonlocal damage variable is the sole stopping criterion of the implicit coupling scheme (recall Equation (8.19)), this offset is largely prevented. In addition to this, it should be remarked that the nonlocal damage, being an independent variable of the coupled problem, is mostly treated as a nodal quantity, as is the temperature in thermomechanics problems. That said, to update the value of the nonlocal damage variable in the beginning of each mechanical problem solution, its value must be interpolated to the integration points, at which the state update and consistent tangent procedures are carried out.

Box 8.1 summarises the main differences between the numerical integration and state update procedure presented in Section 5.3.1 for the local Engelen model and the one adopted for the mechanical code of its gradient-enhanced counterpart.

Consistent tangent procedure

The mechanical consistent tangent modulus for the gradient-enhanced nonlocal damage model coincides to that of its local counterpart, expressed in Equation (5.86), with the sole nuance of employing the nonlocal damage variable to compute the damaged stress tensor. Recalling Equation (8.17), although the expression for the residual vector with respect to the displacement field is dependent on the nonlocal damage variable (Equations (8.11) and (8.13)), tackling the coupled problem in a staggered manner results in the elimination of the non-diagonal terms of the stiffness matrix, in the mechanical case $\mathbf{K}_{uD}$. This is a result of adopting a constant value of the damage variable, meaning that only the standard stiffness matrix, $\mathbf{K}_{uu}$, (Equation (5.86)) need be computed for the partitioned solution of the mechanical equilibrium problem, as expressed in Equation (8.17).

That said, the new OO routines for computing the consistent tangent and assembling the mechanical stiffness matrix are conceptually similar to the ones required by the standard local damage model. To keep consistency with the state update procedure, the consistent tangent is computed at the beginning of a given coupling iteration, k, before the nonlocal damage variable is updated. That said, since the updated damage variable already corresponds to the previous coupling iteration, $k-1$, the consistent tangent is determined with the value of the nonlocal damage at iteration $k-2$.

8.4.3 Damage averaging equation

As detailed in Section 4.3.2, the thermal problem analogous to the gradient damage equation (Equation (4.15)) is the quasi-static heat diffusion of a homogeneous material, subjected to heat dissipation through mechanical means and a linear temperature-dependent heat source. Since these particular thermal loading conditions were not available in the thermomechanics branch of LINKS,

Box 8.1 Summary of the state update procedure implemented for the gradient-enhanced nonlocal Engelen model.

1. Retrieve the nonlocal damage values found in the last solution of the damage averaging problem and interpolate it to the integration points. If damage is unitary, set stresses to zero and bypass state update, else continue.

2. For each integration point, update the deformation gradient and compute the elastic trial state.

3. Check for plastic admissibility. For elastic steps, the local damage variable, driven by plastic deformation, remains unchanged. For plastic steps:

   (a) Use the Newton-Raphson method to find an admissible solution.

   (b) Thereafter, update the relevant state variables: strains, undamaged stresses, effective plastic strain and, crucially, the local damage variable:

$$D := \begin{cases} \bar{\varepsilon}^p / \varepsilon_f & \text{if } \bar{\varepsilon}^p \leq \varepsilon_f \\ 1 & \text{if } \bar{\varepsilon}^p > \varepsilon_f \end{cases} \tag{8.20}$$

   In a standard setting, the $D \leq 1$ is naturally enforced, since the local damage variable affects the stress tensor. In this case, this constraint must be explicitly enforced, to ensure the consistency of the damage averaging problem.

4. Update the damaged stress tensor:

$$\boldsymbol{\tau}_k^* := \left(1 - \bar{D}_{k-1}\right) \boldsymbol{\tau}_k, \tag{8.21}$$

   where the subscripts, $(\cdot)_k$ and $(\cdot)_{k-1}$, denote the coupling iterations and were included to showcase one of the effects of solving the two problems in a staggered manner.

5. Update the damaged Cauchy stress tensor and compute the element vector of internal forces.

they were implemented in the context of this dissertation, following the strategy presented herein. The main steps required for the implementation of the gradient damage averaging equation include:

1. The introduction of the new linear temperature-dependent heat source in the thermal loadings module, with its corresponding element "thermal" force and stiffness contributions, to allow the implementation of the damage averaging equation;

2. Programming the routines for the required initialisations, reading and allocations;

3. The inclusion of this new thermal load in the main routines of the thermomechanics code for proper integration.

In the following, the numerical treatment of the linear temperature-dependent heat source, i.e. the damage averaging equation is adddressed.

Section 8.2 established the weak form statement of the damage averaging problem and presented its finite element discretisation in general terms. Recalling Equation (8.16), non-diagonal terms of the coupled stiffness matrix emerged due to the simultaneous treatment of the mechanical and damage equations. Nonetheless, these non-diagonal stiffness components, derived in Peerlings et al. (1996b), vanish due to the solution of each problem for a constant value of the converse coupling variable, i.e. since the nonlocal damage problem is solved for a constant displacement and local damage, its residual, $\mathbf{r}_D$, can no longer be differentiated with respect to these variables.

Furthermore, recalling Equations (8.10) and (8.13), the application of the Newton-Raphson algorithm to solve the damage averaging equation reads

$$\mathbf{K}_{DD}\delta\bar{\mathbf{D}}^{(k)} = -\mathbf{r}_D^{(k-1)}, \tag{8.22}$$

where the damage residual is given by the subtraction of the internal and external damage forces:

$$\mathbf{r}_D^{(k-1)} = \left[\int_{\boldsymbol{\varphi}(^h\Omega)} l^2(\nabla_{\boldsymbol{x}}(\bar{\mathbf{N}}^g))^T\nabla_{\boldsymbol{x}}(\bar{D})\,\mathrm{d}v - \int_{\boldsymbol{\varphi}(^h\Omega)}(\bar{\mathbf{N}}^g)^T\left(D-\bar{D}\right)\mathrm{d}v\right]^{(k-1)}. \tag{8.23}$$

The computation of the internal force vector needed not be implemented nor modified, since it was already embedded in the thermomechanics code. In addition, since the local damage variable is passed to the damage problem as mechanical heat dissipation, its contribution to the damage balance problem was also already implemented. Conversely, the contribution of the nonlocal damage itself to the external forces was not available, since this is a specific feature of the linear temperature-dependent heat source, implemented for the solution of the gradinet-enhanced coupled problem. This term of the residual vector, hereafter denoted by $\mathbf{f}_D^{\mathrm{H}}$, may be written, for a given k-th iteration of the Newton-Raphson method, as

$$(\mathbf{f}_D^{\mathrm{H}})^{(k-1)} = \left[\int_{\boldsymbol{\varphi}(^h\Omega)}(\bar{\mathbf{N}}^g)^T\bar{D}\,\mathrm{d}v\right]^{(k-1)}. \tag{8.24}$$

As mentioned in Section 8.2.2, this term is computed with the nonlocal damage evaluated at the integration points of the structure, hence, the nodal nonlocal damage must be interpolated.

Regarding the damage stiffness matrix, the contributions of the internal forces, associated with damage diffusion, were already accounted for in the pre-existing thermal procedures. However, since the external force vectors explicitly depends on the nonlocal damage variable, an additional load-dependent stiffness term arises. This stiffness term, denoted by $\mathbf{K}_{DD}^{\mathrm{H}}$, may be defined as

$$\mathbf{K}_{DD}^{\mathrm{H}} = \int_{\boldsymbol{\varphi}(^h\Omega)}(\bar{\mathbf{N}}^g)^T(\bar{\mathbf{N}}^g)\,\mathrm{d}v. \tag{8.25}$$

The computation of this stiffness term was introduced in LINKS, along with the estimation of $\mathbf{f}^{\mathrm{H}}$. Box 8.2 presents the element loop implemented in the thermal loadings procedure to compute these additional terms of the linearised damage balance equation[1]. For completeness, the total damage consistent tangent stiffness matrix is given by

$$\mathbf{K}_{DD} = \int_{\boldsymbol{\varphi}(^h\Omega)}\left[(\bar{\mathbf{N}}^g)^T(\bar{\mathbf{N}}^g) + l^2(\nabla_{\boldsymbol{x}}(\bar{\mathbf{N}}^g))^T\nabla_{\boldsymbol{x}}(\bar{\mathbf{N}}^g)\right]\mathrm{d}v. \tag{8.26}$$

[1] In Box 8.2, the subscripts $(\cdot)_D$ and $(\cdot)_{DD}$ were dropped for notation compactness.

Box 8.2 Element loop for computing the damage forces and stiffness contributions.

1. Read the relevant element data and allocate the element force vector, the vector and matrix of shape functions, the element nodal nonlocal damage vector and the element load-dependent stiffness contribution.

2. Loop over all integration points in the element:

   (a) Evaluate the shape functions for the gauss point coordinates and construct the shape function vector, $\bar{\mathbf{N}}^e(\boldsymbol{x}_i)$, and matrix, $(\bar{\mathbf{N}}^e(\boldsymbol{x}_i))^T\bar{\mathbf{N}}^e(\boldsymbol{x}_i)$, for Gauss point coordinates $(\boldsymbol{x}_i)$.

   (b) Evaluate the element jacobian and compute the current element volume, v^e.

   (c) Interpolate the nodal nonlocal damage with the shape function to retrieve the Gauss point damage, i.e.:

   $$\bar{D}_i = \sum_{k=1}^{n_{\text{points}}} \bar{\mathrm{D}}_k^e \cdot \bar{\mathrm{N}}_k^e(\boldsymbol{x}_i), \tag{8.27}$$

   where the subscript $(\cdot)_i$ denotes the Gauss point, i.

   (d) Compute the Gauss point contribution to the element damage force vector:

   $$\mathbf{f}_i^{\mathrm{H},e} = (\bar{\mathbf{N}}^e(\boldsymbol{x}_i))^T \bar{D}_i \, v^e. \tag{8.28}$$

   (e) Compute the Gauss point contribution to the element damage load-dependent stiffness:

   $$\mathbf{K}_i^{\mathrm{H},e} = \left[(\bar{\mathbf{N}}^e(\boldsymbol{x}_i))^T \bar{\mathbf{N}}^e(\boldsymbol{x}_i)\right] v^e. \tag{8.29}$$

3. Assemble the gauss point contributions into the element force vector and sitffness matrix.

As mentioned in Section 4.3.2, to make use of the thermomechanics setup to simulate gradient-enhanced damage, a few boundary conditions must be introduced in the damage problem, namely the prescription of initial null damage in the entire domain and also adiabatic boundaries. Furthermore, the square of the nonlocal length-scale parameter, l^2, comes in as the condutivity, with the adoption of a fourier thermal material model. Lastly, the linear temperature-dependent heat source is defined by two coefficients, which are set to -1 and 0 (recall Equation (4.20)).

8.5 Numerical examples

In this section, some preliminary numerical examples are presented to assess the implementation of the implicit gradient-enhanced nonlocal damage model. In the first place, single-element tests are presented in Section 8.5.1, to evaluate the rates of convergence of the Netwon-Raphson method for the new object-oriented version of the Engelen material model. The local and nonlocal responses obtained in the single-element setting are also compared. Section 8.5.2 reports a detailed study of the influence of the coupling scheme setup on the performance of the gradient nonlocal model for the simulation of a rectangular plate with a central circular hole. The choice of the implicit solver, and also the ratio between the time discretisations of the mechanical problem and the coupling scheme were assessed. The rates of convergence of the coupling solution method were also discussed. Finally, Section 8.5.3 showcases the mesh-regularising effect of the implicit gradient nonlocal model, for a double-notched specimen and several values of the nonlocal length-scale parameter. The impact of this material parameter on the overall response of the test piece is also documented.

8.5.1 Single-element tests

Similarly to what was done for the integral nonlocal model (Section 5.5.2), single-element tests were employed to perform a preliminary assessment of the consistency of the implementation presented in Section 8.4. The single finite element under tension, illustrated in Figure 8.2, was utilised, with the material properties shown in Table 8.1. Additionally, a nonlocal length parameter of 1 mm was adopted. Regarding the coupling scheme, 100 pseudo-time increments were adopted for both the mechanical problem and the field-coupling procedure, and Broyden's method was selected as the implicit solver.

Figure 8.3 showcases the effective Cauchy stress and damage evolutions found for the 4-noded finite element, with both reduced and complete integration. The responses obtained with the gradient and local models were identical, although the gradient damage was slightly lower. This is probably due to the staggered solution scheme and the employment of the last converged nonlocal damage in the estimation of the damage stress tensor (recall Section 8.4.2). However, these results demonstrate that, while the implicit staggered solution scheme might not produce the exact solution, in comparison to the isolated mechanical problem, it still yields a very accurate prediction of the mechanical response, given the adoption of an adequate coupling setup (incrementation and solver choice). It is also noteworthy that the gradient nonlocal model showed identical responses for reduced and complete integration, contrarily to what was found for the integral nonlocal model (Section 5.5.2). Nonetheless, this observation was expected, since the adopted loading scenario (Figure 8.2) promotes uniform stress and damage distributions in the single finite element. The integral nonlocal averaging procedure relies on the interactions between Gauss points, and impacts the damage found in the finite element as long as more than a single point is included in each nonlocal domain (see Figure 5.7), although the damage distribution remains uniform. In the gradient case, since nonlocality is introduced by the additional damage diffusion equation, and the local damage distribution estimated by the mechanical problem is uniform, no damage diffusion takes place, i.e. nonlocal damage is already in equilibrium.

Furthermore, Figure 8.4 illustrates the rates of convergence of the Newton-Raphson method, obtained for the reduced integration local and nonlocal cases at several load increments. Both cases showed quadratic rates of convegence, validating the object-oriented version of the Engelen material model (Section 8.4.2). The convergence of the coupling scheme was not addressed for the single-element cases, since no damage homogenisation actually took place.

Table 8.1: Material properties of the single finite element. Legend: E denotes the Young's modulus; ν denotes the Poisson coefficient; ε_f denotes the critical accumulated plastic strain; $\sigma_{y,0}$ denotes the initial yield stress; and $\sigma_{y,2}$ denotes the yield stress at $\bar{\varepsilon}^p = 1.0$.

E / GPa	ν / -	ε_f / -	$\sigma_{y,0}$ / MPa	$\sigma_{y,2}$ / MPa
210	0.30	1.00	243	400

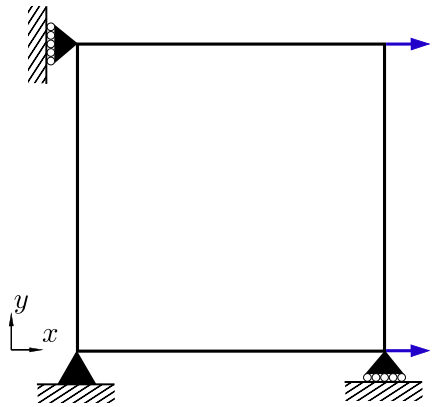

Figure 8.2: Schematic representation of the boundary conditions applied to the single element under tension. Horizontal displacements of 50% of the element's length were prescribed.

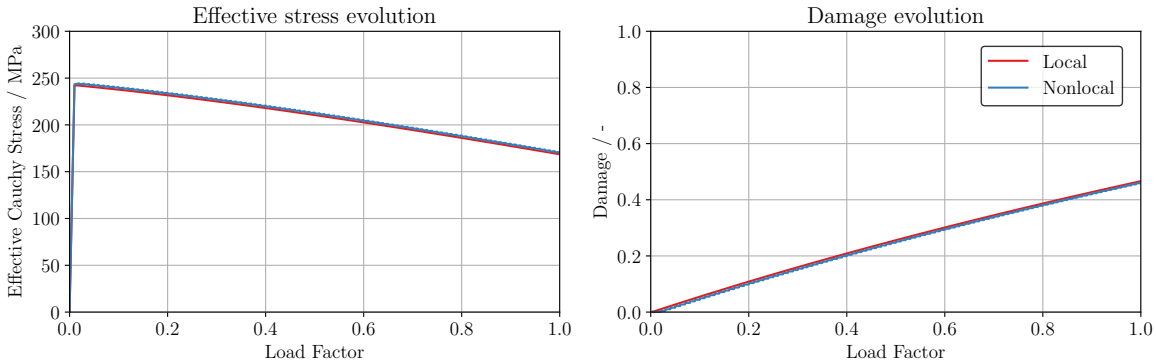

(a) Reduced integration (1 GP).

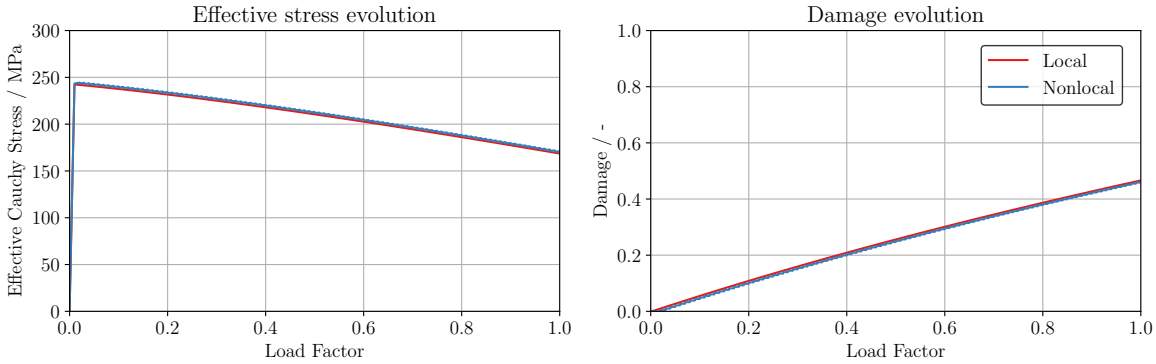

(b) Complete integration (4 GP).

Figure 8.3: Effective Cauchy stress and damage evolutions found with the single-element setup, for the local and the gradient-enhanced nonlocal cases.

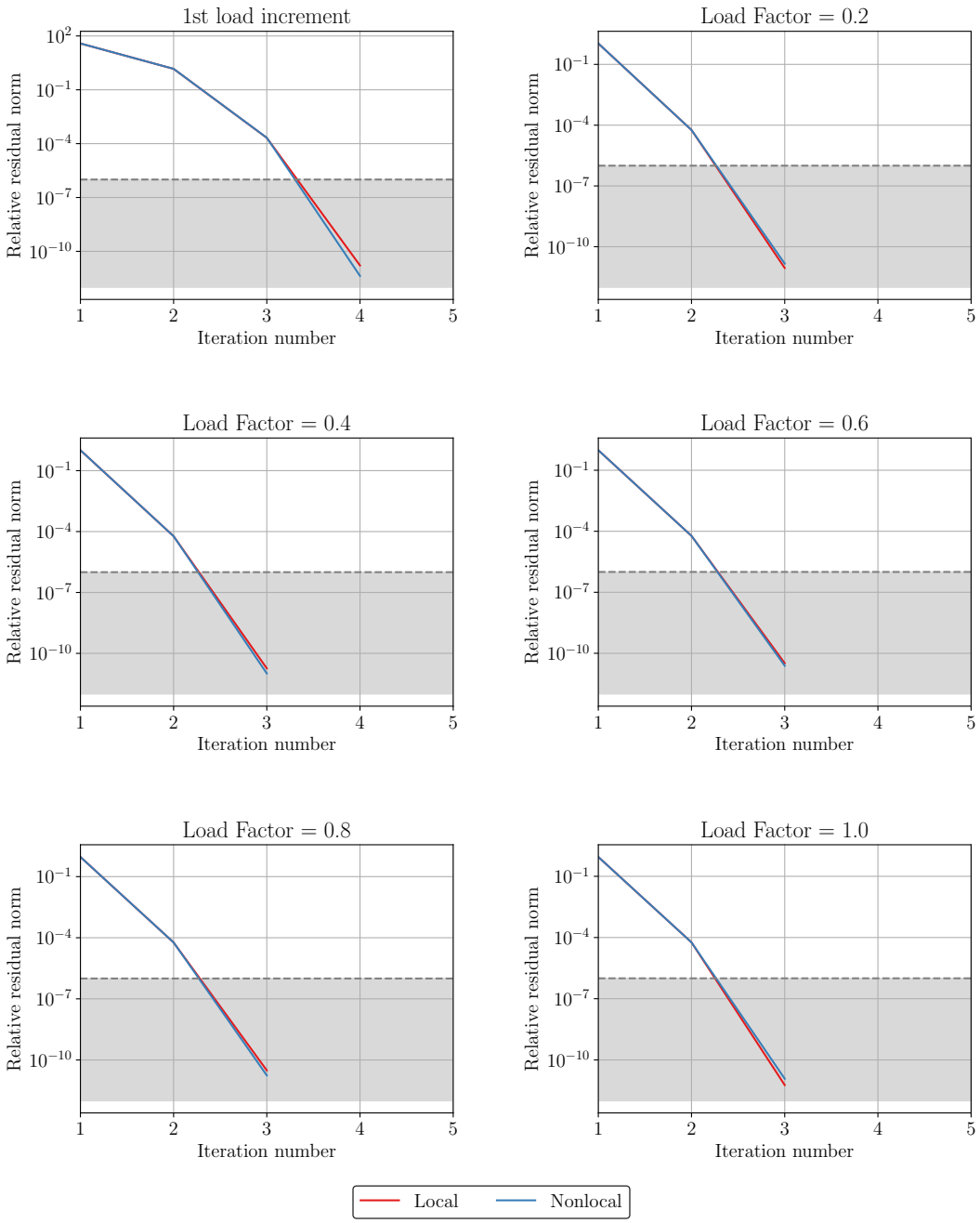

Figure 8.4: Evolution of the norm of the relative residual obtained with the Newton-Raphson method at different load increments, for the single-element setup and the local and gradient nonlocal cases. Relative norms shown in %. A convergence tolerance of 10^{-6} was adopted, as illustrated by the grey dashed lines.

8.5.2 Plate with central hole

In this section, a quarter of a rectangular plate with a central circular hole under a tensile load, illustrated in Figure 8.5a, was utilised to perform a preliminary assessment of the implementation of the gradient-enhancement and the coupled solution scheme. The tensile load was applied by prescribing a 1.0 mm vertical displacement at the top of the plate, as shown in Figure 8.5a. Figure 8.5b depicts the finite element mesh adopted for the discretisation of the plate, while the material prop-

erties utilised in the single-element tests (Table 8.1) were employed again. The values of 1 and 5 mm were considered for the length-scale parameter, to account for distinct extents of nonlocal damage diffusion in this preliminary assessment of the coupled scheme.

That said, the plate was first simulated with local and gradient-enhanced damage to evaluate the effects of these two values of the nonlocal parameter. For these first tests, the gradient cases were run with Broyden's method with the same number of coupling and mechanical problem time steps. Figure 8.6 shows the damage distributions found for the local and gradient-enhanced model, for the two aforementioned values of the nonlocal length-scale. With the local model, the plate failed before half of the prescribed displacement had been applied, whereas both gradient simulations were completed, with two distinct nonlocal damage contours. For a length-scale parameter of 5 mm, the extent of nonlocal diffusion was such that damage initiated at every point of the plate, while the recorded maximum damage was also significantly lower than the one found for a nonlocal length of 1 mm. These results highlight the effects produced by the two selected values of the nonlocal regularisation parameter.

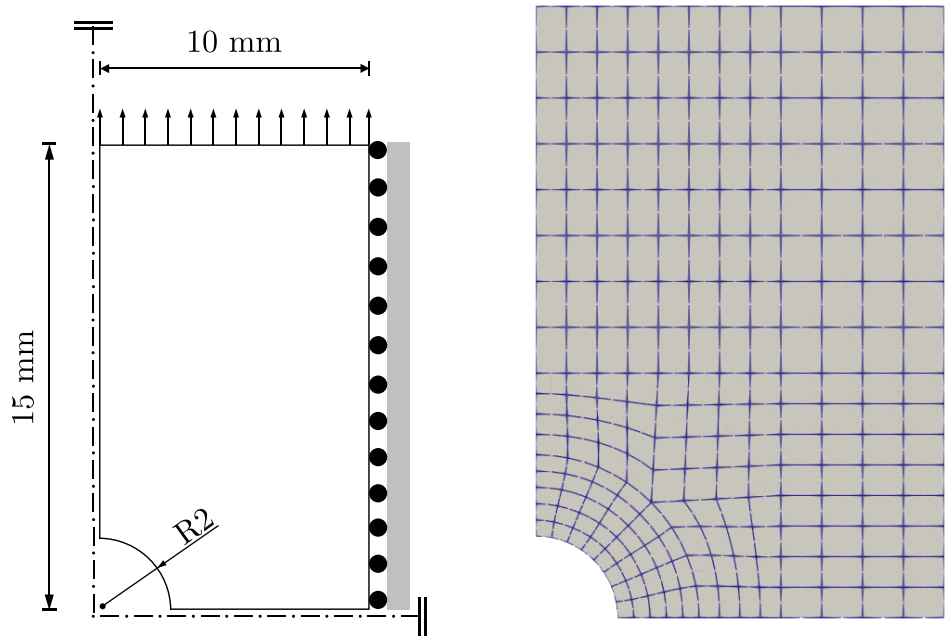

(a) Schematic.

(b) Finite element mesh, containing 216 QUAD8 elements and 715 nodes.

Figure 8.5: Schematic representation of a quarter of a rectangular plate with a circular central hole, under a tensile load, and its finite element discretisation.

Coupling scheme analysis

Having selected two values of the nonlocal length-scale that produce distinct mechanical responses of the plate with a central hole, this section reports a detailed analysis on the influence of the coupling scheme on the computational cost of gradient-enhanced predictions. To that end, the simulations of the plate with the nonlocal lengths of 1 and 5 mm were repeated with the three implicit solvers introduced in Section 8.3 and six different coupling incrementation schemes. In this case, the mechanical problem was discretised in 1000 equally spaced pseudo-time steps. The number of coupling increments, n_c must be equal to or lower than the number of mechanical increments, n_m. Within the adopted staggered coupled scheme, selecting a number of coupling increments lower than the number of mechanical time steps essentially results in solving the coupling problem over a number of mechanical load increments, instead of solving the field-coupling for every load incre-

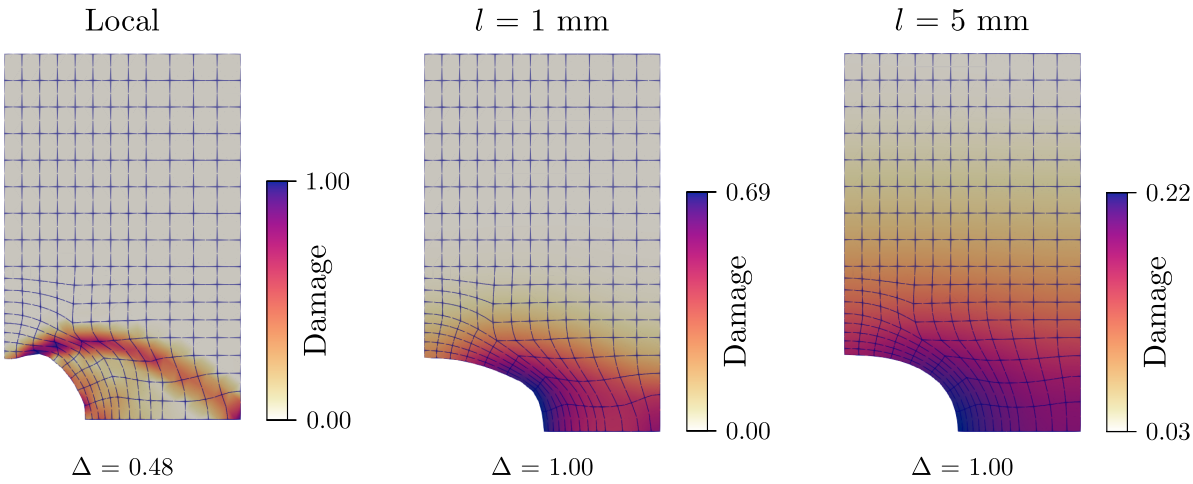

Figure 8.6: Damage distributions found for the plate with a central hole, with local damage and the gradient-enhanced model, with two different values of the nonlocal length-scale parameter. The load increment, Δ, at which these distributions were observed are also shown, since the local case collapsed before the simulation was completed.

ment. With this in mind, six different values of n_c were considered in this section: 50, 100, 250, 500 and 1000. These are associated to different coupling incrementation ratios, $n_c : n_m$: 1:20, 1:10, 1:4, 1:2 and 1:1.

Figure 8.7 presents the evolutions of the computational cost of the gradient simulations, with respect to the number of coupling increments, for the two values of the nonlocal length and the three implicit solvers. For a length of 1 mm, the computational times generally decreased with the increase in the number of coupling increments. Broyden's method recorded the lower computational times, with the fixed-point method as a close second, and the Aitken relaxation coming in third with the largest time measures. Conversely, for a length of 5 mm, increasing the number of coupling increments resulted in generally longer simulations, for the three implicit solvers. Furthermore, as shown in Figure 8.8, identical results are found for the simulation of the plate, with the extreme coupling ratio values. This indicates that, for this particular nonlocal length, adopting a lower number of coupling increments not only reduced the computational cost of the simulation, but also did not equate to any loss of accuracy, compared to the results obtained with a 1:1 ratio. With regard to their relative performance, Broyden's method remains the best-performing solver, while the fixed-point algorithm still recorded similar results.

To visualise the convergence behaviour of the coupling scheme, Figures 8.9 and 8.10 depict the evolutions of the norm of the relative residual, at several values of the Load Factor, for the best performing number of coupling increments for each nonlocal length, i.e. for $l = 1$ mm, $n_c = 1000$ (Figure 8.9), for $l = 5$ mm, $n_c = 50$ (Figure 8.10). In the case of the lower nonlocal length, since the convergence is shown for a 1:1 coupling ratio, both the fixed-point and Broyden's methods converge in two coupling iterations, for most load increments. In spite of this, the Aitken relaxation method required an additional coupling iteration throughout the entire pseudo-time domain. For a length of 5 mm, convergence is shown for a 1:20 ratio, resulting in a larger numbers of iterations before the coupling tolerance is reached. Nonetheless, the stable convergence of the coupling scheme, even for an unbalanced coupling ratio, is an encouraging sign in regards to the implementation of the gradient-enhanced model. Once again, while the convergence of the other two solvers was practically coincident for most coupling increments, the Aitken relaxation method required an additional iteration to achieve the tolerance.

The findings presented in this section show the consistency and robustness of the implementated gradient-enhanced nonlocal model and its coupled solution strategy. Adding to this, it has

been shown that some critical aspects of the coupling scheme have a significant impact on the computational cost of gradient-enhanced simulations, particularly the implicit solver and the coupling increment ratio. Similarly to the observation of Vila-Chã et al. (2023) for the thermomechanical case, Broyden's method was the best performing algorithm for this coupled problem and is employed for the remaining examples presented in this dissertation. It has also been observed that adopting different numbers of coupling increments, relative to the number of mechanical pseudo-time steps, can have a notable effect in the computational time. Nonetheless, this effect was seen to depend on the value of the nonlocal length. This indicates that the selection of the coupling ratio for a particular problem and nonlocal length requires a detailed preliminary analysis, to optimise the performance of gradient-enhanced simulations.

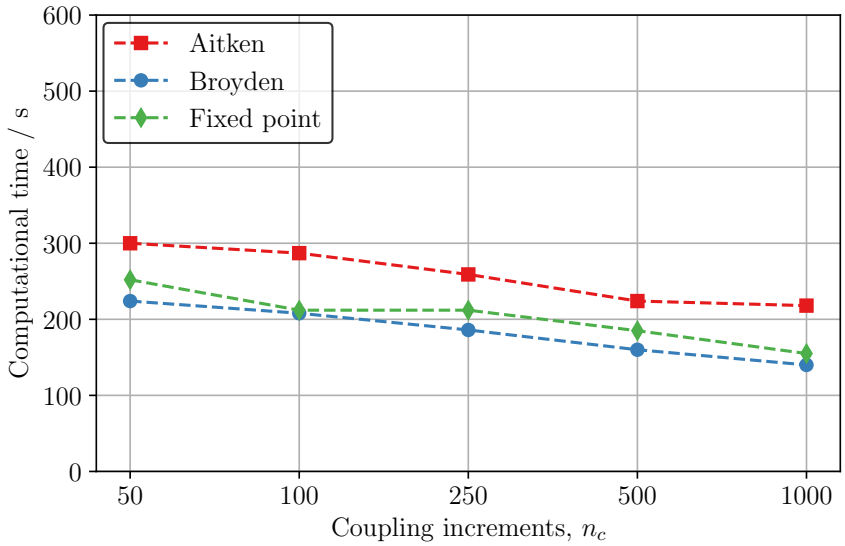

(a) $l = 1$ mm.

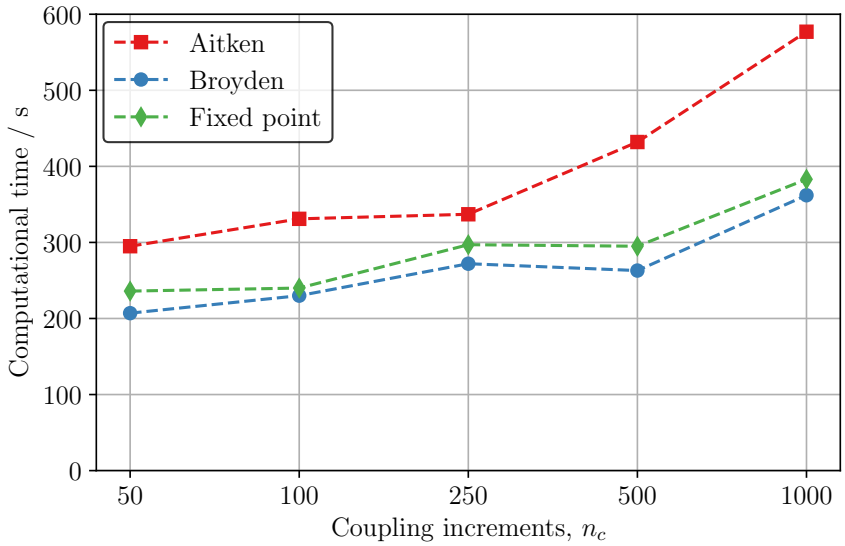

(b) $l = 5$ mm.

Figure 8.7: Computational times recorded for the simulation of the plate with a central hole with two nonlocal lengths, three different implicit solvers and several numbers of coupling increments.

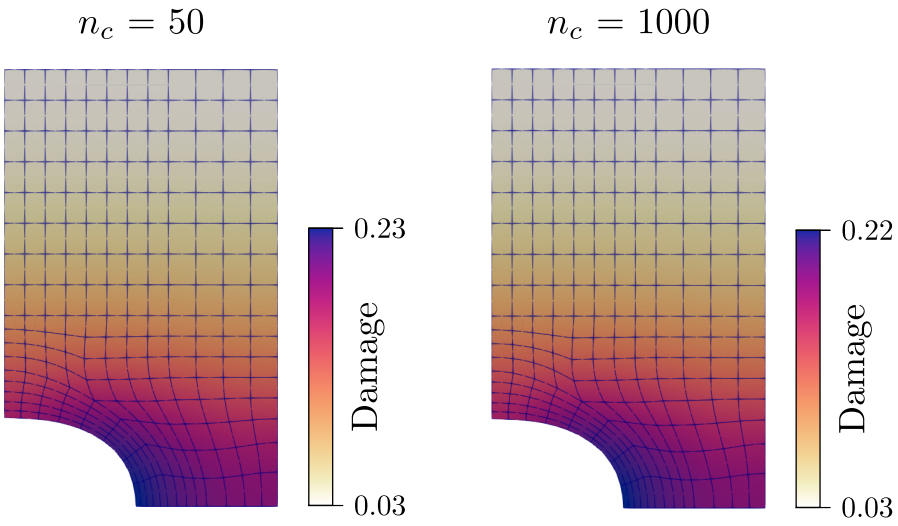

Figure 8.8: Gradient-enhanced damage distributions found for the plate with a central hole, with two different numbers of coupling increments, n_c. Results for l = 5 mm.

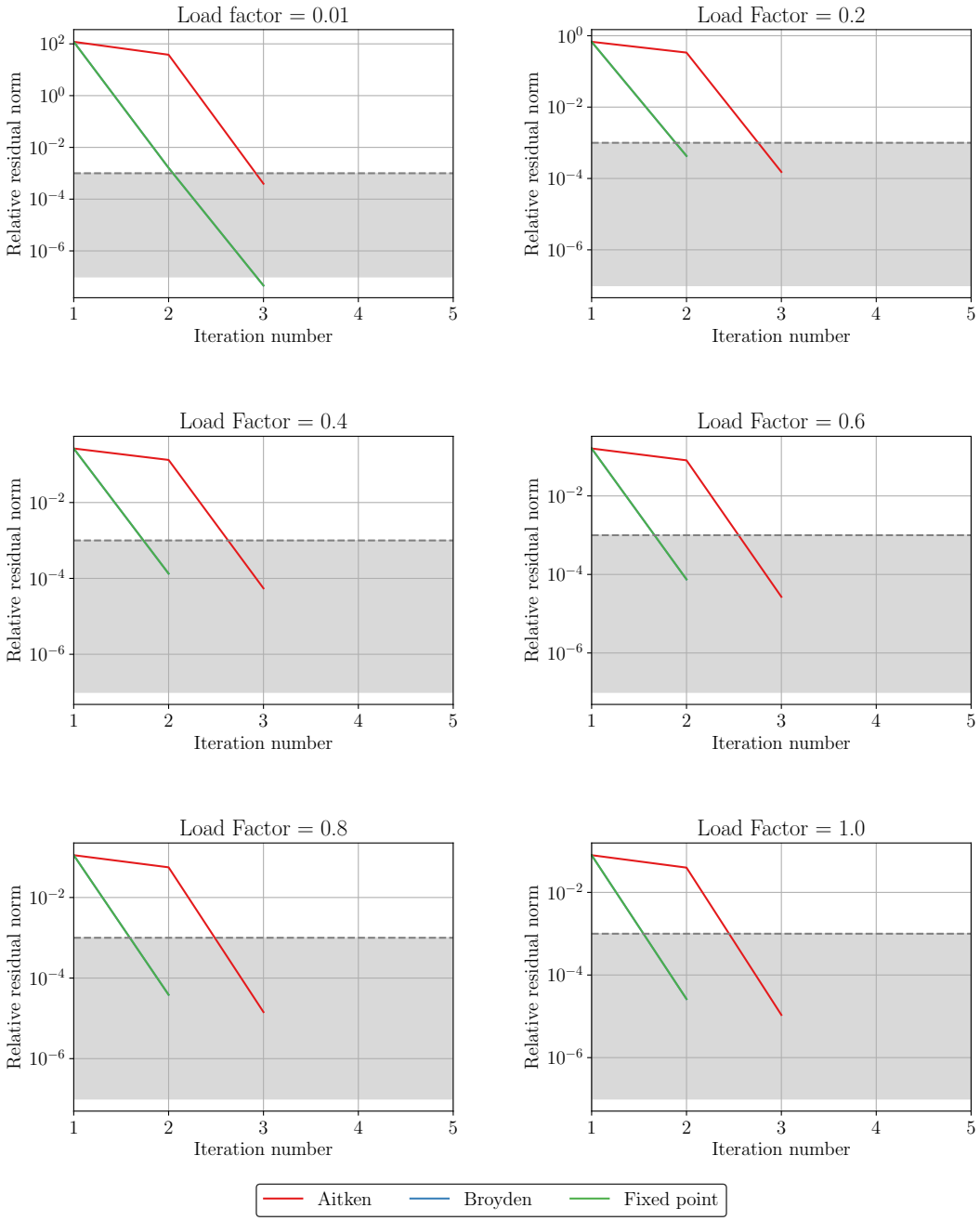

Figure 8.9: Evolution of the norm of the relative residual obtained with the different implict solver, for different load increments, for the plate with central hole, with $l = 1$ mm. Relative norms shown in %. Results obtained for $n_c = 1000$ and $n_m = 1000$. In this case, the first coupling increment couild not be used since damage was yet to initiate. A coupling convergence tolerance of 10^{-3} was adopted, as illustrated by the grey dashed lines.

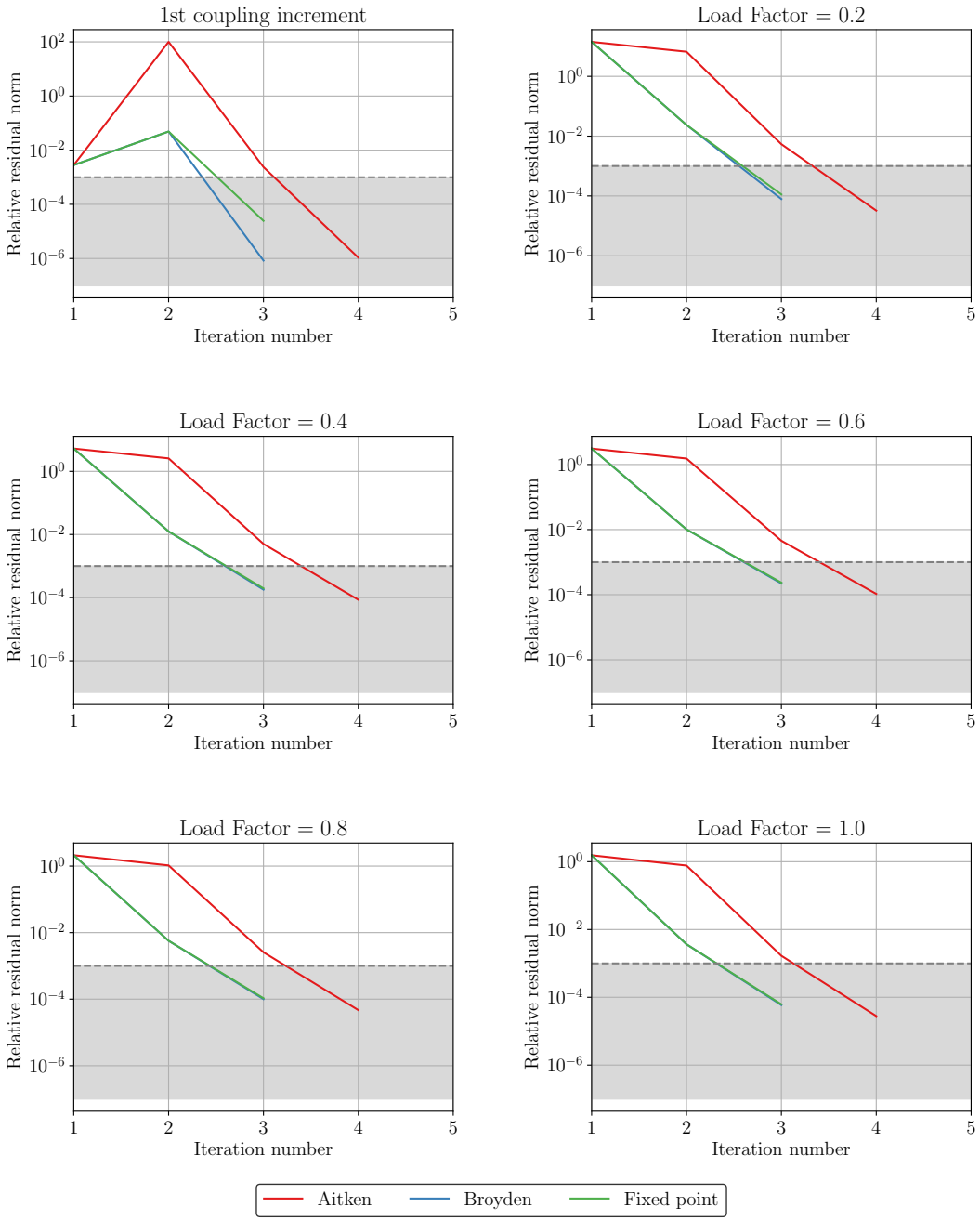

Figure 8.10: Evolution of the norm of the relative residual obtained with the different implict solver, for different load increments, for the plate with central hole, with l = 5 mm. Relative norms shown in %. Results obtained for n_c = 50 and n_m = 1000. A coupling convergence tolerance of 10^{-3} was adopted, as illustrated by the grey dashed lines.

8.5.3 Double-notched specimen

Having assessed the implementation of the gradient-enhanced nonlocal model in previous sections, the analysis presented here is dedicated to the mesh regularisation of a double-notched specimen, illustrated in Figure 8.11, subjected to a vertical displacement of 1 mm. The two finite element meshes shown in Figure 8.12 were used and the material properties shown back in Table 8.1 were adopted. Moreover, bearing the goals of this analysis in mind, the gradient-enhanced simulations of the test piece were performed assuming a 1:1 coupling ratio.

Figure 8.13 shows the reaction curves obtained for the local and gradient models, where the following nonlocal length values were used: 0.1 and 0.2 mm. For the local Engelen model, the simulations of the double-notched specimen collapsed before the total prescribed displacement was applied. Moreover, this occurred at different load increments depending on the finite element discretisation, with the local reaction curves expectedly showcasing spurious mesh sensitivity. The introduction of the gradient-enhancement resulted in an attenuation of the observed mesh dependency, while also avoiding the premature abortion of the simulations. As observed in the case of the integral model (recall Section 5.5), increasing the value of the nonlocal length led to a lower degree of softening, but also to a reduction of the pathological mesh dependency.

Figure 8.14 illustrates the damage contours obtained for the two local and the four nonlocal cases. Adopting a nonlocal length of 0.1 mm did not yield significant changes in the damage distributions found for both mehses, in relation to the local case. Nonetheless, this value of the nonlocal parameter allowed a reasonable reduction in the mesh dependency (Figure 8.13), underscoring the effectiveness of the gradient-enhancement. For a nonlocal length of 0.2 mm, the obtained damage distributions were pratically coincident. The gradient-enhanced simulation of the double-notched specimen was repeated for greater values of the nonlocal length, to assess its impact on the resulting damage distributions. Figure 8.15 depicts the nonlocal damage contours obtained for the values of 0.5, 1 and 5 mm. The observed nonlocal distributions are essentially mesh-independent. Additionally, increasing the value of the nonlocal length led to the diffusion of damage over broader regions of the specimen, culminating in the 5 mm case, in which damage is almost uniform throughout the entire domain. This effect had not been observed with the integral model (recall the analysis of Section 5.5.4), and is further discussed in Section 8.6.

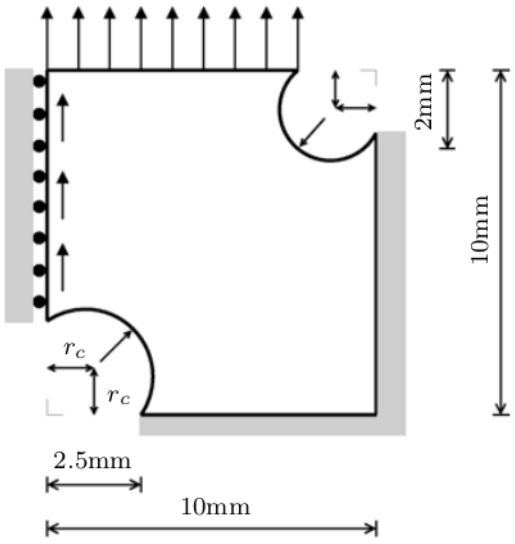

Figure 8.11: Schematic representation of the double-notched specimen, taken from Andrade (2012).

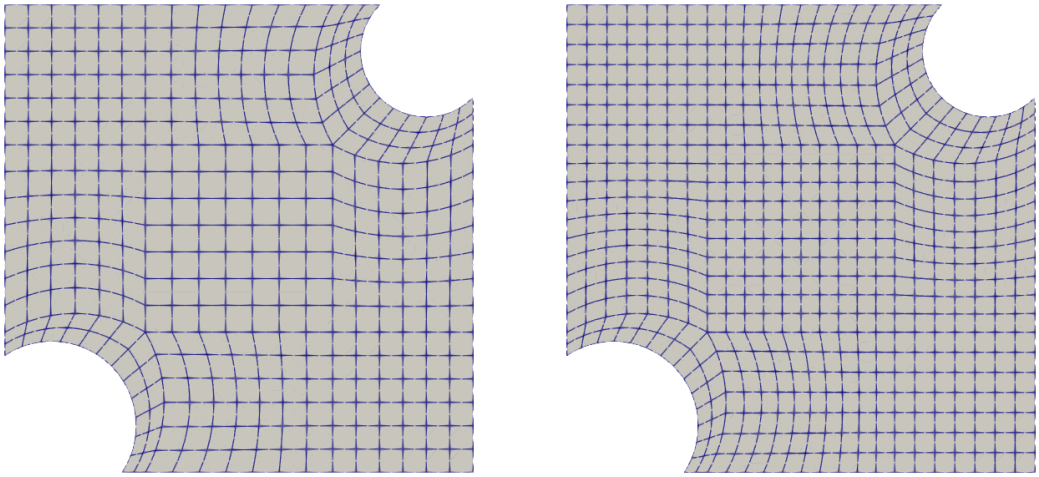

(a) Coarse mesh, containing 349 QUAD8 elements and 1134 nodes.

(b) Fine mesh, containing 548 QUAD8 elements and 1751 nodes.

Figure 8.12: Finite element meshes used to discretise the double-notched specimen.

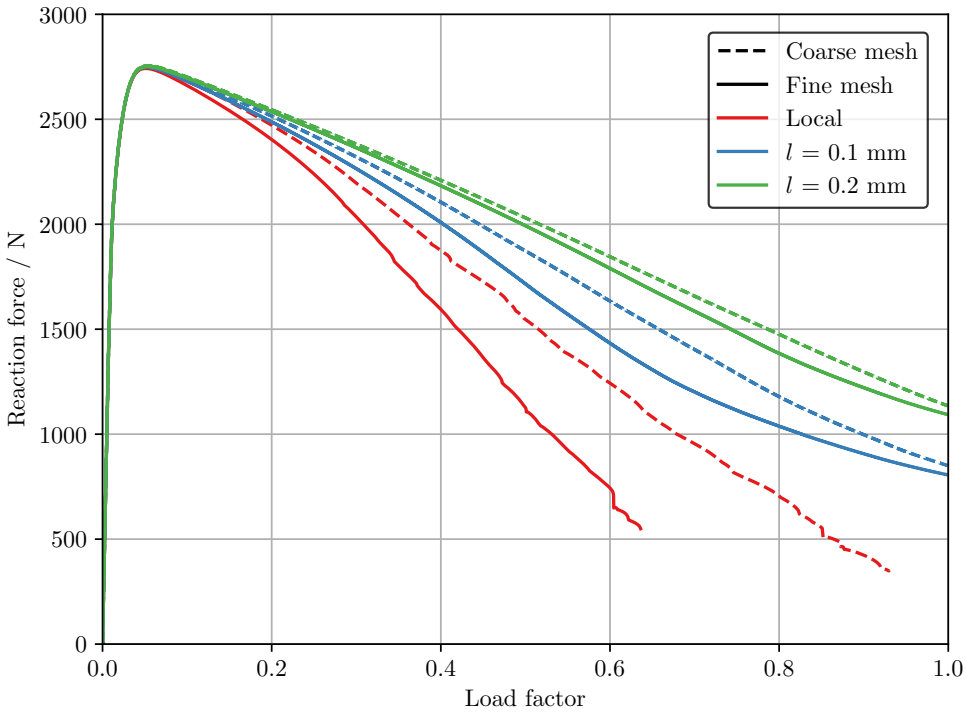

Figure 8.13: Reaction curves obtained with the gradient-enhanced and local models for the double-notched specimen, for the two finite element meshes and two values of the nonlocal length parameter.

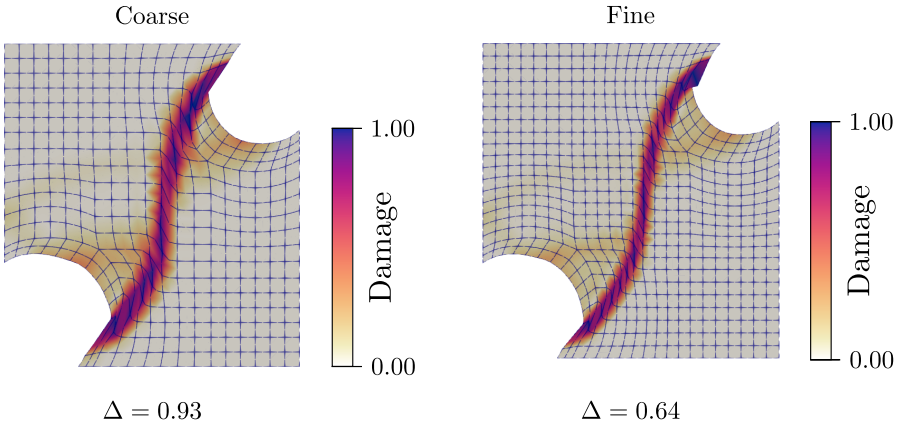

(a) Local model.

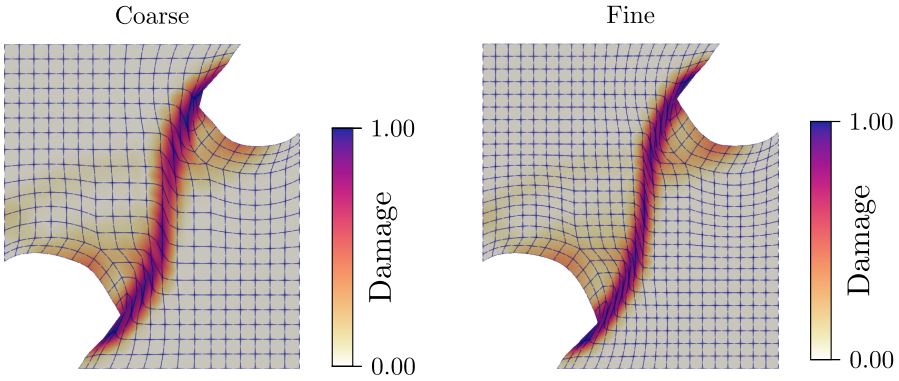

(b) Gradient, $l = 0.1$ mm.

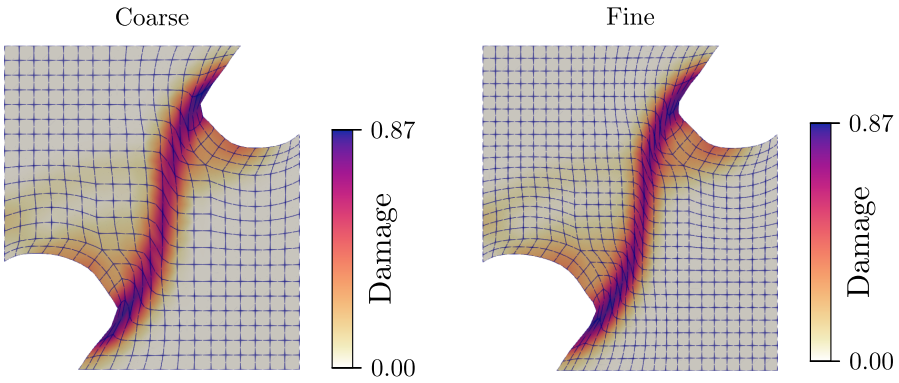

(c) Gradient, $l = 0.2$ mm.

Figure 8.14: Damage distributions found for each mesh of the double-notched specimen, for the local and the two nonlocal cases.

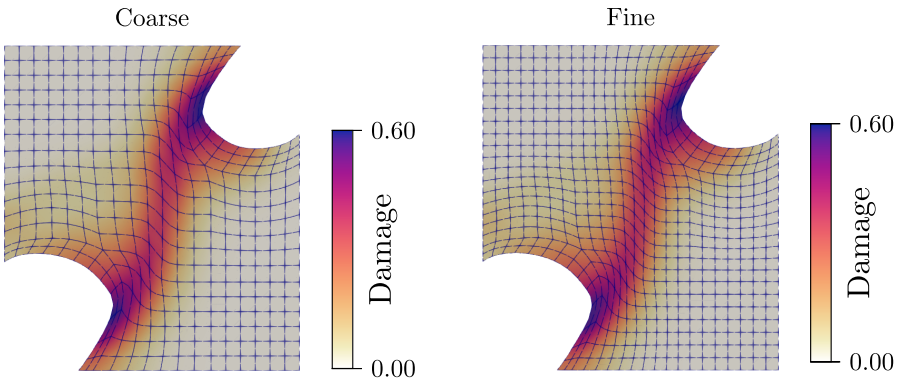

(a) Gradient, $l = 0.5$ mm.

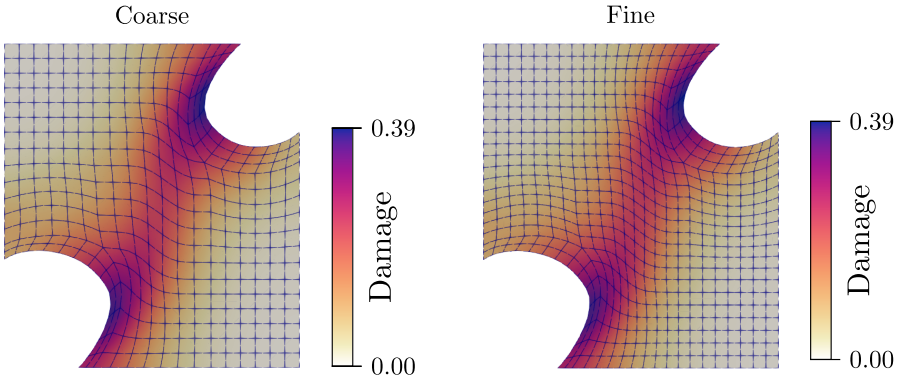

(b) Gradient, $l = 1.0$ mm.

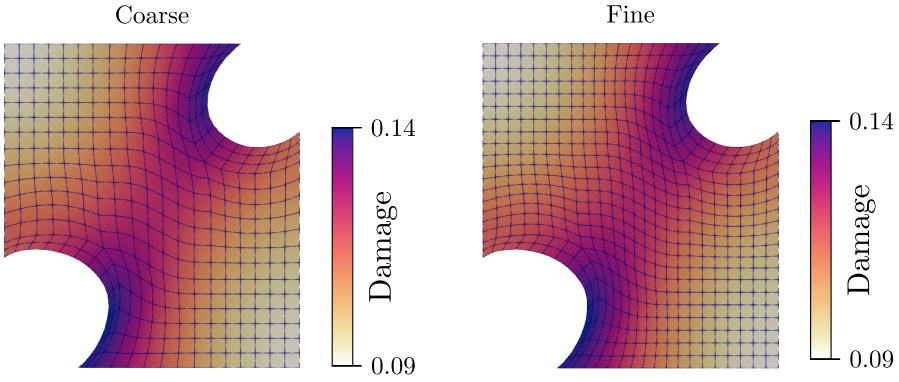

(c) Gradient, $l = 5.0$ mm.

Figure 8.15: Nonlocal damage distributions found for each mesh of the double-notched specimen, for larger values of the nonlocal length parameter.

8.6 Comparison with integral-type strategy

Despite their similar roots, numerical comparisons between gradient-enhanced and integral type nonlocal models are still pratically non-existent. Notable exceptions include the pioneering works by Peerlings et al. (1996a, 2001), which tackled important questions regarding explicit and implicit gradient models and their relation to their integral counterpart. Nevertheless, their analyses is limited to an academic example of a uni-dimensional bar under uniaxial tension. Moreover, de Vaucorbeil et al. (2022) presented an assessment of the two models, for meshless methods and considering the rate of plastic strain as the nonlocal variable. Finally, Nahrmann and Matzenmiller (2021) evaluated the predictive capabilities of integral and gradient models for distinct stress states, while also addressing numerical aspects.

In the following, a detailed juxtaposition of the two nonlocal approaches is detailed. This comparative analysis is done with the compact shear specimen in Section 8.6.1 and the plate with a central hole in Section 8.6.2.

Remark 5 *Since the integral nonlocal radius, R, and the gradient nonlocal length, l, have, up until now, been denoted by distinct symbols. To ease the comparison of the two strategies, these nonlocal characteristic parameters are hereinafter represented, in a unified fashion, by L.*

8.6.1 Compact shear specimen

The first example used to compare the two nonlocal approaches is the compact shear specimen, first employed in Section 5.5.3. Its geometry and the boundary conditions imposed on the specimen are illustrated in Figure 5.9, and the finite element meshes shown in Figure 5.10 were adopted again. However, in this section, the material properties reported in Table 8.1 were utilised.

The simulations of the compact shear specimen were performed with the local model and the two nonlocal approaches, for the two meshes, and adopting a nonlocal length parameter of 2.5 mm. For the gradient approach, a coupling incrementation ratio of 1:10 was employed. Figure 8.16 depicts the resulting reaction curves, where the four nonlocal cases are coincident, contrarily to their mesh-dependent local counterparts. In fact, as observed in Section 5.5.3, this particular example is particularly mesh-dependent is the absence of a nonlocal regularisation parameter. Furthermore, Figure 8.17 shows the obtained nonlocal damage distributions. For the same value of the nonlocal parameter, adopting the gradient-enhanced model resulted in the redistribution of damage over a wider region of the test piece. The gradient damage contours also showcase a smoother evolution of damage, from the shear deformation band to the rest of the specimen. In comparison, the integral nonlocal model is associated with damage distributions which seems to be more confined to the shear deformation band. To further assess these differences in the nonlocal damage distributions, the simulations were repeated for a nonlocal length-scale of 10 mm. Figure 8.18 reports the damage contours obtained with this new value of the nonlocal parameters, where the differences between the results of the two strategies are amplified. In spite of the larger value of the nonlocal radius, the integral damage distributions are still confined to the deformation band region, while the gradient-enhancement resulted in a smooth damage distribution from the band to the rest of the geometry.

These results highlight the fundamental numerical differences between the two strategies. As discussed in Section 5.5.4, the nonlocal model of integral-type can yield damage distributions which showcase particular concentration in the more finely discretised regions of the domain, due to the reliance of the averaging procedure on the locations of Gauss points. Conversely, since the gradient-enhancement is performed in a global damage diffusion problem, it leads to smoother damage contours.

Finally, the simulations were repeated with a nonlocal length-scale of 5 and 7.5 mm, to evaluate the computational cost of nonlocal simulations with the two approaches, depending on the mesh

and the regularisation paramater. Figure 8.19 shows the computational times recorded for all cases, where it can be seen that the gradient simulations were faster than integrals ones. Nonetheless, there is a number of caveats concerning direct computational time comparisons between these two approaches, due to the differences in the adopted solution schemes. While, the integral model is solved through the standard finite element solution scheme, the gradient-enhanced model requires an adequate coupling strategy. In practice, gradient-enhanced simulations, for instance, require the use of two CPUs, in parallel, to address each problem, as mentioned in Section 8.4, contrarily to the integral cases which were all run with a single CPU. Furthermore, as seen in Section 8.5.2, there are several factors within the coupling scheme that affect the computational cost of gradient simulations, and no preliminary analysis was performed for this particular specimen and the adopted nonlocal length values to assess them. Notwithstanding, the computational cost of nonlocal simulations and the influence of the nonlocal parameter and mesh refinement can be evaluated separately for each approach, before drawing a comparison between them. This range of values of the nonlocal length-scale is not sufficient to promote significant changes in the computing times on each approach, thus the difference between the two approaches remains constant with the length-scale parameter. The level of mesh refinement, however, was seen to influence the gap between the computational times recorded between the two strategies, with the finer mesh cases showing a larger differential between the cost of integral and gradient simulations.

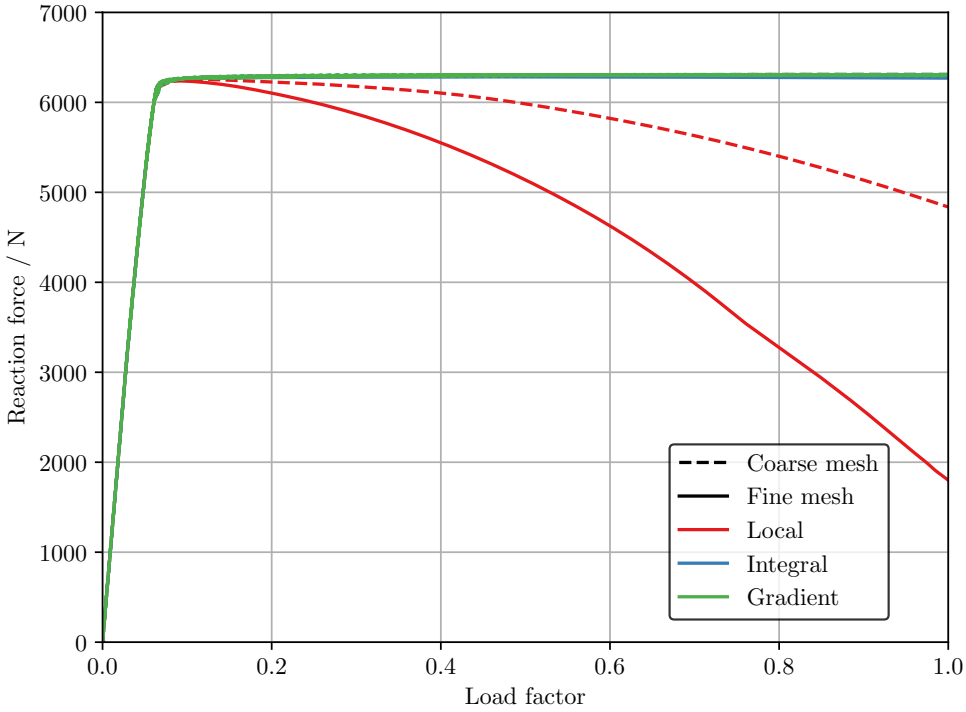

Figure 8.16: Reaction curves obtained with the both nonlocal approaches and the local model for the compact shear specimen, for each finite element mesh.

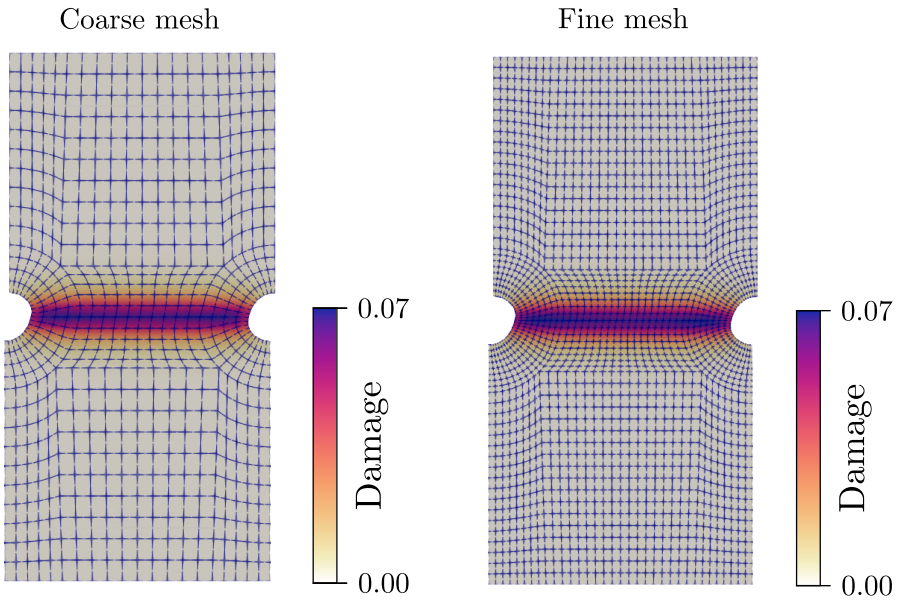

(a) Gradient.

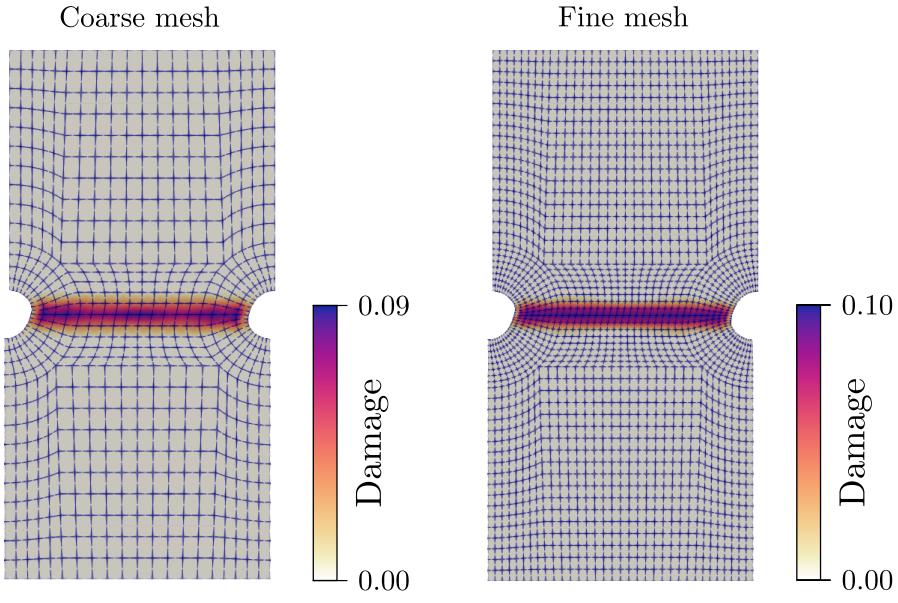

(b) Integral.

Figure 8.17: Nonlocal damage distributions found for each mesh of the compact shear specimen, for the two nonlocal models. A nonlocal length parameter of 2.5 mm was employed in both cases.

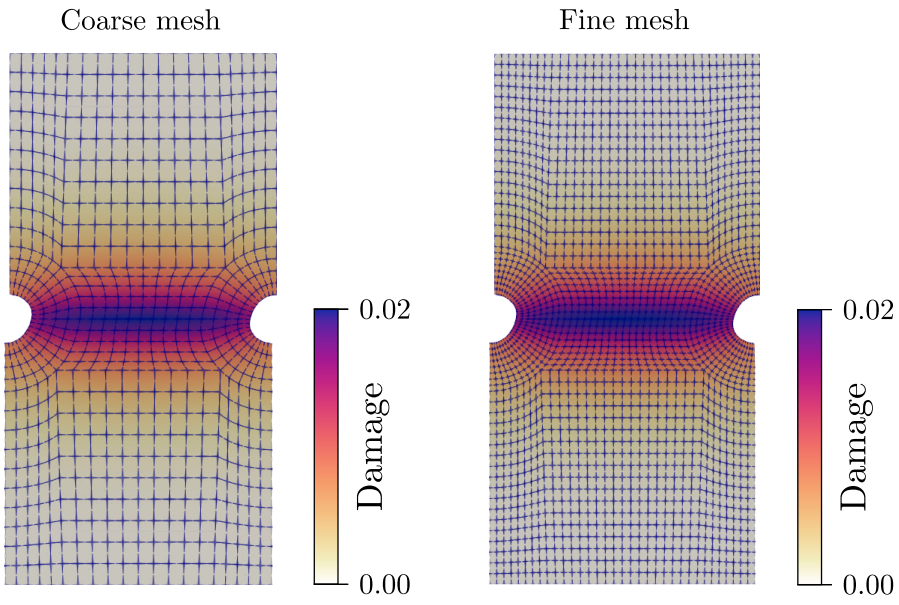

(a) Gradient.

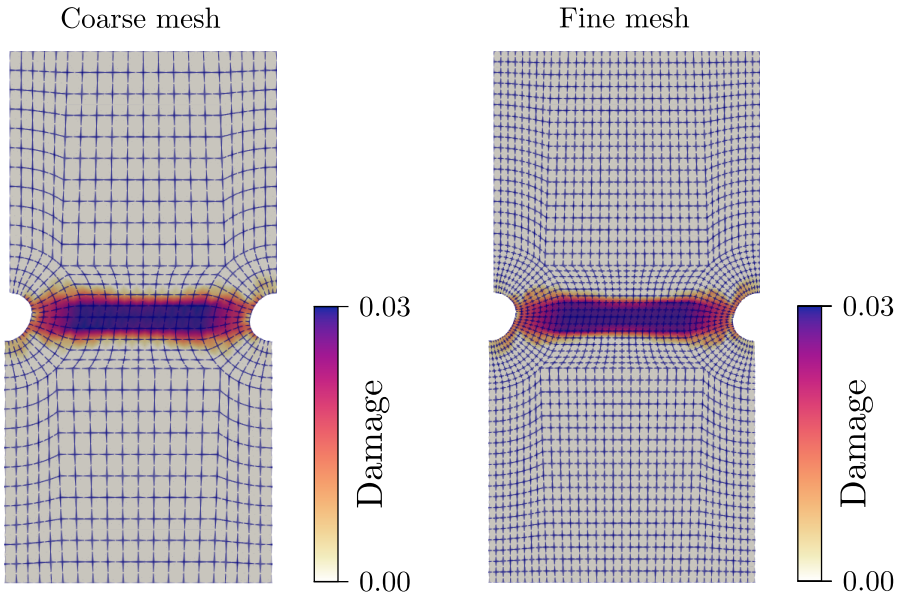

(b) Integral.

Figure 8.18: Nonlocal damage distributions found for each mesh of the compact shear specimen, for the two nonlocal models and a nonlocal length of 10 mm.

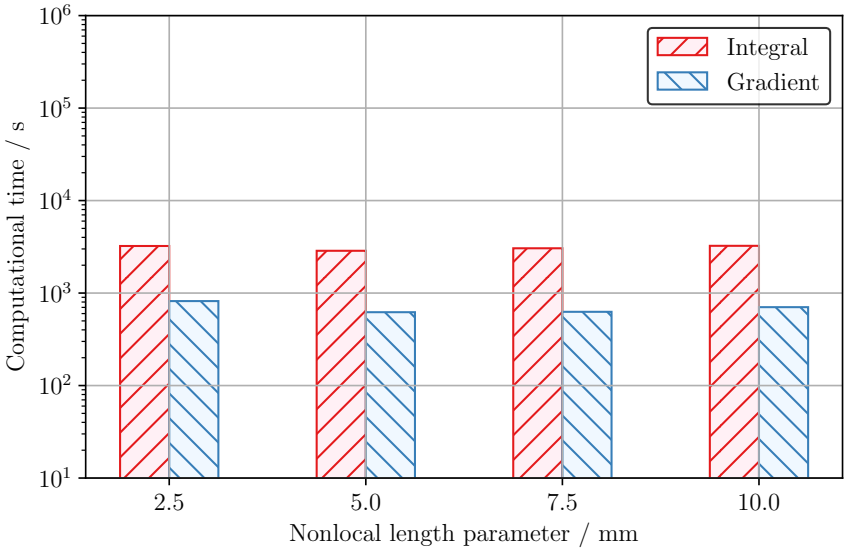

(a) Coarse mesh.

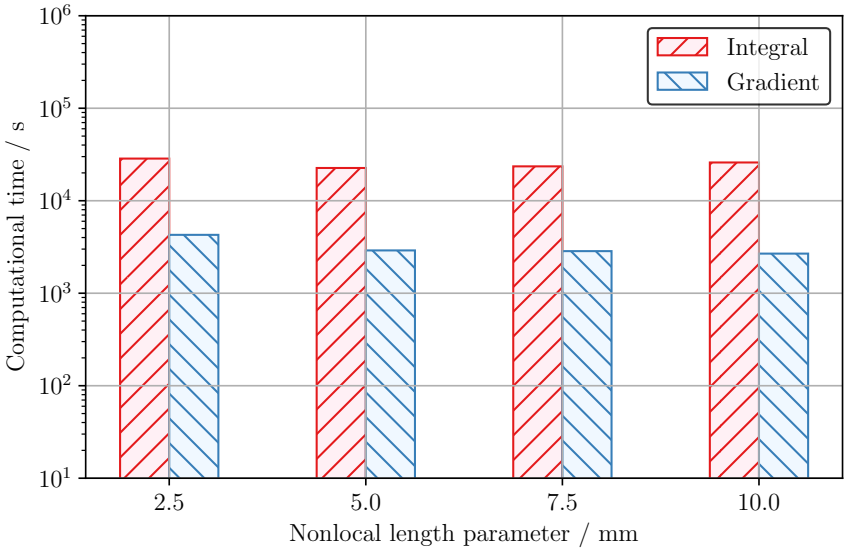

(b) Fine mesh.

Figure 8.19: Computational times recorded for the nonlocal simulations of both meshes of the compact shear specimen.

8.6.2 Plate with central hole

The second example for the comparison between the implicit gradient and integral nonlocal models is the plate with a central hole, first employed in Section 8.5.2. Having assessed the mesh regularisation effects observed with the two strategies, and also compared the resulting damage distributions in Section 8.6.1, a more detailed analysis on the effects of the value of the nonlocal length-scale for the two strategies is presented here. In this section, the same material properties (Table 8.1) and finite element mesh (Figure 8.5b) were adopted, for the same prescribed vertical displacement of 1 mm. For the gradient cases, a coupling ratio of 1:4 was selected.

The first set of simulations was performed for the nonlocal length values of 0.5, 1 and 1.5 mm, for both strategies. Figure 8.20 depicts the resulting reaction curves, where reasonable deviations were observed between the two approaches. For the same nonlocal length values, the integral strategy was associated with greater reductions in the degree of softening. In fact, the gradient-enhanced response for $L = 1.5$ mm is similar to the integral response obtained for $L = 1$ mm. This demonstrates that the fundamental and numerical differences between these two nonlocal approaches are also present in the impact of the value of the nonlocal length-scale on the mechanical response of softening media. This impact may be dependent on several factors. For instance, in the integral nonlocal case, the adoption of a different weighting function modifies the reduction in the degree of softening observed with the increase of the nonlocal radius, as observed in Section 5.5.4. That said, the effect of a given value of the nonlocal characteristic length-scale on the mechanical response of a material undergoing softening is dependent on the adopted nonlocal model, its formulation and features.

It is also worth noting that the simulations for $L = 0.5$ mm both failed due to convergence issues. The damage distributions at failure are depicted in Figure 8.21, where it can be seen that, contrarily to the integral case, the gradient-enhanced simulation aborted before unitary damage was reached. In fact, for this particular value of the nonlocal length, the coupling scheme could not converge past $\Delta = 0.82$. This underscores the main disadvantage of implicit staggered schemes, relative to their monolithic counterparts: altough unconditional stability is assured, it may require an excessive number of coupling iterations or, as occurred here, the implicit solver may fail to converge.

To further study the effects of the nonlocal length on the responses obtained with the two strategies, the simulations were repeated for several values of this parameter: 2, 5 and 10 mm. Figure 8.22 illustrates the damage distributions found for nonlocal lengths of 1, 2 and 5 mm, for both nonlocal models. For $L = 1$ mm, the two damage contours are similar, although the integral one seems to concentrate more in the proximity of the notch and the gradient one is more diffuse, and the maximum nonlocal damage values are also comparable. However, for the greater values of the nonlocal length, the differences between the obtained damage distributions increase, both in qualitative and quantitative terms. For the gradient case, increasing the value of the nonlocal length leads to an increase in the intensity of damage diffusion, resulting in smooth distributions of damage from the notch region to the rest of the geometry. This also leads to the presence of some level of damage in the entire domain, which occurred for both $L = 2$ and $L = 5$ mm. In the integral case, increasing the value of the nonlocal radius slightly increases the domain where damage is confined, while also increasing the uniformisation of damage in said domain. This, in turn, is associated with a decrease in the value of the maximum nonlocal damage. This effect is particularly visible in the comparison between the integral damage contours for $L = 2$ and $L = 5$ mm, where, for the latter value, the boundaries between the damage and undamaged regions of the plate become clearer, and the maximum damage value sharply decreases.

To observe the effects of these different damage distributions on the mechanical response of the plate, Figures 8.23 and 8.24 depict the stress and strain distributions obtained for the two nonlocal models and the nonlocal lengths of 1 and 5 mm. For the first value, although the damage distributions were somewhat akin, the strain and stress contours present some distinctions, similarly to what had been seen for the reactions (Figure 8.20). The integral strain contour is more localised,

recording a larger maximum equivalent strain value. Furthermore, the integral case also obtained a significantly greater maximum value of the effective Cauchy stress, found in the lower right corner of the modelled geometry. This is likely due to the fact that this particular region recorded a lower value of nonlocal damage in the integral case, in comparison to the gradient one, due to the concentration of damage near the notch. That said, since similar values of the equivalent strain were found, less damage resulted in a significantly higher stress. For a nonlocal length of 5 mm, although very distinct damage contours were attained with the two nonlocal models, the resulting strain distributions are almost identical, and the stresses are also relatively comparable.

The final ingredient in this comparison is assessing the impact of the nonlocal length on the computational cost of integral and gradient nonlocal simulations, bearing in mind the discussion of Section 8.6.1 in this regard. Figure 8.25 shows the computational times measured for all nonlocal simulations performed in this section, excluding the nonlocal length of 0.5 mm since both the integral and the gradient cases terminated prematurely. Similarly to what was observed in Section 5.5.4, after a certain point, increasing the value of the nonlocal radius is associated to a considerable increase in the computational cost of integral nonlocal simulations. Conversely, for the gradient-enhanced cases, increasing the nonlocal length does not yield a discernible increase in the computational times. This observation reflects the different numerical effects of increasing this parameter in each nonlocal model: in the integral case, it leads to a progressive loss of global stiffness matrix sparsity, not only increasing the size of the problem, but also hindering the performance of several features of the standard finite element solution scheme, which rely on matrix sparsity for efficiency; in the gradient case, increasing the nonlocal length parameter alters the damage balance problem, however, since nonlocal damage diffusion occurs between adjacent elements, this does not result in any loss of sparsity of the damage stiffnes matrix, nor does it increase the computational cost of solving the damage balance problem.

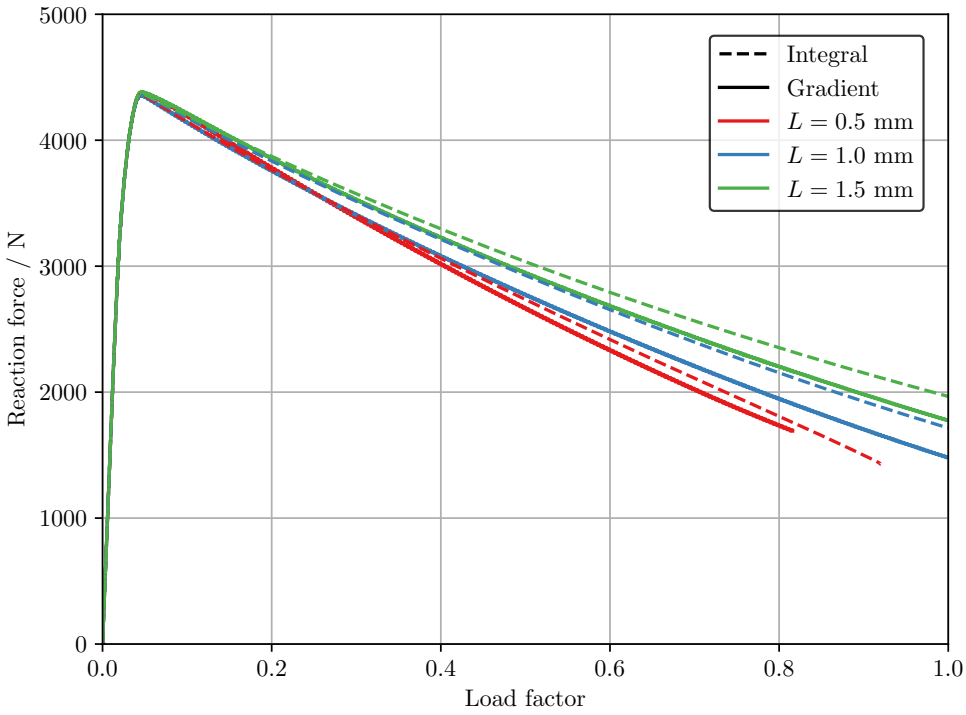

Figure 8.20: Reaction curves obtained with the both nonlocal approaches and the local model for the plate with a central hole, for several values of the nonlocal length parameter.

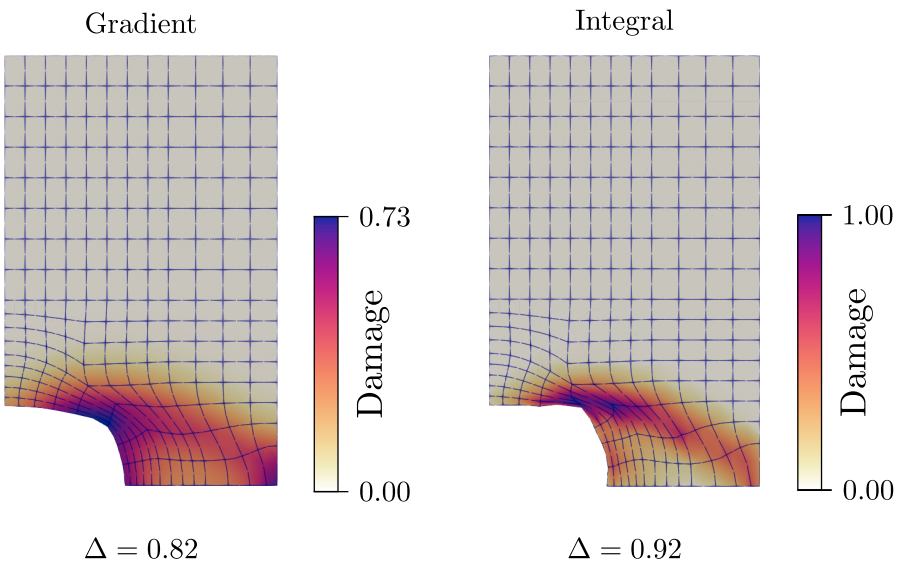

Figure 8.21: Nonlocal damage distributions obtained with the two nonlocal strategies, for the plate with a central hole and $L = 0.5$ mm.

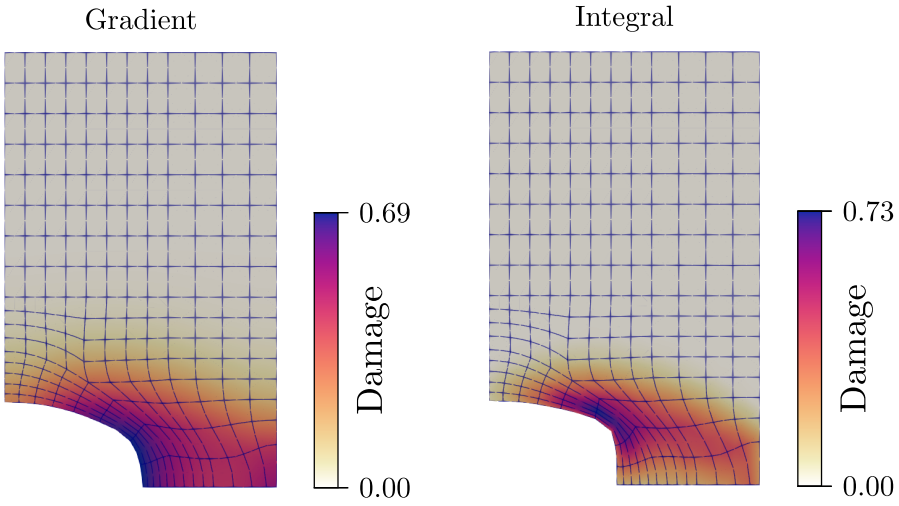

(a) $L = 1.0$ mm.

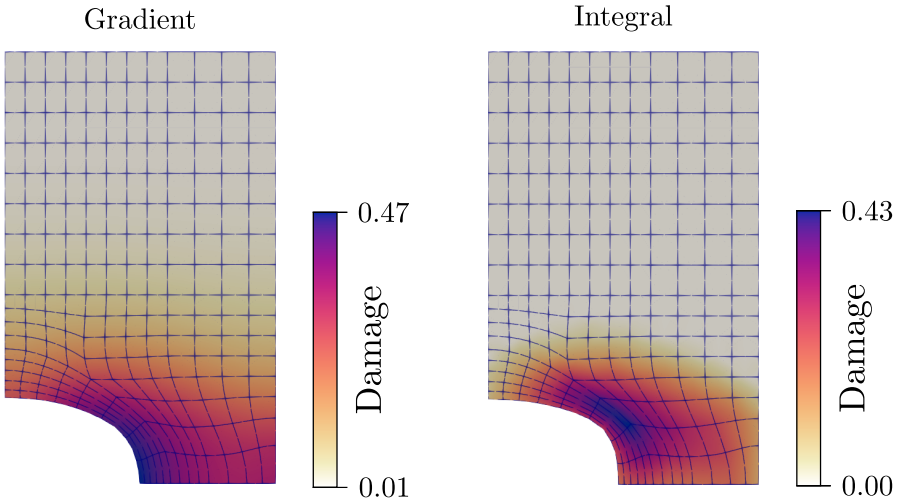

(b) $L = 2.0$ mm.

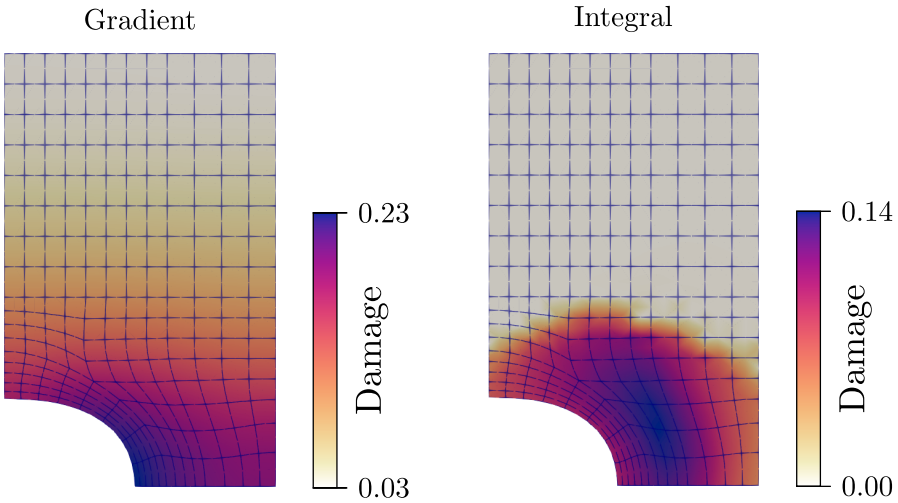

(c) $L = 5.0$ mm.

Figure 8.22: Nonlocal damage distributions obtained with the two nonlocal strategies, for the plate with a central hole and several values of the nonlocal length parameter.

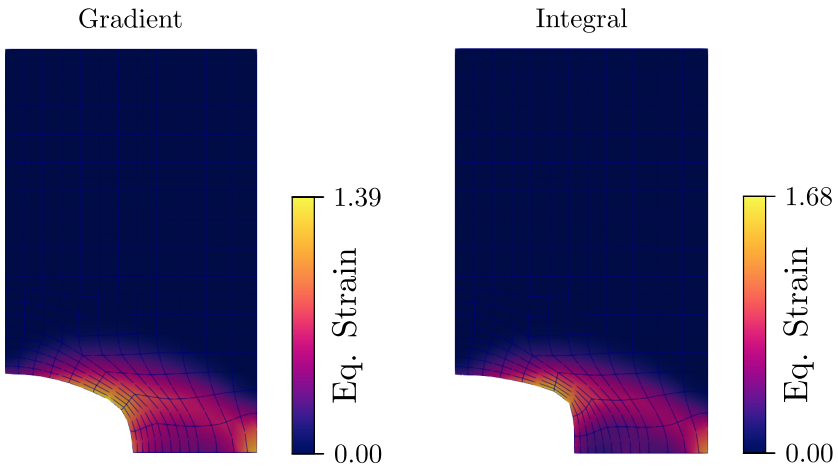

(a) Equivalent strain.

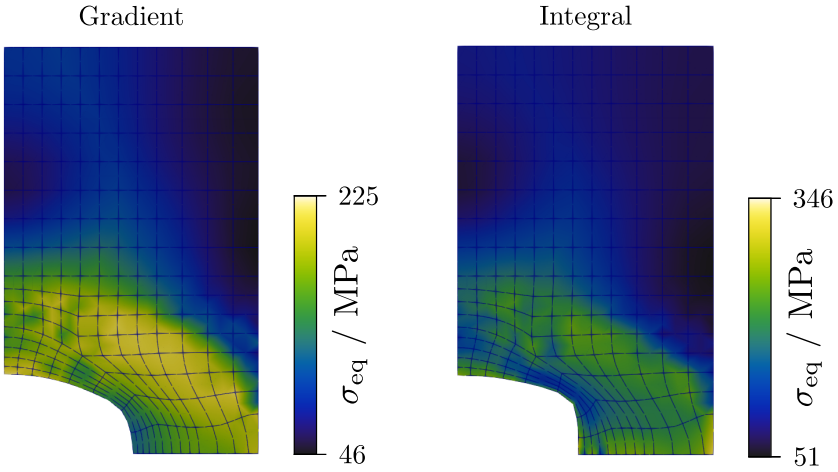

(b) Effective Cauchy stress.

Figure 8.23: Strain and stress distributions obtained with the two nonlocal approaches for the plate with a central hole and a nonlocal length parameter of 1.0 mm.

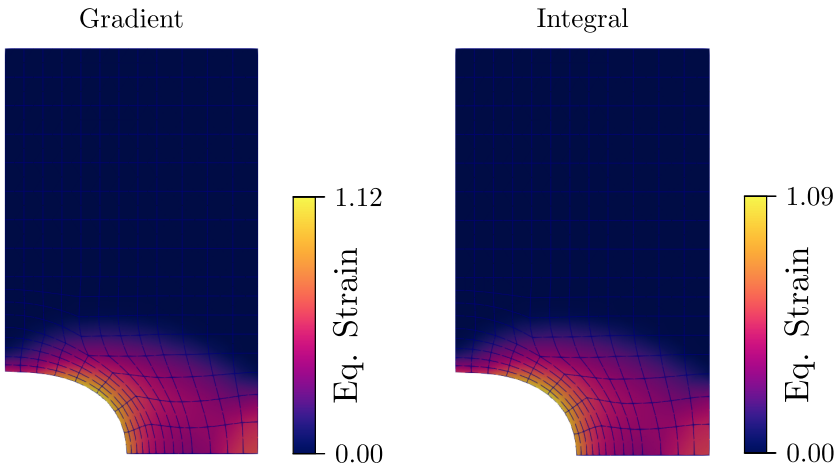

(a) Equivalent strain.

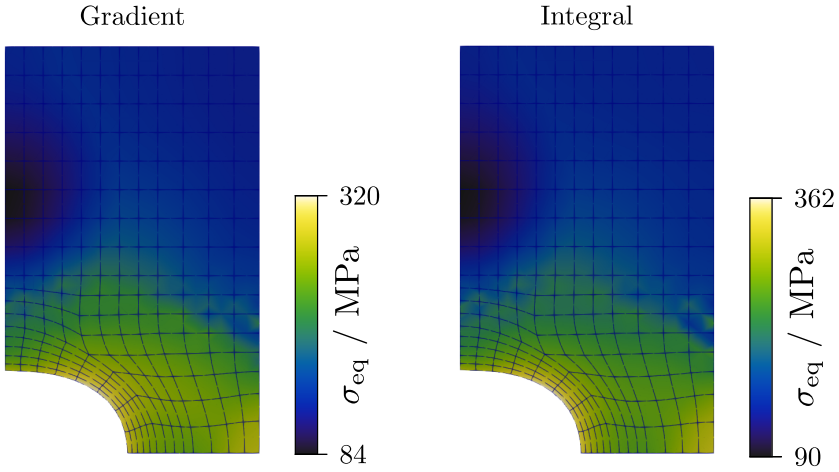

(b) Effective Cauchy stress.

Figure 8.24: Strain and stress distributions obtained with the two nonlocal approaches for the plate with a central hole and a nonlocal length parameter of 5.0 mm.

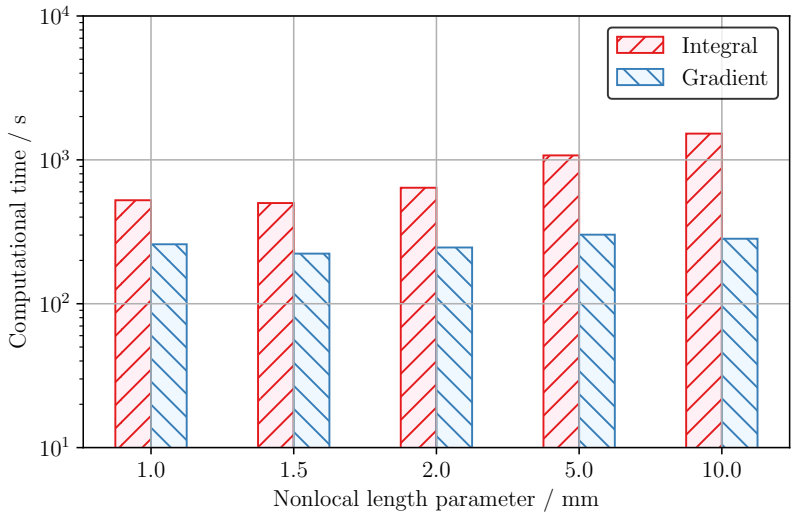

Figure 8.25: Computational times measured for all nonlocal simulations of the plate with a central hole.

8.7 Discussion

In this chapter, the implementation of a gradient-enhanced nonlocal damage model for ductile failure is presented and assessed through various numerical examples. The overall stability and robustness of the staggered solution scheme is showcased, and a detailed numerical comparison between gradient and integral nonlocal models is carried out.

The single-element tests presented in Section 8.5.1 reveal identical mechanical responses and convergence rates for the local and gradient nonlocal Engelen models. In addition, the absence of averaging for any integration scheme of the single finite element contrast with the observations of Section 5.5.2, where integral nonlocal averaging initiates as long as there are neighbouring Gauss points. In the gradient case, since the element is under a homogeneous stress and damage state, no redistribution takes place. Thereafter, a preliminary assessment of the coupling scheme and some of its features is reported in Section 8.5.2. Broyden's method was the best-performing implicit solver for all coupling incrementation ratios and nonlocal length values, in accordance with the observation of Vila-Chã et al. (2023). With regard to the coupling ratio, different tendencies are observed for the two selected values of the nonlocal length, hence this is still an unresolved issue. Lower numbers of coupling increments are associated with a slower convergence of the coupling scheme, even if when these low ratios are the less time-consuming strategy. Section 8.5.3 addressed the mesh regularisation of the double-notched setup, where the impacts of the gradient-enhancement are observed even for relatively low values of the nonlocal length, with a reduction in mesh dependency. Furthermore, the adoption of large values of the nonlocal parameter are related to a greater degree of damage diffusion within the entire domain.

Regarding the comparison between the two nonlocal models, detailed in Section 8.6, both differences and similarities are found. With the compact shear specimen, either strategy is associated to a very effective elimination of pathological mesh dependency, relative to the local model (Section 8.6.1). In spite of this, distinct effects are observed with the increase in the nonlocal length-scale. For the gradient case, damage diffusion occurs within a wider region of the specimen, resulting in a smooth damage contour. Conversely, the integral case is associated with a minor increase in the damaged region, which seems limited to the densely populated area of the finite element mesh. In terms of computing time, although the selected range of nonlocal length values did not bring about any discrepancies between integral and gradient cases, the adoption of the finer discretisation of the specimen promotes a greater increase in the computational cost of integral nonlocal simulations. For the second example, shown in Section 8.6.2, both approaches are associated with a decrease in the observed level of softening, particularly for increasing values of the nonlocal length. Furthermore, the same values of this parameter yield different responses, with the integral model being associated with a greater reduction of softening. This observation, however, is dependent on some of the features of the nonlocal approaches, such as the weighting function of the integral strategy. For larger nonlocal length values, similar effects are observed for the plate and compact shear setups, even if more extreme values are considered for the former case. Additionally, for the plate example, the differences found in the damage distributions are contextualied with the corresponding stress and strain contours. For a lower nonlocal length, although the damage distributions are similar for integral and gradient models, the underlying strain and stress plots present considerable differences. For the larger nonlocal length, the contrary observation is made: even though the damage distributions are poles apart, the associated strain and stress contours are comparable. This analysis showcases the complex differences in numerical behaviour that arise between two nonlocal formulations, which are theoretically adjacent. In the plate example, having considered a larger array of nonlocal length values, the computing times of the gradient case remain essentially constant, while the cost of integral simulations rises consistently with increase in the nonlocal length.

In summary, even though the gradient-enhanced nonlocal model is obtained through the Taylor expansion of the integral kernel, significant computational distinctions are verified between the

two approaches. The root of these differences lies in the numerical strategies for establishing nonlocal interactions. On the one hand, the integral type model employs specific weighting functions to modify the constitutive relations at each integration point to account for size effects. This introduces additional terms in the stiffness matrix, which raises numerical issues, particularly for larger nonlocal radius values. Moreover, since nonlocal interactions are modelled explicitly with the nonlocal kernel, if damage initiates in a particular region of the domain, the length to which this damage is averaged is ultimately limited by the nolocal radius. On the other hand, the gradient approach models nonlocal interactions implicitly, with the addition of the averaging equation, where damage is diffused between adjacent nodes. This justifies the distinctions observed for larger nonlocal lengths, where almost uniform damage distributions could be found for the gradient strategy. Furthermore, the fact that nonlocal connections are accounted for in an implicit manner, meands that the damage stiffness matrix remains sparse even for large nonlocal lengths, rendering the computational cost of gradient simulations essentially insensible to the value of this parameter.

Finally, the premature abortion of the gradient simulation shown in Figure 8.21 raises another significant difference between integral and gradient strategies. While the integral approach is only dependent on the stability and convergence of the Newton-Raphson method, the gradient case also requires the convergence and efficiency of the implicit coupling scheme, which is not guaranteed. That said, a more detailed study of the coupling scheme, its setup and efficiency, for a wider set of problems, spatial discretisations, and nonlocal length values should be pursued in the future.

CHAPTER 9

IMPLEMENTING PHASE-FIELD FRACTURE TOWARDS MULTI-SCALE MODELLING OF DAMAGE

9.1 Introduction

Phase-field approaches to fracture were extensively discussed in Section 4.4, where their versatility and predictive capabilites were highlighted. These models have shown particular potential for modelling severe localisation phenomena at lower spatial scales, where material heterogeneities play a crucial role. In addition, several guides for the implementation of phase-field models in commercial finite element programs can be found in the literature, taking advantage of pre-existing solution schemes for coupled problems. In this dissertation, the implementation of the gradient-enhanced nonlocal model within the thermomechanics branch of LINKS, detailed in Chapter 8, was used as the basis for the implementation of a phase-field model for quasi-brittle fracture.

With this in mind, Section 9.2 presents the hyperelastic constitutive model considered in this section, as well as the finite element discretisation of the phase-field balance equation. Thereafter, the implementation of the phase-field model is described in Section 9.3, and validated with benchmark results from the literature in Section 9.4. Additional numerical examples are shown in Section 9.5, to assess numerical and physical aspects of the model, and demonstrate its potential for modelling the failure of heterogeneous microstructures. The limitations of the implementation presented here are addressed and the next steps towards the multi-scale mdoelling of damage with phase-field approaches are outlined. Section 9.6 draws the main conclusions from this chapter and discusses future prospects.

9.2 Phase-field model for quasi-brittle hyperelastic materials

In the following, the application of phase-field fracture for a hyperelastic constitutive model is described. The main ingredients of the hyperelastic model are addressed in Section 9.2.1. Thereafter, Section 9.2.2 presents the finite element discretisation of the phase-field equation, and briefly summarises the solution of the coupled system of equations with the staggered approach detailed in Section 8.3.

9.2.1 Hyperelastic constitutive model

The logarithmic strain tensor was assumed as the main kinematical quantity of the hyperelastic material model:

$$\boldsymbol{\varepsilon} = \ln \boldsymbol{V} = \ln\left(\boldsymbol{F}\boldsymbol{R}^T\right). \tag{9.1}$$

Its work conjugate stress measure is the Kirchhoff tensor, i.e.

$$\boldsymbol{\tau} = \mathbf{D}^e : \boldsymbol{\varepsilon}, \tag{9.2}$$

where $\mathbf{D}^e$ is the fourt-order isotorpic elasticity tensor. Furthermore, a relatively simple free-energy potential was assumed in this contribution, where

$$\psi_0 = \frac{1}{2}\boldsymbol{\tau} : \boldsymbol{\varepsilon}. \tag{9.3}$$

In light of Equation (9.3), the history-dependent maximum strain energy can be recast as

$$\mathscr{H} = \max_{t\in[0,t_f]}\left[\frac{1}{2}\boldsymbol{\tau} : \boldsymbol{\varepsilon}\right] \tag{9.4}$$

Furthermore, considering the degradation function in Equation (4.38), the damaged energetic potential reads:

$$\psi = \frac{1}{2}\left[(1-\phi)^2 + \chi\right]\boldsymbol{\tau} : \boldsymbol{\varepsilon}. \tag{9.5}$$

Accordingly, the damaged Kirchhoff stress tensor can be computed as

$$\boldsymbol{\tau}^* = \left[(1-\phi)^2 + \chi\right]\boldsymbol{\tau}. \tag{9.6}$$

9.2.2 Finite element discretisation of the phase-field equation

Recalling the generic form of the weak balance statement for phase-field models in Equation (4.22), the expressions for the micro-stresses, ω and ξ, (Equations (4.35) and (4.36)) can be employed to arrive at

$$\int_{\boldsymbol{\varphi}(\Omega)}\left[\boldsymbol{\sigma}^* : \nabla_{\boldsymbol{x}}(\boldsymbol{\eta}) + \left(2(1-\phi)\mathscr{H} + \frac{G_c}{l}\phi\right)\kappa + G_c l \nabla_{\boldsymbol{x}}(\phi)\cdot\nabla_{\boldsymbol{x}}(\kappa)\right]\mathrm{d}v = \int_{\boldsymbol{\varphi}(\partial\Omega)}(\boldsymbol{t}\cdot\boldsymbol{\eta})\mathrm{d}a, \tag{9.7}$$

for admissible virtual displacements, $\boldsymbol{\eta}$, and virtual phase-field, κ. Since the phase-field and mechanical problems are addressed separately, it becomes convenient to de-couple the weak form of equilibrium. Hence, the weak form of momentum balance reads:

$$\int_{\boldsymbol{\varphi}(\Omega)}\boldsymbol{\sigma}^* : \nabla_{\boldsymbol{x}}(\boldsymbol{\eta})\mathrm{d}v = \int_{\boldsymbol{\varphi}(\partial\Omega)}(\boldsymbol{t}\cdot\boldsymbol{\eta})\mathrm{d}a. \tag{9.8}$$

Conversely, the weak form of the phase-field equation is given by

$$\int_{\boldsymbol{\varphi}(\Omega)}\left[\left(2(1-\phi)\mathscr{H} + \frac{G_c}{l}\phi\right)\kappa + G_c l \nabla_{\boldsymbol{x}}(\phi)\cdot\nabla_{\boldsymbol{x}}(\kappa)\right]\mathrm{d}v = 0. \tag{9.9}$$

Similarly to what was done in Section 8.2.2, the phase-field must be discretised and interpolated with recourse to finite element shape functions:

$$\phi \approx {}^h\phi = \mathbf{N}^g_\phi \Phi, \tag{9.10}$$

where $\mathbf{N}^g_\phi$ is the global phase-field interpolation function and Φ is the global phase-field nodal vector, given by

$$\Phi = \left\{\phi_1, \phi_2, \ldots, \phi_j, \ldots, \phi_{n_{\text{points}}}\right\}^T, \tag{9.11}$$

where ϕ_j is the nonlocal damage at global node j. In addition, the virtual phase-field is also discretised with $\mathbf{N}^g_\phi$. With this in mind, the governing equations (Equations (9.8) and (9.9)) can be discretised. In the case of the mechanical balance equation:

$$\int_{\boldsymbol{\varphi}(^h\Omega)} (\mathbf{B}^g)^T \boldsymbol{\sigma}^* \mathrm{d}v = \int_{\boldsymbol{\varphi}(\partial^h\Omega)} (\mathbf{N}^g)^T \mathbf{t} \mathrm{d}a, \tag{9.12}$$

The above equation coincides with the discretised momentum equation obtained for the gradient-enhanced nonlocal model (see Equation (8.9)). However, differences arise by substituting the expression for the damaged Cauchy stress tensor

$$\int_{\boldsymbol{\varphi}(^h\Omega)} \left[(1-\phi)^2 + \chi\right] (\mathbf{B}^g)^T \boldsymbol{\sigma} \mathrm{d}v = \int_{\boldsymbol{\varphi}(\partial^h\Omega)} (\mathbf{N}^g)^T \mathbf{t} \mathrm{d}a. \tag{9.13}$$

Furthermore, the discretised phase-field equation reads

$$\int_{\boldsymbol{\varphi}(^h\Omega)} \left[2(1-\phi)\mathscr{H}(\mathbf{N}^g_\phi)^T + \frac{G_c}{l}(\mathbf{N}^g_\phi)^T\phi + G_c l(\nabla_{\boldsymbol{x}}(\mathbf{N}^g_\phi))^T \nabla_{\boldsymbol{x}}(\phi)\right] \mathrm{d}v = 0. \tag{9.14}$$

Staggered solution scheme

Recalling the discussion in Section 8.3, the adoption of a staggered solution scheme allows effectively de-coupling the nonlinear system of equations, which for the phase-field case, may be expressed as

$$\begin{bmatrix} \mathbf{K}_{uu} & \mathbf{K}_{u\phi} \\ \mathbf{K}_{\phi u} & \mathbf{K}_{\phi\phi} \end{bmatrix}^i_{n+1} \begin{bmatrix} \delta\mathbf{u} \\ \delta\Phi \end{bmatrix}^{i+1}_{n+1} = - \begin{bmatrix} \mathbf{r}_u \\ \mathbf{r}_\phi \end{bmatrix}^i_{n+1}, \tag{9.15}$$

where $\mathbf{r}_u$ and $\mathbf{r}_\phi$ are the mechanical and phase-field residuals, respectively, obtained through the time-discretisation of the finite element equations, shown in Equations (9.13) and (9.14). For brevity, these terms are not derived here, but the reader is referred to Section 8.2.2, where analogous expressions were presented for the gradient-enhanced nonlocal damage model. By making use of the staggered solution scheme, Equation (9.15) is recast as follows

$$\begin{bmatrix} \mathbf{K}_{uu} & \mathbf{0} \\ \mathbf{0} & \mathbf{K}_{\phi\phi} \end{bmatrix}^i_{n+1} \begin{bmatrix} \delta\mathbf{u} \\ \delta\Phi \end{bmatrix}^{i+1}_{n+1} = - \begin{bmatrix} \mathbf{r}_u \\ \mathbf{r}_\phi \end{bmatrix}^i_{n+1}. \tag{9.16}$$

In this context, the coupling stiffness terms, $\mathbf{K}_{\phi u}$ and $\mathbf{K}_{u\phi}$, need not be explicitly considered, and one must only define the stiffness matrices and residuals for each problem in isolation. That being the case, the phase-field residual, $\mathbf{r}_\phi$, can be defined using Equation (9.14), and is split in two terms, for mathematical convenience. For a given pseudo-time increment and the k-th iteration of the Newton-Rpahson method, one may write

$$\mathbf{r}^{(k-1)}_\phi = \left[\int_{\boldsymbol{\varphi}(^h\Omega)} G_c l(\nabla_{\boldsymbol{x}}(\mathbf{N}^g_\phi))^T \nabla_{\boldsymbol{x}}(\phi) \mathrm{d}v + \int_{\boldsymbol{\varphi}(^h\Omega)} \left[2(1-\phi)\mathscr{H} + \frac{G_c}{l}\phi\right](\mathbf{N}^g_\phi)^T \mathrm{d}v\right]^{(k-1)}. \tag{9.17}$$

Conversely, for the same time increment and iteration of the Newton-Raphson method, the phase-field stiffness matrix reads

$$\mathbf{K}_{\phi\phi} = \left[\int_{\boldsymbol{\varphi}(^h\Omega)} G_c l(\nabla_{\boldsymbol{x}}(\mathbf{N}^g_\phi))^T \nabla_{\boldsymbol{x}}(\mathbf{N}^g_\phi) \mathrm{d}v + \int_{\boldsymbol{\varphi}(^h\Omega)} \left(\frac{G_c}{l} - \mathscr{H}\right)(\mathbf{N}^g_\phi)^T (\mathbf{N}^g_\phi) \mathrm{d}v\right]. \tag{9.18}$$

9.3 Implementation

In this section, the implementation of the hyperelastic material model coupled with phase-field fracture, within the thermomechanics branch of LINKS, is detailed. Considering the numerous

similarities between the computational aspects of gradient-enhanced and phase-field models, the presentation in Section 8.4 bears particular relevance here. Once again, the new routines were implemented following a OO approach, in separate mechanical and thermal code structures, due to the underlying staggered solution scheme.

That said, Section 9.3.1 summarises the necessary steps for the implementation of the hyperelastic material model, coupled with the phase-field. Thereafter, Section 9.3.2 presents the implementation of the phase-field equation within the LINKS thermal code.

9.3.1 Hyperelastic material model

The numerical treatment of the hyperelastic material model presented in Section 9.2.1, coupled with phase-field fracture is shown in this section. Its implementation with an OO approach required the development of the six main procedures for material models listed in Section 8.4.2, consisting on: initialisation; reading material properties; state update; consistent tangent; mechanically dissipated heat computation; Gauss point output. Considering its relative simplicity, the state update and consistent tangent procedures are briefly summarised in Box 9.1, along with the remaining steps for the solution of an iteration of the mechanical problem.

Regarding the remaining procedures, since the fracture toughness and phase-field length-scale are not used in the mechanical problem, only the elastic properties of the material are read in this case, while the toughness and length-scale come as properties of the phase-field problem, as cescribed in Section 9.3.2.

Some additional remarks should be made regarding the phase-field variable. Similarly to what done in the gradient-enhanced case (recall Section 8.4.2), the damaged consistent tangent was computed with the phase-field variable from coupling iteration $k-2$, consdering the fact that the stress tensor is affected by its value from coupling iteration $k-1$.

Furthermore, after performing preliminary studies, it was decided that the value of the phase-field driving force, i.e. the maximum strain energy, should only be sent to the phase-field problem in the following coupling iteration. This essentially means that, at coupling iteration k, the mechanical problem sends $\mathscr{H}_{k-1}$ as the phase-field driving force. The introduction of this slight pseudo-time offset, also considered by Navidtehrani et al. (2021b), was seen to improve the stability of the coupling scheme by reducing the level of nonlinearity of the coupled system of equations.

9.3.2 Phase-field equation

In Section 4.4.2, a thermal diffusion problem analogous to the structure of the phase-field balance equation in Equation (4.42) was proposed. This analogous thermal problem was slightly more complex than the one proposed in the gradient-enhanced case (see Sections 4.3.2 and 8.4.3), since the phase-field equilibrium equation contains a linear combination of the history-dependent maximum strain energy, $\mathscr{H}$, and the phase-field variable, ϕ. This results in an equivalent thermal heat source which depends on both the current temperature and the mechanically dissipated heat (Equation (4.44)).

Considering the considerable similarities between the phase-field and gradient nonlocal damage equations, the linear temperature-dependent heat source implemented in the context of the nonlocal model was adopted to also accomodate the its use for the numerical solution of the phase-field problem. With this in mind, the main steps for employing the previously implement heat source to solve the phase-field equation were the following:

1. The introduction of logical conditions to differentiate the numerical procedures for the gradient and phase-field cases, and adopting the input data format to include a keyword for this distinction;

Box 9.1 Summary of the numerical solution of the k-th iteration of the Newton-Raphson method, for the $(n+1)$-th load increment, assuming the hyperelastic material model.

1. Loop over all integration points in the structure to compute the element contributions to the global stiffness matrix. The damaged hyperelastic tangent modulus for plane strain problems is given by:
$$\mathbf{D}^{e*} := \left[(1-\phi)^2 + \chi\right]\left(2G\mathbf{I}_S + (K - \frac{2}{3}G)\boldsymbol{I}\otimes\boldsymbol{I}\right), \tag{9.19}$$
where G and K are the materials shear and bulk moduli, respectively, $\boldsymbol{I}$ is the second-order identity and $\mathbf{I}_S$ is the fourt-order symmetric identity tensor. Having computed the consistent tangent modulus, the global tangent stiffness matrix is obtained with Equations (2.142) to (2.144).

2. Solve the nonlinear system of mechanical balance equations, update nodal displacements and deformation gradients.

3. Perform state update procedure for all Gauss points in the structure:
$$\begin{aligned}
&\boldsymbol{B}_n := \exp\left[2\boldsymbol{\varepsilon}_n\right],\\
&\boldsymbol{B}_{n+1} := \boldsymbol{F}_\Delta \boldsymbol{B}_n \left(\boldsymbol{F}_\Delta\right)^T,\\
&\boldsymbol{\varepsilon}_{n+1} := \ln\left[\boldsymbol{V}_{n+1}\right] = \frac{1}{2}\ln\left[\boldsymbol{B}_{n+1}\right],\\
&\boldsymbol{\tau}_{n+1} := \mathbf{D}^e : \boldsymbol{\varepsilon}_{n+1},\\
&\psi_{0,n+1} := \frac{1}{2}\left(\boldsymbol{\tau}_{n+1} : \boldsymbol{\varepsilon}_{n+1}\right),\\
&\boldsymbol{\tau}^*_{n+1} := \left[(1-\phi)^2 + \chi\right]\left(\mathbf{D}^e : \boldsymbol{\varepsilon}_{n+1}\right),
\end{aligned} \tag{9.20}$$
where $\boldsymbol{F}_\Delta$ is the incremental deformation gradient, previsouly defined in Equation (5.23). In addition, the value of the history-dependent maximum strain energy is updated if necessary:
$$\mathscr{H}_{n+1} := \begin{cases} \psi_{0,n+1} & \text{if } \psi_{0,n+1} > \mathscr{H}_n \\ \mathscr{H}_n & \text{if } \psi_{0,n+1} \leq \mathscr{H}_n \end{cases}, \tag{9.21}$$
and subsequently sent to the phase-field problem.

4. Assemble internal force vector and check convergence of the Newton-Rapshon scheme.

2. The implementation of the numerical procedures for computing the phase-field forces and stiffness.

In this section, the computational treatment of the time- and spatially-discrete phase-field equation is discussed.

Firstly, since the thermal code is constructed with an OO strategy, the mechanically dissipated heat, computed separately from the other thermal loads, is a private attribute of its specific object, due to encapsulation (recall Section 8.4.1). To allow using this quantity in the thermal loadings routine, a public pointer had to be created and compatibilised with the surrounding code. The mechanical heat dissipation, coming directly from the structural problem, is stored in matrix format, for each Gauss point of each finite element.

Moreover, the phase-field residual, expressed in Equation (9.17), contains two components which were addressed by the pre-existing thermomechanics code: its first term including the gradient of the phase-field, analogous to the thermal condutivity forces; and the pure mechanical heat dissipation term, which contains the maximum srain energy de-coupled from the phase-field. This

pure mechanical heat dissipation term of the phase-field residual, $\mathbf{f}_\phi^{\text{mec}}$, for a given time increment and iteration of the Newton-Rapshon method, reads

$$\mathbf{f}_\phi^{\text{mec}} = \int_{\boldsymbol{\varphi}(^h\Omega)} 2\mathscr{H}(\mathbf{N}_\phi^g)^T \mathrm{d}v. \tag{9.22}$$

With this in mind, the remaining terms in Equation (9.17) had to be included in the new version of the linear temperature-dependent heat source. The imeplemented components of the residual vector are hereafter denoted by $\mathbf{f}_\phi^{\text{H}}$, and may be written as

$$\mathbf{f}_\phi^{\text{H}} = \int_{\boldsymbol{\varphi}(^h\Omega)} \left[-2\phi\mathscr{H} + \frac{G_c}{l}\phi\right](\mathbf{N}_\phi^g)^T \mathrm{d}v, \tag{9.23}$$

for a given pseudo-time increment and Newton-Rapshon iteration. Conversely, the first tem of the phase-field stiffness in Equation (9.18), related to the phase-field gradient, is intrinsically computed by the thermal code. The second term in Equation (9.18), however, is a load-dependent stiffness component, which had to be included in the new implemented variant of the linear heat source. This load-dependent stiffness component, denoted by $\mathbf{K}_{\phi\phi}^{\text{H}}$, reads

$$\mathbf{K}_{\phi\phi}^{\text{H}} = \int_{\boldsymbol{\varphi}(^h\Omega)} \left(\frac{G_c}{l} - \mathscr{H}\right)(\mathbf{N}_\phi^g)^T(\mathbf{N}_\phi^g)\mathrm{d}v. \tag{9.24}$$

Box 9.2 Element loop for computing the load-dependent phase-field forces and stiffness contributions.

1. Read the relevant element data and allocate the element force vector, the vector and matrix of shape functions, the element nodal phase-field vector and the element load-dependent stiffness contribution.

2. Loop over all integration points in the element:

   (a) Evaluate the shape functions for the gauss point coordinates and construct the shape function vector, $\mathbf{N}_\phi^e(\boldsymbol{x}_i)$, and matrix, $(\mathbf{N}_\phi^e(\boldsymbol{x}_i))^T\mathbf{N}_\phi^e(\boldsymbol{x}_i)$, for Gauss point coordinates $(\boldsymbol{x}_i)$.

   (b) Evaluate the element jacobian and compute the current element volume, v^e.

   (c) Interpolate the nodal phase-field with the shape function to evaluate it at the Gauss point, i.e.:

   $$\phi_i = \sum_{k=1}^{n_{\text{points}}} \left[\Phi^e \cdot \mathrm{N}_\phi^e(\boldsymbol{x}_i)\right]_k, \tag{9.25}$$

   where the subscript $(\cdot)_i$ denotes the Gauss point, i.

   (d) Compute the Gauss point contribution to the element phase-field force vector:

   $$\mathbf{f}_i^{\text{H},e} = (\mathbf{N}_\phi^e(\boldsymbol{x}_i))^T\phi_i v^e. \tag{9.26}$$

   (e) Compute the Gauss point contribution to the element phase-field load-dependent stiffness:

   $$\mathbf{K}_i^{\text{H},e} = \left[(\mathbf{N}_\phi^e(\boldsymbol{x}_i))^T\mathbf{N}_\phi^e(\boldsymbol{x}_i)\right] v^e. \tag{9.27}$$

3. Assemble the gauss point contributions into the element force vector and sitffness matrix.

Once again, the prescription of adiabatic boundaries and a null initial phase-field in the entire domain is necessary. In this case, the material condutivity is the product of the fracture toughness and length-scale parameter, $G_c l$. Finally, in the gradient nonlocal case the linear temperature-dependent heat source was defined using two input parameter: its linear coefficients. Making use

of this fact, the fracture toughness and phase-field length-scale were introduced into the global phase-field problem as these two input properties of the thermal load.

9.4 Validation with pre-cracked plate benchmark

To validate the implementation of the phase-field model for quasi-brittle materials, reference results from the work of Navidtehrani et al. (2021a) were employed. In that contribution, after a comprehensive review of phase-field fracture and its numerical implementation, the authors present a benchmark example of a pre-cracked plate subjected to a vertical crack opening displacement. The pre-cracked specimen is presented in Figure 9.1, and Table 9.1 reports the material properties adopted in Navidtehrani et al. (2021a). Furthermore, Figure 9.2 depicts the finite element mesh employed by Navidtehrani et al. (2021a) (Figure 9.2a), and the mesh generated to replicate this benchmark (Figure 9.2b). Since fracture problems are inherently sensitive to the spatial discretisation of continua, and considering that the usual values of the phase-field length parameter, which are generally below 0.1 mm, Navidtehrani et al. (2021a) recommendes applying a local seed in the crack path around one fifth of the phase-field parameter. In thi case, since $l = 0.024$ mm was adopted, a local seed of 0.005 mm was introduced in the crack path, to generate the unstructured locally refined mesh shown in Figure 9.2b.

Table 9.1: Material properties employed in the benchmarking example of the pre-cracked plate. Legend: E denotes the Young's modulus; ν denotes the Poisson coefficient; l denotes the phase-field length-scale parameter; and G_c denotes the material's fracture toughness.

E / GPa	ν / -	l / mm	G_c / N/mm
210	0.30	0.024	2.7

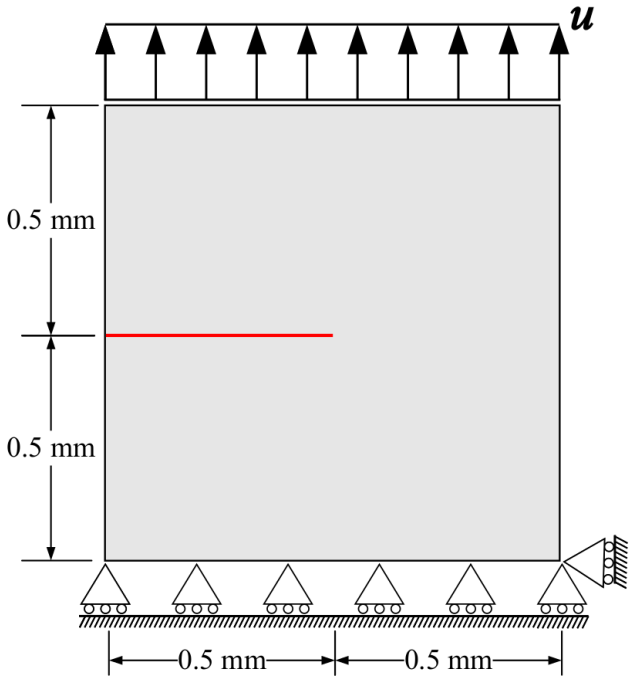

Figure 9.1: Schematic representation of the pre-cracked plate under tension, taken from Navidtehrani et al. (2021a).

Considering the reference results, a displacement of 10 μm was prescribed at the upper edge of the pre-cracked specimen, and the simulation was performed, with a 1:1 coupling incrementation ratio and Broyden's method. Figures 9.3 and 9.4 showcase the resulting reaction curve and phase-field variable contour obtained with the implementation presented in Section 9.3. Both the reactions and the distribution of the phase-field variable obtained for this benchmark are in agreement with the reference results, thus validating the phase-field model for quasi-brittle elastic materials implemented in LINKS. Adding to this, the minor deviations from the reference results are likely related to the difference between the two finite element discretisations shown in Figure 9.2. While the mesh utilised in this benchmark did take into account the need for the introduction of the local seed in the crack path, the width of local refinement is clearly different from the one adopted in the reference mesh (Figure 9.2a). This difference could not only explain the slight deviation in the reaction curves, but also the larger crack neighbourhood observed in Figure 9.4b, since the refinement of the spatial discretisation in this region is considerably lower, in comparison with the reference mesh.

Nonetheless, considering the proximity of the benchmark and reference results, the implementation of the phase-field model was deemed valid, without the need for repeating the simulation for a more adequate mesh.

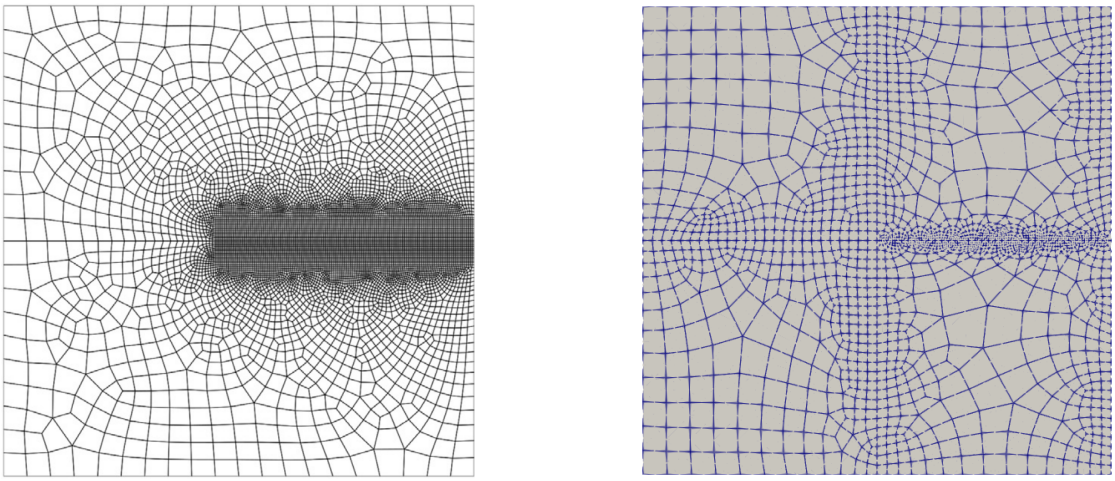

(a) Mesh employed in Navidtehrani et al. (2021a), 8532 CP4T elements in ABAQUS (Smith, 2009).

(b) Mesh employed in this contribution, containing 1828 QUAD8 elements and 5663 nodes.

Figure 9.2: Finite element meshes used to discretise the pre-cracked plate.

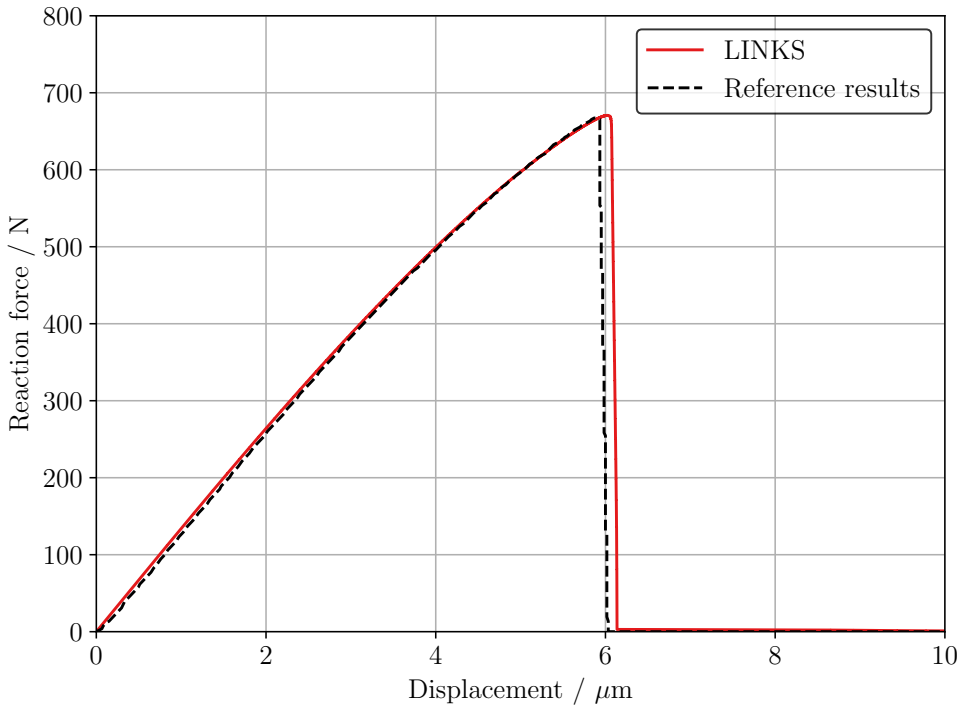

Figure 9.3: Reaction curve obtained for the pre-cracked plate benchmark, in comparison to the reference results (Navidtehrani et al., 2021a).

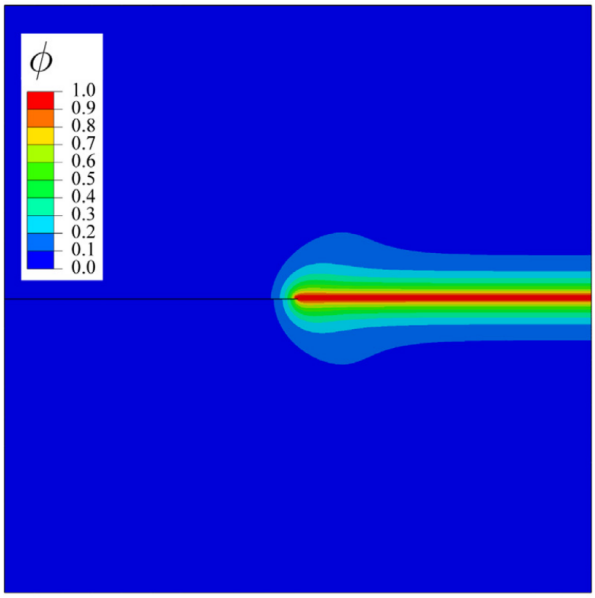

(a) Results from (Navidtehrani et al., 2021a).

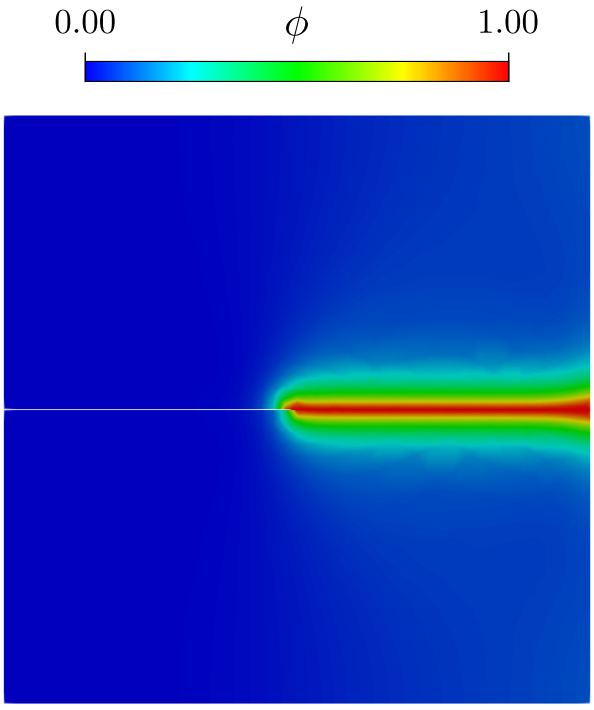

(b) Results from LINKS.

Figure 9.4: Phase-field variable distribution obtained for the pre-cracked benchmark, in comparison to the reference results (Navidtehrani et al., 2021a).

9.5 Numerical examples

In this section, additional numerical examples of the application of the phase-field model are presented, to assess some of its features and explore its capabilities. In Section 9.5.1, the plate with a central hole is utilised to perform several analyses, including an assessment of the coupling scheme, a parametric study, and a mesh sensitivity study. Morever, Section 9.5.2 delves into the application of phase-field models for multi-scale predictions of composite fracture, by analysing several fibre-

reinforced polymer RVEs.

9.5.1 Plate with central hole

The plate with a central hole, utilised in Sections 8.5.2 and 8.6.2, was employed again in this section, this time with the hyperelastic model presented in Section 9.2.1, coupled with phase-field fracture. The geometry of the plate, and the corresponding boundary conditions were shown in Figure 8.5a, as well as its finite element discretisation. The material properties adopted in this section are presented in Table 9.2, although some variations were considered in the parametric and mesh sensitivity studies. That said, the first simulation of the plate with a central hole with the phase-field model was performed with a 1:1 coupling increment ratio, Broyden's method, and a prescribed displacement of 1 mm. Figure 9.5 presents the obtained reaction curve and phase-field variable distribution, which contrast with the results from previous analyses of the plate, in the context of ductile damage.

In what follows, numerical and physical aspects of the simulation of the quasi-brittle failure of the plate, with the phase-field model, are assessed.

Table 9.2: Material properties employed for the plate with central hole. Legend: E denotes the Young's modulus; ν denotes the Poisson coefficient; l denotes the phase-field length-scale parameter; and G_c denotes the material's fracture toughness.

E / GPa	ν / -	l / mm	G_c / N/mm
210	0.30	0.05	1.5

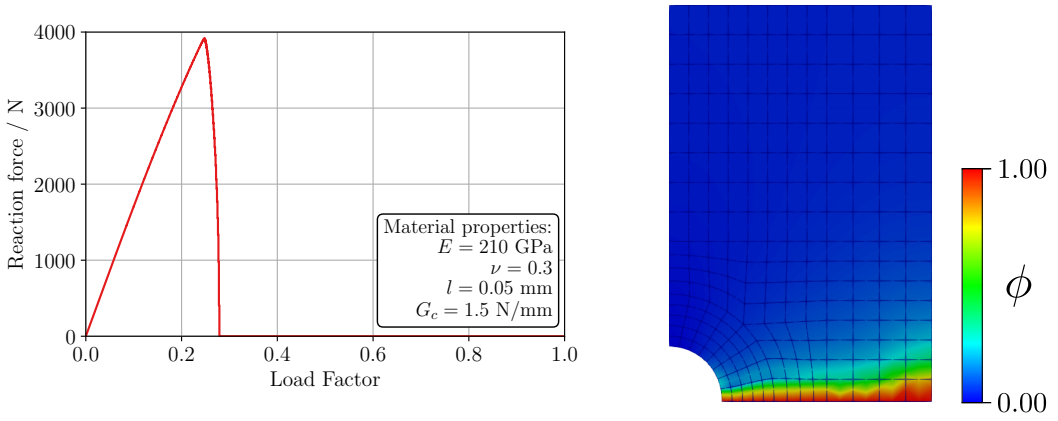

(a) Quasi-brittle reaction curve.

(b) Phase-field variable contour.

Figure 9.5: Results of the first simulation of the plate with a central hole with the phase-field model.

Coupling scheme analysis

In this analysis, the simulation of the plate with a central hole was repeated for several numbers of coupling increments, in relation to the 1000 proportional load steps assumed in the mechanical problem. Moreover, the performances of the fixed-point and Broyden's methods were compared. Figure 9.6 shows the reaction curves obtained for the two solvers and the various numbers of coupling increments. It is observed that the simulation could only be completed for the 1:1 coupling ratio, with all other cases failing to reach coupling convergence near the critical load. In these cases, given that the coupling convergence of the implicit iterative scheme is not guaranteed, the adoption of coarser coupling incrementation, relative to the time discretisation of the mechanical

problem, results in a loss of stability, which could also be related to the time offset introduced in Section 9.3.1. Contrarily to the problems analysed in Chapter 8, the mechanical responses that result from the adoption of phase-field model for quasi-brittle fracture are characterised by an abrupt loss of load bearing capacity, contrasting with the smooth softening responses observed in the case of ductile failure. In this setting, and considering the relevance of being able to simulate the entire crack nucleation and propagation process, adopting a more conservative 1:1 coupling incrementation ratio has proven to be the only reliable approach to guarantee the stability of the coupled solution scheme.

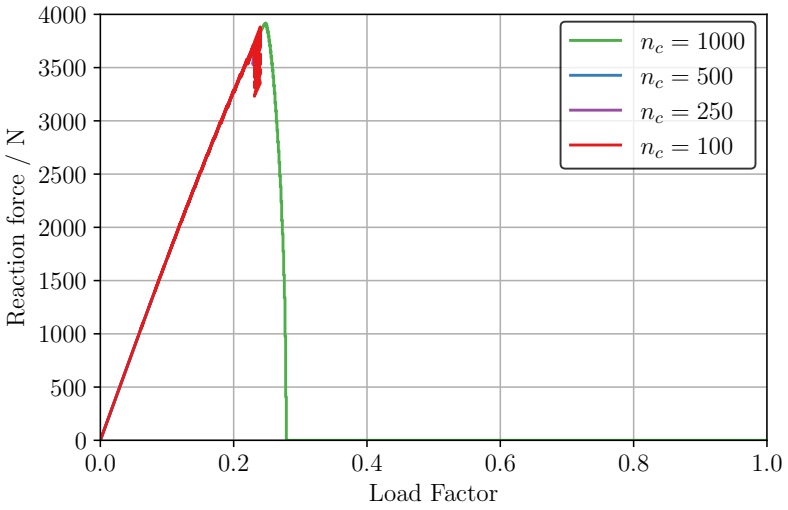

(a) Broyden's method.

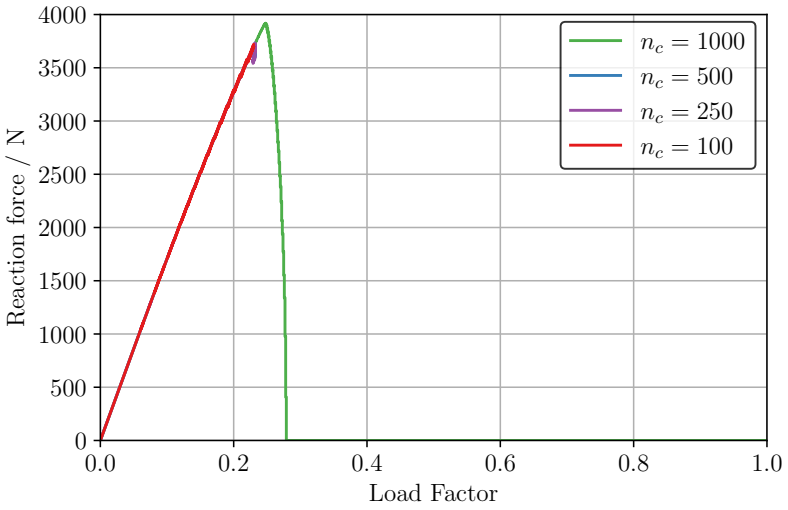

(b) fixed-point method.

Figure 9.6: Reaction curves obtained with the two implicit solvers and different coupling increment ratios. The mechanical and phase-field problems were discretised in 1000 time increments.

Moreover, the computational times recorded for each of these cases are reported in Table 9.3, where it can be seen that, despite having computed the solution of the coupled problem for the entire pseudo-time domain, the 1:1 simulations still outperformed the remaining coupling ratios, which did not reach 30% of the prescribed displacement. Tables 9.4 and 9.5 present the coupling

convergence behaviour observed for each ratio, at two different load increments, for Broyden's method and the fixed-point algorithm, respectively. It was found that decreasing the number of coupling increments led to coupling convergence issues, which were aggravated in the case of the fixed-point method. Conversely, the adoption of a 1:1 coupling ratio led to identical coupling solutions for the two implicit solvers, where null residual vectors were achieved. The efficacy of the coupling scheme with the 1:1 ratio is inseparable from the use of the phase-field driving forces from the previous iteration in the actual phase-field problem, as detailed in Section 9.3. For a sufficiently fine time discretisation, employing a 1:1 coupling increment ratio allows taking advantage of the reduced nonlinearity of the phase-field equation, achieving remarkable convergence results, without loss of accuracy or overestimation of the material toughness. That said, a 1:1 ratio was adopted for all phase-field examples presented hereinafter. For this coupling strategy, the performances of the fixed-point and Broyden's methods were identical, hence the choice for Broyden's method, made in Chapter 8, was maintained.

Table 9.3: Computational times recorded for the two implicit coupling solvers and the different time discretisation ratios. Mechanical and phase-field problems discretised in 1000 time steps. Time measures shown in seconds.

Coupling increments, n_c	Coupling ratio, $n_c : n_m$	Broyden's method	fixed-point method
1000	1:1	72	72
500	1:2	81	115
250	1:4	96	128
100	1:5	150	158

Table 9.4: Coupling convergence rates obtained with Broyden's method and different coupling incrementation ratios. Mechanical and phase-field problems discretised in 1000 time steps.

Load increment $\Delta = 0.1$		Load increment $\Delta = 0.2$	
Iterations	Relative norm of the residual / %	Iterations	Relative norm of the residual / %
1000 coupling increments			
0	2.07×10^{0}	0	1.10×10^{0}
1	**0.00**	**1**	**0.00**
500 coupling increments			
0	4.12×10^{0}	0	1.94×10^{0}
1	1.16×10^{-1}	1	2.82×10^{-1}
2	6.22×10^{-3}	2	8.18×10^{-2}
3	$\mathbf{1.98\times10^{-4}}$	3	1.89×10^{-2}
		4	7.32×10^{-3}
		5	1.78×10^{-3}
		6	$\mathbf{7.23\times10^{-4}}$
250 coupling increments			
0	8.51×10^{0}	0	4.03×10^{0}
1	2.29×10^{-1}	1	5.38×10^{-1}
2	1.23×10^{-2}	2	1.45×10^{-1}
3	$\mathbf{3.91\times10^{-4}}$	3	3.03×10^{-2}
		4	1.09×10^{-2}
		5	2.41×10^{-3}
		6	$\mathbf{9.28\times10^{-4}}$
100 coupling increments			
0	2.35×10^{1}	0	1.03×10^{1}
1	5.51×10^{-1}	1	1.33×10^{0}
2	2.94×10^{-2}	2	3.75×10^{-1}
3	$\mathbf{9.36\times10^{-4}}$	3	8.42×10^{-2}
		4	3.23×10^{-2}
		5	7.93×10^{-3}
		6	3.23×10^{-3}
		7	$\mathbf{6.29\times10^{-4}}$

Table 9.5: Coupling convergence rates obtained with the fixed-point method and different coupling incrementation ratios. Mechanical and phase-field problems discretised in 1000 time steps.

Load increment $\Delta = 0.1$		Load increment $\Delta = 0.2$	
Iterations	Relative norm of the residual / %	Iterations	Relative norm of the residual / %
1000 coupling increments			
0	2.07×10^{0}	0	1.10×10^{0}
1	**0.00**	**1**	**0.00**
500 coupling increments			
0	4.12×10^{0}	0	1.97×10^{0}
1	1.16×10^{-1}	1	2.82×10^{-1}
2	8.08×10^{-3}	2	9.86×10^{-2}
3	$\mathbf{6.57\times10^{-4}}$	3	4.12×10^{-2}
		4	1.92×10^{-2}
		5	9.69×10^{-3}
		6	5.10×10^{-3}
		7	2.77×10^{-3}
		8	1.53×10^{-3}
		9	$\mathbf{8.58\times10^{-4}}$
250 coupling increments			
0	8.51×10^{0}	0	3.94×10^{0}
1	2.29×10^{-1}	1	5.57×10^{-1}
2	1.59×10^{-2}	2	1.93×10^{-1}
3	1.29×10^{-3}	3	7.99×10^{-2}
4	$\mathbf{1.17\times10^{-4}}$	4	3.72×10^{-2}
		5	1.86×10^{-2}
		6	9.78×10^{-3}
		7	5.30×10^{-3}
		8	2.93×10^{-3}
		9	1.64×10^{-3}
		10	$\mathbf{9.26\times10^{-4}}$
100 coupling increments			
0	2.35×10^{1}	0	1.03×10^{1}
1	5.51×10^{-1}	1	1.33×10^{0}
2	3.81×10^{-2}	2	4.51×10^{-1}
3	3.09×10^{-3}	3	1.84×10^{-1}
4	$\mathbf{2.79\times10^{-4}}$	4	8.47×10^{-2}
		5	4.20×10^{-2}
		6	2.19×10^{-2}
		7	1.18×10^{-2}
		8	6.52×10^{-3}
		9	3.64×10^{-3}
		10	2.05×10^{-3}
		11	1.16×10^{-3}
		12	$\mathbf{6.59\times10^{-4}}$

Material parameter analysis

Having evaluated the coupling scheme setup for phase-field problems, this section assesses the impact of the two material properties related to the fracture model on the mechanical response of the plate. That said, the values of the phase-field length-scale parameter, l, and fracture toughness, G_c, are varied in a sequential fashion, while the remaining material properties are kept at their original values, reported in Table 9.2.

Concerning the fracture toughness, two additional values were tested: 15 and 150 N/mm. Figure 9.7 shows the resulting reactions for the two additional toughness values and the original results from Figure 9.5. Furthermore, Figure 9.8 presents the phase-field variable contours obtained for the three toughness values. As expected, increasing the value of the fracture toughness increases the amount of strain energy the material can absorb before the critical load is reached. In this case, adopting a toughness of 150 N/mm meant that the plate did not fail for the prescribed displacement. In regards to diffuse crack width, however, the value of the fracture toughness does not have a discernible impact, as this is exclusively controlled by the phase-field length-scale. That said, the slight differences observed between the phase-field contours for 1.5 and 15 N/mm can be attributed to the coarse spatial discretisation of the crack path.

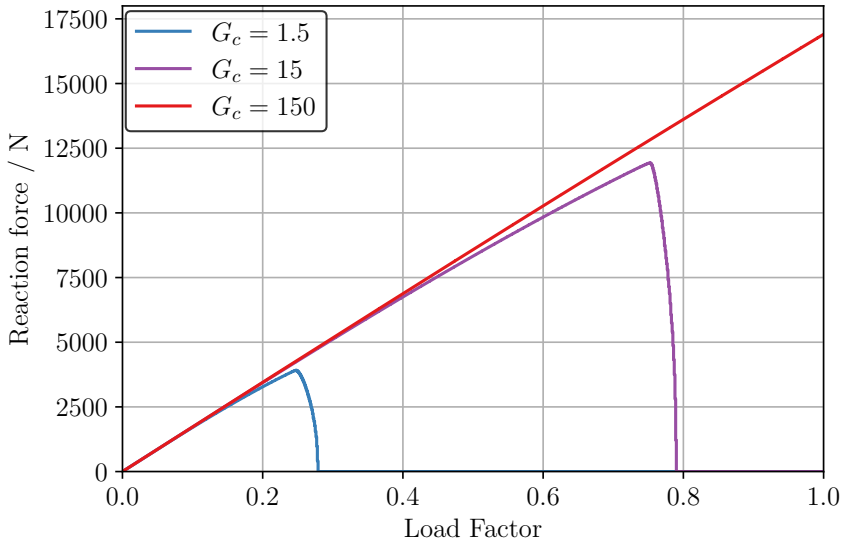

Figure 9.7: Reaction curves obtained for three values of the fracture toughness.

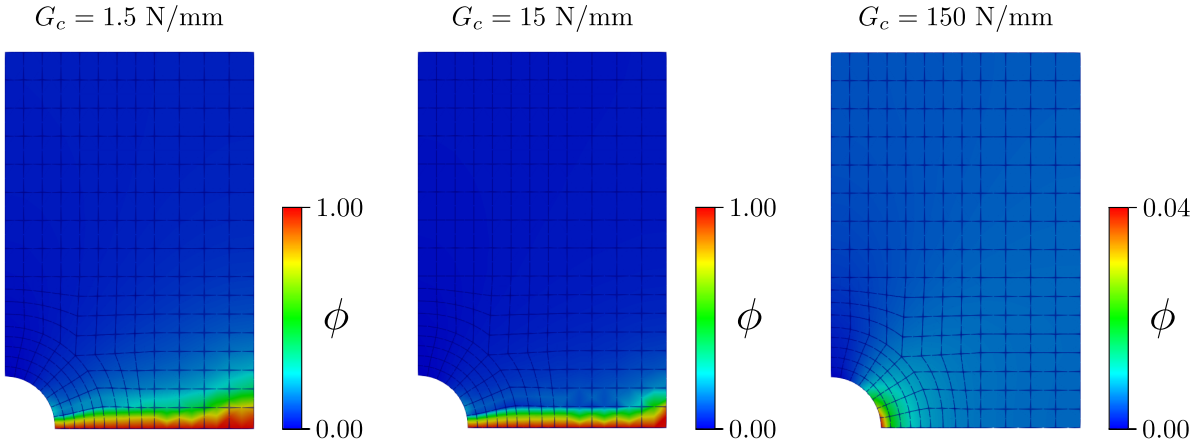

Figure 9.8: Phase-field variable distribution for the three values of the fracture toughness.

For the phase-field length-scale, three additional values were considered: 0.005, 0.5 and 5 mm. Figures 9.9 and 9.10 depict the reactions and phase-field contours obtained for the four values of the length-scale parameter. It was found that lower values of the phase-field length-scale resulted in an increase of the critical load. From a numerical standpoint, this can be traced back to the phase-field equation (Equation (4.42)), where the length-scale parameter not only influences the intensity of gradient diffusion on the right-hand side, but also the term on the phase-field forces related to the fracture toughness, on the left-hand side, where decreasing the phase-field length-scale increases the critical strain energy value that must be surpassed for failure to occur. This also bears physical meaning, since a lower length-scale parameter yields a lower crack area and, hence, requires a greater load to reach the critical energy value. However, Borden et al. (2012) observed that excessively low values of the phase-field length-scale yield non-physical increases in material strength. In these cases, in spite of the significant increase in the critical load found for 0.005 mm, the resulting phase-field variable distribution was identical to the one obtained with 0.05 mm, since the finite element mesh was not fine enough such that the differences between these two length-scale values could be adequately captured.

Furthermore, it can be seen that adopting a phase-field length-scale of 5 mm resulted in greater softening levels before failure, which is justified by the large portion of the plate that was damaged. It should be noted that this sort of value of the phase-field length-scale is unlikely in practical fracture problems, where cracks propagate within much smaller domains, more akin to the results obtained with 0.05 and 0.005 mm.

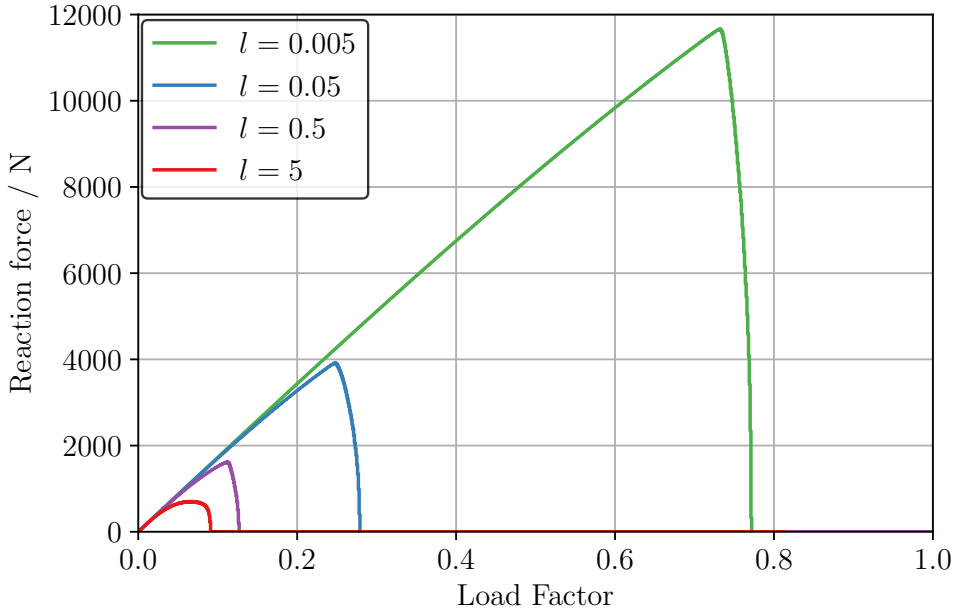

Figure 9.9: Reaction curves obtained for four values of the phase-field length-scale parameter.

Mesh sensitivity in fracture problems

This section presents the final analysis for the plate with a central hole, where the sensitivity of the phase-field response to the spatial discretisation of the geometry is assessed, for different values of the length-scale parameter. To this end, the two finite element meshes depicted in Figure 9.11 were generated, by assigning local seeds on the crack path with the values of 0.1 and 0.05 mm, while adopting a global seed of 0.9 mm. Furthermore, it should be remarked that a fracture toughness of 2.5 N/mm was adopted in this section, while the elastic properties remain the ones reported in

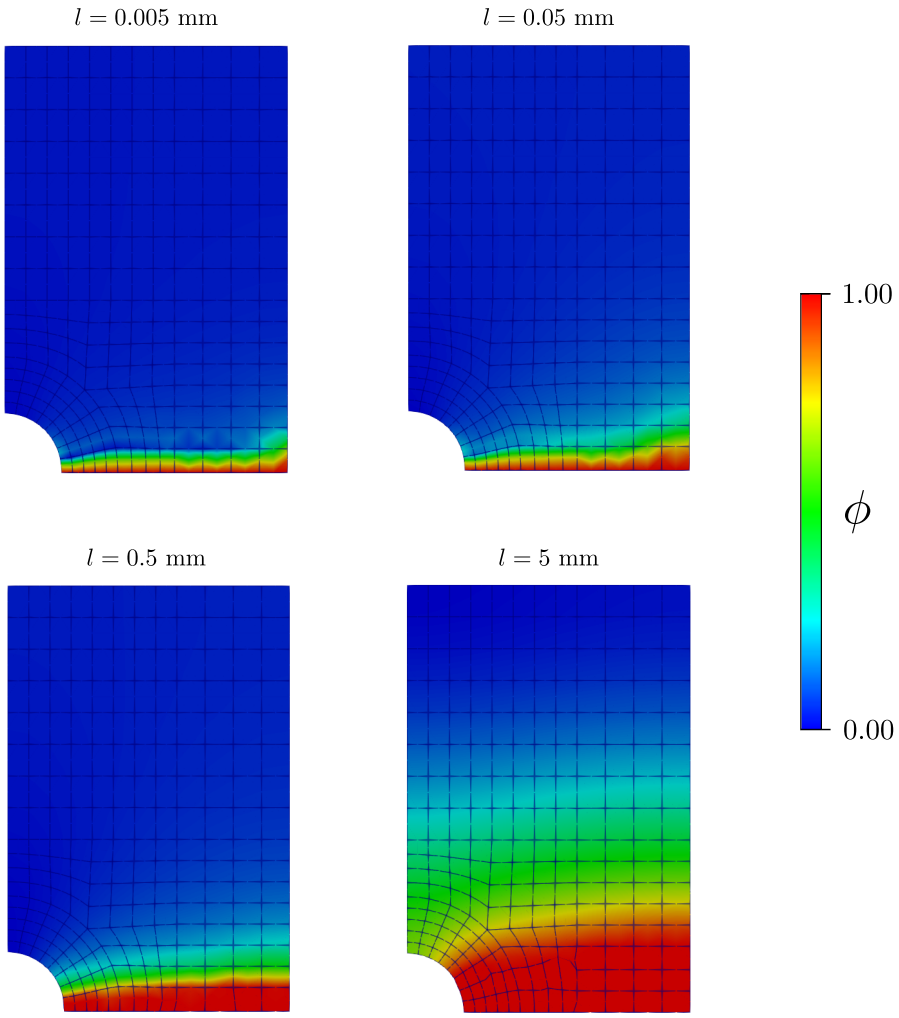

Figure 9.10: Phase-field variable contours obtained for four values of the length-scale parameter.

Table 9.2. That said, the four discretisations of the plate were simulated for the following values of the phase-field length-scale parameter: 0.1, 0.05 and 0.01 mm.

Figure 9.12 illustrates the reaction curves obtained with the four meshes for each value of the phase-field length-scale. Some level of mesh sensitivity was found for every value of the length-scale parameter, which was expected due to the significant differences in the mesh refinement among the four cases. Adding to this, the level of mesh sensitivity increased as the value of this parameter decreased, since more meshes were progressively incapable of capturing the failure of the plate for lower crack widths. In spite of this, the reactions of the two finer meshes were essentially coincident for all three values of the phase-field length-scale.

Remark 6 *The meshes employed in this section do not abide by the meshing suggestion of Navidtehrani et al. (2021a), of applying a local seed on the crack path equal to one fifth of the phase-field length-scale, for the three considered values. Nonetheless, the main goal of this study, which is assessing mesh dependency in phase-field fracture, remains valid.*

Remark 7 *The simulation of the plate with a central hole with a length-scale parameter of 0.01 mm terminated prematurely in the case of Mesh 4 (see Figures 9.11d and 9.12). This was due to the occurrence of significant element distortion in the crack path, yielding negative jacobians in the mechanical problem and inhibiting its convergence. Therefore, the premature abortion of this particular case is not related to coupling issues.*

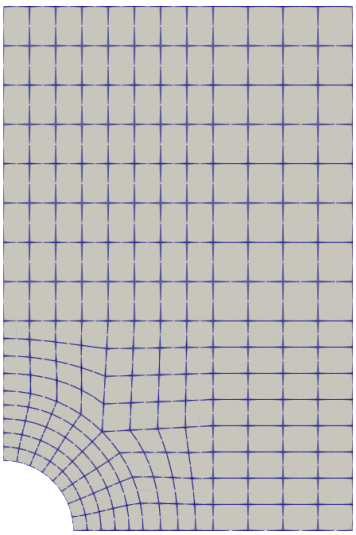

(a) Mesh 1: structured mesh from Chapter 8, containing 216 QUAD8 elements and 715 nodes.

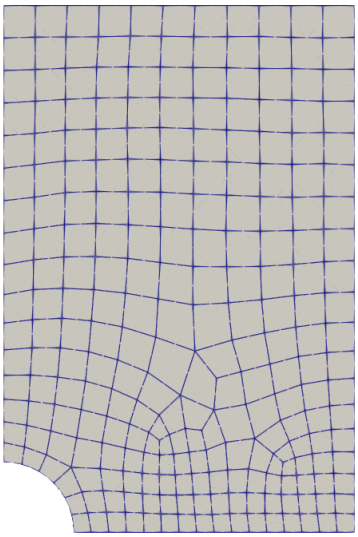

(b) Mesh 2: mesh with local seed of 0.1 mm, containing 235 QUAD8 elements and 774 nodes.

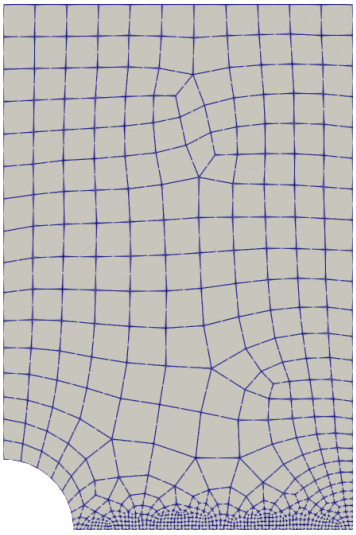

(c) Mesh 3: mesh with local seed of 0.1 mm, containing 581 QUAD8 elements and 1888 nodes.

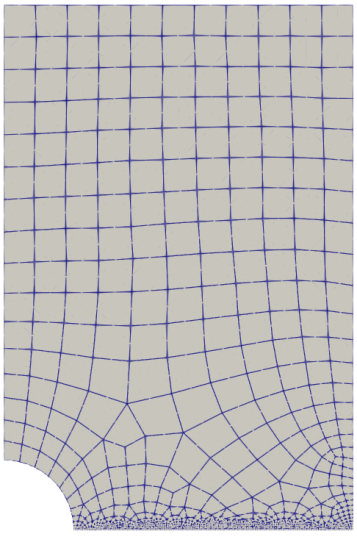

(d) Mesh 4: mesh with local seed of 0.05 mm, containing 1066 QUAD8 elements and 3429 nodes.

Figure 9.11: Finite element meshes utilised with the plate with central hole.

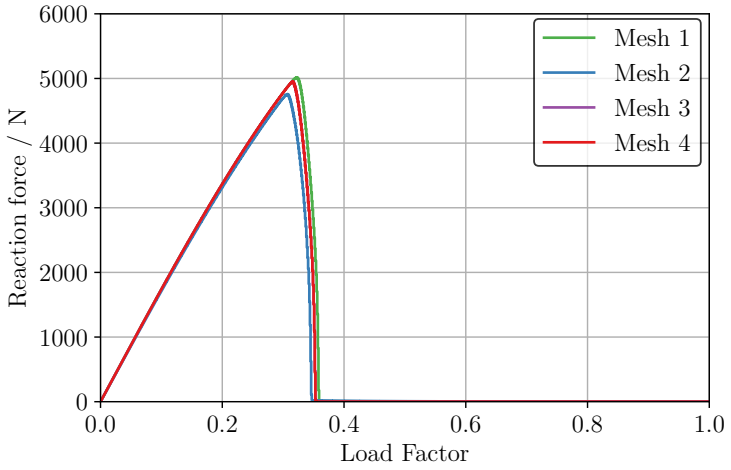

(a) $l = 0.1$ mm.

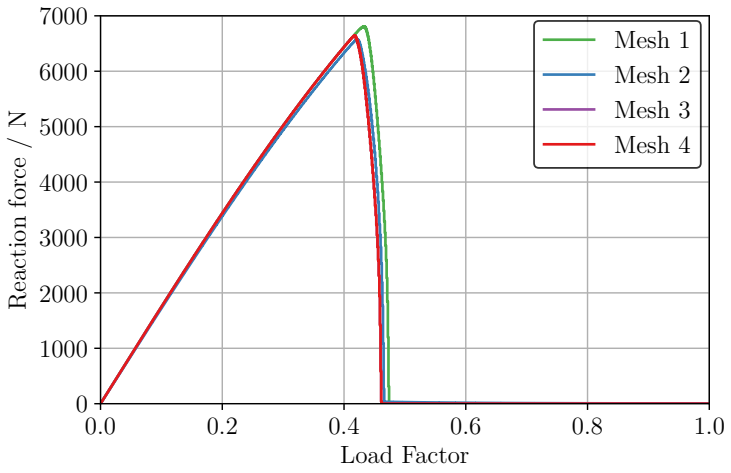

(b) $l = 0.05$ mm.

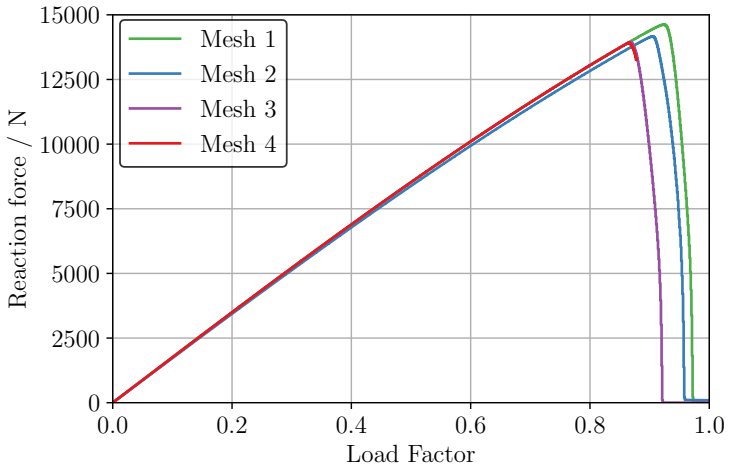

(c) $l = 0.01$ mm.

Figure 9.12: Reaction force curves obtained with the four different mesh sizes for the plate with central hole for different values of the phase-field length-scale parameter. Mesh labels shown in Figure 9.11.

9.5.2 Composite RVE

In the final analysis of this dissertation, the phase-field model, implemented for 2D plane strain analysis at the macro-scale, is employed to perform preliminary tests with fibre reinforced composite RVEs. Three 1×1 mm^2 RVEs were generated with GMMD (Vila-Chã et al., 2021), with different volume fractions and fibre diameters, to provide a broader set of examples. In addition, the RVEs were fixed vertically at the lower edge, while an upward 0.1 mm displacement was applied at its top edge. This tensile loading scenario should result in transverse (horizontal) crack propagation, i.e. perpendicular to the loading direction.

A relevant caveat regarding the use of the implemented phase-field model to simulate heterogeneous microstructures is the fact that, since the fracture toughness and length-scale come in as parameters of the global phase-field balance problem (recall Section 9.3.2), only one set of fracture properties can be explicitly defined. Distinct materials can be defined, but their only property is the equivalent condutivity, equal to the product of the two fracture parameters, $G_c l$. That said, since damage was only desired in the matrix, the equivalent condutivity of the fibres was artificially set to 1×10^{-15}. Although this did not totally inhibit fibre damage, its magnitude was negligible.

Remark 8 *Throughout this section, the term "critical displacement" is utilised to compare the load bearing capacity of the different RVEs and sets of fracture properties. It should be noted that this refers to the value of the displacement for which the phase-field simulations aborted. Premature termination is verified for all cases, due to excessive deformation levels found at specific finite elements along the crack paths, in which negative jacobians were obtained. This, in turn, impeded the convergence of the mechanical Newton-Raphson scheme. That being the case, these premature abortions are not linked to coupling issues.*

RVE 1: 10 fibres with 20% volume fraction

The first RVE is shown in Figure 9.13, and is composed of 10 fibres, with a 20% volume fraction. Its elastic properties are reported in Table 9.6. This RVE was simulated considering three distinct phase-field length-scales: 0.005, 0.01 and 0.03 mm, while a fracture toughness of 3.5 N/mm was adopted. The resulting phase-field contours are showcased in Figure 9.14, and the critical displacement for each case is reported in Table 9.7.

Increasing the value of the length-scale parameter resulted in propagation of the crack from the RVE's left side to its bottom edge, while also increasing the region of the domain where the phase-field is not null. Conversely for the lower value of the length-scale, failure was reeasonably localised. Moreover, consistently with the observations of Section 9.5.1, decreasing the value of the length-scale parameter results in a greater RVE strength, i.e. results in a larger value of the critical displacement. Once again, it is noted that the finite element discretisation adopted here might not comply with recommendable standards for acquiring accurate solutions of the fracture problem. Nonetheless, for all three cases, cracks propagated in the expected horizontal direction.

Table 9.6: Elastic properties of RVE 1. Legend: E denotes the Young's modulus; ν denotes the Poisson coefficient.

Fibres		Matrix	
E / GPa	ν / -	E / GPa	ν / -
74	0.2	20	0.3

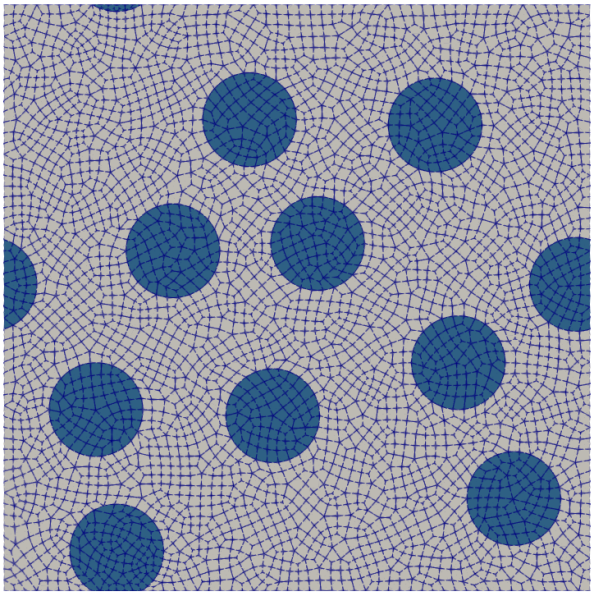

Figure 9.13: RVE 1: 10 fibres with 20% volume fraction, discretised in 3592 QUAD8 and TRI6 elements and 10987 nodes.

Table 9.7: Critical displacements found for RVE 1 and each value of the length-scale parameter. Legend: l denotes the matrix phase-field length-scale.

l / mm	Critical displacement / mm
0.005	0.0528
0.01	0.0406
0.03	0.0300

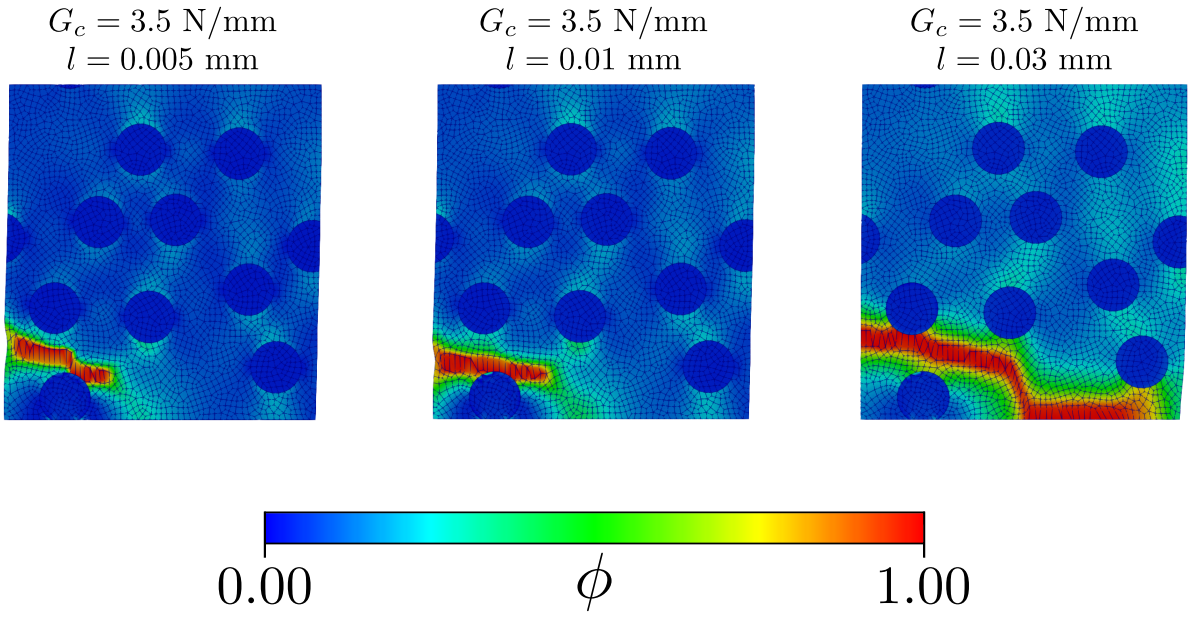

Figure 9.14: Phase-field variable contours obtained for RVE 1 and three different values of the length-scale parameter.

RVE 2: 39 fibres with 30% volume fraction

The second RVE is illustrated in Figure 9.15, and contains of 39 fibres, with a 30% volume fraction. In addition, the same elastic properties from RVE 1 were utilised (Table 9.6). This RVE was simulated considering three distinct fracture toughness values: 3.5, 5 and 10 N/mm, while a phase-field length-scale of 0.01 mm was assumed. The resulting phase-field contours are depicted in Figure 9.16, and the critical displacements are reported in Table 9.8.

In this case, the applied boundary conditions, combined with the particular morphology of RVE 2, led to excessive element distortion in the lower right corner of the microstructure. Together with the overall complexity of this RVE, containing a considrably higher number of fibres, this inhibits drawing any pattern regarding the effect of the fracture toughness on the observed crack path and length. Despite this, the critical displacements are, again, aligned with the observations of Section 9.5.1, since greater fracture toughness values led to greater RVE strengths, and crack propagation is transverse.

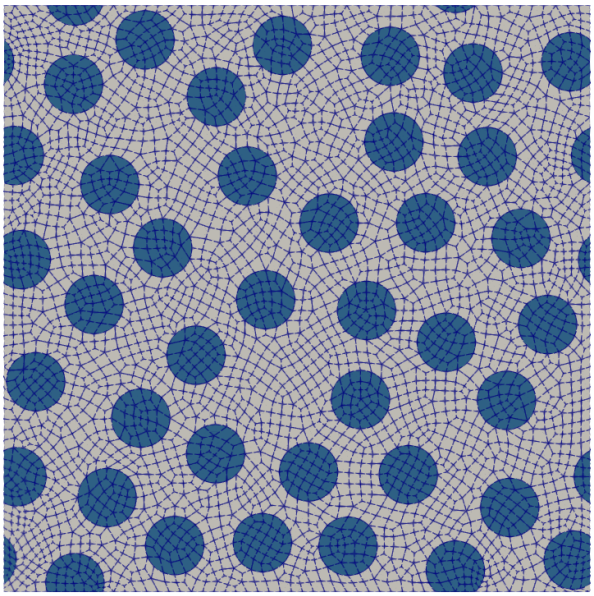

Figure 9.15: RVE 2: 39 fibres with 30% volume fraction, discretised in 3690 QUAD8 and TRI6 elements and 11297 nodes.

Table 9.8: Critical displacements found for RVE 2 and each value of the fracture toughness. Legend: G_c denotes the matrix fracture toughness.

G_c / N/mm	Critical displacement / mm
3.5	0.0347
5.0	0.0414
10.0	0.0550

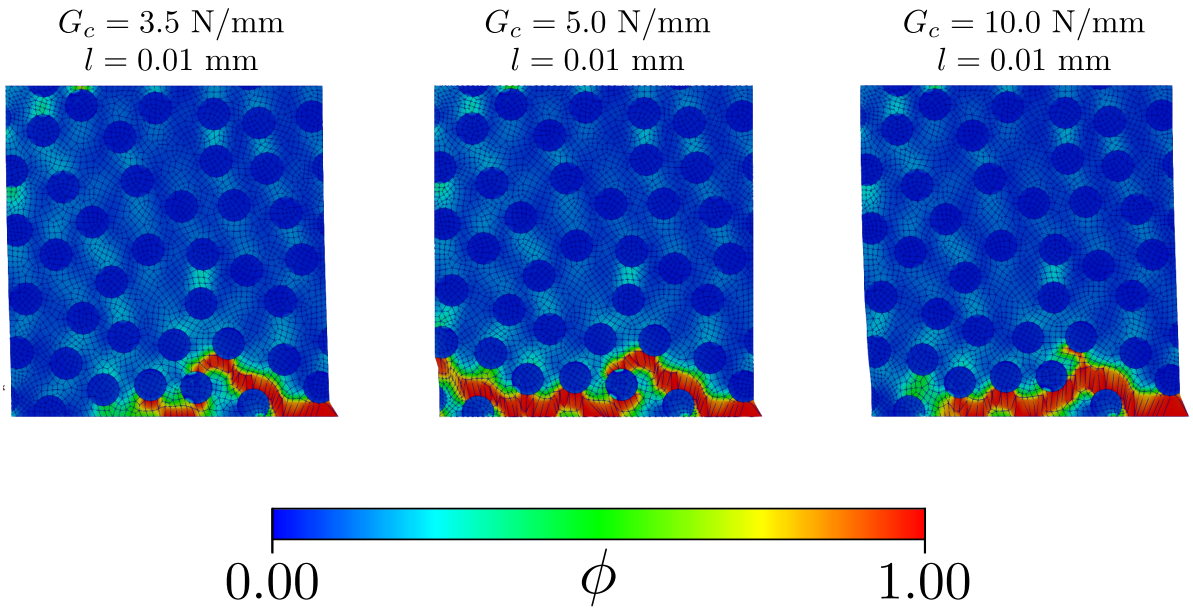

Figure 9.16: Phase-field variable contours obtained for RVE 2 and three different values of the fracture toughness.

RVE 3: 8 fibres with 15% volume fraction and finer mesh

The final RVE analysed in this section is depicted in Figure 9.17 and is associated with a considerably finite element discretisation, to increase the fidelity of the fracture predictions. In an attempt to avoid excessive computing time increases, the previously employed QUAD8 elements were replaced with 4-noded F-bar bilinear elements (Neto et al., 2005) with complete integration. It also has a simpler morphology, relative to RVE 2, containing 8 fibres with a 15% volume fraction. The elastic properties employed for this RVE are shown in Table 9.9. RVE 3 was simulated for nine combinations of fracture properties, including three values of the length-scale: 0.005, 0.01 and 0.03 mm; and three values of the fracture toughness: 1 N/mm, 3.5 N/mm and 7 N/mm. The resulting phase-field contours and critical displacmeents are reported in Figure 9.18 and table 9.10, respectively.

In this case, the adoption of larger values of the fracture toughness led to more localised failure, irregardless of the phase-field length-scale. In spite of this, greater length-scale parameters are, again, associated with broader regions of the domain in which the phase-field is not null, even for the higher toughness values. Conversely, lower toughness cases exhibited generally longer crack lengths, while the paths seemed to vary depending on the adopted length-scale, which controls crack coalescense. Regarding the critical displacements, the same patterns remain, larger toughness cases recording the greater values. Finally, for all cases, the tensile loading scenario yields transverse cracks, even though their extensions were varied.

Table 9.9: Elastic properties of RVE 3. Legend: E denotes the Young's modulus; ν denotes the Poisson coefficient.

Fibres		Matrix	
E / GPa	ν / -	E / GPa	ν / -
74	0.2	30	0.3

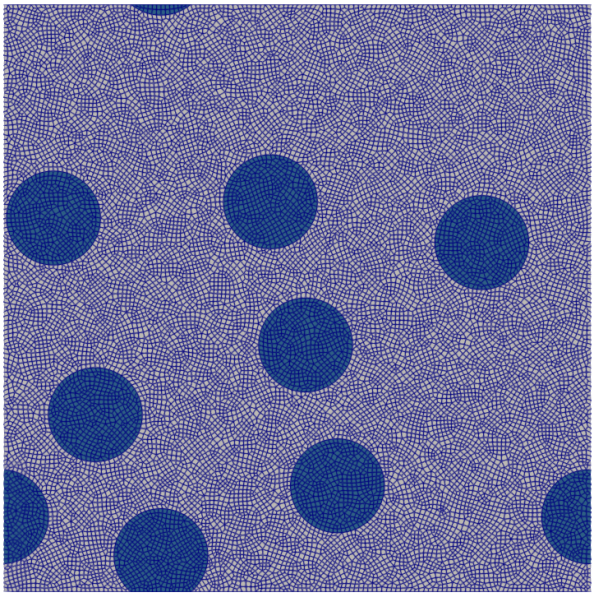

Figure 9.17: RVE 3: 8 fibres with 15% volume fraction, discretised in 20800 F-bar QUAD4 elements and 21055 nodes.

Table 9.10: Critical displacements found for RVE 3 and each combination of fracture properties. Legend: l denotes the matrix length-scale parameter; G_c denotes the matrix fracture toughness.

l / mm	G_c / N/mm	Critical displacement / mm
0.03	1.0	0.0222
0.01	1.0	0.0237
0.005	1.0	0.0314
0.03	3.5	0.0295
0.01	3.5	0.0423
0.005	3.5	0.0548
0.03	7.0	0.0399
0.01	7.0	0.0578
0.005	7.0	0.0754

The analyses presented here are only a preliminary study, containing a few relevant limitations, but showcasing the potential of phase-field approaches to fracture for modelling multi-scale damage phenomena. Apart from the incompatibility of the implementation with heterogeneous microstructures and the finite element discretisations of RVEs 1 and 2, the application of macroscopic boundary conditions to these heterogeneous microstructures restricts these analyses to simpler morphologies, since more intricate ones may lead to element distortion problems, as observed for RVE 2. Moreover, some of the phase-field length-scales adopted in this section may be excessive, considering that the phase-field model only approaximates the original sharp crack representation as this parameter tends to zero (Quintanas-Corominas et al., 2019). Lastly, alternative definitions of the fracture driving force, neglecting the crack-closing strain energy, should be pursued (recall Equation (4.30) and Section 4.4.1), to avoid underestimating material strength in the presence of compressive strain modes. Bearing these limitations and issues in mind, the implementation presented here may be enhanced in the future to allow solving these problems for heterogeneous materials (explicitly), with micro-scale boundary conditions, while also employing more approapriate finite element meshes and phase-field length-scales.

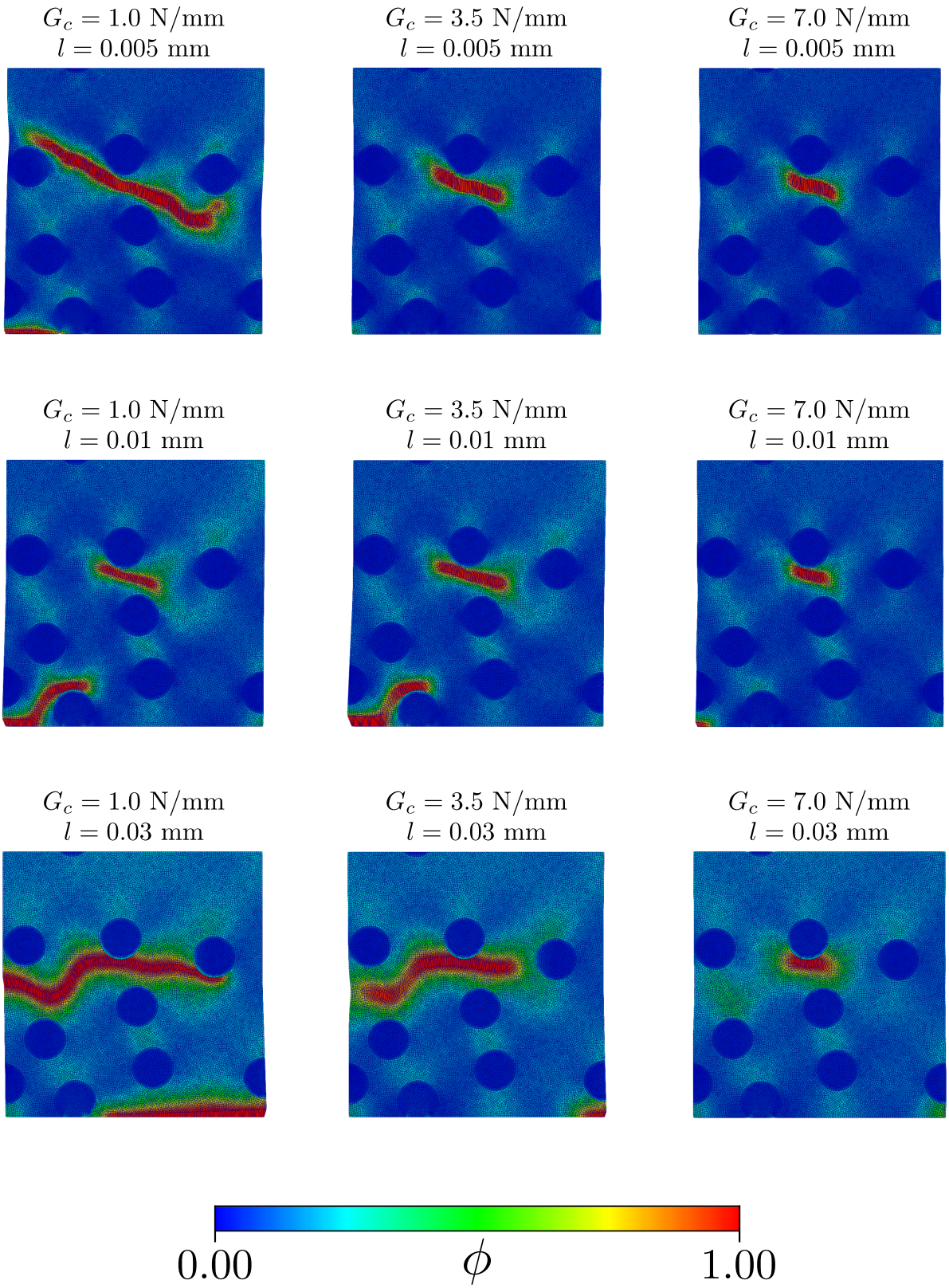

Figure 9.18: Phase-field variable contours obtained for RVE 3, for three different values of the fracture toughness and three values of the phase-field length-scale.

9.6 Discussion

In this chapter, the implementation of a phase-field model for brittle and quasi-brittle materials is described and validated with a reference from the literature (Navidtehrani et al., 2021a) in Section 9.4. In addition, brief parametric and coupling scheme studies are performed in Section 9.5.1 with the plate with a central hole, where a 1:1 coupling ratio is seen to provide the required stability to predict the response of the specimen until failure. The fracture toughness is seen to influence the plate strength, while the length-scale parameter affected both strength and crack width. Mesh sensitivity analyses are also reported in Section 9.5.1, where it is shown that, for the same set of spatial discretisations, mesh dependency increases with the decrease in the phase-field length-scale.

Finally, preliminary simulations of fibre reinforced composite RVEs are carried out, demonstrating the possibility of utilising these models for modelling multi-scale damage phenomena. Several limitations to the reported setup are identified, as well as routes for future improvements, emphasising the need to account for heterogeneous materials and also solving the RVE balance problem with adequate micro-scale boundary conditions. Moreover, it is seen that the phase-field length-scale effectively controls the crack path, while large values for this parameter lead to broad regions of the RVE being damaged and, thus, generally longer cracks. Larger fracture toughness values lead to more localised failure for the cases in which excessive element distortion is avoided. For all RVEs and fracture properties, the tensile loading scenario result in transverse crack propagation, as expected.

CHAPTER 10

CONCLUSIONS AND FINAL REMARKS

10.1 Conclusions

The main focus of this dissertation is the assessment of different strategies for the multi-scale modelling of damage and structural failure. The problem of pathological macro-mesh dependency is addressed in single- and multi-scale settings, with nonlocal damage models and second-order computational homogenisation, respectively. These macro-regularisation strategies, and their respective numerical parameters, are related with an optimisation-based strategy. Micro-mesh dependent effects in a multi-scale setup and their connection with macro-mesh dependency are analysed, while also performing a detailed study on the impact of the RVE length. Moreover, a recent solution strategy for coupled problems is utilised to implement a gradient-enhanced nonlocal model. A comprehensive numerical assessment of integral and gradient nonlocal approaches is carried out. The same solution scheme is employed to implement a phase-field fracture model, which was validated with benchmark results from the literature, before conducting a preliminary analysis on the failure of heterogeneous microstructures.

To provide a suitable theoretical basis to the different contributions developed throughout this dissertation, Part I includes an extensive review of continuum mechanics, multi-scale models based on computational homogenisation, and damage and fracture. Chapter 2 addresses the formulations of first- and second-order continua, as well as the finite element method and its different ingredients. Chapter 3 presents the foundations of multi-scale models based on first- and second-order homogenisation, with particular emphasis on porous microstructures. Lastly, Chapter 4 contains a thorough review on nonlocal damage models and phase-field approaches to fracture.

Part II tackles the issue of macro-mesh dependency in single- and multi-scale problems, while aiming to establish a connection between strategies for macro-regularisation for each case. Chapter 5 details the implementation of the nonlocal model of integral type for macro-analyses, and its enhancement for micro-scale problems. Chapter 6 includes a systematic assessment of multi-scale mesh-dependent effects arising for softening media, employing second-order homogenisation and RVE nonlocal damage of integral type for macro- and micro-regularisation. Chapter 7 proposes an optimisation-based strategy to relate the numerical parameters of the macro-scale nonlocal damage and the second-order multi-scale models.

In Part III, a staggered solution scheme is exploited for the implementation of additional damage and fracture models. A gradient-enhanced nonlocal model is implemented in Chapter 8, before assessing its main numerical aspects, in comparison to the integral approach. Finally, Chapter 9 describes the implementation and validation of a phase-field model for fracture.

In the following, the main contributions of this dissertation are outlined, before enumerating additional outcomes and observations.

10.1.1 Main contributions

Section 1.2 highlights the three main ingredients of the numerical studies performed in this dissertation: nonlocal strategies for macro- and micro-regularisation, second-order homogenisation for macro-regularisation in FE^2, and phase-field models towards micro-scale fracture. In this section, the key contributions to each of these topics are listed.

With regard to nonlocal strategies for single-scale regularisation, the existing micro-scale nonlocal damage model of integral type is enhanced, and extended for macro-analyses in Chapter 5. The comparative efficiency of the new implementation is demonstrated, relative to its previous version, and quadratic rates of convergence of the Newton-Rapshon method are reported for several numerical examples at the macro-scale. Furthermore, the effectiveness of the integral model in attenuating macro-mesh dependency is shown, while also discussing its numerical aspects. Particular attention is given to the increase in the number of non-zero stiffness coefficients caused by larger nonlocal domains, and its effects are examined. Conversely, a gradient nonlocal model is implemented in Chapter 8, making use of a staggered scheme for the solution of coupled problems, hitherito only employed in the context of thermomechanics. A preliminary study of the coupling setup is included, and convergence analyses showcase the consistency of the implementation. Mesh regularisation is carried out with the gradient nonlocal approach, before establishing a comparison between both nonlocal models. This assessment reveals that, even when both nonlocal strategies yield similar mechanical responses, their underlying numerical frameworks are completely distinct. The explicit modelling of nonlocal interactions of the integral model, associated with the loss of stiffness matrix sparsity, contrasts with the gradient approach, which includes nonlocality through an additional balance equation, resulting in damage diffusion between adjacent nodes. Crucially, this yields negligible computing time increases for larger nonlocal lengths, in the gradient case, since the damage stiffness matrix remains diagonal. Conversely, broader nonlocal domains result in increasingly non-sparse stiffness matrices for the integral model (this is illustrated in Figure 5.20), which pose numerical concerns. In the case of gradient-enhanced models, the main numerical issue identified here is the possibly slow convergence of the implicit coupling scheme, which is reported for one of the setups in Section 8.6.2 Furthermore, notable differences between the predictions of the two nonlocal strategies are identified in particular cases, namely the distinct damage averaging patterns.

The employment of second-order homogenisation for the regularisation of a multi-scale problem involving macro-softening, promoted by porous RVEs including damage, is comprehensively analysed in Chapter 6. In contrast with first-order FE^2, second-order approaches attenuate macro-mesh dependency, which is also related to mesh-dependent effects at the micro-scale. The ill-posedness of the macro-scale equilibrium problem, in this multi-scale setting, leading to mesh-dependent localisation, results in different degrees of macro-softening and also the arisal of distinct macroscopic strain bands, some of which are deemed non-physical. The impact of the RVE length on the macro-regularisation effects obtained with second-order homogenisation is assessed, with FE^2 responses for distinct macro-meshes converging for larger length values. In addition, an upper bound for exploiting the RVE length as a numerical parameter for macro-regularisation is reported, resulting in the appearance of non-physical behaviour. The simultaneous regularisation of the macro- and micro-problems is seen to enable a remarkable reduction of multi-scale mesh-dependency, although additional studies should be conducted in this regard. In Chapter 7, a numerical relation between the nonlocal radius and the RVE length is established, with larger values of the former corresponding to larger values of the latter. The single-scale nonlocal model replicates the macro-strain distributions found with second-order FE^2. Conversely, the evolving nature of the macroscopic length-scale arising in second-order homogensation inhibits the approximation of the

FE^2 reactions with the nonlocal model. The effectiveness of the proposed two-step optimisation-based strategy is proven with four distinct calibration cases.

A phase-field model for quasi-brittle materials implemented in Chapter 9 is validated with reference results from the literature. Preliminary parametric, coupling scheme, and mesh sensitivity analyses are conducted. Lastly, the phase-field model is applied to simulate the fracture of 3 fibre reinforced composite RVEs, within a macro-scale setup. Promising results are obtained for most cases, with the prediction of failure through the nucleation and coalescense of transverse cracks, whose length and path are analysed for the three morphologies and several combinations of fracture properties. The potential of phase-field approaches to model multi-scale damage and fracture phenomena is showcased, and this first implementation for macro-analyses paves the way for future enhancements.

10.1.2 Additional outcomes

Additional observations and remarks on the investigations conducted in this dissertation are included here, summarising the discussions in Sections 5.6, 6.6, 7.5, 8.7 and 9.6.

In Chapter 5, a limit on the minimum nonlocal radius value that allowed macro-regularisation, dependent on the selected mesh size, is identified. Below this limit, the nonlocal model recovers the local response, even though computing time still increases, as the nonlocal finite element loops are carried out. Slighly lower rates of convergence are also obtained for a smaller value of the nonlocal radius in Section 5.5.3. It is argued that several factors could be behind this observation, so it cannot be generalised before additional analyses are performed. Moreover, the adoption of distinct nonlocal weighting functions results in identical mechanical responses, as reported by Andrade et al. (2011), although it influences the computing times of nonlocal simulations. Alternative numerical methods for the solution of the global system of equations are assessed, for several values of the nonlocal radius and, hence, varying degrees of stiffness matrix non-sparsity, although the tendency of computational cost increase for larger nonlocal domains cannot be circumvented.

Chapter 6 examines the interdependency of mesh-regularisation effects at both spatial scales. With second-order FE^2 and local damage at the RVE level, even though macro-mesh dependency is greatly reduced, the degree of micro-softening also plays an important role. Conversely, with first-order homogenisation and micro-scale nonlocal damage, since the macro-problem is still ill-posed, numerous unrealistic macroscopic strain bands are obtained. This observation highlights the connection between mesh-regularising effects at both scales. In this setting, the level of micro-softening, dependent on the value of the RVE nonlocal radius, influences the arisal of these non-physical strain bands. For second-order FE^2 and nonlocal micro-damage, both problems are regularised, with all combinations of finite element meshes yielding identical responses, for two values of the RVE nonlocal radius and two RVE lengths. However, these findings are accompanied by a significant reduction of macro-softening, which may also have contributed to the attenuation of mesh dependency. The reduction of micro-softening, through the adoption of RVE nonlocal damage, also accelerates the convergence of second-order multi-scale predictions, for distinct macro-scale spatial discretisations, with RVE length increase, underscoring the intricate link between multi-scale mesh-dependent effects.

Chapter 7 proposes two strategies for the identification of the local Engelen model parameters. The first one, presented by Fonseca Gonçalves (2022), is based on the employment of FE^2 single-element simulations at low deformation levels, to up-scale the micro-constitutive response of porous RVEs. In the presence of micro-localisation, this framework does not produce robust calibrated models. It is also argued that the macroscopic Engelen model could be inadequate for capturing the complex load-dependent behaviour of RVEs containing voids, highlighted by the different elastic properties calibrated for RVEs under tension and shear loading setups. Alternatively, a direct calibration strategy is adopted, aiming at replicating the degree of macro-softening observed for specific FE^2 simulations. This approach yields accurate macro-models, which can be used to

relate the introduction of nonlocal damage of integral type and second-order homogenisation, in single- and multi-scale schemes, respectively.

Preliminary coupling scheme studies included in Chapter 8 show that Broyden's method is the most efficient implicit solver for the gradient-enhanced staggered setup, in accordance with the observations of Vila-Chã et al. (2023). Various coupling incrementation ratios are tested, and their effects on the computing time of gradient simulations depend on the value of the nonlocal length. Considering the importance of coupling scheme stability to the numerical efficiency and robustness of gradient nonlocal approaches, this analysis should be revisited. Additionally, identical values of the nonlocal length parameter result in distinct nonlocal predictions for the integral and gradient strategies, which are associated with different softening reductions. In this regard, complex effects are brought about by the adoption of the two nonlocal models. For a lower nonlocal length, similar damage contours are related with distinct strain and stress distributions for each case. Conversely, for a larger nonlocal parameter, identical strain and stress responses are attained, in spite of the underlying damage distributions, which present considerable differences.

Chapter 9 contains a preliminary coupling scheme analysis for the phase-field model. The time offset between the fracture driving force and the phase-field variable, discussed in Section 9.3.2 and by Navidtehrani et al. (2021b), leads to a remarkably robust coupling, considering a 1:1 incrementation ratio, while alternative numbers of coupling increments yield the premature termination of phase-field simulations due to the lack of coupling convergence. Moreover, a larger fracture toughness is associated with increased material strength, while the value of the length-scale parameter is seen to influence both the spatial diffusion of cracks, but also material strength. Lower values of the phase-field length-scale resulted in larger critical loads, in accordance with the observations of Borden et al. (2012). A mesh sensitivy study showcases the dependence of phase-field predictions on the refinement of the spatial discretisation throughout the crack path. Lastly, the simulation of the failure of heterogeneous RVEs with the phase-field model leads to similar observations in regard to the fracture parameters. In addition, conducting these preliminary studies within a macro-scale setup is associated with various limitations, particularly due to the set of boundary conditions to which the RVEs are subjected. For a composite microstructure containing a larger number of fibres, severe localisation near the constrained edges results in significant element distortion and likely non-physical results.

10.2 Future challenges

With the developments of this dissertation in mind, numerous prospects of future enhancement come to mind. In this section, some of these future challenges are discussed.

The main challenge in the aftermath of the contributions presented in this work is the improvement and extension of the phase-field model, towards the multi-scale modelling of fracture. The present implementation should be modified to explicitly account for heterogeneous materials, with several sets of fracture properties. The efficiency of the coupling solution scheme could also be revisited, although reasonable robustness has been achieved here. The formulation of the fracture driving force must be revised to avoid underestimating material strength in the presence of significant compressive strain modes. Furthermore, this phase-field model should be extended for micro-analyses, to allow a more reliable assessment of micro-scale fracture. Its integration with cohesive zone models, already explored by Paggi et al. (2018), could also be considered, to account for competing interface and bulk failure mechanisms, while the implementation may also be extended for elastoplastic fracture. Crucially, a variationally consistent framework for the computational homogenisation of the fracture of heterogeneous microstructures modelled with the phase-field approach should be pursued, following the contributions by Bharali (2024), Bharali et al. (2021).

In addition, the implementation of the nonlocal model of integral type could be revisited, to enhance its computational efficiency. Several suggestions in this regard are made in Section 5.6.

The numerical issues posed by the loss of stiffness matrix sparsity associated with larger nonlocal domains should be addressed, pursuing strategies for minimising the associated computing time increases. The influence of the nonlocal radius on the convergence rates of the Newton-Raphson method sould also be further explored. In the case of the gradient-enhanced model, a more detailed coupling scheme study should be carried out, to ensure its robustness and stability. For both integral and gradient nonlocal approaches, the adoption of evolving length-scale parameters could be considered in the future.

The employment of second-order homogenisation and micro-scale nonlocal damage for multi-scale regularisation should be revisited with more adequate loading conditions, to ensure the occurrence of reasonable macro-softening. In this context, the convergence of FE^2 responses for different meshes, with the increase in the RVE length, must be reassessed. Concerning the relationship between macro-scale nonlocal damage and second-order multi-scale approaches, the two-step calibration strategy could be repeated considering the gradient-enhanced Engelen model, to compare the resulting numerical connection between the nonlocal parameter and RVE length with the one obtained for the integral approach. Even for the nonlocal model of integral type, adopting the bell-shaped weighting function could be equated, since this would likely yield different results. Finally, if nonlocal strategies with evolving length-scale parameters are implemented, the optimisation-based procedure should be repeated, to see if these approaches allow replicating the nonlinearity of the second-order FE^2 response.

BIBLIOGRAPHY

Abali, B. E., Klunker, A., Barchiesi, E., and Placidi, L. (2021). A novel phase-field approach to brittle damage mechanics of gradient metamaterials combining action formalism and history variable. *ZAMM - Journal of Applied Mathematics and Mechanics / Zeitschrift für Angewandte Mathematik und Mechanik*, 101(9):e202000289.

Ackbarow, T., Chen, X., Keten, S., and Buehler, M. J. (2007). Hierarchies, multiple energy barriers, and robustness govern the fracture mechanics of alpha-helical and beta-sheet protein domains. *Biological Sciences*, 107(42):16410–16415.

Aifantis, E. C. (1984). On the Microstructural Origin of Certain Inelastic Models. *Journal of Engineering Materials and Technology*, 106(4):326–330.

Andrade, F. X. C. (2012). *Non-local Modelling of Ductile Damage: Formulation and Numerical Issues*. PhD thesis, Faculdade de Engenharia da Universidade do Porto.

Andrade, F. X. C., Andrade Pires, F. M., and César de Sá, J. M. A. (2014a). Consistent tangent operators for implicit non-local models of integral type. *Computers & Structures*, 141:59–73.

Andrade, F. X. C., Andrade Pires, F. M., César de Sá, J. M. A., and Malcher, L. (2009). Improvement of the numerical prediction of ductile failure with an integral nonlocal damage model. *International Journal of Material Forming*, 2:439–442.

Andrade, F. X. C., de Sa, J. M. A. C., and Andrade Pires, F. M. (2011). A ductile damage nonlocal model of integral-type at finite strains: formulation and numerical issues. *International Journal of Damage Mechanics*, 20:515–557.

Andrade, F. X. C., de Sá, J. M. A. C., and Pires, F. M. A. (2014b). Assessment and comparison of non-local integral models for ductile damage. *International Journal of Damage Mechanics*, 23(2):261–296.

Andrade-Campos, A., Thuillier, S., Pilvin, P., and Teixeira-Dias, F. (2007). On the determination of material parameters for internal variable thermoelastic–viscoplastic constitutive models. *International Journal of Plasticity*, 23(8):1349–1379.

Azinpour, E., Cruz, D., and de Sá, J. (2021). Phase-field approach in elastoplastic solids: application of an iterative staggered scheme and its experimental validation. *Computational Mechanics*, 68:255–269.

Azinpour, E., Ferreira, J. P. S., Parente, M. P. L., and de Sá, J. C. (2018). A simple and unified implementation of phase field and gradient damage models. *Advanced Modeling and Simulation in Engineering Sciences*, 5(15).

Bagni, C. and Askes, H. (2015). Unified finite element methodology for gradient elasticity. *Computers & Structures*, 160:100–110.

Barker, A. T. and Cai, X.-C. (2010). Scalable parallel methods for monolithic coupling in fluid–structure interaction with application to blood flow modeling. *Journal of Computational Physics*, 229(3):642–659.

Bažant, Z. P. (1991). Why continuum damage is nonlocal: Micromechanics arguments. *Journal of Engineering Mechanics*, 117(5):1070–1087.

Bažant, Z. P. (1994). Nonlocal damage theory based on micromechanics of crack interactions. *Journal of Engineering Mechanics*, 120(3):593–617.

Bažant, Z. P., Belytschko, T. B., and Chang, T. (1984). Continuum theory for strain-softening. *Journal of Engineering Mechanics*, 110(12):1666–1692.

Bažant, Z. P. and Pijaudier-Cabot, G. (1988). Nonlocal Continuum Damage, Localization Instability and Convergence. *Journal of Applied Mechanics*, 55:287–290.

Becke, A. D. (1992). Density-functional thermochemistry. I. The effect of the exchange-only gradient correction. *Journal of Chemical Physics*, 96:2155–2160.

Belnoue, J. P., Nguyen, G. D., and Korsunsky, A. M. (2009). Consistent tangent stiffness for local-nonlocal damage modelling of metals. *Procedia Engineering*, 1(1):177–180. Mesomechanics 2009.

Belytschko, T., Bažant, Z. P., Yul-Woong, H., and Ta-Peng, C. (1986). Strain-softening materials and finite-element solutions. *Computers & Structures*, 23(2):163–180.

Belytschko, T., Liu, W. K., Moran, B., and Elkhodary, K. (2014). *Nonlinear Finite Elements for Continua and Structures*. John Wiley & Sons, second edition edition.

Benvenuti, E., Borino, G., and Tralli, A. (2002). A thermodynamically consistent nonlocal formulation for damaging materials. *European Journal of Mechanics - A/Solids*, 21(4):535–553.

Bertram, A. (2017). *Compendium on Gradient Materials*. Springer Cham.

Bharali, R. (2024). *Numerical Methods and Multi-scale Modelling for Phase-field Fracture with Applications in Linear Elastic and Poro-elastic Media*. PhD thesis, Chalmers University of Technology.

Bharali, R., Goswami, S., Anitescu, C., and Rabczuk, T. (2022). A robust monolithic solver for phase-field fracture integrated with fracture energy based arc-length method and under-relaxation. *Computer Methods in Applied Mechanics and Engineering*, 394:114927.

Bharali, R., Larsson, F., and Jänicke, R. (2021). Computational homogenisation of phase-field fracture. *European Journal of Mechanics - A/Solids*, 88:104247.

Bijaya, A., Roy Chowdhury, S., and Chowdhury, R. (2023). Multiscale phase-field approach for investigation of anisotropic fracture properties of architected materials. *Mechanics of Materials*, 176:104528.

Blanco, P., Sánchez, P., de Souza Neto, E., and Feijóo, R. (2016a). The method of multiscale virtual power for the derivation of a second order mechanical model. *Mechanics of Materials*, 99:53–67.

Blanco, P., Sánchez, P., Rocha, F., Toro, S., and Feijóo, R. (2023). A consistent multiscale mechanical formulation for media with randomly distributed voids. *International Journal of Solids and Structures*, 283:112494.

Blanco, P. J., Sánchez, P. J., de Souza Neto, E. A., and Feijóo, R. A. (2016b). Variational foundations and generalized unified theory of rve-based multiscale models. *Archives of Computational Methods in Engineering*, 23:191–253.

Bobrow, D. G. and Stefik, M. J. (1982). Loops: data and object oriented programming for interlisp. In *European AI Conference*.

Bonet, J., Gil, A. J., and Wood, R. D. (2016). *Nonlinear Solid Mechanics for Finite Element Analysis: Statics*. Cambridge University Press.

Bonet, J. and Wood, R. D. (1997). *Nonlinear Continuum Mechanics for Finite Element Analysis*. Cambridge University Press.

Borden, M. J., Hughes, T. J., Landis, C. M., Anvari, A., and Lee, I. J. (2016). A phase-field formulation for fracture in ductile materials: Finite deformation balance law derivation, plastic degradation, and stress triaxiality effects. *Computer Methods in Applied Mechanics and Engineering*, 312:130–166. Phase Field Approaches to Fracture.

Borden, M. J., Verhoosel, C. V., Scott, M. A., Hughes, T. J., and Landis, C. M. (2012). A phase-field description of dynamic brittle fracture. *Computer Methods in Applied Mechanics and Engineering*, 217-220:77–95.

Bouhala, L., Shao, Q., Koutsawa, Y., Younes, A., Núñez, P., Makradi, A., and Belouettar, S. (2013). An xfem crack-tip enrichment for a crack terminating at a bi-material interface. *Engineering Fracture Mechanics*, 102:51–64.

Bourdin, B., Francfort, G., and Marigo, J.-J. (2000). Numerical experiments in revisited brittle fracture. *Journal of the Mechanics and Physics of Solids*, 48(4):797–826.

Bourdin, B., Francfort, G., and Marigo, J.-J. (2008). The variational approach to fracture. *Journal of Elasticity*, 91(4):5–148.

Brochu, E., Cora, V. M., and de Freitas, N. (2010). A tutorial on bayesian optimization of expensive cost functions, with application to active user modeling and hierarchical reinforcement learning.

Cardoso Coelho, R., Carvalho Alves, A. F., and Andrade Pires, F. (2024). Efficient constitutive parameter identification through optimisation-based techniques: A comparative analysis and novel composite bayesian optimisation strategy. *Computer Methods in Applied Mechanics and Engineering*, 427:117039.

Cardoso Coelho, R., Vieira de Carvalho, M., and Andrade Pires, F. (2023). A multi-scale model combining martensitic transformations with multi-phase crystallographic slip. *Computers & Structures*, 289:107174.

Carvalho Alves, A. F., Ferreira, B. P., and Andrade Pires, F. (2023). On the modeling of cavitation and yielding in rubber-toughened amorphous polymers: Fully implicit implementation and optimization-based calibration. *International Journal of Solids and Structures*, 283.

Coelho, R. P. C. (2019). Ductile Failure Analysis in Metallic Materials through Computational Homogenization.

Coleman, B. D. and Gurtin, M. E. (1967). Thermodynamics with Internal State Variables. *The Journal of Chemical Physics*, page 597–613.

Comi, C. (1999). Computational modelling of gradient-enhanced damage in quasi-brittle materials. *Mechanics of Cohesive-frictional Materials*, 4(1):17–36.

Comi, C. (2001). A non-local model with tension and compression damage mechanisms. *European Journal of Mechanics - A/Solids*, 20(1):1–22.

Cosserat, E. and Cosserat, F. (1909). *Théorie des Corps déformables*. A. Hermann et Fils.

César de Sá, J., Areias, P., and Zheng, C. (2006). Damage modelling in metal forming problems using an implicit non-local gradient model. *Computer Methods in Applied Mechanics and Engineering*, 195(48):6646–6660. Computational Metal Forming.

Danowski, C. (2014). *Computational Modelling of Thermo-Structure Interaction with Application to Rocket Nozzles*. PhD thesis, Technical University of Munich.

de Borst, R., Crisfield, M. A., Remmers, J. J. C., and Verhoosel, C. V. (2012). *Non-Linear Finite Element Analysis of Solids and Structures*. John Wiley & Sons.

de Borst, R., Geers, M., Peerlings, R., and Benallal, A. (1998). Some remarks on gradient and nonlocal damage theories. In Voyiadjis, G. Z., Ju, J.-W. W., and Chaboche, J.-L., editors, *Damage Mechanics in Engineering Materials*, volume 46 of *Studies in Applied Mechanics*, pages 223–236. Elsevier.

De Borst, R. and Muehlhaus, H. B. (1992). Gradient-dependent plasticity: formulation and algorithmic aspects. *International Journal for Numerical Methods in Engineering*, 35:521–539.

de Borst, R. and Verhoosel, C. V. (2016). Gradient damage vs phase-field approaches for fracture: Similarities and differences. *Computer Methods in Applied Mechanics and Engineering*, 312:78–94. Phase Field Approaches to Fracture.

de Borst, R., Benallal, A., and Heeres, O. M. (1996). A gradient-enhanced damage approach to fracture. *J. Phys. IV France*, 06:C6–491–C6–502.

de Carvalho, M. V., de Bortoli, D., and Andrade Pires, F. M. (2022). Consistent modeling of the coupling between crystallographic slip and martensitic phase transformation for mechanically induced loadings. *International Journal for Numerical Methods in Engineering*, 123(14):3179–3236.

De Cola, F., Pellegrino, A., Barbieri, E., Penumadu, D., and Petrinic, N. (2016). Void ratio based representative volume element for modelling the high strain rate behaviour of granular materials. *International Journal of Impact Engineering*, 91:46–55.

de Souza Neto, E., Blanco, P., Sánchez, P., and Feijóo, R. (2015). An rve-based multiscale theory of solids with micro-scale inertia and body force effects. *Mechanics of Materials*, 80:136–144.

de Souza Neto, E., Perić, D., and Owen, D. (1994). A model for elastoplastic damage at finite strains: algorithmic issues and applications. *Engineering Computations*, 11(3):257–281.

de Souza Neto, E. A. (2002). A fast, one-equation integration algorithm for the lemaitre ductile damage model. *Communications in Numerical Methods in Engineering*, 18(8):541–554.

de Souza Neto, E. A. and Feijóo, R. A. (2010). *Variational Foundations of Large Strain Multiscale Solid Constitutive Models: Kinematical Formulation*, chapter 9, pages 341–378. John Wiley & Sons, Ltd.

de Souza Neto, E. A., Peric, D., and Owen, D. R. J. (2008). *Computational Methods for Plasticity: Theory and Applications*. Wiley.

de Vaucorbeil, A., Nguyen, V. P., and Mandal, T. K. (2022). Mesh objective simulations of large strain ductile fracture: A new nonlocal johnson-cook damage formulation for the total lagrangian material point method. *Computer Methods in Applied Mechanics and Engineering*, 389:114388.

de Vree, J., Brekelmans, W., and van Gils, M. (1995). Comparison of nonlocal approaches in continuum damage mechanics. *Computers & Structures*, 55(4):581–588.

dos Santos, W. F., Ferreira, A. R., and Proença, S. P. B. (2022). Complete geometric representation of yield surfaces for porous ductile media by a 3d computational homogenization approach: an assessment of the gurson yield criterion. *J Braz. Soc. Mech. Sci. Eng.*, 44.

dos Santos, W. F., Ferreira, A. R., and Proença, S. P. B. (2023). Isotropic yield surfaces for porous ductile materials: complete geometric representation by a computational homogenisation procedure. *Engineering Computations*, 40(4):737–771.

dos Santos, W. F., Rodrigues Lopes, I. A., Andrade Pires, F. M., and Proença, S. P. (2023). Second-order multi-scale modelling of natural and architected materials in the presence of voids: Formulation and numerical implementation. *Computer Methods in Applied Mechanics and Engineering*, 416:116374.

dos Santos, W. F., Rodrigues Lopes, I. A., Andrade Pires, F. M., and Proença, S. P. (2024). Exploring novel mechanical metamaterials: Unravelling deformation mode coupling and size effects through second-order computational homogenisation. *International Journal of Solids and Structures*, 292.

Edelen, D. G. B., Green, A. E., and Laws, N. (1971). Nonlocal continuum mechanics. *Archive for Rational Mechanics and Analysi*, 43:36–44.

Edelen, D. G. B. and Laws, N. (1971). On the thermodynamics of systems with nonlocality. *Archive for Rational Mechanics and Analysis*, 43:24–35.

Elmasry, A., Azoti, W., El-Safty, S. A., and Elmarakbi, A. (2023). A comparative review of multiscale models for effective properties of nano- and micro-composites. *Progress in Materials Science*, 132:101022.

Engelen, R. A., Geers, M. G., and Baaijens, F. P. (2003). Nonlocal implicit gradient-enhanced elastoplasticity for the modelling of softening behaviour. *International Journal of Plasticity*, 19(4):403–433.

Fang, J., Wu, C., Rabczuk, T., Wu, C., Ma, C., Sun, G., and Li, Q. (2019). Phase field fracture in elasto-plastic solids: Abaqus implementation and case studies. *Theoretical and Applied Fracture Mechanics*, 103:102252.

Feijóo, R. A., Blanco, P. J., de Souza Neto, E. A., and Sánchez, P. J. (2023). Novel multiscale models in a multicontinuum approach to divide and conquer strategies. *Computational and Applied Mechanics*, 42(143).

Felder, S., Kopic-Osmanovic, N., Holthusen, H., Brepols, T., and Reese, S. (2022). Thermomechanically coupled gradient-extended damage-plasticity modeling of metallic materials at finite strains. *International Journal of Plasticity*, 148:103142.

Felippa, C. and Park, K. (1980). Staggered transient analysis procedures for coupled mechanical systems: Formulation. *Computer Methods in Applied Mechanics and Engineering*, 24(1):61–111.

Felippa, C. A., Park, K., and Farhat, C. (2001). Partitioned analysis of coupled mechanical systems. *Computer Methods in Applied Mechanics and Engineering*, 190(24):3247–3270. Advances in Computational Methods for Fluid-Structure Interaction.

Fermi, E., Pasta, P., Ulam, S., and Tsingou, M. (1955). Studies on the nonlinear problems. Technical report, Los Alamos National Laboratory (LANL), Los Alamos, NM, USA.

Ferreira, B. P. (2017). Avaliação da Precisão de um Modelo de Dano Contínuo através de um Modelo Multi-escala baseado em Homogeneização Computacional.

Ferreira, B. P. (2022). *Towards Data-driven Multi-scale Optimization of Thermoplastic Blends: Microstructural Generation, Constitutive Development and Clustering-based Reduced-Order Modeling*. PhD thesis, Faculdade de Engenharia da Universidade do Porto.

Ferreira, B. P., Andrade Pires, F., and Bessa, M. (2022a). Adaptivity for clustering-based reduced-order modeling of localized history-dependent phenomena. *Computer Methods in Applied Mechanics and Engineering*, 393:114726.

Ferreira, B. P., Carvalho Alves, A. F., and Andrade Pires, F. (2023). An efficient finite strain constitutive model for amorphous thermoplastics: Fully implicit computational implementation and optimization-based parameter calibration. *Computers and Structures*, 281.

Ferreira, B. P., Vila-Chã, J. L. P., and Pires, F. M. A. (2022b). An adaptive multi-temperature isokinetic method for the rve generation of particle reinforced heterogeneous materials, part ii: Numerical assessment and statistical analysis. *Mechanics of Materials*, 165:104068.

Ferreira Rocha, P. R., Fonseca Gonçalves, G., dos Reis, G., and Guedes, R. M. (2024). Mechanisms of component degradation and multi-scale strategies for predicting composite durability: Present and future perspectives. *Journal of Composites Science*, 8(6).

Feyel, F. and Chaboche, J.-L. (2000). Fe2 multiscale approach for modelling the elastoviscoplastic behaviour of long fibre sic/ti composite materials. *Computer Methods in Applied Mechanics and Engineering*, 183(3):309–330.

Fish, J. (2006). Bridging the scales in nano engineering and science. *Journal of Nanoparticle Research*, 8:577–594.

Fish, J., Jiang, T., and Yuan, Z. (2012). A staggered nonlocal multiscale model for a heterogeneous medium. *Numerical Methods in Engineering*, 91:142–157.

Fleck, N., Muller, G., Ashby, M., and Hutchinson, J. (1994). Strain gradient plasticity: Theory and experiment. *Acta Metallurgica et Materialia*, 42(2):475–487.

Fonseca Gonçalves, G. (2022). Determination of macroscopic constitutive parameters from multi-scale simulations. Technical report, Faculdade de Engenharia da Universidade do Porto.

Francfort, G. and Marigo, J.-J. (1998). Revisiting brittle fracture as an energy minimization problem. *Journal of the Mechanics and Physics of Solids*, 46(8):1319–1342.

Frazier, P. I. (2018). A tutorial on bayesian optimization.

Fu, Q., Yi, S., Chen, B., Bui, T. Q., Hu, X., and Yao, W. (2020). A crack-tip element for modelling arbitrary crack propagations. *Theoretical and Applied Fracture Mechanics*, 105:102422.

Gamma, E., Helm, R., Johnson, R., Vlissides, J., and Booch, G. (1995). *Design Patterns: Elements of Reusable Object-Oriented Software*. Addison-Wesley.

Geerlings, P., Proft, F. D., Proft, F. D., Langenaeker, W., and Langenaeker, W. (2003). Conceptual density functional theory. *Chemical Reviews*, 103(5):1793–1874.

Geers, M., de Borst, R., Brekelmans, W., and Peerlings, R. (1998). Strain-based transient-gradient damage model for failure analyses. *Computer Methods in Applied Mechanics and Engineering*, 160(1):133–153.

Gerasimov, T. and De Lorenzis, L. (2016). A line search assisted monolithic approach for phase-field computing of brittle fracture. *Computer Methods in Applied Mechanics and Engineering*, 312:276–303. Phase Field Approaches to Fracture.

Ghosh, S., Lee, K., and Moorthy, S. (1995). Multiple scale analysis of heterogeneous elastic structures using homogenization theory and voronoi cell finite element method. *International Journal of Solids and Structures*, 32(1):27–62.

Gitman, I. (2006). *Representative volumes and multi-scale modelling of quasi-brittle materials*. PhD thesis, Technische Universiteit Delft.

Gitman, I., Askes, H., and Sluys, L. (2007). Representative volume: Existence and size determination. *Engineering Fracture Mechanics*, 74(16):2518–2534.

Griebel, M. and Hamaekers, J. (2004). Molecular dynamics simulations of the elastic moduli of polymer-carbon nanotube composites. *Computer Methods in Applied Mechanics and Engineering*, 193(17):1773–1788. Multiple Scale Methods for Nanoscale Mechanics and Materials.

Griffith, A. A. (1921). Vi. the phenomena of rupture and flow in solids. *Philosophical transactions of the royal society of london. Series A, containing papers of a mathematical or physical character*, 221(582-593):163–198.

Grimme, S., Ehrlich, S., and Goerigk, L. (2011). Effect of the damping function in dispersion corrected density functional theory. *Journal of Computational Chemistry*, 32(7):1456–1465.

Groot, R. D. and Warren, P. B. (1997). Dissipative particle dynamics: Bridging the gap between atomistic and mesoscopic simulation. *Journal of Chemical Physics*, 107:4423–4435.

Guedes, J. and Kikuchi, N. (1990). Preprocessing and postprocessing for materials based on the homogenization method with adaptive finite element methods. *Computer Methods in Applied Mechanics and Engineering*, 83(2):143–198.

Gurson, A. L. (1977). Continuum Theory of Ductile Rupture by Void Nucleation and Growth: Part I—Yield Criteria and Flow Rules for Porous Ductile Media. *Journal of Engineering Materials and Technology*, 99(1):2–15.

Hambli, R. (2001). Finite element simulation of fine blanking processes using a pressure-dependent damage model. *Journal of Materials Processing Technology*, 116(2):252–264.

Han, Y. and Elliott, J. (2007). Molecular dynamics simulations of the elastic properties of polymer/-carbon nanotube composites. *Computational Materials Science*, 39(2):315–323.

He, B., Schuler, L., and Newell, P. (2020). A numerical-homogenization based phase-field fracture modeling of linear elastic heterogeneous porous media. *Computational Materials Science*, 176:109519.

Hill, R. (1965). A self-consistent mechanics of composite materials. *Journal of the Mechanics and Physics of Solids*, 4:213–222.

Hirshikesh, Natarajan, S., Annabattula, R. K., and Martínez-Pañeda, E. (2019). Phase field modelling of crack propagation in functionally graded materials. *Composites Part B: Engineering*, 169:239–248.

Hofacker, M. and Miehe, C. (2012). Continuum phase field modeling of dynamic fracture: variational principles and staggered fe implementation. *International Journal of Fracture*, 178:113–129.

Holzapfel, G. A. (2000). *Nonlinear Solid Mechanics: A Continuum Approach for Engineering*. John Wiley and Sons, London.

Horstemeyer, M. F. (2012). *Integrated Computational Materials Engineering (ICME) for Metals: Using Multiscale Modeling to Invigorate Engineering Design with Science*. The Minerals, Metals & Materials Society.

Horstemeyer, M. F. (2018). *Integrated Computational Materials Engineering (ICME) for Metals: Concepts and Case Studies*. John Wiley & Sons, Inc.

Irons, B. M. and Tuck, R. C. (1969). A version of the aitken accelerator for computer iteration. *International Journal for Numerical Methods in Engineering*, 1(3):275–277.

Irwin, G. R. (1957). Analysis of Stresses and Strains Near the End of a Crack Traversing a Plate. *Journal of Applied Mechanics*, 24(3):361–364.

Jamshidian, M., Boddeti, N., Rosen, D., and Weeger, O. (2020). Multiscale modelling of soft lattice metamaterials: Micromechanical nonlinear buckling analysis, experimental verification, and macroscale constitutive behaviour. *International Journal of Mechanical Sciences*, 188:105956.

Javili, A., Saeb, S., and Steinnmann, P. (2017). Aspects of implementing constant traction boundary conditions in computational homogenization via semi-dirichlet boundary conditions. *Computer Mechanics*, 59:21–35.

Jirásek, M. (1998). Nonlocal models for damage and fracture: Comparison of approaches. *International Journal of Solids and Structures*, 35(31):4133–4145.

Jirásek, M. and Desmorat, R. (2019). Localization analysis of nonlocal models with damage-dependent nonlocal interaction. *International Journal of Solids and Structures*, 174-175:1–17.

Jirásek, M. and Patzak, B. (2002). Consistent tangent stiffness for nonlocal damage models. *Computers and Structures*, 80:1279–1293.

Junker, P., Riesselmann, J., and Balzani, D. (2022). Efficient and robust numerical treatment of a gradient-enhanced damage model at large deformations. *International Journal for Numerical Methods in Engineering*, 123(3):774–793.

Kachanov, L. (1958). Time of the rupture process under creep condition. *Izvestiya Akademii Nauk SSSR, Otdelenie Tekhn Nauk*, 8:26–31.

Kaczmarczyk, L., Pearce, C. J., and Bićanić, N. (2008). Scale transition and enforcement of rve boundary conditions in second-order computational homogenization. *International Journal for Numerical Methods in Engineering*, 74(3):506–522.

Kanouté, P., Boso, D. P., Chaboche, J. L., and Schrefler, B. A. (2009). Multiscale methods for composites: A review. *Archives of Computational Methods in Engineering*, 16:31–75.

Khadyko, M., Frodal, B. H., and Hopperstad, O. S. (2024). Modelling ductile fracture in an al alloy with crystal plasticity models. *Materials Research Proceedings*, 41:2190–2199.

Kochmann, D. M., Hopkins, J. B., and Valdevit, L. (2019). Multiscale modeling and optimization of the mechanics of hierarchical metamaterials. *MRS Bulletin*, 44(10):773–781.

Kouznetsova, V., Brekelmans, W. A. M., and Baaijens, F. P. T. (2001). An approach to micro-macro modeling of heterogeneous materials. *Computational Mechanics*, 27:37–48.

Kouznetsova, V., Geers, M., and Brekelmans, W. (2004a). Multi-scale second-order computational homogenization of multi-phase materials: a nested finite element solution strategy. *Computer Methods in Applied Mechanics and Engineering*, 193(48):5525–5550. Advances in Computational Plasticity.

Kouznetsova, V., Geers, M., and Brekelmans, W. (2004b). Size of a representative volume element in a second-order computational homogenization framework. *International Journal for Multiscale Computational Engineering*, 2(4):575–598.

Kouznetsova, V. G. (2002). *Computational homogenization for the multi-scale analysis of multi-phase materials*. PhD thesis, Technische Universiteit Eindhoven.

Kristensen, P. K., Niordson, C. F., and Martínez-Pañeda, E. (2020). Applications of phase field fracture in modelling hydrogen assisted failures. *Theoretical and Applied Fracture Mechanics*, 110:102837.

Krueger, R. (2004). Virtual crack closure technique: History, approach, and applications. *Applied Mechanics Reviews*, 57(1-6):109 – 143.

Kröner, E. (1967). Elasticity theory of materials with long range cohesive forces. *International Journal of Solids and Structures*, 3(5):731–742.

Kuhn, J., Spitz, J., Sonnweber-Ribic, P., Schneider, M., and Böhlke, T. (2022). Identifying material parameters in crystal plasticity by bayesian optimization. *Optimization and Engineering*, 23:1489–1523.

Kumar, P. A. V., Dean, A., Reinoso, J., Lenarda, P., and Paggi, M. (2021). Phase field modeling of fracture in functionally graded materials: γ-convergence and mechanical insight on the effect of grading. *Thin-Walled Structures*, 159:107234.

Labergere, C., Guelorget, B., and Francois, M. (2014). Strain rate distribution and localization band width evolution during tensile test. *International Journal of Solids and Structures*, 51(23):3944–3961.

Lacy, T. E., McDowell, D. L., and Talreja, R. (1999). Gradient concepts for evolution of damage. *Mechanics of Materials*, 31(12):831–860.

Lasry, D. and Belytschko, T. (1988). Localization limiters in transient problems. *International Journal of Solids and Structures*, 24(6):581–597.

Lemaitre, J. (1985a). A Continuous Damage Mechanics Model for Ductile Fracture. *Journal of Engineering Materials and Technology*, 107(1):83–89.

Lemaitre, J. (1985b). Coupled elasto-plasticity and damage constitutive equation. *Computer Methods in Applied Mechanics and Engineering*, 51:31–49.

Lenz, P. and Mahnken, R. (2023). Non-local integral-type damage combined to mean-field homogenization methods for composites and its parallel implementation. *Composite Structures*, 314:116911.

Lesičar, T. (2015). *Multiscale modeling of heterogeneous materials using second-order homogenizations*. PhD thesis, University of Zagreb.

Lesičar, T., Sorić, J., and Tonković, Z. (2016). Large strain, two-scale computational approach using c1 continuity finite element employing a second gradient theory. *Computer Methods in Applied Mechanics and Engineering*, 298:303–324.

Li, C., E., D., and Yi, N. (2016). Analysis on fracture initiation and fracture angle in ductile sheet metal under uniaxial tension by experiments and finite element simulations. *Journal of Materials Research*, 31(24):3991–3999.

Li, G., Sharifpour, F., Bahmani, A., and Montesano, J. (2018). A new approach to rapidly generate random periodic representative volume elements for microstructural assessment of high volume fraction composites. *Materials & Design*, 150:124–138.

Li, X. and Xu, Y. (2022). Phase field modeling scheme with mesostructure for crack propagation in concrete composite. *International Journal of Solids and Structures*, 234-235:111259.

Lu, Y., Helfer, T., Bary, B., and Fandeur, O. (2020). An efficient and robust staggered algorithm applied to the quasi-static description of brittle fracture by a phase-field approach. *Computer Methods in Applied Mechanics and Engineering*, 370:113218.

Lu, Y. and Tong, L. (2023). Concurrent multiscale topology optimization of metamaterials for mechanical cloak. *Computer Methods in Applied Mechanics and Engineering*, 409:115966.

Luo, C. (2023). Fast staggered schemes for the phase-field model of brittle fracture based on the fixed-stress concept. *Computer Methods in Applied Mechanics and Engineering*, 404:115787.

Luscher, D. J. (2010). *A hierarchical framework for the multiscale modeling of microstructure evolution in heterogeneous materials*. PhD thesis, Georgia Institute of Technology.

Maekawa, K. and Itoh, A. (1995). Friction and tool wear in nano-scale machining—a molecular dynamics approach. *Wear*, 188(1):115–122.

Maia, M., Rocha, I., Kerfriden, P., and van der Meer, F. (2023). Physically recurrent neural networks for path-dependent heterogeneous materials: Embedding constitutive models in a data-driven surrogate. *Computer Methods in Applied Mechanics and Engineering*, 407:115934.

Mandal, T. K., Nguyen, V. P., and Heidarpour, A. (2019). Phase field and gradient enhanced damage models for quasi-brittle failure: A numerical comparative study. *Engineering Fracture Mechanics*, 207:48–67.

Marques da Silva, J. A., Vieira de Carvalho, M., Cardoso Coelho, R. P., Rodrigues Lopes, I. A., and Andrade Pires, F. M. (2023). On the representativeness of polycrystalline models with transformation induced plasticity. *Finite Elements in Analysis and Design*, 215:103875.

Martins, J., Andrade-Campos, A., and Thuillier, S. (2018). Comparison of inverse identification strategies for constitutive mechanical models using full-field measurements. *International Journal of Mechanical Sciences*, 145:330–345.

Matouš, K., Geers, M. G. D., Kouznetsova, V., and Gillman, A. (2017). A review of predictive nonlinear theories for multiscale modeling of heterogeneous materials. *Journal of Computational Physics*.

Matsushima, T., Chambon, R., and Caillerie, D. (2002). Large strain finite element analysis of a local second gradient model: application to localization. *International Journal for Numerical Methods in Engineering*, 54(4):499–521.

McAuliffe, C. and Waisman, H. (2016). A coupled phase field shear band model for ductile–brittle transition in notched plate impacts. *Computer Methods in Applied Mechanics and Engineering*, 305:173–195.

Mediavilla Varas, J. (2005). *Continuous and discontinuous modelling of ductile fracture*. PhD thesis, Technische Universiteit Eindhoven.

Meng, M., Rizvi, M., Le, H., and Grove, S. (2016). Multi-scale modelling of moisture diffusion coupled with stress distribution in cfrp laminated composites. *Composite Structures*, 138:295–304.

Metcalf, M., Reid, J., and Cohen, M. (2011). *Modern Fortran Explained*. Oxford University Press.

Mi, Y., Crisfield, M. A., Davies, G. A. O., and Hellweg, H. B. (1998). Progressive delamination using interface elements. *Journal of Composite Materials*, 32(14):1246–1272.

Miehe, C., Aldakheel, F., and Raina, A. (2016). Phase field modeling of ductile fracture at finite strains: A variational gradient-extended plasticity-damage theory. *International Journal of Plasticity*, 84:1–32.

Miehe, C. and Bayreuther, C. G. (2007). On multiscale fe analyses of heterogeneous structures: from homogenization to multigrid solvers. *International Journal for Numerical Methods in Engineering*, 71(10):1135–1180.

Miehe, C., Welschinger, F., and Hofacker, M. (2010). Thermodynamically consistent phase-field models of fracture: Variational principles and multi-field fe implementations. *International Journal for Numerical Methods in Engineering*, 83(10):1273–1311.

Mindlin, R. and Eshel, N. (1968). On first strain-gradient theories in linear elasticity. *International Journal of Solids and Structures*, 4(1):109–124.

Mindlin, R. D. (1964). Micro-structure in linear elasticity. *Archive for Rational Mechanics and Analysis*, 16:51–78.

Mir, A., Nguyen, G. D., and Sheikh, A. H. (2018). A thermodynamics-based model for brittle to ductile behaviour and localised failure of porous rocks. *International Journal of Solids and Structures*, 152-153:161–184.

Mirkhalaf, S., Andrade Pires, F., and Simoes, R. (2017). Modelling of the post yield response of amorphous polymers under different stress states. *International Journal of Plasticity*, 88:159–187.

Mockus, J. (1994). Application of bayesian approach to numerical methods of global and stochastic optimization. *Journal of Global Optimization*, 4:347–365.

Moon, D. A. (1986). Object-oriented programming with flavors. *SIGPLAN Not.*, 21(11):1–8.

Moës, N., Dolbow, J., and Belytschko, T. (1999). A finite element method for crack growth without remeshing. *International Journal for Numerical Methods in Engineering*, 46(1):131 – 150.

Msekh, M. A., Sargado, J. M., Jamshidian, M., Areias, P. M., and Rabczuk, T. (2015). Abaqus implementation of phase-field model for brittle fracture. *Computational Materials Science*, 96:472–484. Special Issue Polymeric Composites.

Mühlhaus, H.-B., Borst, de, R., Sluys, L., and Pamin, J. (1994). A thermodynamic theory for inhomogeneous damage evolution. In Siriwardana, H. and Zaman, M., editors, *Computer methods and advances in geomechanics : proceedings of the 8th international conference on computer methods and advances in geomechanics, Morgantown, West Virginia, USA, 22-28 May 1994*, pages 635–640. Balkema.

Murakami, S. (2012). *Continuum Damage Mechanics*. Springer Dordrecht.

Mühlhaus, H. B. and Alfantis, E. C. (1991). A variational principle for gradient plasticity. *International Journal of Solids and Structures*, 28(7):845–857.

Nahrmann, M. and Matzenmiller, A. (2021). Modelling of nonlocal damage and failure in ductile steel sheets under multiaxial loading. *International Journal of Solids and Structures*, 232:111166.

Navidtehrani, Y., Betegón, C., and Martínez-Pañeda, E. (2021a). A simple and robust abaqus implementation of the phase field fracture method. *Applications in Engineering Science*, 6:100050.

Navidtehrani, Y., Betegón, C., and Martínez-Pañeda, E. (2021b). A unified abaqus implementation of the phase field fracture method using only a user material subroutine. *Materials*, 14(8).

Neto, E. A. S., Pires, F. M. A., and Owen, D. R. J. (2005). F-bar-based linear triangles and tetrahedra for finite strain analysis of nearly incompressible solids. part i: formulation and benchmarking. *International Journal for Numerical Methods in Engineering*, 62(3):353–383.

Nguyen, V.-D. and Noels, L. (2014). Computational homogenization of cellular materials. *International Journal of Solids and Structures*, 51(11):2183–2203.

Nguyen, V.-D., Wu, L., and Noels, L. (2017). Unified treatment of microscopic boundary conditions and efficient algorithms for estimating tangent operators of the homogenized behavior in the computational homogenization method. *Computer Mechanics*, 59:483–505.

Orifici, A., Herszberg, I., and Thomson, R. (2008). Review of methodologies for composite material modelling incorporating failure. *Composite Structures*, 86(1):194–210. Fourteenth International Conference on Composite Structures.

Ostwald, R., Kuhl, E., and Menzel, A. (2019). On the implementation of finite deformation gradient-enhanced damage models. *Computational Mechanics*, 64:847–877.

Oñate, E. (2009). *Structural Analysis with the Finite Element Method. Linear Statics. Volume 1: Basis and Solids.* Springer Dordrecht.

Oñate, E. (2013). *Structural Analysis with the Finite Element Method. Linear Statics. Volume 2: Beams, Plates and Shells.* Springer Dordrecht.

Paggi, M., Corrado, M., and Reinoso, J. (2018). Fracture of solar-grade anisotropic polycrystalline silicon: A combined phase field-cohesive zone model approach. *Computer Methods in Applied Mechanics and Engineering*, 330:123–148.

Paggi, M. and Reinoso, J. (2017). Revisiting the problem of a crack impinging on an interface: A modeling framework for the interaction between the phase field approach for brittle fracture and the interface cohesive zone model. *Computer Methods in Applied Mechanics and Engineering*, 321:145–172.

Papanicolopulos, S.-A., Zervos, A., and Vardoulakis, I. (2009). A three-dimensional c1 finite element for gradient elasticity. *International Journal for Numerical Methods in Engineering*, 77(10):1396–1415.

Patil, R., Mishra, B., and Singh, I. (2018a). An adaptive multiscale phase field method for brittle fracture. *Computer Methods in Applied Mechanics and Engineering*, 329:254–288.

Patil, R., Mishra, B., and Singh, I. (2019). A multiscale framework based on phase field method and xfem to simulate fracture in highly heterogeneous materials. *Theoretical and Applied Fracture Mechanics*, 100:390–415.

Patil, R., Mishra, B., Singh, I., and Bui, T. (2018b). A new multiscale phase field method to simulate failure in composites. *Advances in Engineering Software*, 126:9–33.

Peerlings, R., Borst, de, R., Brekelmans, W., Vree, de, J., and Spee, I. (1996a). Some observations on localisation in non-local and gradient damage models. *European Journal of Mechanics. A, Solids*, 15:937–953.

Peerlings, R., Geers, M., de Borst, R., and Brekelmans, W. (2001). A critical comparison of nonlocal and gradient-enhanced softening continua. *International Journal of Solids and Structures*, 38(44):7723–7746.

Peerlings, R. H. J., De Borst, R., Brekelmans, W. A. M., and De Vree, J. H. P. (1996b). Gradient enhanced damage for quasi-brittle materials. *International Journal for Numerical Methods in Engineering*, 39(19):3391–3403.

Perdahcioglu, E. S., Geijselaers, H. J. M., and Groen, M. (2008). Influence of plastic strain on deformation-induced martensitic transformation. *Scripta Materialia*, 58:947–950.

Petera, J. and Pittman, J. F. T. (1994). Isoparametric hermite elements. *International Journal for Numerical Methods in Engineering*, 37(20):3489–3519.

Phunpeng, V. and Baiz, P. (2015). Mixed finite element formulations for strain-gradient elasticity problems using the fenics environment. *Finite Elements in Analysis and Design*, 96:23–40.

Pijaudier-Cabot, G. and Bažant, Z. P. (1987). Nonlocal damage theory. *Journal of Engineering Mechanics*, 113(10):1512–1533.

Pijaudier-Cabot, G., Haidar, K., and Dubé, J.-F. (2004). Non-local damage model with evolving internal length. *International Journal for Numerical and Analytical Methods in Geomechanics*, 28(7-8):633–652.

Pijaudier-Cabot, G. and Huerta, A. (1991). Finite element analysis of bifurcation in nonlocal strain softening solids. *Computer Methods in Applied Mechanics and Engineering*, 90(1):905–919.

Pinto Carvalho, R. (2021). *Multi-scale Modelling of Contact Interfaces*. PhD thesis, Faculdade de Engenharia da Universidade do Porto.

Pinto Carvalho, R., Rodrigues Lopes, I. A., and Andrade Pires, F. M. (2018). Prediction of the yielding behaviour of ductile porous materials through computational homogenization. *Engineering Computations*, 35(2):604–621.

Plews, J. and Duarte, C. (2015). Bridging multiple structural scales with a generalized finite element method. *International Journal for Numerical Methods in Engineering*, 102(3-4):180–201.

Poh, L. H. and Sun, G. (2017). Localizing gradient damage model with decreasing interactions. *International Journal for Numerical Methods in Engineering*, 110(6):503–522.

Polizzotto, C. (2009). A nonlocal strain gradient plasticity theory for finite deformations. *International Journal of Plasticity*, 25(7):1280–1300.

Polizzotto, C. (2016). A note on the higher order strain and stress tensors within deformation gradient elasticity theories: Physical interpretations and comparisons. *International Journal of Solids and Structures*, 90:116–121.

Quintanas-Corominas, A., Reinoso, J., Casoni, E., Turon, A., and Mayugo, J. (2019). A phase field approach to simulate intralaminar and translaminar fracture in long fiber composite materials. *Composite Structures*, 220:899–911.

Quintanas-Corominas, A., Turon, A., Reinoso, J., Casoni, E., Paggi, M., and Mayugo, J. (2020). A phase field approach enhanced with a cohesive zone model for modeling delamination induced by matrix cracking. *Computer Methods in Applied Mechanics and Engineering*, 358:112618.

Rabotnov, Y. N. (1963). Paper 68: On the equation of state of creep. *Proceedings of the Institution of Mechanical Engineers, Conference Proceedings*, 178(1):2–117–2–122.

Rajput, A., Subhash Shedbale, A., and Khan, D. (2023). A robust staggered localizing gradient enhanced isotropic damage model for failure prediction in heterogeneous materials. *Engineering Fracture Mechanics*, 293:109708.

Rastiello, G., Giry, C., Gatuingt, F., and Desmorat, R. (2018). From diffuse damage to strain localization from an eikonal non-local (enl) continuum damage model with evolving internal length. *Computer Methods in Applied Mechanics and Engineering*, 331:650–674.

Reis, F. and Andrade Pires, F. (2013). An adaptive sub-incremental strategy for the solution of homogenization-based multi-scale problems. *Computer Methods in Applied Mechanics and Engineering*, 257:164–182.

Reis, F. and Andrade Pires, F. (2014). A mortar based approach for the enforcement of periodic boundary conditions on arbitrarily generated meshes. *Computer Methods in Applied Mechanics and Engineering*, 274:168–191.

Reis, F. J. P., Rodrigues Lopes, I. A., Andrade Pires, F. M., and Andrade, F. X. C. (2018). Microscale analysis of heterogeneous ductile materials with nonlocal damage models of integral type. *Computers and Structures*, 201:37–57.

Rocha, F. F., Blanco, P. J., Sánchez, P. J., and Feijóo, R. A. (2018). Multi-scale modelling of arterial tissue: Linking networks of fibres to continua. *Computer Methods in Applied Mechanics and Engineering*, 341:740–787.

Rochus, V., Rixen, D. J., and Golinval, J.-C. (2006). Monolithic modelling of electro-mechanical coupling in micro-structures. *International Journal for Numerical Methods in Engineering*, 65(4):461–493.

Rodrigues Lopes, I. A. (2019). *Multi-Scale Modelling and Analysis of Multi-Phase Solids Using Second-Order Computational Homogenisation at Finite Strains with Parallel Computing*. PhD thesis, Faculdade de Engenharia da Universidade do Porto.

Rodrigues Lopes, I. A. and Andrade Pires, F. M. (2021). Unlocking the Potential of Second-order Computational Homogenisation: An Overview of Distinct Formulations and a Guide for their Implementation. *Archive for Rational Mechanics and Analysis*, 29:1339–1393.

Rodrigues Lopes, I. A. and Andrade Pires, F. M. (2022a). An assessment of multi-scale models based on second-order computational homogenisation. *Computers & Structures*, 259:106679.

Rodrigues Lopes, I. A. and Andrade Pires, F. M. (2022b). Formulation and numerical implementation of a variationally consistent multi-scale model based on second-order computational homogenisation at finite strains for quasi-static problems. *Computer Methods in Applied Mechanics and Engineering*, 392:114714.

Rodrigues Lopes, I. A. and Andrade Pires, F. M. (2022). A fully second-order homogenization formulation for the multi-scale modeling of heterogeneous materials. *International Journal for Numerical Methods in Engineering*, 123(21):5274–5318.

Rodrigues Lopes, I. A., Andrade Pires, F. M., and Reis, F. J. P. (2018). A mixed parallel strategy for the solution of coupled multi-scale problems at finite strains. *Computational Mechanics*, 61:157–180.

Rodrigues Lopes, I. A., Ferreira, B. P., and Andrade Pires, F. M. (2021). On the efficient enforcement of uniform traction and mortar periodic boundary conditions in computational homogenisation. *Computer Methods in Applied Mechanics and Engineering*, 384:113930.

Rodrigues Lopes, I. A., Vieira de Carvalho, M., Marques da Silva, J. A., Cardoso Coelho, R. P., and Andrade Pires, F. M. (2023). Second-order homogenisation of crystal plasticity and martensitic transformation. *European Journal of Mechanics - A/Solids*, 102:105104.

Romano, G., Barretta, R., and Diaco, M. (2017). On nonlocal integral models for elastic nano-beams. *International Journal of Mechanical Sciences*, 131-132:490–499.

Romero, I. (2010). Algorithms for coupled problems that preserve symmetries and the laws of thermodynamics: Part i: Monolithic integrators and their application to finite strain thermoelasticity. *Computer Methods in Applied Mechanics and Engineering*, 199(25):1841–1858.

Rudd, R. E. and Broughton, J. Q. (1998). Coarse-grained molecular dynamics and the atomic limit of finite elements. *Phys. Rev. B*, 58:R5893–R5896.

Runge, E. and Gross, E. K. U. (1984). Density-functional theory for time-dependent systems. *Phys. Rev. Lett.*, 52:997–1000.

Rybicki, E. and Kanninen, M. (1977). A finite element calculation of stress intensity factors by a modified crack closure integral. *Engineering Fracture Mechanics*, 9(4):931–938.

s. Saroukhani, Vafadari, R., and Simone, A. (2013). A simplified implementation of a gradient-enhanced damage model with transient length scale effects. *Computer Methods in Applied Mechanics and Engineering*, 51:899–909.

Salnikov, V., Choi, D., and Karamian-Surville, P. (2015). On efficient and reliable stochastic generation of RVEs for analysis of composites within the framework of homogenization. *Computational Mechanics*, 55:127–144.

Sarkar, S., Singh, I., and Mishra, B. (2020). A thermo-mechanical gradient enhanced damage method for fracture. *Computational Mechanics*, 66:1399–1426.

Sarkar, S., Singh, I., Mishra, B., Shedbale, A., and Poh, L. (2019). A comparative study and abaqus implementation of conventional and localizing gradient enhanced damage models. *Finite Elements in Analysis and Design*, 160:1–31.

Schellekens, J. and de Borst, R. (1993). A non-linear finite element approach for the analysis of mode-i free edge delamination in composites. *International Journal of Solids and Structures*, 30(9):1239–1253.

Schenk, O. and Gärtner, K. (2011). *PARDISO*, pages 1458–1464. Springer US, Boston, MA.

Schreiber, C., Müller, R., and Kuhn, C. (2021). Phase field simulation of fatigue crack propagation under complex load situations. *Archive of Applied Mechanics*, 91:563–577.

Seleš, K., Lesičar, T., Tonković, Z., and Sorić, J. (2019). A residual control staggered solution scheme for the phase-field modeling of brittle fracture. *Engineering Fracture Mechanics*, 205:370–386.

Seupel, A., Hütter, G., and Kuna, M. (2018). An efficient fe-implementation of implicit gradient-enhanced damage models to simulate ductile failure. *Engineering Fracture Mechanics*, 199:41–60.

Shutov, A. and Klyuchantsev, V. (2023). Integral-based non-local approach to ductile damage and mixed-mode fracture. *Engineering Fracture Mechanics*, 292:109656.

Silva, J. A. M. (2021). Multi-Scale Analysis of Martensitic Transformation Based on Second-Order Homogenisation.

Simo, J. C. and Hughes, T. J. R. (1998). *Computational Inelasticity*. Springer New York, NY.

Simoes, M. and Martínez-Pañeda, E. (2021). Phase field modelling of fracture and fatigue in shape memory alloys. *Computer Methods in Applied Mechanics and Engineering*, 373:113504.

Simone, A., Wells, G. N., and Sluys, L. J. (2003). From continuous to discontinuous failure in a gradient-enhanced continuum damage model. *Computer Methods in Applied Mechanics and Engineering*, 192(41):4581–4607.

Smit, R., Brekelmans, W., and Meijer, H. (1998). Prediction of the mechanical behavior of nonlinear heterogeneous systems by multi-level finite element modeling. *Computer Methods in Applied Mechanics and Engineering*, 155(1):181–192.

Smith, M. (2009). *ABAQUS/Standard User's Manual, Version 6.9*. Dassault Systèmes Simulia Corp, United States.

Somer, D., de Souza Neto, E., Dettmer, W., and Perić, D. (2009). A sub-stepping scheme for multi-scale analysis of solids. *Computer Methods in Applied Mechanics and Engineering*, 198(9):1006–1016.

Song, C. and Wolf, J. P. (1997). The scaled boundary finite-element method—alias consistent infinitesimal finite-element cell method—for elastodynamics. *Computer Methods in Applied Mechanics and Engineering*, 147(3):329–355.

Soutis, C. and Beaumont, P. W. R. (2005). *Multi-scale modelling of composite material systems: The art of predictive damage modelling*. Woodhead Publishing.

Storvik, E., Both, J. W., Sargado, J. M., Nordbotten, J. M., and Radu, F. A. (2021). An accelerated staggered scheme for variational phase-field models of brittle fracture. *Computer Methods in Applied Mechanics and Engineering*, 381:113822.

Stuart, S. J., Tutein, A. B., Harrison, J. S., and Harrison, J. A. (2000). A reactive potential for hydrocarbons with intermolecular interactions. *Journal of Chemical Physics*, 112(14):6472–6486.

Tadmor, E. B., Miller, R. E., and Elliott, R. S. (2011). *Continuum Mechanics and Thermodynamics: From Fundamental Concepts to Governing Equations*. Cambridge University Press.

Tadmor, E. B., Ortiz, M., and Phillips, R. (1996). Quasicontinuum analysis of defects in solids. *Philosophical Magazine A*, 73(6):1529–1563.

Tan, W. and Martínez-Pañeda, E. (2021). Phase field predictions of microscopic fracture and r-curve behaviour of fibre-reinforced composites. *Composites Science and Technology*, 202:108539.

Tang, B., Xiang, L., Cheng, L., Liu, D., Kou, H., and Li, J. (2018). The formation and evolution of shear bands in plane strain compressed nickel-base superalloy. *Metals*, 8(2).

Tang, Z., Guo, L., Li, Z., Huang, K., Zheng, T., and Sun, R. (2022). A comparative study of void characteristics on the mechanical response of unidirectional composites. *Mechanics of Materials*, 174:104456.

Temizer, I. and Wriggers, P. (2011). An adaptive multiscale resolution strategy for the finite deformation analysis of microheterogeneous structures. *Computer Methods in Applied Mechanics and Engineering*, 200(37):2639–2661. Special Issue on Modeling Error Estimation and Adaptive Modeling.

Tipper, C. F. (1949). The fracture of metals. *Metallurgia*, 39:133–137.

Toupin, R. A. (1964). Theories of elasticity with couple-stress. *Archive for Rational Mechanics and Analysis*, 17:85–112.

Tran, H. T., Bui, T. Q., Chijiwa, N., and Hirose, S. (2023). A new implicit gradient damage model based on energy limiter for brittle fracture: Theory and numerical investigation. *Computer Methods in Applied Mechanics and Engineering*, 413:116123.

Triantafyllidis, N. and Aifantis, E. C. (1986). A gradient approach to localization of deformation. i. hyperelastic materials. *Journal of Elasticity*, 16:225–237.

Truesdell, C. (1984). *Rational Thermodynamics*. New York: Springer-Verlag, 2nd edition.

Turon, A., Dávila, C., Camanho, P., and Costa, J. (2007). An engineering solution for mesh size effects in the simulation of delamination using cohesive zone models. *Engineering Fracture Mechanics*, 74(10):1665–1682.

Tvergaard, V. and Needleman, A. (1984). Analysis of the cup-cone fracture in a round tensile bar. *Acta Metallurgica*, 32(1):157–169.

Vieira, R. (2018). Numerical Micromechanical Analysis on the Influence of Monocrystalline Parameters on the Elastic and Yielding Response of Polycrystalline Aggregates.

Vieira de Carvalho, M., Cardoso Coelho, R. P., and Pires, F. M. A. (2022). On the computational treatment of fully coupled crystal plasticity slip and martensitic transformation constitutive models at finite strains. *International Journal for Numerical Methods in Engineering*, 123(21):5155–5200.

Vila-Chã, J. L., Couto Carneiro, A. M., Ferreira, B. P., and Andrade Pires, F. (2023). A numerical assessment of partitioned implicit methods for thermomechanical problems. *Computers & Structures*, 277-278:106969.

Vila-Chã, J. L., Ferreira, B. P., and Pires, F. A. (2021). An adaptive multi-temperature isokinetic method for the rve generation of particle reinforced heterogeneous materials, part i: Theoretical formulation and computational framework. *Mechanics of Materials*, 163:104069.

Vu-Bac, N., Bessa, M. A., Rabczuk, T., and Liu, W. K. (2015). A multiscale model for the quasi-static thermo-plastic behavior of highly cross-linked glassy polymers. *Macromolecules*, 48.

Walhorn, E., Kölke, A., Hübner, B., and Dinkler, D. (2005). Fluid–structure coupling within a monolithic model involving free surface flows. *Computers & Structures*, 83(25):2100–2111.

Weck, A. and Wilkinson, D. (2008). Experimental investigation of void coalescence in metallic sheets containing laser drilled holes. *Acta Materialia*, 56(8):1774–1784.

Wick, T. (2017). Modified newton methods for solving fully monolithic phase-field quasi-static brittle fracture propagation. *Computer Methods in Applied Mechanics and Engineering*, 325:577–611.

Wolf, D., Yamakov, V., Phillpot, S., Mukherjee, A., and Gleiter, H. (2005). Deformation of nanocrystalline materials by molecular-dynamics simulation: relationship to experiments? *Acta Materialia*, 53(1):1–40.

Wu, J.-Y., Huang, Y., and Nguyen, V. P. (2020). On the bfgs monolithic algorithm for the unified phase field damage theory. *Computer Methods in Applied Mechanics and Engineering*, 360:112704.

Wu, J.-Y., Huang, Y., Zhou, H., and Nguyen, V. P. (2021). Three-dimensional phase-field modeling of mode i + ii/iii failure in solids. *Computer Methods in Applied Mechanics and Engineering*, 373:113537.

Xie, J., Zhang, R., Liu, T., Zhou, C., and Jia, L.-J. (2022). Effect of initial void shape on void growth of structural steels based on micromechanical rve models. *Journal of Materials in Civil Engineering*, 34(4):04022010.

Zervos, A. (2008). Finite elements for elasticity with microstructure and gradient elasticity. *International Journal for Numerical Methods in Engineering*, 73(4):564–595.

Zhang, H. W., Wu, J. K., and Lv, J. (2012). A new multiscale computational method for elasto-plastic analysis of heterogeneous materials. *Computational Mechanics*, 49:149–169.

Zhang, X., Nguyen, H., Paci, J. T., Sankaranarayanan, S. K. R. S., Mendoza-Cortés, J. L., and Espinosa, H. D. (2021). Multi-objective parametrization of interatomic potentials for large deformation pathways and fracture of two-dimensional materials. *npj Computational Materials*, 7.

Zhou, S., Zhuang, X., Zhu, H., and Rabczuk, T. (2018). Phase field modelling of crack propagation, branching and coalescence in rocks. *Theoretical and Applied Fracture Mechanics*, 96:174–192.

Zienkiewicz, O. C., Taylor, R. L., and Fox, D., editors (2014). *The Finite Element Method for Solid and Structural Mechanics*. Butterworth-Heinemann, Oxford, seventh edition edition.